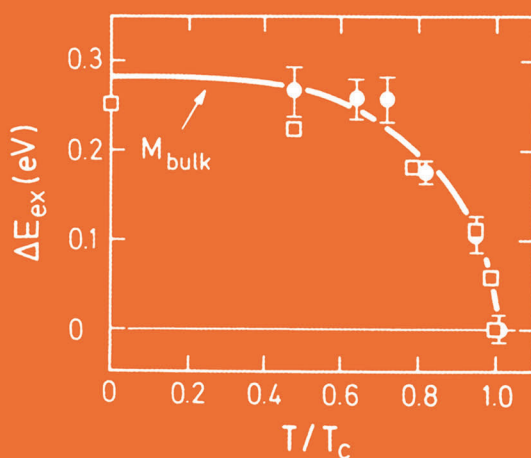


K. Baberschke M. Donath W. Nolting (Eds.)

Band- Ferromagnetism

Ground-State and Finite-
Temperature Phenomena



Springer

Lecture Notes in Physics

Editorial Board

R. Beig, Wien, Austria
J. Ehlers, Potsdam, Germany
U. Frisch, Nice, France
K. Hepp, Zürich, Switzerland
W. Hillebrandt, Garching, Germany
D. Imboden, Zürich, Switzerland
R. L. Jaffe, Cambridge, MA, USA
R. Kippenhahn, Göttingen, Germany
R. Lipowsky, Golm, Germany
H. v. Löhneysen, Karlsruhe, Germany
I. Ojima, Kyoto, Japan
H. A. Weidenmüller, Heidelberg, Germany
J. Wess, München, Germany
J. Zittartz, Köln, Germany

Springer

*Berlin
Heidelberg
New York
Barcelona
Hong Kong
London
Milan
Paris
Singapore
Tokyo*

Physics and Astronomy



<http://www.springer.de/phys/>

Editorial Policy

The series *Lecture Notes in Physics* (LNP), founded in 1969, reports new developments in physics research and teaching -- quickly, informally but with a high quality. Manuscripts to be considered for publication are topical volumes consisting of a limited number of contributions, carefully edited and closely related to each other. Each contribution should contain at least partly original and previously unpublished material, be written in a clear, pedagogical style and aimed at a broader readership, especially graduate students and nonspecialist researchers wishing to familiarize themselves with the topic concerned. For this reason, traditional proceedings cannot be considered for this series though volumes to appear in this series are often based on material presented at conferences, workshops and schools (in exceptional cases the original papers and/or those not included in the printed book may be added on an accompanying CD ROM, together with the abstracts of posters and other material suitable for publication, e.g. large tables, colour pictures, program codes, etc.).

Acceptance

A project can only be accepted tentatively for publication, by both the editorial board and the publisher, following thorough examination of the material submitted. The book proposal sent to the publisher should consist at least of a preliminary table of contents outlining the structure of the book together with abstracts of all contributions to be included.

Final acceptance is issued by the series editor in charge, in consultation with the publisher, only after receiving the complete manuscript. Final acceptance, possibly requiring minor corrections, usually follows the tentative acceptance unless the final manuscript differs significantly from expectations (project outline). In particular, the series editors are entitled to reject individual contributions if they do not meet the high quality standards of this series. The final manuscript must be camera-ready, and should include both an informative introduction and a sufficiently detailed subject index.

Contractual Aspects

Publication in LNP is free of charge. There is no formal contract, no royalties are paid, and no bulk orders are required, although special discounts are offered in this case. The volume editors receive jointly 30 free copies for their personal use and are entitled, as are the contributing authors, to purchase Springer books at a reduced rate. The publisher secures the copyright for each volume. As a rule, no reprints of individual contributions can be supplied.

Manuscript Submission

The manuscript in its final and approved version must be submitted in camera-ready form. The corresponding electronic source files are also required for the production process, in particular the online version. Technical assistance in compiling the final manuscript can be provided by the publisher's production editor(s), especially with regard to the publisher's own LaTeX macro package which has been specially designed for this series.

Online Version/ LNP Homepage

LNP homepage (list of available titles, aims and scope, editorial contacts etc.):

<http://www.springer.de/phys/books/lnpp/>

LNP online (abstracts, full-texts, subscriptions etc.):

<http://link.springer.de/series/lnpp/>

K. Baberschke M. Donath W. Nolting (Eds.)

Band-Ferromagnetism

Ground-State and Finite-Temperature Phenomena



Springer

Editors

Prof. Klaus Baberschke
Freie Universität Berlin
Institut für Experimentalphysik
Arnimallee 14
14195 Berlin, Germany

Prof. Wolfgang Nolting
Humboldt-Universität zu Berlin
Institut für Physik
Invalidenstr. 110
10115 Berlin, Germany

Prof. Markus Donath
Westfälische Wilhelms-Universität
Physikalisches Institut
Wilhelm-Klemm. Str. 10
48149 Münster, Germany

Cover picture: see contribution by M. Donath in this volume

Library of Congress Cataloging-in-Publication Data applied for

Die Deutsche Bibliothek - CIP-Einheitsaufnahme

Band ferromagnetism : ground state and finite temperature phenomena / K. Baberschke ... (ed.). - Berlin ; Heidelberg ; New York ; Barcelona ; Hong Kong ; London ; Milan ; Paris ; Singapore ; Tokyo : Springer, 2001
(Lecture notes in physics ; 580)
(Physics and astronomy online library)
ISBN 3-540-42389-3

ISSN 0075-8450

ISBN 3-540-42389-3 Springer-Verlag Berlin Heidelberg New York

This work is subject to copyright. All rights are reserved, whether the whole or part of the material is concerned, specifically the rights of translation, reprinting, reuse of illustrations, recitation, broadcasting, reproduction on microfilm or in any other way, and storage in data banks. Duplication of this publication or parts thereof is permitted only under the provisions of the German Copyright Law of September 9, 1965, in its current version, and permission for use must always be obtained from Springer-Verlag. Violations are liable for prosecution under the German Copyright Law. Springer-Verlag Berlin Heidelberg New York

a member of BertelsmannSpringer Science+Business Media GmbH <http://www.springer.de>

© Springer-Verlag Berlin Heidelberg 2001

Printed in Germany The use of general descriptive names, registered names, trademarks, etc. in this publication does not imply, even in the absence of a specific statement, that such names are exempt from the relevant protective laws and regulations and therefore free for general use.

Typesetting: Camera-ready by the authors/editor

Camera-data conversion by Steingraeber Satztechnik GmbH Heidelberg

Cover design: *design & production*, Heidelberg

Printed on acid-free paper

SPIN: 10847373 57/3141/du - 5 4 3 2 1 0

Preface

The fascinating phenomenon ferromagnetism is far from being fully understood, although it surely belongs to the oldest problems of solid state physics. For any investigation it appears recommendable to distinguish between materials whose spontaneous magnetization stems from localized electrons of a partially filled atomic shell and those in which it is due to itinerant electrons of a partially filled conduction band. In the latter case one speaks of band-ferromagnetism, prototypes of which are the classical ferromagnets Fe, Co, and Ni. The present book is a status report on the remarkable progress that has recently been made towards a microscopic understanding of band-ferromagnetism as an electron correlation effect.

The authors of the various chapters of this book “Band-Ferromagnetism: Ground-State and Finite-Temperature Phenomena” participated as selected experts in the 242nd WE-Heraeus-Seminar (4-6 October 2000) held under almost the same title in Wandlitz near Berlin (Germany). It was the second seminar of this type in Wandlitz. (The first in 1998 dealt with the complementary topic of the physics of local-moment ferromagnets such as Gd). Twenty-six invited speakers from ten different countries together with fifty-five further participants, who presented contributions in form of posters, spent three days together discussing in an enthusiastic and fertile manner the hot topics of band-ferromagnetism.

Generous financial support by the Wilhelm und Else Heraeus-Stiftung, by the Sonderforschungsbereich 290 (Metallische dünne Filme: Struktur, Magnetismus und elektronische Eigenschaften) of the Deutsche Forschungsgemeinschaft, and also by the Wohnungsbaugenossenschaft Hellersdorfer Kiez e. G. made it possible to bring together experimentalists and theoreticians working in different areas and with different techniques in the field of band-ferromagnetism. The idea was to document the present state of affairs, to learn from each other, and to pinpoint important areas for future research. The support of the sponsors is gratefully acknowledged.

Many colleagues have helped to organize the workshop and to prepare the manuscript of the accompanying book. We wish to thank the members of the Lehrstuhl Festkörpertheorie at the Humboldt-Universität zu Berlin for doing an excellent and active job. Special thanks are due to Priv.-Doz. Dr. Michael Potthoff who really worked hard in composing the various contributions to this book. The collaboration with the Springer-Verlag was always effective and delightful.

Berlin, Münster
April 2001

*K. Baberschke
M. Donath
W. Nolting*

Contents

Introduction

<i>K. Baberschke, M. Donath, W. Nolting</i>	1
---	---

Part I Ground-State Properties

On the Way to a Gutzwiller Density Functional Theory

<i>W. Weber, J. Bünenmann, F. Gebhard</i>	9
---	---

Anisotropy in Magnetism

<i>K. Baberschke</i>	27
----------------------------	----

Anisotropic Magnetic Ground-State Moments

Probed by Soft X-Ray Spectroscopy

<i>H.A. Dürr</i>	46
------------------------	----

First Principles Determination of Magnetic Anisotropy and Magnetostriction in Transition Metal Alloys

<i>R. Wu</i>	60
--------------------	----

Part II Finite-Temperature Electronic Structure

Magnetism of Correlated Systems: Beyond LDA

<i>A.I. Lichtenstein, M.I. Katsnelson</i>	75
---	----

Probing the Electronic States of Band Ferromagnets with Photoemission

<i>T. Greber</i>	94
------------------------	----

Temperature Dependence

of Spin- and Angle-Resolved Photoemission of Ni

<i>A. Kakizaki</i>	111
--------------------------	-----

Spin Fluctuations in Itinerant Electron Systems

<i>P. Mohn, S. Khmelevskyi</i>	126
--------------------------------------	-----

VIII Contents

Itinerant Electron Magnets: Curie Temperature and Susceptibility in Density-Functional Theory	
<i>J. Kübler</i>	143

Band Magnetism near a Quantum Critical Point	
<i>S.G. Mishra</i>	158

Non-equilibrium Physics of Magnetic Solids: Time Dependent Changes of Magnetism	
<i>K.H. Bennemann</i>	173

Part III Models of Band-Ferromagnetism

Metallic Ferromagnetism – An Electronic Correlation Phenomenon	
<i>D. Vollhardt, N. Blümer, K. Held, M. Kollar</i>	191

Ferromagnetism in the Hubbard Model	
<i>W. Nolting, M. Potthoff, T. Herrmann, T. Wegner</i>	208

Orbital Order Versus Orbital Liquid in Doped Manganites	
<i>A.M. Oleś, L.F. Feiner</i>	226

Part IV Low-Dimensional Systems

First Principles Theory of Magnetism for Materials with Reduced Dimensionality	
<i>O. Eriksson</i>	243

Surface Electronic Structure of Band Ferromagnets	
<i>M. Donath</i>	267

Phase Transitions in Coupled Two-Dimensional Ferromagnetic Layers	
<i>P. Poulopoulos, K. Baberschke</i>	283

Theory of Spin Excitations and the Microwave Response of Cylindrical Ferromagnetic Nanowires	
<i>D. Mills</i>	297

Transmission of Electron Beams Through Thin Magnetic Films	
<i>W. Weber, S. Riesen, H.C. Siegmann</i>	320

Part V Understanding Spectroscopies

**New Developments in UPS and XPS
from Ferromagnetic Materials***J. Braun* 341**Theory of Electron Spectroscopies***M. Potthoff* 356**Magnetic Dichroism in Electron Spectroscopy***H. Ebert, J. Minár, V. Popescu* 371**Neutrons as a Probe of the Magnetic Moment Stability
in Itinerant Electron Ferromagnets***K.-U. Neumann, K.R.A. Ziebeck* 386

Introduction

K. Baberschke, M. Donath, and W. Nolting

Ferromagnetism and in particular the so-called band-ferromagnetism belongs to the oldest phenomena discussed in solid state physics, but on the other hand continues to be a very hot topic of modern research. The only explanation for this fact is that up to now this very complicated and very fascinating phenomenon is not yet fully understood. The main shortcoming for our understanding of ferromagnetism is the lack of a unified theory which would be able to describe the rich variety of magnetic features within one and the same theoretical framework. The full microscopic explanation of ferromagnetism as a consequence of strong electron correlations is still absent, in spite of some obvious progress just in the recent past, and remains therewith a challenging task for experimentalists as well as theoreticians. Fundamental precondition for collective magnetic ordering is of course the existence of permanent magnetic moments. However, it makes already a big difference whether these moments are localized or itinerant. The investigations presented in this book aim exclusively at the situation of itinerant ferromagnetism as realized by the classical prototypes Fe, Co, and Ni. It is commonly accepted that itinerant ferromagnetism results from an interplay between the Pauli principle, the spin-independent normal Coulomb interaction, the kinetic energy, and the lattice structure. Consequently it belongs to the most fundamental phenomena in condensed matter physics. Understanding ferromagnetism means to understand the spontaneous spin-dependent splitting of the density of states of a narrow, partially filled energy band below a critical temperature, the Curie temperature T_c . With electrons occupying band states up to the spin-independent Fermi edge, a spin asymmetry is realized and therewith a resulting spontaneous finite magnetization.

In the past there have been two different strategies to come to a better insight into ferromagnetism. The first refers to single-electron bandstructure calculations in the framework of Density Functional Theory (DFT). In principle DFT is an exact ground state theory, which, however cannot be treated rigorously. The achievements and merits of the respective Local Density Approximation (LDA) as a ground state approach to the physics of real materials are very well-known. LDA-DFT has the great advantage of being an *ab initio* procedure which does not need any adjustable parameter. The electronic structure of many real materials could be calculated with astonishing accuracy. However, it is also undoubtedly clear, that LDA seems to underestimate electron correlation effects delivering therefore in cases of highly correlated systems very often a non-satisfactory description of experimental (photoemission) data. This holds in particular for ferromagnetic systems, even for the pure *3d* ferromagnets. Let us mention as an example for the failure of LDA the fundamental

$T = 0$ -exchange splitting, which comes out at least twice bigger than in the experiment. Another example is the intensively discussed 6eV satellite, observed in Ni but not in Fe, and by no means reproducible by an LDA treatment. The LDA, when applied to paramagnetic Ni, e. g. , obviously denies the existence of local moments (or short-range magnetic order) in the paramagnetic phase, in contradiction to experiments (susceptibility) performed for temperatures above the Curie point. The general shortcoming of LDA is its restriction to $T = 0$. A key quantity of ferromagnetism as the Curie temperature is therefore out of reach. The finite-temperature extension DFT, being in principle available, has not yet led to acceptable results.

The other strategy uses model Hamiltonians which are approximately evaluated by many-body techniques. The advantage is that in principle there does not exist any restriction with respect to temperature, carrier concentration, lattice structure, Coulomb coupling and screening, external magnetic field and so on, and the full thermodynamics of the ferromagnet is accessible. Furthermore, analytical investigations can lead more directly to an understanding of the microscopic mechanisms responsible for the spontaneous magnetic order. On the other hand, a theoretical model cannot represent more than a caricature of reality, stressing the supposedly important things and neglecting all the details which are not directly related to the phenomenon. Strictly speaking, however, the neglected details imply that, from the very beginning, a quantitative comparison to experimental data will be excluded. Only qualitative tendencies can be conveyed by such model studies. Further disadvantages are the uncertainty in the choice of the model parameters, which, because of the inherent model simplifications, cannot be brought into contact unambiguously with *ab initio* calculated matrix elements, and, very often, a certain degree of uncontrollability in the approximative treatment of the normally not exactly solvable many-body problem.

The mentioned two strategies are more or less complementary tools for theoretically tackling the magnetism problem. Highly promising are therefore recent attempts to combine the methods in order to exploit their advantages and simultaneously to eliminate to a great part their shortcomings. First results for temperature-dependent quasiparticle structures with reasonable inclusion of correlation effects are available which allow to understand magnetic phenomena as being caused by the electronic structure, only, i. e. without referring to effective spin models.

From a more phenomenological point of view a similar idea is realized by the combination of spin-fluctuation theories with LDA bandstructure calculations. Spin fluctuation theories are based on a Landau expansion of the free energy of the ferromagnetic solid up to fourth order in the magnetization, the local statistical fluctuations of which are explicitly taken into account. A weighty criterion for such finite-temperature theories of ferromagnetism is their ability to reproduce the experimental Curie temperature.

Supreme judge of each theory is the experiment. To learn from the experiment and to test a theory by the experiment, however, meets the requirement to

understand what is really measured. Which kind of information is transmitted by which spectroscopy? Do the data refer to ground state or to excited state properties of the solid? Which input-parameter for the theory can directly be taken from the experiment to understand the magnetism of real substances on an atomistic microscopic level?

The book in hand tries to define what is our today's understanding of ferromagnetism by gathering and interpreting most recent experimental as well as theoretical investigations. It is not at all intended to formulate something like a provisional solution of the very complicated problem, but rather to illustrate the progress made so far and to list up and to classify open questions. Five main groups of problems with respect to ferromagnetism are selected and commented on:

Ground State Properties

Enormous progress in the understanding of magnetism has been brought in by ab initio bandstructure calculations. Starting from Density Functional Theory (DFT) as an exact ground state theory various approaches to the not exactly known exchange-correlation potential have proved to yield excellent descriptions of ground state properties of bandferromagnets. Strictly speaking DFT and therewith all the approximative DFT-related versions (local (spin) density approximations (L(S)DA)) are restricted to total energy calculations. The Kohn-Sham eigenenergies are, in principle, only auxiliary quantities (Lagrange multipliers) for the total energy calculation. Nevertheless they are also used to represent bandstructures and different spectral properties, and that in many cases with astonishing success. The above-mentioned shortcomings, which become evident, when DFT- LDA is applied to strong correlation effects as the metal-insulator transition in transition metal monoxides, the high- T_c superconductor physics or heavy-fermion properties, have been attacked by introducing modifications known in literature as LDA+U, GW approach, selfinteraction correction (SIC), generalized gradient approximation (GGA), Within limits these modifications are able to remove some of the shortcomings, although in some cases at cost of corrupting a little bit the idea of first principles calculations.

Very promising attempts to incorporate correlation effects adequately into the calculation of ground state properties of the ferromagnet are based on combinations of multiband-Gutzwiller variational approaches with the DFT-LSDA concept. Clear improvements for effective masses, bandwidths and above all exchange splittings become possible.

The above-cited advances in ab initio theories together with the enormous increase in computational capacities allow today full relativistic calculations of the total energy and its magnetic anisotropy contributions. The magnetic anisotropy is measured as the dependence of the ground state energy on the direction of the magnetization. There are two sources for magnetic anisotropy, the dipole-dipole interaction between magnetic moments and an electronic contribution due to spin-orbital coupling in the sample (orbital moment magnetism). In bulk

3d transition metals the spin-orbital coupling plays a minor role, while becoming important in films and nanostructures where orbital moments are not fully quenched. It has become possible to calculate and to measure the projection of the spin and the orbital momentum on the total angular momentum to fix the spin and the orbital contribution to the magnetic moment. This gives new insight in fundamental magnetic anisotropy effects. A detailed discussion is given in the book.

The most fundamental ground-state feature of the bandferromagnet is the exchange splitting, in particular that of the states near the Fermi edge. It remains furtheron a challenging task, even for refined LSDA calculation, to determine the correct wavevector- and energy- dependent value. There are possibly other correlation-caused splittings which must not be misinterpreted as exchange splitting.

Finite Temperature Electronic Structure

Characteristic for a ferromagnetic material is a temperature-dependent electronic structure. Of central importance is again the exchange splitting and its behaviour when the temperature goes up towards the Curie temperature. Is the increasing demagnetization due to a collapsing behaviour of the exchange splitting, i. e. to an increasing overlap of spin bands as it is observed for Ni by spinpolarized (inverse) photoemission, or is the spin asymmetry continuously removed simply by a redistribution of spectral weight? A persisting splitting above T_c is sometimes claimed for Fe.

The old Stoner picture of collapsing spin bands with vanishing local magnetic moments above T_c is known to be incorrect. An entirely unsatisfactory result following from this picture concerns the derived values for the transition temperature. Another contradiction to experimental facts is the Pauli-like susceptibility in the paramagnetic phase with no indication of a Curie-Weiß law behaviour. Collective excitations as spin waves do not fit the model picture. Short range order above T_c as observed in neutron scattering experiments is not explainable.

The other extreme is that of stable localized moments, as in the Heisenberg model, with an orientation disorder above T_c . This picture is also unacceptable, because it neglects the itinerant nature of the magnetic electrons in bandferromagnets being therefore not able to generate the non-integer magneton number of a typical bandferromagnet. Nevertheless, it is an interesting question why strong itinerant ferromagnets indeed resemble Heisenberg-ferromagnets (ferromagnetic insulators) at least as far as low-energy properties are considered. Spin waves do exist and are responsible for the suppression of long-range magnetic order at the Curie temperature. A theory for magnons in the band-picture is necessary. The same theory should explain the rather large magnetic moments even in the paramagnetic phase. Furthermore, the Curie temperature as the key-quantity of the bandferromagnet should be selfconsistently calculable without any fit to experimental data. Respective proposals are presented in the book.

Models of Band-Ferromagnetism

Some of the questions addressed above are to be investigated in the frame of simplifying model concepts in order to work out as clearly as possible the basic mechanisms responsible for the spontaneous long-range moment order. The simplest and most frequently applied model is the single-band Hubbard model. In spite of the fact that it was invented to gain insight into the origin of itinerant ferromagnetism, it was not clear up to very recently whether or not the model can really reproduce a ferromagnetic phase over an extended region of the model variables (coupling strength, band occupation). Sophisticated new approaches to the non-trivial many-body problem of the Hubbard Hamiltonian permit the conclusion that the essentials of ferromagnetism can indeed be studied within the framework of this model. The Dynamical Mean-Field Theory (DMFT) has proved to be an effective method for the investigation of correlated electron systems with strong local interactions. It maps the correlated electron problem on an effective single-impurity Anderson model. The latter is very much simpler and can even rigorously be solved by numerically exact methods. The mapping is exact for infinite lattice dimensions and is believed to represent a trustworthy approach for two- or three-dimensional systems, too. Non-perturbative, analytical theories different from DMFT can then be tested by the infinite-dimension results of the DMFT. Such analytical approximations are sometimes more helpful for an microscopic interpretation of magnetic phenomena. Systematically refined schemes can lead to a classification of the decisive factors, which may influence the stability of ferromagnetism (shape of the Bloch density of states, spin-dependent band shifts, correlated electron hopping, quasiparticle damping, Fermi liquid behaviour, ...).

While the simple single-band Hubbard model has to be accepted as a reasonable basis for an at least qualitative understanding of band-ferromagnetism, it is nevertheless rather far away from the situation of real magnetic materials. It is therefore absolutely necessary to investigate how the stability of band-ferromagnetism is influenced by orbital degeneracy and Hund's rule coupling. How important is it to incorporate into the model study uncorrelated s and p bands which hybridize to a certain degree with the correlated d bands? Questions like these are urgent topics, which are tackled by some contributions to this book.

Dimension-Reduced Systems

The magnetism of films, multilayers, surfaces, interfaces, clusters, nanostructures, ... has provoked intensive research activities in the recent past. One reason is certainly the technological potential. However, there are also more fundamental reasons to study dimension-reduced magnetic systems, since they introduce special degrees of freedom (lattice constant, structure, anisotropy, broken translational symmetry, film thickness, cluster size, ...), which may help to develop new ideas with respect to the microscopic conditions of ferromagnetism.

The investigation of layer-dependent, finite temperature electronic excitation spectra and the therefrom resulting magnetic properties of thin films are important experimental as well as theoretical research problems. The thickness-dependence of the Curie temperature of thin Ni and Fe films is a prominent example. One should bear in mind that in bulk band-ferromagnetism only very few fixed Curie temperatures (Fe, Co, Ni) are really known. In this respect, thin film and nanostructure experiments have opened a completely new field by permitting to manipulate T_c to almost any arbitrary value. A further and special challenge is given by the critical behaviour of thin films, with a possible dimensional cross-over as function of increasing thickness. What is the influence of the anisotropy, e. g. in view of reorientation transitions of the magnetization in thin Ni and Fe films? Following the Mermin-Wagner theorem anisotropy is absolutely necessary to allow collective magnetic order at finite temperatures for films of arbitrary, but finite thickness. The phase transition in magnetic multilayers, where two ferromagnetic films interact through a non-ferromagnetic spacer, is far from being fully understood.

What can be said about magnetic stability at surfaces? Is it possible to have a magnetic depth profile, e. g. a ferromagnetic surface for temperatures, for which the bulk is already paramagnetic? Further interesting questions aim at the spin-dependent electronic states of dimension-reduced systems: surface states, interface states, quantum-well states, their origin, their temperature behaviour and their impact on the magnetic behaviour.

Understanding of Spectroscopies

All the above-listed physical problems and questions require for satisfactory solutions the complementary interplay of theory and experiment. Decisive precondition for a successful interplay of theory and experiment, however, is an unambiguous understanding of the applied spectroscopies. This holds of course in general, but in particular for magnetic phenomena. For the explanation of band-ferromagnetism one needs exclusively information about the electronic structure of the respective material. In order to understand the basic physics, experimental data have to be compared with theoretically derived or modelled electron correlations and quasiparticle effects as well as calculated dependencies on temperature, carrier concentration and structure. It is a non-trivial question, which information can reliably be drawn from direct and inverse photoemission data, from Auger-electron and appearance-potential spectroscopy, from the magnetic circular dichroism, from neutron scattering, How directly are the terms of many-body evaluations (correlation functions, spectral densities, quasiparticle bandstructures, electronic and magnonic selfenergies, quasiparticle lifetimes, ...) manifested in experimental spectroscopies? Last but not least, the influence of apparatus functions must distinctly be known to get physically correct statements. Some important contributions to this book are therefore focussed on the interpretation and classification of spectroscopies which are widely used to investigate magnetic materials.

On the Way to a Gutzwiller Density Functional Theory

Werner Weber¹, Jörg Bünemann², and Florian Gebhard²

¹ Institut für Physik, Universität Dortmund, D-44221 Dortmund, Germany

² Fachbereich Physik, Philipps-Universität Marburg, D-35032 Marburg, Germany

Abstract. Multi-band Gutzwiller-correlated wave functions reconcile the contrasting concepts of itinerant band electrons versus electrons localized in partially filled atomic shells. The exact evaluation of these variational ground states in the limit of large coordination number allows the identification of quasi-particle band structures, and the calculation of a variational spinwave dispersion. The study of a generic two-band model elucidates the co-operation of the Coulomb repulsion and the Hund’s-rule exchange for itinerant ferromagnetism. We present results of calculations for ferromagnetic nickel, using a realistic 18 spin-orbital basis of $4s$, $4p$ and $3d$ valence electrons. The quasi-particle energy bands agree much better with the photo-emission and Fermi surface data than the band structure obtained from spin-density functional theory (SDFT).

1 Exchange Versus Correlations

More than 50 years ago two basically different scenarios had emerged from early quantum-mechanical considerations on electrons in metals with partly filled d bands.

Scenario I: As proposed by Slater [1] and Stoner [2], band theory alone was argued to account for itinerant ferromagnetism. Due to the Pauli principle, electrons with parallel spins cannot come arbitrarily close to each other (“Pauli” or “exchange hole”), and, thus, a ferromagnetic alignment of the electron spins reduces the total Coulomb energy with respect to the paramagnetic situation (“exchange field energy”).

Scenario II: As emphasized by van Vleck [3], electronic correlations are important in narrow-band materials. Due to the strong electron-electron interaction, charge fluctuations in the atomic d shells are strongly suppressed (“minimum polarity model”). The atomic magnetic moments arise due to the local Coulomb interactions (in particular, Hund’s-rule couplings) and the electrons’ motion through the crystal may eventually align them at low enough temperatures.

In principle, such a dispute can be resolved in natural sciences. The corresponding theories have to be worked out in detail, and their results and predictions have to be compared to experiments.

This was indeed done for scenario I [4,5]. The (spin-)density functional theory is a refined band theory which describes some iron group metals with considerable success. Unfortunately, progress for scenario II was much slower. It calls

for a theory of correlated electrons, i.e., a genuine many-body problem has to be solved. It was only recently that reliable theoretical tools became available which allow to elucidate scenario II in more detail [6,7,8,9,10,11].

A first step in this direction was the formulation of appropriate model Hamiltonians which allowed to discuss matters concisely, e.g., the Hubbard model [12,13,14,15]. This model covers both aspects of d electrons on a lattice: they can move through the crystal, and they strongly interact when they sit on the same lattice site. The model is discussed in more detail in Sec. 2.

Even nowadays, it is impossible to calculate exact ground-state properties of such a model in three dimensions. In 1963/1964 Gutzwiller introduced a trial state to examine variationally the possibility of ferromagnetism in such a model [12,13]. His wave function covers both limits of weak and strong correlations and should, therefore, be suitable to provide qualitative insights into the magnetic phase diagram of the Hubbard model. Gutzwiller-correlated wave functions for multi-band Hubbard models are defined and analyzed in Sec. 3.

The evaluation of multi-band Gutzwiller wave functions itself poses a most difficult many-body problem. Perturbative treatments [16,17] are constrained to small to moderate interaction strengths. The region of strong correlations could only be addressed within the so-called “Gutzwiller approximation” [12,13,18] and its various extensions [19,20]. Some ten years ago, the Gutzwiller approximation was found to become exact for the one-band Gutzwiller wave function in the limit of infinite spatial dimensions, $d \rightarrow \infty$ [21,22,23], and Gebhard [24] developed a compact formalism which allows the straightforward calculation of the variational ground-state energy in infinite dimensions. Recently, Gebhard’s approach was generalized by us to the case of multi-band Gutzwiller wave functions [10]. Thereby, earlier results by Bünemann and Weber [25], based on a generic extension of the Gutzwiller approximation [26], were found to become exact in infinite dimensions [27].

As shown in Sect. 4 for a two-band toy model, the Gutzwiller variational scheme approach also allows the calculation of spinwave spectra [28]. In this way, the dispersion relation of the fundamental low-energy excitations can be derived consistently. Albeit the description is based on itinerant electrons, the results for strong ferromagnets resemble those of a Heisenberg model for localized spins whereby a unified description of localized and itinerant aspects of electrons in transition metals is achieved.

In Sect. 5 we discuss results from a full-scale calculation for nickel. The additional local correlations introduced in the Gutzwiller scheme lead to a much better description of the quasi-particle properties of nickel than in previous calculations based on spin-density functional theory.

2 Hamilton Operator

Our multi-band Hubbard model [14] is defined by the Hamiltonian

$$\hat{H} = \sum_{i,j;\sigma,\sigma'} t_{i,j}^{\sigma,\sigma'} \hat{c}_{i;\sigma}^+ \hat{c}_{j;\sigma'} + \sum_i \hat{H}_{i;\text{at}} \equiv \hat{H}_1 + \hat{H}_{\text{at}}. \quad (1)$$

Here, $\hat{c}_{i;\sigma}^+$ creates an electron with combined spin-orbit index $\sigma = 1, \dots, 2N$ ($N = 5$ for $3d$ electrons) at the lattice site i of a solid.

The most general case is treated in Ref. [10]. In this work we assume for simplicity that different types of orbitals belong to different representations of the point group of the respective atomic state (e.g., s , p , $d(e_g)$, $d(t_{2g})$). In this case, different types of orbitals do not mix locally, and, thus, the local crystal field is of the form $t_{i,i}^{\sigma,\sigma'} = \epsilon_\sigma \delta_{\sigma,\sigma'}$. Consequently, we may later work with normalized single-particle product states $|\Phi_0\rangle$ which respect the symmetry of the lattice, i.e.,

$$\langle \Phi_0 | \hat{c}_{i;\sigma}^+ \hat{c}_{i;\sigma'} | \Phi_0 \rangle = \delta_{\sigma,\sigma'} n_{i;\sigma}^0. \quad (2)$$

We further assume that the local interaction is site-independent

$$\hat{H}_{i;\text{at}} = \sum_{\sigma_1, \sigma_2, \sigma_3, \sigma_4} \mathcal{U}^{\sigma_1, \sigma_2, \sigma_3, \sigma_4} \hat{c}_{i;\sigma_1}^+ \hat{c}_{i;\sigma_2}^+ \hat{c}_{i;\sigma_3} \hat{c}_{i;\sigma_4}. \quad (3)$$

This term represents all possible local Coulomb interactions.

As our basis for the atomic problem we choose the configuration states

$$|I\rangle = |\sigma_1, \sigma_2, \dots\rangle = \hat{c}_{i;\sigma_1}^+ \hat{c}_{i;\sigma_2}^+ \dots |\text{vacuum}\rangle \quad (\sigma_1 < \sigma_2 < \dots), \quad (4)$$

which are the ‘‘Slater determinants’’ in atomic physics. The diagonalization of the Hamiltonian $\hat{H}_{i;\text{at}}$ is a standard exercise [29]. The eigenstates $|I\rangle$ obey

$$|I\rangle = \sum_I T_{I,I'} |I'\rangle, \quad (5)$$

where $T_{I,I'}$ are the elements of the unitary matrix which diagonalizes the atomic Hamiltonian matrix with entries $\langle I | \hat{H}_{i;\text{at}} | I' \rangle$. Then,

$$\hat{H}_{i;\text{at}} = \sum_I E_I \hat{m}_I, \quad \hat{m}_I = |I\rangle \langle I|. \quad (6)$$

The atomic properties, i.e., eigenenergies E_I , eigenstates $|I\rangle$, and matrix elements $T_{I,I'}$, are essential ingredients of our solid-state theory.

3 Multi-band Gutzwiller Wave Functions

3.1 Variational Ground-State Energy

Gutzwiller-correlated wave functions are written as a many-particle correlator \hat{P}_G acting on a normalized single-particle product state $|\Phi_0\rangle$,

$$|\Psi_G\rangle = \hat{P}_G |\Phi_0\rangle. \quad (7)$$

The single-particle wave function $|\Phi_0\rangle$ which obeys (2) contains many configurations which are energetically unfavorable with respect to the atomic interactions. Hence, the correlator \hat{P}_G is chosen to suppress the weight of these configurations

to minimize the total ground-state energy of (1). In the limit of strong correlations the Gutzwiller correlator \hat{P}_G should project onto atomic eigenstates. Therefore, the proper multi-band Gutzwiller wave function with atomic correlations reads

$$\begin{aligned}\hat{P}_G &= \prod_i \hat{P}_{i;G} , \\ \hat{P}_{i;G} &= \prod_{\Gamma} \lambda_{i;\Gamma}^{\hat{m}_{i;\Gamma}} = \prod_{\Gamma} [1 + (\lambda_{i;\Gamma} - 1) \hat{m}_{i;\Gamma}] = 1 + \sum_{\Gamma} (\lambda_{i;\Gamma} - 1) \hat{m}_{i;\Gamma} .\end{aligned}\quad (8)$$

The 2^{2N} variational parameters $\lambda_{i;\Gamma}$ per site are real, positive numbers. For $\lambda_{i;\Gamma_0} \neq 0$ and all other $\lambda_{i;\Gamma} = 0$ all atomic configurations at site i but $|I_0\rangle$ are removed from $|\Phi_0\rangle$. Therefore, by construction, $|\Psi_G\rangle$ covers both limits of weak and strong coupling. In this way it incorporates both itinerant and local aspects of correlated electrons in narrow-band systems.

The class of Gutzwiller-correlated wave functions as specified in (8) was evaluated exactly in the limit of infinite dimensions in Ref. [10]. The expectation value of the Hamiltonian (1) reads [30]

$$\begin{aligned}\langle \hat{H} \rangle &= \frac{\langle \Psi_G | \hat{H} | \Psi_G \rangle}{\langle \Psi_G | \Psi_G \rangle} \\ &= \sum_{i \neq j; \sigma, \sigma'} t_{i,j}^{\sigma, \sigma'} \sqrt{q_{i;\sigma}} \sqrt{q_{j;\sigma'}} \langle \Phi_0 | \hat{c}_{i;\sigma}^+ \hat{c}_{j;\sigma'} | \Phi_0 \rangle + \sum_{i;\sigma} \epsilon_{\sigma} n_{i;\sigma}^0 + \sum_{i;\Gamma} E_{\Gamma} m_{i;\Gamma} .\end{aligned}\quad (9)$$

Here, $n_{i;\sigma}^0 = \langle \Phi_0 | \hat{n}_{i;\sigma} | \Phi_0 \rangle$ is the local particle density in $|\Phi_0\rangle$. The local q factors are given by [10]

$$\begin{aligned}\sqrt{q_{\sigma}} &= \sqrt{\frac{1}{n_{\sigma}^0(1 - n_{\sigma}^0)}} \sum_{\Gamma, \Gamma'} \sqrt{\frac{m_{\Gamma} m_{\Gamma'}}{m_{\Gamma}^0 m_{\Gamma'}^0}} \sum_{I, I' (\sigma \notin I, I')} f_{\sigma}^I f_{\sigma}^{I'} \sqrt{m_{(I' \cup \sigma)}^0 m_{I'}^0} \\ &\quad \times T_{\Gamma, (I \cup \sigma)}^+ T_{(I' \cup \sigma), \Gamma} T_{\Gamma', I}^+ T_{I, \Gamma'} ,\end{aligned}\quad (10)$$

where $m_{i;I}^0$ ($m_{i;\Gamma}^0$) is the probability to find the configuration $|I\rangle$ (the atomic eigenstate $|\Gamma\rangle$) on site i in the single-particle product state $|\Phi_0\rangle$. The fermionic sign function $f_{\sigma}^I \equiv \langle I \cup \sigma | \hat{c}_{\sigma}^+ | I \rangle$ gives a minus (plus) sign if it takes an odd (even) number of anticommutations to shift the operator \hat{c}_{σ}^+ to its proper place in the sequence of electron creation operators in $|I \cup \sigma\rangle$.

Eqs. (9) and (10) show that we may replace the original variational parameters $\lambda_{i;\Gamma}$ by their physical counterparts, the atomic occupancies $m_{i;\Gamma}$. They are related by the simple equation [10]

$$m_{i;\Gamma} = \lambda_{i;\Gamma}^2 m_{i;\Gamma}^0 .\quad (11)$$

The probability for an empty site ($|I| = 0$) is obtained from the completeness condition,

$$m_{i;\emptyset} = 1 - \sum_{\Gamma (|\Gamma| \geq 1)} m_{i;\Gamma} .\quad (12)$$

The probabilities for a singly occupied site ($|I| = 1$) are given by [30]

$$m_{i;\sigma} = n_{i;\sigma}^0 - \sum_{I (|I| \geq 2) (\sigma \in I)} m_{i;I} , \quad (13a)$$

$$m_{i;I} = \sum_K \left| \sum_{\Gamma} \sqrt{\frac{m_{i;\Gamma}}{m_{i;\Gamma}^0}} T_{\Gamma,I}^+ T_{K,\Gamma} \right|^2 m_{i;K}^0 . \quad (13b)$$

The parameters $m_{i;\emptyset}$ and $m_{i;\sigma}$ must not be varied independently. All quantities in (9) are now expressed in terms of the atomic multi-particle occupancies $m_{i;\Gamma}$ ($|\Gamma| \geq 2$), the local densities $n_{i;\sigma}^0$, and further variational parameters in $|\Phi_0\rangle$.

It is seen that the variational ground-state energy can be cast into the form of the expectation value of an effective single-particle Hamiltonian with renormalized electron transfer amplitudes $\tilde{t}_{i,j}^{\sigma,\sigma'}$,

$$\begin{aligned} \hat{H}_{\text{eff}} &= \sum_{i \neq j; \sigma, \sigma'} \tilde{t}_{i,j}^{\sigma,\sigma'} \hat{c}_{i;\sigma}^+ \hat{c}_{j;\sigma'} + \sum_{i;\sigma} \epsilon_{\sigma} \hat{n}_{i;\sigma} + \sum_{i;\Gamma} E_{\Gamma} m_{i;\Gamma} , \\ \tilde{t}_{i,j}^{\sigma,\sigma'} &= \sqrt{q_{i;\sigma}} \sqrt{q_{j;\sigma'}} t_{i,j}^{\sigma,\sigma'} . \end{aligned} \quad (14)$$

Therefore, $|\Phi_0\rangle$ is the ground state of \hat{H}_{eff} whose parameters have to be determined self-consistently from the minimization of $\langle \Phi_0 | \hat{H}_{\text{eff}} | \Phi_0 \rangle$ with respect to $m_{i;\Gamma}$ and $n_{i;\sigma}^0$. For the optimum set of parameters, $\hat{H}_{\text{eff}}^{\text{opt}}$ defines a band structure for *correlated* electrons. Similar to density-functional theory, this interpretation of our ground-state results opens the way to detailed comparisons with experimental results; see Sect. 5.3.

3.2 Spinwaves

The variational principle can also be used to calculate excited states [31]. If $|\Phi\rangle$ is the ferromagnetic, exact ground state with energy E_0 , the trial states

$$|\Psi(q)\rangle = \hat{S}_q^- |\Phi\rangle \quad (15)$$

are necessarily orthogonal to $|\Phi\rangle$, and provide an exact upper bound to the first excited state with momentum q and energy $\epsilon(q)$

$$\epsilon(q) \leq E_s(q) \equiv \frac{\langle \Psi(q) | \hat{H} | \Psi(q) \rangle}{\langle \Psi(q) | \Psi(q) \rangle} - E_0 . \quad (16)$$

Here, $\hat{S}_q^- = (\hat{S}_q^+)^+ = \sum_{l,b} \exp(-iq l) \hat{c}_{l,b,\downarrow}^+ \hat{c}_{l,b,\uparrow}$ flips a spin from up to down in the system whereby it changes the total momentum of the system by q . In this way, the famous Bijl-Feynman formula for the phonon-roton dispersion in superfluid Helium was derived [32]. In the case of ferromagnetism the excitation energies $E_s(q)$ can be identified with the spinwave dispersion if a well-defined spinwave exists at all [28]. Experimentally this criterion is fulfilled for small momenta q and energies $E_s(q)$.

Unfortunately, we do not know the exact ground state or its energy in general. However, we may hope that the Gutzwiller wave function $|\Psi_G\rangle$ is a good approximation to the true ground state. Then, the states

$$|\Psi_G(q)\rangle = \hat{S}_q^- |\Psi_G\rangle \quad (17)$$

will provide a reliable estimate for $E_s(q)$,

$$E_s(q) \approx E_s^{\text{var}}(q) = \frac{\langle \Psi_G | \hat{S}_q^+ \hat{H} \hat{S}_q^- | \Psi_G \rangle}{\langle \Psi_G | \hat{S}_q^+ \hat{S}_q^- | \Psi_G \rangle} - \frac{\langle \Psi_G | \hat{H} | \Psi_G \rangle}{\langle \Psi_G | \Psi_G \rangle}. \quad (18)$$

Naturally, $E_s^{\text{var}}(q)$ does not obey any strict upper-bound principles.

The actual calculation of the variational spinwave dispersion is rather involved. However, explicit formulae are available [28] which can directly be applied once the variational parameters have been determined from the minimization of the variational ground-state energy.

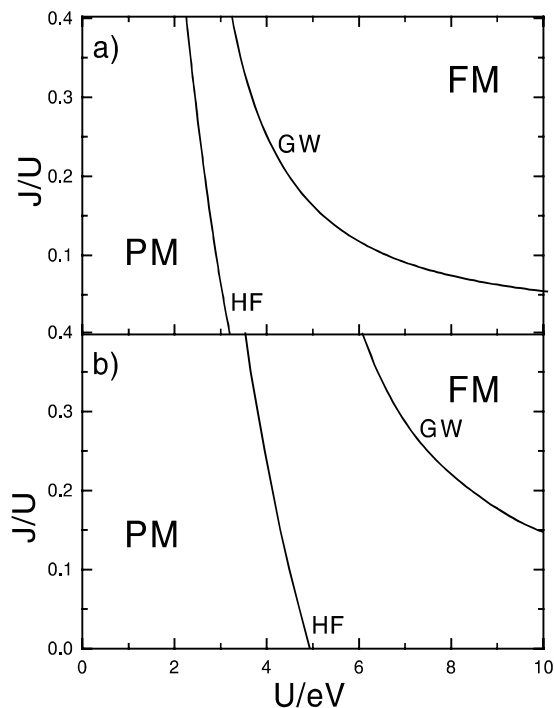


Fig. 1. Phase diagram as a function of U and J for the Hartree–Fock–Stoner theory (HF) and the Gutzwiller wave function (GW) for **(a)** $n = 1.17$ and **(b)** $n = 1.40$; PM: paramagnet, FM: ferromagnet

4 Results for a Generic Two-Band Model

4.1 Ground-State Properties

The atomic Hamiltonian for a two-band model ($b = 1, 2$) can be cast into the form

$$\begin{aligned} \hat{H}_{i;\text{at}} = & U \sum_b \hat{n}_{b,\uparrow} \hat{n}_{b,\downarrow} + U' \sum_{\sigma,\sigma'} \hat{n}_{1,\sigma} \hat{n}_{2,\sigma'} - J \sum_{\sigma} \hat{n}_{1,\sigma} \hat{n}_{2,\sigma} \\ & + J \sum_{\sigma} \hat{c}_{1,\sigma}^+ \hat{c}_{2,-\sigma}^+ \hat{c}_{1,-\sigma} \hat{c}_{2,\sigma} + J_C \left(\hat{c}_{1,\uparrow}^+ \hat{c}_{1,\downarrow}^+ \hat{c}_{2,\downarrow} \hat{c}_{2,\uparrow} + \hat{c}_{2,\uparrow}^+ \hat{c}_{2,\downarrow}^+ \hat{c}_{1,\downarrow} \hat{c}_{1,\uparrow} \right) \end{aligned} \quad (19)$$

For two $d(e_g)$ orbitals, \hat{H}_{at} exhausts all possible two-body interaction terms. Since we assume that the model describes two degenerate $d(e_g)$ orbitals, the following restrictions are enforced by the cubic symmetry [29]: (i) $J = J_C$, and (ii) $U - U' = 2J$. Therefore, there are two independent Coulomb parameters, the local Coulomb repulsion U (of the order of 10 eV) and the local exchange coupling J (of the order of 1 eV, as typical for atomic Hund's rule couplings). For the one-particle part \hat{H}_1 we use an orthogonal tight-binding Hamiltonian with first and second nearest neighbor hopping matrix elements, resulting in a bandwidth $W = 6.6$ eV.

In the following we concentrate on two band-fillings, (a), $n = 1.17$, where the non-interacting density of states (DOS) shows a pronounced peak at the Fermi energy, most favorably for ferromagnetism, and, (b), $n = 1.40$, a position near the DOS peak, where the DOS exhibits a positive curvature as a function of the magnetization.

In Fig. 1 we display the J - U phase diagram for both fillings. It shows that Hartree-Fock theory always predicts a ferromagnetic instability. In contrast, the correlated-electron approach strongly supports the ideas of van Vleck [3] and Gutzwiller [13]: (i) a substantial on-site exchange J is required for the occurrence of ferromagnetism if, (ii), realistic Coulomb repulsions U are assumed. At the same time the comparison of Figs. 1a and 1b shows the importance of band-structure effects which are the basis of the Stoner theory. The ferromagnetic phase in the U - J phase diagram is much bigger when the density of states at the Fermi energy is large. Therefore, the Stoner mechanism for ferromagnetism is well taken into account in our correlated-electron approach.

In Fig. 2, we display the energy differences between the paramagnetic and ferromagnetic ground states ("condensation energy", E_{cond}) as a function of the interaction strength for $J = 0.2U$. This quantity should be of the order of the Curie temperature which is in the range of 100 K–1000 K in real materials. The Hartree-Fock-Stoner theory yields such small condensation energies only in the range of $U \approx 4$ eV; for larger U , E_{cond} is of order U . In any case, the interaction parameter U has to be tuned very precisely to give condensation energies which concur with experimental Curie temperatures [1]. In contrast, for the Gutzwiller-correlated wave function, we find relatively small condensation energies $E_{\text{cond}} = 0.5 \cdot 10^3$ K even for interaction values as large as twice the

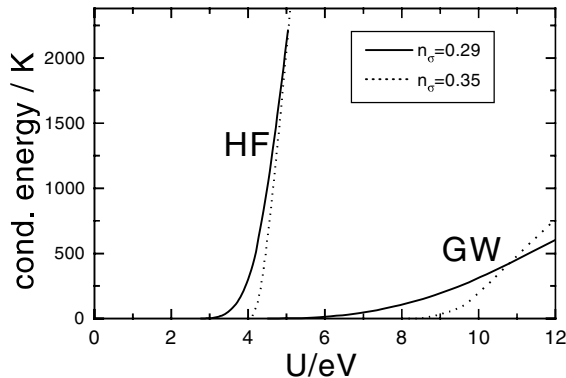


Fig. 2. Condensation energy as a function of U for $J = 0.2U$ for the Hartree-Fock theory (HF) and the Gutzwiller wave function (GW) for $n = 1.17$ (full lines) and $n = 1.40$ (dashed lines)

bandwidth ($U \approx 12$ eV). Moreover, the dependence of the condensation energy on U is rather weak such that uncertainties in U do not drastically influence the estimates for the Curie temperature.

4.2 Spinwave Dispersions

In Fig. 3 we show $E_s^{\text{var}}(q, 0, 0)$, the variational spinwave dispersion (18), in x direction for the model parameters $n = 1.17$, $J = 0.2U$, and the four different values $U/\text{eV} = 7.8, 10, 12, 13.6$ which correspond to a magnetization per band of $m = 0.12, 0.20, 0.26, 0.28$. This quantity is defined as $0 \leq m = (n_{b,\uparrow} - n_{b,\downarrow})/2 \leq n/4$. Note that our last case corresponds to an almost complete ferromagnetic polarization. The data fit very well the formula

$$E_s^{\text{var}}(q, 0, 0) = Dq^2(1 + \beta q^2) + \mathcal{O}(q^6), \quad (20)$$

in qualitative agreement with experiments on nickel [33]. The corresponding values $D = 1.4 \text{ eV } \text{\AA}^2$ and $D = 1.2 \text{ eV } \text{\AA}^2$ for $m = 0.26$ and $m = 0.28$, respectively, are of the right order of magnitude for nickel where $D = 0.43 \text{ eV } \text{\AA}^2$. As lattice constant of our simple-cubic lattice we chose $a = 2.5 \text{ \AA}$.

As shown in the inset of Fig. 3, the dispersion relation is almost isotropic for q values up to half the Brillouin zone boundary [28], in particular for large magnetizations. This is in contrast to the strong dependence of the electron-transfer amplitudes $t_{i,j}$ on the lattice direction. This implies for *strong* ferromagnets that the collective motion of the local moments is similar to that of *localized* spins in an *insulator* [34]. Such ferromagnetic insulators are conveniently described by the Heisenberg model with exchange interactions between neighboring sites $\langle i, j \rangle$ on a cubic lattice,

$$\hat{H}_S = -J \sum_{\langle i, j \rangle} \hat{S}_i \hat{S}_j. \quad (21)$$

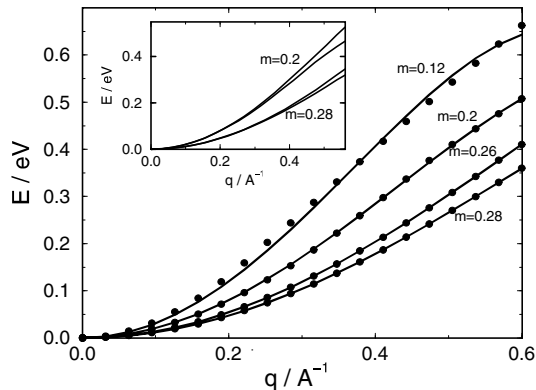


Fig. 3. Variational spinwave dispersion in x direction, $E_s^{\text{var}}((q, 0, 0))$, for the two-band model defined in Sect. 4; $n = 1.17$, $J = 0.2U$, and the values $U/\text{eV} = 7.8, 10, 12, 13.6$ correspond to $m = 0.12, 0.20, 0.26, 0.28$. The lattice constant is $a = 2.5 \text{ \AA}$. Inset: $E_s^{\text{var}}((q, 0, 0))$ and $E_s^{\text{var}}((q/\sqrt{2}, q/\sqrt{2}, 0))$ for $m = 0.2$ and $m = 0.28$, respectively. The spinwave dispersion is almost isotropic

For such a model one finds $D = 2SJ a^2$. The length of the effective local spins can be calculated from $|\Psi_G\rangle$ as $S(S+1) \approx 0.95$ ($S = 0.6$) for $m \geq 0.20$ [10]. Therefore, $J \approx D/(1.2a^2)$, which gives the typical value $J = 0.17 \text{ eV}$. For an estimate of the Curie temperature T_C we use the result from quantum Monte-Carlo calculations [35]

$$T_C = 1.44JS^2 \quad (22)$$

for spins S on a simple-cubic lattice. In this way we find $T_C \approx 0.5J = 0.09 \text{ eV} = 1 \cdot 10^3 \text{ K}$. This is the same order of magnitude as the condensation energy for these values of the interaction, $E_{\text{cond}} = 5 \cdot 10^2 \text{ K}$, see Sect. 4. Given the arbitrariness in the relation between E_{cond} and T_C , and the application of the Heisenberg model to our itinerant-electron system, we may certainly allow for difference of a factor two in these quantities. Nevertheless, the results of this section clearly show that, (i), E_{cond} gives the right order of magnitude for T_C , and that, (ii), the spinwave dispersion of *strong itinerant* ferromagnets resembles the physics of *localized* spins.

5 Correlated Band-Structure of Nickel

5.1 Discrepancies Between Experiment and SDFT

Of all the iron group magnetic metals, nickel is the most celebrated case of discrepancies between the results from experiment and from spin-density functional theory (SDFT) [36]. From very early on, the photo-emission data have indicated that the width of the occupied part of the d bands is approximately $W_{\text{occ}}^* = 3.3 \text{ eV}$ [37] whereas all SDFT results yield values of $W_{\text{occ,SDFT}}^* = 4.5 \text{ eV}$ or larger [4,37]. Similarly, the low temperature specific heat data [38] give a much

larger value of $N^*(E_F)$, the quasi-particle density of states at the Fermi energy (3.0 vs. 1.9 states/(eV atom)), which indicates a quasi-particle mass enhancement by a factor of approximately 1.6. Here, the Sommerfeld formula is used to convert the specific heat data; the theoretical value follows directly from the quasi-particle band structure. Furthermore, very detailed photo-emission studies at symmetry points and along symmetry lines of the Brillouin zone show discrepancies to SDFT results for individual band-state energies which are of similar magnitude as seen in the overall d bandwidth.

The studies revealed even bigger discrepancies in the exchange splittings of majority spin and minority spin bands. The SDFT results give a rather isotropic exchange splitting of about 600 meV [4,37,39]. In contrast, the photo-emission data show small and highly anisotropic exchange splittings between 160 meV for pure $d(e_g)$ states such as X_2 and 330 meV for pure $d(t_{2g})$ states, the latter value estimated from the exchange splitting of A_3 states along Γ to L [40,41]. The much larger and much too isotropic exchange splitting of the SDFT results has further consequences.

1. The experimental magnetic moment of the strong ferromagnet Ni is $\mu = 0.61\mu_B$; yet of relevance is its spin-only part $\mu_{\text{spin-only}} = 0.55\mu_B$ [42]. The SDFT result is $\mu_{\text{spin-only}} = 0.59\mu_B$ [4], an overestimate related to the too large exchange splitting.
2. the X_2 state of the minority spin bands lies below E_F [43], whereas all SDFT results predict it to lie above the Fermi level [4,44,45]. As a consequence, the SDFT Fermi surface exhibits *two* hole ellipsoids around the X point of the Brillouin zone whereas in the de-Haas-van-Alphen experiments only *one* ellipsoid has been found [44,46].
3. The strong t_{2g} - e_g anisotropy is also reflected in the total d hole spin density, i.e., in the observation that the d -hole part of the Ni magnetic moment has 81% $d(t_{2g})$ and 19% $d(e_g)$ character [42], whereas the SDFT results give a ratio of 74% to 26% [47].

In the late 70's and early 80's various authors have investigated in how far many-body effects improve the agreement between theory and experiment, see, e.g., Refs. [48,49]. For example, Cooke et al. [48] introduced an anisotropic exchange splitting as a fit parameter.

5.2 Present Status of the Gutzwiller-DFT

Limitations: By construction, the Gutzwiller approach naturally combines with density-functional theory (DFT) which provides a basis of one-particle wave functions and a 'bare' band structure. The Gutzwiller-DFT introduces important local correlations and provides a variational ground-state energy, a quasi-particle band structure, and a spin-wave dispersion.

Nevertheless, the Gutzwiller-DFT has its own limitations which we collect here for further reference.

1. It starts from a model Hamiltonian whose parameters need to be determined from a DFT calculation; we shall comment on this procedure below.

2. The true ground state is approximated by a variational many-body wave function; however, our experience from the two-band model supports our hope that the variational freedom of our wave function is big enough to capture the essential features of itinerant ferromagnetism in real materials as well.
3. The variational ground-state energy is evaluated exactly only in the limit of infinite dimensions; however, from the one-band case, we expect $1/d$ corrections to be small [24].
4. Similar in spirit to density-functional theory, we *interpret* the ground-state energy in terms of a quasi-particle band structure; it should be kept in mind, though, that this quantity is, in general, not identical to the quasi-particle dispersion in the sense of standard many-body theory [50].
5. Most dynamic quantities, e.g., the spectral function, cannot be determined within our approach; the example of the spinwave dispersion in Sect. 4.2 shows, however, that we can calculate low-order moments of spectral functions consistently.

Despite all these restrictions, the method remedies many problems of the SDFT in the description of the quasi-particle band structure of nickel, see Sect. 5.3.

Parameterization of the One-Particle Hamiltonian: In the present study, we determine the hopping matrix elements $t_{i,j}^{\sigma,\sigma'}$ in (1) from a least squares' fit to the energy bands obtained from a density-functional-theory calculation for non-magnetic nickel. An orthogonal nine orbital basis is used, and the root-mean-square deviation of the d band energies is about 60 meV.

A more complete description should include the flexibility of the wave functions to relax in the magnetic state. This could be achieved by enhancing the orbital basis by $4d$ states. Moreover, spin-orbit coupling is of significance in nickel, as it leads to a 10% enhancement of the total magnetic moment. In principle, the spin-orbit coupling, or, more generally, an arbitrarily large orbital basis can be treated within our formalism [10], yet it leads to complications such as local q factors which now depend on two spin-orbital indices instead of one as in (10). These extensions not only enhance the numerical complexity of the problem but also require different methods for extracting the single-particle Hamiltonian from DFT, for example by a more direct evaluation of DFT results obtained from local basis methods.

Since we start from a DFT basis, the 'bare' band structure incorporates already some important exchange and correlation effects. In particular, we may expect that the non-local Coulomb terms are well taken into account because the electron-electron interaction is screened at a length scale of the order of the inverse Fermi wave number. In this way, we can restrict all explicit Coulomb interaction terms in \hat{H} to local interactions. This assumption is supported by the fact that the Hartree-Fock approximation becomes exact in infinite dimensions for density-density interactions, $\hat{V}^{\sigma,\sigma'}(r \neq 0) = \sum_l \hat{n}_{l,\sigma} \hat{n}_{l+r,\sigma'} \rightarrow \hat{V}_{\text{HF}}^{\sigma,\sigma'}(r \neq 0)$ [51]. Therefore, we expect that interaction terms beyond the purely local Hubbard

interaction should be properly taken into account in the density-functional approach in three dimensions. However, the proper treatment of the “double counting” problem for both local and non-local interactions remains a serious problem for all methods which try to combine density-functional approaches with model-based many-particle theories; see, e.g., the contributions by Lichtenstein, Vollhardt, and Potthoff in this volume.

Chemical Potentials: In the translationally invariant system under investigation, the local occupation densities are the same as their system averages,

$$\langle \hat{n}_{i,\sigma} \rangle = \langle \hat{N}_\sigma \rangle / L, \quad (23)$$

where $\hat{N}_\sigma = \sum_i \hat{c}_{i,\sigma}^\dagger \hat{c}_{i,\sigma}$ counts the number of electrons with spin-orbit index σ . Therefore, we may equally work with chemical potentials μ_σ for each spin-orbit index in the Hamiltonian

$$\hat{H}_{\text{gc}} = \hat{H} - \sum_\sigma \mu_\sigma \hat{N}_\sigma. \quad (24)$$

In this grand-canonical view, the chemical potentials rather than the particle densities act as variational parameters. Naturally, not all of these parameters may be varied independently. For example, as a consequence of the hybridization of the $4sp$ and the $3d$ electrons, the $3d$ levels would be depleted for a strong d - d repulsion which needs to be compensated using one of the parameters. Presently we keep fixed the values of the $4s$ and $4p$ partial charges, and thus also the $3d$ total charge, to the values of the non-magnetic calculation. This is achieved by using two of the four chemical potentials for $4s$ and $4p$ electrons.

As can be seen from (14), the chemical potentials act as a shift of the ‘bare’ (DFT) values of the fields ϵ_σ ,

$$\epsilon_\sigma^{\text{eff}} = \epsilon_\sigma - \mu_\sigma. \quad (25)$$

In this way, the variational approach naturally contains the flexibility to adjust the magnetic (or “exchange”) splitting between majority bands (b, \uparrow) and minority bands (b, \downarrow),

$$\Delta_b = \epsilon_{b,\uparrow}^{\text{eff}} - \epsilon_{b,\downarrow}^{\text{eff}}. \quad (26)$$

In particular, we may allow for an anisotropy in the exchange splittings of the $d(e_g)$ and $d(t_{2g})$ electrons.

Interaction Parameters of the Atomic Hamiltonian: Presently we employ only the on-site Coulomb interaction within the $3d$ shell, i.e., all interactions within the $4s$, $4p$ shell and between $4sp$ and $3d$ are neglected. In spherical atom approximation, which is found to be well justified, all matrix elements in (3) can either be expressed as a function of the Slater integrals $F(k)$ ($k = 0, 2, 4$) or of the Racah parameters A, B, C [29]. We use $C/B \approx 4$ –5 [29] and determine A and C in order to give an optimal agreement with experimental data (effective mass

and bandwidth, condensation energy, t_{2g}/e_g ratio of the d part of the magnetic moment, Fermi surface topology).

Currently, there is a big debate on the magnitude of the interaction parameters. In principle, the interaction parameters could also be deduced from DFT results. However, there is no consensus on how to calculate these parameters consistently. For example, they could be calculated from atomic or Wannier functions, or they could be found using constrained DFT methods (see, e.g., Ref. [52]).

Minimization: The number of multi-electron states $|I\rangle$ is $2^{2N} = 2^{10}$. Because of the cubic site symmetry, the number of independent variational parameters m_I reduces to approximately 200 for the paramagnetic and to approximately 400 for the ferromagnetic cases. These “internal” variational parameters obey $2N + 1$ sum rules (12) and (13a); in cubic symmetry there remain three for the paramagnetic and five for the ferromagnetic cases. There is freedom to choose those $m_{I'}$ which, through the sum rules, are dependent on the other m_I . It is advisable to pick those $m_{I'}$ which can be expected to have large values. This avoids unphysical negative values of $m_{I'}$ to occur during the variational procedure.

The chemical potentials of (25) are the “external” variational parameters. In the present case these are eight, however three are fixed to yield the total $4s$, $4p$, and $3d$ densities, such that the space of the external parameters is five-dimensional. Given a fixed set of external variational parameters, the procedure to determine the internal ones begins to put them equal to their uncorrelated values $m_I = m_I^0$. Thus, $q_{d,\sigma}^0 = 1$. Note that $q_{s,\sigma} = q_{p,\sigma} = 1$ always holds, as there is no interaction for $4s$, $4p$ orbitals. From this, the ‘bare’ (DFT) band structure and $|\Phi_0\rangle^{\text{bare}}$ follow as an initial guess for the quasi-particle band structure and one-particle product state. Then, the following self-consistent scheme is employed:

1. Calculate the ground-state energy for $|\Phi_0\rangle_\alpha^{\text{old}}$ where α labels the set of external variational parameters. This requires momentum-space integrations up to the respective Fermi surface.
2. Minimize the ground-state energy (9) with respect to the internal variational parameters.
3. Calculate the q factors and derive $|\Phi_0\rangle_\alpha^{\text{new}}$ as the ground state of the \hat{H}_{eff} (14) with the renormalized hopping matrix elements $\tilde{t}_{i,j}$; repeat steps 1–3 until convergence to $|\Phi_0\rangle_\alpha^{\text{opt}}$ is reached.

Self-consistency is usually reached rather quickly, i.e., $|\Phi_0\rangle_\alpha^{\text{opt}}$ is found after three to five iterations.

The global minimum, $|\Phi_0\rangle_{\text{global}}^{\text{opt}}$ is found by a search through the space of the external variational parameters keeping the average d and sp occupations. This search can be sped up by first optimizing with respect to the most important external variational parameter which is the isotropic exchange splitting $\Delta_d = (\Delta_{e_g} + \Delta_{t_{2g}})/2$, putting the difference to zero as a first approximation.

In a second step, the anisotropy of the exchange splitting is investigated, i.e., we introduce Δ_{e_g} and $\Delta_{t_{2g}}$ in the minimization procedure, keeping Δ_d at the value of Δ_d^{opt} obtained in the first optimization step. The searches for Δ_d^{opt} , and for $\Delta_{e_g}^{\text{opt}}$ and $\Delta_{t_{2g}}^{\text{opt}}$ can be carried out starting with $|\Phi_0\rangle^{\text{bare}}$. Only then the self-consistency procedure for $|\Phi_0\rangle^{\text{opt}}$ has to be launched.

Typical energy gains are (in meV):

$$E_0^{\text{bare}} - E_0^{\text{bare}}(\Delta_d^{\text{opt}}) \approx 10\text{--}100, \quad (27a)$$

$$E_0^{\text{bare}}(\Delta_d^{\text{opt}}) - E_0^{\text{bare}}(\Delta_{e_g}^{\text{opt}}, \Delta_{t_{2g}}^{\text{opt}}) \approx 5\text{--}10, \quad (27b)$$

$$E_0^{\text{bare}}(\Delta_{e_g}^{\text{opt}}, \Delta_{t_{2g}}^{\text{opt}}) - E_0^{\text{opt}}(\Delta_{e_g}^{\text{opt}}, \Delta_{t_{2g}}^{\text{opt}}) \approx 5\text{--}10. \quad (27c)$$

The energy gains from the variations of Δ_s and Δ_p are of the order of 0.1 meV.

5.3 Comparison to Experiments

The results for nickel of our DFT-based Gutzwiller calculations agree best with experiment when we choose the following values of the interaction parameters: $A \approx 10\text{--}12\text{ eV}$, $C \approx 0.1\text{--}0.4\text{ eV}$ with $C/B \approx 4.5$ [53]. The width of the d bands is predominantly determined by A (essentially the Hubbard U) via the values of the hopping reduction factors $q_{d,\sigma}$. The exchange splittings and, consequently, the magnetic moment are mainly governed by C and to some extent also by A . The Racah parameter C causes the Hund's-rule splitting of the d^8 multiplets; in the hole picture, d^8 is the only many-particle configuration which is significantly occupied (by 1.90 electrons), while 5.94 electrons are in d^9 , 0.89 electrons are in d^{10} , and 1.18 electrons have s or p character.

In our present study, the parameter C is found to be rather small (0.1 eV) compared to A in order to reproduce the measured spin-only moment $\mu_{\text{spin-only}} = 0.55$. Larger values of C move the minimum of the total energy curve E_{tot} vs. magnetization m to values of $m \approx 0.60\text{--}0.65\mu_B$.

There are two points to discuss here. The first concerns the large value of A , which seems incompatible with the position of the satellite peak in the photoemission data at about 6 eV below the Fermi energy E_F [36]. Model calculations for this many-body excitation peak use values of $U \approx 3\text{--}5\text{ eV}$. However, these models use single of few d band models, excluding hybridization with the $4s$, $4p$ bands, see, e.g., Ref. [49]. When, in our calculation, the hybridization effects are switched off, and only the d band contribution to the total energy matters, we also find that values of $A \approx 3\text{--}5\text{ eV}$ agree best with experiment, and $A \approx 10\text{ eV}$ would be way out of a reasonable range of parameter values.

The second point concerns the shape of the total energy curve $E_{\text{tot}}(m)$ at large values of m in the limit of strong ferromagnetism. In this limit, the increase of the magnetic moment is fed from the d admixture in the majority $4s$, $4p$ bands. Compared to analogous curves obtained from SDFT, the curvature at large m values is much smaller in our results. We presume that the larger SDFT curvature is related to the balance between $4s$, $4p$ and $3d$ electrons. It is well known that this balance in a delicate manner determines the stability of transition metals

as well as of noble metals; see, e.g., Ref. [54], and the discussion of this problem in Ref. [55]. The balance between $4sp$ and $3d$ electrons is the more influenced the larger the exchange splitting fields are because the minority band $3d$ level is shifted towards the $4s$, $4p$ levels and the majority band $3d$ level is shifted away. Only in first order of the splitting energy, we can expect that no change in the overall $4s$, $4p$ population happens, as is imposed by the choice of our $4s$, $4p$ chemical potentials. Presently, the flow between $4s$, $4p$ and $3d$ electrons cannot be described with our model Hamiltonian as the electron-electron interaction within the $4s$, $4p$ shell and between $4sp$ and $3d$ is not included.

The exchange splittings not only determine the magnetic moment but also influence strongly the shape of the single-particle bands in the vicinity of E_F (not the overall bandwidth). For the detailed comparison with photo-emission data we have thus either chosen calculations with small C values (0.1 eV), where the minimum of $E_{\text{tot}}(m)$ yields $m = 0.55\mu_B$, or, for larger C values, with a fixed moment constraint, using the experimental spin-only moment of $\mu_{\text{spin-only}} = 0.55$. The resulting quasi-particle bands do not differ much from each other. There is however a tendency that values $C \approx 0.4$ eV and larger appear to agree somewhat better with the bulk of the photo-emission data.

Generally, the Gutzwiller results agree much better with experiment than the SDFT results. For example, this is the case for, (i), the value for the quasi-particle density of states at the Fermi energy ($N_{\text{G-DFT}}^*(E_F) = 2.6$ vs. 3.0 states/(eV atom)), (ii), the positions of individual quasi-particle energies, (iii), the values of the exchange splittings, (iv), their t_{2g-e_g} anisotropy, and, (v), the t_{2g}/e_g ratio of the d part of the magnetic moment ($(t_{2g}/e_g)_{\text{G-DFT}} = 83/17$ vs. 81/19). As a consequence of the small $d(e_g)$ exchange splitting, the $X_{2\downarrow}$ state lies below E_F and, thus, the Fermi surface exhibits only *one* hole ellipsoid around X , in nice agreement with experiment.

The large anisotropy of the exchange splittings is a result of our ground-state energy optimization, which allows $\Delta_{t_{2g}}$ and Δ_{e_g} to be independent variational parameters. We find $\Delta_{t_{2g}} \approx 3\Delta_{e_g} \approx 800$ meV. Note that these values enter $|\Phi_0\rangle^{\text{bare}}$ and are renormalized by factors $q_{d,\uparrow} \approx 0.7$, $q_{d,\downarrow} \approx 0.6$, when $|\Phi_0\rangle^{\text{opt}}$ is reached. This also implies that the width of the majority spin bands is about 10% bigger than that of the (higher lying) minority spin bands. It causes a further reduction of the exchange splittings of states near E_F , especially for those with strong t_{2g} character. Note that this band dispersion effect causes larger exchange splittings near the bottom of the d bands, e.g., 0.45 eV splitting of X_1 and 0.74 eV splitting of X_3 . There, however, the quasi-particle linewidths have increased to 1.25 eV and 1.4 eV, respectively [37], so that an exchange splitting near the bottom of the d bands could, so far, not be observed experimentally.

The large anisotropy may originate from peculiarities special to Ni with its almost completely filled d bands and its fcc lattice structure. Near the top of the d bands, the t_{2g} states dominate because they exhibit the biggest hopping integrals to nearest neighbors, $t_{dd\sigma}^{(1)} \approx 0.5$ eV. The e_g states have $t_{dd\pi}^{(1)} \approx -0.3$ eV to nearest neighbors, and $t_{dd\sigma}^{(2)} \approx 0.1$ eV to next-nearest neighbors; the latter are small because of the large lattice distance to second neighbors. The e_g states

also mix with the nearest-neighbor t_{2g} states with $t_{dd\pi}^{(1)}$ -type coupling. Therefore, the system can gain more band energy by avoiding occupation of anti-bonding t_{2g} states in the minority spin bands via large values of $\Delta_{t_{2g}}$, at the expense of allowing occupation of less anti-bonding e_g states via small Δ_{e_g} values. This scenario should not apply to materials with a bcc lattice structure which have almost equal nearest and next-nearest neighbor separations. Since the bands in nickel are almost completely filled, the suppression of charge fluctuations actually reduces the number of atomic configurations where the Hund's-rule coupling is active. It is also in this respect that nickel does not quite reflect the generic situation of other transition metals with less completely filled d bands.

The results for nickel presented here must be seen as preliminary inasmuch some important interaction terms were not yet included; see Sect. 5.2. However, the present study already shows that the Gutzwiller-DFT is a working approach. It should allow us to resolve many of the open issues in itinerant ferromagnetism in nickel and other transition metals.

6 Conclusions and Outlook

Which scenario for itinerant ferromagnetism in transition metals is the correct one?

Band theory along the lines of Slater and Stoner could be worked out in much detail whereas a correlated-electron description of narrow-band systems was lacking until recently. Our results for a two-band model and for nickel show that the van-Vleck scenario is valid. Band theory alone does not account for the strong electronic correlations present in the material which lead to the observed renormalization of the effective mass, exchange splittings, bandwidths, and Fermi surface topology. Moreover, charge fluctuations are indeed small, and large local moments are present both in the paramagnetic and the ferromagnetic phases.

Roughly we may say that the electrons' motion through the crystal leads to a ferromagnetic coupling of pre-formed moments which eventually order at low enough temperatures. In this way, strong itinerant ferromagnets resemble ferromagnetic insulators as far as their low-energy properties are concerned: spinwaves exist which destroy the magnetic long-range order at the Curie temperature.

Our present scheme allows us a detailed comparison with data from refined photo-emission experiments on nickel which are currently carried out [56]. It should be clear that our approach is applicable not only to nickel but to all other itinerant electron systems.

Despite all recent progress much work remains to be done. The present implementation of the Gutzwiller-DFT needs to be improved by the inclusion of more orbitals, their mutual Coulomb interaction terms, and the spin-orbit coupling. Ultimately, some of the principle limitations of our variational approach will have to be overcome by a fully dynamic theory. Most probably, such a theory will require enormous numerical resources such that a fully developed Gutzwiller-DFT will always remain a valuable tool to study ground-state properties of correlated electron systems.

Acknowledgments

We gratefully acknowledge helpful discussions with all participants of the Heraeus seminar *Ground-State and Finite-Temperature Bandferromagnetism*. This project is supported in part by the Deutsche Forschungsgemeinschaft under WE 1412/8-1.

References

1. J.C. Slater, Phys. Rev. **49**, 537 (1936); *ibid.*, 931 (1936).
2. E.C. Stoner, Proc. Roy. Soc. A **165**, 372 (1938); for early reviews, see J.C. Slater, Rev. Mod. Phys. **25**, 199 (1953) and E.P. Wohlfarth, *ibid.*, 211 (1953).
3. J.H. van Vleck, Rev. Mod. Phys. **25**, 220 (1953).
4. V.L. Moruzzi, J.F. Janak, and A.R. Williams, *Calculated Electronic Properties of Metals* (Pergamon Press, New York, 1978).
5. See also the contributions in this volume by O. Erikson; R. Wu; J. Kübler and K.H. Bennemann; R. Brinzanik; P.J. Jensen.
6. W. Nolting, W. Borgiel, V. Dose, and Th. Fauster, Phys. Rev. B **40**, 5015 (1989); W. Borgiel and W. Nolting, Z. Phys. B **78**, 241 (1990).
7. H. Hasegawa, J. Phys. Soc. Jpn **66**, 3522 (1997); Phys. Rev. B **56**, 1196 (1997); R. Frésard and G. Kotliar, Phys. Rev. B **56**, 12909 (1997).
8. Th. Obermeier, Th. Pruschke, and J. Keller, Phys. Rev. B **56**, 8479 (1997); Th. Maier, M.B. Zöfl, Th. Pruschke, and J. Keller, Euro. Phys. J. B **7**, 377 (1999); M.B. Zöfl, Th. Pruschke, J. Keller, A.I. Poteryaev, I.A. Nekrasov, and V.I. Anisimov, Phys. Rev. B **61**, 12810 (2000).
9. D. Vollhardt, N. Blümer, K. Held, M. Kollar, J. Schlipf, M. Ulmke, and J. Wahle, Adv. in Solid-State Phys. **38**, 383 (1999); I.A. Nekrasov, K. Held, N. Blümer, A.I. Poteryaev, V.I. Anisimov, D. Vollhardt, preprint cond-mat/0005207 (2000).
10. J. Bünnemann, W. Weber, and F. Gebhard, Phys. Rev. B **57**, 6896 (1998).
11. See also the contributions in this volume by A.I. Lichtenstein; D. Vollhardt; W. Nolting, M. Potthoff, T. Herrmann, and T. Wegner; A.M. Oleś and L.L. Feiner.
12. M.C. Gutzwiller, Phys. Rev. Lett. **10**, 159 (1963).
13. M.C. Gutzwiller, Phys. Rev. **134**, A923 (1964); *ibid.* **137**, A1726 (1965).
14. J. Hubbard, Proc. Roy. Soc. London Ser. A **276**, 238 (1963); *ibid.* **277**, 237 (1964).
15. J. Kanamori, Prog. Theor. Phys. **30**, 275 (1963).
16. G. Stollhoff and P. Fulde, J. Chem. Phys. **73**, 4548 (1980); G. Stollhoff and P. Thalmeier, Z. Phys. B **43**, 13 (1981); A.M. Oleś and G. Stollhoff, Phys. Rev. B **29**, 314 (1984); for further details on the “local ansatz” technique, see P. Fulde, *Electron Correlations in Molecules and Solids*, Springer Series in Solid-State Sciences **100** (Springer, Berlin, 1991).
17. D. Baeriswyl and K. Maki, Phys. Rev. B **31**, 6633 (1985); D. Baeriswyl, J. Carmelo, and K. Maki, Synth. Met. **21**, 271 (1987).
18. D. Vollhardt, Rev. Mod. Phys. **56**, 99 (1984).
19. K.A. Chao and M.C. Gutzwiller J. Appl. Phys. **42** 1420 (1971); K.A. Chao, Phys. Rev. B **4** 4034 (1971); *ibid.* 1088 (1973); J. Phys. C **7** 127 (1974).
20. P. Fazekas, *Lecture Notes on Electron Correlation and Magnetism*, Series in Mod. Cond. Matt. Phys. **5** (World Scientific, Singapore, 1999), gives an introduction to the theory of ferromagnetism, and a concise description and some applications of the Gutzwiller approximation.

21. W. Metzner and D. Vollhardt, Phys. Rev. Lett. **59**, 121 (1987); Phys. Rev. B **37**, 7382 (1988).
22. W. Metzner and D. Vollhardt, Phys. Rev. Lett. **62**, 324 (1989).
23. For a review, see F. Gebhard, *The Mott Metal-Insulator Transition* (Springer, Berlin, 1997).
24. F. Gebhard, Phys. Rev. B **41**, 9452 (1990).
25. J. Bünemann and W. Weber, Phys. Rev. B **55**, 4011 (1997).
26. J. Bünemann, Eur. Phys. J. B **4**, 29 (1998).
27. J. Bünemann, F. Gebhard, and W. Weber, J. Phys. Cond. Matt. **8**, 7343 (1997).
28. J. Bünemann, preprint cond-mat/0005154 (2000).
29. S. Sugano, Y. Tanabe, and H. Kamimura, *Multiplets of Transition-Metal Ions in Crystals*, Pure and Applied Physics **33** (Academic Press, New York, 1970).
30. This holds for our symmetry-restricted basis.
31. A. Messiah, *Quantum Mechanics*, 3rd printing (North Holland, Amsterdam, 1965).
32. R.P. Feynman, *Statistical Mechanics*, Frontiers in Physics **36** (Benjamin, Reading, 1972).
33. R.D. Lowde and C.G. Windsor, Adv. Phys. **19**, 813 (1970).
34. See, e.g., S.V. Halilov, H. Eschrig, A.Y. Perlov, and P.M. Oppeneer, Phys. Rev. B **58**, 293 (1998).
35. K. Chen, A.M. Ferrenberg, and D.P. Landau, Phys. Rev. B **48**, 3249 (1993).
36. For a review, see S. Hüfner, *Photoelectron Spectroscopy* (Springer, Berlin, 1995).
37. W. Eberhardt and E.W. Plummer, Phys. Rev. B **21**, 3245 (1980).
38. M. Dixon, F.E. Hoare, T.M. Holden, and D.E. Moody, Proc. R. Soc. A **285**, 561 (1965).
39. J. Callaway in *Physics of Transition Metals*, ed. by P. Rhodes (Conf. Ser. Notes **55**, Inst. of Physics, Bristol, 1981), p. 1.
40. M. Donath, Surface Science Reports **20**, 251 (1994).
41. K.-P. Kämper, W. Schmitt, and G. Güntherodt, Phys. Rev. B **42**, 10696 (1990).
42. H.A. Mook, Phys. Rev. **148**, 495 (1966).
43. R. Raue, H. Hopster, and R. Clanberg, Phys. Rev. Lett. **50**, 1623 (1983).
44. C.S. Wang and J. Callaway, Phys. Rev. B **15**, 298 (1977).
45. E.P. Wohlfahrt in *Handbook of Magnetic Materials* **1**, ed. by E.P. Wohlfarth (North Holland, Amsterdam, 1980).
46. D.C. Tsui, Phys. Rev. **164**, 561 (1967).
47. O. Jepsen, J. Madsen, and O.K. Andersen, Phys. Rev. B **26**, 2790 (1982).
48. J.F. Cooke, J.W. Lynn, and H.L. Davis, Phys. Rev. B **21**, 4118 (1980).
49. A. Liebsch, Phys. Rev. B **23**, 5203 (1981).
50. A. L. Fetter and J. D. Walecka, *Quantum Theory of Many-Particle Systems* (McGraw-Hill, New York, 1971).
51. E. Müller-Hartmann, Z. Phys. B **74**, 507 (1989); *ibid.* **76**, 211 (1989).
52. G. Vielsack and W. Weber, Phys. Rev. B **54**, 6614 (1996).
53. Some preliminary results can be found in J. Bünemann, F. Gebhard, and W. Weber, Found. Phys. **30** (Dec. 2000).
54. D.G. Pettifor, J. Magn. Magn. Mat. **15–18**, 847 (1980).
55. J. Hafner, *From Hamiltonians to Phase Diagrams: The Electronic and Statistical Mechanical Theory of Sp-Bonded Metals and Alloys* (Springer Series in Solid-State Sciences **70**, 1987), pp. 72.
56. R. Claessen, private communication (2000).

Anisotropy in Magnetism

Klaus Baberschke

Institut für Experimentalphysik, Freie Universität Berlin,
Arnimallee 14, D-14195 Berlin, Germany

Abstract. The enormous research on magnetic properties of ultrathin films and nanostructures produces also new activities in the fundamental understanding of the magnetic anisotropy energy (MAE) and the anisotropy of the orbital magnetic moment/atom. The pseudomorphic growth of Fe, Co, Ni on metallic and non-metallic substrates can change the nearest neighbor distance by ≈ 0.05 Å. This small change in structure and symmetry increases the MAE by several orders of magnitude and lifts the quenching of the orbital moment. Increases of 20 – 30% of the orbital moment μ_L are observed. This experimental finding is confirmed by full relativistic *ab initio* calculations. Various experiments deliver the full temperature dependence of all MAE contributions. The temperature dependence remains a challenge for the theory in itinerant magnetism.

1 Introduction

The anisotropy in magnetic phenomena is well established in theoretical and experimental investigations. We refer to standard textbooks, e.g. [1,2,3,4]. Although this is common knowledge and standard part of teaching in solid state physics, in recent years a revival happened with an enormous number of new results and publications, in particular for itinerant magnets. In our opinion this has at least three independent reasons:

- There is an obvious interest on ultrathin ferromagnetic films and nanostructures for technological applications (we refer to recent reviews [5,6]).
- In 1985-87 the magnetic circular dichroism was introduced in the x-ray regime (XMCD = **X**-ray **M**agnetic **C**ircular **D**ichroism). This new experimental technique became very popular when circular polarized synchrotron radiation was available [7,8]. Theoretical efforts followed immediately [9]; using a localized picture to calculate the transition probability at the $L_{3,2}$ -edges of 3d ferromagnets, the so-called ‘sum rules’ were developed [9,10,11].
- Advances in *ab initio* theories and computational capacities allow today full relativistic calculation of the total energy and its magnetic anisotropic contributions [12,13,14]. In section 2 we will show that the anisotropic magnetic energy is in the order of $\approx \mu\text{eV}/\text{atom}$ out of some eV/atom of the total energy. In other words, total energy calculations for particular systems are that precise and reliable that $\approx 10^{-6}$ contributions can be calculated (analogy in 1960’s can be seen for the core polarization in the hyperfine fields).

We prefer to see these three reasons (and more) as an accidental ‘coincidence’. It is not only the demand for new technologies in magnetic storage media, but

also the progress in the fundamental understanding which reactivate the discussion of magnetic anisotropies. I.e. in the history of magnetism [15] the MAE was always treated in a thermodynamical phenomenological way by expanding the free energy [16]. In nowadays magnetism is interpreted from an atomistic, microscopic point of view: New artificial structures can be grown with different symmetries and lattice constants (changes by few 1/100 Å only). These real structures serve as input for *ab initio* theories (see the chapters by R. Q. Wu and O. Eriksson in this book) and it appears that these small changes in the nearest neighbor distance (≈ 0.05 Å) change the magnetic anisotropy energy by 2-3 orders of magnitude! This will be a main aspect of the present contribution.

Table 1. Characteristic energies of metallic ferromagnets (MAE values are given at room temperature) [17]

binding energy	1 – 10 eV/atom
exchange energy	$10 - 10^3$ meV/atom
cubic MAE (Ni)	0.2 μ eV/atom
uniaxial MAE (Co)	70 μ eV/atom

Unfortunately the history of magnetism and magnetic anisotropy went different routes and were uncoupled from other areas of solid state magnetism, that is to say, magnetoelastic theory had sometimes very little contact with crystal field theory (e.g. [18]). As a consequence, the classification of magnetic anisotropy contribution went a different route than Legendre polynom expansion in crystal field theory. Moreover, as a consequence various units are used in the historical part of magnetoelasticity, namely erg/cm³ and erg/cm², that is to say energy per volume and area, respectively. Other parts of solid state physics and in particular the theory prefers eV/atom, that is to say energy per particle (see Tab.1). This newer notation started to be used in surface and thin film magnetism and we strongly advocate in favor of it, since it facilitates the communication with theory and gives an easier insight. For example, in thin film magnetism Fe, Co and Ni ions contribute equally strong to the anisotropy energy, be it a surface atom or an atom in the inner part of a nanostructure, namely 10–100 μ eV/atom. In the older version it would read $1.5 - 15 \cdot 10^6$ erg/cm³ and $0.03 - 0.3 \cdot$ erg/cm² which is not so easy to be compared.

In the following we distinguish only two effects of anisotropy in magnetism:

- In Sec.2 we discuss the magnetic anisotropy energy (MAE), which is the energy to rotate the magnetization of a single magnetic domain from its easy axis into the hard axis. At first glance this energy is largest at $T = 0$ and reduces to 0, if T approaches the ordering temperature T_C [16]. On a closer look we note that details of the temperature dependence depend on

the origin of the anisotropy, namely a single particle or pair interaction [1]. Gd metal for example has a finite anisotropy above T_C [3,17].

- In Sec.3 we discuss the anisotropic magnetic moment/atom. This is in first order a *temperature independent* observable and originates from the anisotropic orbital magnetic moment which is in films and nanostructures not fully quenched.

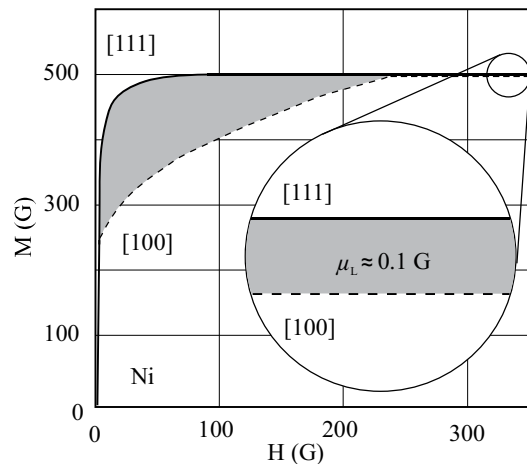


Fig. 1. Room temperature magnetization curve for Ni along the easy ([111]) and hard ([100]) direction [17]

Both effects are schematically shown in Fig.1: The MAE corresponds to the gray triangle and amounts at 300 K to $\approx 0.2 \mu\text{eV}/\text{atom}$ for fcc Ni (Tab.1). The anisotropy in the magnetic moments $\Delta\mu_L/\mu \approx 10^{-4}$ for bulk cubic Ni. In the following we will see that both may increase by orders of magnitude for nanostructures. The latter effect survives far in the paramagnetic regime. It is well known [17] that the magnetic moments of Fe, Co, Ni are larger along the easy axis (see inset of Fig.1) than in other directions.

2 Magnetic Anisotropy Energy (MAE)

In common phenomenology of MAE several origins can be listed: magneto-crystalline, magneto-elastic, etc.. In view of its physical origin we prefer to distinguish only two types:

- The intrinsic anisotropy K . It originates from the non spherical charge distribution, be it in a localized or itinerant picture. It is the only mechanism for anisotropic energy in an infinite sized crystal (here we ignore the small dipolar contributions for non cubic symmetry). As discussed in Sec.1 this can be treated in *ab initio* theories in full-relativistic and full-potential treatments.

- The only other mechanism is the dipole-dipole interaction which may become dominant in finite sized samples. It depends entirely on the sample shape.

In the following we discuss exclusively ‘single-domain physics’ for two reasons: (i) There exist excellent literature for multi-domain magnetism [19]. (ii) The thermodynamic ground state for many nanostructures investigated in recent literature is a single domain state. Note that for example ultrathin Co/Cu(001) films of few atomic layers thickness is a single domain system in its thermodynamic ground state with easy axis in plane. This is not in contradiction to PEEM microscopy. There, the as grown film shows a multi-domain state which is not the thermodynamic ground state of the system. Depending on stiffness constant and other parameters all structures with dimensions smaller than a few nm are single-domain in the ground state [1]. In the following we use the letter ‘ K ’ exclusively for this intrinsic anisotropy (orbital moment induced), it is the focal point of the experiments presented here. The experimentally measured total value of the MAE includes also the dipolar contribution, which can be calculated (Sec.2.2) and is subtracted from the raw experimental data before discussing the intrinsic MAE ‘ K ’.

2.1 Intrinsic Anisotropy K

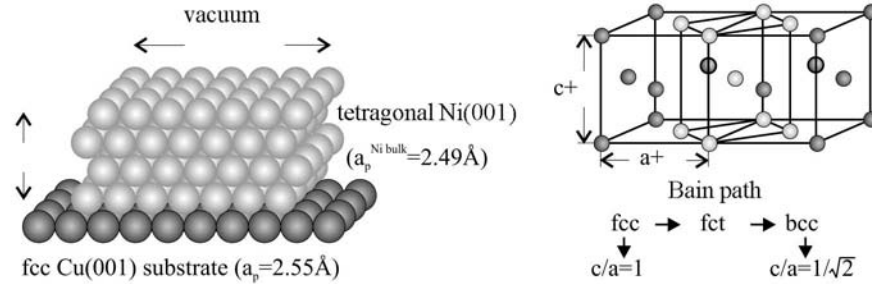


Fig. 2. Schematic drawing of pseudomorphic growth of Ni on a Cu(001) substrate. On the right hand side an fcc lattice is shown for $c/a = 1$. If the c/a -ratio reduces down to $c/a = 1/\sqrt{2}$, the lighter spheres indicate the new bcc lattice cell. [20]

In Fig.2 an ultrathin film grown in register on a substrate crystal is shown schematically, e.g. Ni/Cu(001). The nearest neighbor distance in bulk Cu is $a_{\text{Cu}} = 2.55 \text{ \AA}$ and in Ni $a_{\text{Ni}} = 2.49 \text{ \AA}$. The pseudomorphic growth of Ni on Cu(001) results in an in-plane tensile strain of $\varepsilon_1 = 2.5 \%$. Keeping the total energy at a minimum or $\delta V = 0$ results in a contraction along the c -axis of $\varepsilon_2 = -3.2 \%$. In other words, the cubic symmetry of Ni reduces to a tetragonal symmetry, face centered tetragonal (fct). In the right panel of Fig.2 this lattice is schematically shown. If one compresses the c -axis down to $c/a = 1/\sqrt{2}$, we end up again in cubic symmetry (light spheres) with a bcc lattice (the so-called

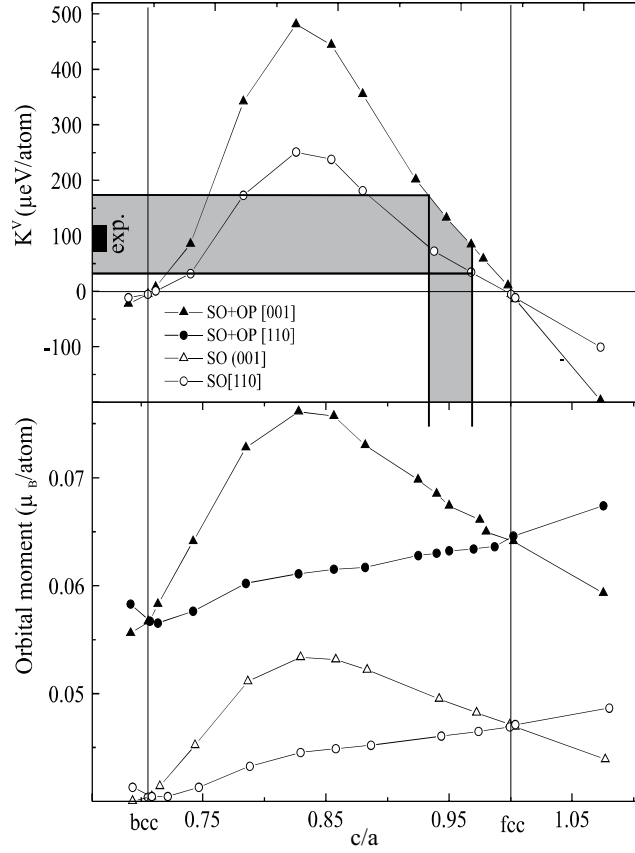


Fig. 3. An all electron and full relativistic calculation of the intrinsic anisotropy K and anisotropy of the orbital moment for an infinitely sized Ni single crystal as function of uniaxial deformation of the c/a -ratio [21]. All symbols are calculated values for two crystallographic orientations. Open symbols correspond to spin-orbit-coupling-only, full symbols to SO+orbital polarization(OP). The grey area on the x -axis indicates the uncertainty of the c/a -ratio from LEED measurements [22]. This uncertainty can be projected on the y -axis, depending on SO-only or SO+OP calculations. It results in an anisotropy energy of the order of 100 $\mu\text{eV}/\text{atom}$, which agrees nicely with the experiments [23].

Bain path, see the chapter by O. Eriksson in this book). Hjortstam et al. [21] have calculated for such an artificial structure with infinite size the total energy E as well as the magnetic anisotropy energy (see Fig.3).

$$K = \Delta E = E_{[001]} - E_{[110]} \quad (1)$$

At exact cubic fcc and bcc symmetry $K \approx 0 \mu\text{eV}/\text{atom}$ (see Tab.1). This calculation shows very nicely that K increases dramatically by orders of magnitude,

if Ni departs from cubic symmetry. Similar calculations have been performed by Wu et al. for Co/Cu(001) [24]. Fig.3 shows also the difference between spin-orbit(SO)-only calculations and adding orbital polarization (OP) (for details see theoretical contributions by O. Eriksson and R. Q. Wu in this volume). Oversimplifying one might say that SO-only calculation corresponds to Hund's third rule, namely the coupling of the orbital (L) and spin momentum (S). The SO- and SO+OP-calculation in Fig.3 shows that there is a significant difference, a detailed discussion goes beyond this contribution, but the figure shows clearly that the non-spherical charge distribution ($L \neq 0$) contributes significantly to the intrinsic magnetic anisotropy energy. Strictly speaking, the non-vanishing orbital momentum (non-spherical charge distribution) is the only origin of the intrinsic MAE (it includes magneto-elastic, magneto-crystalline and other effects). For Ni/Cu(001) the c/a -ratio was determined to be $c/a \approx 0.95$ [22]. The hatched area in Fig.3 shows nicely that this ends up in a MAE of $K \approx 100 \mu\text{eV}/\text{atom}$. In Sec.3 we will discuss the lower panel of Fig.3, showing the anisotropy of μ_L . So far we have not included any surface or interface effects. Fig.4 shows schematically the K^{S1} , the surface facing vacuum and the interface regime K^{S2} . Following Néel [25] and Gradmann [26] one can decompose the total intrinsic ' K ' of a thin film into a surface and interface effect and into a contribution arising from the inner part, the so-called K^{V} , where ' V ' stands for volume.

$$K_{\text{i}} = K_{\text{i}}^{\text{V}} + \frac{2K_{\text{i}}^{\text{S}}}{d} \quad (2)$$

Note that this is an energy density and consequently the first term K^{V} is a constant contribution originating from the inner part of the sample. The second term in Eq.(2) yields an average term for the surface contribution K^{S} , which contributes with $1/d$ to the total K . The subscript i stands for various contributions of K being explained in Sec.2.3.

In the right part of Fig.4 we show for Ni/Cu(001) that the experimentally determined K follows exactly the linear dependence of $K \propto 1/d$. To our experience this is the most sensitive method to determine real pseudomorphic growth. For Ni/Cu(001) we have found that Ni grows pseudomorphically in a fct structure up to $d \approx 15$ ML. For thicker films with $d \geq 20$ ML the system relaxes (producing misfit dislocations) into its original bulk fcc structure, while the MAE decreases again to $K \rightarrow 0$. Performing experiments for various thicknesses in the range of $2 - 10$ ML one also changes the Curie temperature of the ferromagnet due to finite size effects. Therefore, it is all important to plot this type of diagram as function of the reduced temperature $t = T/T_{\text{C}}$. Fig.4 shows this for $t = 0.56$ and $t = 0.74$. If, for example, thickness dependent measurements are performed only at ambient temperature, $T \approx 300$ K, the $K(1/d)$ -plots are misleading and lead to wrong conclusions, as we have shown recently for Co/Cu(111) [27]. In earlier literature of thin film magnetism it has been said that the Néel (surface) contribution to the MAE is dominant because of symmetry breaking and is the main reason for large MAE in ultrathin films. Such a statement would be only true, if the inner part of a thin film would not contribute to the MAE, which is in obvious contrast to Fig.4. In nowadays the high precision of surface

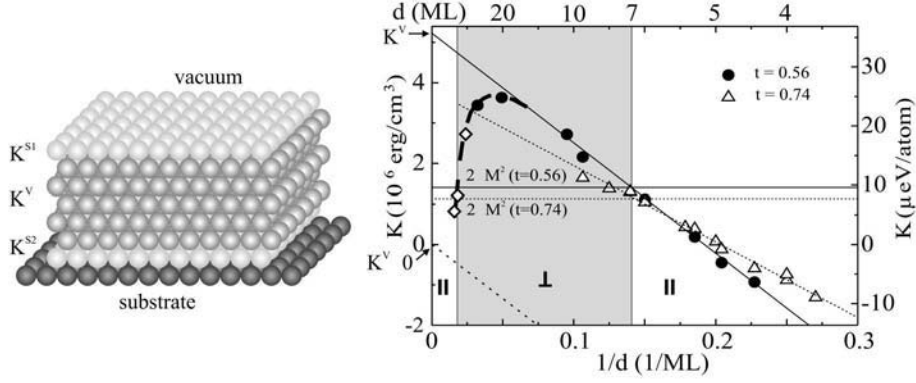


Fig. 4. Left panel: Schematic drawing of a pseudomorphic grown thin film with 3 contributions of anisotropy energy contributions, the surface term K^{S1} , the interface term K^{S2} and the central or volume term K^V . Right hand panel: Experimental data for Ni/Cu(001) taken from [28]. If, hypothetically, the Ni film would grow in a pseudomorphic structure up to infinite thickness ($1/d = 0$), K^V would reach a value indicated on the y -axis. This is by orders of magnitude larger than for unperturbed bulk fcc Ni as indicated close to the '0' of the y -axis. The 3 regimes indicate parallel, perpendicular and again parallel easy axis of magnetization. For details of the spin reorientation transition see [28,30].

structure analysis techniques proves that most of the grown nanostructures in thin films do not have bulk cubic symmetry, but perturbed lower symmetric artificial structures. The extrapolation of $K(1/d)$ in Fig.4 shows clearly that for $1/d \rightarrow 0$ we end up with a $K^V \approx 30 \mu\text{eV/atom}$ at a reduced temperature of $t = 0.56$ which is two orders of magnitude larger than for bulk Ni (Fig.1, Tab.1). This simple argumentation has been nicely proven in the theoretical calculation by Uiberacker et al. [29], displayed in Fig.5. They have taken a thin film of 12ML of Ni, facing on the right hand side the vacuum surface and on the left the Cu substrate. The surface layer (layer 15 in Fig.5) gives a huge negative contribution corresponding to the negative slope in Fig.4. They also found a negative contribution at the interface layer (layer 4), but less dramatic than in the vacuum facing surface. In the present context however, it is most important to see that the central part of the film (layers 5 to 14) also contributes very much to the magnetic anisotropy, if the cubic symmetry is broken. For -5.5% relaxation approximately 10 layers contribute each with $K \approx 100 \mu\text{eV/atom}$. This overcomes definitely the surface and interface contribution which count only for 1 layer.

In summary, for the analysis of MAE in nanostructures and ultrathin films it is all important to consider the real structure and symmetry and not to assume that the inner part of the structures behave like bulk cubic Fe or Ni. High precision structure analysis of these materials serves as an ideal input for theoretical *ab initio* calculations. In previous publications we have discussed thickness and

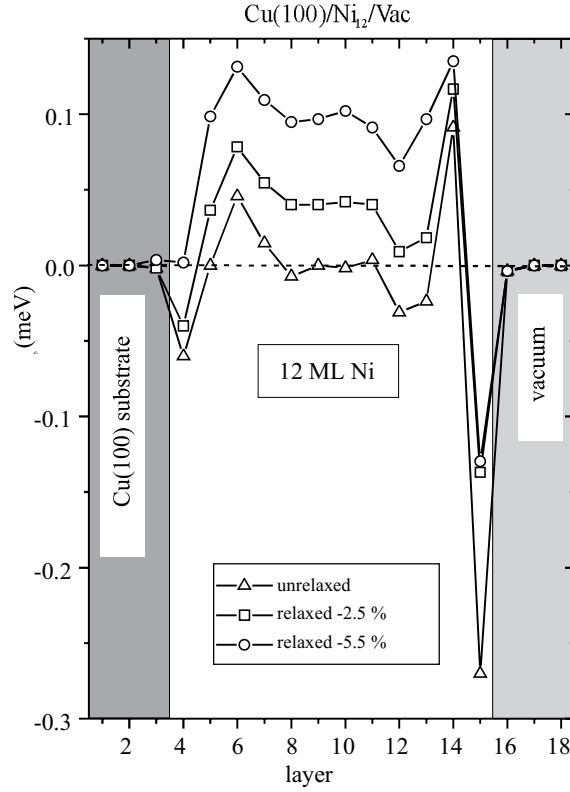


Fig. 5. Magnetic Anisotropy energy calculated for 12 ML Ni/Cu(001) [29]. The energy difference ΔE , defined in Eq.1, was calculated for each layer, starting with 3 layers of Cu substrate, followed by 12 layers of Ni atoms and 3 layers on the vacuum side above Ni. The open triangles denote an unrelaxed, cubic fcc-lattice, squares and circles correspond to a relaxed tetragonal structure.

temperature dependent spin reorientation transition [30]; for the present focus it is all important to note that the main reason for the reorientation is the above discussed K^V contribution of the fct Ni. Only the tetragonal distortion produces in Fig.4 an intercept of the y -axis at large K -values. Taking the same negative slope (negative K^S), but assuming a cubic fcc structure $K(1/d)$ would cross the y -axis at $K \approx 0$ (dotted line in Fig.4), resulting in the fact that the Ni film would never have an easy axis perpendicular to the film plane. So far all theoretical calculations were done for $T = 0$, but experiments were not. We will come back to this in Sec.2.3.

2.2 Dipolar (Shape) Anisotropy

The only other anisotropic interaction between magnetic moments $\boldsymbol{\mu}_i$ and $\boldsymbol{\mu}_j$ with a distance of \mathbf{r}_{ij} is the dipole-dipole interaction:

$$H_{\text{dip}} = \sum_{i \neq j} r_{ij}^{-3} \left[(\boldsymbol{\mu}_i \cdot \boldsymbol{\mu}_j) - \frac{3}{r_{ij}^2} (\boldsymbol{\mu}_i \cdot \mathbf{r}_{ij}) (\boldsymbol{\mu}_j \cdot \mathbf{r}_{ij}) \right] \quad (3)$$

The second term in the dipolar interaction shows clearly that the dipole energy depends on the orientation of the magnetic moments $\boldsymbol{\mu}_i$, $\boldsymbol{\mu}_j$ with respect to \mathbf{r}_{ij} : E_{dip} is lowest, if the magnetization \mathbf{M} points parallel to \mathbf{r}_{ij} and it costs energy to rotate the two dipole moments perpendicular to the \mathbf{r}_{ij} -axis. This simple argument demonstrates clearly that an exchange coupling by $J\mathbf{S}_i \cdot \mathbf{S}_j$ is per definition isotropic. A scalar product $\mathbf{S}_i \cdot \mathbf{S}_j$ does not depend on the space coordinates, i.e. the exchange energy depends on the angle between the neighboring spins, but is independent of their orientation relative to their bond direction. Consequently, it costs no energy to rotate two spin moments in space as long as one keeps them parallel or antiparallel to each other. It is worth-while to note that a so-called anisotropic exchange interaction cited in the literature originates from the projection of spin-orbit coupling into spin space. One may project part of the orbital momentum and interaction into spin space. We prefer to keep the orbital magnetism as what it is, originating from non-spherical charge distributions described by the orbital angular momentum, be it as orbital polarization or as spin-orbit coupling. Another quite common way of interpretation for 3d ferromagnetism is to state a quenching of the orbital momentum and replace the magnetic moment $\boldsymbol{\mu}$ by a spin vector \mathbf{S} resulting from Eq.(3) with an ‘effective anisotropic exchange’.

The summation over all lattice sites i, j in cubic symmetry and infinite-sized samples vanishes. We know that for non-cubic specimen like hcp cobalt or fct Ni small finite dipolar contributions remain, even if the sample is infinite-sized as discussed in the beginning of Sec.2.1 (we ignore this in the following discussion). For finite-sized samples like ultrathin films two approaches are commonly used:

- *The continuum model* assuming a dipole density: This leads to the well-known demagnetizing factor N times the magnetization M^2 :

$$E_{\text{dip}} = 2\pi (N_{\perp} - N_{\parallel}) M^2 \quad (4)$$

- *The discrete lattice sum* over point dipoles: Here a magnetic moment per lattice site is assumed and the summation (Madelung-sum) is taken over the whole specimen.

Today’s experiments in metallic ferromagnets and ultrathin films are that precise and demonstrate that non of the two models is good enough. In the continuum model one cannot assume that $N_{\parallel} = 0$ is and $N_{\perp} = 1$ respectively. A better approximation is $N_{\parallel} \approx \frac{\pi d}{4D}$, where d is the film thickness and D the diameter of the film. N_{\parallel} can directly be measured via susceptibility experiments because

the maximum in the susceptibility peak is limited by $1/N_{||}$:

$$\chi_{\text{exp}} = \frac{1}{\frac{1}{\chi_{\text{int}}} + N_{||}} \quad (5)$$

In recent susceptibility measurements of ultrathin Gd films we have measured $\chi_{\text{max}} \approx 10^4$ for films in the order of 1 nm thickness. From that we deduced that the lower limit for the lateral diameter is in the order of $D \approx 0.5 \mu\text{m}$ [31]. This was later confirmed in a STM experiment [32]. Summation over discrete dipoles has been performed in bulk and ultrathin films [33,34]. This leads to a small demagnetizing energy [33,34]. In conclusion: The true demagnetizing energy lies between the two limits. What needs to be done in the future is the calculation of a lattice sum using a finite magnetic moment profile (measured by neutron form factor analysis, for example).

Another and more important effect is to consider the proper temperature dependence $M(T)$. In the next section we will discuss the temperature dependence of the intrinsic anisotropy ‘ K ’. A priori it is not clear that the temperature dependence $K(T)$ and $M(T)$ are known or well understood. In earlier literature of thin film magnetism an effective anisotropy was introduced as the sum of two contributions $K_{\text{eff}} = K + 2\pi M^2$. Since $K(T)$ and $M(T)$ may have a completely different temperature dependence $f(T)$, be it an analytical function or not, the sum of the two and an effective K mixes both effects and makes the situation less transparent. A more transparent way of analysis is to separate immediately the temperature dependence of dipolar interaction $M^2(T)$ and the intrinsic anisotropy $K(T)$ and discuss both contributions separately, even if a very precise temperature determination of E_{dip} is still not available.

2.3 Angular and Temperature Dependence of the MAE

Following Eq.(3) the dipolar anisotropy is described in a reasonable approximation by a $\cos^2(\theta)$ -law. The intrinsic anisotropy ‘ K ’, however, consists out of several contributions with twofold, fourfold, etc. symmetry following a $\cos^2(\theta)$ -, $\cos(2\varphi)$ -, $\cos^4(\theta)$ -, $\cos(4\varphi)$ -, ... angular dependence. For the anisotropy of bulk ferromagnets this is well tabulated in the literature [1,2,3]. We note that there exists no common nomenclature. In [3] one finds an expansion in Legendre polynomials (in analogy to crystal field theory), whereas in [1,2] one finds an expansion in trigonometrical functions. The latter is listed in [17]. Unfortunately no unique systematic has been used in the majority of literature on thin film magnetism, most publications use only an effective uniaxial term. In Eq.(6) we give some frequently used notation for the intrinsic free energy density for systems of tetragonal symmetry:

$$E = E_{\text{eff}} - E_{\text{dip}} = -K_{2\perp} \cdot \cos^2(\theta) - K_{2||} \cdot \cos(2\varphi) \sin^2(\theta) - \frac{1}{2}K_{4||} \frac{1}{4} [3 + \cos(4\varphi)] \cdot \sin^4(\theta) - \frac{1}{2}K_{4\perp} \cdot \cos^4(\theta) + \dots \quad (6)$$

We note here that this expansion of the anisotropy energy is used by the majority but it has also some disadvantages: Legendre polynom expansion used in [3] has the advantage that one finds a monotonic decrease as function of temperature and not a crossing of the sign as it is listed e.g. for Fe, Co and Ni in [17]. The higher (fourth) order terms are of principle importance because only a higher than quadratic function in the free energy can lead to energy minima (easy axis of magnetization) at arbitrary angles. That is to say all interpretations of thin film magnetism which restrict themselves to an uniaxial $\cos^2(\theta)$ -dependence will find only easy axis being in- or out-of-plane. However there exist examples (prototype Ni/Cu(001)) with a continuous rotation of the easy axis [35,36,37]. A detailed description of this effect has been given in [38]. In Fig.6 we demonstrate these dependencies for a Fe_4/V_4 -multilayer. For this multilayer structure the ferromagnetic resonance was measured angular dependent as function of the polar angle θ_H and the azimuthal angle φ_H .

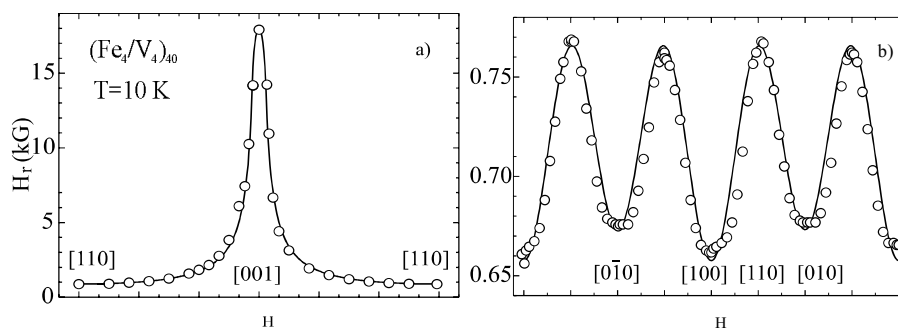


Fig. 6. Polar (θ_H) and azimuthal (φ_H) angular dependence of the FMR resonance field H_r for a Fe_4/V_4 -multilayer at 10 K [36].

In Fig.6 we clearly see a 180° -dependence with the resonance field H_r being largest along the film normal [001] (i.e. the hard axis) and H_r being lowest in the film plane [100] (i.e. easy axis). It is all important to measure the full angular dependence as indicated by the open circles and to fit it to the Eq.(6). We note that measuring only the hard axis and easy axis leads to a misinterpretation of pseudo-uniaxial symmetry. The fitted solid line has very large components of fourth order terms (for details see [39]). On the right hand panel we show the azimuthal in-plane angular dependence which is obviously smaller and superimposes a 90° - and 180° angular dependence. The very small 180° angular dependence is produced by steps within the surface plane of the film structure. In Fig.7 we show the K_2 , $K_{4\perp}$ and $K_{4\parallel}$ as function of temperature. First of all we note that K_2 and $K_{4\perp}$ are in the same order of magnitude at low temperature (left hand y -axis) but of opposite sign. $K_{4\perp}$ is negative, whereas K_2 is positive. The in-plane component $K_{4\parallel}$ is about one order of magnitude smaller than the out-of-plane contributions (right hand y -axis). The ferromagnetic resonance is

the technique of choice to measure each of these contributions also as function of temperature. The experimental results shown in Fig.7 reveal that each has a different temperature dependence.

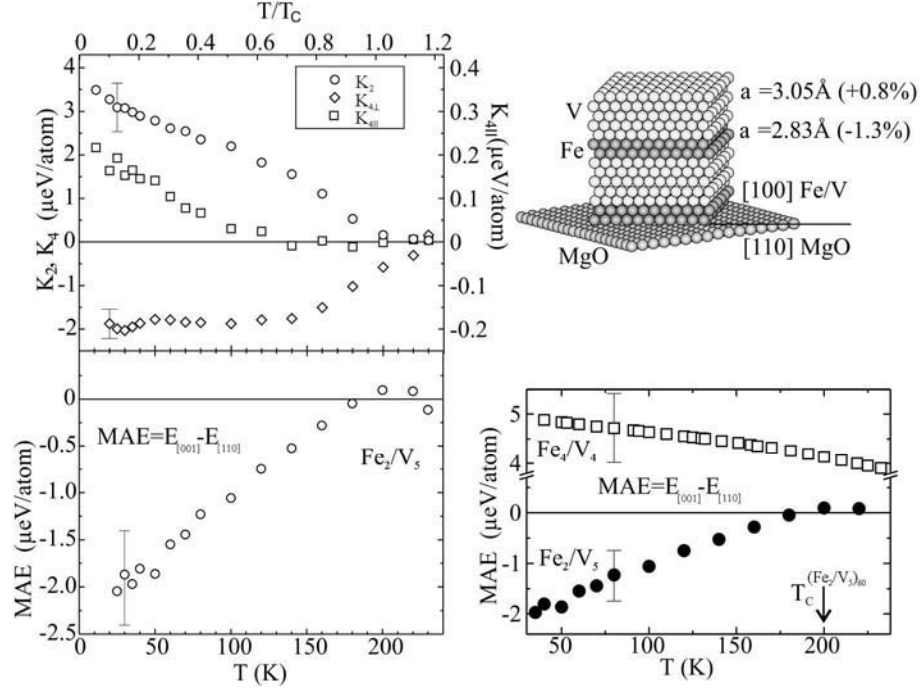


Fig. 7. Schematic drawing of a Fe₂/V₅-multilayer structure grown on an MgO single crystal. Temperature dependence of the various anisotropy components K_i as function of the absolute and reduced temperature for both multilayer structures Fe₂/V₅ and Fe₄/V₄ [39].

In the lower panel we show similar results for a thinner Fe₂/V₅ film. From the lower right hand part of Fig.7 it is obvious that Fe₄/V₄ and Fe₂/V₅ show completely different temperature dependencies. This again is an unambiguous demonstration that not only the interface term at the Fe/V-interface contributes to the anisotropy but also the layer 2 and 3 in the film of 4 ML Fe.

A similar type of analysis has been performed for our prototype system Ni/Cu(001). For various samples ranging between 7 and 8 ML a full set of angular dependent FMR measurements over a large range of reduced temperatures $t = 0.2 - 0.9$ were performed (Fig.8). Again K_2 and $K_{4\perp}$ have different signs. For $T \rightarrow 0$ K_2 is only about 3 times larger than $K_{4\perp}$. The fourfold in-plane anisotropy $K_{4\parallel}$ is smaller by about one order of magnitude.

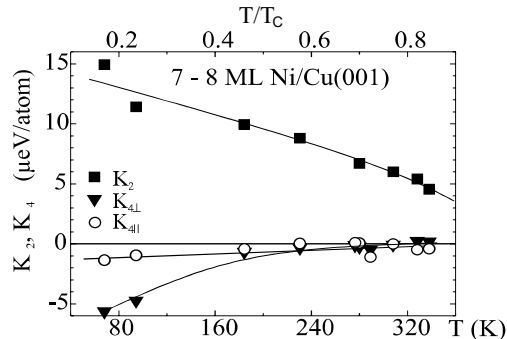


Fig. 8. Temperature dependence of K_2 , $K_{4\perp}$ and $K_{4\parallel}$ for ≈ 7.5 ML Ni/Cu(001) [38].

Finally we turn (Sec.2.1) to the separation of volume and surface part of the anisotropy in thin films. To separate K^S and K^V many thicknesses between 2 and 10 and 15 layers were measured. The result is shown in Fig.9 and compared to a similar experiment for Ni/W(110) films. Within the experimental error bars we see that both systems show the same surface term K_2^S but the volume term K_2^V differs by a factor of 3. In the framework of pseudomorphic growth this can be easily understood: The vacuum and interface contributions for the Ni film may be approximately the same, be it on a Cu or W substrate (mostly Néel type). However the growth and that is to say the tetragonal distortion is very much different for the two systems. On Cu(001) substrate the film grows up to 15 ML pseudomorphic with a tetragonal distortion described in Sec.2.1. On W(110) only the first 2-3 layers are distorted. For thicker films Ni grows bulk-like. In other words the K^V contribution is much smaller. A more detailed description goes beyond the present overview, we refer to [38].

In conclusion: the angular dependence of the intrinsic anisotropy is in theory and experiment well understood and explains nicely continuous as well as abrupt spin reorientation transitions. The temperature dependence of the anisotropy as shown experimentally in Fig.6-9 needs new theoretical input. The classical work for magnetic insulators is based on a discrete multiplet structure which is populated by Boltzmann statistics. For Fe, Co, Ni ferromagnets an itinerant theory of ferromagnetism at finite temperatures would be adequate.

3 Anisotropic Magnetic Moments

Several of the recent popular experimental techniques to investigate itinerant ferromagnets depend on the existence of a uniform magnetization (be it macroscopic or microscopic), e.g. spin-polarized photoemission, magneto-optic Kerr effect, etc.. The magnetic response in these techniques vanishes if the magnetization, that is to say the expectation value $\langle S_z \rangle$, vanishes. In some of the literature it is stated that the ‘magnetic moment vanishes at T_C ’. Similar interpretation is

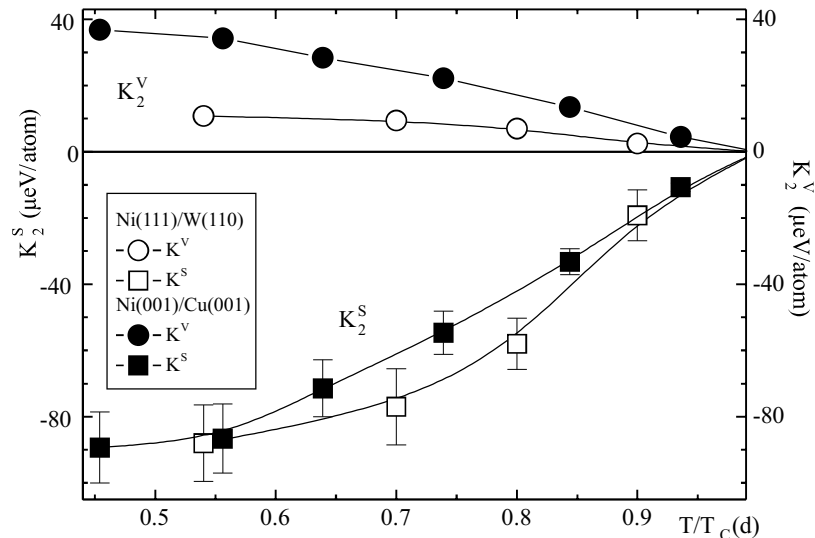


Fig. 9. Separation of the intrinsic anisotropy into surface and volume contributions for Ni(111)/W(110) and Ni(001)/Cu(001) and its temperature dependence. Note that such a diagram should be only plotted as function of the reduced temperature because by changing the thickness of the film also the Curie-temperature $T_C(d)$ changes.

given if experimental findings are explained within the Stoner-Wolfarth model only. This can hardly explain the existence of magnetic moments per atom above T_C . On the other hand it is well established for more than 70 years that Fe, Co and Ni show a Curie-Weiss like behaviour above their Curie-temperatures. In the discussion of band ferromagnetism we would like to turn the focus again on the expectation value $\langle S^2 \rangle$. If for simplicity we ignore higher order effects of kT at the Fermi energy E_F , one might say that the magnetic moment per atom in ferromagnets like Fe, Co and Ni has a fixed (not integer) value which is temperature independent above and below T_C . For a detailed discussion of the distinction between $\langle S_z \rangle$ and $\langle S^2 \rangle$ see [40]. A good quantity to describe the magnetic moment/atom is the g -value or the g -tensor in solids respectively. Appropriate experimental techniques to determine this quantity are for example the susceptibility or the paramagnetic resonance. In [41] we did follow the magnetic resonance signal in thin Ni films starting in the paramagnetic phase through the phase transition (with spin fluctuations at T_C) into the ferromagnetic phase. Furthermore it is also clear from bulk magnetism that the magnetic moment of Fe, Co, Ni is anisotropic in the bulk, e.g. the magnetic moment for a Ni single crystal along the [111]-direction is larger than along the [001]-direction (Fig.1). This anisotropy in the bulk is quite small, but finite [17].

3.1 g-Tensor

The tensor character of g originates from the non-spherical charge distribution of the d-shell, that is to say of a not complete quenching of the orbital momentum. Strictly speaking $\langle L_z \rangle \neq 0$. We refer to Kittel's formula

$$\frac{g-2}{2} = \frac{\mu_L}{\mu_S} \quad (7)$$

It is known that the ' g -factor' for bulk Fe, Co, Ni is $g \geq 2$. It ranges from $g = 2.09$ for Fe to $g = 2.18$ for Co and $g = 2.21$ for Ni. In other word we have always an admixture of 4 – 10 % of orbital magnetism. For bulk magnetism this is tabulated in textbooks [18]. We also see that within second order perturbation theory the departure from $g = 2$ comes from the same type of matrix element the anisotropy energies [28]. We note that this reason for anisotropy in the magnetic moment and anisotropy energy does not depend on the use of a localized picture; it applies equally for d-bands within an itinerant picture [42].

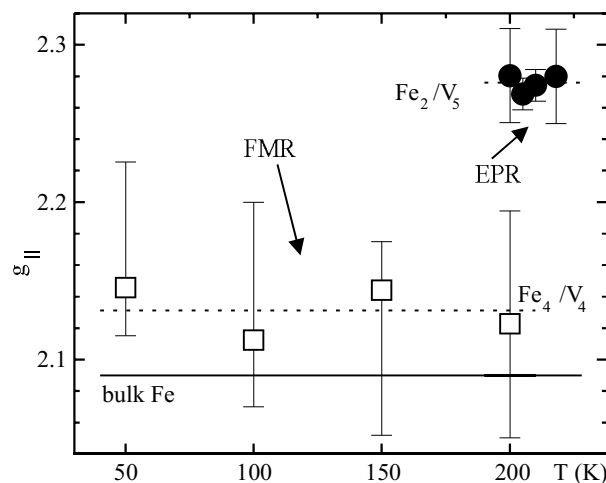


Fig. 10. g -tensor component in the film plane ($g_{||}$) of Fe_n/V_m -multilayers [43]. Note that within the error bars the g -values (i.e. the magnetic moment) are temperature independent.

In Sec.2.1 we have demonstrated that in thin film magnetism the departure of the crystallographic structural from cubic symmetry caused by pseudomorphic growth leads to lower (tetragonal) symmetries. On that basis we must conclude that also the g -value for itinerant ferromagnets departs stronger from $g = 2$ compared to bulk single crystals. As an example we show in Fig.10 $g_{||}$ (in plane) for ultrathin Fe_n/V_m -multilayers. The figure shows the bulk g -value of Fe to be

$g = 2.09$. The Fe_4/V_4 -multilayer has a Curie-temperature $T_C \geq 500$ K. In Fig.10 we show the determination of $g_{||}$ in the ferromagnetic phase from 50 – 200 K to be $g = 2.13$. If one reduces the Fe-thickness down to Fe_2/V_5 the Curie-temperature decreases to $T_C \approx 200$ K. Its g -value in the paramagnetic phase was determined to be $g = 2.26$. Qualitatively this can be easily understood from the schematic drawing in Fig.7. For two layers of Fe, each of the Fe-layers faces an interface with a ‘stronger symmetry breaking’ and one ends with less quenching of $\langle L_z \rangle$. A detailed discussion with correlation to the change of the easy axis of magnetization etc. will be published elsewhere.

3.2 X-ray Magnetic Circular Dichroism at 3d L-Edges

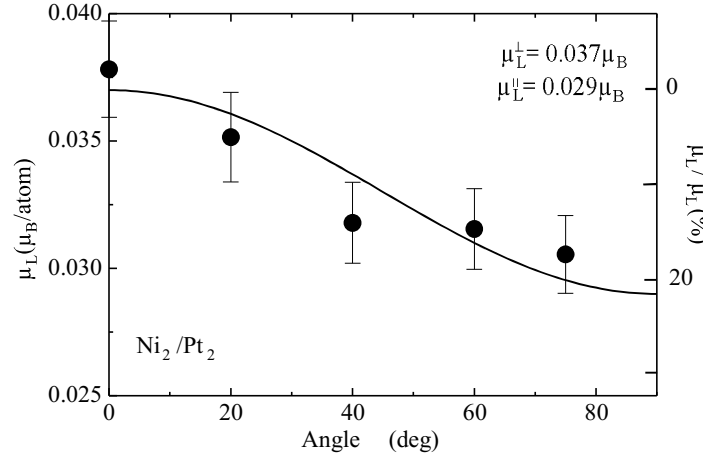


Fig. 11. Anisotropy of the orbital moment μ_L for Ni_2/Pt_2 -multilayers determined from XMCD [44]. Although the absolute value of μ_L is small its relative change is dramatically large, namely 22 %.

The recent progress in XMCD [7,8,9,10,11] allows also to determine the orbital moment μ_L and spin moment μ_S (see also the chapter by H. A. Dürr in this book). Using the sum rules for the analysis of $L_{3,2}$ edge XMCD one may determine the orbital moment μ_L and its anisotropy $\Delta\mu_L$. As an example [44] we show the angular dependent XMCD for a Ni_2/Pt_2 -multilayer structure in Fig.11. This film has its easy axis of magnetization perpendicular to the film plane, i.e. at $\theta = 0^\circ$. Fig.11 shows that for this direction the orbital moment is largest and reduces for the in-plane ($\theta = 90^\circ$) direction. This is in accordance with the general rule that the magnetic moment is largest along the easy axis of magnetization (this rule has some exceptions). One might say that μ_L/atom is very small (left hand y -axis). On the other hand the relative change in % is extremely large, namely 22 %. Since the total moment per Ni-atom is very small

$\approx 0.6\mu_B$, it is no surprise that the orbital moment is only a few % of μ_S . Important is the relative change of μ_L . Indeed the MAE (Sec.2) for these ultrathin Ni/Pt-multilayers is 10 – 100 times larger compared to a bulk Ni single crystal [44].

Finally we note that a precise determination of μ_L from XMCD relies on a proper determination of the area under the dichroic signal at the L_3 - and L_2 -edges. The application of the sum rules [9,10] is underlying a localized picture, namely to assume a step-like change of the absorption coefficient at the $L_{3,2}$ -edges. Further theoretical work will be needed for an adequate description of itinerant systems [45]. These authors separate the configuration of occupied electron states in Ni into a localized and delocalized part. First attempts to separate one-electron and multi-electron features as well as localized and delocalized parts in the analysis of XMCD for Ni has been made [46].

4 Summary

In this contribution we tried to distinguish between anisotropic magnetic moments and macroscopic anisotropy energies. In most solids with lower than cubic symmetry the magnetic moment per atom is anisotropic also in the paramagnetic phase. The moments are randomly oriented: with equal population along \pm -direction and the net magnetization is zero ($\langle\mu_z\rangle = 0$). Only below the ordering temperature at which a cooperative alignment of the moments starts we measure a net magnetization $\langle\mu_z\rangle \neq 0$. To rotate this magnetization from the easy axis (lowest energy) into the hard direction costs energy. This energy increases by reducing the temperature up to its maximum value at $T = 0$. In the framework of second order perturbation theory it is said that the anisotropy energy is proportional to the anisotropy of the orbital magnetic moment $K \propto \Delta\mu_L$. That can hold only for $T = 0$.

The enormous research on ultrathin films and nanostructures opened a complete new field in experiment and theory to study the fundamental understanding of magnetism: In the research of bulk magnetism we did have only three fixed Curie-temperatures for Fe, Co and Ni (≈ 1000 K, ≈ 1300 K, ≈ 600 K). In ultrathin films due to finite size effects we are now in a position to manipulate for each of the 3 ferromagnets the Curie-temperature from its bulk value down to almost zero K (for 1.6ML Ni a T_C of 36 K has been measured). Consequently, susceptibility, g -tensor, MAE and other measurements can be performed for the whole temperature range. That is to say, a reduction in film thickness offers not only a transition from 3D \rightarrow 2D, it is equally interesting to manipulate the ordering temperature. New experiments and theory which clearly distinguish between the two observables $\langle\mu^2\rangle$ and $\langle\mu_z\rangle$ will lead to a better understanding of basic properties of magnetism.

Acknowledgment

We enjoyed fruitful collaboration with theory groups of B. Johansson, O. Eriksson, K. H. Bennemann, W. Nolting, P. Weinberger, H. Ebert, R. Wu as well as

the experimental groups of K. Heinz, D. Arvanitis. J. Lindner is acknowledged for preparation of this manuscript and helpful comments. The work is supported by BMBF, Grant 05 SC8 KEA-3 and DFG, SFB 290.

References

1. S. Chikazumi: *Physics of Magnetism*, 2nd edn. (John Wiley, New York 1964) and S. Chikazumi, C. D. Graham, JR: *Physics of Ferromagnetism*, 2nd edn. (Oxford University Press, 1997)
2. E. Kneller: *Ferromagnetismus*, (Springer, Berlin, Göttingen, Heidelberg 1962)
3. B. Coqblin: *The electronic Structure of Rare-Earth Metals and Alloys: The magnetic Heavy Rare-Earths*, (Academic Press London, New York, San Francisco 1977)
4. J. Kübler: *Theory of Itinerant Electron Magnetism*, (Clarendon Press, Oxford 2000)
5. B. Heinrich and J. A. C. Bland: *Ultrathin Magnetic Structures*, (Springer, Berlin 1994)
6. A. J. Freeman, S. D. Bader: *Magnetism beyond 2000*, (Elsevier, Amsterdam, Lausanne, New York, Oxford, Shannon, Singapore, Tokyo 1999)
7. B. T. Thole et al.: Phys. Rev. Lett. **55**, 268 (1985); G. van der Laan et al.: Phys. Rev. B **34**, 6592 (1986)
8. G. Schütz, W. Wagner, W. Wilhelm, P. Kienle, R. Zeller, R. Frahm, G. Materlik: Phys. Rev. Lett. **58**, 737 (1987)
9. B.T. Thole, P. Carra, F. Sette, G. van der Laan: Phys. Rev. Lett. **68**, 1943 (1992); P. Carra, B. T. Thole, M. Altarelli, X. Wang: Phys. Rev. Lett. **70**, 694 (1993)
10. M. Altarelli: Phys. Rev. B **47**, 597 (1993)
11. A. Ankudinov, J. J. Rehr: Phys. Rev. B **51**, 1282 (1995)
12. R. Q. Wu, L. J. Chen, A. Shick, A. J. Freeman: J. Magn. Mater. **177-181**, 1216 (1998)
13. J. Trygg, B. Johansson, O. Eriksson, J. M. Wills: Phys. Rev. Lett. **75**, 2871 (1995); O. Eriksson, B. Johansson, R. C. Albers, A. M. Boring, M. S. S. Brooks: Phys. Rev. B **42**, 2707 (1990)
14. G. Y. Guo, H. Ebert, W. M. Temmerman: J. Phys.: Condensed Matter **3**, 8205 (1991)
15. G. T. Rado, H. Suhl: *Magnetism*, vol. 1-5, (Academic Press New York, London 1973)
16. Callen H B and Callen E R: J. Phys. Chem. Solids **27**, 1271 (1966)
17. Landolt-Börnstein: *Vol.III/19a, ed. by H.P.J. Wijn*, (Springer-Verlag, Heidelberg 1986)
18. A. Abragam, B. Bleaney: *Electron Paramagnetic Resonance of Transition Ions*, (Clarendon Press, Oxford 1970)
19. A. Hubert, R. Schäfer: *Magnetic Domains* (Springer, Heidelberg 1998)
20. K. Baberschke: Surf. Sci. Lett. **6**, 735 (1999)
21. O. Hjortstam, K. Baberschke, J. M. Wills, B. Johansson, O. Eriksson: Phys. Rev. B **55**, 15026 (1997)
22. W. Platow, U. Bovensiepen, P. Pouloupoulos, M. Farle, K. Baberschke, L. Hammer, S. Walter, S. Müller, K. Heinz: Phys. Rev. B **59**, 12641 (1999)
23. B. Schulz and K. Baberschke: Phys. Rev. B **50**, 13467 (1994)
24. X. Wang, R. Wu, D.-S. Wang, A. J. Freeman: Phys. Rev. B **54**, 61 (1996)
25. L. Néel: J. Physique Radium **15**, 376 (1954)

26. U. Gradmann: J. Magn. Magn. Mater. **100**, 481 (1991); U. Gradmann: J. Magn. Magn. Mater. **54/57**, 733 (1986)
27. M. Farle, W. Platow, E. Kosubek, K. Baberschke: Surf. Sci. **439**, 146 (1999)
28. K. Baberschke: Appl. Phys. A **62**, 417 (1996)
29. C. Uiberacker, J. Zabloudil, P. Weinberger, L. Szunyogh, C. Sommers: Phys. Rev. Lett. **82**, 1289 (1999)
30. K. Baberschke, M. Farle: J. Appl. Phys. **81**, 5038 (1997)
31. A. Aspelmeier, F. Gerhardter, K. Baberschke: J. Magn. Magn. Mater. **132**, 22 (1994)
32. E. D. Tober, R. X. Ynzunsa, C. Westphal, C. S. Fadley: Phys. Rev. B **53**, 5444 (1996)
33. M. Farle, K. Baberschke: Phys. Rev. Lett. **58**, 511 (1987) and M. Farle, A. Berghaus, K. Baberschke: Phys. Rev. B **39**, 4838 (1989)
34. B. Heinrich, K. B. Urquhart, A. S. Arrott, J. F. Cochran, K. Myrtle, S. T. Purcell: Phys. Rev. Lett. **59**, 1756 (1987)
35. A. Berghaus, M. Farle, Yi Li, K. Baberschke: Springer Proc. in Physics **50**, 61 (1989)
36. P. Poulopoulos, K. Baberschke: J. Phys.: Condensed Matter **11**, 9495 (1999)
37. M. Farle, B. Mirwald-Schulz, A. Anisimov, W. Platow, K. Baberschke: Phys. Rev. B **55**, 3708 (1997) and M. Farle, W. Platow, A. Anisimov, B. Schulz, K. Baberschke: J. Magn. Magn. Mater. **165**, 74 (1997)
38. M. Farle: Rep. Prog. Phys. **61**, 755 (1998)
39. A. N. Anisimov, W. Platow, P. Poulopoulos, W. Wisny, M. Farle, K. Baberschke, P. Isberg, B. Hjörvarsson, R. Wäppling: J. Phys.: Condens. Matter **9**, 10581 (1997)
40. D. K. Wohlleben, B. R. Coles in vol. 5 of ref. 15 and references therein
41. Y. Li, K. Baberschke: Phys. Rev. Lett. **68**, 1208 (1992)
42. P. Bruno: Phys. Rev. B **39**, 865 (1989)
43. A. N. Anisimov, M. Farle, P. Poulopoulos, W. Platow, K. Baberschke, P. Isberg, R. Wäppling, A. M. N. Niklasson, O. Eriksson : Phys. Rev. Lett. **82**, 2390 (1999)
44. F. Wilhelm, P. Poulopoulos, P. Srivastava, H. Wende, M. Farle, K. Baberschke, M. Angelakeris, N. K. Flevaris, W. Grange, J.-P. Kappler, G. Ghiringhelli, N. B. Brookes: Phys. Rev. B **61**, 8647 (2000)
45. A. L. Ankudinov, A. I. Nesvizhskii, J. J. Rehr: J. Synchrotron Rad. **8**, XXX (2001)
46. A. I. Nesvizhskii, A. L. Ankudinov, J. J. Rehr, K. Baberschke: Phys. Rev. B **62**, 15295 (2000)

Anisotropic Magnetic Ground-State Moments Probed by Soft X-Ray Spectroscopy

H.A. Dürr

Institut für Festkörperforschung, Forschungszentrum Jülich, 52425 Jülich, Germany

Abstract. The description of the itinerant ferromagnetic ground state in terms of a bandstructure approach has been very successful in providing detailed information about valence-band exchange splitting, quasiparticle effects, etc. An alternative picture is the expansion of electronic and magnetic ground-state properties into multipole moments. Vector moments such as orbital and spin magnetic moments are their best-known representatives. This approach allows a very natural extension to describe higher-order spin-orbit correlation effects. Spin-orbit coupling is known to link the electron spins to the crystal lattice, thus, causing a preferred direction of magnetization in ferromagnetic materials. Of special interest is the directional anisotropy of the orbital magnetic moment and the spin-orbit expectation value. These two quantities probe directly the microscopic origin of the magneto-crystalline anisotropy. We will demonstrate for several examples how these properties can be measured element and atomic site resolved with soft x-ray resonant scattering techniques.

1 Introduction

The interfaces between magnetic and non-magnetic layers are of high importance for many magnetic properties such as the magneto-crystalline anisotropy (MCA). A spin orientation perpendicular to the layers is, for instance, preferred for magneto-optical recording applications. When the layer thickness is only a few atomic layers the electronic structure displays a quasi two-dimensional behavior. This and the anisotropy of the electronic bonding at the interfaces can lead to a spin orientation perpendicular to the layers [1]. The MCA then overcomes an in-plane shape anisotropy which is caused by dipole-dipole interactions between the magnetic moments.

The microscopic origin of MCA is thought to be spin-orbit coupling. In bulk $3d$ transition metals the spin-orbit coupling is nearly quenched due to a large crystalline field and it is only the small orbital part of the wavefunction that ties the spins to a crystalline direction. The broken symmetry at interfaces can strongly enhance the orbital moment. Bruno [2] has shown that under certain conditions the MCA is directly proportional to the anisotropy of the orbital moment expectation value. This model was qualitatively corroborated using magnetic circular x-ray dichroism (MCXD) [3,4,5,6] (for a more in-depth review we refer the interested reader to the chapter by K. Baberschke). In the Bruno model spin-flip terms were neglected which can contribute significantly to the MCA [7]. This has lead van der Laan to propose a direct measurement of the MCA by probing the anisotropy of the spin-orbit expectation value with magnetic linear

x-ray dichroism (MLXD) [8]. Recently Dhesi et al. have shown the experimental feasibility of this approach [9]. All of these methods are based on x-ray absorption spectroscopy and suffer from the drawback that interface properties such as MCA are only indirectly accessible through a variation of the magnetic and non-magnetic layer thicknesses. The lattice mismatch at the interface can then easily lead to undesired structural changes.

These problems can be overcome by utilizing x-ray resonant magnetic scattering (XRMS) techniques [10,11,12,13]. The observation of huge resonant enhancements of the x-ray magnetic diffraction intensity near an absorption edge in actinide compounds, and the more modest, but still useful, enhancements in lanthanides has made this technique a unique element-sensitive magnetic probe for these materials. The largest class of magnetic materials in technological applications and fundamental research contains transition metals which were so far inaccessible to conventional XRMS studies since they display no strong resonances in the hard x-ray region. However, in the soft x-ray region the $L_{2,3}$ edges of 3d transition metals are displaying very strong resonant enhancements which can be utilized for XRMS experiments. Soft x-ray resonances at the rare earth $M_{4,5}$ edges are also vastly more intense than their hard x-ray counterparts, enabling unprecedented sensitivity and a wide range of experimental configurations. It is in general possible but cumbersome to disentangle geometry and magnetism in the scattering signal. In the following we want to review XRMS experiments on 3d transition metals where through a special choice of the magnetic domain structure the magnetic scattering signal can be measured directly. This will allow us to probe the interface MCA as proposed in ref. [8].

2 Magneto-Crystalline Anisotropy and Ground-State Moments

The magnetic anisotropy measures the change in ground-state energy with the direction of magnetization. It consists of two contributions due to the dipole-dipole interaction between magnetic moments and an electronic contribution, the MCA. The MCA energy, E_{MCA} is given by the spin-orbit coupling in the material. In 3d transition metals the crystalline field is of the order 1-2 eV. Spin-orbit coupling is much weaker, ca. 40-80 meV, and can be treated as a perturbation [2]. Its contribution to the Hamiltonian is

$$\mathbf{H}_{ls} = \xi \mathbf{l} \cdot \mathbf{s} = \xi l_z s_z + \xi \frac{1}{2} [l_+ s_- + l_- s_+] \quad (1)$$

where ξ and $\lambda = \mathbf{l} \cdot \mathbf{s}$ are the radial and angular part, respectively, of the spin-orbit operator [14]. In a perturbation expansion \mathbf{H}_{ls} mixes an unperturbed state $|gr\rangle$ of energy E_{gr} with excited states $|ex\rangle$ of energy E_{ex} . The first non-zero contribution to the spin-orbit expectation value is of second order and given by [2,14,8,15]

$$\langle \mathbf{l} \cdot \mathbf{s} \rangle = 2\xi \sum_{ex} \frac{|\langle gr | \mathbf{l} \cdot \mathbf{s} | ex \rangle|^2}{E_{gr} - E_{ex}} \quad (2)$$

Comparing Eq. (2) with the second-order contribution to the ground-state energy, $E^{(2)}$, gives

$$E^{(2)} = \frac{1}{2}\xi\langle\mathbf{l} \cdot \mathbf{s}\rangle \quad (3)$$

If we neglect spin-flip terms caused by the ladder operators $\mathbf{l}_{\mp}\mathbf{s}_{\pm}$ in Eq. (1) and assume that the majority spin states are completely filled as would be the case for a 'hard' ferromagnet we obtain the Bruno formula [16]

$$E^{(2)} = -\frac{1}{4}\xi\mathbf{M} \cdot \langle\mathbf{l}\rangle \quad (4)$$

Here \mathbf{M} is a unit vector along the spin direction and $\langle\mathbf{l}\rangle$ is the expectation value of the orbital magnetic moment. The minimum energy in Eq. (4) corresponds to the easy magnetization direction, ε , along which a spontaneous magnetization would occur. The MCA energy, E_{MCA} , can now be obtained by a difference measurement with the spins aligned parallel and perpendicular to ε , i.e. $E_{MCA} = E_{\perp}^{(2)} - E_{\parallel}^{(2)}$. This can be done using MCXD to probe $\langle\mathbf{l}\rangle$ [3,4] or MLXD to obtain $\langle\mathbf{l} \cdot \mathbf{s}\rangle$ [8,9]. If, however, E_{MCA} is large which is usually the case for a perpendicular easy magnetization axis [17] this method has the drawback that large magnetic fields are required to magnetically saturate the sample along the hard magnetization axis. It would, therefore, be advantageous to measure E_{MCA} , through the anisotropy of $\langle\mathbf{l} \cdot \mathbf{s}\rangle$, directly. From Eq. (2) we can calculate the angular dependence of $\langle\mathbf{l} \cdot \mathbf{s}\rangle$ when the spins are forcefully aligned along \mathbf{M} and obtain [8]

$$\langle\mathbf{l} \cdot \mathbf{s}\rangle = \langle\lambda_i\rangle + \langle\lambda_a\rangle\frac{1}{2}[3(\varepsilon \cdot \mathbf{M})^2 - 1] \quad (5)$$

In a difference measurement the isotropic part, $\langle\lambda_i\rangle$, cancels and the anisotropy of $\langle\mathbf{l} \cdot \mathbf{s}\rangle$ is given directly by the spin-orbit quadrupole moment $\langle\lambda_a\rangle = \frac{1}{2}[3\langle l_z s_z \rangle - \langle\mathbf{l} \cdot \mathbf{s}\rangle]$. Eq. (5) shows that $E_{MCA} = \frac{3}{4}\langle\lambda_a\rangle$ can be determined by obtaining $\langle\lambda_a\rangle$ in a collinear geometry, e.g. with $\mathbf{M} \parallel \varepsilon$. We will demonstrate in the following how $\langle\lambda_a\rangle$ can be measured directly with XRMS.

3 The X-Ray Resonant Magnetic Scattering Amplitude

The scattering signal measured in a diffraction experiment, $I \propto |\sum_n e^{i\mathbf{q} \cdot \mathbf{r}_n} f_n|^2$ (where \mathbf{q} is the wavevector transferred in the scattering process), is the modulus square of the sum over all lattice sites, \mathbf{r}_n , of the scattering amplitudes, f_n , weighted by a phase factor. In this chapter we will review how to derive the resonant scattering amplitude and describe its relation to ground-state properties. This is of considerable importance for the interpretation of XRMS experiments. It is not intended to give a rigorous derivation but rather to highlight the salient features and give an application to the important case of 3d transition metal $L_{2,3}$ -edge dipole XRMS.

The resonant scattering amplitude is determined by the $\mathbf{p} \cdot \mathbf{A}$ interaction between x-rays and matter. It is advantageous to expand this term into spherical

Bessel functions $g_l(k_i r)$ and spherical harmonics of $\hat{\mathbf{k}}_i$ and $\hat{\mathbf{r}}$ as: $\mathbf{p} \cdot \mathbf{e}_i g_l(k_i r) \sum_m Y_m^{l*}(\hat{\mathbf{k}}_i) Y_m^l(\hat{\mathbf{r}}_i)$. Here, $\hat{\mathbf{k}}_i$ and \mathbf{e}_i denote a unit vector of the photon momentum of the incident x-ray beam and the x-ray polarization, respectively [18]. Since the Y_m^l are angular momentum eigenfunctions it is possible to apply the framework of angular momentum coupling and obtain the scattering amplitude for 2^L -pole transitions [18,19,20]

$$f^{EL}(\omega) = 2\lambda \sum_{\mu=0}^{2L} \sum_{M=-L}^L T_M^{(\mu)}(\mathbf{e}_0, \hat{\mathbf{k}}_0, \mathbf{e}_f, \hat{\mathbf{k}}_f)_{EL} F_M^{(\mu)}(\omega)_{EL} \quad (6)$$

The significance of Eq. (6) is that it separates the x-ray polarization from the expectation value of the frequency dependent transition operator, $F_M^{(\mu)}(\omega)$. $F_M^{(\mu)}(\omega)$ depends only on the physical properties of the sample. The scattering amplitude is described by the linear combination of tensors of increasing rank μ . The summation can be simplified by considering the symmetry properties of the physical system. A layered magnetic structure is characterized by cylindrical symmetry with the z-axis perpendicular to the layers. In this case only $M = 0$ is a totally symmetric representation that contributes to the M -sums in Eq. (6) [18].

In the following we will be only concerned with the case of electric dipole (E1) transitions of $2p$ core electrons into the magnetic $3d$ shell. The tensor

$$T_0^{(\mu)}(\mathbf{e}_0, \mathbf{e}_f)_{EL} = \frac{1}{2} \sum_{\rho=-1}^1 \langle 1, \rho, 1, -\rho | \mu, 0 \rangle Y_\rho^1(\mathbf{e}_0) Y_\rho^1(\mathbf{e}_f) \quad (7)$$

and similarly

$$F_0^{(\mu)}(\omega) = \sum_{\rho=-1}^1 \langle 1, \rho, 1, -\rho | \mu, 0 \rangle \sum_I \frac{1}{2\lambda_{Ig}} \frac{|\langle g | J_\rho^1 | I \rangle|^2}{\Delta E_{Ig} - \hbar\omega - i\Gamma/2} \quad (8)$$

is then given by the coupling of two vector moments into a scalar ($\mu = 0$), a vector ($\mu = 1$), and a tensor of rank 2 ($\mu = 2$) [18]. This can be visualized by writing out $T_0^{(\mu)}$ in cartesian coordinates as [19]

$$\begin{aligned} T_0^{(0)} &= \frac{3}{16\pi} \mathbf{e}_0 \cdot \mathbf{e}_f \\ T_0^{(1)} &= -\frac{3i}{16\pi} (\mathbf{e}_0 \times \mathbf{e}_f) \cdot \hat{\mathbf{z}} \\ T_0^{(2)} &= \frac{1}{16\pi} [3(\mathbf{e}_0 \cdot \hat{\mathbf{z}})(\hat{\mathbf{z}} \cdot \mathbf{e}_f) - \mathbf{e}_0 \cdot \mathbf{e}_f] \end{aligned} \quad (9)$$

It is important to note that $T_0^{(2)}$ has the angular dependence of a quadrupole moment with a quantization axis along $\hat{\mathbf{z}}$. A similar structure will become apparent in $F_0^{(2)}$ and it will turn out to be this term that measures the quadrupole moments of interest here.

A great simplification of $F_0^{(\mu)}$ is obtained if the energy spread of the intermediate states, $|I\rangle$, is much smaller than the lifetime, Γ , of the core hole. In

this so-called 'fast collision approximation' the resonant denominator in Eq. (8) together with radial integrals can be taken out of the sums and be treated as a constant factor, $R(\omega)$ [20,18]. The resulting expression

$$f^{E1}(\omega) = 2\lambda R(\omega) \sum_{\mu} T_0^{(\mu)}(\mathbf{e}_0, \mathbf{e}_f) M_0^{(\mu)} \quad (10)$$

probes only ground-state properties since the I -sum in Eq. (8) extends over the complete intermediate-state manifold, $|I\rangle$, i.e. $\sum_I |I\rangle\langle I| = 1$. This treatment is identical to the well-known sum-rule analysis in MCXD and MLXD [21,22,8].

Luo et al. [20] showed that the functions $M^{(\mu)}$ in Eq. (10) can be written as linear combinations of spin and orbital coupled tensor operators, $\underline{w}^{xy\mu}$. An orbital moment, x , is coupled with a spin moment, y , into a total moment, μ , which is the multipole moment of the charge and spin distribution in the valence shell [8]. The underscore denotes that the sum over single particle operators is taken over holes instead of electrons. The $3d$ shell contains moments such as the number of holes, $\langle \underline{w}^{000} \rangle = \langle n_h \rangle$, the spin magnetic moment, $\langle \underline{w}^{011} \rangle = -2S_z$, the magnetic dipole term, $\langle \underline{w}^{211} \rangle = -\frac{7}{2}T_z$, the charge quadrupole moment, $\langle \underline{w}^{202} \rangle = \frac{1}{2} \langle l_z^2 - \frac{1}{3}l^2 \rangle$ that are determined by crystalline field effects and the exchange interaction. Of particular interest are, however, such moments that are influenced by spin-orbit coupling such as the spin-orbit coupling itself, $\langle \underline{w}^{110} \rangle = \langle l \cdot s \rangle$, the spin-orbit quadrupole moment, $\langle \underline{w}^{112} \rangle = \frac{3}{2} \langle \lambda_a \rangle$, the orbital magnetic moment, $\langle \underline{w}^{101} \rangle = -\frac{1}{2}L_z$, and the coupling of charge octupole moment and spin moment to a quadrupole moment, $\langle \underline{w}^{312} \rangle$ [20,18,8].

The scattering amplitude for $\mu = 0$ is mainly proportional to the number of holes, i.e. $T^{(0)}M^{(0)} \propto n_h \mathbf{e}_0 \cdot \mathbf{e}_f$. The higher-order moments have to be evaluated relative to a quantization axis, $\hat{\mathbf{z}}$. In general, $\hat{\mathbf{z}}$ and the quantization axes of the orbital, ε , and spin distribution, \mathbf{M} , are different. Van der Laan [8] has shown that this leads to an extra angular dependence $\langle \underline{w}^{xy\mu}(\varepsilon, \mathbf{M}) \rangle$. For instance, we obtain for $\langle \underline{w}^{011}(\varepsilon, \mathbf{M}) \rangle = -2S_z C_0^0(\varepsilon) C_0^1(\mathbf{M})$ where $C_M^L(\theta, \varphi)$ are normalized spherical harmonics [8]. In $3d$ -transition metals the spin moment is much larger than the orbital moment and the magnetic dipole term [21,22,3]. The main contribution to the $\mu = 1$ scattering amplitude, therefore, is from the $\langle \underline{w}^{011} \rangle$ term, i.e. $T^{(0)}M^{(0)} \propto S_z(\mathbf{e}_0 \times \mathbf{e}_f) \cdot \mathbf{M}$. This is identical to the angular dependence derived for the case of a magnetic ion with the magnetic moment oriented along, $\hat{\mathbf{z}}$, given in Eq. (9) [19].

The angular dependence of the quadrupolar scattering amplitude ($\mu = 2$) is more complicated. It consists of a linear combination of $\langle \underline{w}^{202} \rangle$, $\langle \underline{w}^{112} \rangle$ and $\langle \underline{w}^{312} \rangle$ [20,8]. The charge octupole moment ($x = 3$) should be small and we will, therefore, neglect the last term. The charge quadrupole moment is independent of \mathbf{M} , i.e. $\langle \underline{w}^{202} \rangle = q_{zz} C_0^2(\varepsilon) C_0^0(\mathbf{M})$ with $q_{zz} = \frac{1}{2} \langle l_z^2 - \frac{1}{3}l^2 \rangle$ obtained along the quantization axis, ε . This term contributes to the scattering amplitude as $T^{(2)}\langle \underline{w}^{202} \rangle \propto q_{zz}[3(\mathbf{e}_0 \cdot \hat{\varepsilon})(\hat{\varepsilon} \cdot \mathbf{e}_f) - \mathbf{e}_0 \cdot \mathbf{e}_f]$. The spin-orbit quadrupole moment, on the other hand, is determined by crystalline field effects and spin-orbit coupling.

Its angular dependence is given by [8]

$$\langle \underline{w}^{112}(\varepsilon, \mathbf{M}) \rangle = \frac{3}{2} \langle \lambda_a \rangle \sum_{\xi} n^{-1} \begin{pmatrix} 2 & 2 & 2 \\ \xi & -\xi & 0 \end{pmatrix} C_{\xi}^2(\varepsilon) C_{-\xi}^2(\mathbf{M}) \quad (11)$$

where n^{-1} is a normalization factor. This translates into a rather lengthy expression in cartesian coordinates [23] which will not be given here. For our purposes it is sufficient to emphasize that $\underline{w}^{112}(\varepsilon, \mathbf{M})$ is quadratic in both ε and \mathbf{M} . We will see in the next chapter that it is exactly this quadratic dependence on \mathbf{M} that allows us to measure $\langle \lambda_a \rangle$ and to separate it from the other ground-state moments.

4 Applications

In this chapter we will review several experiments that were aimed at separating the three contributions to the $E1$ resonant scattering amplitude in Eq. (6). This approach is based on a well defined magnetic domain structure as shown in Fig. 1. Regular domain patterns are a characteristic feature of many low-dimensional systems with phases stabilized by competing interactions [24]. In ultrathin magnetic films such a domain structure can occur when the electron spins favor to align in a direction perpendicular to the film plane. It is the competition between a perpendicular MCA and the dipolar spin-spin interaction that leads to the regular domain pattern in Fig. 1 [25]. The lowest energy state is characterized by magnetic flux lines that are partially outside the sample. It was predicted already by Kittel [26] half a century ago that internal flux closure should produce a high degree of order in the magnetic domains. In spite of the important fundamental and technological implications for ultrathin films such closure domains with a magnetization direction in the film plane are almost impossible to observe even with modern imaging techniques capable of sufficient lateral resolution such as magnetic force microscopy (MFM). This is due to the fact that these

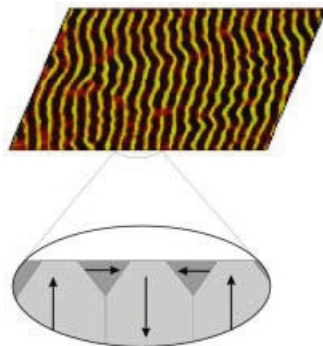


Fig. 1. Magnetic force microscopy image of a $2\mu\text{m} \times 2\mu\text{m}$ area of a 400 Å-thick FePd film grown epitaxially on a MgO(001) substrate [28]

techniques often monitor the magnetic stray field outside the sample as it is the case for MFM and provide hardly any information about the magnetic depth profile within the layer. We will show in the next section that XRMS can easily perform such a task utilizing the first-order ($\mu = 1$) magnetic scattering contribution. The following section will then describe experiments that determine the interface MCA in magnetic multilayers via the $\mu = 2$ scattering term.

4.1 Magnetic Depth Profile of Ultrathin FePd Films

Epitaxial FePd(001) films grow in a crystalline structure that is characterized by alternating Fe and Pd atomic layers. The driving force for the perpendicular spin arrangement in Fig. 1 is the electronic hybridization between Fe 3*d* and Pd 4*d* electrons. At the Fe L_3 absorption edge the magnetic 3*d* valence shell is probed. The x-ray wavelength is with 17.5 Å larger than the atomic spacing but still small enough to probe the magnetic domain periodicity of 900 Å.

The case of regular domain patterns results in an elegant way to separate the three $E1$ scattering contributions in Eq. (6). Using a scattering geometry as shown schematically in Fig. 2(a) the lateral domain periodicity leads to purely magnetic superstructure scattering peaks located symmetrically around the specularly reflected x-ray beam. For structurally well ordered films with smooth interfaces the charge scattering term in Eq. (6) contributes only to the specular peak. The two magnetic terms are linear and quadratic in \mathbf{M} and cause

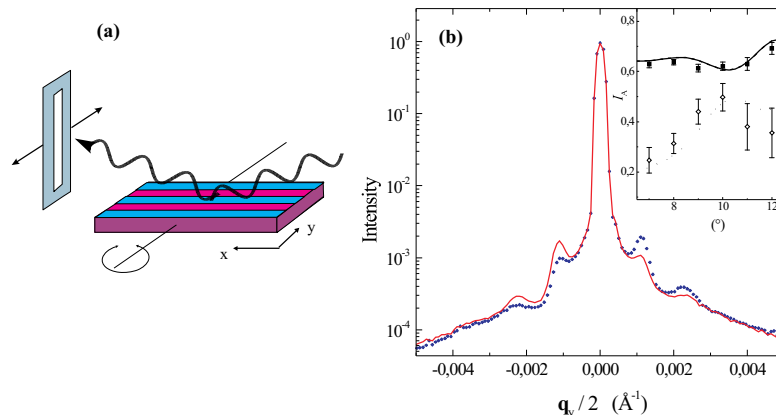


Fig. 2. (a) Experimental geometry with x-rays incident along the stripe direction at grazing angle, Θ . Scattered x-rays were detected by a photodiode mounted behind a rectangular aperture. (b) Diffraction scans with the wavevector, \mathbf{q}_y transferred along the y -axis. Left-circularly polarized (dotted line, I^-) and right-circularly polarized (solid line, I^+) x-rays with energy tuned to the Fe L_3 absorption edge impinge at an angle of $\Theta = 12^\circ$ relative to the surface plane. The inset shows the values of $I_A = (I^+ - I^-)/(I^+ + I^-)$ for first-order (solid symbols) and second-order (open symbols) magnetic satellite peaks. [27]

magnetic peaks at wavevectors τ and 2τ , respectively ($2\pi/\tau$ is the domain periodicity) [10]. The observation of circular dichroism in the XRMS signal, I , i.e. its difference between left- and right-circularly polarized photons, was used in ref. [27] to recover the phase information that is generally lost in diffraction experiments.

In order to assess the scattering from the individual domains in Fig. 1 it is conventional to divide the light polarization into the two linear components σ and π that are perpendicular and parallel to the scattering plane, respectively. For the scattering geometry shown in Fig. 2A and concentrating on the ($\mu = 1$) term in Eq. (9) there are mainly two scattering paths producing π -polarized scattered light [27]. Perpendicular to the film σ -polarized incident radiation experiences a Faraday rotation producing a π component [12,29]. The other channel is $\pi - \pi$ scattering leaving the incident π -polarization unchanged [13]. It occurs when \mathbf{M} has a component perpendicular to the scattering plane as it is the case for the closure domains. Since bulk and closure domains are located at different lateral positions the x-rays scattered from them will experience a phase shift of $\pi/2$. Unfortunately, this phase shift between the $\sigma - \pi$ and $\pi - \pi$ scattering is lost when only one incident light polarization is used. However, the phase information can be retrieved with circularly polarized radiation. Left- and right-circularly polarized light is a combination of σ and π -polarizations where the π component is advanced or retarded with respect to the σ -polarization by a phase shift of $\pi/2$, respectively. As a consequence the scattering of circularly polarized x-rays from bulk and closure domains in Fig. 1 will result in a total phase shift of 0 or π depending on the helicity, i.e. there will be either constructive or destructive interference, respectively, between the two scattering channels. This is expected to result in intensity changes of the magnetic superstructure peaks with incident light helicity that are indicative for the existence of closure domains.

Typical XRMS scans obtained in ref. [27] are displayed in Fig. 2(b). The spectra taken with opposite light helicities show clearly the first-order ($q_y = \pm\tau$) and second-order ($q_y = \pm 2\tau$) magnetic peaks located symmetrically around the specularly reflected x-ray beam. As expected from symmetry arguments the strong circular dichroism in the magnetic peaks reverses sign for negative q_y [27]. The magnetization depth profile was obtained from XRMS spectra measured at different incidence angles [27,30]. The results are collected in the inset of Fig. 2(b) where the ratio of the difference to sum intensities, $I_A = (I^+ - I^-)/(I^+ + I^-)$, is plotted for the first-order (solid symbols) and second-order (open symbols) magnetic peaks. The signals for both magnetic satellite peaks show strong modulations with Θ . This is caused by a change in the phase relationship between closure and bulk domain layer as the wavevector perpendicular to the film is varied. By modeling this variation (lines in the inset of Fig. 2) the closure domain layer thickness of 83 Å was obtained [30]. This corresponds to a significant fraction of the total film thickness (400 Å).

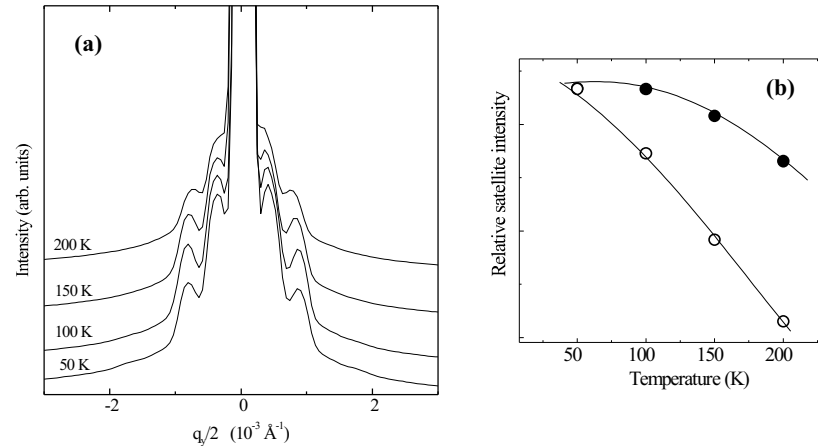


Fig. 3. (a) Fe L_3 -edge XRM scans from a Fe(16Å)/CeH₂(10Å) multilayer measured at the indicated temperatures. (b) Temperature dependence of the normalized and background corrected intensity of the first-order (open circles) and second-order (solid circles) magnetic peaks of the spectra shown in (a) [34]. The lines serve as guides to the eye

4.2 Interface Magneto-Crystalline Anisotropy of Fe/CeH₂ Multilayers

Fe/CeH₂ multilayers display a spin reorientation transition as the temperature is lowered below about $T_R \approx 240\text{K}$ [31]. While above T_R an in-plane spin orientation is favored the spins rotate out-of-plane when the perpendicular MCA overcomes the in-plane shape anisotropy. It has been demonstrated that the MCA is an interface property since the spin reorientation is absent in samples where a LaH₂ layer was inserted at the Fe/CeH₂ interfaces [32]. The microscopic nature of the MCA is, however, still under debate. One explanation could be a strongly temperature dependent MCA of the interface Fe layer. Similar effects have been observed in other itinerant ferromagnets [33]. For the Ce interface atoms a different mechanism can lead to a perpendicular MCA. This is especially pronounced at low temperatures when the indirect exchange coupling between the Fe $3d$ and Ce $4f$ shell mediated by the Ce $5d$ electrons induces a significant $4f$ magnetic moment. In this single-ion anisotropy picture the strong crystalline field of the transition metal interface atoms acting on the large orbital quadrupole moment of the $4f$ shell pulls the spins out-of-plane [35]. In this chapter we will discuss experiments that allow us to differentiate between these two mechanisms by probing the magnetic domain configurations and the MCA element resolved.

Below T_R the magnetic structure of Fe/CeH₂ is again characterized by a multidomain configuration similar to the one shown in Fig. 1. This is apparent from Fe $L_{2,3}$ -edge XRM scans displayed in Fig. 3(a). The spectra were measured with linearly polarized x-rays at an x-ray incidence angle of 15° . As

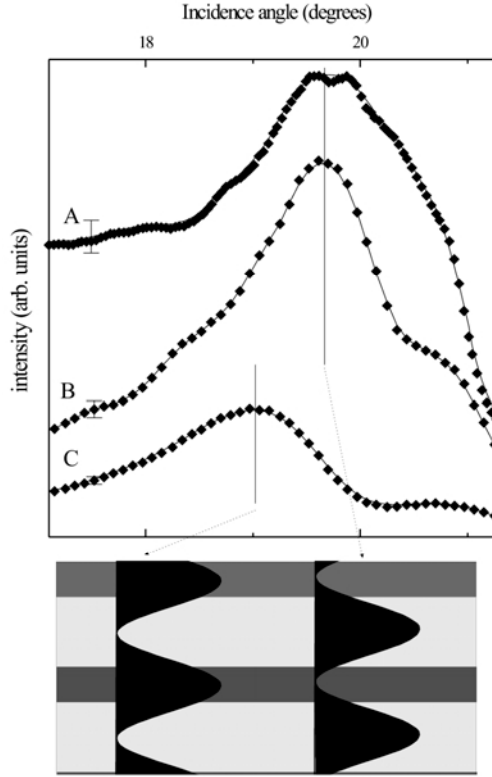


Fig. 4. Intensity changes of A) the specular peak, B) the first-order magnetic peak and C) the second-order magnetic peak as the x-ray incidence angle is varied through the first-order multilayer Bragg condition. The spectra are offset vertically for clarity. Measurements were taken at the Fe L_3 edge for a sample temperature of 200 K. The lower part of the figure shows schematically how the x-ray standing wave field intensity (black sinusoidal areas) varies across the Bragg condition. The Fe and CeH_2 layers are indicated as light and dark shaded areas, respectively [34]

expected for a stripe domain structure they show clearly the two magnetic satellite features located symmetrically around the specular peak. The satellite peaks appear below the spin reorientation transition and become more pronounced as the temperature is lowered further. Also weak fourth-order magnetic peaks become discernible at temperatures of 50 K and below. In addition the domain size, L , varies with temperature. This is evident from the changing position of the magnetic superstructure peaks, $\tau=2\pi/L$. This results in domain sizes between 2200\AA and 2500\AA . The two magnetic scattering signals show distinctly different temperature behaviors. This is clearly visible in Fig. 3(b) which shows the background corrected intensity of the two scattering features for various sample temperatures. While the second-order scattering yield saturates below 100 K the first-order intensity increases down to the lowest measured temperature.

This is a clear indication that the two satellite features measure indeed different magnetic properties as described in section 4.

A further proof would be to show that first- and second-order magnetic scattering originates from different parts of the Fe layer. To this end dynamical scattering effects were used in ref. [34] as a more direct approach to interface magnetism. This technique is well known from structural studies in single crystals where standing x-ray wave fields are set up near certain Bragg conditions [36]. As the transferred wavevector is scanned through the Bragg peak two types of standing wave fields can be produced. They have their intensity maxima either at the position of the atoms or in-between them. Therefore, the amount of absorbed photons and, thus, the diffracted intensity depends on the type of standing wave field. In analogy to this technique wave fields were set up in Fe/CeH₂ multilayers. Interface sensitivity is achieved by tuning the scattering conditions so that the x-ray intensity maxima in the multilayer coincide with the position of the interfaces. This is demonstrated in Fig. 4 where the specular intensity (curve A) together with the first- (curve B) and second-order scattering peak height (curve C) is plotted as the x-ray incidence angle is varied through the first multilayer Bragg condition. At resonance the x-ray structure factor is large enough so that a diffracted wave with sufficient intensity is formed in order to create standing wave fields inside the multilayer. Since at the Fe L₃ resonance the 3*d* valence shell is probed the reflected specular intensity monitors the case when the wave field maxima pass through the Fe layers. With decreasing incidence angle the wave field maxima are continuously shifted towards the CeH₂ layer center [36] and the specular intensity decreases. The sharp intensity decrease at the high-angle side is caused by the reflected x-rays moving partly off the detector. The first-order magnetic satellite intensity follows closely that of

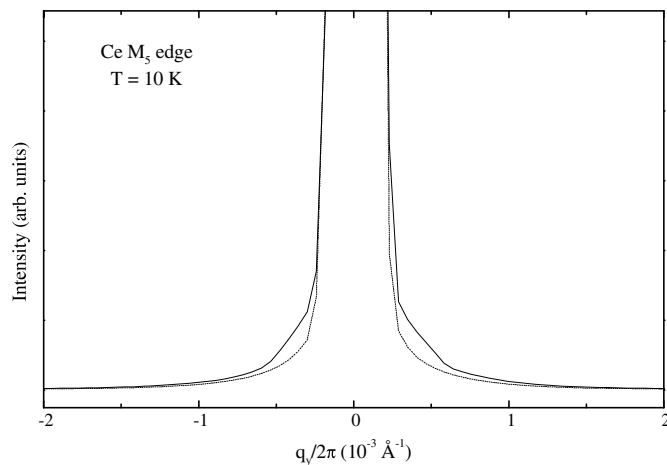


Fig. 5. Ce M_5 -edge X RMS scans from a Fe(16 Å)/CeH₂(10 Å) multilayer measured at 10 K without (solid line) and with an applied field of 1 T (dashed line) [34]

the specular intensity. In contrast the second-order magnetic satellite intensity peaks at significantly different incidence angles corresponding to the position when the wave field maxima move towards the CeH_2 layer centers.

This demonstrates that the first-order scattering contribution probes mainly the Fe $3d$ magnetic moment and is strongest when the wave field maxima are within the Fe layers. The second-order contribution is a measure of the spin-orbit quadrupole moment, $\langle\lambda_a\rangle$. It is localized at the Fe interface layer and largely responsible for the observed spin reorientation. The Fe interface MCA as monitored by the second-order scattering intensity shown in Fig. 3(b) first increases and saturates below 100 K. The first-order scattering intensity still increases in this temperature range indicating that the Fe spins are still not completely aligned along the sample normal. This points to an additional contribution to the total MCA at low temperatures possibly due to a Ce $4f$ single-ion anisotropy. Evidence for such a mechanism comes from XRMS scans at the Ce $M_{4,5}$ -edges in Fig. 5 that monitor the temperature dependence of the Ce $4f$ domain structure. At 100 K and below weak first-order satellite peaks are observed [34] when the domain structure is quenched in an applied magnetic field of 1 T. Although the second-order scattering contribution is too weak to be discernible in these XRMS measurements the strong $4f$ spin-orbit interaction will give rise to a quadrupole moment which can then become aligned by crystalline field effects at the Fe interface, thus, leading to a single-ion anisotropy at the interface.

5 Summary and Outlook

Soft x-ray resonant magnetic scattering has developed into a very valuable tool for element and site resolved studies of magnetic properties. Especially for $3d$ transition metals the magnetic scattering effects are large and allowed a detailed investigation of the magnetic dipole scattering contributions which were shown to probe different magnetic ground-state moments. Although the experiments presented here were restricted to a specific magnetic domain configuration the concepts can be generalized and applied also to single-domain samples. There have even been first attempts to obtain the magnetic moments quantitatively using sum-rule analysis [11]. A vast potential for applications exists. The large magnetic scattering yield makes it possible to study 'dilute' systems such as surfaces of single-layer films [37,38]. Stripe domains seem to be a rather common phenomena in low-dimensional systems. The described scattering experiments can then be applied to study directly the valence shell responsible for spin, charge and orbital ordering in transition metal compounds [39]. With the recent development of high-brilliance synchrotron radiation sources it is possible to use coherent x-rays in order to probe the temporal correlation functions [40] of the various ground-state properties. Furthermore, there have been first attempts to generate femtosecond x-ray pulses [41]. This will enable pump-probe experiments in the not too distant future. Resembling laboratory based laser experiments [42] an optical laser pump-pulse would then be used to drive the system into a non-equilibrium state which is then probed with a time delayed x-ray pulse.

Using soft x-ray resonant magnetic scattering this can be expected to result in unprecedented sensitivity to magnetic relaxation processes.

Acknowledgments

I would like to thank my colleagues and collaborators, especially G. van der Laan, S.S. Dhesi, E. Dudzik, M. Münzenberg, W. Felsch, J.B. Goedkoop and M. Belakhovsky for their help in the experiments described in this chapter and for valuable discussions. The support of the staff of the European Synchrotron Radiation Facility in Grenoble is gratefully acknowledged.

References

1. G.H.O. Daalderop, P.J. Kelly, M.F.H. Schuurmans: 'Magnetic Anisotropy from First Principles'. In: *Ultrathin Magnetic Structures I*, ed. by J.A.C. Bland, B. Heinrich (Springer, Berlin Heidelberg 1994) pp. 40-65.
2. P. Bruno, Phys. Rev. B **39**, 865 (1989).
3. D. Weller, et al. Phys. Rev. Lett. **75**, 3752 (1995).
4. H.A. Dürr, G.Y. Guo, G. van der Laan, J. Lee, G. Lauhoff, J.A.C. Bland, Science **277**, 213 (1997).
5. F. Wilhelm, P. Poupoulos, C. Ceballo, H. Wende, K. Baberschke, S. Srivastava, D. Benea, H. Ebert, M. Angelakeris, N.K. Flevaris, D. Niarchos, A. Rogalev, N.B. Brookes, Phys. Rev. Lett. **85**, 413 (2000).
6. W. Kuch, J. Gilles, S.S. Kang, S. Imada, S. Suga, J. Kirschner, Phys. Rev. B **62**, 3824 (1997).
7. H.A. Dürr, G. van der Laan, J. Vogel, M. Finazzi, J.B. Goedkoop, IEEE Trans. Magn. **MAG-34**, 1201 (1998).
8. G. van der Laan, Phys. Rev. Lett. **82**, 640 (1999); G. van der Laan, Phys. Rev. B **57**, 5250 (1998).
9. S.S. Dhesi, et al., unpublished.
10. D. Gibbs, D.R. Harshman, E.D. Isaacs, D.B. McWhan, D. Mills, C. Vettier, Phys. Rev. Lett. **61**, 1241 (1988).
11. J.-M. Tonnerre, L. Seve, D. Raoux, G. Soullie, B. Rodmacq, P. Wolfers, Phys. Rev. Lett. **75**, 740 (1995).
12. M. Sacchi, C.F. Hague, L. Pasquali, A. Mirone, J.-M. Mariot, P. Isberg, E.M. Gullikson, J.H. Underwood, Phys. Rev. Lett. **81**, 1521 (1998).
13. C. Kao J.B. Hastings, E.D. Johnson, D.P. Diddons, G.C. Smith, G.A. Prinz, Phys. Rev. Lett. **65**, 373 (1990).
14. M. Cinal, D.M. Edwards, Phys. Rev. B **55**, 3636 (1997).
15. D.S. Wang, R. Wu, A.J. Freeman, Phys. Rev. B **47**, 14932 (1993).
16. H.A. Dürr, G. van der Laan, Phys. Rev. B **54**, R760 [1996].
17. W.J.M. de Jonge, P.J.H. Bloemen, F.J.A. den Broeder: 'Experimental Investigation of Magnetic Anisotropy'. In: *Ultrathin Magnetic Structures I*, ed. by J.A.C. Bland, B. Heinrich (Springer, Berlin Heidelberg 1994) pp. 65-86.
18. P. Carra, B.T. Thole, Rev. Mod. Phys. **66**, 1509 (1994).
19. J.P. Hannon, G.T. Trammell, M. Blume, D. Gibbs, Phys. Rev. Lett. **61**, 1245 (1988).
20. J. Luo, G.T. Trammell, J.P. Hannon, Phys. Rev. Lett. **71**, 287 (1993).

21. B.T. Thole, P. Carra, F. Sette, G. van der Laan, Phys. Rev. Lett. **68**, 1943 (1992).
22. P. Carra, B.T. Thole, M. Altarelli, X. Wang, Phys. Rev. Lett. **70**, 694 (1993).
23. M. Blume: 'Magnetic effects in anomalous dispersion'. In: *Resonant Anomalous X-Ray Scattering*, ed. by G. Materlik, C.J. Sparks, K. Fischer (Elsevier Science B.V. 1994) pp. 495-512.
24. M. Seul, D. Adelman, Science **267**, 476 (1995).
25. V. Gehanno, Y. Samson, A. Marty, B. Gilles, A. Chamberod, J. Mag. Mat. **172**, 26 (1997).
26. C. Kittel, Phys. Rev. **70**, 965 (1946).
27. H.A. Dürr, E. Dudzik, S.S. Dhesi, J.B. Goedkoop, G. van der Laan M. Belakhovsky, C. Mocuta, A. Marty, Y. Samson, Science **284**, 2166 (1999).
28. H.A. Dürr, E. Dudzik, S.S. Dhesi, J.B. Goedkoop, G. van der Laan M. Belakhovsky, C. Mocuta, A. Marty, Y. Samson, J. Synch. Rad. **7**, 178 (2000).
29. J.B. Kortright, M. Rice, R. Carr, Phys. Rev. B **51**, 10240 (1995).
30. E. Dudzik, S.S. Dhesi, H.A. Dürr, S.P. Collins, M.D. Roper, G. van der Laan, K. Chesnel, M. Belakhovsky, A. Marty, Y. Samson, Phys. Rev. B **62**, 5797 (2000); E. Dudzik, S.S. Dhesi, S.P. Collins, H.A. Dürr, G. van der Laan, K. Chesnel, M. Belakhovsky, A. Marty, Y. Samson, J.B. Goedkoop, J. Appl. Phys. **87**, 5469 (2000).
31. O. Schulte, F. Klose, W. Felsch, Phys. Rev. B **52**, 6480 (1995).
32. M. Arend, W. Felsch, G. Krill, A. Delobbe, F. Baudet, E. Dartyge, J.-P. Kappler, M. Finazzi, A. San Miguel-Fuster, S. Pizzini, A. Fontaine, Phys. Rev. B **59**, 3707 (1999).
33. P. Pouloupoulos, K. Baberschke, J. Phys.: Condens. matter **11**, 9495 (1999).
34. H.A. Dürr, M. Münzenberg, W. Felsch, S.S. Dhesi, Appl. Phys. A, in press (2001).
35. L.T. Baczewski, M. Piecuch, J. Durand, G. Marchal, P. Delcroix, Phys. Rev. B **40**, 11237 (1989).
36. B.W. Batterman, H. Cole, Rev. Mod. Phys. **36**, 681 (1964).
37. J.F. MacKay, C. Teichert, D.E. Savage, M.G. Lagally, Phys. Rev. Lett. **77**, 3925 (1996).
38. J.W. Freeland, K. Bussmann, P. Lublitz, Y.U. Idzerda, Appl. Phys. Lett. **73**, 2206 (1998).
39. C.W.M. Castleton, M. Altarelli, Phys. Rev. B **62**, 1033 (2000).
40. M. Sutton, et al., Nature **353**, 609 (1991).
41. R.W. Schoenlein, S. Chattopadhyay, H.H.W. Chong, T.E. Glover, P.A. Heimann, C.V. Shank, A.A. Zholents, and M.S. Zolotarev, Science **287**, 2237 (2000).
42. A.Scholl, L. Baumgarten, R. Jacquemin, W. Eberhardt, Phys. Rev. Lett. **79**, 5146 (1997).

First Principles Determination of Magnetic Anisotropy and Magnetostriction in Transition Metal Alloys

Ruqian Wu

Department of Physics & Astronomy, California State University,
Northridge, CA 91344-8268

Abstract. First-principles electronic structure studies based on local spin density functional theory and performed on extremely complex simulations of ever increasingly realistic systems, play a very important role in explaining and predicting various magnetic properties. This review deals with one of the most challenging issues for first-principles theory, namely the determination of magnetostriction in transition metal systems. As is demonstrated, extensive first-principles calculations and model analyses provide simple physical insights for this complex phenomenon.

1 Introduction

State-of-the-art ab initio density functional electronic structure calculations have achieved great success in the exciting field of thin film magnetism, in both explaining existing phenomena and, more importantly, in predicting the properties of new systems [1,2]. The prediction of enhanced magnetic moments with lowered coordination number at clean metal surfaces and interfaces has stimulated theoretical and experimental investigations for new magnetic systems and phenomena in man-made transition metal thin films, which has accompanied the renaissance of magnetism in the last decade. The giant magneto-resistance in spin valves and other magnetic multilayers has already had a major impact on the magnetic recording industry [3,4,5].

Anisotropic magnetostriction, as sketched in Fig. 1, is generally described as the deformation of a body in response to a change in its direction of magnetization through application of a magnetic field. In many technical applications such as for electric transformers, motor shielding, and magnetic recording, magnetic materials with extremely small magnetostrictive coefficient, λ (defined as $\lambda \propto \Delta l/l$), are required. By contrast, materials with large λ are needed for many applications in electromagnetic micro devices as actuators and sensors [6,7]. The strongest magnetostriction (λ can be up to 10^{-2}) was found in either elementary rare earth metal (under low temperature and high magnetic field) and in various compounds with rare earth metals and transition metals [8,9].

Despite the tremendous advances in modern electronic structure theory for studies in materials science, magnetostriction has been rarely attacked until very recently, due to its intrinsic complexity. In principle, the magnetostrictive coefficient λ can be determined through two separate total energy optimizations

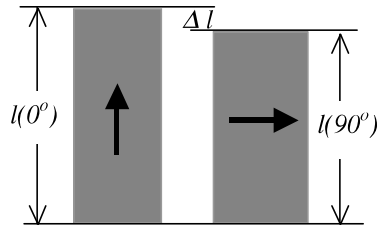


Fig. 1. Sketch of anisotropic magnetostriction.

for $\lambda(0^\circ)$ and $\lambda(90^\circ)$ of a given system. The main difficulty is that the energy separation for these two directions, the so-called magneto-crystalline anisotropy (MCA) energy ($E_{MCA} = E(90^\circ) - E(0^\circ)$) due to spin-orbit coupling (SOC), is extremely small (a few meV/atom) in most of transition metal systems, especially those with cubic symmetry. Using the torque[10] approaches based on the full-potential linearized augmented plane wave (FLAPW) method [11], we can now obtain a highly reliable MCA energy (with a precision up to $0.2 \mu\text{eV}/\text{atom}$ in some cases) and its strain dependence, a key gradient for magnetostriction.

The aim of the present review is to provide some examples of our recent theoretical developments for the determination of magnetostriction using the expanded capabilities and new functionalities of the FLAPW method. The results presented here indicate that high quality ab initio calculations of magnetic systems can achieve high accuracy and precision for magnetostriction in a wide range of transition metal and rare-earth metal systems.

2 Methodology

2.1 FLAPW Approach

In the thin film version of the FLAPW method, the space is divided into three regions, namely, the near nucleus muffin-tin region, the vacuum region and the remaining interstitial region [11]. The wave function, potential and charge density are expanded in a “natural” way without any artificial shape approximations, which ensures the accuracy and precision of electronic properties obtained through FLAPW calculations. Single particle Kohn-Sham equations are solved self-consistently until the root-mean-square difference between the input and output charge densities is less than $1.0 \times 10^{-4} \text{ e/a.u.}^3$. The exchange-correlation interactions among electrons are described by using either the local density approximation (LDA, von-Barth-Hedin formula [12]) or the generalized gradient approximation (GGA, Perdew-Burke-Ernzerhof formula [13]). The core states are treated fully relativistically (by solving the Dirac equations), while the valence states are treated semi-relativistically [14]. To investigate magnetostriction and magneto-crystalline anisotropy, the SOC is invoked second-variationally. Atomic structures are optimized using total energies and atomic forces.

2.2 Spin-Orbit Coupling and Magneto-crystalline Anisotropy

As known, the spin-orbit coupling ($H^{SOC} = \xi \mathbf{s} \cdot \mathbf{L}$) is the most important origin of magnetic crystalline anisotropy (MCA). The so-called shape anisotropy term, which results from the magnetostatic dipole-dipole interactions between local magnetic moments, is usually negligible. In most ab initio calculations, the MCA force theorem [15,16]

$$E_{MCA} \equiv E(90^\circ) - E(0^\circ) = \sum_{occ'} \varepsilon_i(90^\circ) - \sum_{occ''} \varepsilon_i(0^\circ) + O(\rho^n) \quad (1)$$

has been adopted for the determination of E_{MCA} . Here ε_i stands for the band energy of the i -th state. Strong numerical uncertainties have been inherent in most previous ab initio MCA calculations [17] because the sets of occupied states, i.e., $\{occ'\}$ and $\{occ''\}$, were determined through the Fermi filling scheme which relies on the very limited information from the eigenvalues, ε_i . Hence, one had to use a huge number of k -points ($>10,000$ in the two dimensional Brillouin zone for thin films) to obtain reliable E_{MCA} values and thus only few systems (e.g., free monolayers or simple alloys) could be treated.

We proposed a simple solution for this problem by using the state tracking approach in which the $\{occ'\}$ and $\{occ''\}$ states are determined according to their projections back to the occupied set of unperturbed states [18]. Since this procedure ensures the minimum change in the charge and spin densities, as required by the force theorem, and excludes possible randomness in the Brillouin zone (tracking at a given k -point), very stable E_{MCA} results have been obtained with a relatively small number of k -points for magnetic thin films.

The torque method can further depress the remaining uncertainties resulting from the SOC interaction between near-degenerate states around the Fermi level (so called surface pair coupling) [10]. To demonstrate the idea of the torque method, recall that the total energy of a uniaxial system can be well approximated in the form

$$E = E_0 + k_2 \sin^2 \theta + k_4 \sin^4 \theta \quad (2)$$

Its angular derivative (torque) is thus

$$T \equiv \frac{dE}{d\theta} = \sin 2\theta (k_2 + k_4 \sin^2 \theta) \quad (3)$$

Here θ is the angle between the normal axis and the direction of magnetization. If we apply the Feynman-Hellman theorem, E_{MCA} can be evaluated finally (note that only $H^{SOC} = \xi \mathbf{s} \cdot \mathbf{L}$ depends on θ in the Hamiltonian as

$$E_{MCA} = \sum_{occ} \langle \Psi'_i | \frac{\partial H}{\partial \theta} | \Psi'_i \rangle_{\theta=45^\circ} = \sum_{occ} \langle \Psi'_i | \frac{\partial H^{SOC}}{\partial \theta} | \Psi'_i \rangle_{\theta=45^\circ} \quad (4)$$

where Ψ'_i is the i -th perturbed wave function.

Very stable results of MCA energies can be obtained through the state-tracking and torque approaches with a reasonable number of k -points (about

200 in the 2D-BZ for thin films). This allows us to (1) make explanations and predictions for many magnetic thin films of practical importance; (2) provide physical insights for E_{MCA} at the most fundamental level (e.g., band structure, wave functions and ligand interaction), which was thought to be extremely complex; and (3) as elaborated below, to study magneto-elastic coupling and magnetostriction [19].

2.3 Magnetostriction

In general, the size of the magneto-elastic strain induced by rotation of the magnetization depends on the directions of the measured strain and of the spin moment with respect to the crystalline axes of the material. For a cubic material, the directional dependence of the fractional change in length can be expressed in terms of the direction cosines of the magnetization (a) and of the strain measurement direction (b) with respect to the crystalline axes [7]

$$\frac{\Delta l}{l_0} = \frac{3}{2}\lambda_{001} \left[\sum_{i=1}^3 \alpha_i^2 \beta_i^2 - \frac{1}{3} \right] + 3\lambda_{111} \sum_{i \neq j} \alpha_i \beta_i \alpha_j \beta_j \quad (5)$$

If the measurement is carried out along the (001) direction, for example, $\beta_x = \beta_y = 0$ and $\beta_z = 1.0$ then Eq. 5 can be simplified as

$$\frac{\Delta l}{l_0} = \frac{3}{2}\lambda_{001} [\alpha_z^2 - 1] \quad (6)$$

or further, for systems with a single domain

$$\lambda_{001} = \frac{2}{3} \frac{l(0^\circ) - l(90^\circ)}{l_0} \quad (7)$$

Clearly, λ_{001} represents the change in length along (001) when the magnetization turns from the x,y plane to the z direction.

The equilibrium lengths, $l(\theta)$, can be obtained by fitting the calculated total energies as quadratic functions of l

$$E(0^\circ) = al^2 + bl + c; \quad E(90^\circ) = al^2 + bl + c + E_{MCA} \quad (8)$$

and so

$$\lambda_{001} = -\frac{2E'_{MCA}}{3l_0} \quad (9)$$

Here $E'_{MCA} = \frac{dE_{MCA}}{dl}$, which is much smaller than the value of b . Note that b is always negative (since both a and the equilibrium length are positive), and thus λ and E'_{MCA} always have the same sign.

3 Results and Discussion

Magnetostrictive coefficients were calculated for many systems in the last few years by us and also by several other authors (e.g., Eriksson et al [20], Guo [21], Fähnle et al [22]). Here we discuss results for a few selected systems, mainly through our FLAPW calculations.

3.1 Cubic Transition Metal Bulks

As an important benchmark test, the magnetostriction coefficients of cubic bulk magnetic transition metals are studied first. The calculated total and MCA energies for bcc bulk Fe are plotted in Fig. 2. Clearly, E_{MCA} can be fitted well by a smooth curve versus the vertical strain. This validates the usage of the large range of lattice strain ($\sim 10\%$) in calculations. The slope of E_{MCA} and thus the magnetostrictive coefficient are positive, indicating that the bulk Fe stretches along the direction of magnetization, a conclusion that agrees well with experiment. Note that theory also predicted a large non-linear term in the $E_{MCA} - l$ dependence. This term may contribute to the strain-induced magnetic anisotropy (an inverse effect of magnetostriction), especially in magnetic thin films grown epitaxially with large lattice mismatches.

Quantitatively, the value of λ_{001} depends sensitively on the distortion mode (i.e., Poisson's ratio). As listed in Table 1, the value of Poisson's ratio for Fe, Co and Ni optimized through total energy minimization is in the range of 0.37-0.48, which is reasonably close to that obtained using the measured elastic stiffness constants ($\sigma = -c_{12}/(c_{11} + c_{12})$) for bulk Fe and Ni (0.37-0.38) [23]. As a result, satisfactory quantitative agreement is achieved for λ_{001} between our (zero temperature) theory and experiment for all these three metals.

The theoretical result can be further improved by using the GGA formula. As seen in Table 1, LDA leads to a 3% underestimation for the lattice constant and a more substantial difference for the spin magnetic moments at the equilibrium geometry. With GGA, the calculated values of most magnetic properties are

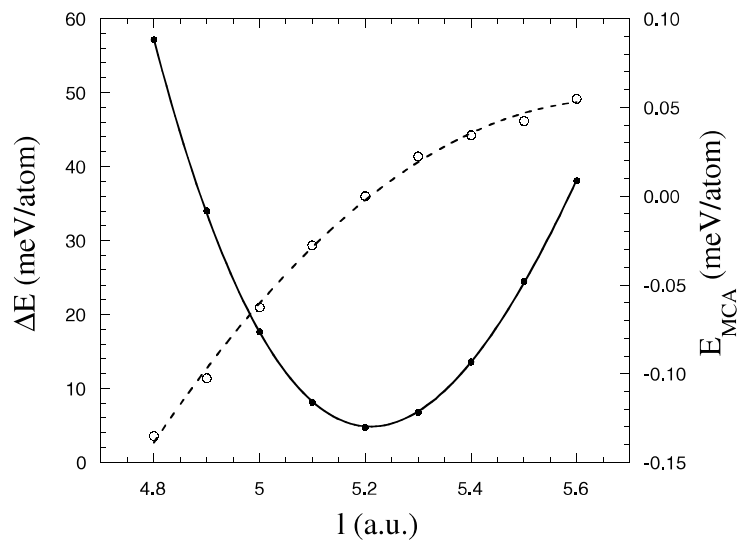


Fig. 2. The calculated total energy (solid line) and MCA energy (dashed line) for the bcc bulk Fe using LDA.

Table 1. The lattice constant, a Poisson's ratio, σ , spin moment, M_s , orbital moment, M_L , and magnetostrictive coefficient, λ_{001} , for bulk Fe, Co and Ni obtained with FLAPW calculations.

	a(a.u.)	σ	$M_s(\mu_B)$	$M_L(\mu_B)$	$\lambda_{001}(10^{-6})$
bcc Fe					
LDA	5.20	-0.409	2.05	0.048	52
GGA	5.37	-0.486	2.17	0.045	29
EXP	5.41	-0.368	2.22	0.05-0.08	21
fcc Co					
LDA	6.48	-0.374	1.59	0.076	92
GGA	6.67	-0.396	1.66	0.073	56
EXP	6.70	-	1.72	0.12	79
fcc Ni					
LDA	6.46	-0.332	0.62	0.049	-63
GGA	6.64	-0.376	0.66	0.050	-56
EXP	6.66	-0.376	0.57	0.05	-49

improved, especially for Fe in which the number of holes in its majority spin band is very sensitive to the change of environment. Changes for Co and Ni are less dramatic since their majority spin bands are full in both LDA and GGA calculations.

Physically, the strain induced E_{MCA} results from changes in the band structure. For instance, a lattice shrinkage along the z-axis for bcc Fe induces some charge transfer from the $d_{x^2-y^2}$ state to d_{z^2} the state, which in turn increases negative contributions to the MCA energy [24].

An orbital polarization term has been employed in some first principle calculations to improve results of orbital magnetic moments. This term was introduced to take account the effect of Hund's second rule and indeed improves some results such as for the orbital magnetic moment, however, was found to significantly overestimate E_{MCA} and thus magnetostriction. For bulk fcc Ni, for example, Hjortstam et al [20] obtained magnetostrictive coefficients, $\lambda_{001} = -270 \times 10^{-6}$ and $\lambda_{111} = -107 \times 10^{-6}$, that are more than three times larger in magnitude than experiment [25,26,27], $\lambda_{001} = -49 \sim -71 \times 10^{-6}$ and $\lambda_{111} = -39 \times 10^{-6}$.

3.2 Fe, Co and Ni Alloys

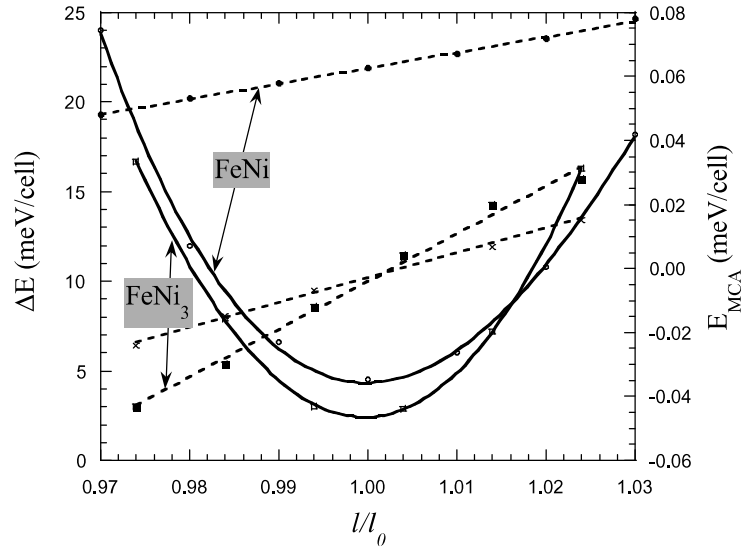
Fe, Co and Ni magnetic alloys are widely used in magnetic recording technology and invar materials. Despite the fact that their magnetic properties are being studied in great detail both experimentally and phenomenologically[28], until very recently there was no microscopic theoretical description of the magnetic anisotropy and magnetostriction for these systems. Results obtained through our FLAPW-GGA calculations are listed in Table 2. The optimized lattice constants, elastic constants and magnetic properties agree very well with experiment [29]. FeCo₃, FeNi₃ and CoNi₃ alloys have the L1₂ structure while FeCo adopts the B₂ structure. They have cubic symmetry and thus zero E_{MCA} (since the x and

Table 2. Calculated lattice constants, E_{MCA} , Poisson's ratio and magnetostrictive coefficient for Fe, Co, and Ni ordered alloys, accompanied by corresponding experimental data in parentheses .

	FeCo	FeCo ₃	FeNi	FeNi ₃	CoNi	CoNi ₃
a(a.u.)	5.38	6.70	6.76	6.70	6.62	6.66
	(5.39)		(6.76)	(6.71)	(6.67)	(6.65)
c(a.u.)	5.38	6.70	6.76	6.70	6.78	6.66
	(5.39)		(6.76)	(6.71)	(6.67)	(6.65)
E_{MCA}	0	0	63	0	143	0
σ	-0.35	-0.36	-0.33	-0.35	-0.34	-0.36
$\lambda_{001}(10^{-6})$	83	-68	10	27	42	33
	(125)		(12)	(13)	(40-120)	

z axes are identical). By contrast, the cubic symmetry is broken in the FeNi and CoNi alloys, and they have a uniaxial E_{MCA} as large as 63 meV/cell and 143 meV/cell, respectively. FeNi adopts the cubic L1₀ geometry, while the c-axis of CoNi is 2.4% longer than its a-axis. The calculated spin magnetic moments of Fe, Co and Ni atoms are enhanced significantly from their bulk values. For example, the spin magnetic moment of Fe (Co) is as large as 2.85 (1.83) μ_B in FeCo.

To calculate the magnetostrictive coefficients, the length of the c-axis is used as a parameter. The E_{MCA} appears to be a smooth function of the lattice strain

**Fig. 3.** The lattice constant, a, Poisson's ratio, σ , spin and orbital magnetic moments (M_s and M_L) and the magnetostrictive coefficient, λ_{001} , for cubic magnetic bulks using GGA.

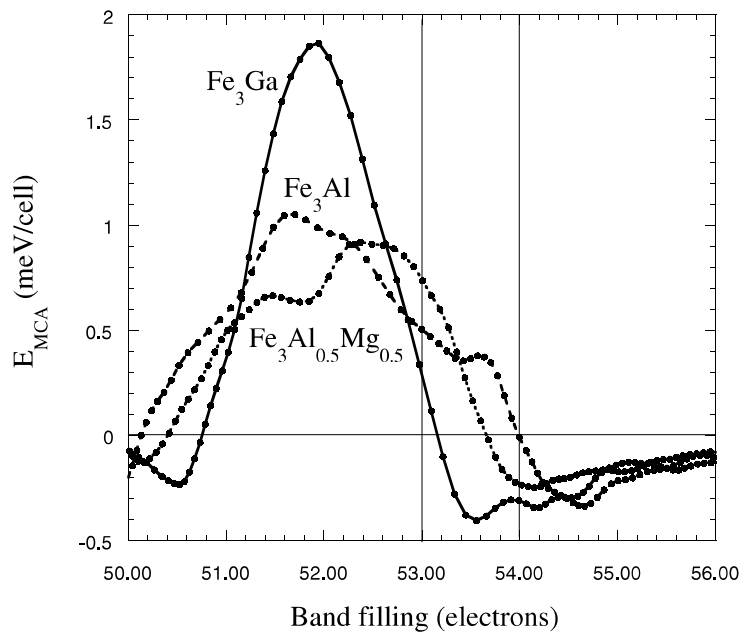


Fig. 4. Band filling dependence of MCA energy for Fe_3Ga , Fe_3Al , $Fe_3Ga_{0.5}Al_{0.5}$ using GGA. Vertical lines show the positions of real Fermi levels.

for each system studied. For instance, the calculated total energy and MCA energy for $FeNi_3$ are plotted in Fig. 3 versus the lattice distortion along the z-axis (l is 6.66 a.u.; the minimum-energy distortion mode is adopted here). The calculated magnetostrictive coefficient from the curvature of the total energy curve and the slope of the E_{MCA} curve is 23×10^{-6} for $FeNi_3$, a value which is much larger than the measured results for a $Fe_{30}Ni_{70}$ polycrystalline sample, 13×10^{-6} [29]. The measured data, however, strongly depend on the temperature and composition. The calculated magnetostrictive coefficients for $FeNi$ and $CoNi$ also agree well with experiments [29].

The values of E_{MCA} for permalloy ($Fe_{20}Ni_{80}$) are also given in Fig. 3. Note that these results are obtained from the $FeNi_3$ band structure using a rigid band model; they thus reflect only the effects of a change of composition (or more exactly, the change of number of valence electrons in the unit cell). The calculated magnetostrictive coefficient for this pseudo-permalloy (11.7×10^{-6}) is much smaller than that of the $FeNi_3$ crystal. Experimentally, it is known that the magnetostrictive coefficient of permalloy is close to zero. The change in number of valence electrons certainly plays a very important role in weakening the magnetostriction.

Magnetostriction in Fe-Ga and Fe-Ga-Al alloys attract some interest recently due to potency of making strong magnetostrictive materials [30]. FLAPW calculations found that the magnetostrictive coefficient of Fe_3Al is very small

Table 3. Calculated and measured (in parentheses) lattice constant, a , total magnetic moment per primitive unit cell, M , spin magnetic moment of itinerant electrons in rare-earth (M_{RE}) and transition metal M_{TM} , and magnetostrictive coefficient, λ_{001} for different compounds.

	a (a.u.)	$M(\mu_B)$	$M_{RE}(\mu_B)$	$M_{TM}(\mu_B)$	$\lambda_{001}(10^{-6})$
GdCo ₂	13.72(13.68)	4.99(4.9)	0.46	-1.24	-407(-1200)
NdCo ₂	13.84(13.77)	5.28(3.8)	0.32	-1.14	-171
SmCo ₂	13.74(13.71)	2.73(2.0)	0.52	-1.26	-290
ErCo ₂	13.70(13.50)	7.06(7.0)	0.28	-1.10	-516(-1000)
GaFe ₂	13.85(13.94)	3.85(2.8)	0.58	-1.96	44(39)

($< 5 \times 10^{-6}$). Rigid band model analyses indicate, however, a strong sensitivity of λ_{001} on the band filling as shown in Fig. 4. If some Al atoms are substituted by Mg atoms (e.g., Fe₆AlMg), we found from both rigid band model analyses and FLAPW calculations for Fe₆AlMg that the magnetostrictive coefficient λ_{001} indeed becomes large (ca. $+150 \times 10^{-6}$). The calculated λ_{001} for Fe₃Ga is -106×10^{-6} , a value which indeed much larger than that for bulk Fe (cf. Table 1). Electronic structure analyses indicate that the magneto-elastic coupling in Fe₃Ga is linked to the strain dependence of Fermi surface of the Fe- d_{xz-yz} state (majority spin) around the center of Brillouin zone [31].

3.3 Rare Earth Intermetallic Compounds

Rare-earth intermetallic compounds have attracted great attention since the late 1960's due to their extraordinary magnetic properties, especially their large magnetostrictive coefficients (10^{-3}) at room temperature [6,7,8,9]. While it was believed that the localized rare-earth 4f states play a dominant role in magnetization and magneto-elastic coupling, recent experiments found that the effects of itinerant states can be equally important [6,7]. Although a phenomenological approach was developed long ago to describe the dependence of single crystal magnetostriction on magnetization and measurement directions, the magnetostrictive coefficient for a given material, especially the contribution of itinerant electrons, has never been accurately calculated.

Very recently, we investigated the magnetostrictive properties of two prototype rare-earth intermetallic compounds, namely, GdCo₂ and GdFe₂ [32]. Both compounds adopt the C15 cubic Laves phase structure, a close-packed arrangement of spheres with two different sizes. Through total energy minimization, the calculated equilibrium lattice constants for GdCo₂ and GdFe₂ are 13.65 a.u. and 13.85 a.u., respectively. These values agree very well with their experimental counterparts, 13.69 a.u. and 13.94 a.u. [9] – indicating the validity and accuracy of our local density FLAPW calculations for these compounds. As expected, the calculated atomic forces on all the atoms are zero in a range of $\pm 2.5\%$ lattice expansion/compression. Thus the C15 cubic Laves phase is a very stable structure for these materials.

The spin magnetic moment for Gd is $7.46 \mu_B$ ($7.0 \mu_B$ from the 4f shell and $0.45 \mu_B$ from the valence band) in GdCo_2 , while it is enhanced to $7.58 \mu_B$ ($0.58 \mu_B$ from the valence band) in GdFe_2 . For both systems, the orbital magnetic moment of Gd remains very small ($0.021\text{--}0.025 \mu_B$). In agreement with experiment, the magnetic moments of Co and Fe align anti-parallel to that of Gd. The spin and orbital magnetic moments of the Co atom in GdCo_2 are $-1.24 \mu_B$ and $-0.11 \mu_B$, respectively. The calculated total magnetic moment (spin and orbital parts, including contributions from the interstitial region) for GdCo_2 is $4.99 \mu_B$, which agrees very well with experiment ($4.9 \mu_B$). As listed in Table 3, although the magnetic moments of rare earth atoms vary significantly in different compounds, the spin magnetic moment of Co retain almost as a constant ($1.10 \sim 1.26 \mu_B$).

The calculated total energies (ΔE) and E_{MCA} for GdCo_2 are plotted in Fig. 5 versus the length of the unit cell along the z-axis. The total energy can be well fitted by a third order polynomial but not by a parabola – indicating the importance of nonlinear elasticity in this system. The calculated E_{MCA} in Fig. 5 is also a monotonic smooth function of l . The large negative slope of the $E_{MCA}(l)$ curve indicates that GdCo_2 contracts along the direction of magnetization. The calculated λ_{001} is -407×10^{-6} . While this value is much larger than the magnetostrictive coefficients for magnetic transition metals ($20 \sim 70 \times 10^{-6}$), it is still considerably smaller than the early experimental value of -1200×10^{-6} , which is under scrutiny by experimentalists now. The calculated magnetostrictive coefficients for other compounds are also listed in Table 3. Note that the 4f-states of all rare earth elements are treated as atomic core levels with spherical charge distributions; thus the magnetostrictive coefficients are only due

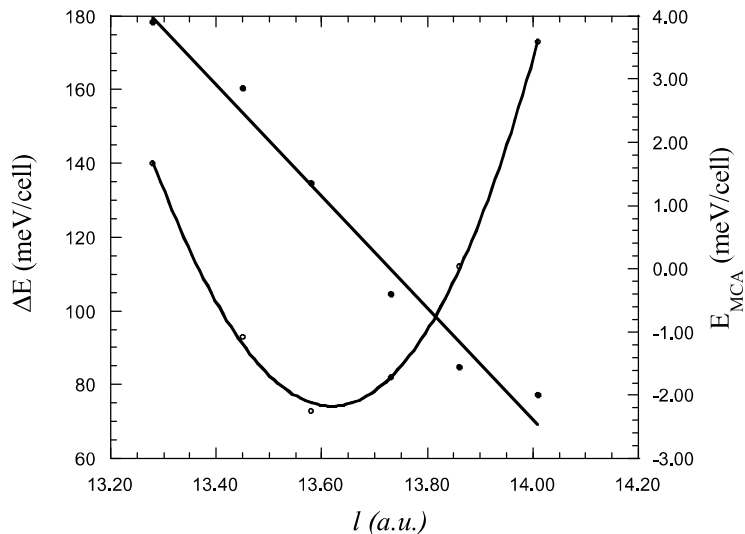


Fig. 5. Calculated total and MCA energies for cubic GdCo_2 using LDA.

to the contributions of H^{SOC} among the itinerant electrons and thus not subject to direct comparison with experiment. Significantly, the contributions are a few hundreds ppm (10^{-6}) large, which are obviously comparable to those from the stiff anisotropic charge distributions of the $4f$ electrons [7,8].

We also investigated the spatial anisotropy of magnetostriction in GdCo_2 . The calculated λ_{111} for GdCo_2 is positive (19×10^{-6}), a result which agrees with experimental data ($\sim 10 \times 10^{-6}$). The Young's modulus for a distortion along the (111) direction is found to be about four times larger than that along the (100) direction.

The calculated magnetostrictive coefficient for GdFe_2 is positive, $+44 \times 10^{-6}$, and very close to experiment, $\lambda_s = +39 \times 10^{-6}$ [7]. Using a rigid band picture, we found that the difference in the magnetostrictive behaviors of GdFe_2 and GdCo_2 is mainly due to the change in band filling. A compound, $\text{GdFe}_x\text{Co}_{2-x}$ ($x=0.9-1.2$) is predicted to be a strong magnetostrictive material with a positive sign for λ_{001} ($+450 \times 10^{-6}$).

Acknowledgments

I thank Drs. K.B. Hathaway, A.E. Clark, A.J. Freeman and V.G. Gavrilenko for stimulating discussions and collaborations. Work supported by the ONR (Grant Nos. N00014-95-1-0489), and by computing grants at ARSC and NAVO.

References

1. See review articles edited by A.J. Freeman and S.D. Bader, *J. Magn. Magn. Mater.*, **200** (1999).
2. A.J. Freeman and R.Q. Wu, *J. Magn. Magn. Mater.*, **100**, 497 (1991).
3. M. N. Baibich, J. M. Broto, A. Fert, F. Nguyen Van Dau, F. Petroff, P. Etienne, G. Creuzet, A. Friederich, and J. Chazelas, *Phys. Rev. Lett.*, **61**, 2472 (1988).
4. S.S.P. Parkin, N. More and K.P. Roche, *Phys. Rev. Lett.*, **64**, 2304 (1990).
5. B. Dieny, V. S. Speriosu, S. S. P. Parkin, B. A. Gurney, D. R. Wilhoit, and D. Mauri, *Phys. Rev. B*, **43**, 1297 (1991).
6. A. Clark and K.B. Hathaway, in "Handbook of Giant Magnetostrictive Materials", edited by G. Engdahl (Academic Press, London, 2000).
7. J. R. Cullen, A.E. Clark and K.B. Hathaway, in "Materials Science and Technology", edited by R.W. Cahn, P. Hasen and E.J. Kramer, Vol. IIIB (1994) 529.
8. A.E. Clark, in "Ferromagnetic Materials", Vol. 1, edited by E.P. Wohlfarth, (Amsterdam, North-Holland, 1971), page 531.
9. K.N.R. Taylor, *Advance in Physics*, **2**, 551 (1971).
10. X.D. Wang, R.Q. Wu, D.S. Wang, and A.J. Freeman, *Phys. Rev. B*, **54**, 61 (1996).
11. E. Wimmer, H. Krakauer, M. Weinert and A. J. Freeman, *Phys. Rev. B*, **24**, 864 (1981) 864; M. Weinert, E. Wimmer and A. J. Freeman, *Phys. Rev. B*, **26**, 4571 (1982), and references therein.
12. U. von Barth and L. Hedin, *J. Phys. C*, **5**, 1629 (1972).
13. J. P. Perdew and W. Yue, *Phys. Rev. B*, **33**, 8800 (1986); J. P. Perdew, J. A. Chevary, S. H. Vosko, K. A. Jackson, M. R. Pederson, D. J. Singh, and C. Fiolhais, *Phys. Rev. B*, **46**, 6671 (1992); J. P. Perdew, K. Burke, and M. Ernzerhof, *Phys. Rev. Lett.*, **61**, 2472 (1988).

14. D.D. Koelling and B.N. Harmon, *J. Phys. C* **10**, 3107 (1972).
15. X.D. Wang, D.S. Wang, R.Q. Wu and A.J. Freeman, *J. Magn. Magn. Mater.* **159**, 337 (1996).
16. J.G. Gay and R. Richter, *Phys. Rev. Lett.* **56**, 2728 (1986); G.H.O. Daalderop, P.J. Kelly and M.F.H. Schuurmans, *Phys. Rev. B* **41**, 11919 (1990); G.Y. Guo, W.M. Temmerman and H. Ebert, *J. Phys. C* **3**, 8205 (1991); *J. Magn. Magn. Mater.* **104-107**, 1772 (1992); C. Li, A.J. Freeman, H.J.F. Jansen and C.L. Fu, *Phys. Rev. B* **42**, 5433 (1990).
17. G.H.O. Daalderop, P.J. Kelly and M.F.H. Schuurmans, *Phys. Rev. B* **42**, 1533 (1990); A.R. Mackintosh and O.K. Andersen, in "Electrons at the Fermi Surface", edited by M. Springford (Cambridge University Press, Cambridge, 1980).
18. D.S. Wang, R.Q. Wu and A.J. Freeman, *Phys. Rev. Lett.* **70**, 869 (1993); **71**, 2166 (1993).
19. R.Q. Wu and A.J. Freeman, A.J. Freeman and R.Q. Wu, *J. Magn. Magn. Mater.*, **200**, 498 (1999).
20. O. Hjorstam, K. Baberschke, J.M. Wills, B. Johansson and O. Eriksson, *Phys. Rev. B* **55**, 15026 (1997).
21. G.Y. Guo, *J. Magn. Magn. Mater.* **209**, 33 (2000).
22. S. Buck and M. Fähnle, *Phys. Rev. B* **57**, 14044 (1998).
23. see C. Kittel, "Introduction to Solid State Physics", (7th edition, Wiley 1997).
24. R.Q. Wu, L.J. Chen, A. Shick and A.J. Freeman, *J. Magn. Magn. Mater.* **177-181**, 1216 (1998).
25. D. Bonnenberg, K.A. Hempel and H.P.J. Wijn, in "Numerical Data and Functional Relationships in Science and Technology", edited by H.P.J. Wijn, Landolt-Bornstein, New Series, Group 3 Vol. 19a (Springer-verlag, Berlin, 1986).
26. E.W. Lee and M.A. Asgar, *Proc. R. Soc. London Ser. A* **326**, 73 (1971).
27. M. Farle, W. Platow, A.N. Anisimov, P. Pouloupoulos and K. Baberschke, *Phys. Rev. B* **55**, 3708 (1997); **56**, 5100 (1997).
28. S. Chikazumi, "Physics of Magnetism", (Krieger, Malabar, FL, 1986).
29. see "Data in Science and Technology: Magnetic Properties of Metals", edited by H.P.J. Wijn, (Springer-verlag, Berlin, 1986).
30. S. Guruswamy S, N. Srisukhumbowornchai, A.E. Clark, J.B. Restorff, and M. Wun-Fogle, *Scripta Materialia*, **43**, 239-244 (2000).
31. R.Q. Wu, *Phys. Rev. Lett.*, submitted.
32. R.Q. Wu, *J. Appl. Phys.* **85**, 6217 (1999), V.G. Gavrilenko and R.Q. Wu, *J. Appl. Phys.* (2001), in press.

Magnetism of Correlated Systems: Beyond LDA

A.I. Lichtenstein¹ and M.I. Katsnelson²

¹ University of Nijmegen, 6525 ED Nijmegen, The Netherlands

² Institute of Metal Physics, 620219 Ekaterinburg, Russia

Abstract. A novel approach to electronic correlations in magnetic crystals which takes into account a dynamical many-body effects is present. In order to find a frequency dependence of the electron self energy, an effective quantum-impurity many-particle problem need to be solved within the dynamical mean-field theory. The numerically exact QMC-scheme and the spin-polarized fluctuation exchange approximation are used for the self-consistent solution of this single-site many-particle problem. The calculations of effective exchange interaction parameters based on the realistic electronic structure of correlated magnetic crystals have been discussed.

1 Introduction

The calculation of thermodynamic properties and excitation spectra of different magnetic materials is one of the most important problems of the microscopic theory of magnetism. A modern computational material science is based on the density functional (DF) approach [1]. It is a common practice to use this scheme not only for the total energy calculations and related quantities such as charge and spin densities, but also for different spectral characteristics. Sometimes an agreement of the computational results with the experimental data is very impressive, despite the absence of a reliable theoretical background. In principle, the energies of Kohn-Sham quasiparticles [1] which are calculated in a standard band theory are just auxiliary quantities for the total energy calculation. Among all achievements of the quantitative electronic theory a list of difficulties and shortcomings grows, especially when one consider the magnetic d- and f-electron systems. In a number of cases the theory appeared to be *qualitatively* inadequate. First, the DF scheme cannot describe correctly the phenomenon of “Mott insulators” [2], as it was first shown by Terakura *et al* [3] in attempt to calculate the electronic structure of 3d-metal oxides. Later we faced similar problems in field of the high- T_c superconductors [4] and other compounds [5]. The Ce- and U- based “heavy fermion” compounds such as CeCu₆, UPt₃, etc, are another “hot-spots”: normally the calculated values of effective masses are orders of magnitude smaller than the experimentally observed ones [6]. Even for the pure 3d metals some qualitative differences between the theory and experiments exists. For example, there are at least three difficulties with the photoelectron spectra of ferromagnetic nickel [7]: (i) the measured width of the occupied part of d-band is 30% narrower than the calculated one (ii) the spin splittings is twice smaller than in the LSDA and (iii) the band structure cannot describe a famous 6 eV - satellite. Calculations for paramagnetic spin-disordered states

[8] lead to the conclusion that Ni has no local magnetic moments above the Curie temperature T_c , in a clear contradiction with experimental results [9]. For iron, a standard band theory cannot explain the data about spin polarization of thermionic electrons [10,11,12] and some features of angle-resolved photoemission spectra [13,14,12]. All these difficulties put many questions to the DF approach: what are the “electron spectrum” which we really calculated and how one can improve the electronic theory for magnetic d- and f- systems?

It was understood many years ago that all this problems are connected with inadequate description of many-body effects in DF calculations of the excitation spectra. Such methods as GW [15], LDA+U [5] and SIC (Self-Interaction Correction approximation) [16] have been proposed to improve the situation. This methods are very useful for the description of antiferromagnetic transition-metal oxides as the Mott insulators [16,5]. However, one should note that both LDA+U and SIC are just the mean-field approximations and cannot describe the *correlation* effects which are, by definition, the many-body effects *beyond* the Hartree-Fock. For example, in these approaches one need spin or orbital ordering to describe the Mott insulator and it is impossible to describe correctly electronic structure of NiO or MnO in paramagnetic phase. At the same time, the magnetic ordering should not be important for the basic physics of Mott insulators [2]. All the “Hartree-Fock-like” approaches fail to describe the renormalization of the effective mass in the heavy fermion systems. There are also many problems concerning the electronic structure and itinerant magnetism of 3d metals as described above. Thus, one need some practical ways to incorporate *correlation* effects in the electronic structure of solids.

In principle, there are two ways to include them into DF calculations. The first one is the use of *time-dependent* DF formalism which can guarantee, in principle, an opportunity to calculate exact response functions [17], in the same sense as the Hohenberg-Kohn theorem guarantees the total energy in usual “static” DF [1]. However, all the expressions for this time-dependent non-local DF in real calculations are based on RPA-like approximations which described not satisfactory the really highly correlated systems. They are excellent for investigation the plasmon spectrum of aluminum, but not for understanding a nature of high- T_c superconductivity or the heavy fermion behavior. Another way is to use an “alternative” many-body theory developed in the 50-th by Gell-Mann and Brueckner, Galitskii and Migdal, Beliaev and many others in terms of the Green functions rather than in the electron density [18]. We try to formulate such computational approach as a generalization of LDA+U scheme, a so-called “LDA++” method. The main difference of LDA++ approach from LDA+U one is an account in the former dynamical fluctuations, or the real correlation effects, described by local but energy dependent self-energy $\Sigma(E)$, so the LDA++ means $LDA + U + \Sigma(E)$.

The comparison of the standard DF theory in the local spin density approximation (LSDA) and LDA++ approach is represented in the table I.

First of all the LSDA theory is based on the Hohenberg - Kohn theorem that the total energy E_{tot} is a functional of charge and spin densities, while the

Table 1. Comparison of different schemes

LSDA	LDA++
Density functional	Baym-Kadanoff functional
Density $\rho(\mathbf{r})$	Green-Function $G(\mathbf{r}, \mathbf{r}', E)$
Potential $V_{xc}(\mathbf{r})$	Self-energy $\Sigma_i(E)$
$E_{tot} = E_{sp} - E_{dc}$	$\Omega = \Omega_{sp} - \Omega_{dc}$
$E_{sp} = \sum_{\lambda < \lambda_F} \varepsilon_\lambda$	$\Omega_{sp} = -Tr \ln[-G^{-1}]$
$E_{dc} = E_H + \int \rho V_{xc} d\mathbf{r} - E_{xc}$	$\Omega_{dc} = Tr \Sigma G - \Phi_{LW}$

LDA++ scheme considers the thermodynamic potential Ω as a functional of exact one-particle Green functions. This approach in many-particle theory has been introduced in the works by Luttinger and Ward [19] and Baym and Kadanoff [20]. The Green function in LDA++ theory plays the same role as the density matrix in LSDF formalism. We stress the dynamic nature of the correlation effects which are taken into account in the LDA++ approach since the density in the LSDA is just the static limit of the local Green function. Further, the self energy Σ is analogous to the exchange-correlation potential; local approximation for Σ , which is assumed to be energy-dependent but not momentum-dependent corresponds to the local approximation for V_{xc} . In both formalisms the thermodynamic potential can be represented as a “single-particle” one, Ω_{sp} minus the contributions of the “double counted terms”, Ω_{dc} . It will be important for the consideration of so-called “local force theorem” and the computation of magnetic interaction parameters (Sect. III). The single-particle contribution to the thermodynamic potential in the LDA++ would have the same form as in the LSDA if we take into account only a pole part of the Green function and neglect the quasiparticle damping. However, even in that case the quasiparticle energies are not the same since the poles of the Green functions are not coincide, generally speaking, with the “Kohn-Sham” energies. The quantity Φ_{LW} is the Luttinger-Ward generating functional for the self energy, or the sum of all the skeleton diagrams without free legs [19].

The difficulty with the finite temperature effects is one of the main shortcomings of a standard DF formalism. In all realistic calculations the temperature is included in the Fermi distribution functions and in the lattice constants via the thermal expansion [21]. At the same time, for the itinerant electron magnets the temperature effects connected with the “Bose” degrees of freedom due to spin waves and paramagnons are much more important [22]. In principle, these effects could be taken into account in the DF theory via the temperature dependence of the exchange-correlation potential, the corresponding terms being nonlocal. It is not easy to propose an adequate expression for such temperature-dependent non-local potential. One of the first attempts in this direction based on simple

RPA-like considerations [23]. On the other hand, in LDA++ type of scheme all the calculations are naturally carried out for finite temperatures by the using of Matsubara frequencies, as in the usual many-body theory [18].

The main assumption of the LDA++ approach is the importance of only intrasite “Hubbard correlations” with the local approximation for the self-energy. It is worthwhile to stress a difference of this kind of locality from the locality in DF theory. In the latter, the local approximation means that the exchange-correlation energy is calculated for the homogeneous electron gas [24]. It is known from exact QMC calculations that the correlation effects could lead to some instabilities of the state of homogeneous electron gas (magnetism, charge ordering, etc) only for electron densities which are order of magnitude smaller than ones typical for real metals (the critical values of the parameter r_s are of order of hundred in comparison with the “normal” range 2-6 for metals). At the same time, magnetism and charge ordering are rather usual for real compounds with the d- and f- elements. It seems that the “atomic-like” features of d- and f- states are of the crucial importance to describe the correlation effects in real compounds. Only these features are taken into account in the Hubbard-like terms for the d- or f-states in LDA++ approach. Therefore one can view the LDA++ as a simplest way for quantitative considerations of the correlation effects in the transition metals, and their compounds, based on the LSDA description for all non-correlated electrons in the systems.

The investigation of correlation effects in the electronic structure and magnetism of iron-group metals is still far from the final picture and attracts continuous interest (see, e.g., [8,25,26,27] and Refs therein). Despite of many attempts, the situation is still unclear both theoretically and experimentally. For example, there is no agreement on the presence of 5 eV satellite in photoemission spectrum of iron [13,14], and on the existence of local spin splitting above Curie temperature in nickel [28]. From the theoretical point of view, different approaches such as the second-order perturbation theory [29,26], the T-matrix approximation [25,30], the three-body Faddeev approximation [31], and the moment expansion method [32] were used. Unfortunately, the applicability of these schemes are not clear. Here we present the version of “LDA++” approach [12,33,34] which is based on the combination of standard band theory technique with so-called dynamical mean-field theory (DMFT) or LDA+DMFT scheme [35].

2 Computational Technique

We start from LDA+U Hamiltonian in the diagonal density approximation:

$$H = \sum_{\{im\sigma\}} t_{im,i'm'}^{LDA} c_{im\sigma}^+ c_{i'm'\sigma} + \frac{1}{2} \sum_{imm'\sigma} U_{mm'}^i n_{im\sigma} n_{im'-\sigma} + \frac{1}{2} \sum_{im \neq m'\sigma} (U_{mm'}^i - J_{mm'}^i) n_{im\sigma} n_{im'\sigma} \quad (1)$$

where i is the site index and m is the orbital quantum numbers; $\sigma = \uparrow, \downarrow$ is the spin projection; c^+, c are the Fermi creation and annihilation operators ($n = c^+ c$);

t^{LDA} is effective single-particle Hamiltonian obtained from the non-magnetic LDA with the correction for double counting of the average interactions among d-electrons. In the general case of spin-polarized LSDA Hamiltonian this correction is presented in Refs. [33,12,36]. In the non-magnetic LDA this is just a shift “back” of correlated d-states with respect to s,p-states by the average Coulomb and exchange potential: $\Delta_d = U(n_d - \frac{1}{2}) - \frac{1}{2}J(n_d - 1)$, where U and J are the average values of $U_{mm'}$ and $J_{mm'}$ matrices and n_d is the average number of d-electrons.

The screened Coulomb and exchange vertex for the d-electrons

$$U_{mm'} = \langle mm' | V_{scr}^{ee}(\mathbf{r} - \mathbf{r}') | mm' \rangle, J_{mm'} = \langle mm' | V_{scr}^{ee}(\mathbf{r} - \mathbf{r}') | m'm \rangle \quad (2)$$

are expressed via the effective Slater integrals. We use the minimal *spd*-basis in the LMTO-TB formalism [37] and numerical orthogonalization for $t^{LDA}(\mathbf{k})$ matrix [33]. Local density approximation [1] was used for the self-consistent electronic structure calculation.

In order to find the best local approximation for the self-energy we use the DMFT method [38] for real systems. This scheme become exact in the limit of infinite lattice coordination number [39]. The DMFT approach reduce the lattice many-body problem (Eq.(2)) to the self-consistent solution of effective one-site Andersen model. In this case we need a local Green-function matrix which has the following form in the orthogonal LMTO-representation:

$$G(i\omega) = \sum_{\mathbf{k}} \{i\omega + \mu - t^{LDA}(\mathbf{k}) - \Sigma(i\omega)\}^{-1} \quad (3)$$

where μ is the chemical potential. Note that due to cubic crystal symmetry of ferromagnetic bcc-iron the local Green function without spin-orbital interactions is diagonal both in the orbital and the spin indices. The so-called bath Green function which defined the effective Andersen model and preserve the double-counting of the local self-energy is obtained as a solution of the following impurity model [38]:

$$G_{0m}^{-1}(i\omega) = G_m^{-1}(i\omega) + \Sigma_m(i\omega) \quad (4)$$

The local Green functions for the imaginary time interval $[0, \beta]$ with the mesh $\tau_l = l\Delta\tau$, $l = 0, \dots, L-1$, and $\Delta\tau = \beta/L$, where $\beta = \frac{1}{T}$ is calculated in the path-integral formalism [38,40]:

$$G_m^{ll'} = \frac{1}{Z} \sum_{s_{mm'}} \det[O(s)] * G_m^{ll'}(s) \quad (5)$$

here we redefined for simplicity $m \equiv \{m, \sigma\}$, Z is the partition function and the so-called fermion-determinant $\det[O(s)]$ as well as the Green function for arbitrary set of the auxiliary fields $G(s) = O^{-1}(s)$ are obtained via the Dyson equation [41] for imaginary-time matrix ($\mathbf{G}_m(s) \equiv G_m^{ll'}(s)$):

$$\mathbf{G}_m = [\mathbf{1} - (\mathbf{G}_m^0 - \mathbf{1})(e^{V_m} - \mathbf{1})]^{-1} \mathbf{G}_m^0$$

where the effective fluctuation potential from the Ising fields $s_{mm'}^l = \pm 1$ is

$$V_m^l = \sum_{m'(\neq m)} \lambda_{mm'} s_{mm'}^l \sigma_{mm'}, \text{ where } \sigma_{mm'} = \begin{cases} 1, m < m' \\ -1, m > m' \end{cases}$$

and the discrete Hubbard-Stratonovich parameters are $\lambda_{mm'} = \text{arccosh}[\exp(\frac{1}{2}\Delta\tau U_{mm'})]$ [41]. Using the output local Green function from QMC and input bath Green functions the new self-energy is obtained via Eq.(4) and the self-consistent loop can be closed through Eq.(3). The main problem of the multiband QMC formalism is the large number of the auxiliary fields $s_{mm'}^l$. For each time slices l it is equal to $M(2M - 1)$ where M is the total number of the orbitals which gives 45 Ising fields for the d-states case. We compute the sum over this auxiliary fields in Eq.(5) using important sampling QMC algorithm and performed a dozen of self-consistent iterations over the self-energy Eqs.(3,4,5). The number of QMC sweeps was of the order of 10^5 on the CRAY-T3e supercomputer. The final $G_m(\tau)$ has very little statistical noise. We use maximum entropy method [42] for analytical continuations of the QMC Green functions to the real axis. Comparison of the total density of states (DOS) with the results of LSDA calculations (Fig.1) shows a reasonable agreement for single-particle properties of not “highly correlated” ferromagnetic iron. We calculate the bcc iron at experimental lattice constant with 256 **k**-points in the irreducible part of Brillouin zone. The Matsubara frequencies summation corresponds to the temperature of about $T=850$ K. The average magnetic moment is about $1.9 \mu_B$ which corresponds to a small reduction of the LSDA-value of $2.2 \mu_B$ for such a high temperature. The DOS curves in the LDA+ Σ approach with exact QMC solution of on-site multiorbital problem is similar to that obtained within the simple perturbative fluctuation-exchange (FLEX) approximation described below. The discussion of the results and the comparison with the experimental data will be given in Section 4.

The QMC method described above is probably the most rigorous real way to solve an effective impurity problem in the framework of DMFT theory. However, it is rather time consuming. Besides that, in the previous section we did not work with *complete* four-indices Coulomb matrix:

$$\langle 12|v|34 \rangle = \int d\mathbf{r} d\mathbf{r}' \psi_1^*(\mathbf{r}) \psi_2^*(\mathbf{r}') v_{scr}(\mathbf{r} - \mathbf{r}') \psi_3(\mathbf{r}) \psi_4(\mathbf{r}'), \quad (6)$$

where we define for simplicity $m_1 \equiv 1$.

For moderately strong correlations (which is the case of iron group metal) one can propose an approximate scheme which is more suitable for the calculations. It is based on the fluctuation exchange (FLEX) approximation by Bickers and Scalapino [43] generalized to multiband spin-polarized case [33,12,44]. The electronic self-energy in the FLEX is equal to:

$$\Sigma = \Sigma^{HF} + \Sigma^{(2)} + \Sigma^{(ph)} + \Sigma^{(pp)}, \quad (7)$$

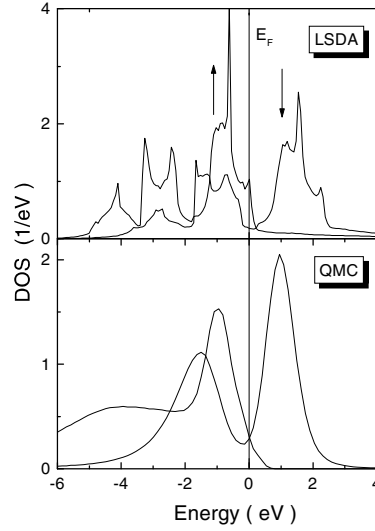


Fig. 1. Spin-resolved density of d-states and magnetic moments for ferromagnetic iron in the LSDA and the LDA+QMC calculations for different average Coulomb interactions with $J=0.9$ eV and temperature $T=1500$ K.

where the Hartree-Fock contribution has a standard form:

$$\Sigma_{12,\sigma}^{HF} = \sum_{34} \left[\langle 13 | v | 24 \rangle \sum_{\sigma'} n_{34}^{\sigma'} - \langle 13 | v | 42 \rangle n_{34}^{\sigma} \right], \quad (8)$$

with the occupation matrix $n_{12}^{\sigma} = G_{21}^{\sigma}(\tau \rightarrow -0)$; this contribution to Σ is equivalent to spin-polarized “rotationally-invariant” LDA+U method [36].

The second-order contribution in the spin-polarized case reads:

$$\begin{aligned} \Sigma_{12,\sigma}^{(2)}(\tau) = & - \sum_{\{3-8\}} \langle 13 | v | 74 \rangle G_{78}^{\sigma}(\tau) * \\ & * \left[\langle 85 | v | 26 \rangle \sum_{\sigma'} G_{63}^{\sigma'}(\tau) G_{45}^{\sigma'}(-\tau) - \langle 85 | v | 62 \rangle G_{63}^{\sigma}(\tau) G_{45}^{\sigma}(-\tau) \right], \end{aligned} \quad (9)$$

and the higher-order particle-hole (or particle-particle) contribution

$$\Sigma_{12,\sigma}^{(ph)}(\tau) = \sum_{34,\sigma'} W_{13,42}^{\sigma\sigma'}(\tau) G_{34}^{\sigma'}(\tau), \quad (10)$$

with p-h (p-p) fluctuation potential matrix:

$$W^{\sigma\sigma'}(i\omega) = \begin{bmatrix} W^{\uparrow\uparrow}(i\omega) & W^{\uparrow\downarrow}(i\omega) \\ W^{\downarrow\uparrow}(i\omega) & W^{\downarrow\downarrow}(i\omega) \end{bmatrix}, \quad (11)$$

where the spin-dependent effective potentials has a generalized RPA-form and can be found in [12]. Note that for both p-h and p-p channels the effective

interactions, according to Eq.(11), are non-diagonal matrices in *spin space* as in the QMC-scheme, in contrast with any mean-field approximation like LSDA. This can be important for the spin-dependent transport phenomena in transition metal multilayers.

We could further reduce the computational procedure by neglecting dynamical interaction in the p-p channel since the most important fluctuations in itinerant electron magnets are spin-fluctuations in the p-h channel. We take into account static (of T -matrix type) renormalization of effective interactions replacing the bare matrix $U_{12,34} = \langle 12|v|34 \rangle$ in FLEX-equations with the corresponding spin-dependent scattering T -matrix

$$\langle 12|T^{\sigma\sigma'}|34 \rangle = \langle 12|v|34 \rangle - \sum_{5678} \langle 12|v|56 \rangle \int_0^\beta d\tau G_{56}^\sigma(\tau) G_{78}^{\sigma'}(\tau) \langle 78|T^{\sigma\sigma'}|34 \rangle \quad (12)$$

Similar approximation has been checked for the Hubbard model [45] and appeared to be accurate enough for not too large U . Finally, in the spirit of DMFT-approach $\Sigma = \Sigma[G_0]$, and all the Green functions in the self-consistent FLEX-equations are in fact the bath Green-functions G_0 .

3 Exchange Interactions

An useful scheme for analyses of exchange interactions in the LSDF approach is a so called "local force theorem". In this case the calculation of small total energy change reduces to variations of the one-particle density of states [46,47]. First of all, let us prove the analog of local force theorem in the LDA++ approach. In contrast with the standard density functional theory, it deals with the real dynamical quasiparticles defined via Green functions for the correlated electrons rather than with Kohn-Sham "quasiparticles" which are, strictly speaking, only auxiliary states for the total energy calculations. Therefore, instead of the working with the thermodynamic potential as a *density* functional we have to start from the general expression for Ω in terms of exact Green function in the Table I. We have to keep in mind also Dyson equation $G^{-1} = G_0^{-1} - \Sigma$ and the variational identity $\delta\Phi_{LW} = Tr \Sigma \delta G$. Here $Tr = Tr_{\omega i L \sigma}$ is the sum over Matsubara frequencies $Tr_{\omega...} = T \sum_{\omega} ...$, $\omega = \pi T(2n+1)$, $n = 0, \pm 1, ...$, T is the temperature, and $iL\sigma$ are site numbers (i), orbital quantum numbers ($L = l, m$) and spin projections σ , correspondingly. We represent the expression for Ω as a difference of "single particle" (*sp*) and "double counted" (*dc*) terms as it is usual in the density functional theory. When neglecting the quasiparticle damping, Ω_{sp} will be nothing but the thermodynamic potential of "free" fermions but with exact quasiparticle energies. Suppose we change the external potential, for example, by small spin rotations. Then the variation of the thermodynamic potential can be written as

$$\delta\Omega = \delta^* \Omega_{sp} + \delta_1 \Omega_{sp} - \delta \Omega_{dc} \quad (13)$$

where δ^* is the variation without taking into account the change of the "self-consistent potential" (i.e. self energy) and δ_1 is the variation due to this change of Σ . To avoid a possible misunderstanding, note that we consider the variation of Ω in the general "non-equilibrium" case when the torques acting on spins are nonzero and therefore $\delta\Omega \neq 0$. In order to study the response of the system to general spin rotations one can consider either variations of the spin directions at the fixed effective fields or, vice versa, rotations of the effective fields, i.e. variations of Σ , at the fixed magnetic moments. We use the second way. Taking into account the variational property of Φ one can be easily shown (cf. Ref. [19]) that $\delta_1\Omega_{sp} = \delta\Omega_{dc} = TrG\delta\Sigma$ and hence

$$\delta\Omega = \delta^*\Omega_{sp} = -\delta^*Tr \ln [\Sigma - G_0^{-1}] \quad (14)$$

which is an analog of the "local force theorem" in the density functional theory [47].

Further considerations are similar to the corresponding ones in LSDF approach. In the LDA++ scheme, the self energy is local, i.e. is diagonal in site indices. Let us write the spin-matrix structure of the self energy and Green function in the following form

$$\Sigma_i = \Sigma_i^c + \Sigma_i^s \sigma, \quad G_{ij} = G_{ij}^c + \mathbf{G}_{ij}^s \sigma \quad (15)$$

where $\Sigma_i^{(c,s)} = \frac{1}{2}(\Sigma_i^\uparrow \pm \Sigma_i^\downarrow)$, $\Sigma_i^s = \Sigma_i^s \mathbf{e}_i$, with \mathbf{e}_i being the unit vector in the direction of effective spin-dependent potential on site i , $\sigma = (\sigma_x, \sigma_y, \sigma_z)$ are Pauli matrices, $G_{ij}^c = \frac{1}{2}Tr_\sigma(G_{ij})$ and $\mathbf{G}_{ij}^s = \frac{1}{2}Tr_\sigma(G_{ij}\sigma)$. We assume that the bare Green function G^0 does not depend on spin directions and all the spin-dependent terms including the Hartree-Fock terms are incorporated in the self energy. Spin excitations with low energies are connected with the rotations of vectors \mathbf{e}_i : $\delta\mathbf{e}_i = \delta\boldsymbol{\varphi}_i \times \mathbf{e}_i$. According to the "local force theorem" (14) the corresponding variation of the thermodynamic potential can be written as $\delta\Omega = \delta^*\Omega_{sp} = \mathbf{V}_i \delta\boldsymbol{\varphi}_i$ where the torque is equal to

$$\mathbf{V}_i = 2Tr_{\omega L} [\Sigma_i^s \times \mathbf{G}_{ii}^s] \quad (16)$$

Using the spinor structure of the Dyson equation one can write the Green function in this expression in terms of pair contributions (a similar trick has been proposed in Ref. [48] in the framework of LSDF approach). As a result, we represent the total thermodynamic potential of spin rotations or the effective Hamiltonian in the form [34]

$$\Omega_{spin} = - \sum_{ij} Tr_{\omega L} \{ (\mathbf{G}_{ij}^s \Sigma_j^s) (\mathbf{G}_{ji}^s \Sigma_i^s) - \Sigma_i^s G_{ij}^c \Sigma_j^s G_{ji}^c - i (\Sigma_i^s \times G_{ij}^c \Sigma_j^s) \mathbf{G}_{ji}^s \} \quad (17)$$

one can show by direct calculations that $\left[\frac{\delta\Omega_{spin}}{\delta\boldsymbol{\varphi}_i} \right]_{G=const} = \mathbf{V}_i$. This means that $\Omega_{spin} \{\mathbf{e}_i\}$ is the effective spin Hamiltonian. The last term in Eq.(17) is nothing but Dzialoshinskii-Moriya interaction term. It is non-zero only in relativistic case

where Σ_j^s and G_{ji}^s can be, generally speaking, “non-parallel” and $G_{ij} \neq G_{ji}$ for the crystals without inversion center.

In the nonrelativistic case one can rewrite the spin Hamiltonian for small spin deviations near collinear magnetic structures in the following form $\Omega_{spin} = -\sum_{ij} J_{ij} \mathbf{e}_i \mathbf{e}_j$ where

$$J_{ij} = -Tr_{\omega L} \left(\Sigma_i^s G_{ij}^\uparrow \Sigma_j^s G_{ji}^\downarrow \right) \quad (18)$$

are the effective exchange parameters. This formula generalizes the LSDA expressions of [47] to the case of correlated systems.

Spin wave spectrum in ferromagnets can be considered both directly from the exchange parameters or by the consideration of the energy of corresponding spiral structure (cf. Ref. [47]). In nonrelativistic case when the anisotropy is absent one has

$$\omega_{\mathbf{q}} = \frac{4}{M} \sum_j J_{0j} (1 - \cos \mathbf{q} \mathbf{R}_j) \equiv \frac{4}{M} [J(0) - J(\mathbf{q})] \quad (19)$$

where M is the magnetic moment (in Bohr magnetons) per magnetic ion.

It should be noted that the expression for spin stiffness tensor $D_{\alpha\beta}$ defined by the relation $\omega_{\mathbf{q}} = D_{\alpha\beta} q_\alpha q_\beta$ ($\mathbf{q} \rightarrow \mathbf{0}$) in terms of exchange parameters has to be exact as the consequence of phenomenological Landau-Lifshitz equations which are definitely correct in the long-wavelength limit. Direct calculation basing on variation of the total energy under spiral spin rotations (cf. Ref. [47]) leads to the following expression

$$D_{\alpha\beta} = -\frac{2}{M} Tr_{\omega L} \sum_{\mathbf{k}} \left(\Sigma^s \frac{\partial G^\uparrow(\mathbf{k})}{\partial k_\alpha} \Sigma^s \frac{\partial G^\downarrow(\mathbf{k})}{\partial k_\beta} \right) \quad (20)$$

where \mathbf{k} is the quasimomentum and the summation is over the Brillouin zone. The expressions Eqs.(18) and (19) are reminiscent of usual RKKY indirect exchange interactions in the s-d exchange model (with Σ^s instead of the s-d exchange integral).

We prove in the Appendix that the expression for the stiffness is exact within the local approximation. At the same time, the exchange parameters themselves, generally speaking, differ from the exact response characteristics defined via static susceptibility since the latter contains vertex corrections. The derivation of approximate exchange parameters from the variations of thermodynamic potential can be useful for the estimation of J_{ij} in the different magnetic systems.

4 Computational Results

We have started from the spin-polarized LSDA band structure of ferromagnetic iron within the TB-LMTO method [37] in the minimal s, p, d basis set and used numerical orthogonalization to find the H_t part of our starting Hamiltonian. We take into account Coulomb interactions only between d -states. The correct

parameterization of the H_U part is indeed a serious problem. For example, first-principle estimations of average Coulomb interactions (U) [49,26] in iron lead to unreasonably large value of order of 5-6 eV in comparison with experimental values of the U -parameter in the range of 1-2 eV [26]. Semiempirical analysis of the appropriate interaction value [50] gives $U \simeq 2.3$ eV. The difficulties with choosing the correct value of U are connected with complicated screening problems, definitions of orthogonal orbitals in the crystal, and contributions of the intersite interactions. In the quasiatomic (spherical) approximation the full U -matrix for the d -shell is determined by the three parameters U , J and δJ or equivalently by effective Slater integrals F^0 , F^2 and F^4 [33,5]. For example, $U = F^0$, $J = (F^2 + F^4)/14$ and we use the simplest way of estimating δJ or F^4 keeping the ratio F^2/F^4 equal to its atomic value 0.625 [51].

Note that the value of intra-atomic (Hund) exchange interaction J is not sensitive to the screening and approximately equals to 0.9 eV in different estimations [49]. For the most important parameter U , which defines the bare vertex matrix Eq.(6), we use the value $U = 2.3$ eV for Fe [50], $U = 3$ eV for Co and Mn and $U = 4$ eV for Ni and Cu. To calculate the spectral functions: $A_\sigma(\mathbf{k}, E) = -\frac{1}{\pi} \text{Tr}_L G_\sigma(\mathbf{k}, E + i0)$ and DOS as their sum over the Brillouin zone we first made analytical continuation for the matrix self-energy from Matsubara frequencies to the real axis using the Pade approximation [52], and then numerically inverted the Green-function matrix as in Eq. (3) for each \mathbf{k} -point. In the self-consistent solution of the FLEX equations we used 1024 Matsubara frequencies and the FFT-scheme with the energy cut-off at 100 eV. The sum over irreducible Brillouin zone have been made with 72 \mathbf{k} -points for SCF-iterations and with 1661 \mathbf{k} -points for the final total density of states.

The depolarization of states near the Fermi level is another important correlation effect. The decrease of the ratio $P = [N_\uparrow(E_F) - N_\downarrow(E_F)] / [N_\uparrow(E_F) + N_\downarrow(E_F)]$ is a typical sign of spin-polaron effects [27,53]. In our approach this effects are taken into account through the $W_{\uparrow\downarrow}^{(ph)}$ terms in the effective spin-polarized LDA++ potential (Eq. (11)).

The energy dependence of self-energy in Fig.2 shows characteristic features of moderately correlated systems. At low energies $|E| < 1$ eV we see a typical Fermi-liquid behavior $\text{Im}\Sigma(E) \sim -E^2$, $\partial \text{Re}\Sigma(E) / \partial E < 0$. At the same time, for the states beyond this interval within the d -bands the damping is rather large (of the order of 1 eV) so these states corresponds to ill-defined quasiparticles, especially for occupied states. This is probably one of the most important conclusions of our calculations. Qualitatively it was already pointed out in Ref. [29] on the basis of a model second-order perturbation theory calculations. We have shown that this is the case of realistic quasiparticle structure of iron with the reasonable value of Coulomb interaction parameter.

Due to noticeable broadening of quasiparticle states the description of the computational results in terms of effective band structure (determined, for example, from the maximum of spectral density) would be incomplete. We present on the Fig.3 the *full* spectral density $A_\sigma(\mathbf{k}, E)$ including both coherent and incoherent parts as a function of \mathbf{k} and E . We see that in general the maxima of the

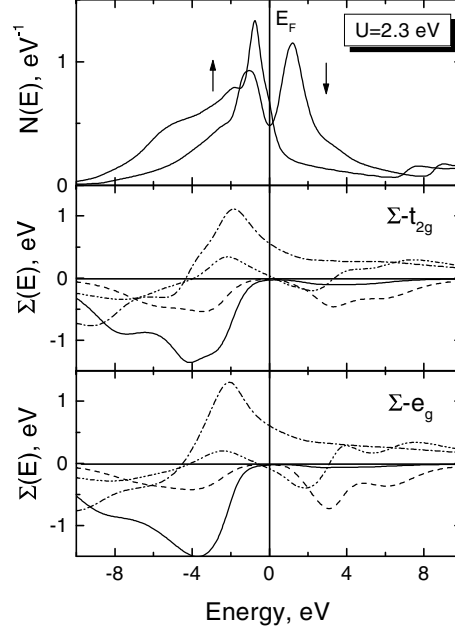


Fig. 2. Total spin-polarized density of states and d-part of self-energy for iron with $U=2.3$ eV and $J=0.9$ eV for the temperature $T=750$ K. Two different self-energies for t_{2g} and e_g d-states in the cubic crystal field symmetry are presented and four different lines corresponds to imaginary part spin-up (full line) and spin-down (dashed line) as well as real part spin-up (dashed-dot line) and spin-down (dashed-double-dot line).

spectral density (dark regions) coincide with the experimentally obtained band structure. However, for occupied majority spin states at about -3 eV the distribution of the spectral density is rather broad and the description of this states in terms of the quasiparticle dispersion is problematic. This conclusion is in complete quantitative agreement with raw experimental data on angle-resolved spin-polarized photoemission [54] with the broad non-dispersive second peak in the spin-up spectral function around -3 eV.

Comparison of the DOS for transition metals in the Fig. 4 shows an interesting correlations effects. First of all, the most prominent difference from the LSDA calculation is observed for the antiferromagnetic fcc-Mn. There is clear formation of the lower and upper Hubbard bands around ± 3 eV. Such behavior is related with the half-filled Mn d-shell which corresponds to a large phase space for particle-hole fluctuations. For the ferromagnetic bcc-Fe the p-h excitations are suppressed by the large exchange splitting and a bcc structural minimum in the DOS near the Fermi level. In the case of ferromagnetic fcc-Co and Ni the correlation effects are more important then for Fe, since there is no structural bcc-dip in the density of states. One could see a formation of a "three-peak" structure for the spin-down DOS for Co and Ni and satellite formation around -5 eV. In order to describe the satellite formation more carefully one need to

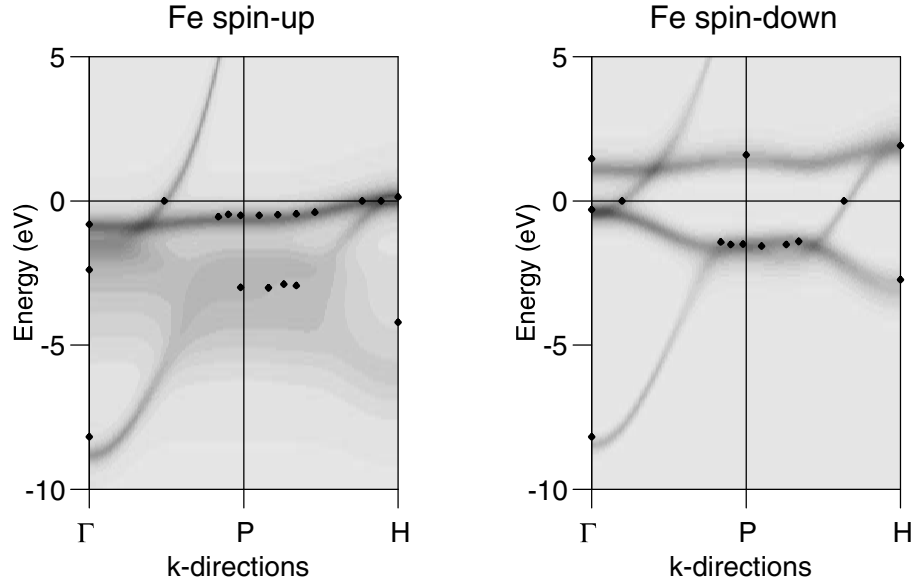


Fig. 3. Spectral function of ferromagnetic iron for spin-up (a) and spin-down (b) and the two k-directions in the Brillouin zone compare with the experimental angle resolved photoemission and de Haas - van Alphen (at the $E_F=0$) points

include T-matrix effects [25,30] or use the QMC scheme in LDA+DMFT calculations. Finally, there is no big correlation effects in non-magnetic fcc-Cu, since the d-states are located well below the Fermi level.

Using the self-consistent values for $\Sigma_m(i\omega)$ computed by QMC technique (Section II) we calculate the exchange interactions (Eq.18) and spin-wave spectrum (Eq.19) using the four-dimensional fast Fourier transform (FFT) method [55] for $(\mathbf{k}, i\omega)$ space with the mesh $20^3 \times 320$. The spin-wave spectrum for ferromagnetic iron is presented in Fig.5 in comparison with the results of LSDA-exchange calculations [47] and with different experimental data [56,57,58]. This room-temperature neutron scattering experiments has a sample dependence (Fe-12%Si in Ref. [56,58] and Fe-4%Si in Ref. [57]) due to problems with the bcc-Fe crystal growth. Note that for high-energy spin-waves the experimental data [58] has large error-bars due to Stoner damping (we show one experimental point with the uncertainties in the \mathbf{q} space). On the other hand, the expression of magnon frequency in terms of exchange parameters itself becomes problematic in that region due to breakdown of adiabatic approximation, as it is discussed above. Therefore we think that comparison of theoretical results with experimental spin-wave spectrum for the large energy needs additional investigation of Stoner excitation and required calculations of dynamical susceptibility in the LDA++ approach [38]. Within the LSDA scheme one could use the linear-response formalism [59] to calculate the spin-wave spectrum with the Stoner renormalizations, which should give in principle the same spin-wave stiffness

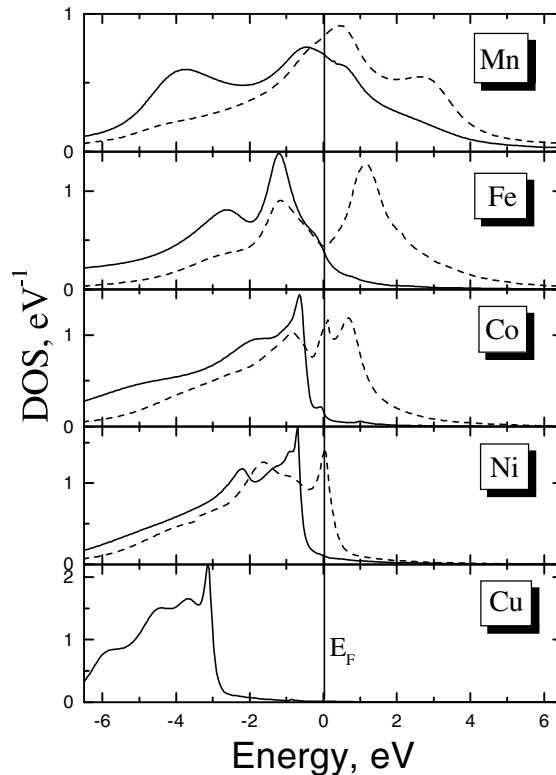


Fig. 4. The spin-polarized partial 3d density of states for different transition metals at the temperature $T=750$ K. The full line is the spin-up DOS and the dashed line is the spin-down DOS.

as our LSDA calculations. Our LSDA spin-wave spectrum agree well with the results of frozen magnon calculations [60,61].

At the lower-energy, where the present adiabatic theory is reliable, the LDA++ spin-waves spectrum agree better with the experiments then the result of the LSDA calculations. Experimental value of the spin-wave stiffness $D=280$ meV/Å² [57] agrees well with the theoretical LDA++ estimations of 260 meV/Å² [34].

Appendix

Here we prove that the expression for the stiffness constant Eq.(20) is exact in the framework of DMFT scheme.

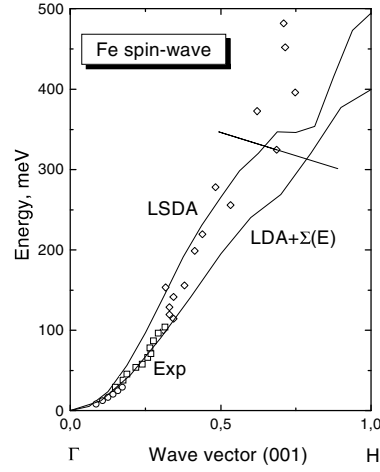


Fig. 5. The spin-wave spectrum for ferromagnetic iron in the LSDA and LDA+ Σ approximations compared with different experiments (circles [16], squares [17], and diamonds [18]) (a); The corresponding spin-wave spectrum from LDA+ Σ scheme in the (110) plane (b).

A rigorous expression for the stiffness constant has been obtained in Ref. [62]:

$$2 \langle S^z \rangle D_{\alpha\beta} q_\alpha q_\beta = C(\mathbf{q}) - i\mathbf{q} \cdot \int \frac{d^4k}{(2\pi)^4} \boldsymbol{\gamma}(k \downarrow, k \uparrow) G_\downarrow(k) G_\uparrow(k) (\mathbf{v}_\mathbf{k} \cdot \mathbf{q}) \quad (21)$$

where

$$C(\mathbf{q}) = \frac{1}{2} q_\alpha q_\beta \text{Tr}_L \sum_{\mathbf{k}} \frac{\partial^2 t(\mathbf{k})}{\partial k_\alpha \partial k_\beta} (n_{\mathbf{k}\uparrow} + n_{\mathbf{k}\downarrow}),$$

$k = (\mathbf{k}, k_0)$ is a momentum-energy 4-vector, $G(k)$ is the electron Green function, $t(\mathbf{k})$ is the one-particle (band) Hamiltonian, $n(\mathbf{k})$ is the one-particle distribution function, $\boldsymbol{\gamma}$ is the irreducible vector three-leg vertex. The irreducible scalar and vector vertices, γ and $\boldsymbol{\gamma}$, are connected with the total ones, Γ_0 and $\boldsymbol{\Gamma}$, by Bethe-Salpeter equations and the total vertices satisfy the Ward-Takahashi identity which is the consequence of the rotational invariance. Taking into account the Bethe-Salpeter equations one can rewrite them in terms of the irreducible vertices (for more details, see [62]). Let us assume now that the scalar irreducible vertex γ and Σ are momentum-independent (which is the real case in DMFT approach). Considering the \mathbf{q} -dependent part of the Ward-Takahashi identity in the limit $\mathbf{q} \rightarrow \mathbf{0}$ we have: $\boldsymbol{\gamma}(k \downarrow, k \uparrow) = \frac{\partial t(\mathbf{k})}{\partial \mathbf{k}} \equiv \mathbf{v}(\mathbf{k})$. Substituting this into Eq.(21) one has

$$D_{\alpha\beta} = \frac{1}{2 \langle S^z \rangle} \text{Tr}_L \left\{ \sum_{\mathbf{k}} \frac{\partial^2 t(\mathbf{k})}{\partial k_\alpha \partial k_\beta} n_{\mathbf{k}} - i \int \frac{d^4k}{(2\pi)^4} v_{\mathbf{k}\alpha} G_\downarrow(k) v_{\mathbf{k}\beta} G_\uparrow(k) \right\} \quad (22)$$

On the other hand, our Eq.(19) reads $2 \langle S^z \rangle D_{\alpha\beta} = \frac{1}{2} \frac{\partial^2 J(\mathbf{q})}{\partial q_\alpha \partial q_\beta} |_{\mathbf{q} \rightarrow 0}$ where $J(\mathbf{q})$ is defined by Eq.(18). Calculating the derivatives of the exchange parameters we obtain

$$\frac{\partial J(\mathbf{q})}{\partial q_\alpha} = i \int \frac{d^4 k}{(2\pi)^4} Tr_L S(k) G_\downarrow(k) \frac{\partial t(\mathbf{k})}{\partial k_\alpha} G_\downarrow(k) S(k) G_\uparrow(k+q)$$

(we shift here $k \rightarrow k+q$ in the integrand). Then

$$\frac{\partial^2 J(\mathbf{q})}{\partial q_\alpha \partial q_\beta} |_{\mathbf{q} \rightarrow 0} = i \int \frac{d^4 k}{(2\pi)^4} Tr_L S(k) G_\downarrow(k) \frac{\partial t(\mathbf{k})}{\partial k_\alpha} G_\downarrow(k) S(k) G_\uparrow(k) \frac{\partial t(\mathbf{k})}{\partial k_\beta} G_\uparrow(k)$$

This expression can be simplified by using the sum rule $(G_\uparrow - G_\downarrow) = G_\uparrow S G_\downarrow$ (where $S = \Sigma_\uparrow - \Sigma_\downarrow$) which is the consequence of the Dyson equation provided that only Σ is spin-dependent. Taking it into account in Eq.(22) one has

$$\frac{\partial^2 J(\mathbf{q})}{\partial q_\alpha \partial q_\beta} |_{\mathbf{q} \rightarrow 0} = i \int \frac{d^4 k}{(2\pi)^4} Tr_L \{ 2G_\uparrow(k) \frac{\partial t(\mathbf{k})}{\partial k_\alpha} G_\downarrow(k) \frac{\partial t(\mathbf{k})}{\partial k_\beta} + \sum_\sigma G_\sigma^2(k) \frac{\partial t(\mathbf{k})}{\partial k_\alpha} \frac{\partial t(\mathbf{k})}{\partial k_\beta} \}$$

The first term is exactly coincide with the last one in Eq.(21) and the first term can be transformed further using the identity: $G_\sigma^2(k) = \frac{\partial G_\sigma(k)}{\partial t(\mathbf{k})}$ Then

$$\int \frac{d^4 k}{(2\pi)^4} \sum_\sigma G_\sigma^2(k) \frac{\partial t(\mathbf{k})}{\partial k_\alpha} \frac{\partial t(\mathbf{k})}{\partial k_\beta} = \sum_{\mathbf{k}\sigma} \frac{\partial n_\sigma(\mathbf{k})}{\partial t(\mathbf{k})} \frac{\partial t(\mathbf{k})}{\partial k_\alpha} \frac{\partial t(\mathbf{k})}{\partial k_\beta}$$

Since $n_\sigma(\mathbf{k}) = n_\sigma[t(\mathbf{k})]$ we have: $\frac{\partial}{\partial k_\alpha} n_\sigma[t(\mathbf{k})] = \frac{\partial n_\sigma(\mathbf{k})}{\partial t(\mathbf{k})} \frac{\partial t(\mathbf{k})}{\partial k_\alpha}$ and finally, integrating by part, one obtains:

$$- \sum_{\mathbf{k}} \frac{\partial n_\sigma}{\partial k_\alpha} \frac{\partial t(\mathbf{k})}{\partial k_\beta} = \sum_{\mathbf{k}} n_\sigma(\mathbf{k}) \frac{\partial^2 t(\mathbf{k})}{\partial k_\alpha \partial k_\beta}$$

Thus, our expression (Eq.(20)) coincides with the exact one (Eq.(21)). We use here the only assumption that both the self-energy and three-leg irreducible vertex are momentum independent as well as the Ward-Takahashi identities which are exact consequences of the rotational invariance of the spin system.

5 Conclusions

We have proposed a general scheme for investigation of the correlation effects in the quasiparticle band structure calculations for itinerant-electron magnets. This approach is based on the combination of the dynamical mean-field theory and the fluctuating exchange approximation. Application of LDA+DMFT method gives an adequate description of the quasiparticle electronic structure for ferromagnetic iron. The main correlation effects in the electron energy spectrum are strong damping of the occupied states below 1 eV from the Fermi level E_F and essential depolarization of the states in the vicinity of E_F . We obtained a

reasonable agreement with different experimental spectral data (spin-polarized photo- and thermoemission). The method is rather universal and can be applied for other magnetic systems, both ferro- and antiferromagnets.

We discussed as well a general method for the investigation of magnetic interactions in the correlated electron systems. This scheme is not based on the perturbation theory in “ U ” and could be applied for rare-earth systems where both the effect of the band structure and the multiplet effects are crucial for a rich magnetic phase diagram. Our general expressions are valid in relativistic case and can be used for the calculation of both exchange and Dzialoshinskii-Moriya interactions, and magnetic anisotropy [34]. An illustrative example of ferromagnetic iron shows that the correlation effects in exchange interactions may be noticeable even in such moderately correlated systems. For rare-earth metals and their compounds, colossal magnetoresistance materials or high- T_c systems, this effect may be much more important. For example, the careful investigations of exchange interactions in MnO within the LSDA, LDA+ U and optimized potential methods for MnO [63] show the disagreement with experimental spin-wave spectrum (even for small \mathbf{q}), and indicate a possible role of correlation effects.

This work demonstrates an essential difference between spin density functional approach and LDA++ formalism. The latter method deals with the thermodynamic potential as a functional of the local Green function rather than the electron density. Nevertheless, there is a close connection between two techniques (the self-energy corresponds to the exchange-correlation potential, etc). In particular, an analog of local force theorem can be proved for LDA++ approach. It may be useful not only for the calculation of magnetic interactions but also for elastic stresses, in particular, pressure, and other physical properties.

Acknowledgments

We are grateful to O.K. Andersen, C. Carbone, P. Fulde, O. Gunnarsson, G. Kotliar, and A. Georges for helpful discussions. The work was supported by the Netherlands Organization for Scientific Research (NWO project 047-008-16) and partially supported by Russian Basic Research Foundation, grant 00-15-96544.

References

1. P. Hohenberg and W. Kohn, Phys. Rev. **136**, B864 (1964); W. Kohn and L.J. Sham, *ibid.* **140**, A1133 (1965); R. O. Jones and O. Gunnarsson, Rev. Mod. Phys. **61**, 689 (1989)
2. N.F.Mott, *Metal-Insulator Transitions* (Taylor and Francis, London 1974)
3. K. Terakura, A. R. Williams, T. Oguchi, and J. Kubler, Phys. Rev. Lett. **52**, 1830 (1984)
4. W. E. Pickett, Rev. Mod. Phys. **61**, 433 (1989)
5. V. I. Anisimov, F. Aryasetiawan, and A. I. Lichtenstein, J. Phys.: Condens. Matter **9**, 767 (1997)
6. P. Fulde, J. Keller, and G. Zwicknagl, Solid State Phys. **41**, 1 (1988)

7. D.E. Eastman, F.J. Himpsel, and J.A. Knapp, Phys. Rev. Lett. **44**, 95 (1980)
8. J. Staunton, B. L. Gyorffy, A. J. Pindor, G. M. Stocks, and H. Winter, J. Phys. F **15**, 1387 (1985)
9. P. Genoud, A. A. Manuel, E. Walker, and M. Peter, J. Phys.: Cond. Matter **3**, 4201 (1991)
10. A. Vaterlaus, F. Milani, and F. Meier Phys. Rev. Lett. **65**, 3041 (1990)
11. R. Monnier, M. M. Steiner, and L. J. Sham, Phys. Rev. B **44**, 13678 (1991)
12. M. I. Katsnelson and A. I. Lichtenstein, J. Phys.: Cond. Matter **11**, 1037 (1999)
13. D. Chandleris, J. Lecante, and Y. Petroff, Phys. Rev. B **27**, 2630 (1983); A. Gutierrez and M. F. Lopez, Phys. Rev. B **56**, 1111 (1997)
14. R. E. Kirby, B. Kisker, F. K. King, and E. L. Garwin, Solid State Commun. **56**, 425 (1985)
15. L. Hedin, Phys. Rev. **139**, A796 (1965); F. Aryasetiawan and O. Gunnarsson, Rep. Prog. Phys. **61**, 237 (1998)
16. A. Svane and O. Gunnarsson, Phys. Rev. Lett. **65**, 1148 (1990)
17. E. K. U. Gross and W. Kohn, Adv. Quant. Chem. **21**, 255 (1990)
18. A. A. Abrikosov, L. P. Gorkov, and I. E. Dzialoshinskii, *Methods of Quantum Field Theory in Statistical Physics* (Pergamon Press, New York 1965); G. Mahan, *Many-Particle Physics* (Plenum Press, New York 1981)
19. J. M. Luttinger and J. C. Ward, Phys. Rev. **118**, 1417 (1960); see also G. M. Carneiro and C. J. Pethick, Phys. Rev. B **11**, 1106 (1975)
20. G. Baym and L. P. Kadanoff, Phys. Rev. **124**, 289 (1961); G. Baym, Phys. Rev. **127**, 1391 (1962)
21. T. Jarlborg, Rep. Prog. Phys. **60**, 1305 (1997)
22. T. Moriya, *Spin Fluctuations in Itinerant Electron Magnetism* (Springer, Berlin 1985)
23. T. Kotani, Phys. Rev. B **50**, 14816 (1994); T. Kotani and H. Akai, Phys. Rev. B **54**, 16502 (1996); N. E. Zein, V. P. Antropov, and B. N. Harmon, J. Appl. Phys. **87**, 5079 (2000)
24. D. Ceperley and B. J. Alder, Phys. Rev. Lett. **45**, 4264 (1980)
25. A. Liebsch, Phys. Rev. Lett. **43**, 1431 (1979); Phys. Rev. B **23**, 5203 (1981);
26. M. M. Steiner, R. C. Albers, and L. J. Sham, Phys. Rev. B **45**, 13272 (1992)
27. V. Yu. Irkhin, M. I. Katsnelson, and A. V. Trefilov, J. Phys. : Cond. Matter **5**, 8763 (1993); S. V. Vonsovsky, M. I. Katsnelson, and A. V. Trefilov, Phys. Metals Metallography **76**, 247, 343 (1993)
28. T. Greber, T. J. Kreuntz, and J. Osterwalder, Phys. Rev. Lett. **79**, 4465 (1997); B. Sinkovich, L. H. Tjeng, N. B. Brooks, J. B. Goedkoop, R. Hesper, E. Pellegrin, F. M. F. de Groot, S. Altieri, S. L. Hulbert, E. Shekel, and G. A. Sawatzky, Phys. Rev. Lett. **79**, 3510 (1997)
29. G. Treglia, F. Ducastelle, and D. Spanjaard, J. Phys. (Paris) **43**, 341 (1982)
30. V. Drchal, V. Janiš, and J. Kudrnovský in *Electron Correlations and Material Properties*, edited by A. Gonis, N. Kioussis, and M. Ciftan, Kluwer/Plenum, New York 1999, p. 273.
31. J. Igarashi, J. Phys. Soc. Japan **52**, 2827 (1983); F. Manghi, V. Bellini, and C. Arcangeli, Phys. Rev. B **56**, 7149 (1997)
32. W. Nolting, S. Rex, and S. Mathi Jaya, J. Phys. : Cond. Matter **9**, 1301 (1987)
33. A. I. Lichtenstein and M. I. Katsnelson, Phys. Rev. B **57**, 6884 (1998)
34. M. I. Katsnelson and A. I. Lichtenstein, Phys. Rev. B **61**, 8906 (2000)
35. V. I. Anisimov, A. I. Poteryaev, M. A. Korotin, A. O. Anokhin, and G. Kotliar, J. Phys. Cond. Matter **9**, 7359 (1997).

36. A. I. Liechtenstein, V. I. Anisimov, and J. Zaanen, Phys. Rev. B **52**, R5467 (1995)
37. O.K. Andersen, Phys. Rev. **B12**, 3060 (1975); O.K. Andersen and O. Jepsen, Phys. Rev. Lett. **53**, 2571 (1984)
38. A. Georges, G. Kotliar, W. Krauth, and M. Rozenberg, Rev. Mod. Phys. **68**, 13 (1996)
39. W. Metzner and D. Vollhardt, Phys. Rev. Lett. **62**, 324 (1989).
40. M. J. Rozenberg, Phys. Rev. B **55**, R4855 (1997); K. Takegahara, J. Phys. Soc. Japan **62**, 1736 (1992).
41. J. E. Hirsch and R. M. Fye, Phys. Rev. Lett. **25**, 2521 (1986)
42. M. Jarrell and J. E. Gubernatis, Physics Reports **269**, 133 (1996)
43. N. E. Bickers and D. J. Scalapino, Ann. Phys. (N. Y.) **193**, 206 (1989)
44. G. Esirgren and N. E. Bickers, Phys. Rev. B **57**, 5376 (1998)
45. M. Fleck, A. I. Liechtenstein, A. M. Oles, L. Hedin, and V. I. Anisimov, Phys. Rev. Lett. **80**, 2393 (1998)
46. A. R. Mackintosh, O. K. Andersen, In: *Electron at the Fermi Surface*, ed.M. Springfield (Univ. Press, Cambridge, 1980) p.145
47. A. I. Liechtenstein, M. I. Katsnelson, and V. A. Gubanov, J. Phys. F **14**, L125; Solid State Commun. **54**, 327 (1985); A. I. Liechtenstein, M. I. Katsnelson, V. P. Antropov, and V. A. Gubanov, J. Magn. Magn. Mater. **67**, 65 (1987)
48. V. P. Antropov, M. I. Katsnelson, and A. I. Liechtenstein, Physica B **237-238**, 336 (1997)
49. V. I. Anisimov and O. Gunnarsson, Phys. Rev. B **43**, 7570 (1991)
50. A. M. Oles and G. Stollhoff, Phys. Rev. B **29**, 314 (1984)
51. V. I. Anisimov, I. V. Solovjev, M. A. Korotin, M. T. Czyzyk, and G. A. Sawatzky, Phys. Rev. B **48**, 16929 (1993)
52. H. J. Vidberg and J. W. Serene, J. Low Temp. Phys. **29**, 179 (1977)
53. V. Yu. Irkhin and M. I. Katsnelson, Physics-Uspekhi **37**, 659 (1994)
54. E. Kisker, K. Schroeder, T. Gudat, and M. Campagna, Phys. Rev. B **31**, 329 (1985)
55. S. Goedecker, Comp. Phys. Commun. **76**, 294 (1993)
56. J. W. Lynn, Phys. Rev. B **11**, 2624 (1975)
57. H. A. Mook and R. M. Nicklow, Phys. Rev. B **7**, 336 (1973)
58. T. G. Peerring, A. T. Boothroyd, D. M. Paul, A. D. Taylor, R. Osborn, R. J. Newport, H. A. Mook, J. Appl. Phys. **69**, 6219 (1991)
59. S. Y. Savrasov, Phys. Rev. Lett. **81**, 2570 (1998)
60. L. M. Sandratskii and J. Kübler, J. Phys.: Condens. Matter. **4**, 6927 (1992)
61. S. V. Halilov, H. Eschrig, A. Y. Perlov, and P. M. Oppeneer, Phys. Rev. B **58**, 293 (1998)
62. J. A. Hertz and D. M. Edwards, J. Phys. F **3**, 2174 (1973)
63. I. V. Solovjev and K. Terakura, Phys. Rev. B **58**, 15496 (1998)

Probing the Electronic States of Band Ferromagnets with Photoemission

Thomas Greber

Physik Institut der Universität Zürich, Switzerland

Abstract. Angle scanned photoemission experiments that map the electronic band structure up to $5k_B T$ above the Fermi level are reviewed. After a short tutorial of the basic principles for the interpretation of angular resolved photoemission (ARUPS) experimental data on the band ferromagnet nickel are presented. The exchange splitting of the sp -bands and the d -bands can be accurately determined. The influence of the temperature and adsorbate layers on the magnetism of the surface are investigated.

For clean nickel metal the ferromagnetic – paramagnetic phase transition is observed in detail. It is found that the exchange splitting follows - within the accuracy of the experiment - the bulk magnetization and disappears at the Curie temperature [1]. A magnetically “active” region in k -space, where sp and d minority bands coincide on the Fermi surface is inspected.

A monolayer of hexagonal boron nitride on Ni(111) strongly influences the Fermi surface of the interface. The formally insulating h -BN acts as an atomic grating and induces umklapp processes. It is seen how the exchange splitting is affected and that the overlayer changes the relative spin asymmetry of exchange split sp -bands.

1 Introduction

Photoemission is among the few techniques that gives experimental access to all relevant electronic states at surfaces that constitute e.g. band ferromagnetism, superconductivity or chemical bonding. For the case of band ferromagnets this was realized with the early experiments of Pierce and Spicer [2] who observed the ferro- paramagnetic phase transition in nickel and in the same issue of Bänninger et al. who measured below the Curie temperature spin polarized photoelectrons from nickel [3]. In the mean time the technique of photoemission has matured close to the complete photoemission experiment where all degrees of freedom of the photoelectrons are measured in the same setup.

For the study of phase transitions in metals it is generally accepted that the states at the Fermi level are the key players. All electronic states around the Fermi level should be accessed in order to get a complete picture.

Photoemission is very fast and localized. It suffers, however, from the $N \rightarrow N - 1$ “problem” i.e. the interaction of the hole state that is created in the photoemission process. Its influence on the photoelectron may not be neglected – in particular in correlated systems like a band ferromagnet and makes comparisons with ground state calculations challenging.

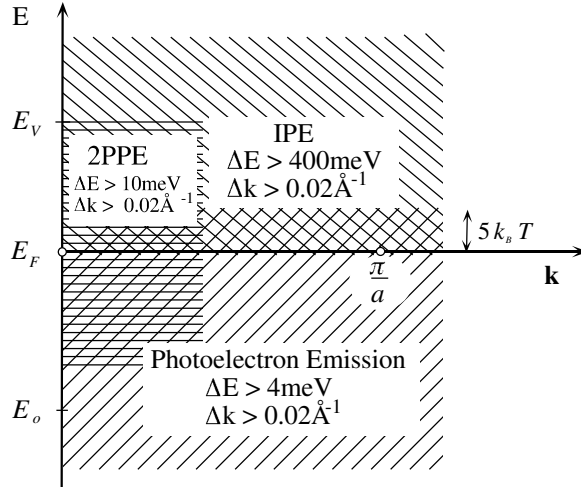


Fig. 1. Accessible energies and k-space for different experimental methods. The energy-resolution ΔE and k-resolution Δk are given for Two Photon Photoelectron Emission (2PPE), Inverse Photoemission (IPE) and photoelectron emission. The relevant energies, the Fermi energy E_F , band bottom E_o and vacuum energy E_v are indicated as well as the Brillouin zone boundary π/a .

2 Experimental

In Fig.1 the electron energies and k-vectors that can be measured with k-resolving techniques like Inverse PhotoEmission (IPE), Two Photon PhotoEmission (2PPE) and PhotoEmission (PE) are shown. 2PPE, as it is performed today, has - like Scanning Tunneling Spectroscopy (STS) - the potential of probing the occupied and unoccupied electronic states. It suffers, however, from the relatively low energies and k-vectors that can be reached and is thus unable to probe the whole Brillouin zone. This is not the case in inverse photoemission and photoemission if photon energies > 10 eV are used. There, in principle, all k-vectors in the Brillouin zone may be probed. It is shown in this article that electron states near the Brillouin zone boundary play a key role in band ferromagnets. The photoemission experiment is senior to inverse photo-emission mainly due to the better energy resolution and detection sensitivity of electron- and photon-spectrometers, respectively. Today, an energy resolution of better than 4 meV and a k resolution of better than 0.02 \AA^{-1} are obtained with photoemission.

The presented data are recorded with a spectrometer with an overall energy (momentum) resolution of about 50 meV (0.02 \AA^{-1}). This is sufficient for studies at room temperature or above since the thermal broadening of the

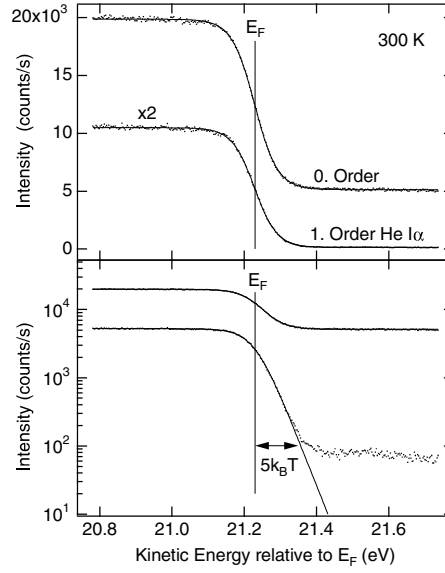


Fig. 2. Photoemission spectra taken around the He I α Fermi level E_F of polycrystalline silver at 300 K. Unmonochromatized (zero order) and monochromatized (1st order) He I α radiation was used for excitation. In the lower panel the same data are shown on a logarithmic intensity scale. From Ref.[4].

Fermi function at room temperature corresponds to the convolution of a step function with a Gaussian of 100 meV ($4k_B T$) full width at half maximum. For problems at non zero temperature as it is e.g. the ferromagnetic – paramagnetic phase transition it is possible to probe thermally populated electronic states *above* the Fermi level [4]. Photoemission has thus the potential to measure all relevant states that drive e.g. phase transitions or electron tunneling. This requires a clean and highly intense photon source. Clean means that it should be monochromatic and not have higher photon energy components as e.g. higher harmonics, since these photons produce photoemission above the Fermi level of the main photon energy. The high intensity is needed since the thermal occupation decreases at energies $\Delta\mathcal{E}$ above the Fermi level with $\approx \exp(-\Delta\mathcal{E}/k_B T)$. In our laboratory this setup is realized with a monochromatized ECR plasma driven He gas discharge lamp [4]. In Fig.2 the performance of such a photon source is shown for the photoemission from the Fermi level of a polycrystalline silver sample at 300 K. The logarithmic intensity scale reveals the Boltzmann wing up to $5k_B T$ above the Fermi level. Such measurements of a Fermi level around which the density of states is constant have to be used in order to normalize the photoemission data for a set of energy distribution curves (EDC's) at various emission angles. Then quantitative information on peak positions in energy E and momentum \mathbf{k} can be recovered [1]. For the normalization it is most convenient to subtract a constant background (in the order of $\approx 0.1\%$) of the

average intensity at the Fermi level from the data before normalizing them with the experimentally determined Fermi function. For the purposes of this article an analytical Fermi function of the form $f(E) = 1/(1 + \exp((E - E_F)/k_B T_{\text{eff}}))$ is sufficient. The “effective” temperature $T_{\text{eff}} = \sqrt{T^2 + (\Delta E/4k_B)^2}$ depends on the sample temperature T and the overall full width at half maximum energy-resolution of the spectrometer ΔE [1]. In the presented experiments the spin polarization is not measured as it is, e.g. done with a Mott polarimeter. This has the drawback of not getting a direct identification of the spin states. On the other hand the sample has not to be macroscopically magnetized over the probed sample area as it is necessary for the measurement of the spin polarization. The assignment of the spin states of direct photoemission transitions is done with help of spin polarized band structure calculations [5]. A further requirement for a band mapping experiment is the accurate control of photoemission direction and an angular resolution below 1° . This is achieved in scanning the sample orientation in front of the detector with an automated high accuracy two angle sample goniometer [4,6,7]. This setup has the advantage of keeping the angle between the photon source and the detector constant and thus avoids matrix element variations that were caused by different light incidences relative to the detector.

3 Angular Resolved Photoemission (ARUPS)

There are excellent reviews on photoemission [8], angular resolved photoemission at UV photon energies (ARUPS) in particular [9] and Fermi surface mapping [10]. Photoemission has the potential of measuring all degrees of freedom of an electron in its initial state. It is a local probe since the momentum for the emission is transferred on the photoelectron on a femto second time scale. Nevertheless, it is able to probe the electronic bands of a solid i.e. the delocalized nature of the electron in its initial state. The mapping of the bands is accompanied with a broadening in energy and momentum that has various reasons. Like in lifetime determination from the spectral width in energy, the broadening in k provides a lower limit of extension of the excited states. A band state with an angular width of 0.1\AA^{-1} has e.g. a spatial extension $\Delta x \geq 10\text{\AA}$.

3.1 Conservation Laws in Photoemission

In order to discuss the basic physics (conservation laws) of photoemission it is convenient to use the three step model. There, the photoemission process is described in a sequence of (i) the photoexcitation, (ii) the transport of the electron to the surface and (iii) its refraction at the surface potential barrier and propagation to the detector.

Step (i), the photoexcitation, obeys energy-, momentum-, spin- and angular momentum conservation. Energy and momentum conservation are shown in an E vs k diagram in Fig. 3 where a periodic zone scheme for an initial state band and the final state is plotted. If at a given k -value, the photon energy matches

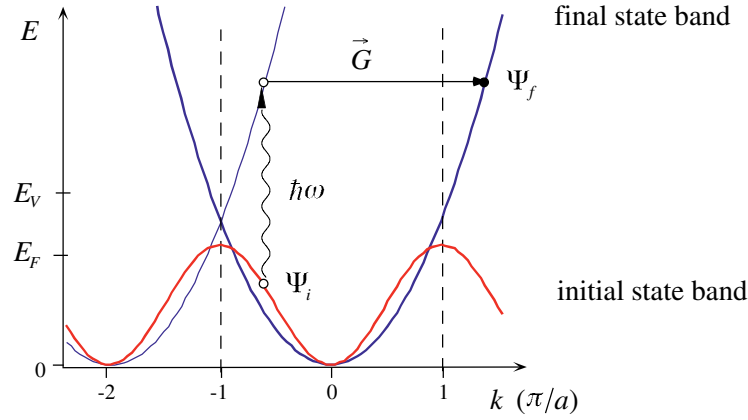


Fig. 3. Photoemission process for band mapping in a periodic crystal in a E vs k scheme. The final state energy, momentum and spin in Ψ_f is related to the initial state Ψ_i via energy, momentum and spin conservation. $\hbar\omega$ is the photon energy and \mathbf{G} is a reciprocal lattice vector.

the energy difference between an occupied initial state and an unoccupied final state the photoemission is at resonance at this particular point in k -space and a so called direct transition can be observed, if the final state propagates into the vacuum. The photoexcitation is treated as a vertical transition, i.e. the momentum of the photon is neglected: $\omega/c \ll \pi/a$, where a is the lattice constant. This is written down as energy conservation:

$$E_f = E_i + \hbar\omega \quad (1)$$

where E_f and E_i are the final and initial state energy and $\hbar\omega$ the photon energy and momentum conservation:

$$\mathbf{k}_f = \mathbf{k}_i + \mathbf{G} \quad (2)$$

where $\hbar\mathbf{k}_f$, $\hbar\mathbf{k}_i$ are the final and initial state momenta and \mathbf{G} is a reciprocal lattice vector that provides the momentum for propagation to the surface.

It has to be noted that the photoemission process leaves a hole state in the solid i.e. is a $N \rightarrow N - 1$ process, where N is the number of electrons in the ground state. Therefore the $N - 1$ final state energies E_f do not directly (via Eqn.1) reflect the ground state energy. The interaction of the photoemission hole state with the rest of the solid and the photoelectron is important. This causes a finite lifetime of the final state i.e. a broadening of the observed transitions in energy and momentum. Therefore shifts in energy and momentum with respect to the ground state may occur. For magnetic systems the response on the perturbation upon photo excitation furthermore depends on the spin polarization of the photoelectron and spin dependent correlation effects are important [11]. Transitions from the Fermi level are, however, least affected by these effects since there is only thermal energy available for final state relaxation.

In the photon energy range of interest, the spin orientation of the electrons is conserved:

$$\boldsymbol{\sigma}_f = \boldsymbol{\sigma}_i \quad (3)$$

where $\boldsymbol{\sigma}_f$ and $\boldsymbol{\sigma}_i$ are the spin of the final and initial state.

Finally, the angular momentum character of the photoelectron final state is determined from the dipole selection rules which read in the non relativistic formulation:

$$\ell_f = \ell_i \pm 1; \quad \ell \geq 0 \quad (4)$$

where $\hbar\ell_f$ and $\hbar\ell_i$ are the angular momenta of the final and initial state. For the magnetic quantum number m ($|m| \leq \ell$) we find:

$$m_f = m_i, \quad (5a)$$

$$m_f = m_i \pm 1. \quad (5b)$$

where Eqn.5a) applies for linearly polarized light and Eqn.5b) for right- or left circularly polarized light, respectively. The quantisation axis points along the propagation of the photons.

The direction and polarization of the incoming light thus provide selection rules that are useful for the identification of particular bands. The dipole selection rules can be exploited for getting information on the magnetism in performing polarization dependent photoemission experiments. If the sample has a magnetization the photoemission depends on the orientation between the magnetisation and the light propagation and/or polarization (dichroism) [12].

In step (ii), the propagation of the photoelectron to the surface, diffraction, elastic and inelastic scattering may occur, but there remains information from the initial state $\Psi_i(E_i, \mathbf{k}_i, \boldsymbol{\sigma}_i)$. In this step differences in the inelastic mean free path between minority and majority spin electrons affect the spectral weight of the observed transitions.

After the last step (iii), where the energy for the emission of the photoelectron into the vacuum is paid, the $(N-1)$ photoemission binding energy E_B measured from the Fermi level E_F gets

$$E_B \equiv \hbar\omega - E_{kin}^{vac} - \Phi \quad (6)$$

where E_{kin}^{vac} is the electron kinetic energy in the vacuum and Φ is the work function. The surface barrier affects the momentum perpendicular to the surface (refraction). If we make the free electron final state approximation (as it is implicitly done in Fig. 3) we set

$$E_f \equiv \frac{\hbar^2 \mathbf{k}_f^2}{2m_e} \quad (7)$$

and note that m_e is the free electron mass and E_f is measured from the valence band bottom. Then the wave numbers of the initial states \mathbf{k}_i can be determined

from the measured photoelectron momentum $\hbar\mathbf{k}_m$ with the following identities for the components of \mathbf{k} parallel and perpendicular to the surface:

$$\mathbf{k}_{i\parallel} = \mathbf{k}_{m\parallel} - (\mathbf{G} - \mathbf{nGn}), \quad (8a)$$

$$k_{i\perp} = \sqrt{k_{m\perp}^2 + 2m_e U/\hbar^2} - \mathbf{nG}. \quad (8b)$$

U is the inner potential, i.e. the energy difference between the vacuum level and the valence band bottom. The surface normal \mathbf{n} is parallel to ∇U . If \mathbf{n} is constant then $\mathbf{k}_{i\parallel}$, the component parallel to the surface of \mathbf{k}_i is conserved up to a reciprocal surface lattice vector $\mathbf{Q} = \mathbf{G} - \mathbf{nGn}$. It has to be noted that the conservation of \mathbf{k}_{\parallel} is given as well without the free final state assumption (Eqn.7). For \mathbf{k}_{\parallel} conservation the direction of ∇U has, however, to be constant over the whole sampling area. This follows from $\mathbf{nG} > 0$ and Eqn.8a. For the experiment it is furthermore important to remember that parallel momentum conservation requires zero electric field between the detector and the sample and therefore work function differences between the detector and the sample have to be compensated with a sample bias voltage. If the inner potential varies as it does e.g. for the two spin components in a ferromagnet [13], the determination of the normal component $k_{i\perp}$ of \mathbf{k}_i is affected. From Eqn.8b and Eqn.2 it is seen that the normal component of \mathbf{k}_f can be measured if $|\mathbf{k}_f| > \sqrt{2m_e U}/\hbar$ and we call this limit photoemission (PE) horizon (see Fig.4).

Therefore, if E_{kin}^{vac} , $\hbar\mathbf{k}_m$ and σ_f are measured, \mathbf{n} and the reciprocal lattice \mathbf{G} are known, the photoemission binding energy E_B , wave numbers \mathbf{k}_i , and spin polarization σ_i can be found out by photoemission. If the free final state approximation is not valid, the parallel component of \mathbf{k}_i only is determined. For 20 eV photoelectrons the free final state approximation works astonishingly well while it is expected to become problematic for lower energies. For two dimensional systems, with no dispersion perpendicular to the surface, the complete information on the electronic states in the Brillouin zone is obtained by a single photon energy. Dispersion perpendicular to the surface can be measured if the photon energy $\hbar\omega$ is scanned as it is conveniently done at synchrotrons.

3.2 k-Space Mapping

A complete photoemission experiment should sample all points in \mathbf{k} -space. If, e.g. the whole second Brillouin zone of nickel down to binding energies of 10 eV shall be scanned, photon energies from 6 eV up to 120 eV have to be at hand and all emission angles should be accessible.

In order to better visualize the angle scanned photoemission experiment it is convenient to redraw Fig. 3. If we sit at a given final state energy E_f , i.e. set the electron analyzer to a fixed kinetic energy E_{kin}^{vac} and use a constant photon energy, the picture in Fig. 3 translates from an E vs. \mathbf{k} picture in a k_{\parallel} vs. k_{\perp} picture (see Fig.4). Normally the initial state bands at the chosen binding energy appear as lines. For the final state band the case is particularly simple in the free final state approximation where the final state is a circle centered at the origin

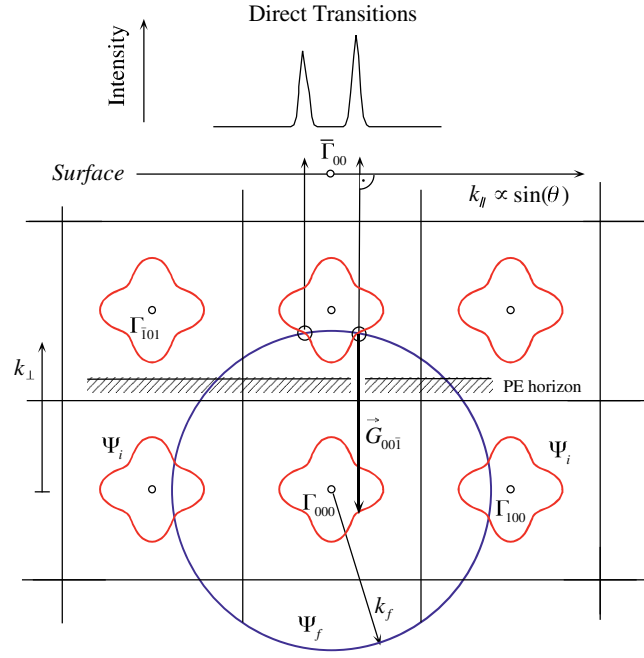


Fig. 4. Photoemission process for band mapping in a k_{\parallel} vs. k_{\perp} picture. Whenever the final state band Ψ_f crosses an initial state band of the periodic zone scheme Ψ_i a direct transition occurs. This transition may be observed above the photoemission (PE) horizon that is a consequence of the surface barrier potential.

of k-space (Γ_{000}) with radius k_f :

$$k_f = \sqrt{2m_e(E_{kin}^{vac} + U)/\hbar} \quad (9a)$$

$$k_f [\text{\AA}^{-1}] = 0.5123 \sqrt{(E_{kin}^{vac} + U) [eV]} \quad (9b)$$

Every intersection point between the initial state band with the periodicity of the reciprocal lattice \mathbf{G} and the final state indicates a direct transition at the given energy E_B (see Eqn. 6). Parallel momentum conservation projects these states normal to the surface, where they can be measured at the corresponding emission angles:

$$k_{\parallel} = \frac{1}{\hbar} \sqrt{2m_e E_{kin}^{vac}} \sin(\theta_m) \quad (10)$$

where θ_m is the measured polar emission angle. The above procedure for k-space mapping is identical to that of Fermi-surface mapping as outlined by Aebi et al. [14]. For Fermi surface maps $E_B \equiv 0$ and correspondingly $E_{kin}^{vac} = \hbar\omega - \Phi$ is the analyzed energy in the detector (see Eqn.6). From Fig.4 it becomes clear that a Fermi surface may be mapped completely, in scanning \mathbf{k}_f , i.e. the photon energy and all emission angles, while the analyzer is set to the Fermi energy E_F .

4 Experimental Results

4.1 The Temperature Dependence of the Exchange Splitting in Nickel

Ferromagnetism in metals, i.e. the long range order of electron spins, must be reflected in the Fermi surfaces. They are splitted in a majority (spin up) and a minority (spin down) surface. The exchange interaction that lifts the spin degeneracy of the electronic bands translates in an analogous splitting in \mathbf{k} -space. Above the Curie temperature ($T_C(\text{Ni}) = 627 \text{ K}$) a ferromagnet becomes paramagnetic and loses the ability to maintain a macroscopic magnetisation. Therefore the \mathbf{k} -space volume that is enclosed by the two Fermi surfaces must be the same for spin up and spin down electrons. This is e.g. achieved if the exchange splitting of the bands that cross the Fermi level vanishes. It does, however, not mean that any magnetic moment disappears - in nickel the d-shell remains open - but that there is no more long range correlation between the magnetic moments on the lattice sites. Photoemission is able to observe the disappearance of the band splitting as well as local correlation effects above the Curie temperature, as they were e.g. observed with neutron scattering [15] or core level photoemission [16].

Aebi et al. have measured a two dimensional cut across the Fermi surface of Ni(110) below and above T_C [5] and found dramatic changes that can not be ascribed to thermal broadening. Fig. 5 shows this kind of He I α excited Fermi surface maps from Ni(111) [1]. The photoelectron emission intensity is

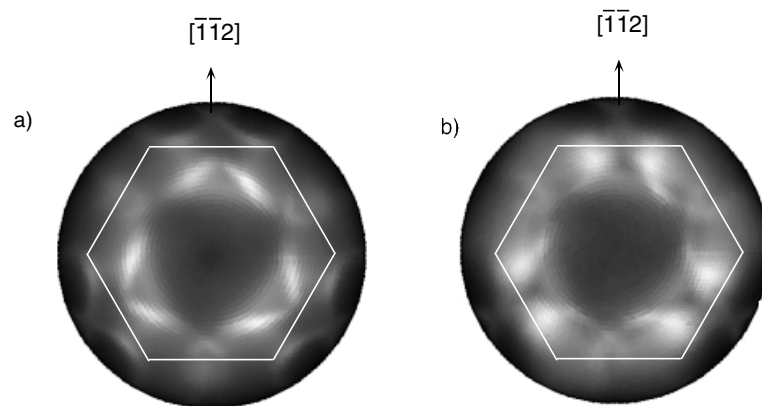


Fig. 5. Fermi surface maps from angular resolved photoemission. The intensity on a linear grey scale (white means high intensity) is displayed as a function of $\sin(\theta)$ and φ , θ being the polar and φ the azimuthal emission angle ($0 \leq k_{\parallel} < 2.06 \text{ \AA}^{-1}$). The hexagons mark the boundary of the first surface Brillouin zone. In a) the He I α excited Fermi surface map from Nickel (111) at room temperature and b) above the Curie temperature $T/T_C = 1.16$. From Ref. [1].

shown on a linear grey scale where white is the highest intensity. The data are displayed in parallel projection $k_{\parallel} \propto \sin(\theta)$ (see Eqn.10) with $0 \leq k_{\parallel} < 2.06 \text{ \AA}^{-1}$. The azimuthal orientation of the surface and the first surface Brillouin zone are indicated as well. Clearly, the Fermi surface map is three fold symmetric as expected from an *fcc* (111) surface where more than one layer contributes to the photoemission and it becomes evident that dispersion normal to the surface is important. The particular bands of interest were identified by band structure calculations [1]. There are direct minority *d*-band transitions in the first surface Brillouin zone, near the zone boundary, and the ∞ -shaped features in the second surface Brillouin zone in the $\bar{1}\bar{1}2$ direction are *sp*-bands and carry minority as well as majority spin electrons (cf. Fig.8a)). It is seen how particular bands move and not simply broaden in *k*-space if the sample crosses the Curie temperature.

The *sp*-bands that are split in *k* “collapse” in approaching the Curie temperature. Collapsing means that *sp*-splitting is not observed anymore and that the angular full width at half maximum broadening of the band is less than 0.2 \AA^{-1} . The observed collapse of the splitting is in line with a Stoner picture where the exchange splitting decreases with the bulk magnetization. In Fig.6 this collapsing of the *sp*-bands is shown with angular distribution curves (ADC's). The ADC's in Fig.6 show the photoemission intensity at the Fermi level as a function of the azimuthal emission angle ϕ . There the *sp*-bands in the ∞ -shaped features at a polar emission angle θ of 78° ($k_{\parallel} = 2.01 \text{ \AA}^{-1}$) are shown (see Fig. 5). The azimuthal angle $\phi = 0$ refers to the azimuth of the $[\bar{1}\bar{1}2]$ direction. Here an angle step $\Delta\phi$ of 1° corresponds to a Δk of 0.035 \AA^{-1} . The spin polarization is assigned from comparison with band structure calculations where the inner peaks reflect the minority *sp*- bands while the outer ones those with majority spin [1]. In Fig.6 b) and c) the angular width of the *sp*-band features at the Fermi level are presented as a function of temperature. In Fig.6 b) the data are shown with the thermally induced broadening that increases linearly above T_C . If this linear increase is subtracted below T_C as well, the data fit the bulk magnetization (solid line in Fig.6c)). The data in Fig.6 contain, besides the exchange splitting in *k*-space, additional information as the width of the individual spin bands and the intensities. This will be further discussed in subsection 4.2..

The *sp*-bands contribute only a few per cent to the magnetic moment of $0.6 \mu_B$ in nickel. The main contribution stems from the hole in the minority *d*-shell. Therefore, the minority *d*-bands at the Fermi level are key players for the magnetism in nickel. In Fig.7 the calculated band structure and measured photoemission cuts across *k*-space, where the interplay between the *d*-bands and the *sp*-bands is seen, were displayed. The LKKR calculation [18] Fig.7a) shows the expected bands. While the *k*-locations of the bands are well reproduced, the energies do not correspond to the measurements since renormalization of the energy scale due to self energy and correlation effects ($N \rightarrow N - 1$) are not taken into account in these calculations [11]. A minority *d*-band crosses the Fermi level and appears - in agreement with inverse photoemission [19] - exchange-split by $280 \pm 20 \text{ meV}$ from its occupied majority sister band. In approaching the Curie temperature the occupied majority band gains energy and merges

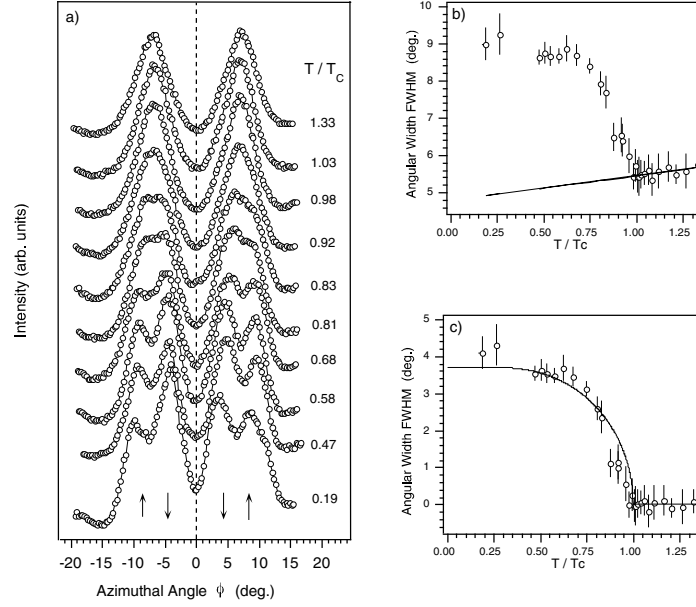


Fig. 6. Temperature dependence of the sp -bands. In a) angular electron distribution curves (ADC's) for the emission from the Fermi level taken at various temperatures T/T_C are shown ($T_C = 627$ K). At lower temperatures the exchange splitting in k -space can be readily observed. In b) the angular full widths at half maximum of the spin split sp -bands are shown. In c) the linear temperature induced broadening is subtracted and it is seen that these data follow the bulk magnetisation (solid line). Data from Ref.[17].

at this particular k -point with the minority band at the Fermi level. In this region of k -space a sp -band is very close to the d -band. We consider this sp - d hybrid to be a zone where scattering between sp_{\downarrow} and d_{\downarrow} electrons may occur within thermal fluctuations. Such scattering events are a strong perturbation of the local magnetic moment and can thus drive the ferro- paramagnetic phase transition. An analysis of the intensity of the minority and the majority band indeed fuels the proposition [20] that this is a magnetically active region which decreases T_C with respect to the expectations from the Stoner model [21].

4.2 Influence of a Commensurate Insulator on the Magnetism of Nickel

The evolution of the electronic structure of band ferromagnets in interfaces is of key importance for the understanding of phenomena like the giant magneto resistance (GMR) [22] where only recently spin sensitive tunneling junctions became a subject of intense research [23]. It is known that the adsorption of atoms or molecules strongly influences the electronic structure of the surface states of

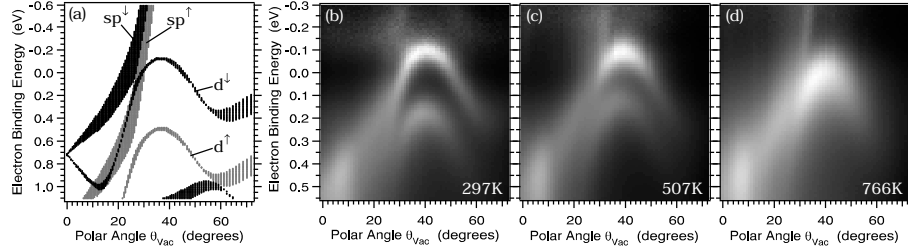


Fig. 7. (a) Spin-polarized LKKR calculation covering the section in \mathbf{k} -space of the measurements. Majority spin bands are given in gray, minority bands in black. (b)–(d): He I α excited polar-angle scanned electron distribution curves EDCs taken from Ni(111) along the azimuth which is clock wise 23° off $[\bar{1}\bar{1}2]$, measured at three different temperatures: (b) $0.47 T_C$, (c) $0.80 T_C$, and (d) $1.21 T_C$. From Ref.[20].

nickel [24,25,26,27,28]. Though, the energy and momentum of bulk states were less involved in the interface forming process. There are reports on “intensity shifts” in the bulk bands of nickel upon adsorption of hydrogen [29]. This means that the adsorption of hydrogen on nickel causes strong matrix element effects but no energy or momentum shifts were reported. However, Boschung et al. interpreted these intensity shifts as an indication for the hybridisation of hydrogen with the nickel d -band [29].

Here we review the system of one layer of hexagonal boron nitride on Ni(111), where bulk band distortions and intensity redistributions in the sp -bands were found [30]. Hexagonal boron nitride forms a perfect commensurate (1x1) overlayer on Ni(111) [31,32]. Nominally h -BN is a closed shell sp^2 network within the single layers and is, due to the ionicity of the BN bond, a wide gap insulator ($E_{\text{gap}} = 5.3 \text{ eV}$). Therefore it should not contribute with metallic bands to the conduction, nor be magnetic. It is, however, classified to be “metallic” on basis of a soft phonon mode as identified by high resolution electron energy loss spectroscopy (HREELS) [33] and one layer is not thick enough in order to prevent electrons to tunnel across [32]. Fig.8 shows the Fermi surface maps of Ni(111) and h -BN/Ni(111). It can be seen that the h -BN overlayer with (nominally) no electronic states on the Fermi surface, strongly influences the shape of the Fermi surface of the underlying nickel and therefore the electronic coupling across the interface. The Fermi surface gets distorted and new features emerge. It is seen that the Ni(111) Fermi surface features are replicated three more times in the h -BN/Ni(111) case (Fig. 8b)). They are shifted by a primitive reciprocal surface lattice vector \mathbf{Q} . This is a (1x1) surface umklapp process where the reciprocal lattice vector \mathbf{G} in the photoemission (see Eqn. 2) contains as well an element of the two dimensional reciprocal surface lattice. The occurrence of such surface umklapps indicates that the h -BN layer acts as a grating for any electrons that cross this interface and therefore such umklapps influence the tunneling characteristics of such junctions. Since the sp -bands are exchange split (see below) this will affect the spin asymmetry in the tunneling current. From the observation of

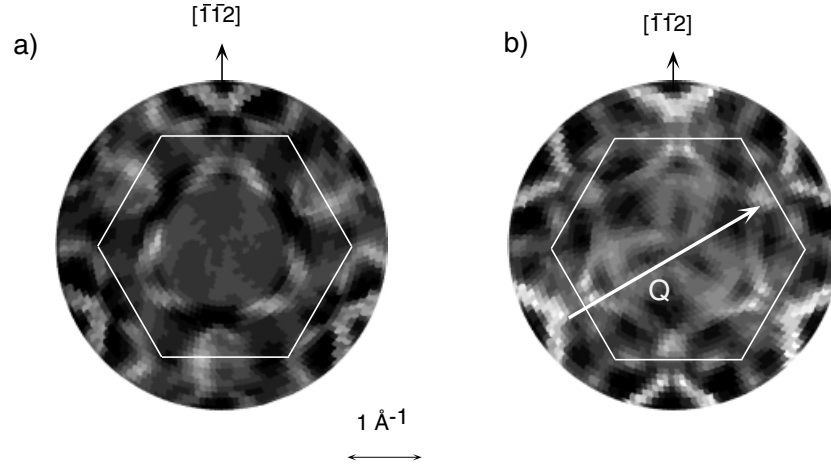


Fig. 8. Fermi surface map from a) Ni(111) measured with He I β radiation ($k_{\parallel} \leq 2.15 \text{ \AA}^{-1}$) and b) $h\text{-BN}/\text{Ni}(111)$ measured with He I α radiation ($k_{\parallel} \leq 2.15 \text{ \AA}^{-1}$) are shown. The differences of a) relative to the Fermi surface maps in Fig.5 are mainly given due to the normalization of the data of each azimuthal scan and much less due to the slightly different photon energy. The hexagons indicate the first surface Brillouin zone. The vector \mathbf{Q} indicates an umklapp process and is a reciprocal vector of the surface lattice. From Ref.[30].

an umklapp in photoemission it is not straightforward to decide to which extent the initial state is affected since diffraction of the photoelectron in step 2 (transport to the surface) may lead as well to umklapps. An unambiguous indication of an interaction of the overlayer with the substrate are energy and momentum shifts of the electronic states. Intensity variations are more difficult to understand since they involve a quantitative understanding of the matrix element in photoemission.

In Fig. 9 two angular cuts across the sp -bands at the Fermi level, in the second surface Brillouin zone of Ni and $h\text{-BN}/\text{Ni}(111)$, are displayed analogous to the cuts shown in Fig.6. For Ni(111) ($h\text{-BN}/\text{Ni}(111)$) the same polar emission angle $\theta_m = 78^\circ$ and the photon energies of 23.1 (21.2) eV were chosen in order to sample the same parallel momenta k_{\parallel} at the same emission angles θ_m [34]. The different photon energies compensate for the work function differences of the two surfaces. The four peaks are characterized by their positions, their width and their area A . The k -exchange splitting between the majority and the minority sp -band is 0.19 (0.16) \AA^{-1} . This decrease of the sp exchange splitting in k -space is not expected to be a consequence of the slightly different k_{\perp} that were probed for the two cases [35]. It is an effect on the initial states at the Fermi energy and thus indicates the influence of the $h\text{-BN}$ on the motion of the electrons in this interface.

The minority sp -band peak width γ_{\downarrow} is about 30% larger than that of the majority bands (γ_{\uparrow}). This is in line with a shorter lifetime of minority excitations

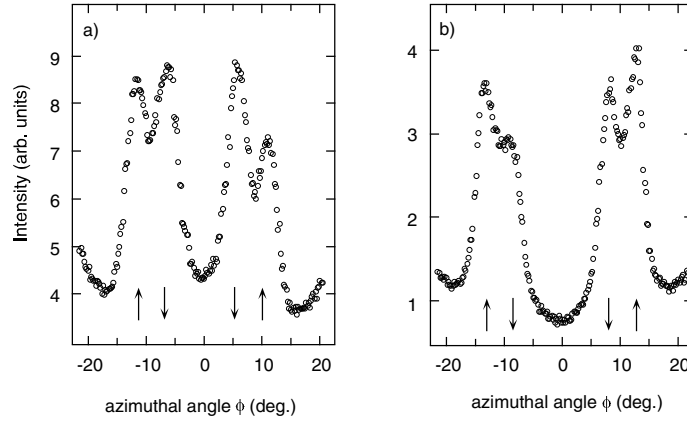


Fig. 9. Photoemission intensity at the Fermi level versus azimuthal angle ϕ . The polar emission angle ($\theta_m = 78^\circ$) is kept constant. $\varphi=0$ is defined along the $[\bar{1}\bar{1}2]$ azimuth. The arrows indicate the minority \downarrow and majority \uparrow sp -bands, respectively. a) Ni(111) measured with He I β radiation. b) h -BN/Ni(111) measured with He I α radiation. Note the strong change in the intensity ratio between minority and majority spin transitions. Data from Ref.[30].

[36]. In three dimensional systems, however, the connection between the angular broadening and the initial- and final state lifetimes is quite involved [37]. The intensity variation of the spin up / spin down “doublets” left and right from the high symmetry plane are caused by the loss of mirror symmetry due to the oblique incidence of the photons in our experimental setup. It provides a rough estimate for the change of the photoemission matrix element with respect to the orientation of the incoming light. In the following the area ratio $\mathcal{Y} = A_\downarrow : A_\uparrow$ shall be discussed. For Ni(111) ($\mathcal{Y}_{Ni(111)}=1.7$) it does not correspond to that on Ni(100) ($\hbar\omega = 44eV$) found by Petrovykh et al. [38,39,40] (0.56) nor to that on Ni(110) (0.8) [38,40]. The data from Ref. [41] indicate for Ni(110) and He I α radiation $\mathcal{Y}_{Ni(110)}=1.3$. Therefore \mathcal{Y} may bank on the experimental parameters and/or the crystal face.

In Fig. 9 an experiment that demonstrates the change of \mathcal{Y} upon the adsorption of a monolayer of hexagonal boron nitride is shown [30]. The change in the area ratio $\mathcal{Y} = A_\downarrow : A_\uparrow = 1.7$ for Ni(111) to 1.1 for h -BN/Ni(111) bears information on the spin dependent electron transmission coefficient. The h -BN overlayer clearly alters the intensities of the spin polarized direct photoemission transitions at these particular places in k -space. This behavior of decreasing \mathcal{Y} upon adsorption of a non-magnetic layer can be related to spin dependent scattering of the electrons during the propagation to the detector (step(ii) in the three step model for photoemission). The data in Fig. 9 emphasize that minority photoelectrons get much more efficiently scattered. This is in line with the Siegmann rule [42] stating that at low kinetic energies the inelastic electron scattering cross section is essentially proportional to the number of valence band

d -holes of a material. Thus for ferromagnets, where the d -holes are polarized, a spin filter effect is expected and in nickel minority spins are scattered more efficiently. In the case of h -BN the Siegmann rule predicts no spin filtering since h -BN has no polarized d -shell. Therefore our finding of a strong asymmetry of the spin transition intensities calls for an extension of the Siegmann rule: it signals that spin filtering may also occur in or due to non-magnetic overlayers that are coupled to a magnetic substrate. This coupling may be mediated by hybridisation of delocalized sp -states extending into the interface and/or by the h -BN grating on Ni(111) that increases the available phase space for electron hole pair excitations in a spin selective way. Though the umklapps may play a crucial role for the understanding of the magnetic coupling across this interface it has to be emphasized that these very same umklapps may influence the matrix elements of the two spin channels shown in Fig. 9. The possible influence of spin selective hybridisation of the h -BN orbitals on the sp -bands seems, however, to be unlikely since it is not expected that the h -BN bond is selective to the spin of the nickel sp -bands. The (essential) assumption of a constant matrix element for a quantitative determination of the spin scattering asymmetry may be hampered by surface umklapp processes [30] and therefore all possible physical mechanisms have to be examined carefully before definite conclusions can be drawn on the absolute value of spin filtering effect of a single layer h -BN on Ni(111).

5 Conclusions

Angle scanned photoemission experiments give a detailed insight in the electron dynamics of magnetic interfaces. At the Fermi energy the exchange interaction induced splitting in k -space can be clearly observed and studied as a function of temperature. Within the accuracy of the experiment this splitting is proportional to the bulk magnetisation. For the h -BN/Ni(111) interface distortions of the Fermi surface indicate an influence of a nominally non magnetic and non conducting overlayer. The overlayer acts as an atomic grating and produces surface umklapp processes in the photoemission final state. The relative photoemission intensities of spin polarized sp -bands are strongly affected by the h -BN overlayer. Implications for a new spin-filter effect in h -BN/Ni(111) are discussed.

Acknowledgments

It is a big pleasure to acknowledge fruitful collaboration with Thomas Kreutz, Willi Auwärter, Philippe Aebi and Jürg Osterwalder. Felix Baumberger and Matthias Hengsberger critically read the manuscript.

References

1. T.J. Kreutz, T. Greber, P. Aebi, J. Osterwalder, Phys. Rev. B, **58** (1998) 1300.
2. D.T. Pierce and W. E. Spicer, Phys. Rev.Lett., **25** (1970) 581.

3. U. Bänniger, G. Busch, M. Campagna, H.C. Siegmann, Phys. Rev.Lett., **25** (1970) 585.
4. T. Greber, O. Raetz, T. J. Kreutz, P. Schwaller, W. Deichmann, E. Wetli and J. Osterwalder, Rev. Sci. Instrum., **68** (1997) 4549.
5. P. Aebi, T.J. Kreutz, J. Osterwalder, R. Fasel, P. Schwaller and L. Schlapbach, Phys. Rev. Lett., **76** (1996) 1150.
6. C.S. Fadley, Prog. Surf. Sci., **16** (1984) 275.
7. J. Osterwalder, T. Greber, A. Stuck, L. Schlapbach, Phys. Rev. B , **44**, 13764 (1991).
8. S. Hüfner, Photoelectron Spectroscopy, (Springer, Berlin, 1995)
9. F.J. Himpsel, Advances in Physics, **32** (1983) 1.
10. J. Osterwalder, Surface Rev. and Letters, **4** (1997) 391.
11. F. Manghi, V.Bellini, J. Osterwalder, T. J. Kreutz, P. Aebi and C. Arcangeli Phys. Rev. B, **59** (1999) 10409.
12. G. Van der Laan, Phys. Rev. B, **51** (1995) 240.
13. D. Oberli, R. Burgermeister, S. Riesen, W. Weber and H.C. Siegmann, Phys. Rev. Lett.,**81** (1998) 4228.
14. P. Aebi, J. Osterwalder, R. Fasel, D. Naumović and L. Schlapbach, Surf. Sci., **307-309** (1993) 917.
15. G. Shirane, O. Steinsvoll, Y.J. Uemura and J. Wicksted, J. Appl. Phys.,**55** (1984) 1887.
16. A. Kakizaki, J. Fujii, K. Shimada, A. Kamata, K. Ono, K.-H. Park, T. Kinoshita, T. Ishii, and H. Fukutani, Phys. Rev. Lett., **73** (1994) 2781.
17. T. J. Kreutz, The temperature-dependent electronic structure of nickel metal, (Thesis, Universität Zürich 1997).
18. J.M. MacLaren, S. Crampin, D.D.Vvedensky, R.C. Albers, J.B. Pendry, Comput. Phys. Commun.,**60** (1990) 365.
19. W. von der Linden, M. Donath and V. Dose, Phys. Rev. Lett., **71** (1993) 899.
20. T. Greber, T.J. Kreutz and J. Osterwalder, Phys. Rev. Lett., **79** (1997) 4465.
21. O. Gunnarson, J. Phys. F, **6** (1976) 587.
22. M.N. Baibich, J.M. Broto, A. Fert, F. Nguyen Van Dau, F. Petroff, P. Etienne, G. Creuzet, A. Friedrich and J. Chazelas, Phys. Rev. Lett.,**61** (1988) 2472.
23. J. Maria De Teresa, A. Barthelemy, A. Fert, JP. Contour, F. Montaigne and P. Senor, Science, **286** (1999) 507.
24. F.J. Himpsel and D.E. Eastman, Phys. Rev. Lett., **41** (1978) 507.
25. M. Donath, F. Passek and V. Dose, Phys. Rev. Lett., **70** (1993) 2802.
26. F. Passek and M. Donath, Phys. Rev. Lett.,**71** (1993) 2122 .
27. H. Namba, N. Nakanishi, T. Yamaguchi and H. Kuroda, Phys. Rev. Lett., **71** (1993) 4027.
28. E. Boschung, Th. Pillo, J. Hayoz, L. Patthey, P. Aebi and L. Schlapbach, J. El. Spectr. and Rel. Phen., **101-103** (1999) 349.
29. E. Boschung, Th. Pillo, J. Hayoz, L. Patthey, P. Aebi and L. Schlapbach, Phys. Rev. B, **58** (1998) R10210.
30. T. Greber, W. Auwärter and J. Osterwalder, In "The Physics of Low Dimensional Systems", Ed. J.L. Morán-López, Plenum, New York, (2001) pg. 411-418.
31. A. Nagashima, N. Tejima, Y. Gamou, T. Kawai and C. Oshima, Phys. Rev. B, **51** (1995) 4606.
32. W. Auwärter, T. J. Kreutz, T. Greber and J. Osterwalder, Surf. Sci., **429** (1999) 229.
33. C. Oshima, A. Itoh, E. Rokuta, T. Tanaka, K. Yamashita, T. Sakurai, Sol. State. Comm., **116** (2000) 37.

34. It is misleading to call this “the same initial state location” as it was done in [30]. Note if the same initial states (\mathbf{k}_i) shall be sampled the same photon energy has to be used, though the polar emission angle depends on the inner potential. In the present case we get from Eqn.9a and Eqn.10 for $k_{f\perp}$ 1.06 and 1.00 \AA^{-1} for Ni(111) and h -BN/Ni(111), respectively. The difference corresponds to 2% of the Brillouin zone diameter.
35. In Ni(111) the k-splitting of He I α excited sp -bands at $\theta_m=78^\circ$ is 0.18 \AA^{-1} .
36. M. Aeschlimann, M. Bauer, S. Pawlik, W. Weber, R. Burgermeister, D. Oberli and H.-C. Siegmann, Phys. Rev. Lett., **79** (1997) 5158.
37. J.K. Grepstadt, B.J. Slagsvold and I. Bartos, J. Phys. F, **12** (1982) 1679.
38. K.N. Altmann, D.Y. Petrovykh, G.J. Mankey, N. Shannon, N. Gilman, M. Hochstrasser, R.F. Willis and F.J. Himpsel, Phys. Rev. B, **61** (2000) 15661.
39. D.Y. Petrovykh, K.N. Altmann, H. Höchst, M. Laubscher, S. Maat, G.J. Mankey and F. Himpsel, Appl. Phys. Lett., **73** (1998) 3459.
40. F.J. Himpsel, K.N. Altmann, G.J. Mankey, J.E. Ortega and D.Y. Petrovykh, J. of Magnet. and Magnet. Mat., **200** (1999) 456.
41. T.J. Kreutz, P. Aebi, and J. Osterwalder, Sol. State Comm., **96** (1995) 339.
42. H.-C. Siegmann, J. El. Spectr. and Rel. Phen., **68** (1994) 505.

Temperature Dependence of Spin- and Angle-Resolved Photoemission of Ni

Akito Kakizaki

Institute of Materials Structure Science,
High Energy Accelerator Research Organization, Tsukuba 305-0801, Japan,
Present address: Institute for Solid State Physics, University of Tokyo,
Kashiwa, Chiba 277-8581, Japan

Abstract. Photoelectron spectroscopy has been continuing to be one of the major experimental techniques to investigate electronic structures of solids and solid surfaces. It is not only by the reason that photoemission spectra give us information on energy-, momentum- and spin-dependent electronic structure of the material under the study, but also that we could obtain information on many-body interactions between photoexcited hole and the electron system in the solid, which accompanies with photoelectron excitation and its decay processes. Especially, the application of synchrotron radiation to photoemission allows easily to change the energy and polarization of incident photons, and to obtain more precise information on the electronic structures. Recently, insertion devices further improve the feasibility of photoemission experiments requiring high incident photon flux such as spin-resolved photoemission and magnetic linear and circular dichroism in photoemission spectra, which provide us complimentary information on the electronic structures of magnetic materials. In the following, we will concern with spin-dependent electronic structures of Ni obtained by spin- and angle-resolved photoemission experiments at finite temperature.

1 Introduction

Now let us consider a solid irradiated by photons with energy, $h\nu$, sufficiently large to extract photoelectrons from a solid surface. The photoelectron intensity from the solid, I , is given in the dipole approximation by [1]

$$I \propto \sum_{i,f} |\langle f | \mathbf{r} | i \rangle|^2 \delta(e_f - e_i - h\nu) \quad (1)$$

where $|i\rangle$ and $|f\rangle$ denote the initial and final states of the electron system of the solid with energy e_i and e_f and with momentum \mathbf{k}_i and \mathbf{k}_f , respectively. The summation is over the indices i and f of all pairs of initial and final states which can participate. When the electronic states of the solid can be described as Bloch states, a term representing momentum conservation including Umklapp process, $\delta(\mathbf{k}_f - \mathbf{k}_i - \mathbf{G})$ with reciprocal vector \mathbf{G} , is to be added to eq. (1), which gives the angular distribution of the photoelectron intensity depending on \mathbf{k}_i . Therefore, each peak which appears in the energy distribution curve (EDC) of photoelectrons corresponds to an initial electronic state of the solid. Although it is not quite simple, one can obtain an energy dispersion of the valence band

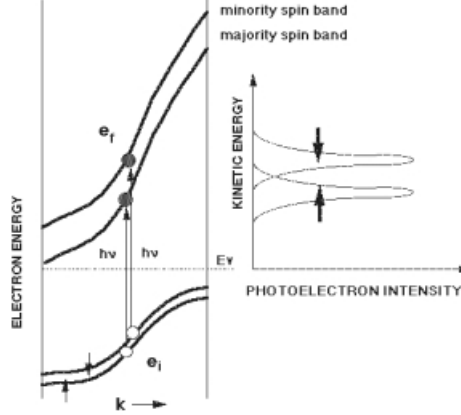


Fig. 1. Energetics of a direct transition from exchange split valence bands at a point along some arbitrary direction in \mathbf{k} -space.

of a solid by comparing the measured EDCs with a valence band structure calculated on the basis of the one-electron approximation (Fig. 1). In addition, if we could identify the spin state of photoelectrons, we can decompose EDCs into two subsets of photoelectrons with spins parallel and anti-parallel to a certain direction. Hence, by taking the macroscopic magnetization direction as the spin quantization axis, we can obtain spin-resolved electronic structures of magnetic materials [2,3].

It is known that a hole produced in the electron system through a photoelectron excitation process relaxes through various decay channels including electron-electron interaction and/or electron-hole interaction. The relaxation process will cause the deviation of the spectral profile from the one simply expected by eq. (1). In the approximation where the interaction between the out-going photoelectrons and the electron system left behind is small, the interaction is renormalized into the self-energy $\Sigma(\mathbf{k}_i, e_i)$. Hence, eq. (1) is modified as

$$I \propto \sum_{i,f} |\langle f | \mathbf{r} | i \rangle|^2 A(\mathbf{k}_i, e_i) \quad (2)$$

where $A(\mathbf{k}_i, e_i) = (1/\pi) \text{Im}[e_f - e_i - h\nu - \Sigma(\mathbf{k}_i, e_i)]^{-1}$ represents the spectral function. In the non-interacting limit, $A(\mathbf{k}_i, e_i) = \delta(e_f - e_i - h\nu)$ and spectral features of an EDC consist of δ -function at the binding energies expected by the one-electron approximation, i.e. eq. (1). In the simplest case where the self-energy is energy and momentum independent, the spectral function has a Lorentzian form with the width of $2|\text{Im}\Sigma|$, and $\text{Re}(\Sigma)$ determines the shift of the binding energy from its value of one-electron approximation. In general case, the self-energy is momentum dependent and spectral features appear at the poles of the spectral function. Hence, manybody effects due to the interaction between a photoexcited hole and the electron system of the solid, i.e. electron correlation

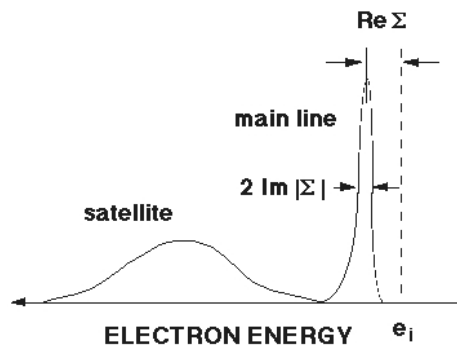


Fig. 2. Photoelectron intensity expected for a correlated electron system.

effects, will appear in the spectra as the shift of peak position from the one-electron band calculation, the appearance of satellites, the asymmetric spectral features of main peaks, etc. (Fig. 2). In other words, the analysis of photoemission spectra reveals the information on electron correlation effects in a solid. We could obtain information on the spin-dependence of the correlation effects by the spin analysis of photoemission spectra, where the photoproduced hole plays not only as a test charge but as a test spin to the electron system.

The electron spin analysis can be achieved by utilizing the spin dependent elastic and inelastic scattering processes between photoelectrons and electrons in a solid [4,5]. Among many kinds of spin-polarimeters developed so far, a Mott scattering polarimeter is one of the most widely used ones with its advantages of a high efficiency, good stability and possibility of self-calibration [6]. Figure 3 shows schematics of a spin- and angle-resolved photoemission experiment. In the Mott polarimeter, transversely polarized photoelectrons are scattered by a target with a large atomic number, which results in a left-right asymmetry of the scattering intensities due to the spin-orbit interaction of photoelectrons in the scattering process. If one knows the effective Sherman asymmetry function, S_{eff} , which is characteristic to the target atom, the transverse polarization component, \mathbf{P} , of the incident photoelectrons can be obtained by the relation, $\mathbf{P} = A/S_{eff}$, where $A = (N_L - N_R)/(N_L + N_R)$ is the left-right scattering asymmetry determined by the number of electrons scattered to the left, N_L , and right, N_R , respectively. Practically, the spin-resolved EDCs of photoelectrons parallel (N_{\uparrow}) and anti-parallel (N_{\downarrow}) to the magnetization direction are more instructive and are derived using measured photoelectron intensities, N_L and N_R , as $N_{\uparrow,\downarrow} = (1 \pm P)/2S_{eff}(N_L + N_R)$.

In the following, we take Ni as a typical example of itinerant ferromagnets, or band-ferromagnets that reveal above mentioned electron correlation effects. We will present the spin- and angle-resolved photoemission spectra of Ni valence band and its satellites and their temperature dependence. We discuss the electron correlation effects and their temperature dependence observed in the spectra by comparing with band calculations.

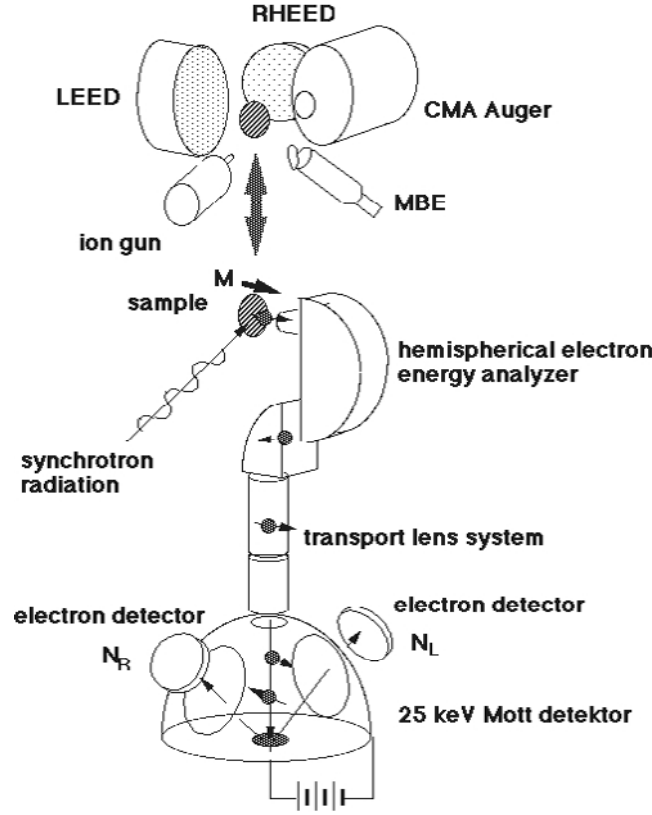


Fig. 3. A schematic diagram of a spin- and angle-resolved photoemission experiment of magnetic materials. Upper part consists of a standard set of sample preparation equipments and lower part a hemispherical electron energy analyzer with a compact Mott scattering type electron spin detector.

2 Correlation Effects in Valence Band Spectra of Ni

The electronic structure of ferromagnetic Ni has been the subjects of intensive studies as a prototype of band-ferromagnets, where the band model reasonably explains the ground state properties such as the existence of the Fermi level in $3d$ bands, non-integral number of Bohr magnetons per atom, etc. [7]. However, the valence band structure of Ni observed by angle-resolved photoemission experiments shows a number of discrepancies from theoretical band calculations based on a one-electron approximation [8]. The photoemission spectra show a reduced exchange splitting and narrower $3d$ bandwidth as well as the existence of valence band satellites down to 30 eV from the Fermi level. These discrepancies have been attributed as consequences of the strong electron correlation effects in the partially filled Ni $3d$ band [9,10,11,12]. So far, a number of calculations of Ni valence band spectra invoking correlation effects, i.e. so-called

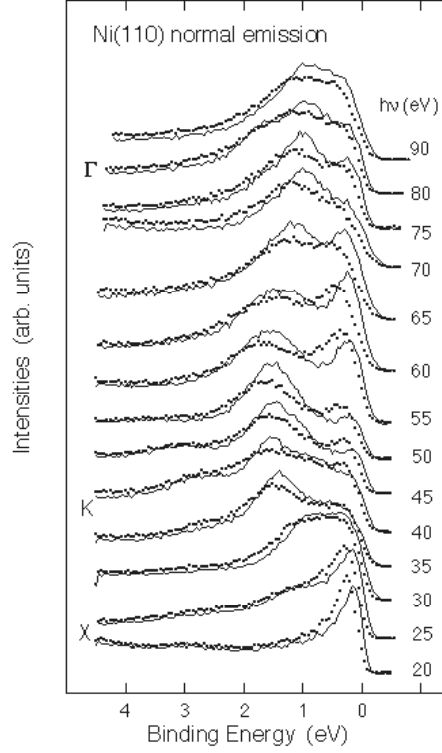


Fig. 4. Majority (dotted curve) and minority spin (solid curve) spectra of Ni(110) observed in the normal emission mode.

quasi-particle band structure, have been carried out and the reduction of exchange splitting and the narrowing of $3d$ bandwidth are interpreted in terms of self-energy [13,14,15,16,17,18,19]. The calculations also reproduce the appearance of the valence band satellites as poles of the self-energy. The electronic structure of Ni was observed by spin- and angle-resolved photoemission experiments to discuss the origin of the discrepancies of the measured spectra from the one-electron approximation [20,21]. Figure 4 shows a set of majority and minority spin photoemission spectra of ferromagnetic Ni(110) measured in the normal emission mode with excitation energies from 20 to 90 eV, which corresponds to the Γ - K - X direction of the Brillouin zone (B.z.) [22]. In both spin spectra the peak positions of the spectral features show an obvious photon energy dependence, which reflects the energy dispersion of the photoexcited final state, or quasi-particle bands. It should be remarked in the figure that the photon energy dependence of the majority spin spectra is different from those of corresponding features in the minority spin spectra. Figure 5 shows the experimentally obtained valence band structure, which plots the positions of spectral

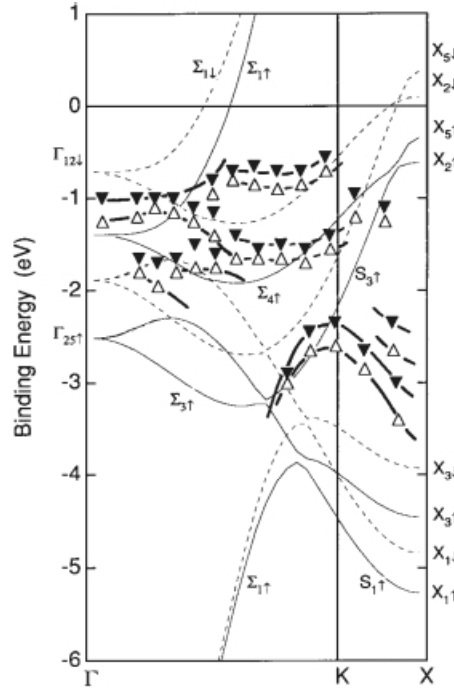


Fig. 5. Experimentally obtained valence bands of Ni(110). \triangle and \blacktriangledown correspond to majority and minority spin bands, respectively. Thin curves (majority spin) and dashed thin curves (minority spin) show calculated band structure based on the LDA.

features appeared in the EDCs by assuming free electron final states for both spin states.

A one-electron band calculation in the local density approximation (LDA) is also shown in the figure [23,24]. In the LDA, the spin-resolved band structure of the ferromagnetic phase was derived by simply introducing a constant exchange potential between the majority and minority spin states. In the figure, one can observe considerable discrepancies between experimentally obtained band structure and the result of the LDA calculation. The observed $3d$ majority and minority spin bands appear at smaller binding energies than those expected by the calculation, which was also observed in the spin-resolved XPS spectra [25]. By comparing with the calculation reducing 30% of the $3d$ bandwidth [7], the observed valence bands are assigned to exchange split s -like $\Sigma_1(S_1)$ bands and d -like $\Sigma_1(S_1)$, $\Sigma_3(S_3)$ and $\Sigma_4(S_4)$ bands. The binding energies and the exchange splitting energies at high symmetry points in the B.z. are given in Table 1. The observed energies are much smaller than those of the LDA calculation.

There have been many attempts to calculate photoemission spectra by taking an electron correlation effect into account. In Table 1, we present the results calculated in the GW approximation (GWA) [16] and those by Hoyland and

Table 1. Experimental and calculated binding energies and exchange splitting (Δ_{ex}) of Ni 3d bands at special points in the B.z. (energies in eV).

	Experiment		LDA calc.		GWA calc. ¹⁶		TDS calc. ¹⁵	
		Δ_{ex}		Δ_{ex}		Δ_{ex}		Δ_{ex}
$\Gamma_{12\uparrow}$	1.05		1.35		0.9		0.60	
		0.30		0.66		0.6		0.12
$\Gamma_{12\downarrow}$	0.85		0.69		0.3		0.48	
$K_{4\uparrow}$	0.70		1.18				0.52	
		0.15		0.63				0.13
$K_{4\downarrow}$	0.55		0.55				0.39	
$K_{3\uparrow}$	1.50		2.07		1.8		1.24	
		0.10		0.50		0.6		0.13
$K_{3\downarrow}$	1.40		1.57		1.2		1.11	
$X_{2\uparrow}$	0.35		0.59		0.5		0.22	
		0.10		0.50		0.3		0.18
$X_{2\downarrow}$	0.25		0.09		0.2		0.03	
$X_{3\uparrow}$	3.35		4.31		3.5			
		0.40		0.50		0.6		
$X_{3\downarrow}$	2.95		3.80		2.9			

Jordan [15] based on the model of Triglia, Ducastelle and Spanjaard (TDS) [13]. Both calculations, TDS and GWA invoking the electron correlation, reproduce the experimental results better than the LDA calculation, which re-confirms the importance of the consideration of the correlation effects. It should be remarked that the differences between observed binding energies and those of the LDA calculation at high symmetry points are larger in the majority spin bands than those in the minority ones. This implies that the quasi-particle energies and hence the electron correlation effects show a spin dependence. In the TDS calculation, it was shown that the difference of the available scattering channels for the majority and minority spin electrons in the photoexcited final state causes the spin dependence of the quasi-particle energies. For a qualitative investigation, we have evaluated the average binding energy shifts of the observed bands from those of the LDA calculation. The energy shifts averaged over high symmetry points are found to be 0.51 eV and 0.14 eV for the majority and minority spin bands, respectively. The larger energy shift in the majority spin bands implies that the electron correlation effect appears more obviously in the majority spin electrons than in the minority ones, which leads to the reduction of the exchange splitting energies.

So far, many of the spin- and angle-resolved photoemission spectra have been restricted to some high symmetry points in B.z. The quantitative comparison with calculated quasi-particle band and the discussion on spin- and wavevector-dependence of the self-energy are not satisfactory. For further analysis of correlation effects observed in photoemission spectra, a more precise information derived from spin- and angle-resolved photoemission spectra with better energy and momentum resolution are needed.

3 Temperature Dependence of Ni(110) Valence Bands

A macroscopic picture of a ferromagnet is explained as a result of a different occupation number of valence electrons with the spin magnetic moment parallel and anti-parallel to the magnetization direction, which results a spontaneous magnetization below a critical temperature (T_c). An energy-, momentum- and probably temperature-dependent exchange interaction separates the energy levels of these subsets of electrons. Hence of particular interests are the temperature dependence of the electronic structure and its energy and momentum dependence as a function of the spin quantum number, which would provide a valuable contribution to a microscopic description of the band-ferromagnetism.

The electronic and magnetic ground state properties of the ferromagnetic $3d$ metals are reasonably understood by the Stoner model based on the mean field approximation for electron-electron interaction and neglecting the spin fluctuation. However, finite temperature properties of ferromagnetic $3d$ metals are not explained by the model. The T_c expected by the model is too high than the observed one [26] and the existence of the short range magnetic order above T_c observed by the neutron scattering experiment does not agree with the model [27]. In the model, the exchange splitting of majority and minority spin states decreases, or collapses with increasing temperature proportional to the macroscopic magnetization and vanishes at T_c . Hence the local magnetic order, i.e. ferromagnetic order vanishes above T_c .

Hopster et al. [13] first reported a spin- and angle-resolved photoemission of Ni at temperatures close to T_c . They observed that in the spectra of Ni [28], the exchange splitting in the valence band collapses to zero as the temperature increases to T_c . The temperature dependence of the exchange splitting of the valence band of Ni was also investigated by means of the spin dependent inelastic electron scattering [29] and the spin polarized electron energy loss spectroscopy experiments [30]. However, the exchange splitting does not temperature dependent in those experiments. In the inverse photoemission experiment [31], collapsing behavior of valence bands were observed. On the other hand, in the spin-resolved valence band spectra of Fe [32,33], the temperature independent peaks were observed in the spectra and the spin polarization of each peak decreases as temperature increases to T_c . The theories based on the fluctuating local magnetic moment have been adopted to solve the controversy and to interpret the temperature- and wavevector-dependence of the spin-resolved valence band spectra.

Korenman and Prange [34] showed that a collapsing and non-collapsing behavior of the exchange split bands in Ni could be explained qualitatively on the basis of the local band theory [35]. The local band theory postulates that a ferromagnetic band structure could be defined locally and the resulting local magnetization fluctuates around the macroscopic magnetization direction at elevated temperatures. Since we extract photoelectrons at finite temperatures through fast photoexcitation process, observed kinetic energies of photoelectrons may reflect the instantaneous local electronic structure. They emphasized the difference of the group velocities of the photoexcited valence holes played an

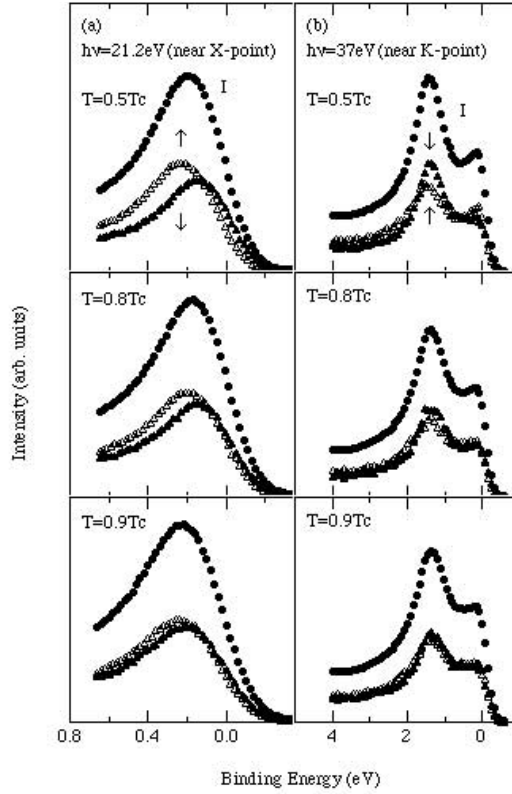


Fig. 6. Temperature dependence of the spin-resolved photoemission spectra of Ni(110) near (a) X -point and (b) K -point in the B.z. Spin integrated spectra (I) are sum of majority (Δ) and minority (\blacktriangle) spin spectra. In both figures, majority and minority spin spectra show collapsing behavior as temperature approaches to T_c .

important role. The SARPES spectra of Fe(100) were successfully interpreted by the local band theory where the amplitude of the local magnetic moments is constant in all temperatures [7,9,10]. However, the local band theory does not directly relate to the temperature dependent quasi-particle band structures.

Figure 6 shows of Ni(110) valence band measured at temperatures between $T/T_c = 0.5$ and $T/T_c = 0.9$ near X - (21.2 eV) and K -point (37 eV) in the B.z. [36]. The spectra show the collapsing behavior at both symmetry points. However, since the spectral features observed near X - and K -points in the B.z. consist of S_1 , S_3 and S_4 states and Σ_1 , Σ_3 and Σ_4 states, respectively, there may exist considerable ambiguities to discuss the temperature and wavevector dependence of the spectra by decomposing each spectral feature into three constituent bands. As described already, discrepancies between the spin- and angle-resolved photoemission spectra and the so-called one-electron band calculations are attributed to the consequences of the strong electron correlation and its spin dependence. The temperature dependence of the spectral profile of

a band-ferromagnetic is also to be explained by quasi-particle bands calculated by the self-energy into account. The principle of the calculation is to evaluate the self-energy combined with the temperature dependent magnetization [21]. To understand the basic role of parameters in the calculation, let us consider the simple model calculation based on a single-band Hubbard Hamiltonian and utilizes a coherent potential approximation (CPA) to approximate many-particle description of the Hamiltonian using single-particle model [37]. The correlation effect by the intra-atomic Coulomb term of the Hamiltonian is concentrated on the coherent potential, which corresponds to a self-energy. The self-energy could be derived from a solution of the CPA equation with an assumption of ideal Lorentzian density of states for the $3d$ band. Hence, the spectral function can be expressed by three parameters, which are magnetization, bandwidth and exchange energy. As a result of the calculation, it was shown that the collapsing and non-collapsing behavior of the spin-resolved valence band is determined by the ratio of the exchange energy to the bandwidth. For small value of the ratio, the spectral density will be a single peak at elevated temperature, while for large value of the ratio it will become a double-peaked structure. In other words, since the bandwidth is considered as the energy gained by the electron system being itinerant in the photoexcited final state, the collapsing and non-collapsing behavior of the valence band near T_c measures the relative strength of the itinerancy or band characteristics of the electron system to the exchange energy. Hence the collapsing behavior observed in Fig. 8 is explained qualitatively due to the comparatively smaller exchange energy (0.3 eV) than the valence bandwidth (2 eV) along the Γ - K - X direction of the Ni(110) B.z. The non-collapsing behavior observed in Fe(001) [32] can be understood due to rather a large exchange energy (2.5 eV) of the band that compared with the bandwidth (4 eV). The model was applied to explain the temperature dependence shown in Fig. 6, which showed qualitative agreement [38].

Quantitatively, however, the simple model is not being applicable to observed spectra without further assumption on the quantities, which are not considered in the model calculation. This may bring a considerable uncertainty in adjusting the experimental results to the calculation. We need a new approach considering the correlation effects. Nolting et al. [39] have adopted generalized Hubbard model considering explicitly the correlation effects and calculated the quasi-particle band structure of Ni at elevated temperature. The theoretical calculation shows good agreement with temperature- and wavevector-dependence of the spin-resolved photoemission and inverse photoemission spectra of Ni. The result also shows the evidence of the temperature-dependent exchange splitting in Ni(110) and not in Ni(111). Since the temperature-dependent spin-resolved photoemission and inverse photoemission spectra are only available of limited surfaces of Ni and Fe, further experimental studies for many band-ferromagnets are needed to describe the microscopic origin of the band-ferromagnetism.

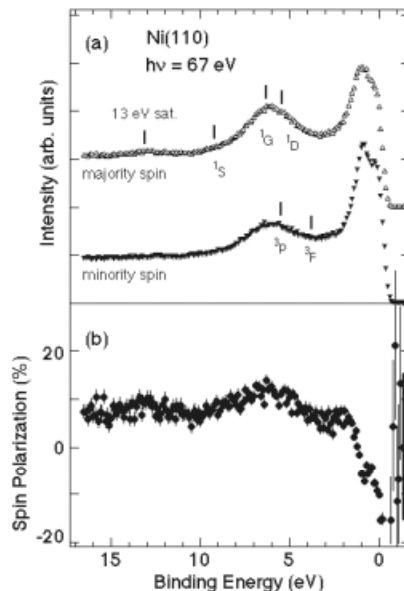


Fig. 7. (a) shows majority (\triangle) and minority (\blacktriangle) spin spectra of Ni(110) observed at the $3d$ threshold (67eV). Vertical bars correspond to the positions of the $3d^8$ final state configurations expected by an atomic model. (b) shows the spin polarization of Ni valence band. The statistical error is indicated by bars.

4 Temperature Dependence of Valence Band Satellites of Ni

The strong electron correlation effects of $3d$ electrons in Ni causes the localization of the photoexcited hole at a Ni atom and the appearance of the satellites in the valence band spectra, the spectral features of which are reasonably explained by an atomic model [8,41]. Actually, both spin-integrated and spin-resolved spectral features of satellites observed at binding energies of 6 eV, 9 eV and 13 eV are interpreted by means of $3d^8$ and $3d^7$ configurations of a Ni atom as shown in Fig. 7 [40,41]. The resonance enhancement of the satellites near the $3p$ threshold (67 eV) is also understood based on an atomic model as being due to the interference effect between the direct $3d$ valence electron excitation ($3p^6 3d^9 \rightarrow 3p^6 3d^8 + el$) and the $3p$ core electron excitation following by the $M_{2,3}VV$ super Coster-Kronig (sCK) transition forming two $3d$ holes in a same atomic site ($3p^6 3d^9 \rightarrow 3p^5 3d^{10} \rightarrow 3p^6 3d^8 + el$) [42,43,44,45,46]. The final state of the resonant photoemission mainly consists of the spin singlet (1S , 1D , 1G) and triplet (3P , 3F) $3d^8$ configurations and the dominant contribution to the 6 eV satellite is due to 1G term. Figure 8 shows the photon energy dependence of the spin polarization of the 1G term of the 6 eV satellite, which reveals characteristic resonant behavior of the satellite near the $3p$ threshold [46]. At

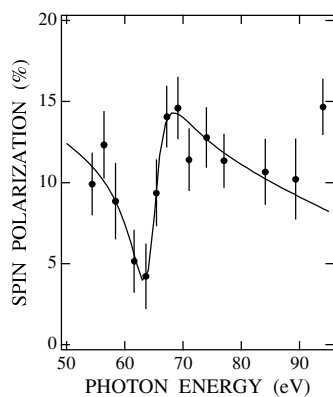


Fig. 8. Photon energy dependence of the spin polarization of the 1G term of the 6 eV satellite.

elevated temperature, the spectral features in the main valence band change as a function of temperature, while the feature of the 6 eV satellite does not show appreciable temperature dependence [46]. Instead the spin polarization of the 6 eV satellite decreases with increasing temperature. These results suggest that the photoelectron excitation process to form the two $3d$ holes is unaltered at elevated temperature. If the exchange splitting of the valence band of Ni decreases with increase of temperature as expected in the Stoner model, the $3d^8$ configuration of the final state is achieved by the $3p$ electron excitation to both unoccupied minority and majority spin states and following sCK decay. Hence the weight of the spin singlet term in the $3d^8$ final state configuration changes as temperature increases and the spectral feature of the 6 eV satellite would show temperature dependence.

Phenomenologically based on the local band theory [34,35], one can assume that the magnitude of the local magnetization is temperature independent and its direction fluctuates around the macroscopic magnetization direction in a time scale ($10^{-12} \sim 10^{-13}$ sec) much longer than the photoelectron excitation process ($10^{-14} \sim 10^{-15}$ sec). Since we extract photoelectrons at finite temperatures through the fast photoexcitation process, an observed photoelectron reflects the instantaneous local electronic structures at a point in the crystal where the direction of the local magnetization is tilted with respect to the macroscopic magnetization direction. Since the spin-resolved photoemission experiment is time integrating and the integrating time (~ 10 sec) is infinitely longer than the spin fluctuating time, we have observed an averaged magnetization over many tilted local magnetization. Hence the spin polarization of the 6 eV satellite observed in the spin-resolved resonant photoemission would decrease with increasing temperature and will trace the same temperature dependence as the macroscopic magnetization. Figure 9 shows the temperature dependence of the characteristic spin polarization of the 6 eV satellite at resonance together with the macro-

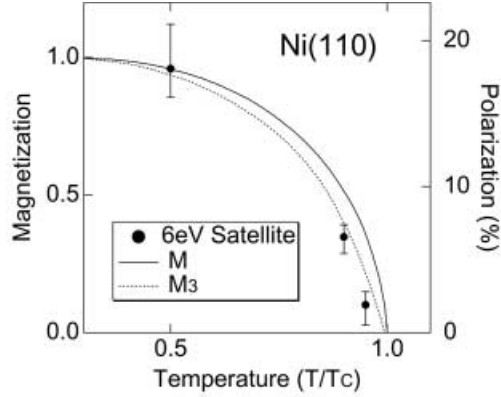


Fig. 9. Temperature dependence of the characteristic spin polarization of the 6 eV satellite. The solid and dotted curves represent the temperature dependence the macroscopic magnetization and the magnetization of 3 ML in the mean field theory, respectively. Experimental results are normalized to the macroscopic magnetization at $T/T_c = 0.5$.

scopic magnetization. The characteristic spin polarization of the 6 eV satellite is normalized to the macroscopic magnetization at $T/T_c = 0.5$. The spin polarization decreases with increasing temperature and shows quite similar temperature dependence as the macroscopic magnetization. The disappearance of the spin polarization at T_c corresponds to the disappearance of the long range magnetic order at T_c .

It should be pointed out that in the figure that the spin polarization decreases slightly faster than the magnetization of the 3 atomic monolayers (ML). This is consistent to the estimated probing depth of photoelectrons for the 6 eV satellite. However, this does not mean that photoemission spectra of Ni films thinner than 3 ML show similar temperature dependence. Electronic structures and magnetic properties of solid surfaces and thin films are rapidly expanding research field in the past decade and intensively studied experimentally and theoretically [48].

5 Conclusion and Outlook

Taking Ni(110) valence band as an example, we have shown that the spin- and angle-resolved photoemission experiments provide not only information on the majority and minority spin states of ferromagnets but also new opportunities to investigate the role of an electron spin in manybody interactions in solids. The temperature dependence of the valence band spectra is also qualitatively interpreted invoking the electron correlation effects. However, quantitative discussion is not quite sufficient. There have been many works on the spin-resolved quasi-particle band structures and their spin dependence, but only a few experiments were actually compared with the theoretical calculations [21,39]. Attempts to

improve the reliability of the experimental resolution are needed as well as the systematic investigations of band-ferromagnets other than Ni and Fe.

As is obvious in Fig. 9, photoemission spectra only prove a few atomic layers from the surface, and by this reason the spin-resolved photoemission is applied to directly observe the electronic structures of solid surfaces and thin films. The experiments on surfaces and thin films of magnetic materials as well as nano-structures grown on magnetic and non-magnetic surfaces will provide information to bridge the gap between two- and three-dimensional magnetic properties of materials. Recently, magnetic circular dichroism and related techniques are applied to investigate the local magnetic moment of atoms at surfaces and interfaces. The cooperation of new experimental techniques with spin-resolved photoemission would show more details of the microscopic origin of surface magnetism.

The development of a free electron laser (FEL) as a future light source in a vacuum ultraviolet region will surely bring new opportunities to investigate the band-ferromagnetism by means of spin-resolved photoemission. The extremely high brightness of FEL will allow us to investigate dynamics of spin relaxation near T_c , time-resolved behavior of the magnetic moments, spatially- and spin-resolved electronic structures of magnetic and non-magnetic solids and solid surfaces, which have not been in the scope of spin-resolved photoemission experiments, so far.

References

1. S. Hüfner: *Photoelectron Spectroscopy* (Springer Verlag, Berlin 1995).
2. H. C. Siegmann et al., *Adv. Electronics and Electron Phys.* **62**, 1 (1984).
3. *Polarized Electrons in Surface Physics*, ed. R. Feder (World Scientific, Singapore 1985).
4. J. Kirschner, *Polarized Electrons at Surfaces*, (Springer, Berlin 1985).
5. J. Kessler, *Polarized Electrons*, 2nd ed., (Springer, Berlin 1985).
6. see for a review, F. B. Dunning, *Nucl. Instr. Meth.*, **A347**, 152 (1994).
7. C. S. Wang and J. Callaway, *Phys. Rev. B* **9**, 4897 (1974), F. Weling and J. Callaway, *Phys. Rev. B* **26**, 710 (1983).
8. W. Eberhardt and E. W. Plummer, *Phys. Rev. B* **21**, 3245 (1980).
9. P. C. Kemny and N. J. Shevchik, *Solid State Commun.* **17**, 255 (1975).
10. A. Liebsch, *Phys. Rev. Lett.* **43**, 1431 (1979).
11. L. A. Feldkamp and L. C. Davis, *Phys. Rev. Lett.* **43**, 151 (1979).
12. L. Hedin and S. Lundqvist, *Solid State Physics*, ed. by H. Ehrenreich, F. Seitz and D. Turnbull (Academic Press, New York 1969).
13. G. Treglia, F. Ducastelle and D. Spanjaard, *J. Physique* **41**, 281 (1980), *Phys. Rev. B* **21**, 3729 (1980).
14. A. Liebsch, *Phys. Rev. B* **23**, 5203 (1981).
15. M. A. Hoyland and R. G. Jordan, *J. Phys. Condens. Matter* **3**, 1337 (1991).
16. F. Aryasetiawan, *Phys. Rev. B* **46**, 13051 (1992).
17. J. Igarashi, P. Unger, K. Hirai and P. Fulde, *Phys. Rev. B* **49**, 16181 (1994).
18. R. H. Victora and L. M. Falicov, *Phys. Rev. Lett.* **55**, 1140 (1985).
19. W. Nolting, W. Borgiel, V. Dose and Th. Fauser, *Phys. Rev. B* **40**, 5015 (1989).

20. H. Hopster, R. Raue and G. Gütherodt: Phys. Rev. Lett. **51**, 829 (1983).
21. K. -P. Kämper, W. Schmitt and G. Gütherodt, Phys. Rev. B **42**, 10696 (1990).
22. K. Ono, A. Kakizaki, K. Tanaka, K. Shimada, Y. Saitoh and T. Sendohda, Solid State Commun. **107**, 153 (1998).
23. V. L. Moruzzi, J. F. Janak and A. R. Williams, *Calculated Electronic Properties of Metals* (Pergamon, New York 1978).
24. J. Harmanson, Solid State Commun. **22**, 9 (1977).
25. A. K. See and L. E. Krebanoff, Surf. Sci. **340**, 309 (1995).
26. O. Gunnarson, J. Phys. F **6**, 587 (1976).
27. G. Shirane, O. Steinsvoll, Y. J. Uemura and J. Wicksted, J. Appl. Phys. **55**, 1887 (1984).
28. R. Raue, H. Hopster and R. Clauberg, Z. Phys. B **54**, 121 (1984).
29. H. Hopster, D. L. Abraham, Phys. Rev. B **40**, 7054 (1989).
30. J. Kirschner and E. Langenbach, Solid State Commun. **66**, 761 (1988).
31. M. Donath and V. Dose, Europhys. Lett. **9**, 821 (1989).
32. E. Kisker, K. Schröder, M. Campagna and W. Gudat, Phys. Rev. Lett. **52**, 2285 (1984).
33. E. Kisker, J. Mag. Mag. Mat. **45**, 23 (1984).
34. V. Korenman and R. E. Prange, Phys. Rev. Lett. **53**, 186 (1984).
35. H. Capellmann, J. Phys. F **4**, 1466 (1974).
36. J. Fujii, A. Kakizaki, K. Shimada, K. Ono, T. Kinoshita and H. Fukutani, Solid State Commun. **94**, 391 (1995).
37. J. Kanamori, *Core-Level Spectroscopy in Condensed Systems*, ed. J. Kanamori and A. Kotani (Springer-Verlag, Berlin 1988) p.160.
38. M. Sawada, A. Kimura, A. Kakizaki and J. Fujii, J. Electron Spectros.Relat. Phenom. **88-91**, 201 (1998).
39. J. Braun, G. Borstel and W. Nolting, Phys. Rev. B **46**, 3510 (1992).
40. O. Björneholm, J. N. Andersen, C. Wigren, A. Nilsson, R. Nyholm and N. Maatensson, Phys. Rev. B **41**, 10408 (1990).
41. A. Kakizaki, J. Fujii, K. Shimada, A. Kamata, K. Ono, K. -H. Park, T. Kinoshita, T. Ishii and H. Fukutani, Phys. Rev. Lett. **72**, 2781 (1994).
42. C. Guillot, Y. Ballu, J. Paigne, J. Lecante, K. P. Jain, P. Thiry, R. Pinchaux, Y. Petroff and L. M. Falicov, Phys. Rev. Lett. **39**, 1632 (1977).
43. L. A. Feldkamp and L. C. Davis, Phys. Rev. Lett. **43**, 151 (1979).
44. R. Clauberg, W. Gudat, E. Kisker, E. Kuhlmann and G.M.Rothberg, Phys. Rev. Lett. **47**, 1314 (1981).
45. L. C. Davis, J. Appl. Phys. **59**, R25 (1986).
46. T. Kinoshita, T. Ikoma, A. Kakizaki, T. Ishii, J. Fujii, H. Fukutani, K. Shimada, A. Fujimori, T. Okane and S. Sato, Phys. Rev. B **47**, 6787 (1993).
47. A. Kakizaki, K. Ono, K. Tanaka, K. Shimada and T. Sendohda, Phys. Rev. B **55**, 6678 (1997).
48. see for example, *Ultrathin Magnetic Structures*, ed. by B. Heinrich and J. A. C. Bland (Springer, Berlin 1994).

Spin Fluctuations in Itinerant Electron Systems

Peter Mohn and Sergei Khmelevskyi

Center for Computational Materials Science, Vienna University of Technology,
Vienna, Austria.

Abstract. Spin fluctuations are introduced to describe the finite temperature properties of itinerant electron ferromagnets. To this end it is shown how Gaussian fluctuations of the magnetic moment can be included in a Landau type free energy expansion. From this model various properties are derived such as the temperature dependence of the magnetic moment and the susceptibility. By including magneto - volume effects an application to Invar alloys is shown. Finally the properties of the spin fluctuations are derived from a Landau - Ginzburg model. A discussion of the Curie temperature in itinerant electron ferromagnets is given.

In the Stoner model of itinerant magnetism the temperature dependence of the magnetic properties arises from the temperature dependence of the Fermi distribution. The results of this model are rather disappointing and lead to an unrealistic description of the magnetic behavior. For localized moments the Heisenberg model and similar approaches yield fair results. For these models collective excitations of the whole spin system (spinwaves) govern the finite temperature properties. In the case of itinerant electrons one can no longer assume the existence of a localized spin so that statistical fluctuations of the magnetic moment must replace the spinwaves. In an itinerant electron system the magnetic moment is carried by the spin density. Figure 1 sketches how such a fluctuation of the free electron spin density could be envisaged.

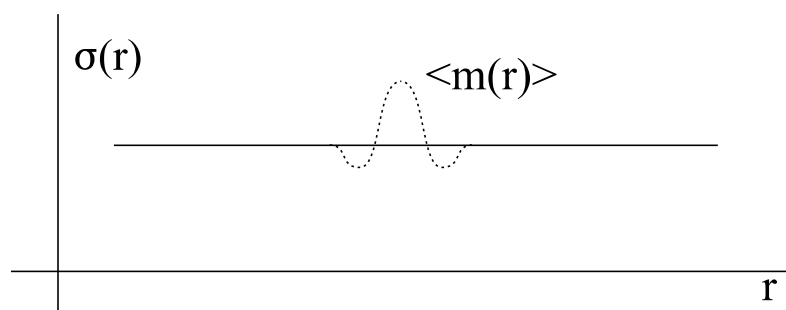


Fig. 1. Sketch of a fluctuation (dotted line) of the spin density $\sigma(r)$.

1 Fluctuations of a Thermodynamical Variable

Those physical quantities, which characterize the equilibrium state of a macroscopic system, are always very close (with high accuracy) to their average value (this is in fact an alternative definition of equilibrium). However, there are (small) deviations from equilibrium, the variables fluctuate and one has the problem of finding the probability distribution for these deviations. One assumes a system in equilibrium and x to be a certain physical quantity which characterizes the system as a whole or a part of it (in the first case, x must not be a quantity which has to be constant due to any conservation law: e.g. the total energy). An elegant way to formulate fluctuations is to use Gaussian statistics:

From Boltzmann's formula one obtains for the probability $w(x)$

$$w(x) = \exp(S(x)) \times \text{const.} \quad (1)$$

Since the entropy $S(x)$ has to be a maximum for the equilibrium one finds that for $x = \langle x \rangle = 0$ ($\langle x \rangle$ is the average value of x) the first derivative of $S(x)$ must vanish and the second derivative be negative.

$$\frac{\partial S(x)}{\partial x} = 0 \quad , \quad \frac{\partial^2 S(x)}{\partial x^2} < 0 \quad \text{for } x = 0 \quad . \quad (2)$$

It should be noted, that these assumptions of equilibrium properties for the entropy causes troubles when approaching a critical point where both the first and the second derivative vanish. The Gaussian statistics for the fluctuations is therefore restricted to parts of phase space, which are far from critical points.

Since the quantity x should be small, one expands $S(x)$ in a Taylor series up to second order

$$S(x) = S(0) - \frac{\eta}{2} x^2 \quad . \quad (3)$$

With (1) one obtains

$$w(x) dx = \kappa \exp\left(-\frac{\eta}{2} x^2\right) dx \quad . \quad (4)$$

The constant κ is given by the condition $\int w(x) dx = 1$. Although the expression for $w(x)$ is only valid for small x , one can carry out the integration from $-\infty$ to $+\infty$ because the integrand vanishes rapidly for larger values of x . The normalization constant κ is thus given by

$$\kappa = \left(\frac{\eta}{2\pi}\right)^{\frac{1}{2}} \quad . \quad (5)$$

The probability distribution for x is now given by

$$w(x) dx = \left(\frac{\eta}{2\pi}\right)^{\frac{1}{2}} \exp\left(-\frac{\eta}{2} x^2\right) dx \quad . \quad (6)$$

A distribution of this kind is called a Gaussian distribution. It shows a maximum for $x = 0$ and decreases monotonically for positive and negative values of x . The statistical averages for even powers of the variable x are given by

$$\langle x^{2k} \rangle = \left(\frac{\eta}{2\pi} \right)^{\frac{1}{2}} \int_{-\infty}^{+\infty} x^{2k} \exp \left(-\frac{\eta}{2} x^2 \right) dx = \eta^{-k} (2k-1)!! \quad . \quad (7)$$

This means in particular that $\langle x^2 \rangle = \eta^{-1}$ and $\langle x^4 \rangle = 3\eta^{-2} = 3 \langle x^2 \rangle^2$. Each higher order average can be expressed in terms of $\langle x^2 \rangle$.

2 Fluctuations of the Magnetic Moment

In the framework of the Landau theory of magnetic phase transitions the magnetic moment M is introduced as an order parameter describing the state of the system and the free energy reads in lowest order

$$F = \frac{A}{2} M^2 + \frac{B}{4} M^4 \quad , \quad (8)$$

where A and B are given by

$$A = -\frac{1}{2\chi_0} \left(1 - \frac{T^2}{T_c^2} \right) \quad , \quad B = \frac{1}{2\chi_0 M_0} \quad . \quad (9)$$

In (8) and (9) M_0 and χ_0 are the magnetic moment and the susceptibility of the ground state, respectively. T_c is the Curie temperature. It should be noted that within the Stoner model T_c is of the order of a few thousand K and thus unrealistically large. This is the reason why this temperature dependence of A , which comes from the Stoner- (single-particle-) excitations, is in most cases neglected. Usually it is assumed that M is a scalar. This is reasonable because time reversal symmetry demands that M appears only in even powers like $M^2 = \mathbf{M} \cdot \mathbf{M}$ which is always scalar. When one now deals with fluctuations one has to recognize the vector properties of both the magnetization and its fluctuations. For reasons of symmetry one can postulate that the volume integral over odd powers in the fluctuation always vanishes. If now $\mathbf{m}(r)$ is the locally fluctuating magnetic moment one assumes

$$\frac{1}{V} \int (\mathbf{m}(r))^n d\tau = \begin{cases} \langle m^n \rangle & \text{for } n = 2k \\ 0 & \text{for } n = 2k + 1 \end{cases} \quad . \quad (10)$$

As an example the lowest two powers of the new order parameter are calculated. Fluctuations appear in all three space directions. The direction of \mathbf{M} is taken as the z axis of a local coordinate system, so that one has two fluctuations perpendicular to \mathbf{M} and one parallel. These three components of the fluctuation are denoted $m_1, m_2, m_3 = m_x, m_y, m_z$ (z is parallel to \mathbf{M}). One now replaces

the original order parameter M^{2n} by the statistical average of the new order parameter (which includes the fluctuation terms)

$$\mathbf{M}^{2n} \rightarrow \left\langle \left(\mathbf{M} + \sum_{i=1}^3 \mathbf{m}_i \right)^{2n} \right\rangle . \quad (11)$$

Put $n = 1$

$$\begin{aligned} \left\langle \left(\mathbf{M} + \sum_{i=1}^3 \mathbf{m}_i \right)^2 \right\rangle &= \left\langle \mathbf{M}^2 + 2\mathbf{M} \sum_{i=1}^3 \mathbf{m}_i + \sum_{i=1}^3 \sum_{j=1}^3 \mathbf{m}_i \mathbf{m}_j \right\rangle \\ &= M^2 + 2 \langle m_{\perp}^2 \rangle + \langle m_{\parallel}^2 \rangle . \end{aligned} \quad (12)$$

On averaging the mixed term vanishes, because \mathbf{m}_i appears as an odd power. From the term $\sum_{i=1}^3 \sum_{j=1}^3 \mathbf{m}_i \mathbf{m}_j$ for the same reason only the diagonal elements remain. On the rhs of (12) it was assumed that the system is isotropic. This means that one describes one component $\langle m_{\parallel}^2 \rangle$ which is parallel to the direction of \mathbf{M} and two components $\langle m_{\perp}^2 \rangle$ which are equal and perpendicular to \mathbf{M} .

Put $n = 2$

$$\begin{aligned} \left\langle \left(\mathbf{M} + \sum_{i=1}^3 \mathbf{m}_i \right)^4 \right\rangle &= \left\langle \left(\mathbf{M}^2 + 2\mathbf{M} \sum_{i=1}^3 \mathbf{m}_i + \sum_{i=1}^3 \sum_{j=1}^3 \mathbf{m}_i \mathbf{m}_j \right)^2 \right\rangle \\ &= M^4 + M^2 \left(6 \langle m_{\parallel}^2 \rangle + 4 \langle m_{\perp}^2 \rangle \right) + 8 \langle m_{\perp}^2 \rangle^2 + \\ &\quad 3 \langle m_{\parallel}^2 \rangle^2 + 4 \langle m_{\perp}^2 \rangle \langle m_{\parallel}^2 \rangle . \end{aligned} \quad (13)$$

To enter the fluctuation terms into the free energy one replaces the bulk magnetization M in (8) by the respective averages (see (12) and (13)). One obtains an expression for the free energy in the variable M which describes the macroscopic magnetic moment (bulk moment) and the variables $\langle m_{\perp}^2 \rangle$ and $\langle m_{\parallel}^2 \rangle$ giving the quadratic average over the locally fluctuating magnetic moment. This dynamical form of (8) now reads

$$\begin{aligned} F &= \frac{A}{2} \left(M^2 + 2 \langle m_{\perp}^2 \rangle + \langle m_{\parallel}^2 \rangle \right) + \\ &\quad \frac{B}{4} \left(M^4 + M^2 \left(6 \langle m_{\parallel}^2 \rangle + 4 \langle m_{\perp}^2 \rangle \right) + \right. \\ &\quad \left. 8 \langle m_{\perp}^2 \rangle^2 + 3 \langle m_{\parallel}^2 \rangle^2 + 4 \langle m_{\perp}^2 \rangle \langle m_{\parallel}^2 \rangle \right) . \end{aligned} \quad (14)$$

The static (without fluctuations) form of the free energy has just been extended by the fluctuations. For $T = 0$ the fluctuation amplitude is zero and (14) reduces to (8). One also notices that the dynamics of the fluctuations scales with the static susceptibility (contained in the coefficient A). The first important result

is obtained for the fluctuation amplitude at T_c . In the framework of the Landau theory, the Curie temperature is given by the point where the susceptibility diverges under the condition $M = 0$. As the bulk magnetization M vanishes at T_c there is no longer a difference between the parallel and perpendicular fluctuations. This means that for $T \geq T_c \Rightarrow \langle m_{\parallel}^2 \rangle = \langle m_{\perp}^2 \rangle = \langle m^2 \rangle$. Calculating $\frac{\partial^2 F}{\partial M^2} = \chi^{-1}$, with $M = 0$, one obtains

$$\chi^{-1} = A + \frac{B}{2} 10 \langle m^2 \rangle = 0 \quad \text{for } T = T_c \quad , \quad (15)$$

which determines the magnitude of the fluctuations at T_c . One recovers the so called Moriya formula [1]

$$\langle m_c^2 \rangle = \frac{M_0^2}{5} \quad \text{for } T = T_c \quad , \quad (16)$$

where $\langle m_c^2 \rangle$ is the fluctuation amplitude at the critical temperature. Equation (16) shows that this amplitude is entirely given by ground state quantities defined at $T = 0$. Equation (16) also allows to formulate an approximation for the temperature dependence of the fluctuations. From the fluctuation dissipation theorem it is obvious that classical fluctuations change essential linear with temperature. Since the fluctuations have to vanish at $T = 0$ and their value at $T = T_c$ is known, one can approximate their temperature variation by

$$\langle m_{\parallel}^2 \rangle (T) = \langle m_{\perp}^2 \rangle (T) \simeq \langle m_c^2 \rangle \frac{T}{T_c} = \frac{M_0^2}{5} \frac{T}{T_c} \quad . \quad (17)$$

In (17) it was also assumed, that $\langle m_{\parallel}^2 \rangle$ and $\langle m_{\perp}^2 \rangle$ are identical, which is largely true for isotropic systems.

From (14) one can now directly calculate the temperature dependence of the bulk moment M

$$\begin{aligned} \frac{\partial F}{\partial M} = 0 &= AM + BM^3 + BM \left(3 \langle m_{\parallel}^2 \rangle + 2 \langle m_{\perp}^2 \rangle \right) \quad , \\ \Rightarrow M^2 &= M_0^2 - 3 \langle m_{\parallel}^2 \rangle + 2 \langle m_{\perp}^2 \rangle \quad . \end{aligned} \quad (18)$$

Using the approximations given in (17) one thus obtains

$$M^2 = M_0^2 \left(1 - \frac{T}{T_c} \right) \quad . \quad (19)$$

This behavior differs from the Stoner model insofar as the reduction of the magnetic moment at low temperature is stronger. The reason is the same as for the comparison between the Weiss- and the Heisenberg model: the collective modes described by the spin fluctuations can readily be excited at low temperature, where the Stoner excitations are still very small. A comparison of these two models is shown in Fig.2

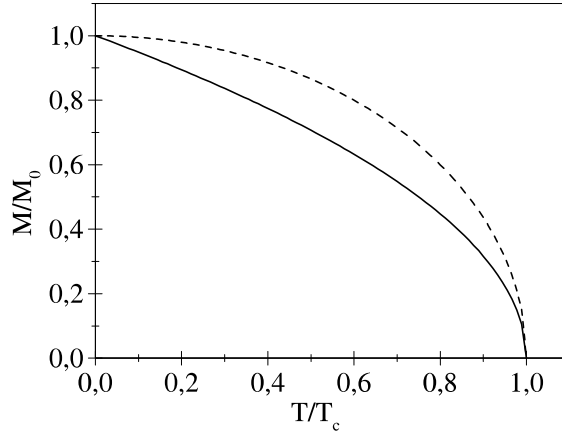


Fig. 2. Temperature dependence of the magnetization for the spinfluctuation model (full curve) and the Stoner model (dashed curve).

It is useful to study also the temperature dependence of the order parameter defined in (12)

$$\begin{aligned} \left\langle \left(\mathbf{M} + \sum_{i=1}^3 \mathbf{m}_i \right)^2 \right\rangle &= M_0^2 \left(1 - \frac{T}{T_c} \right) + 2 \langle m_{\perp}^2 \rangle + \langle m_{\parallel}^2 \rangle \\ &\simeq \begin{cases} M_0^2 \left(1 - \frac{2}{5} \frac{T}{T_c} \right) & T < T_c \\ M_0^2 \frac{3}{5} \frac{T}{T_c} & T \geq T_c \end{cases} . \end{aligned} \quad (20)$$

The temperature behavior of the bulk moment, the fluctuations and the order parameter is shown in Fig.3. The bulk magnetic moment M vanishes at T_c , but the local moments due to the fluctuations exist at all temperatures. This behavior distinguishes the fluctuations from the Stoner model where no magnetic moment exists above T_c so that the paramagnetic state is assumed to be a true non-magnetic state.

The susceptibility below and above T_c is given by

$$\chi = \chi_0 \left(1 - \frac{T}{T_c} \right)^{-1} \quad \text{for } T < T_c \quad , \quad (21)$$

$$\chi = 2\chi_0 \left(\frac{T}{T_c} - 1 \right)^{-1} \quad \text{for } T \geq T_c \quad , \quad (22)$$

which leads to a Curie constant C

$$C = \frac{d(\chi^{-1})}{dT} = \frac{1}{2\chi_0 T_c} \quad , \quad (23)$$

which is no longer temperature dependent as for the Stoner model and thus describes a Curie-Weiss behavior.

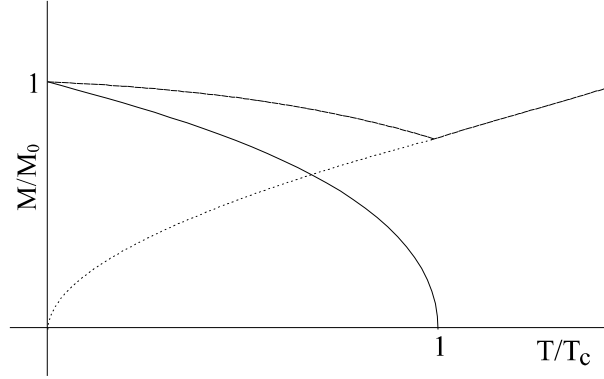


Fig. 3. Temperature dependence of the bulk moment $\sqrt{\left(1 - \frac{T}{T_c}\right)}$ (full curve), the fluctuations $\sqrt{\frac{3}{5} \frac{T}{T_c}}$ (dotted curve), and the order parameter $\sqrt{\left(1 - \frac{2}{5} \frac{T}{T_c}\right)}$ (dashed curve).

Based on these results which were first introduced by Murata and Doniach [2] and the work by Lonzarich and Taillefer [3], Mohn and Wohlfarth [4] derived a simple model for the Curie temperature in weakly itinerant systems

$$T_c \propto T_{SF} = \frac{M_0^2}{10k_B\chi_0} \quad . \quad (24)$$

In (24) T_{SF} is a characteristic temperature which scales with the actual ordering temperature T_c . In Fig.4 the relation between T_{SF} and the experimental Curie temperature T_c is shown.

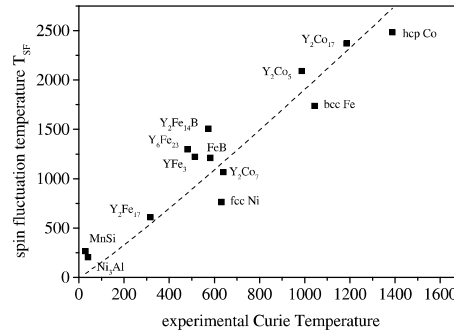


Fig. 4. Relation between T_{SF} and the experimental T_c .

Equation (24) describes the long wave length limit for fluctuations in weakly itinerant systems and is thus an approximation which is based on the assumption

of an effective cut-off for the collective excitations which should be fairly constant. In the literature this approach is known as the Mohn-Wohlfarth model and has triggered considerable interest in the application of spin fluctuation theory. Although this approach can be expected to break down for strong ferromagnets [6] it can still be used to describe the relative change of T_c , e.g. for different concentrations in an alloy system.[7]

From (24) it also becomes clear, why the Curie temperature of Co is larger although the magnetic moment is smaller than that for Fe. The reason is that Fe is just at the verge of an strongly ferromagnetic system, but still has a relatively large susceptibility. Co however is already strongly ferromagnetic and the susceptibility is drastically reduced. This means that in (24) the term M_0^2/χ_0 (and thus T_{SF}) is smaller for Fe than for Co. For Ni the magnetic moment drops to $0.6\mu_B$, so that for a comparable susceptibility with Co the Curie temperature is reduced as well.

3 The Specific Heat of the Spin Fluctuations

The expression for the free energy (14) allows to calculate the specific heat using the thermodynamic relation

$$c_m = -T \frac{\partial^2 F}{\partial T^2} . \quad (25)$$

If one neglects the temperature dependence of the coefficient A (neglecting single particle excitations) one obtains for $T < T_c$ the result [5]

$$\begin{aligned} c_m^< = \frac{B}{2} \langle m_{\parallel}^2 \rangle & \left[6 \frac{\partial \langle m_{\parallel}^2 \rangle}{\partial T} + 4 \frac{\partial \langle m_{\perp}^2 \rangle}{\partial T} \right] \\ & + B \langle m_{\perp}^2 \rangle \left[2 \frac{\partial \langle m_{\parallel}^2 \rangle}{\partial T} - 2 \frac{\partial \langle m_{\perp}^2 \rangle}{\partial T} \right] . \end{aligned} \quad (26)$$

For $T \geq T_c$, the bulk magnetization M and its derivatives are zero so that one finds

$$c_m^> = -\frac{B}{2} \langle m^2 \rangle 15 \frac{\partial \langle m^2 \rangle}{\partial T} . \quad (27)$$

The specific heat of the fluctuations thus shows a discontinuity at T_c which is given by

$$\Delta c_m = \frac{B}{2} \langle m_c^2 \rangle 15 \frac{\partial \langle m^2 \rangle}{\partial T} \Big|_{T=T_c} . \quad (28)$$

Using (16) and (17) one obtains

$$\Delta c_m = \frac{M_0^2}{4\chi_0 T_c} . \quad (29)$$

For *bcc* Fe one calculates a value of about 36 J/mole K which is close to the experimental value of 43 J/mol K. Equation (29) should be compared to the analogous expression derived for the Stoner theory: $\Delta c_m = M_0^2 / (\chi_0 T_c)$. One finds, that the discontinuity at T_c is reduced by a factor 4 (!) with respect to the Stoner theory. The reason for this that in contrast to the Stoner model, in the spin fluctuation model, the state above T_c is not the *nonmagnetic* state but a *paramagnetic* state, where local moments still exist, but long range order has been destroyed by the fluctuations.

4 Magneto-Volume Coupling

In analogy with (8) the interaction between the volume of a system and its magnetic moment is taken into account via a magneto-volume coupling constant δ . With these extensions the free energy reads

$$F = \frac{A}{2} \left(M^2 + 2 \langle m_{\perp}^2 \rangle + \langle m_{\parallel}^2 \rangle \right) + \frac{B}{4} \left(M^4 + M^2 \left(6 \langle m_{\parallel}^2 \rangle + 4 \langle m_{\perp}^2 \rangle \right) + 8 \langle m_{\perp}^2 \rangle^2 + 3 \langle m_{\parallel}^2 \rangle^2 + 4 \langle m_{\perp}^2 \rangle \langle m_{\parallel}^2 \rangle \right) + \alpha + \beta V + \gamma V^2 + \delta V \left(M^2 + 2 \langle m_{\perp}^2 \rangle + \langle m_{\parallel}^2 \rangle \right) . \quad (30)$$

The magnetic and mechanical equations of state are given by

$$H = \left. \frac{\partial F}{\partial M} \right|_V \quad (31)$$

$$= AM + BM^3 + BM \left(3 \langle m_{\parallel}^2 \rangle + 2 \langle m_{\perp}^2 \rangle \right) + 2\delta VM ,$$

$$-P = \left. \frac{\partial F}{\partial V} \right|_M \quad (32)$$

$$= \beta + 2\gamma V + \delta \left(M^2 + 2 \langle m_{\perp}^2 \rangle + \langle m_{\parallel}^2 \rangle \right) .$$

The equilibrium magnetic moment at $T = 0$ is thus

$$M_0^2 = - \frac{A + 2\delta V_0}{B} , \quad (33)$$

where V_0 is the equilibrium volume at $T = 0$. From these results one can determine the critical pressure for the disappearance of magnetism

$$P_c = \frac{\gamma A - \beta \delta}{\delta} , \quad (34)$$

and the pressure dependence of the Curie temperature

$$\begin{aligned} \frac{dT_c}{dP} &= - \frac{T_c(P=0)}{P_c} , \\ \Rightarrow T_c(P) &= T_c(P=0) \left(1 - \frac{P}{P_c} \right) . \end{aligned} \quad (35)$$

For fluctuation systems the Curie temperature depends linearly on the applied pressure. This is again in contrast to the Stoner result which reads

$$T_c(P) = T_c(P=0) \left(1 - \frac{P}{P_c}\right)^{\frac{1}{2}}. \quad (36)$$

A crucial quantity is the magnetic contribution to the thermal expansion α_m since the respective value for the Stoner model was again too large. For the spin-fluctuation model one finds:

$$\alpha_m = \frac{\partial \omega}{\partial T} = \begin{cases} \frac{1}{T_c} \left(\frac{V_{NM}}{V_0} - 1 \right) \frac{2}{5} & \text{for } T < T_c \\ \frac{1}{T_c} \left(1 - \frac{V_{NM}}{V_0} \right) \frac{3}{5} & \text{for } T \geq T_c \end{cases} \quad (37)$$

here ω is the relative volume change ($\frac{V-V_0}{V}$), V_0 is the equilibrium volume at $T = 0K$ and V_{NM} is the hypothetical volume of the non-magnetic phase ($M = 0, \langle m^2 \rangle = 0$), which is also the volume for the Stoner model at T_c . For the fluctuation model the volume at T_c becomes:

$$V(T_c) = V_{NM} - \frac{3}{5} (V_{NM} - V_0), \quad (38)$$

which leads to a considerably smaller spontaneous volume magnetostriction comparable to experiment.

Equation (37) also allows to recover a “rule of thumb“ given by Masumoto in 1927 for Invar [8],[9] alloys: “To observe a large negative value of α_m (and consequently a small overall thermal expansion) the fraction M_0^2/T_c should be large“. If one rewrites (37) in a different form one finds exactly Masumoto’s rule

$$\begin{aligned} \alpha_m &= \frac{1}{T_c} \frac{4B\delta \langle m_c^2 \rangle}{A\delta - 2B\beta} \quad \text{with } \langle m_c^2 \rangle \simeq \frac{M_0^2}{5} : \\ \Rightarrow \quad \alpha_m &= \frac{M_0^2}{T_c} \frac{4B\delta}{5(A\delta - 2B\beta)} \end{aligned} \quad (39)$$

5 Comparing the Spin-Fluctuation- and the Stoner-Model

In this section a comparison between the results from the spin-fluctuation model and the Stoner-model is presented. In both cases the results are based on a Landau-expansion of the free energy up to fourth order in M and up to second order in V . The starting equations are thus (8) or (9) (including a volume dependence when required) for the Stoner model and (14) or (30) for the spin-fluctuation model, respectively.

Spin-fluctuations lead to a different power law behavior for both the susceptibility and the magnetic moment. However, since also spin-fluctuations are treated within a mean field theory, the critical exponents of both models are the same. This different power law is also found for the pressure dependence of the Curie-temperature and its slope. As expected for localized moments, spin-fluctuations

Table 1. Comparison between the Spin-fluctuation and the Stoner-model for the susceptibility χ , the Curie constant C , the magnetic moment $M(T)$, the magnetic contribution α_m to the thermal expansion coefficient, the volume at the Curie temperature $V(T_c)$, the pressure dependence of the Curie temperature $T_c(P)$, the coefficient $\partial T_c / \partial P$ of the pressure dependence of T_c ; the discontinuity of α_m at the Curie temperature $\Delta\alpha_m$, the discontinuity of the specific heat c_m at the Curie temperature Δc_m .

	Spin-fluctuation model	Stoner-model
χ for $T < T_c$	$\chi_0 \left(1 - \frac{T}{T_c}\right)^{-1}$	$\chi_0 \left(1 - \frac{T^2}{T_c^2}\right)^{-1}$
χ for $T \geq T_c$	$2\chi_0 \left(\frac{T}{T_c} - 1\right)^{-1}$	$\chi_0 \left(\frac{T^2}{T_c^2} - 1\right)^{-1}$
$C = \frac{\partial(\chi^{-1})}{\partial T}$	$\frac{1}{2\chi_0 T_c}$	$\frac{1}{\chi_0 T_c} \frac{T}{T_c}$
$M(T)$	$M_0 \left(1 - \frac{T}{T_c}\right)^{\frac{1}{2}}$	$M_0 \left(1 - \frac{T^2}{T_c^2}\right)^{\frac{1}{2}}$
α_m for $T < T_c$	$\frac{1}{T_c} \left(\frac{V_{NM}}{V_0} - 1\right)^{\frac{2}{5}}$	$\frac{2}{T_c} \left(\frac{V_{NM}}{V_0} - 1\right) \frac{T}{T_c}$
α_m for $T \geq T_c$	$\frac{1}{T_c} \left(1 - \frac{V_{NM}}{V_0}\right)^{\frac{3}{5}}$	0
$V(T_c)$	$V_{NM} - (V_{NM} - V_0)^{\frac{3}{5}}$	V_{NM}
$T_c(P)$	$T_c(0) \left(1 - \frac{P}{P_c}\right)$	$T_c(0) \left(1 - \frac{P}{P_c}\right)^{\frac{1}{2}}$
$\frac{\partial T_c}{\partial P}$	$-\frac{T_c}{P_c}$	$-\frac{T_c}{2P_c}$
$\Delta\alpha_m$ at T_c	$\frac{1}{T_c} \left(1 - \frac{V_{NM}}{V_0}\right)$	$\frac{2}{T_c} \left(1 - \frac{V_{NM}}{V_0}\right)$
Δc_m at T_c	$\frac{M_0^2}{4\chi_0 T_c}$	$\frac{M_0^2}{\chi_0 T_c}$

lead to a linear temperature dependence of the inverse susceptibility (Curie-Weiss law), which is expressed by a temperature independent Curie-constant. The magnetic contributions to the thermal expansion coefficient caused by the spin-fluctuations are smaller than that for the Stoner-model and exist also above T_c . Consequently also the volume at T_c is larger than for the Stoner model, which causes a smaller spontaneous volume-magnetostriction. Finally also the discontinuity in the specific heat at T_c is reduced by a factor 4 with respect to the Stoner model.

6 The Landau-Ginzburg Model for Spin Fluctuations

In the beginning of this article spin fluctuations were introduced in a rather phenomenological way. This means that the actual nature of these fluctuations remains unclear and their properties, like the temperature dependence were only introduced in an approximative manner. Although this was sufficient to describe quite a large number of properties, here an “exact” theory within the mean field approximation of the magnetic fluctuations is presented. This means in particular that one has to allow for finite values of the wave-vector \mathbf{q} . If one wants to solve the problem “exactly” one can follow the method of Landau and Ginzburg. The expansion for the free energy now contains a local gradient term which takes the spatial dependence of the fluctuations into account. This treatment is also

called the Ornstein-Zernicke extension to Landau theory or also the “continuum Gaussian” model. The respective hamiltonian becomes

$$\mathcal{H} = \frac{1}{V} \int d\mathbf{r} \left(E \left(\mathbf{M} + \sum_{i=1}^3 \mathbf{m}_i(\mathbf{r}) \right) + \frac{C}{2} \sum_{i,j} (\nabla_j \mathbf{m}_i(\mathbf{r}))^2 \right) \quad . \quad (40)$$

The term $E \left(\mathbf{M} + \sum_{i=1}^3 \mathbf{m}_i(\mathbf{r}) \right)$ is the energy expansion given in (14) while the expression $(\nabla_j \mathbf{m}_i(\mathbf{r}))^2$ accounts for the local fluctuations. The free energy is then given by

$$F = -k_B T \ln Z \quad , \quad Z = \int d\Gamma \exp(-\beta \mathcal{H}) \quad , \quad (41)$$

where $d\Gamma$ means the integration over all fluctuation variables (see (46)) and $\beta = 1/(k_B T)$. The problem is now that the sum of states cannot be calculated analytically for the assumed hamiltonian. An approximate treatment is provided by the Bogoliubov (Peierls- Feynman) [10], [11] inequality which reads

$$F \leq F_0 + \langle \mathcal{H} - \mathcal{H}_0 \rangle_0 \quad . \quad (42)$$

One formulates a parametrized ansatz for F_0 (for which the sum of states can be calculated) and finally minimizes the rhs of (42). In the sense of the variational principle this leads to the best approximation for F under the trial free energy F_0 . It should be noted that this procedure is equivalent to a mean field solution. To have a most general form for \mathcal{H}_0 one chooses a translationally invariant, quadratic form in $\mathbf{m}(\mathbf{r})$

$$\mathcal{H}_0 = \sum_{i=1}^3 \frac{1}{V} \int d^3r \, d^3r' \, \Omega_i(\mathbf{r} - \mathbf{r}') \mathbf{m}_i(\mathbf{r}) \mathbf{m}_i(\mathbf{r}') \quad . \quad (43)$$

With this approach F_0 can be calculated and the function $\Omega_i(\mathbf{r} - \mathbf{r}')$ is the variational parameter. The following derivation is a basic example for the solution of the Landau - Ginzburg Hamiltonian and is therefore given in detail. One starts by defining the Fourier transforms

$$\mathbf{m}_i(\mathbf{r}) = \sum_{\mathbf{k}} \mathbf{m}_{\mathbf{k}i} \exp(i\mathbf{k}\mathbf{r}) \quad , \quad \Omega_i(\mathbf{r}) = \frac{1}{V} \sum_{\mathbf{k}} \Omega_{\mathbf{k}i} \exp(i\mathbf{k}\mathbf{r}) \quad , \quad (44)$$

which allow to write the trial hamiltonian as

$$\mathcal{H}_0 = \sum_{\mathbf{k}, i} \Omega_{\mathbf{k}i} \mathbf{m}_{\mathbf{k}i} \mathbf{m}_{-\mathbf{k}i} = \sum_{\mathbf{k}, i} \Omega_{\mathbf{k}i} |\mathbf{m}_{\mathbf{k}i}|^2 \quad . \quad (45)$$

To calculate the respective sum of states Z_0 one has to integrate over the phase space of the fluctuations which is given by the product over all independent variables

$$d\Gamma = \prod_{\mathbf{k}, i} d\mathbf{m}_{\mathbf{k}i} \quad , \quad (46)$$

and hence

$$\begin{aligned} Z_0 &= \prod_{\mathbf{k}, i} \int_{-\infty}^{+\infty} d\mathbf{m}_{\mathbf{k}i} \exp \left(-\beta \sum_{\mathbf{k}, i} \Omega_{\mathbf{k}i} |\mathbf{m}_{\mathbf{k}i}|^2 \right) \\ &= \prod_{\mathbf{k}, i} \left(\frac{\pi k_B T}{\Omega_{\mathbf{k}i}} \right)^{\frac{1}{2}}, \end{aligned} \quad (47)$$

so that the free energy F_0 becomes

$$\begin{aligned} F_0 &= -k_B T \ln Z \\ &= -\frac{k_B T}{2} \sum_{\mathbf{k}, i} \ln \left(\frac{\pi k_B T}{\Omega_{\mathbf{k}i}} \right). \end{aligned} \quad (48)$$

The Fourier transforms of the averages are

$$\begin{aligned} \langle \mathbf{m}_i(\mathbf{r})^2 \rangle &= \sum_{\mathbf{k}_1, \mathbf{k}_2} \langle \mathbf{m}_{\mathbf{k}_1 i} \mathbf{m}_{\mathbf{k}_2 i} \rangle \exp[-i\mathbf{r}(\mathbf{k}_1 + \mathbf{k}_2)] \\ &= \sum_{\mathbf{k}} \langle |\mathbf{m}_{\mathbf{k}i}|^2 \rangle. \end{aligned} \quad (49)$$

The simplification of the summation to involve only one variable \mathbf{k} is due to the translational symmetry. The thermodynamical average of the fluctuation with respect to \mathcal{H}_0 is given by

$$\begin{aligned} \langle \mathbf{m}_i(\mathbf{r})^2 \rangle &= \sum_{\mathbf{k}} \frac{\int_{-\infty}^{+\infty} |\mathbf{m}_{\mathbf{k}i}|^2 \exp(-\beta \mathcal{H}_0) d\Gamma}{\int_{-\infty}^{+\infty} \exp(-\beta \mathcal{H}_0) d\Gamma} \\ &= \sum_{\mathbf{k}} \frac{\int_{-\infty}^{+\infty} d\mathbf{m}_{\mathbf{k}i} |\mathbf{m}_{\mathbf{k}i}|^2 \exp(-\beta \mathcal{H}_0) d\Gamma}{\int_{-\infty}^{+\infty} d\mathbf{m}_{\mathbf{k}i} \exp(-\beta \mathcal{H}_0) d\Gamma} \\ &= \frac{k_B T}{2} \sum_{\mathbf{k}} \frac{1}{\Omega_{\mathbf{k}i}}. \end{aligned} \quad (50)$$

The thermodynamical average of \mathcal{H}_0 is obtained along the same lines

$$\langle \mathcal{H}_0 \rangle_0 = \sum_{\mathbf{k}i} \Omega_{\mathbf{k}i} \langle |\mathbf{m}_{\mathbf{k}i}|^2 \rangle = \frac{k_B T}{2} \sum_{\mathbf{k}i} 1, \quad (51)$$

giving a contribution which is just proportional to the number of modes (=degrees of freedom). The final step is the calculation of the thermodynamical average of \mathcal{H} . One writes $\langle \mathcal{H} \rangle$ in the form

$$\langle \mathcal{H} \rangle = E(M) + \varphi + \frac{C}{2V} \int d^3r \sum_{i,j} \langle \nabla_j \mathbf{m}_i(\mathbf{r}) \rangle^2. \quad (52)$$

In (51) the function φ has been introduced which is the difference between the Landau expansion at $T = 0$ $E(M)$ and the respective expansion which contains the fluctuations for $T > 0$. It is given by

$$\varphi = \frac{1}{V} \int d^3r \left\langle E \left(\mathbf{M} + \sum_{i=1}^3 \mathbf{m}_i(\mathbf{r}) \right) - E(M) \right\rangle . \quad (53)$$

Using Fourier transforms one can calculate the integral in (52) and obtains

$$\langle \mathcal{H} \rangle_0 = E(M) + \varphi + \frac{C}{2} \frac{k_B T}{2} \sum_{\mathbf{k}i} \frac{\mathbf{k}^2}{\Omega_{\mathbf{k}i}} . \quad (54)$$

Now one can collect all terms and formulate the free energy from the Bogoliubov inequality

$$\begin{aligned} F &\leq F_0 + \langle \mathcal{H} - \mathcal{H}_0 \rangle_0 \\ &= E(M) + \varphi + \frac{C}{2} \frac{k_B T}{2} \sum_{\mathbf{k}i} \frac{\mathbf{k}^2}{\Omega_{\mathbf{k}i}} \\ &\quad - \frac{k_B T}{2} \sum_{\mathbf{k}i} \left(1 + \ln \left(\frac{\pi k_B T}{\Omega_{\mathbf{k}i}} \right) \right) \end{aligned} \quad (55)$$

The function $\Omega_{\mathbf{k}i}$ was introduced as a variational parameter so as to construct an optimal approximation for F . The value of $\Omega_{\mathbf{k}i}$ is now determined from the condition $\frac{dF}{d\Omega_{\mathbf{k}i}} = 0$ which yields

$$\Omega_{\mathbf{k}i} = \frac{C}{2} \mathbf{k}^2 + \frac{\partial \varphi}{\partial \langle \mathbf{m}_i(\mathbf{r})^2 \rangle} . \quad (56)$$

Up to 4th order in the magnetic moment the function φ is given

$$\begin{aligned} \varphi &= \frac{A}{2} (\langle m_1^2 \rangle + \langle m_2^2 \rangle + \langle m_3^2 \rangle) + \\ &\quad \frac{B}{4} \left(M^2 (2 \langle m_1^2 \rangle + 2 \langle m_2^2 \rangle + 6 \langle m_3^2 \rangle) + 4 \langle m_1^2 \rangle^2 \right. \\ &\quad \left. + 4 \langle m_2^2 \rangle^2 + 3 \langle m_3^2 \rangle^2 + 2 \langle m_1^2 \rangle \langle m_3^2 \rangle + 2 \langle m_2^2 \rangle \langle m_3^2 \rangle \right) , \end{aligned} \quad (57)$$

where the obvious \mathbf{r} dependence of $\langle m_i^2 \rangle$ was omitted. As before an isotropic system is assumed so that $\langle m_1^2 \rangle = \langle m_2^2 \rangle = \langle m_{\perp}^2 \rangle$ and $\langle m_3^2 \rangle = \langle m_{\parallel}^2 \rangle$. Calculating the derivative of φ with respect to the fluctuations one obtains

$$\begin{aligned} \frac{\partial \varphi}{\partial \langle m_1^2 \rangle} &= \frac{A}{2} + \frac{B}{4} (2M^2 + 8 \langle m_1^2 \rangle + 2 \langle m_3^2 \rangle) \\ &= \frac{1}{\chi_{\perp}} - \frac{C}{2} k^2 , \end{aligned} \quad (58)$$

for the perpendicular component, and

$$\begin{aligned}\frac{\partial \varphi}{\partial \langle m_3^2 \rangle} &= \frac{A}{2} + \frac{B}{4} (6M^2 + 2 \langle m_1^2 \rangle + 2 \langle m_2^2 \rangle + 6 \langle m_3^2 \rangle) \\ &= \frac{1}{\chi_{\parallel}} - \frac{C}{2} k^2 \quad ,\end{aligned}\tag{59}$$

for the parallel component. From the definition given in (62) the relation to the parallel and perpendicular susceptibility is obvious. It is easy to proof that both derivatives vanish at T_c . Of more interest is their value at $T = 0$. Here the perpendicular component is zero but the parallel component has the value of the inverse bulk susceptibility which is $(2\chi_0)^{-1}$. One can thus interpret these relations as susceptibilities for the excitation of parallel or perpendicular fluctuations. On closer inspection one finds, that the perpendicular susceptibility is much larger than the parallel one, which means that it is much easier to excite a tilting of the moments than a fluctuation along the parallel component. This behavior again resembles the result for the Heisenberg model where also the tilting of the localized spins was found to be the important mechanism.

Combining (50) and (56) allows to calculate the explicit form for the fluctuation amplitude

$$\langle \mathbf{m}_i^2 \rangle = \frac{k_B T}{2} \frac{V}{8\pi^3} \int_0^{k_c} \frac{4\pi k^2}{\frac{C}{2} k^2 + \frac{\partial \varphi}{\partial \langle \mathbf{m}_i(\mathbf{r})^2 \rangle}} dk \quad .\tag{60}$$

In (60) there appear two unknown parameters: the “spin-wave-stiffness“ C and the cut-off wave-vector k_c . The latter quantity must be introduced, since the Ornstein-Zernicke correlation function, which appears in the integrand, leads to a divergence if the integration is carried out to $k \rightarrow \infty$. A physical justification for the introduction of this cut-off may be found in the strong damping of the spin-fluctuations by the single particle excitations (Landau damping). From the zero temperature properties of the derivative of in the integrand of (60) one can replace the spin-wave-stiffness-constant C by ξ^2/χ_0 where ξ is the correlation length and χ_0 is the susceptibility. Equation (60) yields only an implicit definition of $\langle \mathbf{m}_i^2 \rangle$ because the fluctuation amplitude occurs also in the denominator. For practical application (60) must be solved numerically. However, the properties of derivatives of the function φ allows to derive an expression for the Curie temperature of a spin fluctuation system. Since $\frac{\partial \varphi}{\partial \langle \mathbf{m}_i(\mathbf{r})^2 \rangle}$ must vanish at $T = T_c$ one can carry out the integration at T_c and obtains a result similar to the Mohn-Wohlfarth model

$$T_c = \frac{M_0^2}{10\chi_0 k_B} \frac{4\pi^2 \xi^2}{V k_c} \quad .\tag{61}$$

In contrast to the long wavelength expression (24), (61) also contains some information about the finite wavelength dependencies of the fluctuations via the parameter ξ .

It should be noted, that the integrand of (60) can be interpreted as the wavevector dependent susceptibility. The integrand is essentially given by (56) and reads

$$\begin{aligned}\chi_0(\mathbf{k}) &= \frac{1}{\Omega_{\mathbf{k}||}} = \frac{1}{\frac{C}{2}\mathbf{k}^2 + \frac{1}{2\chi_0}} \\ &= \frac{2\chi_0}{1 + \xi^2\mathbf{k}^2},\end{aligned}\quad (62)$$

where the $T = 0$ value for $\frac{\partial\varphi}{\partial\langle\mathbf{m}_{||}(\mathbf{r})^2\rangle}$ was used. ξ is again the correlation length which is also sometimes called “the real space parameter”. The role of ξ becomes clear from Fig.5, which shows that $\frac{1}{\xi}$ determines the halfwidth of the \mathbf{k} -distribution.

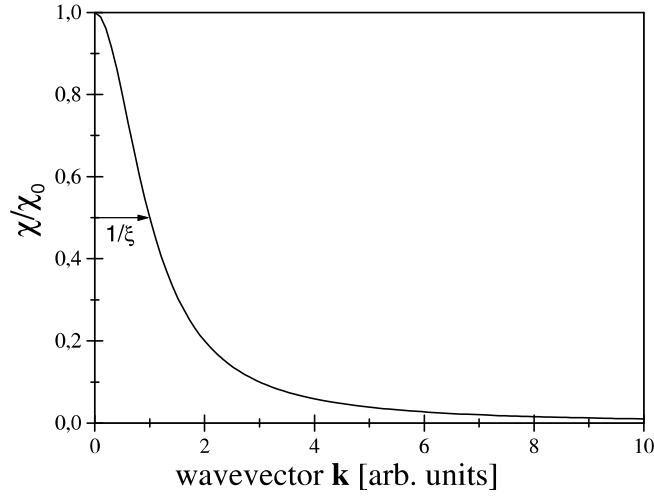


Fig. 5. Wavevector dependent susceptibility of a ferromagnetic fluctuation system.

The function $\chi(\mathbf{k})$ has the shape of a Lorentzian, where the correlation length ξ determines the width of the distribution. The solution given in (62) above is written for low temperatures because ξ also shows a temperature dependence which causes a broadening of the distribution at higher temperature (at $T = T_c$ the correlation length actually diverges). The simple Ornstein-Zernicke form of $\chi(\mathbf{k})$ arises from the assumption of a quadratic form for \mathcal{H}_0 , however, it is found that most ferromagnetic systems are quite well described.

How can one interpret this form for the susceptibility? The susceptibility in its most general form describes the answer of a system to a perturbation. This perturbation can be almost anything (e.g. an electric field or as here our case a magnetic one). When the susceptibility was introduced a static homogenous field H was assumed. The response of the system was a static, homogenous magnetization M . If one now applies a field which varies in space with a wavevector

\mathbf{k} (this field drives the local fluctuations) the answer is $\chi(\mathbf{k})$. A mechanical example is the forced oscillation of a pendulum. The maximum of $\chi(\mathbf{k})$ for $k = 0$ is nothing more but the resonance frequency (ferromagnetic resonance) and for any deviation from the resonance the amplitude becomes smaller and follows exactly the Lorentz curve.

Acknowledgment

This work has been supported by the Austrian Fonds zur Förderung der Wissenschaftlichen Forschung (FWF) grant Nr. P13436-PHY.

References

1. T. Moriya: Prog. Theor. Phys. **16**, 23 (1965)
2. K. K. Murata and S. Doniach: Phys. Rev. Letters **29**, 285 (1972)
3. G. G. Lonzarich and L. Taillefer: J. Phys. C **18**, 4339 (1985)
4. P. Mohn and E. P. Wohlfarth: J. Phys. F: Metal Physics **17**, 2421 (1986)
5. P. Mohn and G. Hilscher: Phys. Rev. B **40**, 9126 (1989)
6. Q. Qi, R. Skomski, J. M. Coey: J. Phys.: Condens. Matter **6**, 3245 (1994)
7. S. S. Jaswal: Phys. Rev. B **48**, 6156 (1993)
8. Ch. E. Guillaume: C. R. Acad. Sci. Paris **125**, 235 (1897)
9. E. F. Wassermann: *Ferromagnetic Materials Volume 5*, ed. by K. H. J. Buschow and E. P. Wohlfarth (North-Holland, Amsterdam 1990)
10. R. Peierls: Phys. Rev. **54**, 918 (1934)
11. R. P. Feynman: Phys. Rev. B **97**, 660 (1955)

Itinerant Electron Magnets: Curie Temperature and Susceptibility in Density-Functional Theory

Jürgen Kübler

Institut für Festkörperphysik, Technische Universität Darmstadt, Germany

1 Introduction

Groundstate properties of solids are astonishingly well described by the local density functional approximation (LDA) [1]. This is also true of metallic magnets for which the situation was recently described by this author [2]. Excited-state properties of magnets (and other systems), however, are still a great challenge and it was believed until recently that the band-picture, based in the LDA, fails entirely in describing magnetism at elevated temperatures. We emphasize here that this is not so, attempting first to expose the reason why it was thought that the band-picture fails. Since historically the underlying physical picture was developed by Stoner and Wohlfarth, we begin with a discussion of their theory using, however, an approach that reveals the essential assumptions. This is Mermin's [3] finite-temperature density functional theory. Two points emerge: one is the essential noncollinearity of the magnetic moments at finite temperatures, the other is the form of the exchange-correlation contribution to the thermodynamic potential. We know how to deal with noncollinear order in the LDA and we explain how we might use this knowledge to advance the issue. Exchange and correlation at finite temperatures are, however, at the present state not well understood. This statement not only applies to density functional theory but also to many-body treatments addressed at this workshop.

We will show in particular that the theory of magnons in the band-LDA-picture at low temperatures is in good shape. At high temperatures we opt for a theory involving spin fluctuations and argue that, although broad features of the magnetic phase transition are described satisfactorily, many details await further improvements.

2 Stoner-Wohlfarth Theory at Non-zero Temperatures

We begin with a brief excursion into density functional theory at finite temperatures essentially using Mermin's [3] approach. We will give an outline of this theory here even though we presently do not know a physically meaningful approximation to the finite-temperature exchange-correlation potential. The discussion given in this section, therefore, serves on the one hand to restate in modern form Stoner-Wohlfarth theory and on the other hand to define our limits of understanding but does not, unfortunately, lead to a useful algorithm.

We consider a many-electron system in an external potential giving first the connection of the external potential with the density matrix:

$$V[\tilde{n}] = \sum_{\alpha\beta} \int v_{\alpha\beta}^{\text{ext}}(\mathbf{r}) n_{\beta\alpha}(\mathbf{r}) d\mathbf{r}, \quad (1)$$

where $\alpha, \beta = 1, 2$ are spin indices and $n_{\beta\alpha}(\mathbf{r})$ are the elements of the density matrix, \tilde{n} , which defines the particle density through the trace

$$n(\mathbf{r}) = \text{Tr } \tilde{n}(\mathbf{r}) \quad (2)$$

and the vector of the magnetization by

$$\mathbf{m}(\mathbf{r}) = \text{Tr } \boldsymbol{\sigma} \tilde{n}(\mathbf{r}), \quad (3)$$

where $\boldsymbol{\sigma}$ is given by the Pauli spin matrices.

Mermin [3] laid the formal foundations for the proof that in the grand canonical ensemble at a given temperature T and chemical potential μ the equilibrium density matrix $\tilde{n}(\mathbf{r})$, i.e. the equilibrium particle density $n(\mathbf{r})$ and the equilibrium magnetization $\mathbf{m}(\mathbf{r})$, are determined by the external potential and magnetic field that make up $v_{\alpha\beta}^{\text{ext}}(\mathbf{r})$. It must be added, however, that Mermin did not discuss magnetic systems and based his theory on the density, not the density matrix. Allowing this generalization we state that the correct $n(\mathbf{r})$ and $\mathbf{m}(\mathbf{r})$ minimize the Gibbs grand potential Ω :

$$\Omega[\tilde{n}] = \sum_{\alpha\beta} \int v_{\alpha\beta}^{\text{ext}}(\mathbf{r}) \tilde{n}_{\beta\alpha}(\mathbf{r}) d\mathbf{r} + \iint d\mathbf{r} d\mathbf{r}' \frac{n(\mathbf{r})n(\mathbf{r}')}{|\mathbf{r} - \mathbf{r}'|} - \mu \int d\mathbf{r} n(\mathbf{r}) + G[\tilde{n}], \quad (4)$$

where G is a unique functional of charge and magnetization at a given temperature T and chemical potential μ . Here we omit the proof and refer the reader interested in these details to Mermin's [3] original paper or to reviews like that by Rajagopal [4] or Kohn and Vashishta [5]. The quantity $G[\tilde{n}]$ in Eq. (4) is written as the sum of three terms, i.e.

$$G[\tilde{n}] = T_0[\tilde{n}] - TS_0[\tilde{n}] + \Omega_{xc}[\tilde{n}] \quad (5)$$

with T_0 , S_0 being, respectively, the kinetic energy and entropy of a system of noninteracting electrons with density matrix \tilde{n} at a temperature T . The quantity Ω_{xc} is the exchange and correlation contribution to the Gibbs grand potential.

We now construct the minimum of the grand potential using a system of noninteracting electrons moving in an effective potential. We thus assume we can determine single-particle functions $\{\psi_{i\alpha}(\mathbf{r})\}$ that permit us to write the elements of the density matrix as

$$n_{\beta\alpha}(\mathbf{r}) = \sum_{i=1}^{\infty} \psi_{i\beta}(\mathbf{r}) \psi_{i\alpha}^*(\mathbf{r}) f(\varepsilon_i), \quad (6)$$

where α and β , due to the electron spin, take on the values 1 and 2 and $f(\varepsilon) = [1 + \exp \beta(\varepsilon - \mu)]^{-1}$ is the Fermi–Dirac distribution function ($\beta = 1/k_B T$). We obtain the single-particle spinor functions by solving the Schrödinger equation

$$\sum_{\beta} [-\delta_{\alpha\beta} \nabla^2 + v'_{\alpha\beta}(\mathbf{r}) - \varepsilon_i \delta_{\alpha\beta}] \psi_{i\beta}(\mathbf{r}) = 0 \quad (7)$$

and attempt to determine the potential, v' , by minimizing the grand potential, thus obtaining the effective potential as

$$v'_{\alpha\beta}(\mathbf{r}) \equiv v_{\alpha\beta}^{\text{eff}}(\mathbf{r}) = v_{\alpha\beta}^{\text{ext}}(\mathbf{r}) + 2 \delta_{\alpha\beta} \int \frac{n(\mathbf{r}')}{|\mathbf{r} - \mathbf{r}'|} d\mathbf{r}' + v_{\alpha\beta}^{xc}(\mathbf{r}), \quad (8)$$

where

$$v_{\alpha\beta}^{xc}(\mathbf{r}) = \frac{\delta}{\delta n_{\beta\alpha}(\mathbf{r})} \Omega_{xc}[\tilde{n}], \quad (9)$$

With the result for the effective potential we may finally rewrite the grand potential as

$$\begin{aligned} \Omega[\tilde{n}] = & -\beta^{-1} \sum_{i=1}^{\infty} \ln[1 + \exp \beta(\mu - \varepsilon_i)] - \iint d\mathbf{r} d\mathbf{r}' \frac{n(\mathbf{r}) n(\mathbf{r}')}{|\mathbf{r} - \mathbf{r}'|} \\ & - \sum_{\alpha\beta} \int d\mathbf{r} v_{\alpha\beta}^{xc}(\mathbf{r}) n_{\beta\alpha}(\mathbf{r}) + \Omega_{xc}[\tilde{n}] \end{aligned} \quad (10)$$

Formally the problem now appears to be solved: the potential in the Schrödinger equation, Eq. (7), is given by the Eqs. (8) and (9) in which the density matrix is given by Eq. (6). For a ferromagnet at zero temperature we know that the basic Schrödinger equation, in the local-density approximation, is diagonal in spin space and hence easily solved. But at finite temperatures the formal expression for the exchange-correlation potential, $v_{\alpha\beta}^{xc}(\mathbf{r})$, Eq. (9), gives no clue concerning its general properties. If we assume it remains diagonal in spin space and use the zero-temperature exchange-correlation potential we may again solve the Schrödinger equation, temperature in this case entering only through the Fermi–Dirac distribution in Eq. (6). This is not a hard calculation and one obtains for the temperature where the magnetization vanishes, values which, compared with the experimental Curie temperatures, are entirely unsatisfactory.

This disagreement is part of what is normally called the failure of Stoner theory. Another, well known defect is the magnetic susceptibility for which one calculates for the temperature range of interest Pauli-like (i.e. temperature independent) behaviour. We have chosen here to discuss the problem using a version of Mermin's finite temperature density-functional theory and see that our basic assumption of a diagonal effective potential is most likely the weak part of this treatment. Restricting the effective potential to diagonal form implies that the magnetization decreases as the temperature increases because of excitations that are of the order of the exchange splitting, i.e. of rather high energies, since

the exchange splitting is large on the scale of the Curie temperatures. We are thus led to look for low-energy excitations to explain the magnetic phase transition. Of course, another unsettling question concerns the form of the exchange correlation grand potential, Ω_{xc} of which nothing is known presently.

Awareness of low-energy excitations arose in the 1970s predominantly through the pioneering work of Moriya [6], Hubbard [7], Hasegawa [8], Korenman et al. [9], Gyorffy et al. [10], Edwards [11], Heine [12], and others. The broad consensus reached was that *orientational fluctuations of the local magnetization* represent the essential ingredients to a thermodynamic theory. This cannot be incorporated in a straightforward way into the Stoner–Mermin theory.

We will not follow the historical development, but, trying to remain in the larger context of noncollinear magnetism in density-functional theory, we begin by deriving the necessary tools to calculate the spin-wave spectrum of an itinerant-electron ferromagnet. Having thus obtained the low-energy excitations of the system, we can subsequently discuss approximations to describe its thermal properties. It should be noticed at the outset that we do *not* initially postulate a model Hamiltonian, like an Ising or Heisenberg model. The contents of the following section can be found in the book by this author [2] where, however, much more detail is given.

3 Adiabatic Spin Dynamics

We want to determine low-lying electronic excitations of the spin system. To do this we calculate a constrained ground-state that possesses a parameter which allows us to continuously tune the system to states with higher energy. This is possible if the constraint consists of an incommensurate spin spiral.

3.1 Incommensurate Spiral Structure

A spiral magnetic structure is defined by giving the Cartesian coordinates of the magnetization vector, \mathbf{m}_n , as

$$\mathbf{m}_n = m [\cos(\mathbf{q} \cdot \mathbf{R}_n) \sin \theta, \sin(\mathbf{q} \cdot \mathbf{R}_n) \sin \theta, \cos \theta] \quad . \quad (11)$$

Here m is the magnitude of the magnetic moment at site \mathbf{R}_n , and $(\mathbf{q} \cdot \mathbf{R}_n)$ as well as θ are polar angles. On first sight it appears that the periodicity is lost with respect to lattice translations nonorthogonal to \mathbf{q} . One should notice, however, that all atoms of the spiral structure separated by a translation \mathbf{R}_n are equivalent, possessing magnetic moments of equal magnitude. This equivalence leads to an interesting property for the single-particle spinor functions.

Indeed, as was first pointed out by Herring [13] and later by Sandratskii [14], [15], transformations combining a lattice translation \mathbf{R}_n and a spin rotation about the z -axis by an angle $\mathbf{q} \cdot \mathbf{R}_n$ leave the spiral structure invariant. The symmetry operators describing this transformation are members of a group that Brinkman and Elliott [16] called a spin-space group (SSG). Quite generally, the

elements of the SSG are denoted by $\{\alpha_S|\alpha_R|\mathbf{t}\}$ and defined by operating on a two-component spinor, $\psi(\mathbf{r})$, in the following way

$$\{\alpha_S|\alpha_R|\mathbf{t}\} \psi(\mathbf{r}) = U(\alpha_S) \psi(\alpha_R^{-1} \mathbf{r} - \alpha_R^{-1} \mathbf{t}). \quad (12)$$

Here $U(\alpha_S)$ is the spin-1/2 rotation matrix for a spin rotation through α_S , α_R denotes a space rotation, and \mathbf{t} a space translation. The operators we seek are now obtained by specifying the spin rotation as

$$\alpha_S = -\mathbf{q} \cdot \mathbf{R}_n, \quad (13)$$

and unity, ε , for the space rotation α_R , giving $\{-\mathbf{q} \cdot \mathbf{R}_n|\varepsilon|\mathbf{R}_n\}$ as generalized translations. They have the following properties:

(i) A spinor is transformed according

$$\{-\mathbf{q} \cdot \mathbf{R}_n|\varepsilon|\mathbf{R}_n\} \psi(\mathbf{r}) = \begin{pmatrix} \exp(-i \mathbf{q} \cdot \mathbf{R}_n/2) & 0 \\ 0 & \exp(i \mathbf{q} \cdot \mathbf{R}_n/2) \end{pmatrix} \psi(\mathbf{r} - \mathbf{R}_n). \quad (14)$$

(ii) They commute with the Kohn–Sham Hamiltonian, $\mathcal{H}_{\mathbf{q}}$, of a spiral structure, where we define $\mathcal{H}_{\mathbf{q}}$ as

$$\mathcal{H}_{\mathbf{q}} = -\mathbf{1} \nabla^2 + \sum_n \Theta(|\mathbf{r}_n|) U^+(\theta, \varphi, \mathbf{q}) \begin{pmatrix} v_+^{\text{eff}}(|\mathbf{r}_n|) & 0 \\ 0 & v_-^{\text{eff}}(|\mathbf{r}_n|) \end{pmatrix} U(\theta, \varphi, \mathbf{q}). \quad (15)$$

Here $|\mathbf{r}_n| = |\mathbf{r} - \mathbf{R}_n|$ and

$$U(\theta, \varphi, \mathbf{q}) = \begin{pmatrix} \cos \frac{\theta}{2} & \sin \frac{\theta}{2} \\ -\sin \frac{\theta}{2} & \cos \frac{\theta}{2} \end{pmatrix} \begin{pmatrix} \exp \left(\frac{i\varphi}{2} + \frac{i \mathbf{q} \cdot \mathbf{R}_n}{2} \right) & 0 \\ 0 & \exp \left(\frac{-i\varphi}{2} - \frac{i \mathbf{q} \cdot \mathbf{R}_n}{2} \right) \end{pmatrix}. \quad (16)$$

By an easy calculation we see that

$$[\mathcal{H}_{\mathbf{q}}, \{-\mathbf{q} \cdot \mathbf{R}_n|\varepsilon|\mathbf{R}_n\}] = 0, \quad (17)$$

which is the desired commutator property. We will say a few more words about the Hamiltonian further below.

(iii) The generalized translations commute thus forming an Abelian group isomorphic to the group of ordinary space translations by vectors \mathbf{R}_n . They

therefore have the same irreducible representation (IR). But the IR of ordinary space translations constitutes Bloch's theorem. Thus one obtains the *generalized* Bloch theorem for a spiral structure:

$$\{-\mathbf{q} \cdot \mathbf{R}_n | \varepsilon | \mathbf{R}_n\} \psi_{\mathbf{k}}(\mathbf{r}) = e^{-i\mathbf{k} \cdot \mathbf{R}_n} \psi_{\mathbf{k}}(\mathbf{r}), \quad (18)$$

where the $\psi_{\mathbf{k}}(\mathbf{r})$ are also eigenspinors of $\mathcal{H}_{\mathbf{q}}$. The vectors \mathbf{k} lie in the first Brillouin zone which is defined in the usual way. This is the central result of this subsection and we may summarize that the spin spiral \mathbf{m}_n defined by Eq. (11) does not break the translational symmetry of the lattice, although, in general, the point-group symmetry may be reduced. This statement is independent of the choice of \mathbf{q} which, therefore, need not be commensurate with the lattice. A practical consequence is that we need no supercells to solve the Kohn–Sham–Schrödinger equation in the presence of spin spirals. Indeed, from the definition of the generalized translation, $\{-\mathbf{q} \cdot \mathbf{R}_n | \varepsilon | \mathbf{R}_n\}$, we see that it suffices to pick any \mathbf{q} inside the first Brillouin zone of the crystal; \mathbf{q} -vectors outside give nothing new.

It is the spiral vector \mathbf{q} that allows us to continuously tune the ferromagnet to states with higher energy.

3.2 How to Treat Noncollinear Structures in Density Functional Theory

We now must say how we deal with the noncollinear spin arrangement that is the result of a spin spiral and, in this connection, must explain Eq. (15). Foundations for the procedure sketched briefly here were developed by Sticht et al. [17], to name only one of a series of publications.

In a first step a local coordinate system is chosen such that the density matrix, defined by Eq. (6), integrated over the atomic sphere is diagonal, i.e. we calculate

$$n_{\alpha\beta} = \int_S \tilde{n}_{\alpha\beta}(\mathbf{r}) \, d\mathbf{r} \quad (19)$$

for the atomic sphere S and diagonalize the matrix $n_{\alpha\beta}$ using the spin-1/2 rotation matrix above:

$$\sum_{\alpha\beta} U_{i\alpha}(\theta, \varphi) n_{\alpha\beta} U_{\beta j}^+(\theta, \varphi) = n_i \delta_{ij} \quad (20)$$

where the polar angles are given by

$$\tan \varphi = -\frac{\text{Im}(n_{12})}{\text{Re}(n_{12})}, \quad (21)$$

$$\tan \theta = 2 \sqrt{(\text{Re}(n_{12}))^2 + (\text{Im}(n_{12}))^2} / (n_{11} - n_{22}). \quad (22)$$

A second step consists in expressing the spin dependent part, $v_{\alpha\beta}^{xc}$ in the effective potential by the polar angles as well. For this we use

$$\frac{\delta n_i}{\delta n_{\alpha\beta}} = U_{i\alpha} U_{\beta i}^+ \quad (23)$$

to eliminate $\delta n_{\alpha\beta}$ in Eq. (9),

$$v_{\alpha\beta}^{xc} = \frac{\delta \Omega_{xc}}{\delta n_{\beta\alpha}} = \sum_{i=1}^2 \frac{\delta \Omega_{xc}}{\delta n_i} \frac{\delta n_i}{\delta n_{\beta\alpha}} = \sum_{i=1}^2 \frac{\delta \Omega_{xc}}{\delta n_i} U_{i\beta} U_{\alpha i}^+ \quad (24)$$

thus obtaining the desired dependence on the polar angles. It can be seen that Eq. (24) used in the Kohn-Sham equations (7) gives the Hamiltonian written out in Eq. (15). Equation (23) is derived from the quadratic equation that is solved to diagonalize the integrated density matrix. Furthermore, since the latter is diagonal in the frame of reference defined by the polar angles, the values of θ and ϕ give the direction of the magnetic moment of a given atom in the crystal. For more detail see Ref.[2].

3.3 Magnons

Assume now we solved the Kohn-Sham equations defined by Eq.(15), then it is not hard to obtain the total energy as a function of the polar angles and the spiral wave vector, \mathbf{q} . Let us denote the total energy at zero temperature counted from the total energy of the ferromagnetic state by $\Delta E(\mathbf{q}, \theta)$. Then it can be shown that the magnon frequency of an elementary ferromagnet is given by

$$\omega(\mathbf{q}) = \lim_{\theta \rightarrow 0} \frac{4}{M} \frac{\Delta E(\mathbf{q}, \theta)}{\sin^2 \theta}. \quad (25)$$

The quantity M is the magnetic moment (in units of μ_B) and the total energy difference $\Delta E(\mathbf{q}, \theta)$ is to be obtained using the force theorem, i.e. from the change of the band energies when the ferromagnetic ground state is changed to a magnetic spiral characterized by the wave vector \mathbf{q} and the polar angle θ . No self-consistency steps are required.

This expression has been derived for the magnon spectrum by Ref. [2], [18], [19] under very general assumptions. A derivation by Halilov et al. [20], though, rests on assuming the Heisenberg model. Their formula agrees with Eq. (25) and so does that of Rosengaard and Johansson [21] who used similar assumptions as Halilov et al. Another derivation of the same result is due to Antropov et al. [22] who also used an equation of motion method, as we did, but determined the total energy part differently. A remark concerning the physics connected with the equation of motion seems in order.

If we set out to describe the motion of the magnetization as a function of time at each point \mathbf{r} in the crystal, we must determine the equation of motion for $\mathbf{m}(\mathbf{r})$ given by Eq. (3). We thus look for the equation of motion of its constituents and are led to the time-dependent Schrödinger equation for the wave functions $\psi_{i\alpha}$,

which in principle should give the time dependence of the spin-density matrix, \tilde{n} , and thus that of $\mathbf{m}(\mathbf{r})$. Knowing that the bandwidths of the d electrons in the crystal are of the order of electron volts, while the low-lying excitations we look for are spin-waves which have energies of the order of milli-electron volts, we may assume that the motion of the electrons is much faster than that of the magnetic moments. This assumption implies that we imagine different time scales govern the physics of the electrons and the magnetic moments. In the adiabatic approximation (see for instance Schiff, [23]) one assumes the time-independent Schrödinger equation holds at any instant of time for a potential that parametrically depends on time. In our case the time-dependent parameters in the Schrödinger equation are the angles θ and ϕ . The essential assumption now is that the time-dependent Schrödinger equation holds in the context of density-functional theory in the adiabatic approximation, an assumption which can only be verified by the answers we obtain.

For the sake of brevity we show the magnon dispersion in Fig. 1 for the case of Ni only, as computed by Halilov et al.[20] by the use of Eq.(25). We see that the overall agreement is good. It should be noted, however, that the Stoner excitations are not included here. The spin-wave stiffness constants can now easily be computed too. They are in fair agreement with the experimental data, although somewhat too large for Ni. The low-temperature properties can now be calculated and are obtained just like in the Heisenberg model. For higher temperatures, however, the magnons interact and we must resort to another model[2].

4 Spin Fluctuations

To deal with high temperatures we now construct a Hamiltonian that is derived from the zero-temperature ground-state properties. We also describe the model

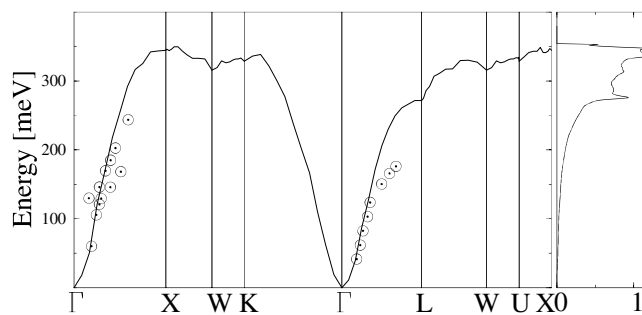


Fig. 1. Adiabatic magnon dispersion relations on high-symmetry lines and magnon densities of states (in states per (meV-cell) $\cdot 10^{-2}$) of fcc Ni. Closed circles are the calculated results of Halilov et al. [20] who kindly supplied this figure. Experimental data are marked as dotted circles and are those of Mook and McK. Paul [24].

which allows us to calculate the magnetization and the susceptibility at high temperatures.

4.1 Hamiltonian

From Fig. 2, which shows the energy changes when Ni becomes magnetic, we read off from the $\mathbf{q} = 0$ curve the total-energy change, ΔE , as

$$\Delta E = \alpha_2 M^2 + \alpha_4 M^4 + \dots, \quad (26)$$

where, for simplicity, we terminate the expansion with the fourth-order term as indicated.

We now postulate that the total energy expansion, Eq. (26), remains valid when the magnetization M is replaced by the corresponding vector quantity

$$\mathbf{M}(\mathbf{R}) = M \mathbf{e}_z + \mathbf{m}(\mathbf{R}) = M \mathbf{e}_z + \sum_{j,\mathbf{k}} m_{j\mathbf{k}} \exp(i\mathbf{k} \cdot \mathbf{R}) \mathbf{e}_j. \quad (27)$$

Here we imply that M is the macroscopic magnetization along some direction, say the z -direction, and \mathbf{m} is a local deviation of the magnetization which is expanded in a Fourier series. Since $\mathbf{m}(\mathbf{R})$ is real we require the Fourier coefficients to obey $m_{j-\mathbf{k}} = m_{j\mathbf{k}}^*$. Physically they describe spin fluctuations. The quantities \mathbf{e}_j ($j = 1, 2, 3$) are Cartesian unit vectors.

The desired Hamiltonian we write as sum of two terms,

$$\mathcal{H} = \mathcal{H}_1 + \mathcal{H}_2. \quad (28)$$

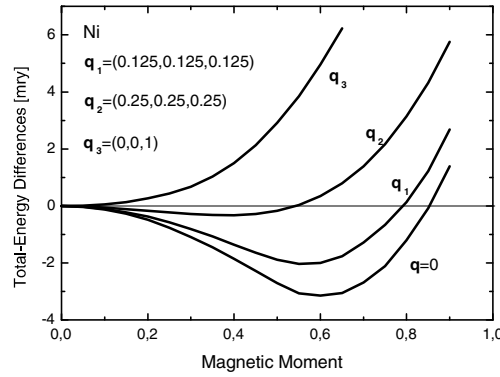


Fig. 2. Total energy differences for Ni as functions of the magnetic moment (in μ_B) for several values of the spiral vector \mathbf{q} (given in units of $2\pi/a$). Polar angle $\theta = 90^\circ$.

The first term on the right-hand side is assumed to consist of single-site terms and, using Eq. (26), we write

$$\mathcal{H}_1 = \frac{1}{N} \sum_i \sum_{n=1}^2 \alpha_{2n} \mathbf{M}(\mathbf{R}_i)^{2n}, \quad (29)$$

where N is the number of atoms in the crystal. Clearly, at $T = 0$ this Hamiltonian reduces to Eq. (26). Next we must include two-site interaction terms and therefore write

$$\mathcal{H}_2 = \frac{1}{N} \sum_{il} J(\mathbf{R}_i - \mathbf{R}_l) \mathbf{M}(\mathbf{R}_i) \cdot \mathbf{M}(\mathbf{R}_l). \quad (30)$$

In keeping with the usual terminology we may call the $J(\mathbf{R} - \mathbf{R}')$ exchange constants, which we obtain from constrained total energy calculations i.e. we substitute a spin spiral of the type given in Eq. (11) and obtain the total energy corresponding to Eq. (30):

$$E_2(M, \mathbf{q}, \theta) = \sum_i J(\mathbf{R}_i) [\sin^2 \theta \cos(\mathbf{q} \cdot \mathbf{R}_i) + \cos^2 \theta]. \quad (31)$$

Transformed exchange constants are defined as

$$j(\mathbf{q}) = \sum_i J(\mathbf{R}_i) \cos(\mathbf{q} \cdot \mathbf{R}_i), \quad (32)$$

thus obtaining

$$E_2(M, \mathbf{q}, \theta) = M^2 [j(\mathbf{q}) \sin^2 \theta + j_n(0) \cos^2 \theta]. \quad (33)$$

The total energy difference corresponding to both \mathcal{H}_1 and \mathcal{H}_2 is therefore

$$\Delta E(M, \mathbf{q}, \theta) = \sum_{n=1}^2 \alpha_{2n} M^{2n} + j(\mathbf{q}) M^2 \sin^2 \theta, \quad (34)$$

the terms $j(0)$ being effectively zero since they are already contained in the first term of the right-hand side. In practice it is sufficient to use $\theta = 90^\circ$ because the total energy is to a good approximation proportional to $\sin^2 \theta$ so that this factor cancels out. The total energy differences are then calculated for a selected set of the spiral wave vectors \mathbf{q} . We give an example of the numerical input in Fig. 2. It should be noted that for Ni the equilibrium magnetization, i.e. the value of M at the minimum, goes to zero long before \mathbf{q} reaches the Brillouin zone boundary.

4.2 Thermodynamics

We are now in the position to deal with the thermodynamics at hand. A manageable method is a variational treatment (e.g. Callen [25]) that defines in a consistent way a mean (or molecular) field theory. We base this on the Bogoliubov-Peierls inequality that states for the free energy

$$F \leq F_0 + \langle \mathcal{H} - \mathcal{H}_0 \rangle_0. \quad (35)$$

The quantity \mathcal{H}_0 is a model Hamiltonian that should possess a rigorous solution defining the free energy F_0 . The right-hand side is made as small as possible by means of variational parameters that may be used in the definition of the model Hamiltonian \mathcal{H}_0 , for which we choose

$$\mathcal{H}_0 = \sum_{j,\mathbf{k}} a_{j\mathbf{k}} |m_{j\mathbf{k}}|^2, \quad (36)$$

where $a_{j\mathbf{k}}$ are variational parameters. This choice of \mathcal{H}_0 leads to Gaussian statistics which is known to allow all thermal averages and the partition function to be carried out analytically obtaining for the zero-order free energy

$$F_0 = -\frac{1}{2\beta} \sum_{j\mathbf{k}} \ln \frac{\pi}{2\beta a_{j\mathbf{k}}}. \quad (37)$$

Furthermore, to evaluate the thermal average of the real Hamiltonian, $\langle \mathcal{H} \rangle_0$, averages of the type

$$\langle |m_{j\mathbf{k}}|^2 \rangle_0 = \frac{1}{2\beta a_{j\mathbf{k}}} \quad , \quad \langle |m_{j\mathbf{k}}|^4 \rangle_0 = 3 \langle |m_{j\mathbf{k}}|^2 \rangle_0^2 \quad (38)$$

are needed which are easily verified. With Eq. (38) we obtain at once

$$\langle \mathcal{H}_0 \rangle_0 = \frac{1}{2\beta} \sum_{j\mathbf{k}} 1. \quad (39)$$

The sums that now occur are restricted to the first Brillouin zone throughout, since the magnetic moments reside on a lattice as a consequence of which the total energy difference, Eq. (31), is periodic as a function of \mathbf{q} with the periodicity volume being the first Brillouin zone. The sum in Eq. (39) is therefore the total number of modes.

In order to write out $\langle \mathcal{H} \rangle_0$ as concisely as possible it is worthwhile to define abbreviations of frequently occurring quantities. There is first the sum $\sum_{\mathbf{k}} \langle |m_{j\mathbf{k}}|^2 \rangle_0$ of the Cartesian component j which can be in the direction of the macroscopic magnetization or perpendicular to it. The former we call the longitudinal (l), the latter the transverse (t) fluctuations, i.e. we define

$$t^2 = \sum_{\mathbf{k}} \langle |m_{t\mathbf{k}}|^2 \rangle_0 \quad (40)$$

and

$$l^2 = \sum_{\mathbf{k}} \langle |m_{l\mathbf{k}}|^2 \rangle_0. \quad (41)$$

The Bogoliubov variational free energy, F_1 , can at this stage be expressed in terms of $\langle |m_{j\mathbf{k}}|^2 \rangle_0$ which, because of Eq. (38), replaces the variational parameter $a_{j\mathbf{k}}$. We therefore collect

$$F_1 = -\frac{k_B T}{2} \sum_{j\mathbf{k}} [1 + \ln (\pi \langle |m_{j\mathbf{k}}|^2 \rangle_0)] + \langle \mathcal{H}_1 \rangle_0 + \langle \mathcal{H}_2 \rangle_0. \quad (42)$$

The averages on the right-hand side are found to be given by

$$\begin{aligned} \langle \mathcal{H}_1 \rangle_0 + \langle \mathcal{H}_2 \rangle_0 &= \alpha_2 (M^2 + 2t^2 + l^2) \\ &+ \alpha_4 [M^4 + 2M^2(2t^2 + 3l^2) + 8t^4 + 4t^2l^2 + 3l^4] \\ &+ 2 \sum_{\mathbf{k}} j(\mathbf{k}) \langle |m_{t\mathbf{k}}|^2 \rangle_0 + \sum_{\mathbf{k}} j(\mathbf{k}) \langle |m_{l\mathbf{k}}|^2 \rangle_0 \end{aligned} \quad (43)$$

Next there are the variational equations that need be determined. One of those is obtained from $\partial F_1 / \partial M = 0$, the others arise from

$$\frac{\partial F_1}{\partial \langle |m_{j\mathbf{q}}|^2 \rangle_0} = 0 \quad (44)$$

for $j = t$ and $j = l$. $\partial F_1 / \partial M = 0$ which gives in the ordered state

$$\frac{M^2}{M_s^2} = 1 - \frac{2t^2 + 3l^2}{M_s^2}, \quad (45)$$

where the saturation magnetization is denoted by M_s and the magnetic energy gain by E_s and we have used

$$\alpha_2 = -\frac{2E_s}{M_s^2}, \quad \alpha_4 = \frac{E_s}{M_s^4}. \quad (46)$$

This result, Eq. (45), was apparently first obtained by Moriya [6].

The optimization condition embodied in Eq. (44) gives the self-consistency equations that follow after some algebra as

$$l^2 = k_B T \sum_{\mathbf{k}} \chi_L(\mathbf{k}), \quad (47)$$

where the temperature-dependent susceptibility is

$$\chi_L^{-1}(\mathbf{k}) = 8\alpha_4 M^2 + 2j(\mathbf{k}) \quad (48)$$

and

$$t^2 = k_B T \sum_{\mathbf{k}} \chi_T(\mathbf{k}), \quad (49)$$

where

$$\chi_T^{-1}(\mathbf{k}) = 8\alpha_4(t^2 - l^2) + 2j(\mathbf{k}). \quad (50)$$

In the paramagnetic case we set $M = 0$ in the free energy and differentiate with respect to the paramagnetic modes which we denote by $\langle |m_{p\mathbf{k}}|^2 \rangle_0$ obtaining for the paramagnetic fluctuations, $p^2 = \sum_{\mathbf{k}} \langle |m_{p\mathbf{k}}|^2 \rangle_0$, the relation

$$p^2 = k_B T \sum_{\mathbf{k}} \chi_P(\mathbf{k}), \quad (51)$$

where

$$\chi_P^{-1}(\mathbf{k}) = 2\alpha_2 + 20\alpha_4 p^2 + 2j(\mathbf{k}). \quad (52)$$

We close this subsection by giving results for nickel in Fig. 3 obtained by solving the total-energy problem using the gradient approximation, GGA (Perdew [26], [27]). Technical details connected with noncollinearity and the GGA can be found in Ref.[28]. The reduced macroscopic magnetization, M , as a function of the temperature is seen to decrease while the reduced transverse, t^2 , and longitudinal, l^2 , fluctuations increase until solutions to the self-consistency equations cease to exist slightly short of 445 K. The solution for the reduced paramagnetic fluctuations, is also shown starting at some arbitrary temperature. The calculated Curie temperature is seen to be smaller than the measured value of $T_c = 627$ K and the magnetization profile is only qualitatively in agreement with the experimental magnetization. The calculated magnetization decreases too fast at low temperatures, which is not surprising since we treat the fluctuations as classical variables. Furthermore, it disappears too abruptly at high temperatures resulting in a first order phase transition. We also show the calculated high-temperature inverse susceptibility multiplied by M_s^2 , in units of mRy. It is seen to be nearly linear in temperature, but the slope of χ^{-1} is too high by nearly a factor of two. We remind the reader that the above results were obtained by truncating the expansion of the Hamiltonian at the lowest nontrivial order. These calculations were improved in the LDA by going to tenth order in the single-site contribution, but leaving the two-site terms at order four (Uhl and Kübler [29]). This improves the calculated Curie temperature somewhat. One might ask how the finite temperature of the electron system influences these results. This question can be answered as follows: the Curie temperature of 445 K is the highest so far obtained by this method and it is calculated using the

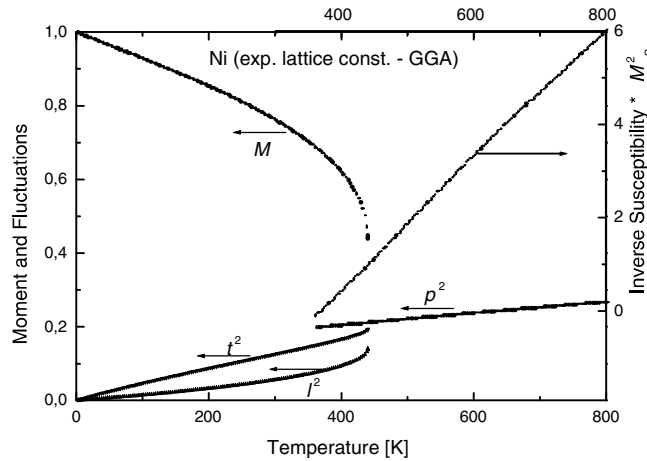


Fig. 3. Calculated magnetization data for fcc Ni as functions of temperature. M is the reduced magnetization, l^2 , t^2 , and p^2 are the reduced fluctuations defined by Eqs. (47), (49) and (51). Inverse paramagnetic susceptibility shown is multiplied by the saturation magnetization squared, M_s^2 , in mRy.

experimental lattice constant which in the GGA is in very good agreement with the total-energy minimum. Estimating the effect of the finite electron temperature by carrying out calculations using the Fermi–Dirac distribution function appropriate for 400 K, one finds a decrease of the Curie temperature by about 10 K. Physically this is due to Stoner excitations.

5 Conclusion

To conclude we collect in Table 1, besides experimental values, the Curie temperatures obtained by us and by other groups. The results of Halilov et al. [31] are rough estimates very similar to results obtained by us [column (4)] using the Langevin formula [2]. The results by Rosengaard and Johansson in column (3) are based on total energy data obtained from density-functional calculations using spin spirals as well. However, the thermodynamics was carried out with a Monte Carlo technique. The magnetization profile they obtained is better than ours, but still does not match the experimental profiles.

The results by Stounton and Gyorffy in column (1) result from a high-temperature treatment assuming a disordered local-moment system; a Curie-Weiss law is obtained for the susceptibility which, however, suffers from the same shortcoming as our high-temperature results. It must be emphasized that the band-picture employed in all cases give local moments above the Curie temperature.

Table 1. Collection of calculated and experimental Curie temperatures in K for the elemental ferromagnets.

(1): Staunton and Gyorffy [32]

(2): Halilov et al. [31]

(3): Rosengaard and Johansson [21] (Monte Carlo calc.)

(4): simple estimate using Langevin formula

(5): our LDA [29], Ni in GGA

	(1)	(2)	(3)	(4)	(5)	exp.
bcc Fe	1015	1037	1060	1316	1095	1044
fcc Co		1250	1080	1558	1012	1388
fcc Ni	450	430	510	642	445	627

References

1. W. Kohn and L.J. Sham: Phys. Rev. A **140**, 1133 (1965).
2. J. Kübler: *Theory of Itinerant Electron Magnetism* (Oxford University Press, Oxford 2000).
3. N.D. Mermin: Phys. Rev. **137**, A1441 (1965).
4. A.K. Rajagopal: Adv. Chem. Phys. **41**, 59 (1980).
5. W. Kohn and P. Vashishta, in: *Theory of the Inhomogeneous Electron Gas*, ed. by S. Lundqvist and N.H. March (Plenum Press, New York 1983).
6. T. Moriya: *Spin Fluctuations in Itinerant Electron Magnetism* (Springer, Berlin 1985).
7. J. Hubbard: Phys. Rev. B **20**, 4584 (1979).
8. H. Hasegawa: J. Phys. Soc. Japan **46**, 1504 (1979).
9. V. Korenman, I.I. Murray and R.E. Prange: Phys. Rev. B **16**, 4032 (1977).
10. B.I. Gyorffy, A.J. Pindor, J. Staunton, G.M. Stocks, and H. Winter: J. Phys. F: Metal Phys. **15**, 1337 (1985).
11. D.M. Edwards: J. Phys. F: Metal Phys. **12**, 1789 (1982).
12. V. Heine and J.H. Samson: J. Phys. F: Metal Phys. **13**, 2155 (1983).
13. C. Herring, in: *Magnetism IV*, Chapter V and XIII, ed. by G. Rado and H. Suhl (Academic Press, New York 1966).
14. L.M. Sandratskii: Phys. Stat. Sol. (b) **135**, 167 (1986).
15. L.M. Sandratskii: J. Phys. F: Metal Phys. **16**, L43 (1986).
16. W. Brinkman and R.J. Elliot: Proc. R. Soc. A **294**, 343 (1966).
17. J. Sticht, K.-H. Höck and J. Kübler: J. Phys.: Condens. Matter **1**, 8155 (1989).
18. Q. Niu and L. Kleinman: Phys. Rev. Lett. **80**, 2205 (1998).
19. Q. Niu, X. Wang, L. Kleinman, W.-M. Liu, D.M.C. Nicholson, and G.M. Stocks: Phys. Rev. Lett. **83**, 207 (1999).
20. S.V. Halilov, H. Eschrig, A.Y. Perlov, and P.M. Oppeneer: Phys. Rev. B **58**, 293 (1998).
21. N.M. Rosengaard and B. Johansson: Phys. Rev. B **55**, 14975 (1997).
22. V.P. Antropov, M.I. Katsnelson, M. van Schilfgaarde, B.N. Harmon, and D. Kuznezov: Phys. Rev. B **54**, 1019 (1996).
23. L.I. Schiff: *Quantum Mechanics* (McGraw-Hill, New York 1955).
24. H.A. Mook and D. McK. Paul: Phys. Rev. Lett. **54**, 227 (1985).
25. H.B. Callen: *Thermodynamics and an Introduction to Thermostatistics*, 2nd ed. (John Wiley & Sons, New York 1985).
26. J.P. Perdew and K. Burke: Int. J. Quantum Chem. **57**, 309 (1996).
27. J.P. Perdew and S. Kurth, in: *Density Functionals: Theory and Applications*, ed. by D.P. Joubert (Springer, Berlin 1998).
28. K. Knöpfle, L.M. Sandratskii and J. Kübler: Phys. Rev. B **62**, 5564 (2000).
29. M. Uhl and J. Kübler: Phys. Rev. Lett. **77**, 334 (1996).
30. J. Weis: Diplomarbeit, Darmstadt 1998 (unpublished).
31. S.V. Halilov, A. Ya. Perlov, P.M. Oppeneer, A.N. Yaresko, and V.N. Antonov: Phys. Rev. B **57**, 9557 (1998).
32. J.B. Staunton and B.I. Gyorffy: Phys. Rev. Lett. **69**, 371 (1992).

Band Magnetism near a Quantum Critical Point

Suresh G. Mishra

Institute of Physics, Bhubaneswar 751005, India

Abstract. We discuss the temperature variation of various quantities in the vicinity of a magnetic quantum critical point within the framework of the spin fluctuation theory. It differs from the Fermi liquid behavior which one expects in normal metals. The reason for this deviation is the presence of the low lying critically damped spin fluctuations in these systems above T_c . The deviation depends upon the space dimension as well as on whether the order parameter is a conserved (ferromagnetic) or a non-conserved (antiferromagnetic) quantity. Away from the critical point there arises an energy scale below which the fermionic behavior is restored. This crossover behavior has an interesting consequence for specific heat of some correlated fermionic systems like liquid ^3He and some heavy fermion materials. In these systems the specific heat versus temperature curves for various pressures or magnetic field have been seen to cross at a point. Within the spin fluctuation theory we find that when the energy scale is a homogeneous function of pressure or magnetic field there is crossing of specific heat at a point.

1 Introduction

The Stoner criteria $1 - UN(\epsilon_F) = 0$ gives instability towards ferromagnetism, while $1 - U\chi(Q) = 0$, gives antiferromagnetic instability corresponding to a wave vector Q . These are examples of phase transition in correlated electronic systems where the transition can be tuned by varying the coupling constant. These are essentially zero temperature transitions, known as quantum phase transition. We are, however, dealing with an interacting fermionic system at low temperature. The temperature dependences of various quantities are expected to be of Fermi liquid form. That is, a linear in temperature specific heat, a temperature independent (Pauli) spin susceptibility, the electrical resistivity varying as T^2 , and a linearly temperature dependent NMR relaxation rate. Here we discuss the possibility of deviation from the Fermi liquid behavior as the quantum critical point approaches.

The normal Fermi liquid behavior as mentioned above is understood within the Landau theory, where the effect of interaction in a Fermi system has been expressed in terms of a few parameters which renormalize the physical quantities with respect to their free Fermi gas values. For example, the modifications in spin susceptibility and isothermal compressibility are given by, $\chi/\chi^0 = (m^*/m)/(1 + F_0^a)$, and $\kappa_s/\kappa_s^0 = (m^*/m)/(1 + F_0^s)$, respectively. The superscript 0 denotes the free Fermi gas values, other notations are standard [1]. It is clear that in this theory, for a certain value of parameters (i.e. F_0 , and F_1), the corresponding

quantities become very large, which in turn may indicate a neighborhood of certain phase transition. For example, $F_0^a \rightarrow -1$ implies magnetic instability, and $F_0^s \rightarrow \infty$, a condensation. The temperature dependence, however, does not change. It remains free fermionic. It seems the Fermi liquid theory gives indication of an incoming electronic phase transition as the coupling constant (or the Landau parameter) is changed, but it does not consider the effect of incipient fluctuations in a self-consistent manner. This has been done in a spin fluctuation theory [2,3,4,5,6,7,8,9,10,11] for a magnetic transition.

We first briefly review the spin fluctuation theory and then write expressions for spin susceptibility, resistivity, specific heat and the nuclear magnetic relaxation rate for ferromagnets as well as for antiferromagnets. The results are presented for the limit of $\alpha(0) \rightarrow 0$ where $\alpha(0) = 1 - UN(\epsilon_f)$ for a ferromagnet and $1 - U\chi^0(Q)$ for an antiferromagnet. Though $T_c = 0$, fluctuation effects are expected to be dominant at finite but low temperatures. The resulting temperature dependence need not be Fermi-Liquid-like because of the low lying fluctuation (bosonic) degrees of freedom. We then discuss the well known case of finite but small $\alpha(0)$, where various quantities exhibit a crossover from non-Fermi liquid to a Fermi liquid behavior. This crossover behavior has an interesting consequence for the specific heat of some heavy fermion materials and liquid ^3He . Finally we make some remarks on non-Fermi liquid behavior arising due to presence of disorder.

2 Spin Fluctuation Theory

The basic motivation for constructing the spin fluctuation theory is that the Stoner factor $\alpha(0)$ is small. In such case a highly paramagnetic system at low temperature can be considered to be in the vicinity of a magnetic transition. The temperature variation of various physical quantities is then governed by transverse and longitudinal spin fluctuations. Though the order parameter vanishes above the transition, it is expected that the effect of fluctuations will be observable well above the transition.

Consider first the Landau expansion for the free energy $F(M, T)$, in power of the order parameter M , viz.

$$F(M, T) = F(0, T) + \frac{1}{2}A(T)M^2 + \frac{1}{4}BM^4 - HM, \quad (1)$$

where H is the field conjugate to M . The temperature dependence of various quantities in this theory arises due to $A(T)$ and B . For example, the spin susceptibility for the paramagnetic phase is given by, $\chi^{-1}(T) = A(T)$. We identify $A(T)$ with $\alpha(T)$ hereafter. In fact $A(T) = \alpha(T)/2N(\epsilon_F)$ for ferromagnets. The expansion coefficients $\alpha(T)$ and B have been calculated in various approximation schemes. In the Ginzburg Landau theory for classical phase transition, $\alpha(T)$ is taken as $(T - T_c)$ and B as independent of temperature. This leads to the Curie Weiss law for the susceptibility. In the mean field (Stoner) theory of itinerant ferromagnet, $\alpha(T) = 1 - UN(\epsilon_F)$, and B is again a constant. In this case the

temperature dependence mainly arises from an integral over density of states through a Sommerfeld expansion. It is weak, of the order of T^2/T_F^2 , and, therefore, it does not give, for example, a Curie-Weiss form for the spin susceptibility. This issue has been tackled in the spin fluctuation theory [5,6], where $\alpha(T)$ turns out to be $\alpha(0) + 5u_4D$. Where D is transverse/longitudinal spin fluctuation amplitude obtained by the internal frequency summation in diagrams for the fluctuation self energy. The leading temperature dependence is governed by these amplitudes. The factor u_4 in the second term is a dimensionless short range four fluctuation coupling constant obtained after integration over fast fermionic degree of freedom. This result has been derived microscopically, within the functional integral scheme on a model of interacting electrons, e.g. Hubbard model as applied to itinerant ferromagnets, considering only the spin degrees of freedom. The Stratanovich- Hubbard transformation changes the partition function for an interacting fermion system to that of an interacting bosonic fluctuation degrees of freedom. Parameters of this model, e.g. fluctuation spectrum, fluctuation coupling vertices are determined by properties of the underlying fermion system. Since these parameters (e.g. the Stoner enhancement factor for ferromagnets or the staggered susceptibility enhancement for antiferromagnets) are such that spin fluctuations are low lying excitations, this transformation is specially helpful for an analysis of temperature dependent properties of weak itinerant electron ferromagnets and antiferromagnets. The free energy functional then expanded in powers of these fluctuation fields up to a quartic term and a self consistent mean fluctuation field approximation (quasi harmonic approximation, or the self consistent renormalization scheme of Moriya) is generated. The mean fluctuation field approximation is shown diagrammatically in a compact manner in Fig. (1), where the double wiggle represents the dressed propagator $D(\mathbf{q})$. One can also estimate corrections due to higher order fluctuation terms within this scheme.

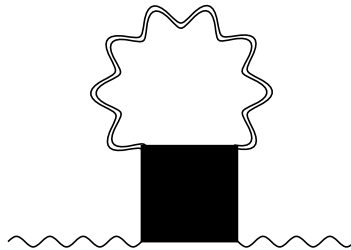


Fig. 1. Mean fluctuation field diagram

3 Physical Properties Near Quantum Critical Point $\alpha = 0$

3.1 Spin Susceptibility

The self consistent equation for the temperature dependence of $\alpha(T)$ can be written explicitly as

$$\alpha(T) = \alpha(0) + \lambda \sum_q \int d\omega n(\omega) \text{Im}\chi(q, \omega^+) \quad (2)$$

where, λ is related to u_4 , $n(\omega)$ is the Bose distribution function, and

$$\chi(q, \omega) = \frac{N(\epsilon_F)}{\alpha(T) + \delta q^2 - i\pi\omega\gamma/2q} \quad (3)$$

is spin susceptibility for the ferromagnetic case. (ω and T are written in units of ϵ_F and q in units of k_F . We have taken $\hbar = 1$ and $k_B = 1$). Performing the frequency integral,

$$\alpha(T) = \alpha(0) + \frac{\lambda}{\pi} \sum_q q \phi(y), \quad (4)$$

where $y = q(\alpha(T) + \delta q^2)/(\pi^2\gamma T)$ and $\phi(y) \equiv \{\ln(y) - \frac{1}{2y} - \psi(y)\}$. For detail calculations $\phi(y)$ can be approximated as $1/(2y + 12y^2)$. This form is valid for small as well as large y . For three dimension,

$$\alpha(T) = \alpha(0) + \frac{\lambda}{2\pi^3} \int \frac{q^3 dq}{(2y + 12y^2)}. \quad (5)$$

For a finite $\alpha(0)$ there arise two regions of temperatures [5]. For $T < \alpha(0)$ which corresponds to $y \gg 1$ and $\phi(y) \sim 1/12y^2$, one gets the standard paramagnon theory results; and for $\alpha(0) < T < 1$, which corresponds to $y < 1$ and $\phi(y) \sim 1/2y$, one gets

$$\alpha(T) = \frac{T}{\delta} \left[q_T - \sqrt{\frac{\alpha(T)}{\delta}} \arctan\left(q_T \sqrt{\frac{\delta}{\alpha(T)}}\right) \right], \quad (6)$$

where, $q_T \approx T^{1/3}$ is a thermal cutoff such that $y_{q_T} \approx 1$. The dominating contribution to $\alpha(T)$ comes from the first term which is given by, $T^{4/3}$. However, since δ is small, the thermal cutoff q_T is high $\approx q_c$ (the spin fluctuation energy rises only slowly with q). Thus, $\alpha(T)$ rises nearly linearly with T . This is the classical spin fluctuation behavior, first pointed out for itinerant ferromagnets by Murata and Doniach [2]. An estimate of the size of the second term is obtained by putting $\alpha(T) \approx T^{4/3}$. We then find it to be of the order $T^{1/3}$ relative to the first term. Since $T^{1/3}$ is not very small, it is essential to do a self consistent calculation. This may lead to a different exponent at finite temperatures. A similar calculation gives a logarithmic temperature dependence, $\alpha(T) = (T/2\delta) \ln(\delta q_c^2/\alpha(T))$ for two dimension.

In case of antiferromagnets, the formalism is identical. One replaces the Pauli susceptibility with the staggered susceptibility for non interacting electron system $\chi^0(\mathbf{Q})$, for brevity we retain the same notation for the enhancement factor which is defined in the present case as $\alpha(0) = \chi^0(\mathbf{Q})/\chi(\mathbf{Q})$. The expansion of the dynamic staggered susceptibility, $\chi(\mathbf{Q} + \mathbf{q}, \omega)$ for small \mathbf{q} and small ω around the static staggered susceptibility is written in the form,

$$\chi(\mathbf{Q} + \mathbf{q}, \omega^+) = \frac{\chi^0(\mathbf{Q})}{\alpha(T) + \delta q^2 - i\gamma\omega}. \quad (7)$$

Making similar transformations as for the ferromagnetic case, we get,

$$\alpha(T) = \alpha(0) + \frac{\lambda}{2} \sum_q \frac{1}{(2z + 12z^2)} \quad (8)$$

where $z = (\alpha(T) + \delta q^2)/2\pi\gamma T$. Thus, for 3D antiferromagnets, the result turns out to be identical to the ferromagnetic case (Eq. 6) once we consider only the case $z < 1$. The momentum cutoff in this case turns out to be $T^{1/2}$ leading to $\alpha(T) \sim T^{3/2}$. In two dimension $\alpha(T) = (T/2\delta) \ln(\delta q_c^2/\alpha(T))$, again a logarithmic behavior.

The terms involving two or more internal thermal spin fluctuations have been calculated in detail earlier [5]. It turns out that apart from a numerical factor the two internal thermal spin fluctuation term has the same temperature dependence as the mean fluctuation field term. However, the three internal thermal spin fluctuation term, $\approx T^2 \ln(1/3\alpha(T))$ in 3D ferromagnet. We see that this term is of the order of $T \ln T$ relative to the simplest non-vanishing contribution. The perturbation expansion therefore converges.

3.2 Resistivity

The electrical resistivity for pure transition and rare earth metals is usually calculated within a two band model [12], where the ‘conducting’ electrons come from s-band while the d-electrons contribute to magnetism. The d-band is assumed to be narrow and the d-electrons heavy. The conducting s-electrons scatter from the spin fluctuations corresponding to d-electrons. The temperature dependent part of the resistivity due to this mechanism for a 3d-ferromagnet is given by [13,14],

$$\rho(T) \propto \frac{1}{T} \int dq q^3 \int Im\chi(q, \omega^+) \omega n(\omega) (1 + n(\omega)) d\omega \quad (9)$$

The frequency integral can be performed by first using the identity, $\omega n(\omega) (1 + n(\omega))/T^2 = \partial n(\omega)/\partial T$ leading to,

$$\rho(T) \approx \int dq q^4 y \phi'(y) \quad (10)$$

where, $\phi(y)$ and y have already been defined. In the limit $y < 1$ the momentum integral gives,

$$\rho(T) = \frac{T}{2\delta} \left[q_c^2 - \frac{\alpha(T)}{\delta} \ln \left(\frac{\alpha(T) + \delta q_c^2}{\alpha(T)} \right) \right]. \quad (11)$$

With $q_c \sim T^{1/3}$ we recover the well known result $\Delta\rho \sim T^{5/3}$ [13]. However, the self consistency correction changes the power of temperature. For two dimensions, $\Delta\rho \sim T^{4/3}$.

The case of 3D antiferromagnets formalism is similar except for the replacement of q^3 in the momentum integral by q^2 . This is due to the fact that the small momentum expansion is not done around $q = 0$ but around $q = Q$, the antiferromagnetic wave vector [15]. The result in the limit of $z < 1$ becomes $\Delta\rho \sim T^{3/2}$. For two dimensions, $\rho(T) = (T/2\delta) \ln(\delta q_c^2/\alpha(T))$.

3.3 Specific Heat

The spin fluctuation contribution to the free energy within the mean fluctuation field approximation [7] (or quasi harmonic approximation) is given by

$$\Delta\Omega = \frac{3T}{2} \sum_{q,m} \ln\{1 - U\chi_{qm}^0 + \lambda T \sum_{q',m'} D_{q'm'}\}. \quad (12)$$

Where $D_{q,m}$ is the fluctuation propagator which is related to inverse dynamical susceptibility, and χ_{qm}^0 is the free Fermi gas (Lindhard) response function. The argument of the logarithm is related to inverse dynamic susceptibility. Considering only the thermal part of the integral and ignoring the zero point part, we perform the frequency summation and obtain,

$$\Delta\Omega_{Thermal} = -\frac{3}{\pi} \sum_q \int_0^\infty \frac{d\omega}{e^{\omega/T} - 1} \arctan\left(\frac{\pi\omega/4q}{\alpha(T) + \delta q^2}\right), \quad (13)$$

From standard thermodynamic result the specific heat can be calculated leading to

$$\frac{\Delta C_v}{k_B} = -6 \int q^2 dq \left[\phi'(y) \left(\frac{q}{\pi^2 \gamma} \frac{\partial \alpha(T)}{\partial T} - y \right)^2 + T \phi(y) \frac{q}{\pi^2 \gamma} \frac{\partial^2 \alpha(T)}{\partial T^2} \right]. \quad (14)$$

Making the small y approximation, finally the terms can be arranged for constant cutoff as,

$$C_v \approx \left[\frac{q_c^3}{3} + T^2 \left(\frac{\partial \alpha(T)}{\partial T} \right)^2 \frac{1}{\sqrt{\alpha(T)}} - \left(T^2 \frac{\partial^2 \alpha(T)}{\partial T^2} + 2T \frac{\partial \alpha(T)}{\partial T} \right) q_c \right]. \quad (15)$$

The first term gives the classical result, the second dominant term gives leading temperature correction, the last term is about two order of magnitude small at the temperature range of interest. For the cutoff $q_T \sim T^{1/3}$ a linear term in the specific heat is obtained. However, a self consistent calculation is needed to get a correct exponent.

The calculation for antiferromagnet is identical except that y is replaced by z in Eq. (15) and the final equation turns out to be identical except that the temperature dependence of $\alpha(T)$ is different in an antiferromagnet.

3.4 Nuclear Spin Relaxation Rate

The nuclear spin relaxation rate in metals is given by the Korringa relation [16], which essentially tells that $1/T_1T$ is related to the static spin susceptibility of metals, which in turn, is independent of temperature for normal metals. However, it has been pointed out by Moriya [17] long ago that this relation gets modified in presence of electron correlations. The nuclear spin-lattice relaxation rate in metals is given by,

$$\frac{1}{T_1T} \sim \sum_q \frac{\text{Im}\chi^{-+}(q, \omega_0^+)}{\omega_0} \quad (16)$$

where ω_0 is the nuclear magnetic resonance frequency which is taken to be very small ($\rightarrow 0$) in the problem of nuclear spin relaxation rate. Substituting the expression for $\chi^{-+}(q, \omega_0^+)$ and taking the limit, we have,

$$\frac{1}{T_1T} \sim \sum_q \frac{1}{q(\alpha(T) + \delta q^2)^2}, \quad (17)$$

leading to $(T_1T)^{-1} \sim \alpha(T)^{-1}$ for a ferromagnet in three dimension. Recall that for normal Fermi liquid $\alpha(T)$ is constant but in the present case it varies as $T^{4/3}$. For antiferromagnets in three dimension $(T_1T)^{-1} \sim \alpha(T)^{-1/2}$.

3.5 Summary

The following table summarizes our results. In the first column Fermi liquid theory results are written, other columns compile the fluctuation theory results. These results are presented in three rows for each property. The first row gives results from a non-self-consistent calculation, i.e., for example, when only the first term in Eq. (6) for $\alpha(T)$ is considered but with a proper momentum cut off. This behavior is expected in the extreme low temperature range. Some of these results are known, but presented in a coherent form here. The second row gives results with the temperature dependence of $\alpha(T)$ taken into account and the integration performed with the functional form for $\phi(y)$ (approximately) valid for all y . The power of temperatures so obtained depends on the temperature regime considered (i.e. whether T is in the range $10^{-3} - 10^{-2}$ or other). These results go over to those presented in the first row as $T \rightarrow 0$. The third row gives the classical spin fluctuation results, obtained when the Bose factor $n(\omega)$ was approximated as T/ω , (one gets essentially the first row result but with a constant cutoff). The experimental results are expected to lie between those given in rows one and three.

3.6 Experimental Results

Results discussed above should apply to weak itinerant ferromagnets and antiferromagnets above their respective T_c which is small in general (see [18] for a brief review). The transition temperature can further be reduced by alloying or

Table 1. Summary of the temperature dependence of various thermal and transport properties near a quantum phase transition point. (from [10])

	Fermi Liquid	Ferro (3D)	Antiferro (3D)	Ferro (2D)	Antiferro (2D)
$(\chi(T))^{-1}$	Const.	$T^{4/3}$ $T^{1.20}$ T	$T^{3/2}$ $T^{1.44}$ T	$T \ln T$ $T^{0.87}$ T	$T \ln T$ T T
$\rho(T)$	T^2	$T^{5/3}$ $T^{1.56}$ T	$T^{3/2}$ $T^{1.45}$ T	$T^{4/3}$ $T^{1.24}$ T	$T \ln T$ T T
$C_v(T)$	T	T $T^{0.74}$ Const.	$T^{3/2}$ $T^{0.99}$ Const.	$T^{2/3}$ $T^{0.52}$ Const.	T $T^{0.86}$ Const.
$(T_1 T)^{-1}$	Const.	$T^{-4/3}$ $T^{-1.284}$ T^{-1}	$T^{-3/4}$ $T^{-0.72}$ $T^{-1/2}$	$(T \ln T)^{-3/2}$ $T^{-1.305}$ $T^{-3/2}$	$(T \ln T)^{-1}$ T^{-1} T^{-1}

by application of pressure. We present here results for one conventional weak itinerant ferromagnet and one heavy fermion material near antiferromagnetic instability. First example is Sc_3In which has a transition temperature of about 6 K. The specific heat above T_c (Fig. 2) curves are due to Ikeda [19]. They show a good fit to the theory with $C_v(T)/T \sim (T - T_c)^{-0.25}$. The other example is heavy fermion material CeCu_6 which is non-magnetic. On alloying with Au the lattice expands and an antiferromagnetic order is observed in $\text{CeCu}_{6-x}\text{Au}_x$ above a critical concentration $x_c \approx 0.1$. The Néel temperature of the anti-ferromagnetic heavy-fermion alloy $\text{CeCu}_{5.7}\text{Au}_{0.3}$ can be continuously tuned to zero with increasing hydrostatic pressure. At the critical pressure the specific heat has been fitted to $C/T \sim \ln T_0/T$ curve [20]. We analyze the data again and fit the curve to our prediction ($T^{0.58}$ corresponding to the temperature range of interest) in the (Fig. 3). Here we compared only the specific heat results. Other results, for example, the resistivity ([21]), and relaxation rate ([22]) have been presented earlier [10].

4 Quantum to Classical Crossover for $\alpha \neq 0$

For a finite α the fermi liquid behavior is restored at low temperatures ($\tau \leq \alpha(0)$) while the non fermi liquid behavior reminiscent of classical spin degrees

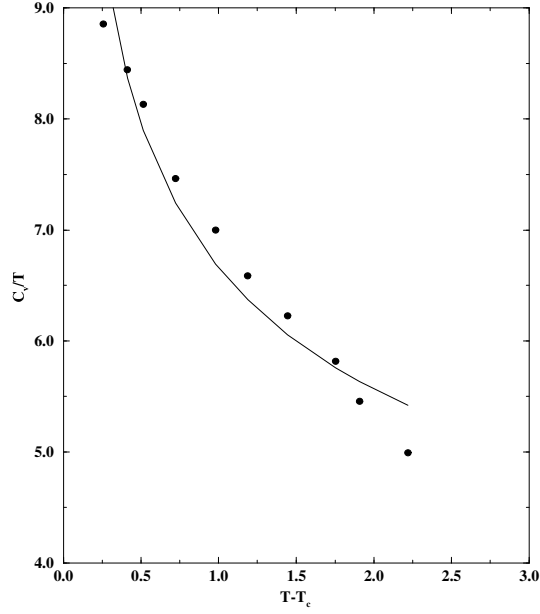


Fig. 2. Plot of C_v/T as a function of $T - T_c$ for Sc_3In . The experimental points [19] are represented by circles and the solid line represents the theoretical fit.

of freedom remains at higher temperatures. This has been seen long ago in susceptibility behavior of liquid 3He [5,23]. We discuss here only an interesting consequence which arises due to presence of a low energy scale and of a crossover from classical to quantum behavior across it.

Consider Eq. 14 for the specific heat. It is clear that the calculation of specific heat correction due to spin fluctuations involves the temperature dependence of spin susceptibility. For low temperatures ($\tau \leq \alpha(0)$) the correction to the specific heat is given by,

$$\frac{\Delta C}{k_B} = \sum_q \frac{\pi^2 \tau}{4q(\alpha + \delta q^2)}. \quad (18)$$

The phase space integral reproduces the standard paramagnon mass enhancement result, $\tau \ln\{1/\alpha\}$ for ΔC . In the classical regime, $\alpha(0) \leq \tau \ll 1$, where the small y approximation holds ΔC falls and vanishes at higher temperatures. Now considered as a function of $\alpha(0)T_F$, specific heat has different functional forms in these two regimes. The figure 4 shows the calculated curves for various temperatures in the case of antiferromagnetic spin fluctuations. The parameters correspond to those used for $CeAl_3$. As seen in the figure, below a certain temperature T_{cr} , specific heat decreases as $\alpha(0)T_F$ increases, while above it the

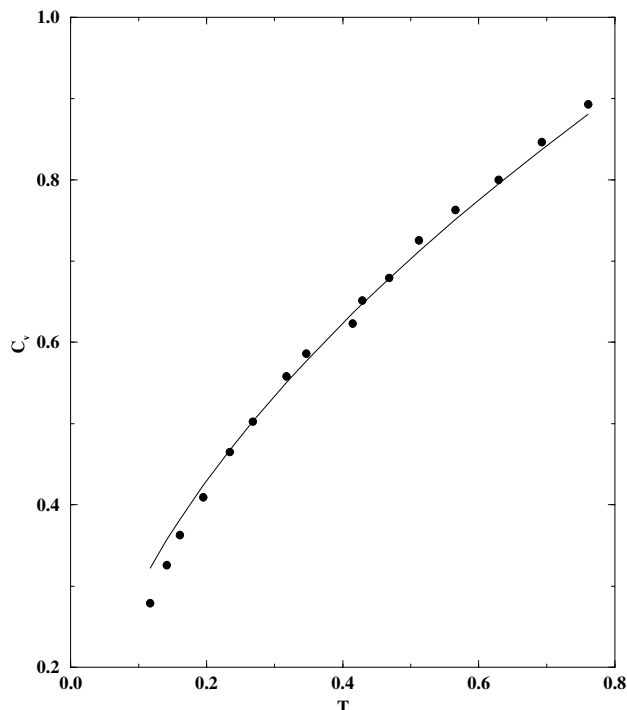


Fig. 3. Plot of C_v as a function of T for $CeCu_{5.7}Au_{0.3}$ at a pressure of 8.2 kbar. The experimental points [20] are represented by circles and the solid line represents the theoretical fit (from [10]).

behavior is reversed. T_{cr} clearly marks a temperature where the ΔC is independent of $\alpha(0)$. T_{cr} is of the order of $\alpha(0)T_F$. Similar features have been obtained for ferromagnetic fluctuations. The spin fluctuation theory has only one parameter, that is, $\alpha(0)T_F$. The pressure or magnetic field dependence of physical quantities is realized through the dependence of $\alpha(0)T_F$ on them. Whenever $\alpha(0)T_F$ is homogeneously increasing or decreasing function of these parameters the specific heat curves will cross at a point. In this case $\partial C / \partial \alpha(0)T_F = 0$ at $T = T_{cr}$ also means $\partial C / \partial X = 0$ at the same temperature, where X is an external control parameter like pressure or magnetic field. The later equation is the condition for crossing of curves at a point.

This crossing behavior was initially observed in ^3He by Brewer *et. al.* [24] and has been seen later on, in a variety of systems ranging from systems close to metal-insulator transition to heavy fermions [25,26,27]. The variety of materials in which this phenomenon has been observed leads one to believe that there is some kind of universality in this behavior. In a recent publication, Vollhardt [28] has given a thermodynamic interpretation to this universality. The argument given there relies on a smooth crossover between behavior of entropy at temperatures low compared to degeneracy temperature and the high temperature classical limit. As such, the question of why such crossings are prominently

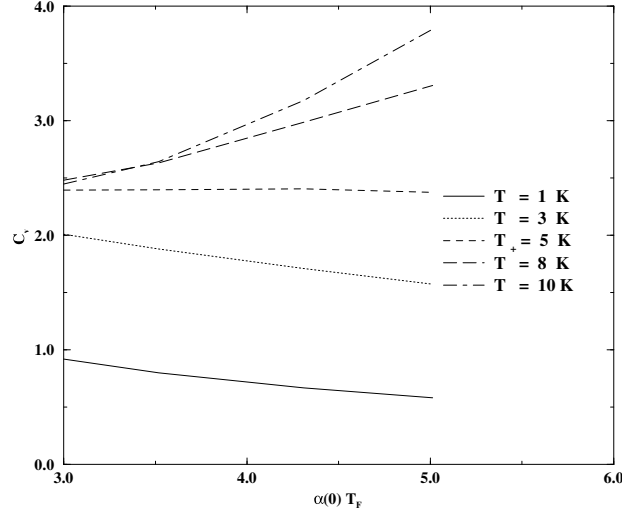


Fig. 4. Specific Heat as a function of $\alpha(0)T_F$ for CeAl_3 for various temperatures calculated from the spin fluctuation theory.

seen in systems with highly enhanced magnetic susceptibility or effective mass remains unanswered. Here we propose that the operative cause is the proximity to a quantum critical point as explained above.

For liquid ^3He the specific heat calculated from spin fluctuation theory is plotted in Fig. 5 as a function of temperature for various values of pressure, assuming a linear reduction of $\alpha(0)T_F$ with pressure. The experimental curves show similar behavior [29]. In Fig. 5 the free Fermi gas part ($\pi^2 T/2T_F$) has been added to $\Delta C(T)$. For heavy fermion materials in which the specific heat curves cross (e.g. CeAl_3 [26] and UBe_{13} [27]); because of the similarity to liquid ^3He , at the phenomenological level it is tempting to apply the spin fluctuation theory, with $\alpha(0)T_F$ playing the role of the crossover temperature T^* . However, there is a difference. While ^3He can be considered close to a ferromagnetic transition, most heavy fermion materials seem to be close to an antiferromagnetic instability. We consider the heavy fermions in the coherence regime as nearly antiferromagnetic Fermi liquid. Moreover to reproduce huge effective mass observed, the fluctuation modes are considered essentially dispersionless [30].

The specific heat curves for CeAl_3 are presented in Fig. 6. The parameter $\alpha(0)T_F$ is of the order of the crossing temperature with a weak linear pressure dependence. In contrast to ^3He , here $\alpha(0)T_F$ increases with pressure. This is because in ^3He pressure brings the atoms closer and thereby increasing the interaction, while in heavy fermions the reduction in the lattice parameter enhances the hybridization between conduction electron and f-electron, thereby the antiferromagnetic exchange between local moment and the conduction electron will be enhanced leading to a non magnetic ground state. It is seen that the curves cross within a small regime close to the experimental crossing point.

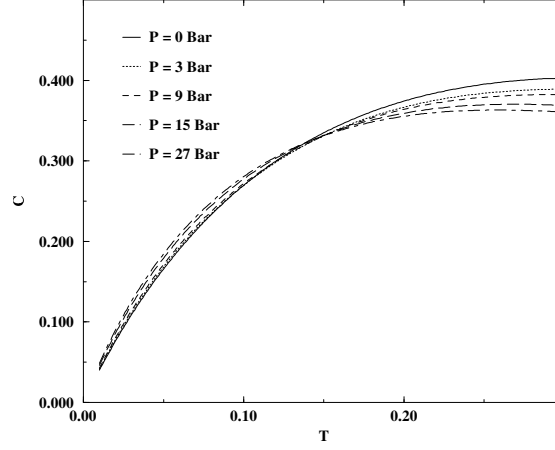


Fig. 5. The calculated curves for $C(P, T)$ of ^3He . Here $\alpha(0)T_F$ has been assumed to vary linearly with pressure (from [11]).

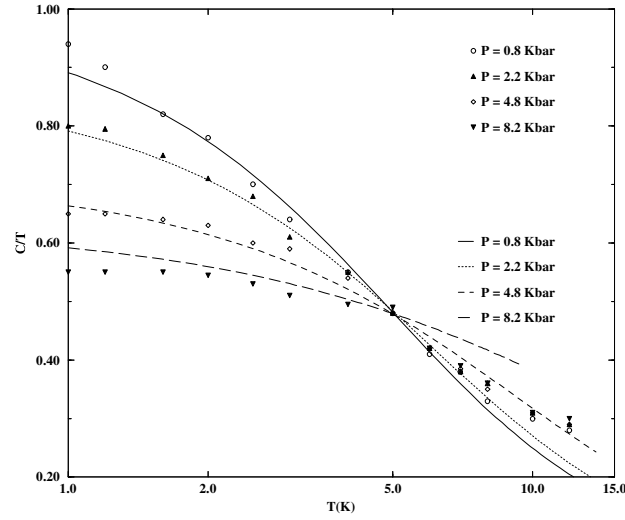


Fig. 6. Semilog plot of $C(P, T)/T$ as a function of T for CeAl_3 for various pressures. The symbols are experimental points [26] and the lines are results from the spin fluctuation theory (from [11]).

Beyond the crossing point the deviation from the experimental curves is large. In fact, in heavy fermions, the curves cross at two points, the second point being away from the crossover temperature T^* . The reason for the second crossing cannot be found within a single parameter theory like the present one.

5 Effect of Disorder

In presence of disorder the electron moves in a random way getting scattered from impurities repeatedly. This introduces a finite mean free path for an electron, and a finite life time τ in the electron propagator, which thereby modifies the free particle-hole propagator (diffuson), free particle-particle propagator (Cooperon) and electron-spin fluctuation vertex. The fluctuation theory gets modified by inclusion of diffusive modes in propagators and vertices in diagrams for the spin fluctuation self energy (for example see [31,32]). The Stoner factor reduces to,

$$\alpha(T) = \alpha_{SF}(T) - \alpha_d(T), \quad (19)$$

where $\alpha_d(T)$ is correction due to diffusive modes. To the leading order in $1/\epsilon_F\tau$, $\alpha_d(T) \sim [1 - \sqrt{(2\pi\tau T)}]/(\epsilon_F\tau)^2$, for low temperatures $T \ll 1/\tau$ and has a vanishing contribution otherwise. This low temperature deviation has indeed been observed experimentally in the susceptibility of Ni_3Ga and Ni_3Al away from stoichiometric composition [33] [31]. Clearly the disorder introduces a new energy scale $(1/\tau)$, in the lowest temperature range. In the case of non-vanishing $\alpha(0)$, in the case of ferromagnet in three dimension, the susceptibility inverse $\alpha(T)$ behaves differently in these regimes, e.g. as $\sim T^{1/2}$ for $T < 1/\tau$, as $T^2/\alpha(0)$ for $1/\tau < T < \alpha(0)$, and as $T^{4/3}$ for $\alpha(0) < T < 1$. Similarly the resistivity correction $\Delta\rho(T)$ behaves as $\sim T^{1/2}$ for $T < 1/\tau$, as $T^2/\sqrt{\alpha(0)}$ for $1/\tau < T < \alpha(0)$, and as $T^{5/3}$ for $\alpha(0) < T < 1$. In the case of vanishing T_c material the quantum fluctuation regime ($T < \alpha(0)$) vanishes and the other two regimes merge. A detailed analysis is needed, which will clarify which of these two contributions, due to fluctuation or due to disorder effect will dominate as the quantum critical point approaches ($\alpha(0) \rightarrow 0$).

6 Conclusion

The temperature dependence of various quantities for system undergoing ferro- or antiferromagnetic transition in two as well as three dimensions near the quantum phase transition point turns out to be non-fermionic in nature at lowest temperatures. The results hold for electronic phase transitions with a finite but small T_c also. This is clear, as the results from the first rows in Table (1) match with some well known results in literature. However, they are pronounced and a clear non-Fermi liquid behavior is obtained when $T_c \rightarrow 0$. Our results are perturbative, but as discussed in the text the fluctuation correlation term is always smaller than the mean fluctuation field term. The behavior of these quantities is different in ferromagnet from the antiferromagnetic system. These two examples, in fact, represent two different types of quantum critical behavior. In ferromagnet the order parameter is a conserved quantity, while in the antiferromagnet it is not. This difference is reflected in the dispersion of their respective order parameter susceptibility as shown in equations (3) and (7). Other approaches based on renormalization group technique also use the same dispersion for calculation of dynamic exponent z [34,35]. In fact, it is possible to express the low

temperature exponents (given in first rows in the table) for susceptibility, resistivity and the NMR rate in three dimension in terms of z , viz. $\alpha(T) \sim T^{1+1/z}$, $\rho(T) \sim T^{2-1/z}$, $1/T_1T \sim \alpha(T)^{(1-z)/2}$, where z is 3 for ferromagnets and 2 for antiferromagnets.

For a finite $\alpha(0)$ there is a crossover from fermionic to a non-fermionic temperature dependence. We have used the terms quantum and classical in our discussion, reason being that for the temperatures below $\alpha(0)T_F$ essentially define a regime where one gets a Fermi liquid behavior, whereas at high temperatures, fluctuations get correlated resulting in the classical behavior for the susceptibility. The distinction, quantum versus classical, becomes clear when one takes the limit $\alpha(0) \rightarrow 0$ (the quantum critical point). In that case the Curie like behavior for susceptibility is obtained down to zero degree [10], while in the opposite limit ($\alpha(0) \rightarrow 1$) one gets the Pauli susceptibility. For specific heat, in either of these limits the curves for various pressures or fields do not cross.

Acknowledgments

It is a pleasure to thank R. Pai and P.A. Sreeram for their contributions to work reviewed here. Thanks also to Prof. Entel for hospitality at Duisburg where the final version of this article was written.

References

1. D. Pines and P. Nozières, *The Theory of Quantum Liquids* (Benjamin, Amsterdam 1966).
2. K. K. Murata and S. Doniach, Phys. Rev. Lett. **29** 285 (1972).
3. T. Moriya and A. Kawabata, J. Phys. Soc. Jpn. **34** (1973) 69; **35** 669 (1973).
4. T. V. Ramakrishnan, *Solid state Comm.* **14** 449 (1974); *Phy. Rev.* **B 10**, 4014 (1974).
5. S. G. Mishra and T. V. Ramakrishnan, Phys Rev. **B 18**, 2308 (1978).
6. S. G. Mishra and T. V. Ramakrishnan, *Inst. Phys. Conf. Series.* **39** 528 (1978).
7. S. G. Mishra and T. V. Ramakrishnan, Phys. Rev. **B 31**, 2825 (1985).
8. G. G. Lonzarich and L. Taillefer, J. Phys **C18** 4339 (1985).
9. T. Moriya, *Spin Fluctuation in Itinerant Electron Magnetism*, Springer Series in Solid State Sciences **56**, (Springer, Heidelberg, 1985).
10. S. G. Mishra and P. A. Sreeram, Phys. Rev. **B 57**, 2188 (1998).
11. S. G. Mishra and P. A. Sreeram, Euro. Phys. Jour. **B 14**, 287 (2000).
12. D. L. Mills and P. Lederer, J. Phys. Chem. Solids **27**, 1805 (1966).
13. J. Mathon, Proc. Roy. Soc. **A 306**, 355 (1968).
14. M. T. Béal-Monod Phys. Rev **B 28**, 1630 (1983).
15. K. Ueda, J. Phys. Soc. Jpn. **43**, 1497 (1977).
16. J. Korrying, Physica **16**, 601 (1950).
17. T. Moriya, Jour. Phys. Soc. Japan **18**, 516 (1963).
18. S. G. Mishra, Mod. Phys. Lett. **B 4**, 83 (1990).
19. K. Ikeda, S. K. Dhar, M. Yoshizawa and K. A. Gschneidner, Jr., J. Mag. and Mag. Mat. **100**, 292 (1991).
20. B. Bogenberger and H. V. Löhneysen, Phys. Rev. Lett. **74**, 1016 (1995).

21. C. Pfleiderer, G. J. McMullan and G. G. Lonzarich, *Physica* **B 199 & 200**, 634 (1994).
22. Y. Masuda, *J. Mag. and Mag. Mat.* **31-34**, 259 (1983).
23. J. R. Thompson Jr., H. Ramm, J. F. Jarvis and Horst Meyer, *Jour. Low. Temp. Phys.* **2**, 521, 539 (1970).
24. D. F. Brewer, J. G. Daunt and A. K. Sreedhar, *Phys. Rev.* **115**, 836 (1959).
25. A. Georges and W. Krauth, *Phys. Rev.* **B 48**, 7167 (1993).
26. G. E. Brodale, R. A. Fisher, N. E. Phillips and J. Flouquet, *Phys. Rev. Lett.* **56** 390 (1986).
27. N. E. Phillips, R. A. Fisher, J. Flouquet, A. L. Giorgi, J. A. Olsen and G. R. Stewart, *J. Mag. Magnetic Materials* **63 & 64**, 332 (1987).
28. D. Vollhardt, *Phys. Rev. Letts.* **78**, 1307 (1997).
29. D. S. Greywall, *Phys. Rev.* **B 27**, 2747 (1983).
30. M. A. Continentino, *Phys. Rev.* **B 57**, 5966 (1998).
31. S. G. Mishra and R. V. Pai, *Solid State Comm.* **81**, 575 (1992).
32. R. V. Pai and S. G. Mishra, *Phys. Rev.* **B48**, 10292 (1993).
33. C. J. Schinkel, F. R. de Boer and B. de Hon, *Jour. Phys. F : Metal Phys.* **3**, 1463 (1973).
34. J. Hertz, *Phys. Rev.* **B14**, 1165 (1976).
35. A. J. Millis, *Phys. Rev.* **B48**, 7183 (1993).

Non-equilibrium Physics of Magnetic Solids: Time Dependent Changes of Magnetism

K.H. Bennemann

Institute of Theoretical Physics, Freie Universität Berlin,
Arnimallee 14, D-14195 Berlin, Germany

Abstract. The characteristic times for reaching from the initial non-equilibrium state the equilibrium are analyzed for the electrons, the magnetization, magnetic reorientation, magnetic nanostructures and magnetic moments. In transition metals, excited d-electrons and itinerant spins have an ultrafast dynamic and relax on a similar time scale of the order of 10 fs or more. In contrast, changes of magnetism involving spin-lattice coupling like the reorientation of the magnetization at surfaces, interfaces and of domains may require times of the order of 100 ps or more.

1 Introduction

Motivated by recent advances in time-resolved spectroscopy, two-photon photoemission (2PPE) and time-resolved magneto-optics (MSHG), for example, studies of the response of electrons in magnetic transition metals, in high T_c -superconductors with antiferromagnetic spin correlations, and of domains in nanostructured thin films have received increasing interest [1]–[10]. On general physical grounds one expects that such dynamics reflect characteristically the forces controlling magnetism, and the relaxation, aging of magnetic structures. For ferromagnetic transition metals like Ni, Fe etc., for example, the response of magnetism to electronic excitations is important. How quickly do excited electrons thermalize, return to the ground state, and how quickly does magnetism, the magnetization and the direction of the magnetization change [5,6]? For itinerant magnetism in transition metals one expects on general physical grounds that the d-electrons and their magnetization respond on the same time scale and that this response reflects band-structure effects and is material specific [6,7,8].

The relaxation of excited electrons is controlled by the electron-electron and also by the weaker electron-phonon interaction and is generally spin-dependent. The distribution of the hot electrons is calculated with the help of the Boltzmann-equation [8]. The resultant electronic temperature $T_{el}(t)$ changes with time and first $T_{el} > T_{latt}$ and as time progresses after the initial electron excitation $T_{el}(t) \rightarrow T_{latt}(t)$, T_{latt} being the lattice temperature [9]. The magnetic response is then after a certain time expected to behave according to $M(T_{el}(t))$. Of course, the changes of the magnetization must obey angular momentum conservation. Electron dynamics in high T_c -superconductors should reflect characteristic energies as indicated by the phase-diagram of the cuprate superconductors. Furthermore, magnetic reorientation and aging of magnetic domain structures in

nanostructured thin films is controlled by magnetic anisotropy and energy barriers due to exchange and magnetic dipole forces [10,11]. Then one expects in contrast to the ultrafast response of itinerant electrons and their spins a relatively slow response during times ranging from ps to seconds. The relaxation of the magnetization in thin nanostructured films will depend on the energy barriers against domain flips and thus characteristically on whether anisotropy, exchange or magnetic dipole interaction dominates the coupling between domains [11].

In the following we support this general physical picture by a simplified theory and by a discussion of the formulae used for the calculation of the non-equilibrium electron distribution, the electronic temperature $T_{el}(t)$ resulting after the thermalization of the hot electrons, of the magnetization $M(T_{el}(t))$, and for the analysis of 2PPE and SHG, and for the dynamics in high T_c -superconductors.

2 Theory for the Dynamics of the Magnetization in Transition-Metals at Nonequilibrium

Generally, the nonequilibrium electrons excited out of the exchange-split d-states in the Fermi sea, see Fig. 1 for illustration, will change the electron dynamics and the magnetization, since this depends generally on the electron distribution. Note, the effective Hubbard-type Coulomb interaction U and the exchange interaction J is changed somewhat in the nonequilibrium state [7]. The redistribution of the hot electrons and of the electrons in the perturbed Fermi sea is calculated using the Boltzmann equation (8), (9). This takes into account effects due to secondary electrons and yields in accordance with Fermi-liquid theory for the lifetimes of the excited electrons $\tau_\sigma^{-1} \propto (\Delta\varepsilon)^2 \sim N_\sigma(\varepsilon_F)$. Here, $\Delta\varepsilon = \varepsilon - \varepsilon_F$, ε_F is the Fermi-energy, and $N_\sigma(\varepsilon)$ is the density of states. However, not only $N_\sigma(\varepsilon)$, but also the strength of the spin-dependent Coulomb interaction $M_{\sigma\sigma'}$ between hot electrons with spin σ and Fermi sea electrons with spin σ' controls the relaxation [8]. The thermalization of the excited initially nonthermal d-electrons together with the thermal ones in the Fermi sea constituting the hot magnetic moments will occur fairly rapidly of the order of several fs and for a time much smaller than ps [9,12,13]. The magnetic d-electrons may have thermalized already before all d- and s-conduction electrons and long before electrons and lattice are again in equilibrium. The time scale for this dynamics follows of course from the characteristic interactions U amongst the d-electrons, typically of the order of eV, and the exchange interaction J amongst the magnetic moments at neighboring lattice sites. In accordance with the Bloch-equation one expects with some restriction due to the Pauli-principle relaxation times of the order of $t \sim U_{eff}^{-1} \lesssim J^{-1}$ for the excited electrons and the magnetization [13]. It is $T_c \sim J$, where T_c is the Curie-temperature. Note, changes of the magnetization must conserve angular momentum and this involves transfer of angular momentum between neighboring spins or between spins and electronic orbits (s. spin-orbit coupling $V_{s.o.}$). The intra-atomic $V_{s.o.}$ is of the order of 50 to 70 meV for Ni, Fe and hence not much smaller than J . Schematically, the time evolution

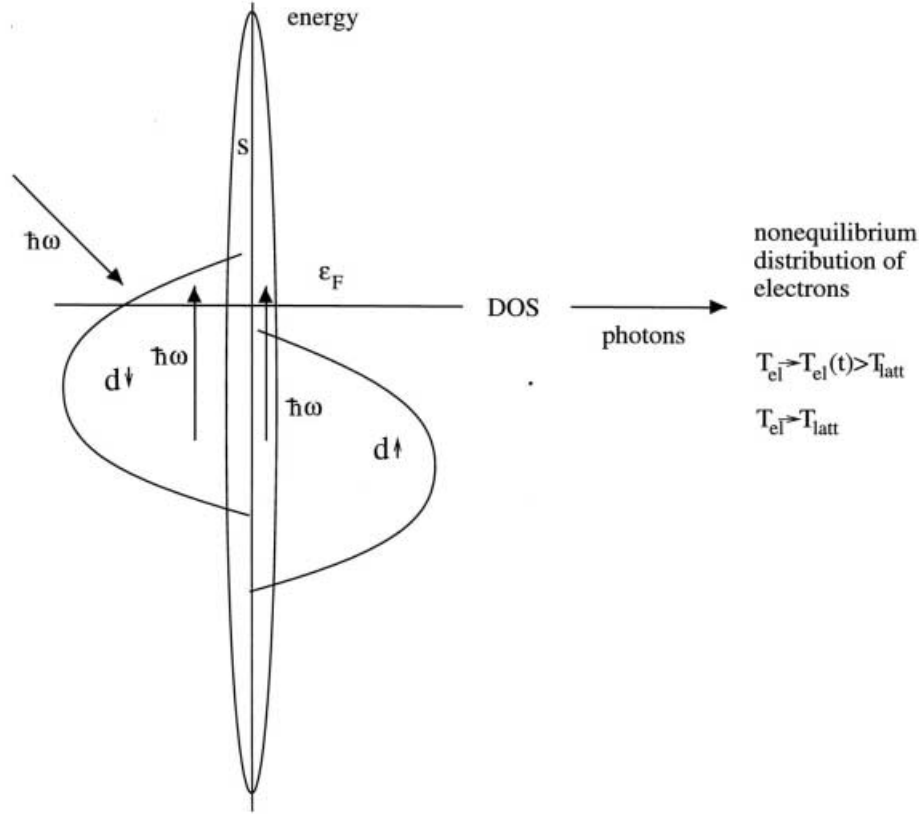


Fig. 1. Illustration of the scenario for the non-equilibrium state produced by exciting optically electrons out of the ground state (the Fermi sea). ε_F is the Fermi-energy. The hot electrons relax first due to electron-electron interactions. The electron thermalization is characterized by the electron temperature $T_{el}(t)$. Energy transfer from the electrons to the lattice occurs via the electron-lattice coupling and which controls $T_{el}(t)$ for longer times. Time resolved spectroscopy observes the dynamics of the hot electron distribution $n(t)$. A spin split density of states $N(E)$ or circularly polarized light creates a spin-polarization of the hot electrons

of the magnetic response to hot electrons shown in Fig. 2 is described by

$$\mathbf{M}[t_o] \rightarrow \mathbf{M}[n'_d(t), T_{el}(t)] \rightarrow \mathbf{M}[T_{el}(t)] . \quad (1)$$

Here, t_o refers to the initial time at which the perturbation (of the pump laser, for example) has stopped, $n'_d(t)$ refers to the number of excited d-electrons which have not yet thermalized at time t , and finally $T_{el}(t)$ is the temperature of the thermalized electrons and which is different from $T_{latt}(t)$ due to the thermalized hot electrons. Of course, $T_{el}(t_o) = T_{latt}(t_o)$. Clearly, if the d-electrons responsible for magnetism have thermalized again the magnetization is approximately given

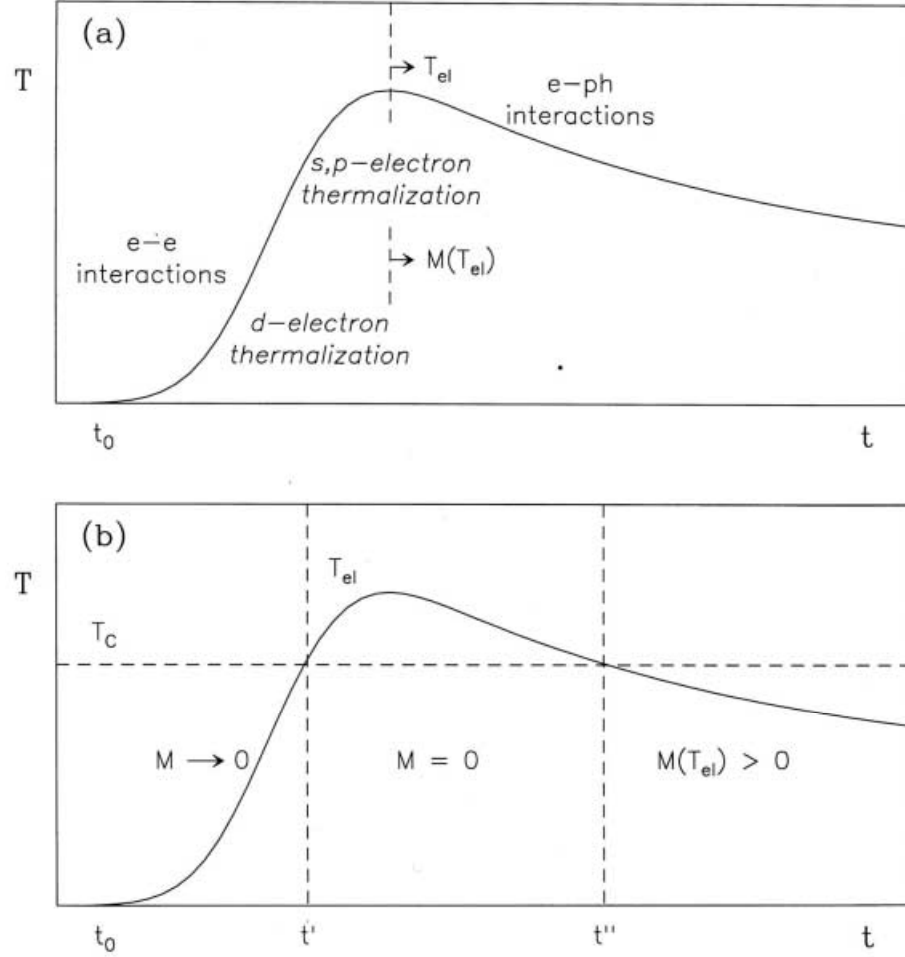


Fig. 2. Illustration of the magnetic response accompanying the time-dependent changes $T_{el}(t)$ of the electrons. Note, for itinerant metals changes of the magnetization happen on the same time scale as those of the electronic distribution

by $M(T_{el})$, where T_{el} is the electronic temperature, and while one has still $T_{el} \neq T_{latt}$ in general. T_{latt} is the lattice temperature.

Since d- and s-, p-electrons establish a common temperature T_{el} and since the s-, p-electrons thermalize more slowly over a time scale of the order of up to a few hundred fs generally, we expect the strongest nonequilibrium reduction of the magnetization $M(T_{el})$ when T_{el} is maximal [6,12]. Note, the interplay of electron-electron interactions and electron-lattice interaction determines at which time t one gets a maximal temperature T_{el} . First, $T_{el}(t)$ increases as time progresses due to the thermalizing hot electrons and then decreases again as energy is transferred from the hot electrons to the lattice via the electron lattice

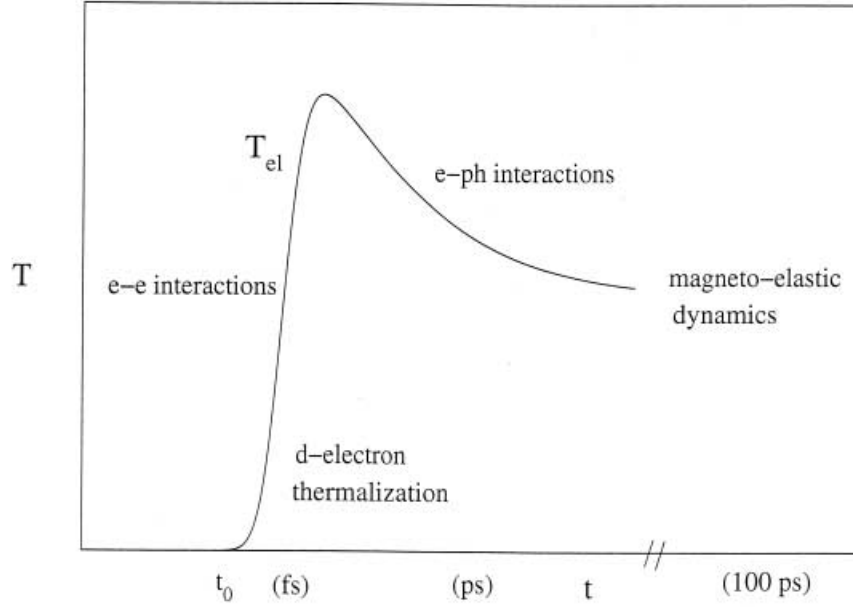


Fig. 3. Time scales for the dynamics of the non-equilibrium state. Electron thermalization occurs during 10–100 fs. Thus, when electron–phonon interaction becomes more and more effective, $T_{el}(T) \rightarrow T_{latt}$ after some ps. After a longer time, $t \gtrsim 100$ ps, magnetoelastic dynamics involving domains, magnetic reorientation and spin-relaxation in a warm lattice occurs. Changes of domain magnetization, in nanostructures, for example, which involve energy barriers may last up to seconds

coupling, see Fig. 3. As a result also the lattice warms up, $T_{latt}(t) > T_{latt}(t_0)$, and after times of a few ps or more $T_{el} \simeq T_{latt}$ again. Note, the diffusion of the hot electrons out of the region where the excitations occur is relatively slow.

It is important to realize that the hot electrons may cause disorder of the spin-directions of neighboring atoms on a time scale of the order of $t \sim J^{-1}$ as well as a change of the magnitude of the local magnetic moments due to an intra-atomic redistribution of the d-electron spins on a time scale of the order of $t \sim U^{-1}$. Generally, flipping locally a spin involves also a change of the acting molecular field and thus of the magnitude of the magnetic moment [14].

To treat the dynamics of excited itinerant electrons and their magnetic moments in Ni, Fe, Co, etc., one may use the Hubbard Hamiltonian [7,14]. In its simplest form this is given by

$$H = \sum_{i,j} t_{ij} c_i^\dagger c_j + \sum_i U n_{i\uparrow} n_{i\downarrow} + \dots \rightarrow H_o + H_{ex} , \quad (2)$$

where the usual notation is used. H_o describes itinerant electrons and H_{ex} the exchange interaction $H_{ex} \sim \sum_{i,j} J \mathbf{S}_i \cdot \mathbf{S}_j$. It is well known that the band char-

acter of the s, d-valence electrons and their kinetic energy is set by the hopping integral t_{ij} and by the interplay of t and U . U is essentially responsible for electronic interactions, correlations and magnetism. The magnetic moment μ_i at atomic site i is given by [14]

$$\mu_i \propto (n_{i\uparrow} - n_{i\downarrow}) . \quad (3)$$

Here, $n_{i\sigma} = \int d\varepsilon f(\varepsilon, T_{el}) N_{i\sigma}(\varepsilon)$ gives the number of electrons at site i with spin σ . Note, within Hubbard Hamiltonian treatment the local density of states $N_{i\sigma}(\varepsilon)$ will depend on the occupation of states. And thus for a given distribution of electrons at time $t = 0$, when the laser irradiation starts and excites many electrons into states above ε_F , one has to recalculate at time t self-consistently $N_{i\sigma}(\varepsilon, T_{el})$, $n_{i\sigma}(T_{el})$ and the magnetic moments $\mu_i(T_{el})$. Here, T_{el} refers to the temperature of the thermalized electrons which is established after a certain time t . Thus, for large T_{el} , $T_{el} \gg T_c$ possibly, one expects $\mu_i(T_{el}) \rightarrow 0$. Note, also depending on the photon energy $\hbar\omega$, s. Fig. 1, electrons are mainly excited into s-states or d-states and also one may get more electrons of spin \uparrow or spin \downarrow due to density of states effects, for example. Clearly this will somewhat affect time-dependently $\mu_i(t > 0)$. One can state quite generally that after a time t ranging from 10 fs to a few hundred fs the hot s- and d-electrons and the remaining cold, not excited valence electrons have thermalized again.

Regarding the spin-dependent lifetimes τ_σ of the hot electrons, note one gets approximately from the Boltzmann equation [8,9,15]

$$\frac{\partial f_\sigma}{\partial t} \simeq P(t) - \frac{1}{\tau_\sigma} f_\sigma \quad (4)$$

and for the change of the distribution function

$$\delta f_\sigma(\varepsilon, t) = \delta f_\sigma(\varepsilon, 0) e^{-t/\tau_\sigma} . \quad (5)$$

This yields then for the lifetime of the excited electrons [8]

$$\tau_\sigma \simeq \tau_0 \varepsilon_F / (\varepsilon - \varepsilon_F)^2 \sim N_\sigma^{-1}(\varepsilon) \quad (6)$$

with

$$\tau_0 = \frac{64}{\pi^2 \sqrt{3\pi}} \sqrt{\frac{m}{e^2 n}} = \frac{128}{\sqrt{3} \pi^2} \frac{1}{\omega_p} . \quad (7)$$

Here, n is the number of electrons per atom and ω_p the plasmon frequency. Evidently, these expressions describe that d-electrons have smaller lifetimes and therefore thermalize faster than s,p-electrons with smaller density of states (DOS) around ε_F for example. The d-electron thermalization speeds up as the DOS available at ε_F for the relaxing electrons increases (for Ni \rightarrow Co \rightarrow Fe: $\tau \sim 15 \rightarrow 5$ fs for $(\varepsilon - \varepsilon_F) \sim 1$ eV [2,8]). Since $N_\uparrow(\varepsilon)$, $N_\downarrow(\varepsilon)$ varies for Ni, Co and Fe, one expects corresponding characteristic behavior of τ_σ or $\tau_\uparrow/\tau_\downarrow$, respectively. With increasing density of excitations, the lifetime τ_σ shortens and then the thermalization will speed up. Also, according to the Boltzmann equation, τ shortens as the electronic temperature T_{el} increases [8,15].

Using these Eqs. one estimates that the excited d-electrons in Ni, Fe, Co have a lifetime of the order of 10 to 100 fs, this compares well with experimental results [2] and this indicates already an electron thermalization during such times. Thus we expect that after 10 fs or more the hot electrons begin to establish a temperature T_{el} . Of course, it may take a time up to a few hundred fs until all s,p-type hot electrons have thermalized [3]. Hence, for noble metals, but less so for magnetic transition metals, the electron temperature T_{el} may increase with time after most of the d-electrons have thermalized, since s-, p- electrons continue to thermalize. As time progresses ($t \rightarrow$ ps), the electron-lattice interaction described by the coupling g_{e-ph} becomes more active with respect to transferring energy from the hot electrons to the lattice and determines the time-dependent change of the electron temperature. Then, the electron temperature T_{el} decreases again, see Fig. 2, 3.

The calculation of the time-dependent electron-temperature caused by the hot electrons is performed as follows: Approximately, $T_{el}(t)$ follows from the coupled master eqs. [16]

$$C_{el}(T_{el}) \frac{\partial T_{el}}{\partial t} = -g_{e-ph}(T_{el} - T_{latt}) + \frac{\partial}{\partial t} \int_0^{\hbar\omega} d\varepsilon \varepsilon N(\varepsilon) f + \dots, \quad (8)$$

and

$$C_{latt}(T_{latt}) \frac{\partial T_{latt}}{\partial t} = g_{e-ph}(T_{el} - T_{latt}) + \dots, \quad (9)$$

where $f(\varepsilon, t)$ includes the exciting laser pulse and where at time t_0 , when the excitation by the laser pulse begins, electron and lattice temperatures are equal, $T_{el} = T_{latt} = T_0$. C_{latt} is the lattice specific heat and $f = f_0 + \delta f$, δf being the contribution to the electronic distribution function due to the nonthermal excited electrons and $C_{el} = \partial E / \partial T$ is the electronic specific heat for the nonequilibrium state. Note, the interplay of the energy distribution amongst the s,p,d-electrons and the lattice determines $T_{el}(t)$. The energy transfer from the hot electrons to the colder lattice is controlled by the electron-lattice coupling g_{e-ph} . Thus the maximal temperature T_{el}^{max} resulting for a given light input energy (fluence F) is given. In general, in transition metals g_{e-ph} is larger for d-electrons than for s-, p-electrons. Of course, T_{el}^{max} depends also on the duration ω of the laser pulse and $T_{el}^{max}(t)$ occurs at shorter times as ω decreases. Note, that for $\omega \rightarrow 0$ the maximal electron temperature is reached at a time set by (g_{ee}/g_{e-ph}) .

Regarding the magnetic response, note as the d-electrons thermalize and feel the temperature $T_{el}(t)$, one gets on general grounds

$$M(t) \rightarrow M(T_{el}(t)) \quad (10)$$

for the time-dependent response of the magnetization to excitations. Usually, one has $M(t_0) > M(t)$. Here, $M(T_0)$ is the magnetization at the temperature $T_0 = T_{latt}$ at the time t_0 before the excitations have increased the temperature. $M(t)$ refers to the magnetization during the time where nonthermal electrons reduce the magnetization. Of course, as the electrons relevant for magnetism reestablish

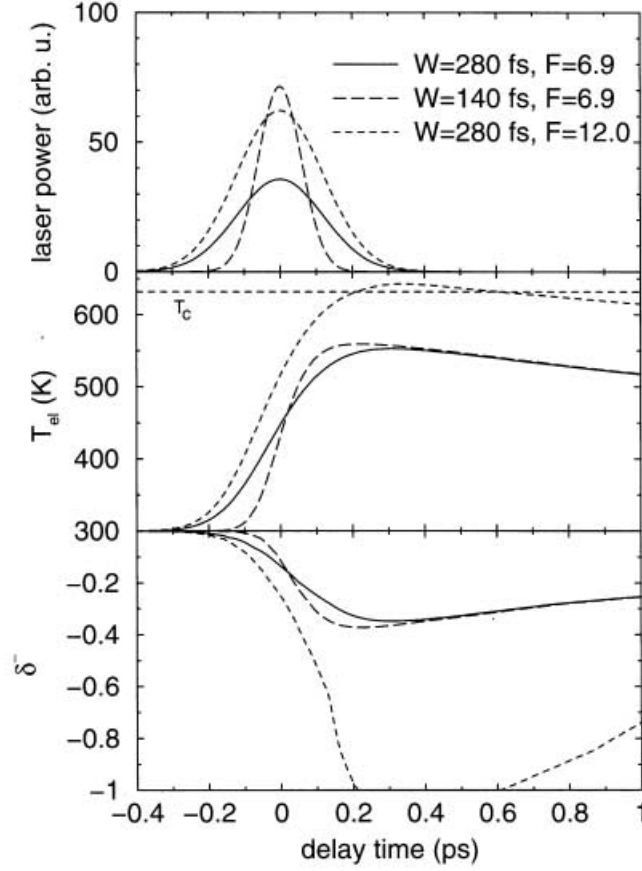


Fig. 4. SHG results showing the dependence of $T_{el}(t)$ and the magnetic response $\Delta^-(t)$ on the duration T of the exciting laser pulse (FWHM) and its intensity. Behaviour of the magnetic response $\Delta^-(t)$ for $T > T_c$, T_c being the Curie-temperature, is also shown

a temperature $T_{el}(t)$, one expects $M(t) \rightarrow M(T_{el})$. Thus, the magnetization will decrease until T_{el}^{max} is reached and then recover again as $T_{el}(t)$ decreases again. This is illustrated in Figs. 3, 4. For $T_{el} > T_C$, of course, $M \rightarrow 0$ and remains zero until T_{el} becomes again smaller than the Curie temperature T_C , see Fig. 5.

Using the Hubbard Hamiltonian or equivalently the Heisenberg Hamiltonian $H_{ex} = \sum_{i,j} J \boldsymbol{\mu}_i \cdot \boldsymbol{\mu}_j$, where J is the exchange coupling between neighboring magnetic moments $\boldsymbol{\mu}_i$, one estimates in accordance with the Bloch equation for the ensemble of local magnetic moments μ_i a spin thermalization or relaxation time of the order of

$$t \gtrsim \frac{1}{zJ\mu^2} \sim \frac{1}{T_C}. \quad (11)$$

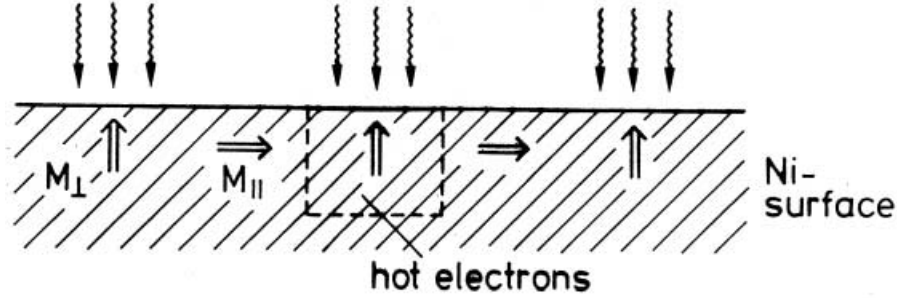


Fig. 5. Light induced magnetic pattern at surfaces due to magnetic reorientation $M_{\perp} \rightarrow M_{\parallel}$ in response to hot electrons, $T_{el}(t)$. Note, the response time for the reorientation transition is given by $t_R \sim E_{anisot} \sim 100ps$ in transition metals, for example

Here, z is the number of nearest neighbors and typically $J \sim 0.1$ eV. Thus, for example, the magnetization of Fe is expected to respond nearly twice as fast as the one of Ni. For Ni we estimate a response time to electronic excitations of the order of 100 fs or even much faster (~ 10 fs), dependent on the number of excitations and the excitation energy range ($\varepsilon - \varepsilon_F$). For Ni, for example, μ_i may decrease by about 30% [14].

Of course, changes of the magnetization must conserve angular momentum and this may involve not only (transversal) local spin excitations, but also the local intra-atomic-like spin-orbit coupling V_{so} ($V_{so} \leq J$ for Ni, Fe). Note, if the nonequilibrium distribution causes also a decrease of μ_i , then the spin-relaxation time increases.

3 Results

We present results (3.1) for the thermalization of the hot electrons, for $T_{el}(t)$, (3.2) for the spin-dependent lifetimes τ_{σ} calculated using the Boltzmann-equation and compare them with 2PPE results obtained by Siegmann, Aeschlimann et al., (3.3) for time resolved nonlinear magneto-optics obtained using general SHG-theory and compare these with experiments by Matthias et al.. These results support the general conclusions discussed in Sect. 2.

3.1 $T_{el}(t)$

In Figs. 2, 3, 4 and 5 results are shown for the thermalization of the excited electrons in Ni. $T_{el}(t)$ and $T_{latt}(t)$ are calculated from the coupled Master-equations. The absolute values of these temperatures depend on the fluence F of the absorbed light, approximately $(T_{el}^{max}(t) - T_{el}(t_0)) \sim F$. The maximal electronic temperature T_{el}^{max} results from the interplay of electron-electron and electron-lattice interaction and at which time $T_{el}(t)$ becomes maximal depends also on

the duration of the laser pulse exciting the electrons, see Fig. 6. Note, the thermalization needs some time and is first mainly controlled by the relatively strong electron-electron interaction. A more complete calculation may also include in addition to the electron-lattice coupling the interaction of the hot electrons with all other excitations, for example spin-excitations (magnons, Stoner-excitations).

3.2 Lifetimes τ_σ of Excited Electrons in Transition Metals

Results obtained from using the Boltzmann-equation are given for the lifetimes of excited electrons in Cu, Co and Ni, for example. For the 2PPE-analysis we use $j_{2PPE}(t) \propto f_{k\sigma}(t)$, where j_{2PPE} is the electron emission current [8,9]. In Fig. 7 we show results for $\tau(\varepsilon - \varepsilon_F)$ in Co and compare with τ in Cu. Note, we get $\tau_\sigma \sim (\varepsilon - \varepsilon_F)^{-2} \sim N_\sigma^{-1}(\varepsilon_F)$. This explains $\tau(Cu) > \tau(Co)$. However, note in order to obtain agreement with experiment we have to use for the Coulomb matrix-element M describing scattering of the hot electrons mainly by the Fermi-sea electrons in Co a value $M \simeq 0.4$ eV rather than $M \simeq 0.8$ eV as for Cu. We expect that this reflects the stronger screening of the Coulomb interaction by the d-electrons in states near ε_F in Co in comparison to Cu [22]. Also, we use in view of the Pauli-principle $M^{\uparrow\uparrow} < M^{\uparrow\downarrow}$. This influences in particular $\tau_\uparrow/\tau_\downarrow$.

Note, the remarkable agreement with experiments and the ultrafast relaxation times ($t \lesssim 100$ fs) which also support the relatively fast thermalization shown in Figs. 2, 4, 5.

3.3 Magneto-optics

Time resolved nonlinear optics (SHG) is a particular sensitive tool for studying the magnetic response in transition metals. We refer to pump-probe spectroscopy where upon variation of the delay time for the action of the probe laser the dynamics of the electron-level population and magnetic changes are obtained [8,9]. Note, SHG probes surfaces and interfaces.

The magnetic SHG signal is given by

$$D^\mp(t) \equiv I(\mathbf{M}, t) \mp I(-\mathbf{M}, t) . \quad (12)$$

The SHG intensity $I(\mathbf{M}, t)$ is calculated by $I(2\omega) \propto |\mathbf{P}(2\omega)|^2$ and the polarization \mathbf{P} is then given in terms of the electric field \mathbf{E} by [17]

$$P_i = F_{ij\ell} \chi_{ij\ell} E_j E_\ell . \quad (13)$$

Here, F denotes Fresnel coefficients and $\chi_{ij\ell}$ is the nonlinear susceptibility. To compare with experiments it is convenient to study the changes (response)

$$\Delta^\pm(t) = \frac{D^\pm(t)}{D^\pm(t_0)} - 1 , \quad (14)$$

where t_0 refers to the time at which the pump laser pulse starts to act and t to the observation time. To simplify the analysis we write [20,21,22]

$$\chi(\mathbf{M}) = \chi_e + \chi_0(\mathbf{M}), \chi_0 \simeq \chi' M . \quad (15)$$

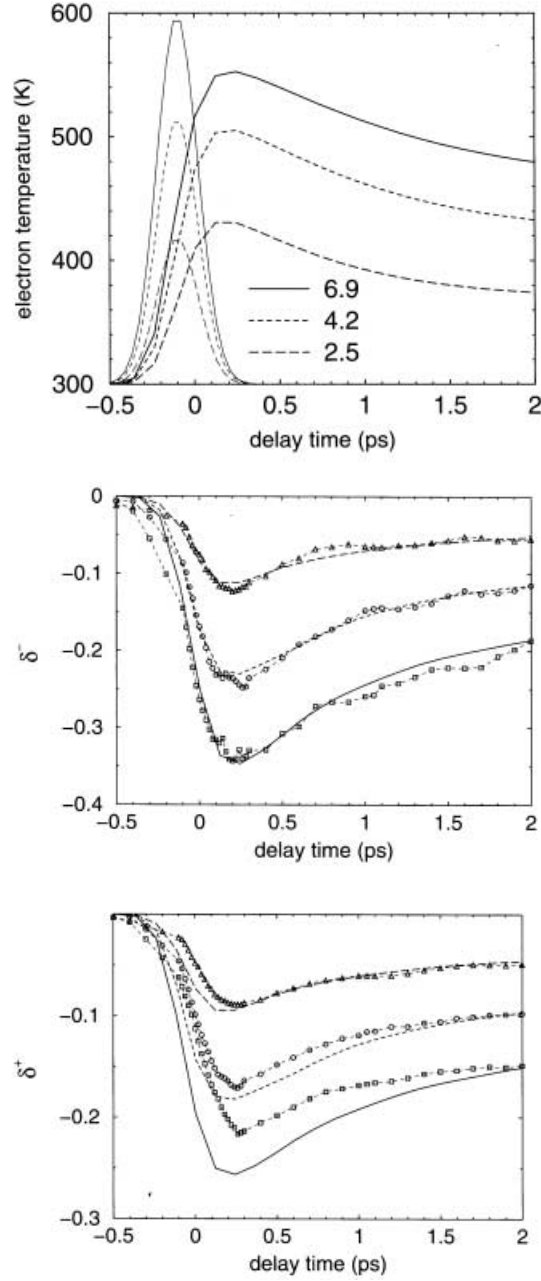


Fig. 6. Results for the electronic temperature and for $\Delta^-(t) \sim I(\mathbf{M}) - I(-\mathbf{M})$ and $\Delta^+(t) \sim I(\mathbf{M}) + I(-\mathbf{M})$. Note, T_{el} is max. when $\Delta^-(t)$ and Δ^+ are minimal. Theory and experiment compare well for $t \gtrsim 200$ fs, but not for small t . Also, $\Delta^- \propto M(T_{el})$ for larger times. F is the fluence and the intensity I refers to SHG light

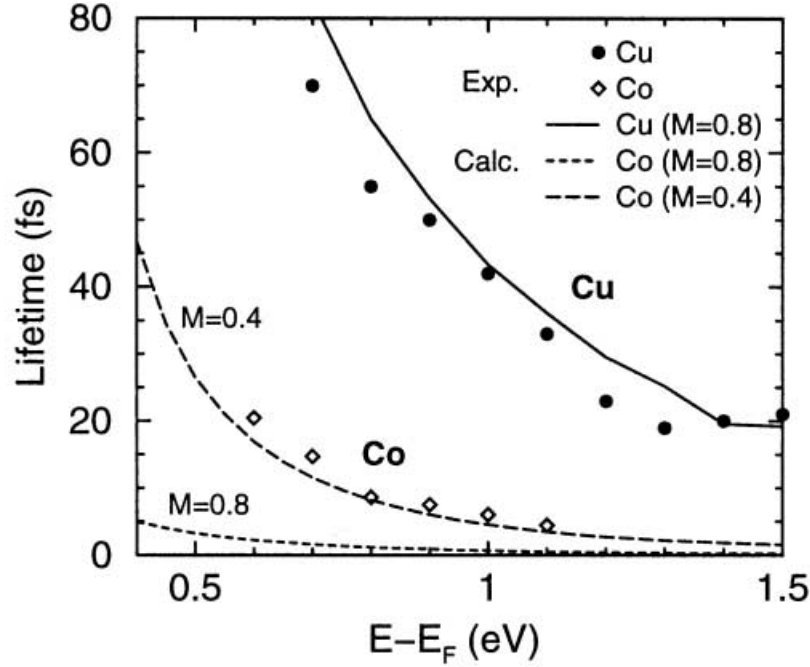


Fig. 7. Lifetime τ of excited electrons in Cu and Co. Note, the Coulombic electron-electron interaction matrix-element M is taken to be smaller for Co than for Cu due to the larger d-electron screening in Co ($V(r) \sim e^{-k_0 r}$, $k_0 \sim N(\varepsilon_F)$)

Here, χ_e and χ_0 denote the contributions to χ which are even and odd in the magnetization, respectively. Note, one has generally to take into account the relative phases ϕ between the tensor elements of χ [20,21,22].

In Fig. 6 results are given for $\Delta(t, M(t))$ and $\Delta^+(t)$. Note, the ultrafast magnetic response for times $t \lesssim 200$ fs which is expected to become even faster as the duration of the exciting laser pulse gets shorter. It is interesting that the minima of $\Delta^+(t)$ and $\Delta^-(t)$ occur at nearly the same time and at a time at which $T_{el}(t)$ is maximal. For longer times it seems valid to use $M(T_{el}(t))$ for the analysis [12,23,24].

In Table 1 we compare results for the minima of $\Delta^+(t)$ and $\Delta^-(t)$ and also indicate the polarization dependence of MSHG and which tensor elements get involved.

In Fig. 4 we show how the results may depend on the absorbed laser energy (fluence F) and the duration W of the exciting laser pulse. Note, for $T_{el}(t) > T_c$, T_c being the Curie-temperature, one expects that $\Delta^-(t) \rightarrow -1$ for the time

Table 1. Values for the tensorelements $\chi_{ij\ell}$ split into even (χ_e) and odd (χ_o) contributions with respect to the magnetization (\mathbf{M}) dependence and for the response quantities Δ^\pm . y, x are in the surface plane, $y \perp$ optical plane. We use $F = 1.15$, $\alpha \simeq 0.9$, $T_{el}^{max} \simeq 500K$, $F_e\chi_e/F_0\chi_0 \approx 10$

$\chi_{ij\ell}(M)$	$s \rightarrow S$	$p \rightarrow P$
χ_e	0	$\chi_{zzz}, \chi_{zxx}, \chi_{xxz}$
$\chi_o(M \parallel x)$	χ_{yyy}	0
$\chi_o(M \parallel y)$	0	$\chi_{xxx}, \chi_{xzz}, \chi_{zzx}$

	response calc	expt
Δ_{min}^-	-0.4	-0.35
Δ_{min}^+	-0.2	-0.2

where $T_{el}(t) > T_c$. This is illustrated. Experiments by Matthias et al. support this [22,24].

For thin films one may get $T_{el}(t) > T_c$ for a given fluence by varying the film thickness, since $T_c = T_c(d)$ where d is the film thickness. Again, $\Delta^-(t)$ will reflect this.

In general one expects that $T_{el}^{max}(t)$ and $M^{min}(t)$ may not coincide and that the magnetic response occurs with a certain time delay, since the coupling between the thermalizing electrons is somewhat stronger than the one between the spins (U versus J in the framework of the Hubbard Hamiltonian and typically $U > J$) [24]. At any rate, the results indicate the possible ultrafast (fs) magnetic response of itinerant ferromagnets in accordance with the general arguments presented in the previous chapter.

Finally it is of interest to study transient magnetism induced by circularly polarized light, for example in Pd, Rh, etc.

Summary

The magnetic response of itinerant metals at non-equilibrium has been studied. We show that of course the relaxation is controlled by the forces causing magnetism. Further MSHG and 2PPE pump-probe experiments and theoretical studies (note SHG \leftrightarrow 2PPE, quantum-mechanical interference effects, calculation of the spin-dependent Coulomb matrix-elements for electron-electron scattering, \mathbf{k} -selective 2PPE, etc.) are needed to refine and sharpen the physics of the dynamics.

Of interest is also to determine time resolved the rotation of the spin of a spin-polarized current through a thin ferromagnetic film, using 2PPE for example, and of spin selectively excited electrons (by circularly polarized light) by the magnetization of Fermi-sea electrons. In layered film structures (Co/Cu/Ni/Cu..., for example) non-equilibrium magnetic response, time resolved alignment in an external field, should also permit fast processes. Hot electrons will change the

interfilm exchange coupling, but may also change selectively the magnetization in the Co or Ni film. Using instead of a Cu film Pd or Rh films, for example, one may change with the help of circularly polarized light (inducing transient magnetization in the non-ferromagnetic transition metal) drastically the interlayer exchange coupling J_{int} .

Acknowledgments

Helpful discussions with Dr. R. Knorren, Prof. E. Matthias, Dr. P. Jensen, and R. Brinzanik are gratefully acknowledged. This study was supported by the DFG through SFB 290.

References

1. I. Hertel, E. Knoesel, M. Wolf, and G. Ertl: Phys. Rev. Lett. **76**, 2, 535 (1996); M. Aeschlimann, M. Bauer, S. Pawlik: Chem. Phys. **205**, 127 (1996).
2. F. Passek, M. Donath, K. Ertl, and V. Dose: Phys. Rev. Lett. **75**, 2746 (1995); M. Aeschlimann, M. Bauer, S. Pawlik, R. Burgemeister, D. Oberli, W. Weber, and H. C. Siegmann: to be published (1997); F. Meier, A. Vaterlaus, M. Aeschlimann, M. Lutz, D. Guarisco, F. Milani, and H.C. Siegmann: J. Magn. Magn. Mater. **93**, 523 (1991)
3. W.S. Fann, R. Storz, H.W.K. Tom, J. Bokor: Phys. Rev. B **46**, 13592 (1992)
4. P. G. Allen: Phys. Rev. Lett. **59**, 1460 (1987)
5. E. Beaupaire, J.-C. Merle, A. Daunois, J.-Y. Bigot: Phys. Rev. Lett. **76**, 4250 (1996)
6. J. Hohlfeld, E. Matthias, R. Knorren and K.H. Bennemann: Phys. Rev. Lett. **78**, 4861 (1997)
7. J. Hubbard: Phys. Rev. B **20**, 4584 (1979)
8. R. Knorren: thesis, FU Berlin (2000)
9. R. Knorren, K.H. Bennemann, R. Burgermeister, and M. Aeschlimann: Phys. Rev. B **61**, 9427 (2000)
10. R. Brinzanik, P. Jensen, K.H. Bennemann: Nano Structured Mat. **12**, 9 (1999)
11. R. Brinzanik, P. Jensen, K.H. Bennemann: preprint FUB (2000)
12. K.H. Bennemann: Ultrafast Spin Dynamics, Revista Mexicana de Fisica **44**, 533 (1998)
13. Of course, the Bloch equation $d\mathbf{S}_i/dt = \frac{2J}{\hbar} \sum_j \mathbf{S}_i \times \mathbf{S}_j + \dots$ conserves angular momentum and should also already serve for an estimate of magnetic dynamics in itinerant ferromagnets. j sums over n.n. spins to i and a relaxation term due to spin-lattice coupling is indicated.
14. J.L. Morán-López, K.H. Bennemann and M. Avignon, Phys. Rev. B **23**, 5978 (1981); the magnetization is approximately given within a Ising-like model by $M \sim (c_+\mu_+ - c_-\mu_-)$, where c_+ is the probability to find a magnetic moment μ_+ pointing in the direction of the magnetization and c_- and μ_- are correspondingly defined. Generally, $\mu_+ \neq \mu_-$ and perturbations cause changes $\mu_+ \rightarrow \mu_-$, for example, and thus a decrease of M due to directional disorder as well as due to a decrease in the magnitude of the magnetic moments.

15. The function $f(\varepsilon, t)$ may be determined by using the Liouville equation for the density operator $\rho(t)$ and $i\hbar\dot{\rho} = [H, \rho]$ or by using the Boltzmann equation $\partial f/\partial t = (\partial f/\partial t)_{opt} + (\partial f/\partial t)_{in} + (\partial f/\partial t)_{out} + (\partial f/\partial t)_{el-ph} + (\partial f/\partial t)_{transp}$. Here, the various terms describe the optically induced transitions, scattering into and out of an electronic level due to electron collisions, changes in f due to electron-phonon interaction and due to transport, respectively; see ref. [8,9] for details.
16. Of course, the time dependence of $T_{el}(t)$ may be determined by using the master equations $c\dot{T}_{el} = -\alpha_1(T_{el} - T_{latt}) - \alpha_2(T_{el} - T_\mu) + P(t)$ for the electrons, $c'\dot{T}_\mu = -\alpha_2(T_\mu - T_{el}) - \alpha_3(T_\mu - T_{latt})$ for the spins, and $c\dot{T}_{latt} = \alpha_1(T_{latt} - T_{el}) + \alpha_3(T_{latt} - T_\mu)$ for the lattice. Here, c , c' and c_{latt} denote the specific heat, P is the laser power and α_i are constants. If diffusion is important, then $c\dot{T}_{el} = \frac{\partial}{\partial z}(K_{el}\frac{\partial}{\partial z}T_{el}) + \dots$, where K_{el} is the thermal diffusion coefficient of the electrons. $T_{el}^{\max}(t)$ will be generally determined by the interplay of the electron-electron and the electron-lattice interaction. Note, for itinerant transition metals it is not strictly valid to separate the conduction electrons from those constituting the magnetic moments and c may change at nonequilibrium.
17. W. Hübner and K.H. Bennemann: Phys. Rev. B **53**, 1 (1996)
18. H.J. Siegmann et al.: private communication; s. also D.R. Penn, S.P. Apell, and S.M. Girvin: Phys. Rev. B **32**, 7753 (1985). M. Aeschlimann, M. Bauer, S. Pawlik, W. Weber, R. Burgermeister, D. Oberli und H.C. Siegmann: Phys. Rev. Lett. **79**, 5158 (1997).
19. $M_{\sigma\sigma'}$ is the matrix element referring to the scattering of excited electrons with spin σ by the (Fermi sea) electrons with spin σ' . Due to the Pauli-principle $M_{\uparrow\uparrow} < M_{\uparrow\downarrow}$ and note the Coulomb potential V is screened by the dielectric function $\varepsilon \simeq 1 + 4\pi\chi_0$, $\chi_0 \propto N(\varepsilon_F)$. Hence, since d-electrons contribute to the screening, one expects $M(Cu) > M(Co)$, for example. Approximately, $V = \frac{e^2}{r}e^{-k_0 r}$, with $k_0 \sim N(\varepsilon_F)$ and $M(Ni) \lesssim M(Co) < M(Fe)$. Recent LDA calculations by Schnell and Czucholl seem to support this, see Wandlitz conf., Oct. 2000. Also, note $(\tau_\uparrow/\tau_\downarrow)$ should depend less sensitively on $M_{\sigma\sigma'}$ than τ_σ .
20. The susceptibility tensor $\chi_{ijl}(\mathbf{M})$ may be expanded into even and odd terms in \mathbf{M} , s. U. Pustogowa, W. Hübner, and K.H. Bennemann: Phys. Rev. B **48**, 8607 (1993): One may write $\chi_{ijl}(\mathbf{M}) = \chi_{ijl}(0) + \chi_{ijlk}M_k + \dots$. It is then straightforward to get $\Delta I^- \propto M$.
21. W. Hübner and K.H. Bennemann: Phys. Rev. B **40**, 5973 (1989).
22. U. Conrad: thesis, FUB (1999); V. Jähnke, thesis: FUB (2000); J. Gütde, U. Conrad, V. Jähnke, J. Hohlfeld, and E. Matthias: Phys. Rev. B **59**, R 6608 (1999); U. Conrad, J. Gütde, V. Jähnke, E. Matthias: J. Appl. Physics B **68**, 511 (1999); J. Hohlfeld, J. Gütde, U. Conrad, O. Dühr, G. Korn, E. Matthias: J. Appl. Physics B **68**, 505 (1999); J. Hohlfeld, J. Gütde and E. Matthias: to be published.
23. J. Hohlfeld: thesis FU Berlin, (1998)
24. E. Matthias: private communications, Oct. (2000)

Metallic Ferromagnetism – An Electronic Correlation Phenomenon

D. Vollhardt¹, N. Blümer^{1,*}, K. Held², and M. Kollar³

¹ Theoretical Physics III, Center for Electronic Correlations and Magnetism,
University of Augsburg, 86135 Augsburg, Germany

² Dept. of Physics, Princeton University, Princeton, NJ 08544, USA

³ Dept. of Physics, Yale University,
P. O. Box 208120, New Haven, CT 06520-8120, USA

Abstract. New insights into the microscopic origin of itinerant ferromagnetism were recently gained from investigations of electronic lattice models within dynamical mean-field theory (DMFT). In particular, it is now established that even in the one-band Hubbard model metallic ferromagnetism is stable at intermediate values of the interaction U and density n on regular, frustrated lattices. Furthermore, band degeneracy along with Hund's rule couplings is very effective in stabilizing metallic ferromagnetism in a broad range of electron fillings. DMFT also permits one to investigate more complicated correlation models, e.g., the ferromagnetic Kondo lattice model with Coulomb interaction, describing electrons in manganites with perovskite structure. Here we review recent results obtained with DMFT which help to clarify the origin of band-ferromagnetism as a correlation phenomenon.

1 Introduction

Since the Curie temperature of ferromagnetic metals like iron, cobalt, and nickel is of the order of electrostatic energies in solids, i.e., is much higher than the interaction energy of the electron spins, itinerant ferromagnetism is expected to be the result of the interplay between the ordinary spin-*independent* Coulomb interaction and the kinetic energy of the electrons, in combination with the Pauli principle [1,2,3]. As such it is one of the fundamental cooperative phenomena in condensed matter physics.

Until recently the theory of itinerant ferromagnetism was investigated by two essentially separate communities, one using model Hamiltonians in conjunction with many-body techniques (or even rigorous mathematical methods [4,5,6]), the other employing density functional theory (DFT) [7,8]. DFT and its local density approximation (LDA) have the advantage of being *ab initio* approaches which do not require empirical parameters as input. Indeed, they are highly successful techniques for the calculation of the electronic structure of real materials. However, in practice DFT/LDA is restricted in its ability to describe strongly correlated materials. Here, the model Hamiltonian approach is more general and powerful since there exist systematic theoretical methods to investigate the

* *Present address:* Institut für Physik, KoMa 337, Johannes Gutenberg-Universität, 55099 Mainz, Germany

many-electron problem with increasing accuracy. Nevertheless, the uncertainty in the choice of the model parameters and the technical complexity of the correlation problem itself prevent the model Hamiltonian approach from being a flexible or reliable enough tool for studying real materials. The two approaches are therefore complementary.

Originally the one-band Hubbard model was introduced to gain insight into the origin of metallic ferromagnetism [9,10,11]. However, even for this simplest possible microscopic model answers are not easily obtained since in general metallic ferromagnetism occurs at *intermediate* couplings and off half filling [3,12]. Thus, this cooperative phenomenon belongs to the class of problems where standard perturbation techniques are not applicable. In particular, weak-coupling theories or renormalization group approaches [13] which are so effective in detecting instabilities with respect to antiferromagnetism or superconductivity meet with limited success here. In general, *non-perturbative* investigations are required.

During the last couple of years significant progress was made in the theoretical understanding of the microscopic foundations of metallic ferromagnetism. They were made possible mainly by the development (i) of new analytic approaches, such as the mathematical methods used to investigate flat-band ferromagnetism [6] and its extensions [14,15] as well as dynamical mean-field theory (DMFT) [16,17,18], (ii) of new numerical techniques, such as the density matrix renormalization group (DMRG) which yields precise results in $d = 1$ [19], and (iii) of new comprehensive approximation schemes such as the multi-band Gutzwiller wave function [20], or the new *ab initio* computational scheme LDA+DMFT [21,22,23] which merges conventional band structure theory (LDA) with a comprehensive many-body technique (DMFT).

In this paper the insights gained with the help of the DMFT will be reviewed. After a short introduction into this approach (Section 2), the microscopic conditions for metallic ferromagnetism in the one-band Hubbard model (Section 3) and in the case of the orbitally degenerate model (Section 4) are explained and the differences discussed. Furthermore, the physics of itinerant ferromagnetism in more complicated models, e.g., the ferromagnetic Kondo lattice model with Coulomb correlations for manganites with perovskite structure, is analyzed. A conclusion and outlook (Section 5) closes the presentation.

2 Dynamical Mean-Field Theory

During the last decade a new many-body approach was developed which is especially well-suited for the investigation of correlated electronic systems with strong local interactions – the dynamical mean-field theory (DMFT) [24]. It becomes exact for $d = \infty$, i.e., for lattices with coordination number $Z = \infty$ [16]. Why is the investigation of this limit useful and interesting? The answer is that already in $d = 3$ the coordination number of regular lattices, such as the fcc lattice, is quite large ($Z_{\text{fcc}} = 12$). It is therefore quite natural to view Z as a large number, and to consider the limit $Z \rightarrow \infty$ as a starting point [16].

To obtain a meaningful model in this limit one has to scale the NN hopping amplitude in the kinetic energy (see below) as $t = t^*/\sqrt{Z}$ (in the following we set $t^* = 1$ and thereby fix the energy scale). Then one obtains a purely local theory where the self-energy $\Sigma_{\mathbf{k}}(\omega)$ becomes \mathbf{k} independent and where the propagator $G(\mathbf{k}, \omega) = G^0(\mathbf{k}, \omega - \Sigma(\omega))$ may be represented by the non-interacting propagator at a shifted frequency [24]. The dynamics of the quantum mechanical correlation problem is then fully included. That is why this theory is referred to as “dynamical mean-field theory” (DMFT). We note that due to the local nature of the theory there is no *short*-range order in position space.

Within DMFT the electronic lattice problem is mapped onto an effective self-consistent single-impurity Anderson model [24]. DMFT is a non-perturbative, thermodynamically consistent theoretical framework within which the dynamics of correlated lattice electrons with local interaction can be investigated at all coupling strengths. This is of essential importance for problems like band-ferromagnetism or the metal-insulator transition [25] which set in at a Coulomb interaction strength comparable to the electronic band width.

In DMFT the information about the lattice or the dispersion of the system under investigation enters only through the density of states (DOS) $N^0(E)$ of the *non*-interacting particles, unless there is long-range order with broken translational symmetry of the lattice as in the case of antiferromagnetism. In finite dimensions, e.g., $d = 3$, DMFT is then an approximation – usually an excellent one as is manifested by the plethora of results obtained within the last decade [24]. DMFT is presently the only comprehensive, thermodynamically consistent computational scheme which allows one to investigate the dynamics of correlated lattice electrons on all energy scales.

Due to its equivalence to an Anderson impurity problem a variety of approximative techniques have been employed to solve the complicated DMFT equations, such as the iterated perturbation theory (IPT) [26] and the non-crossing approximation (NCA) [27], as well as numerically exact techniques like quantum Monte-Carlo simulations (QMC) [28], exact diagonalization (ED) [29], or the numerical renormalization group (NRG) [30]. However, NRG cannot yet be used to solve the DMFT equations for multi-band models.

In the present paper all DMFT results were obtained by QMC. This is a particularly well-tested and reliable, albeit computer-expensive method which may be employed down to temperatures $T \sim 10^{-2}W$ (W : band width) and at not too strong interactions.

3 The One-Band Hubbard Model

The one-band Hubbard model

$$H_{\text{Hub}} = - \sum_{i,j,\sigma} t_{ij} (c_{i\sigma}^\dagger c_{j\sigma} + \text{h.c.}) + U \sum_i n_{i\uparrow} n_{i\downarrow} \quad (1)$$

is the simplest lattice model for correlated electrons, and was originally proposed to understand metallic ferromagnetism in $3d$ transition metals [9,10,11]. Here, t_{ij}

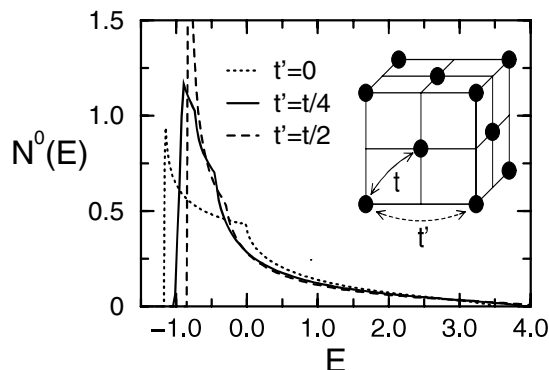


Fig. 1. DOS of noninteracting electrons on a fcc lattice in $d = 3$ with and without additional NNN hopping t' .

is a general hopping matrix element between sites i and j . In the past the kinetic energy in (1) was usually restricted to nearest-neighbor (NN) hopping; then it is useful to divide the underlying lattices into bipartite and non-bipartite ones. This distinction ceases to be useful if, in addition to NN hopping t , longer-range hopping, in particular next-nearest-neighbor (NNN) hopping t' is considered.

The Hubbard model is characterized by a purely local interaction term which is completely independent of the lattice structure and dimension. Therefore in this model the kinetic energy of the electrons (i.e., the dispersion) and the structure of the lattice are very important for the stability of metallic ferromagnetism. This is well-known from the approximate investigations by Gutzwiller [9], Hubbard [10], Kanamori [11] and Nagaoka [31], and has recently been confirmed, and made precise, by detailed investigations [6,32,15,14,17,18].

3.1 Routes to Ferromagnetism

On bipartite lattices the t' -hopping term destroys the antiferromagnetic nesting instability at small U (see, for example [33]) by shifting spectral weight to the band edges and thereby introducing an asymmetry into the otherwise symmetric DOS. It will be shown below that a high spectral weight at the band edge (more precisely: the *lower* band edge for $n < 1$) minimizes the loss of kinetic energy of the overturned spins in the magnetic state and is hence energetically favorable. Therefore frustrated, i.e., non-bipartite lattices, or bipartite lattices with frustration due to further-range hopping (e.g., $t' \neq 0$) support the stabilization of metallic ferromagnetism.

The fcc lattice is an example of a frustrated lattice in $d = 3$. The corresponding DOS of the non-interacting particles is shown in Fig. 1. Switching on an additional NNN hopping t' further increases the spectral weight at the lower band edge. For $t' = t/2$ one even obtains a square-root-like divergence. To understand why a high spectral weight at the band edge is favorable for the kinetic

energy we first consider the case $U = 0$, $n < 1$ [12]. Let us consider a flat, symmetric DOS. The fully polarized state is obtained by inverting the spin of the down electrons, which due to the Pauli principle have to occupy higher energy states. Counting the energy from the lower band edge the Fermi energy of the polarized state, μ_\uparrow , is seen to be twice that of the unpolarized state. This should be contrasted with a DOS having large spectral weight at the lower band edge. Here the Fermi level of the polarized state is not so strongly shifted upwards, i.e., fewer high energy states are populated, which is clearly energetically favorable. The energy difference between the fully polarized state and the unpolarized state

$$\Delta E = \left[\int_{-W_1}^{\mu_\uparrow} - 2 \int_{-W_1}^{\mu} \right] dE N^0(E) E \quad (2)$$

must become negative for the ferromagnetic state to be stable. Of course, in the non-interacting case one has $\Delta E > 0$ [4]. Nevertheless, even for $U = 0$, ΔE attains its lowest value for a DOS with peaked spectral weight at the lower band edge for all $n < 1$ [12]. To show that $\Delta E < 0$ for $U > 0$ requires a reliable calculation of the energy of the *correlated paramagnet*. Indeed, this is one of the central, most difficult problems of electronic correlation theory. It should be noted that the above discussion concerning the shape of the DOS goes beyond the well-known Stoner criterion which predicts a ferromagnetic instability of the paramagnet for U equal to the inverse of the DOS precisely *at* the Fermi level.

3.2 Frustrated Lattices

Since metallic ferromagnetism is an intermediate-coupling problem purely analytic approaches alone cannot provide sufficient information, in particular in dimensions $d > 1$. In this situation the development of new numerical techniques during the last few years was of crucial importance for progress in this field. In particular, for one-dimensional systems the DMRG [19], and for high-dimensional systems the DMFT have led to important insights. Here we restrict ourselves to results obtained by DMFT.

By a suitable generalization of the dispersion relation in three dimensions, frustrated lattices like the fcc lattice can be defined in any dimension, in particular in $d = \infty$ [34]. With the proper scaling of the hopping term (see above) the non-interacting DOS of the generalized *fcc* lattice in $d = \infty$ is obtained as:

$$N_{fcc}^0(E) = e^{-(1+\sqrt{2}E)/2} / \sqrt{\pi(1+\sqrt{2}E)} \quad (3)$$

It has a strong square-root divergence at the lower band edge, $-1/\sqrt{2}$, and no upper band edge.

Investigations of the stability of metallic ferromagnetism on fcc-type lattices within DMFT, in combination with finite-temperature QMC techniques to solve the DMFT equations, were first performed by Ulmke [35]. To detect a ferromagnetic instability one calculates the temperature dependence of the uniform static

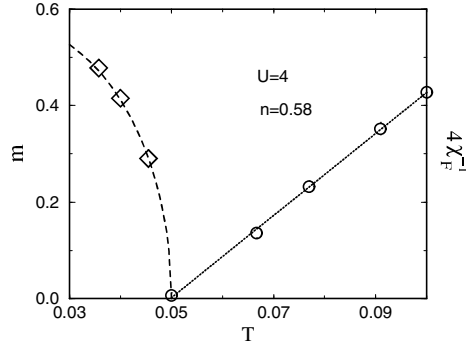


Fig. 2. Magnetization m (diamonds) and inverse ferromagnetic susceptibility χ_F^{-1} (circles; note the factor of 4 in the definition) as calculated by DMFT for the one-band Hubbard model with DOS (3) at $U = 4$ and $n = 0.58$. Error-bars are of the size of the symbols or smaller. The value of χ_F^{-1} at $T = 0.05$ is a data point, not an extrapolation. The dotted line is a linear fit to χ_F^{-1} , the dashed line a fit with a Brillouin function to m [35].

susceptibility χ_F from the corresponding two-particle correlation function [36]. For $N_{gfc}^0(E)$ and at an intermediate interaction strength of $U = 4$ the ferromagnetic response is found to be strongest around quarter filling ($n \simeq 0.5$). The susceptibility χ_F is seen to obey a Curie-Weiss law (Fig. 2). Thus the Curie temperature T_c can be safely extrapolated from the zero of χ_F^{-1} . For $n = 0.58$ this leads to a value of $T_c = 0.051(2)$. Below T_c the magnetization m (a one-particle quantity determined by the local propagator) grows rapidly, reaching more than 80% of the fully polarized value ($m_{max} = n = 0.58$) at the lowest temperature (30% below T_c). The three data points $m(T)$ in Fig. 2 are consistent with a Brillouin function with the same critical temperature of $T_c = 0.05$ and an extrapolated full polarization at $T = 0$. (We note that a saturated ground-state magnetization is also consistent with the single-spin-flip analysis of the fully polarized state by Uhrig [17]). So one finds *simultaneously* a Curie-Weiss-type static susceptibility with Brillouin-function-type magnetization, *and* a non-integer magneton number, in qualitative agreement with experiments on 3d transition metals. In the past, these features were attributed to seemingly opposite physical pictures: the former to localized spins, and the latter to itinerant electrons. However, this was only because of the use of oversimplified, *static* mean-field-type theories like Weiss mean-field theory (for spin models) and Hartree-Fock (for electrons). Here we see that these properties are natural features of *correlated* electronic systems, which are generated by the quantum dynamics of the many-body problem. Within DMFT this “paradoxical” behavior of band ferromagnets is resolved without difficulty.

Collecting the values of $T_c(U, n)$ obtained by $\chi_F^{-1}(T_c, U, n) = 0$, the boundaries between the ferromagnetic and the paramagnetic phases are determined. Thereby one can construct the T vs. n phase diagram for different values of U . The region of stability increases with U [35].

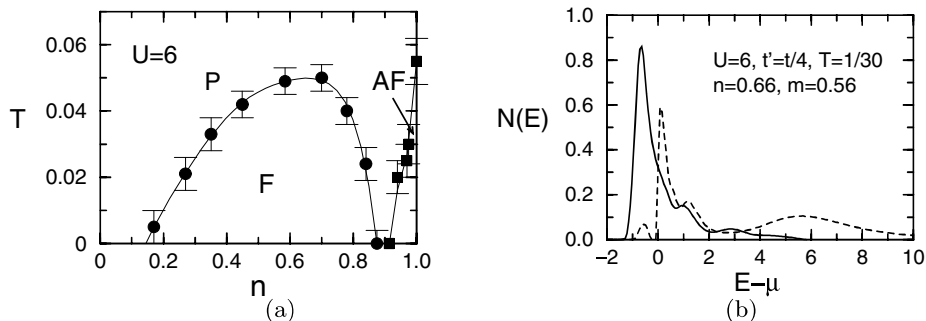


Fig. 3. (a) T vs. n phase diagram of the Hubbard model as obtained within DMFT for the DOS corresponding to a three-dimensional fcc lattice with NN hopping $t' = t/4$ (see Fig. 1); (b) DOS of the interacting electrons in the ferromagnetic phase of (a), solid line: majority spin, dashed line: minority spin [35].

To make contact with $d = 3$ one can use the corresponding fcc DOS shown in Fig. 1. For $t' = 0$ no instability is found at temperatures accessible to QMC. However, already a small contribution of t' -hopping (which is present in any real system) is enough to stabilize a large region of metallic ferromagnetism in addition to an antiferromagnetic phase (which is absent in $d = \infty$), close to half filling (Fig. 3a) [35]. This shows the strong and subtle dependence of the stability on the dispersion and the distribution of spectral weight in the DOS. By developing increasingly refined schemes of iterated perturbation theory to solve the DMFT equations Nolting and collaborator [37] obtained T vs. n phase diagrams which reproduce the QMC results remarkably well.

We note that the maximal transition temperature is $T_c^{\max} = 0.05 \simeq 500$ K for a band width $W = 4$ eV. This is well within the range of real transition temperatures, e.g., in nickel.

So far we only argued on the basis of the shape of the DOS of the *non*-interacting electrons, $N^0(E)$. On the other hand the interaction will renormalize the band and relocate spectral weight. Therefore it is not *a priori* clear at all whether the arguments concerning the kinetic energy discussed in subsection 3.1 still hold at finite U . We note that this effect is also not taken into account in any Stoner theory. To settle this point one may calculate the DOS of the interacting system, $N(E)$, by employing the maximum entropy method for analytic continuation. In Fig. 3b we show $N(E)$ obtained with $N_{fcc}^0(E)$ and the parameter values used to calculate Fig. 2. Clearly the ferromagnetic system is metallic since there is appreciable weight at the Fermi level ($E = \mu$). Furthermore, the spectrum of the majority spins is seen to be affected only slightly by the interaction, the overall shape of the non-interacting DOS being almost unchanged (the magnetization is quite large ($m = 0.56$ at $n = 0.66$) and hence the electrons in the majority band are almost non-interacting). This implies that the arguments concerning the distribution of spectral weight in the non-interacting case and the corresponding kinetic energy are even applicable to the polarized, interact-

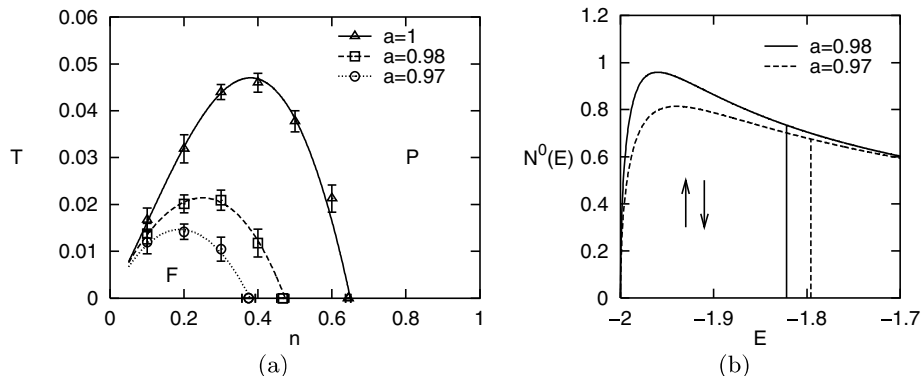


Fig. 4. (a) T vs. n phase diagram of the Hubbard model as obtained within DMFT; (b) corresponding shapes of the non-interacting DOS; Fermi energies for $n = 0.3$ are indicated by vertical lines [38].

ing case. The spectrum of the minority spins is slightly shifted to higher energies and has a pronounced peak around $E - \mu \simeq U = 6$.

From Fig. 3b we find the exchange splitting Δ between the majority and minority bands to be $\Delta = 0.8$. Comparing the quantity Um ($= 3.4$ in the present case) with Δ and T_c we find a characteristic hierarchy of energy scales:

$$Um > \Delta \gg T_c. \quad (4)$$

This is very different from results obtained by Stoner theory or effective one-particle theories like LDA where all three quantities are essentially equal. The generation of *small* energy scales is a genuine correlation effect.

To study the influence of the distribution of spectral weight on the stability of ferromagnetism within the DMFT systematically, Wahle et al. [38] recently solved the DMFT equations with a tunable model DOS,

$$N^0(E) = c \frac{\sqrt{D^2 - E^2}}{D + aE}, \quad (5)$$

with $c = (1 + \sqrt{1 - a^2})/(\pi D)$ and half-band width $D \equiv 2$. Here a is an asymmetry parameter which can be used to change the DOS continuously from a symmetric, Bethe lattice DOS ($a = 0$) to a DOS with a square-root divergence at the lower band edge ($a = 1$), corresponding to a fcc lattice with $t' = t/4$ in $d = 3$ (Fig. 1). The strong dependence of the stability of metallic ferromagnetism on the distribution of spectral weight is shown in Fig. 4a. Already a minute increase in spectral weight near the band edge of the non-interacting DOS, obtained by changing a from 0.97 to 0.98 (see Fig. 4b) is enough to almost double the stability region of the ferromagnetic phase. Obermeier et al. [39] found ferromagnetism even on a hypercubic, i.e., bipartite, lattice, but only at very large U values ($U > 30$).

The importance of genuine correlations for the stability of ferromagnetism is apparent from Fig. 5, where the DMFT results are compared with Hartree-Fock

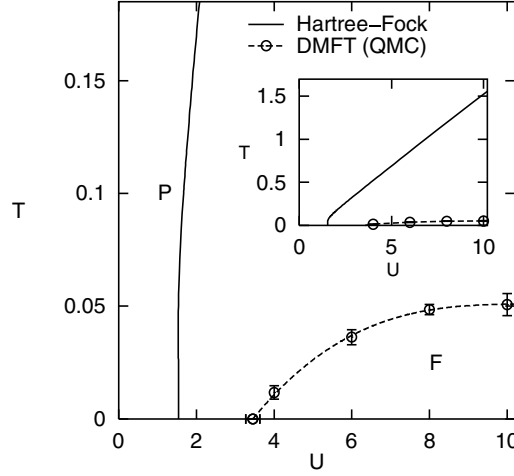


Fig. 5. T vs. U phase diagram for a strongly peaked DOS ($a = 0.98$, see Fig. 4b) at $n = 0.4$ within DMFT (circles; dashed line is guide to the eyes only) in comparison with Hartree-Fock (solid line) [38].

theory [38]. The quantum fluctuations, absent in Hartree-Fock theory, are seen to reduce the stability regime of ferromagnetism drastically. Spatial fluctuations (e.g., spin waves), absent in the DMFT, may reduce the stability regime further.

3.3 Additional Interactions

In the one-band Hubbard model only the local interaction is retained. Thereby several interactions which naturally arise when the Coulomb interaction is expressed in Wannier representation are neglected. Even in the limit of a single band and taking into account only NN contributions, four additional interactions appear [10,40,41,12]:

$$V_{1\text{-band}}^{\text{NN}} = \sum_{\text{NN}} \left[V n_i n_j + X \sum_{\sigma} (c_{i\sigma}^{\dagger} c_{j\sigma} + \text{h.c.}) (n_{i,-\sigma} + n_{j,-\sigma}) - 2F(\mathbf{S}_i \cdot \mathbf{S}_j + \frac{1}{4} n_i n_j) + F' (c_{i\uparrow}^{\dagger} c_{i\downarrow}^{\dagger} c_{j\downarrow} c_{j\uparrow} + \text{h.c.}) \right]. \quad (6)$$

Here the first term corresponds to a density-density interaction, the second term to a density-dependent hopping, and the fourth term describes the hopping of doubly occupied sites. In particular, the third term (with $F = F^*/Z > 0$)

$$H_F = -2 \frac{F^*}{Z} \sum_{\text{NN}} \mathbf{S}_i \cdot \mathbf{S}_j \quad (7)$$

describes the direct ferromagnetic exchange between electrons on NN sites. It is this interaction which Heisenberg singled out in his original spin-model as the

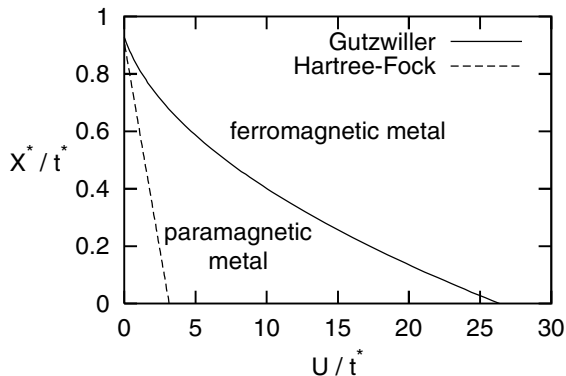


Fig. 6. Bond-charge interaction X vs. U phase diagram for the generalized model $H = H_{\text{Hub}} + H_X$ within the Gutzwiller approximation for the semi-elliptical Bethe DOS at $n = 0.9$ [44].

main source of ferromagnetism. It should be noted, however, that this interaction is present even when the electrons are free to move. The exchange interaction will be quite small, but nevertheless it favors ferromagnetic ordering in the most obvious way. Hirsch [41] argued that this term is the main driving force for metallic ferromagnetism in systems like iron, cobalt, and nickel. Indeed, one can show rigorously that a next-neighbor direct exchange interaction, if only chosen large enough, easily triggers the ferromagnetic instability [42,12,38]. Hence the NN exchange may well be important for systems on the verge of a ferromagnetic instability.

Another term that can be of importance for the stabilization of ferromagnetism is the bond-charge interaction ($X = X^*/\sqrt{Z}$)

$$H_X = \frac{X^*}{\sqrt{Z}} \sum_{\text{NN}\sigma} (c_{i\sigma}^\dagger c_{j\sigma} + \text{h.c.}) (n_{i,-\sigma} + n_{j,-\sigma}). \quad (8)$$

It effectively gives rise to correlated hopping, i.e., the hopping amplitude of an electron now depends on the presence of electrons of the opposite spin polarization. The magnitude of X has been estimated to be of order 0.1-1 eV [10,40], and hence X may be comparable to the hopping t , although typically smaller than U . Hartree-Fock treatment of $H = H_{\text{Hub}} + H_X$ shows that correlated hopping can lead to a spin-dependent band narrowing which may stabilize ferromagnetism [43]. We note that in DMFT H_X does not reduce to its Hartree-Fock contribution. The correlation effects introduced by H_X were recently studied within the Gutzwiller approximation (GA) [44]. The GA yields the exact evaluation of expectation values in terms of the Gutzwiller wave function in the limit of $d \rightarrow \infty$ [45,16] and goes beyond Hartree-Fock theory by including correlations explicitly. It was found that correlated hopping with $X > 0$ can lower the critical value of U for ferromagnetism considerably as shown in Fig. 6. Compared

to Hartree-Fock theory the ferromagnetic region of the phase diagram is seen to be much reduced. Recently it was also shown how to incorporate H_X into DMFT [46], at least in principle. It will be interesting to see how the GA results compare with future DMFT calculations for $H = H_{\text{Hub}} + H_X$.

Clearly, NN interactions may help to stabilize ferromagnetism. However, since the considerably larger Hubbard interaction U , together with a suitable kinetic energy, is already sufficient to trigger a ferromagnetic instability, the ferromagnetic exchange and bond-charge interactions appear to play only a secondary role.

4 Band Degeneracy and Local Exchange

Besides the NN Heisenberg exchange interaction another much larger exchange term is present in ferromagnets like iron, cobalt, and nickel, namely the local exchange between electrons in *different* orbitals on the same lattice site. It has long been speculated that this exchange interaction, which is known to align electrons on isolated atoms (Hund's first rule), may also lead to ferromagnetism in the bulk, being transmitted by the kinetic energy [47]. The simplest model for this mechanism is the two-band Hubbard model with local exchange F_0 and Coulomb repulsion V_0 between two orbitals $\nu = 1, 2$ (Fig. 7):

$$H_{2\text{-band}} = -t \sum_{\text{NN}, \sigma \nu} c_{i\nu\sigma}^\dagger c_{j\nu\sigma} + U \sum_{i\nu} n_{i\nu\uparrow} n_{i\nu\downarrow} + \sum_{i\sigma\sigma'} (V_0 - \delta_{\sigma\sigma'} F_0) n_{i1\sigma} n_{i2'\sigma'} - F_0 \sum_{\sigma \neq \sigma'} c_{i1\sigma}^\dagger c_{i1\sigma'} c_{i2\sigma'}^\dagger c_{i2\sigma}. \quad (9)$$

This two-band model [48] and its multi-band generalizations [49] were studied in considerable detail by various theoretical techniques [50]. Recent investigations [51] were triggered by the renewed interest in the electronic properties of transition metal oxides where the doubly degenerate e_g bands of the d electrons plays a very important role. At quarter filling (one electron per site; $n = 1$), ferromagnetism can be understood by superexchange within strong-coupling perturbation theory (Fig. 8). But away from quarter (or half) filling, the model is much more difficult to treat. In this regime DMFT, solved by QMC, once more provides a powerful tool to investigate this model [52], at least, if the last term in (9), i.e., the spin-flip contribution of F_0 , is neglected.

The calculated T vs. n phase diagram is shown in Fig. 9 for a symmetric Bethe DOS. Without Hund's rule coupling F_0 ferromagnetism is *unstable* for this DOS, at least at moderate values of U (see Sec. 3.2 for the one-band model and [52] for the two-band model). However, when the Hund's rule exchange is included a metallic ferromagnetic phase is stabilized between an alternating (staggered) orbital ordered state at quarter filling and antiferromagnetism at half filling.

While orbital ordering at $n = 1$ and antiferromagnetism at $n = 2$ can be understood by superexchange, the mechanism for metallic ferromagnetism is

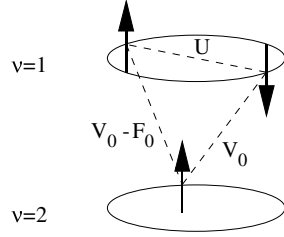


Fig. 7. Illustration of the local interactions (Hubbard U and Hund's rule couplings V_0 , F_0 defined in (9)) between electrons in a two-band model.

$\nu = 1$	$\uparrow \uparrow$	$\uparrow \downarrow$	$\downarrow \downarrow$	$\downarrow \uparrow$
$\nu = 2$	$\uparrow \uparrow$	$\downarrow \downarrow$	$\uparrow \uparrow$	$\downarrow \downarrow$
$\Delta E =$	0	$-2t^2/U$	$-2t^2/V_0$	$-2t^2/(V_0 - F_0)$

Fig. 8. Energy gain in second-order perturbation theory in t for four configurations with two electrons on two sites. Most favorable is ferromagnetism combined with an alternating occupation of orbitals. Note, that the true ground state is not the last configuration above, i.e., $c_{i=1\nu=1\uparrow}^\dagger c_{22\uparrow}^\dagger |0\rangle$, but the corresponding orbital singlet $\frac{1}{2}(c_{11\uparrow}^\dagger c_{22\uparrow}^\dagger - c_{12\uparrow}^\dagger c_{21\uparrow}^\dagger) |0\rangle$.

more subtle. Of course, the virtual superexchange processes described above are still present. But the additional electrons doped to the $n = 1$ system may now move freely between two singly occupied sites, i.e., are unhindered by the Coulomb repulsion U or V_0 . Furthermore, if the electrons on the two sites are spin aligned they do not even have to spend the exchange energy F_0 . Therefore a ferromagnetic alignment of the spins improves the kinetic energy of the electrons. This is essentially the concept of *double exchange* introduced by Zener [53] to explain ferromagnetism in manganites such as $\text{La}_{1-x}\text{Ca}_x\text{MnO}_3$, and put on a firmer theoretical fundament by Anderson and Hasegawa [54].

In manganites, the cubic crystal field splits the five Mn d orbitals into three t_{2g} and two e_g orbitals. The former have a lower energy and hybridize less strongly with the O p orbitals. Thus, the three electrons within the t_{2g} orbitals can be approximately described by a localized spin \mathbf{S}_i , with the remaining $1-x$ electrons occupying the e_g orbitals. If the Coulomb repulsion between e_g electrons is taken into account one arrives at a correlated electron model for manganites:

$$H = H_{2\text{-band}} - 2J \sum_{\nu=1}^2 \sum_i \mathbf{s}_{i\nu} \cdot \mathbf{S}_{i\nu}. \quad (10)$$

Here, $H_{2\text{-band}}$ is defined in (9), $\mathbf{s}_{i\nu} = \frac{1}{2} \sum_{\sigma\sigma'} c_{i\nu\sigma}^\dagger \boldsymbol{\tau}_{\sigma\sigma'} c_{i\nu\sigma'}$ denotes the e_g spin ($\boldsymbol{\tau}$: Pauli matrices), and J is the local exchange between t_{2g} and e_g electrons. Without Coulomb interaction ($U = V_0 = F_0 = 0$), the Hamiltonian (10) reduces to the ferromagnetic Kondo lattice model (KLM) which was investigated intensively in recent years [55]. This model forms the theoretical basis for the double exchange mechanism: at $J \gg t$, the optimization of the kinetic energy of the e_g electrons requires a ferromagnetic environment of t_{2g} spins. The KLM fails

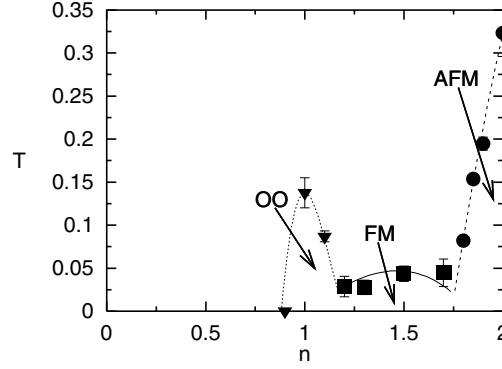


Fig. 9. T vs. n phase diagram of the two-band Hubbard model including antiferromagnetism (AF), ferromagnetism (FM), and orbital ordering (OO) for a Bethe DOS (total width $W = 4$), $U = 6$, $V_0 = 4$, and $F_0 = 2$ [52].

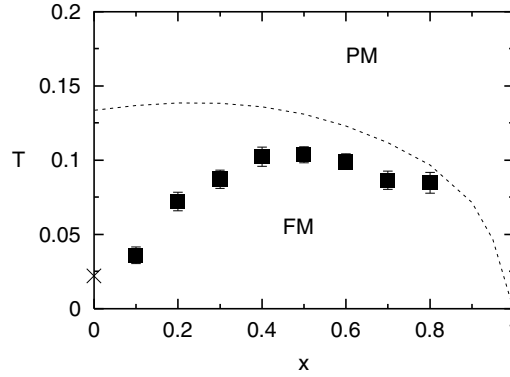


Fig. 10. Curie temperature T_c for the phase transition from the paramagnetic (PM) to the ferromagnetic (FM) phase as a function of Ca doping x ($n = 1 - x$). Dashed line: KLM with Bethe DOS (band width $W = 2$) and Hund's rule coupling $J = 3/2$; squares: correlated electron model (10) which also takes into account the Coulomb interaction between e_g electrons ($U = 8$, $V_0 = 6$, and $F_0 = 1$); cross: Weiss mean-field theory (superexchange) for this model [56]. Note that, without the coupling to the t_{2g} spin, no ferromagnetism is observed in Fig. 9 for $n < 1$ at similar interaction strengths.

to describe the correct behavior for $x \lesssim 0.5$ since it does not penalize double occupations, i.e., two e_g electrons on the same site. The suppression of double occupations induced by the Coulomb repulsions U and V_0 was investigated within DMFT in [56], and was shown to lead to a *crossover* from double exchange to superexchange. This results in a maximum in the Curie temperature (Fig. 10) in qualitative agreement with experiment [57].

5 Conclusion and Outlook

In this paper we reviewed recent developments in our understanding of the origin of metallic ferromagnetism in the one-band Hubbard model and in band-degenerate models on the basis of the dynamical mean-field theory (DMFT). In the one-band Hubbard model metallic ferromagnetism is found to exist in a surprisingly large region of the U vs. n phase diagram. A stabilization of this phase at intermediate U values requires a sufficiently large spectral weight near one of the band edges as is typical for frustrated (e.g., fcc-type) lattices which optimize the kinetic energy of the polarized state and, at the same time, frustrate the parasitic antiferromagnetic order. This finding, together with the results obtained for dimension $d = 1$ [32,15,14,19], finally establishes the stability of band ferromagnetism in the one-band Hubbard model on regular lattices and at intermediate values of the interaction U and density n . Thereby one of the prominent questions of many-body theory in this field is finally answered.

By contrast, the origin of metallic ferromagnetism in the band-degenerate Hubbard model at intermediate U values is not primarily a spectral weight effect but is already caused by moderately strong Hund's rule couplings. In this respect the origin of ferromagnetism in the orbitally degenerate model is more straightforward than that in the (less realistic) one-band case. Nevertheless, in the absence of orbital ordering the resulting magnetic phase diagrams are remarkably similar. The identification of a single main driving force for the stabilization of metallic ferromagnetism in the one-band and the band-degenerate Hubbard model, respectively, helps to differentiate between different mechanisms. However, in real systems these effects will tend to conspire, as is evident, for example, in nickel where an fcc lattice leads to a strongly asymmetric DOS and the band degeneracy brings with it Hund's rule couplings.

These insights also helped to understand the origin of itinerant ferromagnetism in more complicated models, e.g., the ferromagnetic Kondo lattice model with and without Coulomb correlations, which is employed to understand the physics of manganites with perovskite structure, like $\text{La}_{1-x}(\text{Sr,Ca})_x\text{MnO}_3$. It was found that in this model double exchange can explain ferromagnetism only for doping $x \gtrsim 0.5$. At lower values of x the suppression of double occupations by the local Coulomb repulsion becomes more and more important and leads to a crossover from double exchange to superexchange. This results in a maximum of the Curie temperature in qualitative agreement with experiment.

As discussed in the Introduction the problem of metallic ferromagnetism was, until recently, investigated by two essentially separate communities – one using model Hamiltonians together with many-body techniques, the other employing density functional theory (DFT) in the local density approximation (LDA). In view of the individual power of LDA and the model Hamiltonian approach it is highly desirable to combine these techniques, thereby creating an enormous potential for all future *ab initio* investigations of real materials, including, e.g., f -electron systems, Mott insulators and metallic ferromagnets. A combination of these two approaches had already been used to investigate band ferromagnetism some time ago [58]. Recently, a fusion has started to emerge in new

directions. One is the construction of multi-band Gutzwiller wave functions in combination with spin-density functional theory in the limit of large coordination numbers [20]. It was already successfully applied to ferromagnetic nickel, leading to significant improvements over LDA results. The other is the *ab initio* computational scheme LDA+DMFT [23] which was recently used to investigate transition metal oxides and to calculate the magnetic excitation spectrum of ferromagnetic iron [22]. Without doubt these and related methods [59] will rapidly develop into standard tools for future investigations of band ferromagnetism and other electronic correlation phenomena.

Acknowledgments

We thank M. Ulmke and J. Wahle for fruitful discussions. This work was supported in part by the Sonderforschungsbereich 484 of the Deutsche Forschungsgemeinschaft and by a Feodor-Lynen grant of the Alexander von Humboldt-Foundation (KH).

References

1. N. W. Ashcroft, N. D. Mermin: *Solid State Physics* (Saunders College, Philadelphia 1976)
2. D. C. Mattis: *The Theory of Magnetism I* (Springer, Berlin 1988)
3. P. Fazekas: *Lecture Notes on Electron Correlation and Magnetism* (World Scientific, Singapore 1999)
4. E. H. Lieb, D. Mattis: Phys. Rev. **125**, 164 (1962)
5. E. H. Lieb: in *The Hubbard Model: Its Physics and Mathematical Physics*, edited by D. Baeriswyl et al., p. 1, (Plenum, New York 1995)
6. A. Mielke: J. Phys. A **24**, 3311 (1991); H. Tasaki: Phys. Rev. Lett. **69**, 1608 (1992); A. Mielke, H. Tasaki: Commun. Math. Phys. **158**, 341 (1993); H. Tasaki: Phys. Rev. Lett. **73**, 1158 (1994); H. Tasaki: Phys. Rev. Lett. **75**, 4678 (1995); H. Tasaki: Prog. Theor. Phys. **99**, 489 (1998)
7. P. Hohenberg, W. Kohn: Phys. Rev. B **136**, 864 (1964); W. Kohn, L. J. Sham: Phys. Rev. **140**, 4A, A1133 (1965)
8. V. L. Moruzzi, J. F. Janak, A. R. Williams: *Calculated Electronic Properties of Metals* (Pergamon Press, New York 1978)
9. M. C. Gutzwiller: Phys. Rev. Lett. **10**, 59 (1963)
10. J. Hubbard: Proc. Roy. Soc. London A **276**, 238 (1963)
11. J. Kanamori: Prog. Theor. Phys. **30**, 275 (1963)
12. For reviews see D. Vollhardt, N. Blümer, K. Held, M. Kollar, J. Schlipf, M. Ulmke: Z. Phys. B **103**, 283 (1997); D. Vollhardt, N. Blümer, K. Held, M. Kollar, J. Schlipf, M. Ulmke, J. Wahle: *Advances In Solid State Physics* 38, p. 383 (Vieweg, Wiesbaden 1999)
13. R. Shankar: Rev. Mod. Phys. **66**, 129 (1994); C. J. Halboth, W. Metzner: Phys. Rev. B **61**, 7364 (2000); C. Honerkamp: Ph.D. Thesis, Diss. No. 13868, ETH-Zürich (2000)
14. K. Penc, H. Shiba, F. Mila, T. Tsukagoshi: Phys. Rev. B **54**, 4056 (1996)
15. P. Pieri, S. Daul, D. Baeriswyl, M. Dzierzawa: Phys. Rev. B **54**, 9250 (1996)

16. W. Metzner, D. Vollhardt: Phys. Rev. Lett. **62**, 324 (1989)
17. G. S. Uhrig: Phys. Rev. Lett. **77**, 3629 (1996)
18. T. Hanisch, G. S. Uhrig, E. Müller-Hartmann: Phys. Rev. B **56**, 13960 (1997)
19. S. Daul, R. Noack: Z. Phys. B **103**, 293 (1997); S. Daul, R. Noack: Phys. Rev. B **58**, 2635 (1998)
20. J. Bünemann, F. Gebhard, W. Weber: J. Phys. Condens. Matter **9**, 7343 (1997); J. Bünemann, W. Weber, F. Gebhard: Phys. Rev. B **57**, 6896 (1998); J. Bünemann, F. Gebhard, W. Weber: condmat/0006283, to be published in Foundations of Physics (2000)
21. V. I. Anisimov, A. I. Poteryaev, M. A. Korotin, A. O. Anokhin, G. Kotliar: J. Phys.: Cond. Matt. **9**, 7359 (1997)
22. M. I. Katsnelson, A. I. Lichtenstein: Phys. Rev. B **57**, 6884 (1998)
23. For an introduction into LDA+DMFT, see K. Held, I. A. Nekrasov, N. Blümer, V. I. Anisimov, D. Vollhardt: preprint cond-mat/00010395, to be published in Int. J. Mod. Phys. C
24. D. Vollhardt: *Correlated Electron Systems*, ed. by V. J. Emery (World Scientific, Singapore 1993); T. Pruschke, M. Jarrell, J. K. Freericks: Adv. Phys. **44**, 187 (1995); A. Georges, G. Kotliar, W. Krauth, M. Rozenberg, Rev. Mod. Phys. **68**, 13 (1996)
25. G. Moeller, Q. Si, G. Kotliar, M. Rozenberg, D. S. Fisher: Phys. Rev. Lett. **74**, 2082 (1995); J. Schlipf, M. Jarrell, P. G. J. van Dongen, N. Blümer, S. Kehrein, Th. Pruschke, D. Vollhardt: Phys. Rev. Lett. **82**, 4890 (1999); M. J. Rozenberg, R. Chitra, G. Kotliar: Phys. Rev. Lett. **83**, 3498 (1999); R. Bulla: Phys. Rev. Lett. **83**, 136 (1999)
26. A. Georges, G. Kotliar: Phys. Rev. B **45**, 6479 (1992)
27. Th. Pruschke, D. L. Cox, M. Jarrell: Phys. Rev. B **47**, 3553 (1993)
28. J. E. Hirsch, R. M. Fye, Phys. Rev. Lett. **56**, 2521 (1986); M. Jarrell, Phys. Rev. Lett. **69**, 168 (1992); M. Rozenberg, X. Y. Zhang, G. Kotliar, Phys. Rev. Lett. **69**, 1236 (1992); A. Georges, W. Krauth, Phys. Rev. Lett. **69**, 1240 (1992)
29. M. Caffarel, W. Krauth: Phys. Rev. Lett. **72**, 1545 (1994)
30. R. Bulla, Phys. Rev. Lett. **83**, 136 (1999); R. Bulla, T. Costi, D. Vollhardt: in preparation
31. Y. Nagaoka: Phys. Rev. **147**, 392 (1966)
32. E. Müller-Hartmann: J. Low Temp. Phys. **99**, 349 (1995)
33. W. Hofstetter, D. Vollhardt: Ann. Physik **7**, 48 (1998)
34. E. Müller-Hartmann: *Proc. V Symp. Phys. of Metals*, ed. E. Talik and J. Szade, p.22 (Poland 1991)
35. M. Ulmke: Euro. Phys. J. B **1**, 301 (1998)
36. M. Ulmke, V. Janiš, D. Vollhardt: Phys. Rev. B **51**, 10411 (1995)
37. M. Potthoff, T. Herrmann, W. Nolting: Eur. Phys. J. B **4**, 485 (1998); T. Wegner, M. Potthoff, W. Nolting, Phys. Rev. B **57**, 6211 (1998); T. Herrmann, W. Nolting: J. Phys.: Condens. Matter **11**, 89 (1999); W. Nolting: in *Lectures on the Physics of Highly Correlated Electron Systems IV*, AIP Conference Proceedings **527**, p. 118 (Melville, New York 2000)
38. J. Wahle, N. Blümer, J. Schlipf, K. Held, D. Vollhardt: Phys. Rev. B **58**, 12749 (1998)
39. T. Obermeier, T. Pruschke, J. Keller: Phys. Rev. B **56**, R8479 (1997)
40. J. T. Gammel, D. K. Campbell: Phys. Rev. Lett. **60**, C 71 (1988); D. K. Campbell, J. T. Gammel, E. Y. Loh Jr.: Phys. Rev. B **38**, 12043 (1988)
41. J. E. Hirsch: Phys. Rev. B **40**, 2354 (1989); 9061 (1989); S. Tang, J. E. Hirsch: Phys. Rev. B **42**, 771 (1990)

42. R. Strack, D. Vollhardt: Phys. Rev. Lett. **72**, 3425 (1994); M. Kollar, R. Strack, D. Vollhardt: Phys. Rev. B **53**, 9225 (1996)
43. J. Amadon, J. E. Hirsch: Phys. Rev. B **54**, 6364 (1996)
44. M. Kollar, D. Vollhardt: preprint cond-mat/0008015, to be published in Phys. Rev. B **63**(2001)
45. W. Metzner, D. Vollhardt: Phys. Rev. Lett. **59**, 121 (1987)
46. A. Schiller: Phys. Rev. B **60**, 15660 (1999)
47. J. C. Slater: Phys. Rev. **49**, 537 (1936); J. H. van Vleck: Rev. Mod. Phys. **25**, 220 (1953)
48. L. M. Roth: Phys. Rev. **149**, 306 (1966); K. I. Kugel', D. I. Khomskii: Sov. Phys.-JETP **37**, 725 (1973); M. Cyrot, C. Lyon-Caen: J. Phys. C **36**, 253 (1975); K.A. Chao, J. Spalek, A. M. Oleś: Phys. Stat. Sol. (b) **84**, 747 (1977); W. Gill, D. J. Scalapino: Phys. Rev. B **35**, 215 (1987); H. Hasegawa: Phys. Rev. B **56**, 1196 (1997); D. Meyer, W. Nolting: J. Phys.: Condens. Matter **11**, 5811 (1999)
49. A. M. Oleś: Phys. Rev. B **23**, 271 (1981); G. Stollhoff, P. Thalmeier: Z. Phys. B **43**, 13 (1981); A. M. Oleś: Phys. Rev. B **28**, 327 (1983); A. M. Oleś, G. Stollhoff: Phys. Rev. B **29**, 314 (1984); A. M. Oleś, G. Stollhoff: Europhys. Lett. **5**, 175 (1988); W. Nolting, W. Borgiel: Phys. Rev. B **39**, 6962 (1989); G. Stollhoff, A. M. Oleś, V. Heine: Phys. Rev. B **41**, 7028 (1990); R. Frésard, G. Kotliar: Phys. Rev. B **56**, 12909 (1997)
50. Another two-band model for ferromagnetism is the periodic Anderson model, see G. G. Reddy, D. Meyer, S. Schwieger, A. Ramakanth, W. Nolting: J. Phys: Condens. Matter **12**, 7463 (2000); D. Meyer, W. Nolting: Phys. Rev. B **62**, 5657 (2000); D. Meyer, W. Nolting: to be published in Eur. Phys. J. B (2000)
51. J. Kuei, R. T. Scalettar: Phys. Rev. B **55**, 14968 (1997); J. E. Hirsch: Phys. Rev. B **56**, 11022 (1997); M. Fleck, A. M. Oleś, L. Hedin: Phys. Rev. B **56**, 3159 (1997); T. Okabe: Prog. Theor. Phys. **98**, 331 (1997); P. Fazekas: condmat/0011354, to be published in Foundations of Physics (2000)
52. K. Held, D. Vollhardt: Euro. Phys. J. B **5**, 473 (1998)
53. C. Zener: Phys. Rev. **82**, 403 (1951)
54. P. W. Anderson, H. Hasegawa: Phys. Rev. **100**, 675 (1955)
55. See for example, N. Furukawa: J. Phys. Soc. Jap. **63**, 3214 (1994); E. Müller-Hartmann, E. Dagotto: Phys. Rev. B **54**, 6819 (1996); S. Yunoki, A. Moreo, E. Dagotto: Phys. Rev. Lett. **81**, 5612 (1998); A. Moreo, S. Yunoki, E. Dagotto: Science **283**, 2034 (1999); E. Dagotto, S. Yunoki, A. Moreo: in *Physics in Manganites*, ed. T. A Kaplan, S. D. Mahanti (Kluwer Academic/Plenum, New York 1999); N. Furukawa: in *Physics in Manganites*, ed. T. A Kaplan, S. D. Mahanti (Kluwer Academic/Plenum, New York 1999); S. Yunoki, J. Hu, A. L. Malvezzi, A. Moreo, N. Furukawa, E. Dagotto: Phys. Rev. Lett. **80**, 845 (1998); J. van den Brink, D. I. Khomskii: Phys. Rev. Lett. **82**, 1016 (1999)
56. K. Held, D. Vollhardt: Phys. Rev. Lett. **84**, 5168 (2000)
57. P. Schiffer, A. P. Ramirez, W. Bao, S.-W. Cheong: Phys. Rev. Lett. **75**, 3336 (1995)
58. W. Nolting, W. Borgiel, V. Dose, Th. Fauster: Phys. Rev. B **40**, 5015 (1989); W. Borgiel, W. Nolting, M. Donath: Solid State Commun. **78**, 825 (1989); W. Borgiel, W. Nolting: Z. Phys. B **78**, 241 (1990); W. Nolting, A. Vega, Th. Fauster: Z. Phys. B **96**, 357 (1995)
59. T. Wegner, M. Potthoff, W. Nolting, Phys. Rev. B **61**, 1386 (2000)

Ferromagnetism in the Hubbard Model

W. Nolting, M. Potthoff, T. Herrmann, and T. Wegner

Lehrstuhl Festkörpertheorie, Institut für Physik, Humboldt-Universität zu Berlin

Abstract. We investigate the possibility and stability of bandferromagnetism in the single-band Hubbard model. This model poses a highly non-trivial many-body problem the general solution of which has not been found up to now. Approximations are still unavoidable. Starting from a simple two-pole ansatz for the spectral density our approach is systematically improved by focusing on the influence of quasiparticle damping and the correct weak-and strong coupling behaviour. The compatibility of the different approximate steps with decisive moment sum rules is analysed and the importance of a spin-dependent band shift mediated by higher correlation functions is worked out. Results are presented in terms of temperature- and band occupation-dependent quasiparticle densities of states and band structures as well as spontaneous magnetisations, susceptibilities and Curie temperatures for varying electron densities and coupling strengths. Comparison is made to numerically essentially exact Quantum Monte Carlo calculations recently done by other authors using dynamical mean field theory for infinite-dimensional lattices. The main conclusion will be that the Hubbard model provides a qualitatively correct description of bandferromagnetism if quasiparticle damping and selfconsistent spin-dependent bandshifts are properly taken into account.

1 Introduction

Ferromagnetism is bound to the existence of permanent magnetic moments. If these belong to itinerant electrons in a partially filled conduction band one speaks of bandferromagnetism [1]. Archetypical representatives are the classical 3d ferromagnets Fe, Co, Ni. The microscopic interpretation of bandferromagnetism is one of the most interesting and most complicated many-particle problems in solid state physics. The simple but fairly successful “Stoner criterion”

$$U \varrho_0(E_F) > 1 \quad (1)$$

(U : intraatomic Coulomb interaction, ϱ_0 : free Bloch-density of states (B-DOS), E_F : Fermi energy) defines as a minimum set of ingredients for a theoretical model to describe bandferromagnetism the Pauli-principle, the kinetic energy, the Coulomb interaction (strong and strongly screened), and the lattice structure. This minimum set is realized in the Hubbard-Hamiltonian (2) for correlated electrons on a lattice in a non-degenerate energy band,

$$\hat{H} = \sum_{ij,\sigma} (T_{ij} - \mu \delta_{ij}) c_{i\sigma}^\dagger c_{j\sigma} + \frac{1}{2} U \sum_{i\sigma} n_{i\sigma} n_{i-\sigma} \quad (2)$$

(μ : chemical potential). The Coulomb interaction is restricted to its intraatomic part only ($n_{i\sigma} = c_{i\sigma}^\dagger c_{i\sigma}$), while the kinetic energy contains the hopping integrals T_{ij} being strongly related to the lattice structure. The Pauli principle is guaranteed by the formalism of second quantization. $c_{i\sigma}^\dagger$ ($c_{i\sigma}$) is the creation (annihilation) operator for an electron with spin \uparrow or \downarrow at lattice site \mathbf{R}_i .

The physics of the Hubbard-model is decisively determined by the Coulomb coupling U/W (W : Bloch-bandwidth), the lattice structure and the band occupation $n = \frac{1}{N} \sum_{\sigma} \langle n_{\sigma} \rangle$ ($0 \leq n \leq 2$; N : number of lattice sites).

In spite of its simple structure the Hamiltonian (2) provokes a rather sophisticated many-body problem, that could be solved in the past only for a few special cases. In general approximations are unavoidable. So it was not fully clarified until recently whether or not ferromagnetism is possible in the Hubbard-model for finite U , finite temperatures T and band occupations away from half filling $n=1$. Nagaoka showed [2] for the special case $U = \infty$ and electron numbers $N_e = N \pm 1$ on an sc or bcc lattice and $N_e = N + 1$ on an fcc lattice, respectively, that the fully spin-polarized particle system represents the ground state. However, the (numerical) proof of finite-temperature ferromagnetism in an extended parameter region was only recently given by Ulmke [3] for an infinite dimensional ($d = \infty$) fcc-type lattice by use of Quantum Monte Carlo (QMC) calculations in connection with Dynamical Mean Field Theory (DMFT) [4,5]. On the other hand, the certainty that ferromagnetism exists in the Hubbard model does not at all mean that the phenomenon itself is understood. What is the physical mechanism enforcing ferromagnetic spin order of itinerant electrons? This question can be answered, if at all, better by analytical approaches to the highly complicated electron correlation problem than by purely numerical evaluations. Starting from some basic features we shall construct in the following chapters three different theories for the Hubbard model to contribute to an answer of the above question. The theories are constructed in such a way that each differs from the preceding one by eliminating an obvious shortcoming. We start from a simple spectral density approach (SDA) which suggests itself by some rigorous strong coupling features. However, it suffers from a complete neglect of quasiparticle damping and a wrong weak-coupling behaviour. By use of a modified alloy analogy (MAA) the advantages of the SDA are retained but quasiparticle damping is included. Comparison of the SDA- and the MAA-results helps us to recognize the influence of quasiparticle damping on magnetic stability. The weak coupling behaviour, however, remains insufficient. From a modified perturbation theory (MPT) which correctly reproduces the weak- as well as the strong-coupling limit, we learn by comparison with SDA and MAA how decisive the correct weak coupling (low energy) description is for a theoretical approach that aims at the strong-coupling phenomenon ferromagnetism.

2 Hubbard Model Basic Features

It is commonly accepted that ferromagnetism is a strong-coupling phenomenon. A theoretical approach should therefore be reliable first of all in the $U \gg W$

regime. Practically all information we are interested in can be derived from the retarded single-electron Green's function [6]

$$G_{\mathbf{k}\sigma}(E) = \langle\langle c_{\mathbf{k}\sigma}; c_{\mathbf{k}\sigma}^+ \rangle\rangle_E = -i \int_0^\infty dt \exp(\frac{i}{\hbar} Et) \langle [c_{\mathbf{k}\sigma}(t), c_{\mathbf{k}\sigma}^+(0)]_+ \rangle \quad (3)$$

$$c_{\mathbf{k}\sigma} = \frac{1}{\sqrt{N}} \sum_i c_{i\sigma} \exp(-i\mathbf{k}\mathbf{R}_i) \quad (4)$$

$[\dots]_+(-)$ means the anticommutator (commutator) and $\langle \dots \rangle$ the grandcanonical average. \mathbf{k} is a wavevector from the first Brillouin zone. Of equivalent importance is the single-electron spectral density being directly related to the bare line shape of an angle- and spin-resolved (direct or inverse) photoemission experiment:

$$S_{\mathbf{k}\sigma}(E) = -\frac{1}{\pi} \text{Im} G_{\mathbf{k}\sigma}(E + i0^+) \quad (5)$$

According to the pioneering work of Harris and Lange [7] we know that in the strong coupling limit $S_{\mathbf{k}\sigma}(E)$ is built up by two main peaks near T_0 and $T_0 + U$ where T_0 is the centre of gravity of the free Bloch band, and additional satellite peaks at $T_0 + pU$ ($p = -1, -2, \dots; p = 2, 3, \dots$) (s. Fig.1). The spectral weights (\propto peak area) of the satellites, however, decrease rapidly with increasing distance from the main peaks. Already the next neighbours ($p = -1, +2$) acquire only a weight of order $(\frac{W}{U})^4$ being therefore negligible in the strong-coupling regime. So we can assume for $U \gg W$ a two-peak structure of the spectral density. The exact shapes of the peaks are not known, but the centres of gravity are,

$$T_{1\sigma}(\mathbf{k}) = T_0 + (1 - \langle n_{-\sigma} \rangle)(\varepsilon(\mathbf{k}) - T_0) + \langle n_{-\sigma} \rangle B_{\mathbf{k}-\sigma} + 0(\frac{W}{U})^4 \quad (6)$$

$$T_{2\sigma}(\mathbf{k}) = T_0 + U + \langle n_{-\sigma} \rangle(\varepsilon(\mathbf{k}) - T_0) + (1 - \langle n_{-\sigma} \rangle)B_{\mathbf{k}-\sigma} + 0(\frac{W}{U})^4 \quad (7)$$

as well as their spectral weights:

$$\alpha_{1\sigma}(\mathbf{k}) = (1 - \langle n_{-\sigma} \rangle) + 0(\frac{W}{U}) = 1 - \alpha_{2\sigma}(\mathbf{k}) \quad (8)$$

At least formally the centres of gravity carry a spin-dependence which may give rise to an additional exchange splitting of the two main peaks as the fundamental precondition for ferromagnetism. In the following it is demonstrated that such a spin asymmetry is mainly due to the "band correction" $B_{\mathbf{k}-\sigma}$:

$$B_{\mathbf{k}-\sigma} = B_{-\sigma} + F_{\mathbf{k}-\sigma} \quad (9)$$

The local term $B_{-\sigma}$ ("band-shift") can be interpreted as a correlated electron hopping:

$$\langle n_{-\sigma} \rangle (1 - \langle n_{-\sigma} \rangle) B_{-\sigma} = \frac{1}{N} \sum_{i,j}^{i \neq j} T_{ij} \langle c_{i-\sigma}^+ c_{j-\sigma} (2n_{i\sigma} - 1) \rangle \quad (10)$$

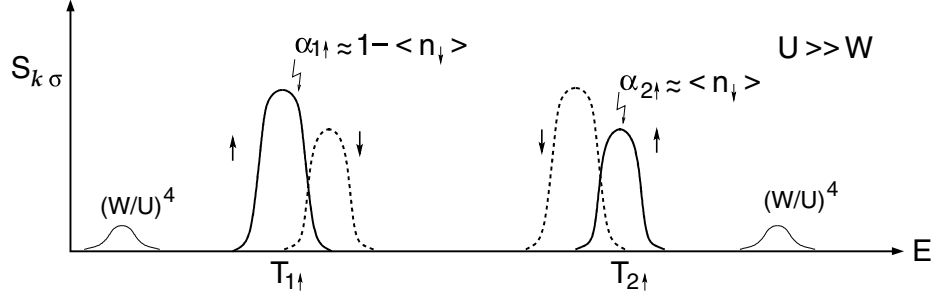


Fig. 1. Single electron spectral density of the Hubbard model in the strong coupling regime ($U \gg W$) as function of energy.

For $U \gg W$ and less than half-filled bands double occupancies are very unlikely so that the second term in the bracket dominates. That means that the shift of the σ -spectrum is correlated with the negative kinetic energy of the $(-\sigma)$ -electrons. For further evaluations it will turn out to be decisive that the band-shift $B_{-\sigma}$ can exactly be expressed by the single-electron spectral-density [8,9]

$$\langle n_{-\sigma} \rangle (1 - \langle n_{-\sigma} \rangle) B_{-\sigma} = \frac{1}{N\hbar} \sum_{\mathbf{k}} (\varepsilon(\mathbf{k}) - T_0) \int_{-\infty}^{\infty} dE f_{-}(E) \left(\frac{2}{U} (E - \varepsilon(\mathbf{k}) - 1) \right) S_{\mathbf{k}-\sigma}(E - \mu) \quad (11)$$

$f_{-}(E) = (\exp \beta(E - \mu) + 1)^{-1}$ is the Fermi function. $B_{-\sigma}$ obviously disappears in the zero-bandwidth limit ($\varepsilon(\mathbf{k}) \rightarrow T_0 \forall \mathbf{k}$).

The \mathbf{k} -dependent part of the band correction (9) is built up by density-density, double hopping and spinflip correlation terms

$$\begin{aligned} \langle n_{-\sigma} \rangle (1 - \langle n_{-\sigma} \rangle) F_{\mathbf{k}-\sigma} = & \frac{1}{N} \sum_{i,j}^{i \neq j} T_{ij} \exp(-i\mathbf{k}(\mathbf{R}_i - \mathbf{R}_j)) (\langle n_{i-\sigma} n_{j-\sigma} \rangle - \langle n_{j-\sigma} \rangle^2 \\ & + \langle c_{j-\sigma}^{\dagger} c_{j\sigma}^{\dagger} c_{i-\sigma} c_{i\sigma} \rangle + \langle c_{j\sigma}^{\dagger} c_{j-\sigma} c_{i-\sigma}^{\dagger} c_{i\sigma} \rangle) \end{aligned} \quad (12)$$

It vanishes in the zero-bandwidth limit and has no direct influence on the centres of gravity $T_{1,2\sigma}$ of the quasiparticle subbands (Hubbard bands) that emerge from the two spectral density peaks (Fig. 1):

$$\hat{T}_{1\sigma} = \frac{1}{N} \sum_{\mathbf{k}} T_{1\sigma}(\mathbf{k}) = T_0 + \langle n_{-\sigma} \rangle B_{-\sigma} \quad (13)$$

$$\hat{T}_{2\sigma} = \frac{1}{N} \sum_{\mathbf{k}} T_{2\sigma}(\mathbf{k}) = T_0 + U + (1 - \langle n_{-\sigma} \rangle) B_{-\sigma} \quad (14)$$

$F_{\mathbf{k}-\sigma}$ may, however, lead to a spin-dependent bandwidth correction competing then with the other band narrowing terms in (6) and (7), respectively. The importance of $F_{\mathbf{k}-\sigma}$ with respect to ferromagnetism shall be discussed in Sect.III.

Unfortunately, it cannot be expressed by the spectral density as the band shift $B_{-\sigma}$ by eq. (11). A determination of $F_{\mathbf{k}-\sigma}$ therefore requires further approximations.

If $B_{\mathbf{k}-\sigma}$ has indeed such vital implications a theoretical approach should handle this term with special care. That can effectively be controlled by the spectral moments of the spectral density,

$$M_{\mathbf{k}\sigma}^{(n)} = \frac{1}{\hbar} \int_{-\infty}^{\infty} dE E^n S_{\mathbf{k}\sigma}(E) \quad n = 0, 1, 2, 3, \dots \quad (15)$$

which can be calculated independently of $S_{\mathbf{k}\sigma}(E)$ via

$$M_{\mathbf{k}\sigma}^{(n)} = \langle [(\hbar \frac{\partial}{\partial t})^n c_{\mathbf{k}\sigma}(t), c_{\mathbf{k}\sigma}^\dagger(t')]_+ \rangle_{t=t'} \quad (16)$$

In practice, however, the moments are useful only for low order n because with increasing n eq.(16) produces higher expectation values which are usually unknown and not expressible by the spectral density, either. The important band correction $B_{\mathbf{k}-\sigma}(E)$ first appears in $M_{\mathbf{k}\sigma}^{(3)}$ [8,9].

$$M_{\mathbf{k}\sigma}^{(0)} = 1 \quad (17)$$

$$M_{\mathbf{k}\sigma}^{(1)} = \hat{\varepsilon}(\mathbf{k}) + U \langle n_{-\sigma} \rangle \quad (18)$$

$$M_{\mathbf{k}\sigma}^{(2)} = \hat{\varepsilon}^2(\mathbf{k}) + 2\hat{\varepsilon}(\mathbf{k})U \langle n_{-\sigma} \rangle + U^2 \langle n_{-\sigma} \rangle \quad (19)$$

$$M_{\mathbf{k}\sigma}^{(3)} = \hat{\varepsilon}^3(\mathbf{k}) + 3\hat{\varepsilon}^2(\mathbf{k})U \langle n_{-\sigma} \rangle + \hat{\varepsilon}(\mathbf{k})U^2 \langle n_{-\sigma} \rangle (2 + \langle n_{-\sigma} \rangle) + U^3 \langle n_{-\sigma} \rangle + U^2 \langle n_{-\sigma} \rangle (1 - \langle n_{-\sigma} \rangle) (B_{\mathbf{k}-\sigma} + T_0 - \mu) \quad (20)$$

($\hat{\varepsilon}(\mathbf{k}) = \varepsilon(\mathbf{k}) - \mu$). A necessary condition for a theoretical approach to be consistent with the strong-coupling results (6),(7),(8) is that the first four moments $M_{\mathbf{k}\sigma}^{(n)}$, $n = 0, 1, 2, 3$ are correctly reproduced. The condition becomes even sufficient when additionally the zero-bandwidth limit [10] is fulfilled. One can elegantly check the strong coupling consistency by use of the high-energy expansion of the single-electron Green's function

$$G_{\mathbf{k}\sigma}(E) = \int_{-\infty}^{+\infty} dE' \frac{S_{\mathbf{k}\sigma}(E')}{E - E'} \longrightarrow \hbar \sum_{n=0}^{\infty} \frac{M_{\mathbf{k}\sigma}^{(n)}}{E^{n+1}} \quad (21)$$

which can also be used in the Dyson equation,

$$G_{\mathbf{k}\sigma}(E) = G_{\mathbf{k}}^{(0)}(E) + G_{\mathbf{k}}^{(0)}(E) \frac{1}{\hbar} \Sigma_{\mathbf{k}\sigma}(E) G_{\mathbf{k}\sigma}(E), \quad (22)$$

where

$$G_{\mathbf{k}}^{(0)}(E) = \hbar(E + \mu - \varepsilon(\mathbf{k}))^{-1} \quad (23)$$

is the $U = 0$ Green's function, to yield a respective expansion for the selfenergy:

$$\Sigma_{\mathbf{k}\sigma}(E) = \sum_{m=0}^{\infty} \frac{C_{\mathbf{k}\sigma}^{(m)}}{E^m} \quad (24)$$

The coefficients $C_{\mathbf{k}\sigma}^{(m)} = f_m(M_{\mathbf{k}\sigma}^{(0)}, \dots, M_{\mathbf{k}\sigma}^{(m+1)})$ are simple functions of the moments up to order $m + 1$:

$$C_{\mathbf{k}\sigma}^{(0)} = M_{\mathbf{k}\sigma}^{(1)} - (\varepsilon(\mathbf{k}) - \mu) \quad (25)$$

$$C_{\mathbf{k}\sigma}^{(1)} = M_{\mathbf{k}\sigma}^{(2)} - (M_{\mathbf{k}\sigma}^{(1)})^2 \quad (26)$$

$$C_{\mathbf{k}\sigma}^{(2)} = M_{\mathbf{k}\sigma}^{(3)} - 2M_{\mathbf{k}\sigma}^{(2)}M_{\mathbf{k}\sigma}^{(1)} + (M_{\mathbf{k}\sigma}^{(1)})^3 \quad (27)$$

...

For a given theoretical approach one can easily control whether or not the leading term in the expansions (21) and (24), respectively, match with the rigorously calculated moments. However, even the opposite procedure may be useful, inferring approximately the overall energy dependence of the Green's function and the selfenergy, respectively, from the first few exactly calculated terms. A proposal how this can be done is exemplified in the next Section.

Rigorous statements are of course also possible in the weak coupling regime ($U \ll W$). As mentioned in Sect. I it remains a challenging problem to find out how decisive weak coupling and low-energy properties are for a theoretical approach to correctly describe the strong-coupling phenomenon "ferromagnetism". In the "diagram-language" the Dyson equation (22) reads

$$\begin{array}{c} \text{Diagram: Double line with arrow} = \text{Diagram: Single line with arrow} + \text{Diagram: Single line with arrow and a loop labeled } \Sigma \\ G_{\mathbf{k}\sigma}(E) = G_{\mathbf{k}}^{(0)}(E) + G_{\mathbf{k}}^{(0)}(E) \frac{1}{\hbar} \Sigma_{\mathbf{k}\sigma}(E) G_{\mathbf{k}\sigma}(E) \end{array}$$

Using standard perturbation theory [6,11,12] one has to sum up for the selfenergy $\Sigma_{\mathbf{k}\sigma}(E)$ all dressed skeleton diagrams. A "skeleton diagram" is a selfenergy diagram that does not contain any selfenergy insertion in its propagators. If in addition the propagators are "full" Green's functions $G_{\mathbf{k}\sigma}(E)$ then the skeleton is "dressed". That means for the Hubbard model up to second order:

$$\begin{array}{c} \text{Diagram: Loop with } \Sigma \text{ and } \sigma \\ = \text{Diagram: Loop with } -\sigma \text{ and } \sigma \\ + \text{Diagram: Loop with } -\sigma \text{ and } \sigma \\ + \dots \end{array}$$

Conventional diagram rules [6,11,12] yield as selfconsistent second order perturbation theory in $\frac{U}{W}$:

$$\Sigma_{\mathbf{k}\sigma}(E) = U\langle n_{-\sigma} \rangle + U^2 \Delta_{\mathbf{k}\sigma}(E) + 0(U^3) \quad (28)$$

The linear term is the Hartree-Fock (Stoner) part while the more complicated second order contribution is in general non-local, complex, and energy dependent:

$$\begin{aligned} \Delta_{\mathbf{k}\sigma}(E) = & \frac{1}{\hbar^3 N^2} \sum_{\mathbf{q}\mathbf{p}} \int \int \int d\varepsilon_1 d\varepsilon_2 d\varepsilon_3 \frac{S_{\mathbf{q}+\mathbf{k}\sigma}(\varepsilon_1 - \mu) S_{\mathbf{p}-\sigma}(\varepsilon_2 - \mu) S_{\mathbf{p}-\mathbf{q}-\sigma}(\varepsilon_3 - \mu)}{E + \mu - \varepsilon_1 + \varepsilon_2 - \varepsilon_3 + i0^+} \\ & \times (f_{-}(\varepsilon_1) f_{-}(-\varepsilon_2) f_{-}(\varepsilon_3) + f_{-}(-\varepsilon_1) f_{-}(\varepsilon_2) f_{-}(-\varepsilon_3)) \end{aligned} \quad (29)$$

S is the full spectral density which has to be determined self-consistently. Several alternatives are thinkable which are correct and equivalent up to order U^2 . One of these is to replace the “full” spectral density in (29) by its Hartree-Fock version [13,14]

$$S_{\mathbf{k}\sigma}^{(1)}(E) = S_{\mathbf{k}\sigma}^{(0)}(E - U\langle n_{-\sigma} \rangle^{(1)}) \quad (30)$$

To avoid an ambiguity we require that the Hartree-Fock particle densities are the same as those in the full calculation:

$$\langle n_{\sigma} \rangle^{(1)} = \langle n_{\sigma} \rangle \quad (31)$$

that can be regulated by considering the chemical potential $\mu^{(1)}$ in (30) as a proper fit parameter. There are of course other possibilities to avoid the mentioned ambiguity [15].

Several very important conclusions can be drawn from (28), e.g. for the low-energy behaviour of the selfenergy [16] at $T = 0$ (α, β, γ , *real*),

$$\Sigma_{\mathbf{k}\sigma}(E) = \alpha_{\mathbf{k}\sigma} + \beta_{\mathbf{k}\sigma} E + i\gamma_{\mathbf{k}\sigma} E^2 + \dots \quad (32)$$

That means that the imaginary part of Σ disappears at the Fermi edge ($E = 0$) indicating quasiparticles with infinite lifetimes. At low but finite temperatures holds

$$Im \Sigma_{\mathbf{k}\sigma}(0) \propto T^2 \quad (T \rightarrow 0) \quad (33)$$

(32) and (33) are necessary to guarantee the correct Fermi liquid behaviour.

3 Analytical Approaches

We can now use the basic features of the last section to construct and control three different analytical approaches. The main goal is to work out the essentials for ferromagnetism in the Hubbard model by a critical comparison of these theories.

3.1 Spin-Dependent Band Shift

Having in mind the two-peak structure of the spectral density in the strong-coupling regime (Fig.1) we can construct a simple “spectral density approach” (SDA). If we initially assume that quasiparticle damping, responsible for the finite peak widths, does not play a dominant role for magnetic properties then the following two-pole ansatz appears to be plausible:

$$S_{\mathbf{k}\sigma}(E) = \hbar \sum_{j=1}^2 \alpha_{j\sigma}(\mathbf{k}) \delta(E + \mu - E_{j\sigma}(\mathbf{k})) \quad (34)$$

The quasiparticle energies $E_{j\sigma}(\mathbf{k})$ and their spectral weights $\alpha_{j\sigma}(\mathbf{k})$ are easily fixed by equating the first four moments. The resulting selfenergy has a remarkable structure [8,9,17,18], in particular the important “band correction” $B_{\mathbf{k}-\sigma}$ is involved:

$$\Sigma_{\mathbf{k}\sigma}^{SDA}(E) = U \langle n_{-\sigma} \rangle \frac{E + \mu - T_0 - B_{\mathbf{k}-\sigma}}{E + \mu - T_0 - B_{\mathbf{k}-\sigma} - U(1 - \langle n_{-\sigma} \rangle)} \quad (35)$$

According to (10) and (12) $B_{\mathbf{k}-\sigma}$ vanishes in the zero-band-width limit ($W \rightarrow 0$). $\Sigma_{\mathbf{k}\sigma}^{SDA}(E)$ is then the exact $W = 0$ selfenergy [10,17]. Additionally the SDA fulfills by construction the first four moments so that the strong-coupling behaviour must be correct according to (6)-(8). The first three terms of the high-energy expansion of $\Sigma_{\mathbf{k}\sigma}^{SDA}(E)$ agree exactly with (25)-(27).

We note in passing that the so-called “Hubbard-I approach” [10] leads to a selfenergy being identical to that of the $W = 0$ limit. It thus coincides with that of the SDA for $B_{\mathbf{k}-\sigma} = 0$. Comparing the results of SDA and Hubbard-I therefore helps to understand the implications due to $B_{\mathbf{k}-\sigma}$.

Two severe shortcomings of the SDA are also very obvious. The first is the neglect of quasiparticle damping by the delta-function ansatz (34) which leads to a real selfenergy $\Sigma_{\mathbf{k}\sigma}^{SDA}(E)$. The second concerns the weak-coupling regime, which is surely violated by the strong-coupling theory SDA. It is not to expect that Fermi liquid behaviour is correctly described by the SDA. These two points shall be attacked and eliminated by the subsequent approaches. But let us first inspect what the SDA tells about bandferromagnetism in the Hubbard model.

For a full SDA-solution we have to determine the “band correction” $B_{\mathbf{k}-\sigma}$ (9). The local part $B_{-\sigma}$ does not need a special treatment because of its direct connection (11) to the spectral density itself. The \mathbf{k} -dependent part $F_{\mathbf{k}-\sigma}$ appears a bit more complicated. Assuming translational invariance and next neighbour hopping, only, the \mathbf{k} -dependence can be separated [17,18]:

$$\langle n_{-\sigma} \rangle (1 - \langle n_{-\sigma} \rangle) F_{\mathbf{k}-\sigma} = (\varepsilon(\mathbf{k}) - T_0) \sum_{i=1}^3 F_{-\sigma}^{(i)} \quad (36)$$

$$F_{-\sigma}^{(1)} = \langle n_{i-\sigma} n_{j-\sigma} \rangle - \langle n_{-\sigma} \rangle^2 \quad (37)$$

$$F_{-\sigma}^{(2)} = \langle c_{j-\sigma}^+ c_{j\sigma}^+ c_{i-\sigma} c_{i\sigma} \rangle \quad (38)$$

$$F_{-\sigma}^{(3)} = \langle c_{j\sigma}^+ c_{j-\sigma} c_{i-\sigma}^+ c_{i\sigma} \rangle \quad (39)$$

i, j are numbering next neighbours. The method used to determine the higher correlations $F_{-\sigma}^{(i)}$ shall be exemplified for $F_{-\sigma}^{(3)}$. First we rewrite $F_{-\sigma}^{(3)}$ as

$$F_{-\sigma}^{(3)} = \sum_l \delta_{jl} \langle c_{l\sigma}^+ c_{j-\sigma} c_{j+\Delta-\sigma}^+ c_{j+\Delta\sigma} \rangle \quad (40)$$

where the index Δ corresponds to the lattice vector which connects two neighbouring sites \mathbf{R}_i and \mathbf{R}_j . Because of translational invariance $F_{-\sigma}^{(3)}$ does not depend on the explicit value of Δ . We now introduce a “higher” spectral density $S_{\mathbf{k}\sigma}^{(3)}(E)$ as the (\mathbf{k}, E) -dependent Fourier transform of

$$S_{jl\sigma}^{(3)}(t, t') = \frac{1}{2\pi} \langle [(c_{j-\sigma} c_{j+\Delta-\sigma}^+ c_{j+\Delta\sigma})(t), c_{l\sigma}^+(t')]_+ \rangle \quad (41)$$

The spectral theorem yields:

$$F_{-\sigma}^{(3)} = \frac{1}{\hbar N} \sum_{\mathbf{k}} \int_{-\infty}^{\infty} dE f_{-}(E) S_{\mathbf{k}\sigma}^{(3)}(E - \mu) \quad (42)$$

According to the definition (41) the poles of $S_{\mathbf{k}\sigma}^{(3)}(E)$ must belong to the single-electron excitations of the Hubbard system. From the spectral representation of $S_{\mathbf{k}\sigma}^{(3)}(E)$ and by comparison with the respective representation of the single-electron spectral density $S_{\mathbf{k}\sigma}(E)$ again a two pole ansatz appears to be consistent,

$$S_{\mathbf{k}\sigma}(E) = \hbar \sum_{j=1}^2 \hat{\alpha}_{j\sigma}(\mathbf{k}) \delta(E + \mu - E_{j\sigma}(\mathbf{k})) \quad (43)$$

where the quasiparticle energies $E_{j\sigma}(\mathbf{k})$ are the same as those in (34) so that the spectral weights $\hat{\alpha}_{j\sigma}$ are the only unknown parameters. They are fixed by the first two spectral moments of $S_{\mathbf{k}\sigma}^{(3)}(E)$ leading via (42) then to an (approximate) expression for $F_{-\sigma}^{(3)}$.

In an analogous manner the correlation terms $F_{-\sigma}^{(1)}$ and $F_{-\sigma}^{(2)}$ are determined by two-pole ansatzes of properly chosen “higher” spectral densities $S_{\mathbf{k}\sigma}^{(1,2)}$ [17]. We note in passing that the same procedure can of course also be applied to the term $\langle n_{i\sigma} c_{i-\sigma}^+ c_{j-\sigma} \rangle$ in the “band shift” $B_{-\sigma}$ (10) yielding then the exact result (11).

Fig.2 demonstrates for an sc lattice that the just-described SDA allows for bandferromagnetism in the Hubbard model. The zeros of the inverse paramagnetic susceptibility χ^{-1} as a function of the band occupation n indicate instabilities of the paramagnetic state towards ferromagnetism ($T = 0K$). The instabilities appear as soon as U exceeds the critical value $U_C \approx 4W$. It is a special feature of the SDA [17,19], maybe even of the Hubbard model itself, that there appear for $U > U_C$ two ferromagnetic solutions, i.e. two zeros of χ^{-1} . The first solution sets in at $n_C \geq 0.34$ where the actual value only slightly depends on

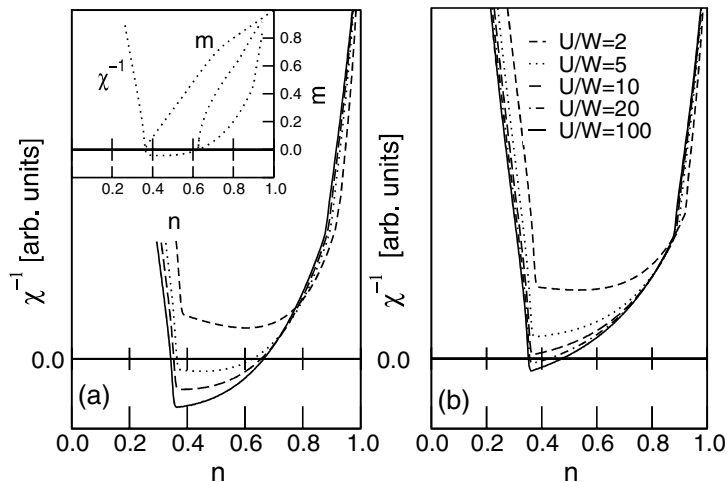


Fig. 2. Inverse paramagnetic static susceptibility χ^{-1} for the sc lattice as a function of the band occupation n for various values of U . (a) System with the full \mathbf{k} -dependent selfenergy. (b) System with a local selfenergy ($F_{\mathbf{k}-\sigma} \equiv 0$). The inset shows the magnetic moment as a function of n for $U/W = 5$.

U running into saturation ($m=n$) for $n \geq 0.68$ (see inset Fig.2). The second solution appears for higher band occupation, but does never reach saturation and is always less stable than the other solution. Two important aspects of the SDA solution in Fig.2 should be stressed. The first concerns the comparison with the corresponding results of the Hubbard-I approach [10], which does not allow ferromagnetism on the sc lattice. On the other hand, the Hubbard-I selfenergy differs from (35) “only” by neglecting the “band correction” $B_{\mathbf{k}-\sigma}$. Consequently, the stronger magnetic stability in the SDA must be due to $B_{\mathbf{k}-\sigma}$. The second remark aims at the non-locality (\mathbf{k} -dependence) of the electronic selfenergy provoked by the “bandwidth correction” $F_{\mathbf{k}-\sigma}$ (36) in $B_{\mathbf{k}-\sigma}$. Part (b) of Fig.2 demonstrates its importance. Switching off this term leads to a dramatic further increase of the critical coupling $\frac{U_C}{W}$ from 4 to 14. More detailed studies [19], however, show that the influence of $F_{\mathbf{k}-\sigma}$ on magnetic stability strongly depends on the lattice type. Increasing coordination number (sc \rightarrow bcc \rightarrow fcc) drastically diminishes the importance of the non-locality leaving the local spin-dependent band shift $B_{-\sigma}$ as the pushing mechanism for ferromagnetic stability.

It can be shown [17] that the SDA gives a qualitatively convincing picture of bandferromagnetism. The main message is that the spin-dependent “band-shift” $B_{-\sigma}$ and the lattice structure are the most important ingredients. However, we should not forget the disadvantages of the method. One of them is the neglect of quasiparticle damping, which is assumed to destabilize the collective spin order.

3.2 Quasiparticle Damping

More or less by construction the SDA selfenergy (35) is real except for a single δ -peak in $Im\Sigma_{\mathbf{k}\sigma}(E + i0^+)$ at the pole $E = T_0 + B_{\mathbf{k}-\sigma} + U(1 - \langle n_{-\sigma} \rangle) - \mu$. It

has, however, no influence since it falls into the Hubbard gap. The quasiparticles are stable. We are therefore looking for an approach that retains the obvious advantages of the SDA but improves it by a reasonable inclusion of quasiparticle lifetime effects.

Starting point is an alloy-analogy for the Hubbard model which traces back to Hubbard himself [20]. The idea is to consider the propagation of a σ electron through the lattice with the $-\sigma$ electrons being “frozen” at their lattice sites and randomly distributed over the crystal. When the σ electron enters a lattice site it can encounter two different situations. It can meet a $-\sigma$ electron or not. That can be interpreted as a hopping through a fictitious binary alloy, the two constituents of which are characterized by atomic levels $E_{1\sigma}, E_{2\sigma}$ and by concentrations $x_{1\sigma}, x_{2\sigma}$. The “coherent potential approximation” (CPA) is a standard method to perform the configurational average over the alloy [21]. The resulting σ selfenergy obeys the following implicit equation [11],

$$0 = \sum_{p=1}^2 x_{p\sigma} \frac{E_{p\sigma} - \Sigma_{\sigma}(E) - T_0}{1 - \frac{1}{\hbar} G_{\sigma}(E)(E_{p\sigma} - \Sigma_{\sigma}(E) - T_0)} \quad (44)$$

$G_{\sigma}(E) = \frac{1}{N} \sum_{\mathbf{k}} G_{\mathbf{k}\sigma}(E)$ is the local propagator. CPA is a single-site approximation, the resulting selfenergy therefore wave vector independent. To proceed one has to specify the two-component alloy. The natural way (“conventional alloy analogy” CAA) would be to use the zero-bandwidth results of the Hubbard model: $E_{1\sigma} = T_0, E_{2\sigma} = T_0 + U, x_{1\sigma} = 1 - \langle n_{-\sigma} \rangle = 1 - x_{2\sigma}$. The resulting $\Sigma_{\sigma}^{CAA}(E)$ includes quasiparticle damping but excludes any spontaneous ferromagnetism [22,23]. Does quasiparticle damping really kill any spontaneous moment order? This is a serious question because it has been shown [24] that for infinite lattice dimensions CPA is an exact (!) treatment of the alloy problem. On the other hand, the CAA selfenergy disagrees with the strong as well as weak coupling behaviour (24), (28). This discrepancy can only be removed by the conclusion that the zero-bandwidth limit constitutes the wrong alloy analogy [25].

The fictitious binary alloy is indeed by no means predetermined. We consider $E_{1,2\sigma}$ and $x_{1,2\sigma}$ at first as free parameters and fix them via the high-energy expansions (21) and (24), which we insert into the CPA equation (44). Then we expand eq. (44) with respect to powers of $\frac{1}{E}$. Comparing coefficients we can use the following set of equations to determine an “optimum alloy analogy”:

$$\begin{aligned} \sum_{p=1}^2 x_{p\sigma} &= 1 & \sum_{p=1}^2 x_{p\sigma}(E_{p\sigma} - T_0) &= U \langle n_{-\sigma} \rangle \\ \sum_{p=1}^2 x_{p\sigma}(E_{p\sigma} - T_0)^2 &= U^2 \langle n_{-\sigma} \rangle \\ \sum_{p=1}^2 x_{p\sigma}(E_{p\sigma} - T_0)^3 &= U^3 \langle n_{-\sigma} \rangle + U^2 B_{-\sigma} \langle n_{-\sigma} \rangle (1 - \langle n_{-\sigma} \rangle) \end{aligned} \quad (45)$$

Deriving from these equations $E_{p\sigma}$ and $x_{p\sigma}$ automatically guarantees the correct strong-coupling behaviour. One finds (p=1,2) (“modified alloy analogy” MAA).

$$\begin{aligned} E_{p\sigma}^{MAA} &= \\ T_0 + \frac{1}{2}[U + B_{-\sigma} + (-1)^p \sqrt{(U + B_{-\sigma})^2 - 4\langle n_{-\sigma} \rangle B_{-\sigma}}] \\ &\equiv (E_{p\sigma}^{SDA}(\mathbf{k}))_{\varepsilon(\mathbf{k})=T_0} \equiv f_p(T_0, U, \langle n_{-\sigma} \rangle, B_{-\sigma}) \end{aligned} \quad (46)$$

$$\begin{aligned} x_{1\sigma}^{MAA} &= \frac{B_{-\sigma} + T_0 + U(1 - \langle n_{-\sigma} \rangle) - E_{1\sigma}^{MAA}}{E_{2\sigma}^{MAA} - E_{1\sigma}^{MAA}} = 1 - x_{2\sigma}^{MAA} \\ x_{p\sigma}^{MAA} &\equiv (\alpha_{p\sigma}^{SDA})_{\varepsilon(\mathbf{k})=T_0} \equiv g_p(T_0, U, \langle n_{-\sigma} \rangle, B_{-\sigma}) \end{aligned} \quad (47)$$

Surprisingly, the energies and weights coincide exactly with the corresponding SDA entities if $\varepsilon(\mathbf{k})$ is simply replaced by T_0 . Because of the single-site aspect of the CPA [21,11] the “band-correction” $B_{\mathbf{k}-\sigma}$ is restricted here to its local part $B_{-\sigma}$, the decisive band shift. Inserting (46) and (47) into (44) yields the MAA selfenergy for all E which exhibits some remarkable features [25]:

- (1) As a CPA result the MAA includes quasiparticle damping ($Im\Sigma_{\sigma}^{MAA}(E) \neq 0$), and that without giving up the advantages of the SDA.
- (2) The expectation values $\langle n_{-\sigma} \rangle$ and $B_{-\sigma}$ are to be determined selfconsistently. In principle, they take care for a carrier concentration-, temperature- and spin-dependence of the atomic data (46),(47) of the alloy constituents. Furthermore, and that is quite an important aspect, $B_{-\sigma}$ brings into play in a certain sense the itineracy of the $-\sigma$ electrons (“correlated” electron hopping), completely neglected in the CAA.
- (3) Strong-coupling and high-energy behaviour are correctly reproduced, more or less by construction.
- (4) The general CPA theory [21] comes for the so-called split-band regime (here, $U \gg W$) to the conclusion that the spectral density $S_{\mathbf{k}\sigma}(E)$ should consist of two separated peaks with centres at

$$T_{p\sigma}^{CPA} = E_{p\sigma} + x_{p\sigma}(\varepsilon(\mathbf{k}) - T_0); \quad p = 1, 2 \quad (48)$$

Inserting (46) and (47) for $U \gg W$ yields exactly the Harris-Lange results (6-8), a further strong confirmation of the MAA.

- (5) Contrary to the CAA the MAA allows for spontaneous bandferromagnetism.

For a typical example the possibilities of the MAA are demonstrated in Fig.3, which shows $S_{\mathbf{k}\sigma}(E)$ for strongly correlated electrons ($\frac{U}{W} = 5$) on an fcc lattice. For less than half-filled bands ($n < 1$) the system is paramagnetic. The band occupation $n=1.6$ used in Fig.3 allows for a spontaneous collective order provided U exceeds a critical value. Two types of splitting occur. At first the spectral density consists for each \mathbf{k} -vector of a high-energy and a low-energy peak separated by an energy of order U . The finite widths of the peaks are due to quasiparticle damping and obviously energy-, wave-vector-, spin- and temperature-dependent.

The spectral weight (area) of the low-energy peak scales with the probability that the propagating (\mathbf{k}, σ) -electron in the more than half-filled band enters an empty lattice site, the weight of the upper peak that it meets anywhere a $-\sigma$ electron. This splitting is general and not at all bound to ferromagnetism. It demonstrates the correct strong-coupling behaviour (6,7). Ferromagnetism appears when the two spectral density peaks show a spin asymmetry. For the low temperature example $T = 100K$ (Fig.3a) the system is close to saturation ($m = 2 - n$), i.e. the up-spin states are almost fully occupied. A down-spin electron cannot avoid to meet an up-spin electron at every lattice site being therefore forced to perform a Coulomb interaction. Consequently the low-energy peak of $S_{\mathbf{k}\downarrow}(E)$ disappears. At higher temperatures (Fig.3b) the peak reappears because of a partial demagnetisation, i.e. a finite density of holes in the up-spin spectrum. At low temperatures the high-energy peaks of $S_{\mathbf{k}\downarrow}(E)$ are very sharp indicating long-living quasiparticles. A \downarrow -hole has no chance to meet an \uparrow -hole to be scattered.

An interesting \mathbf{k} -dependence of the exchange splitting is observed. At the branch-top (X-point) a “normal” splitting appears, i.e. the down-spin peak is above the up-spin peak. At the bottom (Γ -point), however, the \uparrow -peak is higher in energy than the \downarrow -peak (“inverse exchange splitting”). The quasiparticle dispersions of the two spin-parts are crossing as a function of \mathbf{k} . This behaviour is a result of two competing correlation effects. The one is the spin-dependent exchange shift of the centres of gravity of the quasiparticle subbands, the other a spin-dependent band narrowing. The latter may overcompensate the first. In any case the exchange splitting exhibits a strong wave-vector dependence, even with a sign change.

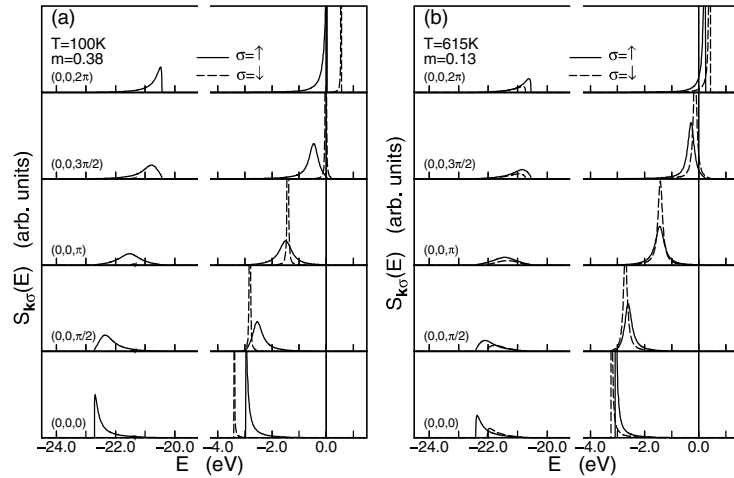


Fig. 3. Spectral density as a function of energy for an fcc lattice calculated within the MAA, (a) $T = 100K$, (b) $T = 615K$ for different \mathbf{k} -vectors equidistant along the (001)-direction of the 1. Brillouin zone. Further parameters: $n = 1.6$, $U = 20\text{eV}$, $W = 4\text{eV}$. The vertical line indicates the position of the chemical potential.

We can conclude that the MAA improves the SDA in a systematic manner by including quasiparticle damping. As will be discussed in Sect. 4, the main modification consists in a substantial destabilisation of ferromagnetism in the Hubbard model. One reason is the finite overlap of the spectral density peaks, in the SDA because of (34) excluded, which weakens the ferromagnetic solution of the selfconsistently evaluated model theory.

The second shortcoming of the SDA, the incorrect weak-coupling behaviour, persists in the MAA. In the following we have to inspect its consequences for the strong-coupling phenomenon ferromagnetism.

3.3 Weak-Coupling Behaviour

Neither the SDA selfenergy (35) nor the MAA selfenergy does fulfill the weak-coupling expansion (28). We are now looking for an approach which interpolates reasonably between the strong- and weak-coupling regimes. It should extend the preceding approaches SDA and MAA by inclusion of weak coupling and Fermi liquid behaviour without giving up the convincing essentials from the SDA and MAA: spin-dependent band shift $B_{-\sigma}$ and quasiparticle damping. Following an idea of Kajueter and Kotliar [15] we start with a selfenergy ansatz [26], which we call the “modified perturbation theory” (MPT):

$$\Sigma_{\mathbf{k}\sigma}(E) = U\langle n_{-\sigma} \rangle + \frac{a_{\mathbf{k}\sigma}U^2\Delta_{\mathbf{k}\sigma}(E)}{1 - b_{\mathbf{k}\sigma}U^2\Delta_{\mathbf{k}\sigma}(E)} \quad (49)$$

The second order contribution $\Delta_{\mathbf{k}\sigma}(E)$ is defined in eq. (29). We use in $\Delta_{\mathbf{k}\sigma}(E)$ for the spectral densities the Hartree-Fock version (30) with the selfconsistency condition (31). By construction the selfenergy (49) is correct in the weak-coupling regime up to order U^2 . In order to fulfill simultaneously the strong-coupling regime we expand (49) in powers of the inverse energy $1/E$ and compare this with the exact selfenergy expansion (24). The first two terms are automatically fulfilled, the third and the fourth fit the coefficients $a_{\mathbf{k}\sigma}$, $b_{\mathbf{k}\sigma}$ [26]. For the results presented in the next section we have implemented the MPT (49) in a “dynamical mean field theory” (DMFT) procedure [26,27]. The main assumption is then a local selfenergy $\Sigma_{\mathbf{k}\sigma}(E) \rightarrow \Sigma_{\sigma}(E)$, exact in infinite lattice dimensions [4]. Furthermore, we exploit the fact that the Hubbard problem can be mapped under such conditions on the single-impurity Anderson model (SIAM) (see contribution of D. Vollhardt) as long as a special selfconsistency condition is fulfilled [26]. The idea of the MPT is then applied to the simpler SIAM problem. It can be shown, however, that the direct application of the MPT-concept to the Hubbard model gives almost the same results.

The MPT fulfills a maximum number of limiting cases: The weak-coupling behaviour is correct up to U^2 -terms, for all bandoccupations n Fermi liquid properties are recovered. The Luttinger theorem,

$$S_{ii\sigma}(0) \stackrel{!}{=} S_{ii\sigma}^{(0)}(0) \leftrightarrow \mu = \mu|_{U=0} + \Sigma_{\sigma}(0), \quad (50)$$

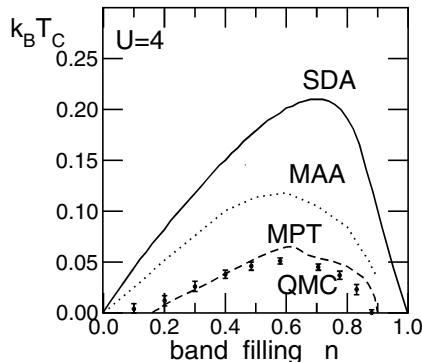


Fig. 4. Curie temperature as a function of band “filling” (hole concentration) for an fcc-type $d = \infty$ -lattice (51). The points with error bars are the Quantum-Monte-Carlo results from ref. [3]. SDA, MAA and MP are explained in the text.

is fulfilled for all bandoccupations n , at least if not too far from half-filling ($n = 1$). For low temperatures a Kondo resonance appears at the chemical potential μ . The zero-bandwidth limit ($W \rightarrow 0$) comes out exact for all n as well as the strong-coupling behaviour gathered in eqs. (6)-(8). Eventually bandferromagnetism is possible within the framework of MP. According to the number of correctly reproduced limiting cases the MP appears to be an optimum approach to the many-body problem of the Hubbard model.

4 Discussion

Let us compare the analytical approaches presented in the preceding Section with respect to the most important magnetic key-quantity, the Curie temperature T_C . For comparison with the numerically essentially exact Quantum Monte Carlo results of Ulmke [3] we have evaluated the three theories for an fcc- $d = \infty$ type lattice described by the Bloch density of states:

$$\rho_0(E) = \frac{\exp\left(-\frac{1}{2}\left(1 - \frac{\sqrt{2}E}{t^*}\right)\right)}{t^* \sqrt{\pi\left(1 - \frac{\sqrt{2}E}{t^*}\right)}} \quad (51)$$

The energy unit is chosen to $t^* = t\sqrt{2d(d-1)} \stackrel{!}{=} 1$. The density of states (51) is strongly asymmetric with a square root divergency at the upper edge.

All the presented methods predict that ferromagnetism exists only for more than half-filled energy bands. In Fig. 4 bandfilling therefore means the hole-density and the DOS is that for holes following from (51) by $t^* \rightarrow -t^*$.

The role of the spin-dependent band shift $B_{-\sigma}$ (10) for the magnetic stability becomes evident by comparison of the three methods with their $B_{-\sigma} = 0$ counterparts. That is for SDA the Hubbard I-solution [10] which yields ferromagnetism only for very asymmetric DOS. In the case of (51) there appears

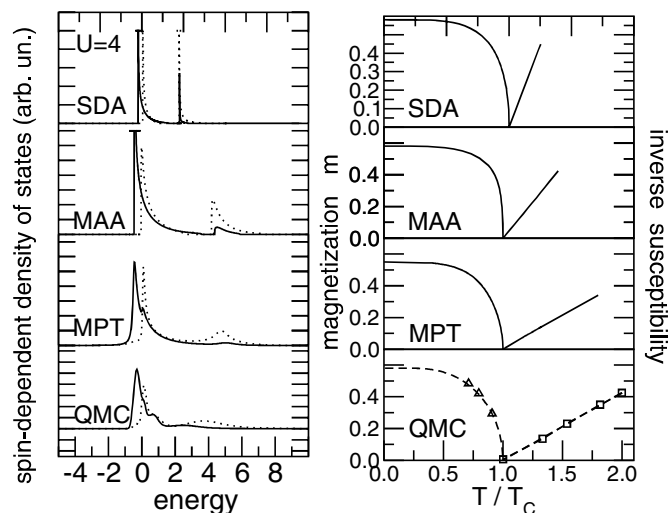


Fig. 5. Left: Quasiparticle density of states as function of energy for the fcc-type lattice (51). Solid lines for $\sigma = \uparrow$, dotted lines for $\sigma = \downarrow$. QMC results from [3]. Temperature T is chosen so that for all presented methods a magnetization $m = 0.4$ is found. Right: For the same parameters as in the left part the magnetisation m and the inverse paramagnetic susceptibility χ^{-1} as function of the reduced temperature T/T_C . Bottom figure: QMC results, dashed line for $T/T_C \leq 1$: $S = 1/2$ -Brillouin function.

ferromagnetism in a strongly restricted region of very low hole densities. The band shift $B_{-\sigma}$ in the SDA obviously leads to a drastic enhancement of ferromagnetic stability. The counterpart of MAA is the conventional alloy analogy (CAA) that does not allow for any n ferromagnetic order [22,23]. Finally, the MPT-counterpart, that neglects the bandshift, is the Kajueter-Kotliar approach [15]. It indeed exhibits ferromagnetism but with substantially lower Curie temperatures T_C .

The influence of quasiparticle damping can best be judged by comparing the results of SDA and MAA. The inclusion of lifetime effects in MAA presses the Curie temperature to half the SDA-values. The ferromagnetic coupling strength is therefore substantially weakened by quasiparticle damping. The incorporation of the correct weak-coupling behaviour by MPT leads to a further T_C -reduction possibly because of the screening tendency with respect to the effective magnetic moments manifesting itself in the appearance of a Kondo resonance. The MPT-results for $T_C(n)$ are closest to the essentially exact numerical results of Ulmke [3], which have been read off from the zeros of the inverse paramagnetic susceptibility.

The similarities and the differences of the various methods come out by the quasiparticle density of states in Fig. 5a. All theories show the splitting into the two Hubbard bands and the additional exchange splitting which takes care for the spin asymmetry. As a consequence of the neglect of damping effects the DOS-structures are rather sharp in the SDA. They appear smoother in MAA.

The correct low-energy behaviour of the MPT leads to the best approach to the Q-DOS found by “Quantum Monte Carlo” (QMC)-evaluation of a “Dynamical Mean Field Theory”. Note that for a reasonable comparison of the Q-DOS we have chosen in Fig. 5a for the various theories temperatures which lead to the same magnetization $m = 0.4$.

Fig. 5b demonstrates impressively the qualitative equivalence of the presented methods when we plot the spontaneous magnetization and the paramagnetic susceptibility as function of the reduced temperature T/T_C . There are indeed strong similarities. All magnetization curves are Brillouin function-like with full polarization at $T = 0$. The only exception is MPT, which shows up a slight deviation from saturation at $T = 0$. For the chosen parameter set all methods predict a second order transition at T_C . The paramagnetic susceptibility follows in all theories a ideal Curie-Weiß behaviour: $\chi = C(T - \Theta)^{-1}$. The paramagnetic Curie temperature Θ equals in any case the Curie temperature T_C and even the Curie constants C are all very similar: $C = 0.42$ (SDA), 0.52 (MAA), 0.57 (MPT), 0.47 (QMC). One important consequence of this striking qualitative equivalence and correctness of SDA, MAA and MPT compared to QMC is that even the rather simple SDA can be used to describe the magnetism of more complicated structures (films, surfaces, multilayer, real substances).

We conclude that ferromagnetism does exist in the Hubbard model depending on lattice structure, band occupation, Coulomb coupling and temperature. By a critical comparison of three different analytical approaches we could demonstrate the essentials for ferromagnetic stability, in a positive sense the spin-dependent band shift $B_{-\sigma}$, which represents the correlated hopping of opposite spin electrons, and in a negative sense the finite lifetime of quasiparticles, which results in a drastic lowering of the ferromagnetic coupling strength. The correct inclusion of Fermi liquid properties eventually leads to the most convincing description of ferromagnetism in the Hubbard model.

References

1. H. Capellmann: ‘Metallic Magnetism’. Vol. **42** of: *Springer Topics in Current Physics*, (Springer, Berlin 1987).
2. Y. Nagaoka: Phys. Rev. **147**, 392 (1966).
3. M. Ulmke: Eur. Phys. J. B **1**, 301 (1998).
4. W. Metzner, D. Vollhardt: Phys. Rev. Lett. **62**, 324 (1989).
5. E. Müller-Hartmann: Z. Phys. B **74**, 507 (1989).
6. G. D. Mahan, ‘Many Particle Physics’, Vol. **42**, (Plenum Press, New York 1990).
7. A. B. Harris, R. Lange: Phys. Rev. **157**, 295 (1967).
8. G. Geipel, W. Nolting: Phys. Rev. B **38**, 2608 (1988).
9. W. Nolting, W. Borgiel: Phys. Rev. B **39**, 6962 (1989).
10. J. Hubbard: Proc. Roy. Soc. **A276**, 238 (1963).
11. W. Nolting: ‘Vielteilchentheorie’. Bd. 7 of: *Grundkurs: Theoretische Physik*. (Vieweg, Wiesbaden 1997).
12. A. A. Abrikosov, L. P. Gorkov, I. E. Dzyaloshinsky: ‘Methods of Quantum Field Theory in Statistical Physics’. (Prentice Hall, New Jersey 1964).
13. H. Schweitzer, G. Czycholl: Solid State Commun. **74**, 735 (1990).

14. V. Zlatic, B. Horvatic: Phys. Rev. B **28**, 6904 (1983).
15. H. Kajueter, G. Kotliar: Phys. Rev. Lett. **77**, 131 (1996).
16. J. M. Luttinger: Phys. Rev. **121**, 942 (1961).
17. T. Herrmann, W. Nolting: J. Magn. Magn. Mater. **170**, 253 (1997).
18. L. M. Roth: Phys. Rev. **184**, 451 (1969).
19. T. Herrmann, W. Nolting: Solid State Commun. **103**, 351 (1997).
20. J. Hubbard: Proc. Roy. Soc. **A281**, 401 (1964).
21. B. Velický, S. Kirkpatrick, H. Ehrenreich: Phys. Rev. **175**, 747 (1968).
22. H. Fukuyama, H. Ehrenreich: Phys. Rev. B **7**, 3266 (1973).
23. J. Schneider, V. Drchal: phys. stat. sol. (b) **68**, 207 (1975).
24. R. Vlaming, D. Vollhardt: Phys. Rev. B **45**, 4637 (1992).
25. T. Herrmann, W. Nolting: Phys. Rev. B **53**, 10579 (1996).
26. M. Potthoff, T. Wegner, W. Nolting: Phys. Rev. B **50**, 16132 (1997).
27. T. Wegner, M. Potthoff, W. Nolting: Phys. Rev. B **57**, 6211 (1998).

Orbital Order Versus Orbital Liquid in Doped Manganites

Andrzej M. Oleś^{1,2} and Louis Felix Feiner^{3,4}

¹ Institute of Physics, Jagellonian University, Reymonta 4, PL-30059 Kraków, Poland

² Max-Planck-Institut FKF, Heisenbergstrasse 1, D-70569 Stuttgart, Germany

³ Utrecht University, Princetonplein 5, NL-3584 CC Utrecht, The Netherlands

⁴ Philips Research Labs, Prof. Holstlaan 4, NL-5656 AA Eindhoven, The Netherlands

Abstract. Doped manganites provide an interesting example of metallic ferromagnetism which occurs in a strongly correlated e_g band. We analyze the magnetic interactions in manganites and show that the superexchange promotes an antiferromagnetic state accompanied by orbital ordering in the insulating LaMnO_3 , while double-exchange favors metallic ferromagnetism observed in doped $\text{La}_{1-x}\text{A}_x\text{MnO}_3$ compounds. In contrast to the common spin-Hubbard model, we find that the orbital-Hubbard model with two orbital flavours, which describes a partly filled e_g band in a ferromagnetic phase, does not exhibit instabilities towards orbital ordering, but gives instead an orbital liquid state. This state explains the cubic symmetry of the spin waves observed in the ferromagnetic manganites, and the magnon stiffness constant which is proportional to the hole doping x and measures the electron correlations.

1 Superexchange Interactions and Orbital Order

The complex phase diagrams of doped manganites with many magnetic phases, some accompanied by orbital or charge ordering, have attracted a lot of attention recently [1]. Although these compounds are known since about fifty years, the metal-insulator phase transition observed both under increasing doping x and with increasing temperature T , as well as the colossal magnetoresistance (CMR) phenomenon itself, are not yet fully understood. The undoped LaMnO_3 is a Mott insulator due to the strong on-site repulsion U , and thus the magnetic interactions are of superexchange (SE) type. As the e_g electrons occupy partly-filled degenerate e_g orbitals, it is necessary to consider the orbital degrees of freedom on an equal footing with the electron spins. This leads to effective spin-orbital models to describe the magnetic interactions and low-energy excitations [2,3,4]. Although the coupling between the e_g electrons of Mn^{3+} [$d^4(t_{2g}^3 e_g)$] ions in LaMnO_3 might look similar to those between the e_g holes of Cu^{2+} [$d^9(t_{2g}^6 e_g^3)$] ions in KCuF_3 [2], an important difference arises due to the local Hund's rule coupling J_H between an e_g electron and the $t_{2g}^3 S_t = \frac{3}{2}$ core, leading to SE interactions between large $S = 2$ spins of Mn^{3+} ions [5,6], in contrast to SE between small $s = \frac{1}{2}$ spins of Cu^{2+} ions. Thus in the cuprate case the quantum fluctuations are quite strong, and new quantum effects might occur which stabilize a spin liquid state instead of magnetic order [7]. In contrast, the situation in undoped manganites such as LaMnO_3 is more classical and spin order occurs more easily.

A very interesting physical situation is found in doped manganites, such as $\text{La}_{1-x}\text{Sr}_x\text{MnO}_3$ or $\text{La}_{1-x}\text{Ca}_x\text{MnO}_3$, when the e_g electrons start to move, but the hopping elements depend on the orientation of the t_{2g}^3 spins by the well-known double-exchange (DE) mechanism [8]. This gives minimum kinetic energy for parallel spins, and thus favors a ferromagnetic (FM) phase. Indeed, FM phases, both insulating and metallic, have been observed in manganites at finite doping. However, the present understanding of the DE interactions and the resulting FM state is highly unsatisfactory, as it is based on a model which describes the e_g electrons as being in a nondegenerate band [9]. If this simplification is made, several properties of the real systems with degenerate e_g orbitals, such as incoherence observed in the optical conductivity of doped materials [10], and the onset of the metallic state below the Curie temperature [11], cannot be correctly described. Moreover, two fundamental questions: (i) Why are the exchange constants observed in the FM metallic phase *isotropic*? and (ii) What kind of an *orbital liquid* (OL) state is realized in doped manganites? – are avoided.

The manganites have a strong tendency towards orbital order. The structural phase transition occurs in LaMnO_3 at $T_s = 750$ K, well above the magnetic transition at the Néel temperature $T_N = 140$ K to the anisotropic A-type antiferromagnetic (AF) order, with the FM (a, b) planes staggered along the c axis. This A-AF phase is stabilized by the underlying orbital order. Thus, in the undoped material the orbitals order first and the spins follow. Although the observed alternating orbital order [12] might in principle originate from the purely electronic interactions of the SE type, it has been argued that it is primarily driven by the cooperative Jahn-Teller (JT) effect, taking the realistic parameters of LaMnO_3 [5,13]. This situation is different from the A-AF phase observed in KCuF_3 , in which the electronic interactions play a dominating role [14].

In the present paper we address the question of the orbital state in the FM manganites. The FM states observed in manganites at doping $x \simeq 0.3$ are in most cases metallic [1], and have *isotropic* magnetic properties, with very similar stiffness constants $D \simeq (175 \pm 15) \text{ meV} \times \text{\AA}^2$ in the magnon dispersion $\omega_{\mathbf{k}} \propto Dk^2$ [15]. However, models which combine SE interactions with the kinetic energy of a partially filled e_g band predict typically *anisotropic* FM states with orbital order (OO) [16,17]. As we discuss below, such states result from a competition between the SE and the kinetic energy of the e_g electrons, if the on-site Coulomb repulsion is treated in the Hartree-Fock (HF) approximation, or if the problem is solved with additional approximations, for instance in a restricted space.

We start with the undoped insulating compound LaMnO_3 which has to be understood before the full problem of DE interactions in doped materials is addressed. The on-site Coulomb interaction $U \simeq 7.3$ eV [5] is the dominating effect which suppresses the charge fluctuations, and leads to an effective low-energy Hamiltonian, where spin and orbital degrees of freedom are interrelated. The SE interactions are obtained by starting from the $d^4(t_{2g}^3 e_g)$ Hund's rule high-spin 5E ground state of Mn^{3+} , and considering the virtual processes which lead to d_i^5 excited states of Mn^{2+} ions. These involve either $d_i^4 d_j^4 \Rightarrow d_i^5(t_{2g}^3 e_g^2) d_j^3(t_{2g}^3)$ transitions by an e_g electron, or $d_i^4 d_j^4 \Rightarrow d_i^5(t_{2g}^4 e_g) d_j^3(t_{2g}^2 e_g)$ transitions by a

t_{2g} electron. Such processes have to be analyzed carefully and the intermediate states projected on the d_i^5 (d_j^3) eigenstates of Mn^{2+} (Mn^{4+}) ions, yielding the SE Hamiltonian, $H_J = H_J^e + H_J^t$, between spins $S = 2$.

Consider first the excitations due to e_g electrons, which involve the orbital degrees of freedom. If an e_g electron is transferred, either a high-spin 6A_1 state ($S = 5/2$), or one of the low-spin ($S = 3/2$) states, 4A_1 , 4E or 4A_2 , of Mn^{2+} is excited, with Mn^{4+} ending up in the 4A_2 state. The excitation energies depend on the three Racah parameters A , B , and C , but it is more convenient to use simplified formulae which involve only the Coulomb element $U = A + 2B + 5C$ and the Hund's rule exchange $J_H = 2B + C$ [5]: $\varepsilon({}^6A_1) = U - 5J_H$, $\varepsilon({}^4A_1) = U$, $\varepsilon({}^4E) = U + \frac{2}{3}J_H$, $\varepsilon({}^4A_2) = U + \frac{10}{3}J_H$. Since hopping of an e_g electron between two Mn^{3+} ions is a two-step process which goes via the oxygen orbitals, $t \propto t_{dp}^2/\Delta$ depends on the d - p hopping t_{dp} and on the charge-transfer gap Δ in the respective multiband model [18]. For such processes, with characteristic energy $J = t^2/U = 23$ meV, which follows from realistic parameters of LaMnO_3 , one finds the SE (n_i is the number operator for e_g electrons) [5]:

$$H_J^e = \frac{1}{16} \sum_{\langle ij \rangle} n_i n_j \left\{ -\frac{8}{5} \frac{t^2}{\varepsilon({}^6A_1)} (\mathbf{S}_i \cdot \mathbf{S}_j + 6) \mathcal{P}_{\langle ij \rangle}^{\zeta\zeta} + (\mathbf{S}_i \cdot \mathbf{S}_j - 4) \right. \\ \left. \times \left[\left(\frac{t^2}{\varepsilon({}^4E)} + \frac{3}{5} \frac{t^2}{\varepsilon({}^4A_1)} \right) \mathcal{P}_{\langle ij \rangle}^{\zeta\xi} + \left(\frac{t^2}{\varepsilon({}^4E)} + \frac{t^2}{\varepsilon({}^4A_2)} \right) \mathcal{P}_{\langle ij \rangle}^{\xi\xi} \right] \right\}. \quad (1)$$

Hopping occurs only between two directional orbitals $|\zeta\rangle$ parallel to the considered bond $\langle ij \rangle$, while hopping to/from the orbitals $|\xi\rangle$ perpendicular to the bond vanishes due to compensating orbital phases. Thus, the SE on the bond $\langle ij \rangle$ involves only either the pair of two different orbitals, $|\zeta\rangle$ and $|\xi\rangle$, or the pair of directional orbitals $|\zeta\rangle$ occupied, as expressed by the projection operators:

$$\mathcal{P}_{\langle ij \rangle}^{\zeta\xi} = P_{i\zeta} P_{j\xi} + P_{i\xi} P_{j\zeta}, \quad \mathcal{P}_{\langle ij \rangle}^{\zeta\zeta} = 2P_{i\zeta} P_{j\zeta}, \quad (2)$$

where $P_{i\zeta} = \frac{1}{2} - \tau_i^\alpha$ and $P_{j\xi} = \frac{1}{2} + \tau_j^\alpha$ are the respective local projection operators on orbital $|\zeta\rangle$ and $|\xi\rangle$ at site i . They are represented by the orbital operators τ_i^α associated with the three cubic axes ($\alpha = a, b$, or c),

$$\tau_i^{a(b)} = \frac{1}{4}(-\sigma_i^z \pm \sqrt{3}\sigma_i^x), \quad \tau_i^c = \frac{1}{2}\sigma_i^z, \quad (3)$$

where the σ 's are Pauli matrices acting on the orbital pseudospins: $|x\rangle = \begin{pmatrix} 1 \\ 0 \end{pmatrix}$ and $|z\rangle = \begin{pmatrix} 0 \\ 1 \end{pmatrix}$, corresponding to the usual basis in the e_g subspace defined by $|x\rangle \equiv |x^2 - y^2\rangle$ and $|z\rangle \equiv |3z^2 - r^2\rangle$ orbitals, corresponding to $|\uparrow\rangle$ and $|\downarrow\rangle$ pseudospin components.

The t_{2g} -hopping leads to an approximately isotropic SE [19],

$$H_J^t = \sum_{\langle ij \rangle} \left\{ \frac{1}{4} J_t n_i n_j (\mathbf{S}_i \cdot \mathbf{S}_j - 4) + \frac{4}{9} \hat{J}_t (1 - n_i)(1 - n_j) \left(\mathbf{S}_i \cdot \mathbf{S}_j - \frac{9}{4} \right) \right. \\ \left. + \frac{1}{3} \bar{J}_t [n_i(1 - n_j) + (1 - n_i)n_j] (\mathbf{S}_i \cdot \mathbf{S}_j - 3) \right\}, \quad (4)$$

with SE constants (as estimated using the spectroscopic data [5,19]): $J_t = 2.1$ meV, $\hat{J}_t = 4.6$ meV, and $\bar{J}_t = 5.5$ meV for the pairs of $\text{Mn}^{3+}\text{--Mn}^{3+}$, $\text{Mn}^{4+}\text{--Mn}^{4+}$, and $\text{Mn}^{3+}\text{--Mn}^{4+}$ ions, respectively, and \mathbf{S}_i is an $S = 2$ ($S = \frac{3}{2}$) spin operator for a Mn^{3+} (Mn^{4+}) ion with $n_i = 1$ ($n_i = 0$) e_g electrons.

The intersite JT interaction leads to purely orbital interactions [20] which favor orbital alternation, and one finds [5]:

$$H_{\text{JT}} = \kappa \sum_{\langle ij \rangle} n_i n_j \left(\mathcal{P}_{\langle ij \rangle}^{\zeta\zeta} - 2\mathcal{P}_{\langle ij \rangle}^{\zeta\xi} + \mathcal{P}_{\langle ij \rangle}^{\xi\xi} \right) - E_z \sum_i \tau_i^c n_i, \quad (5)$$

where $\mathcal{P}_{\langle ij \rangle}^{\xi\xi} = 2P_{i\xi}P_{j\xi}$, and $\kappa \simeq 11$ meV is determined from the experimental temperature of the structural phase transition $T_s = 750$ K [5]. The tetragonal crystal-field splitting $\propto E_z$ acts as a magnetic field in the pseudospin space.

The SE interaction due to e_g electrons (1) depends on the Hund's rule coupling J_H/U and on the type of occupied orbitals. As in the d^9 model [7], the e_g interactions are frustrated in the $J_H/U \rightarrow 0$ limit at $E_z = 0$, but the t_{2g} SE removes this degeneracy and stabilizes the G-type AF phase for small J_H/U , while for the actual values of the interaction parameters the A-AF phase is stable [Fig. 1(a)]. Due to the particular stability of the high-spin 6A_1 state of Mn^{2+} ions, the system is quite close to the FM insulating (FI) state, and one might expect that a transition to this state occurs under doping.

In the weakly doped regime the holes are localized and form Mn^{4+} lattice polarons with energy E_p . They interact with the surrounding Mn^{3+} ions by FM SE $\propto J_p = K_p/(1 + E_p/2J_H)$, where $K_p = t^2/2E_p$ stands for the effective charge interaction in which the polaronic energy is lost at both sites [19],

$$H_{\text{pol}} = -E_p \sum_i (1 - n_i) - \sum_{\langle ij \rangle} (1 - n_i) \left[K_p + \frac{1}{8} J_p (\mathbf{S}_i \cdot \mathbf{S}_j - 3) \right] P_{j\zeta} n_j. \quad (6)$$

Taking the Hamiltonian $\mathcal{H}_{eff} = H_J^e + H_J^t + H_{\text{JT}} + H_{\text{pol}}$, we determined the total exchange constants on the bonds within the FM (a, b) planes $J_{(a,b)}$, and along the c axis J_c , assuming a random distribution of polarons over the lattice. In addition, we weighted the polaron energy E_p by the number of holes at the first neighbors of the polaron, $\sum_j (1 - n_j)/6$, which suppresses partly the polaronic energy when doped holes are close to each other and block the corresponding lattice distortion. As a consequence of the FM contribution $\propto J_p$, the (average) AF interaction J_c is affected much stronger by doping than the FM $J_{(a,b)}$, and the order changes from A-AF to the FI state at $x \simeq 0.11$, where $x = 1 - n$ and $n = \langle n_i \rangle$ is the e_g electron density. The model gives the values $J_{(a,b)} = -1.15$ meV and $J_c = 0.88$ meV for LaMnO_3 [5], thus reproducing well the experimental values -0.83 and 0.58 meV, respectively. Furthermore, the observed doping dependence of $J_{(a,b)}$ and J_c in $\text{La}_{1-x}\text{Ca}_x\text{MnO}_3$ [21] could also be reproduced, but only if a (close to) rigid OO was assumed [Fig. 1(b)]. Instead, if the local OO was modified to form orbital polarons around a doped hole [22], the transition to the FI phase occurs already at $x \simeq 0.047$. This suggests that the lattice plays an important role in the manganites, and prevents the formation of orbital polarons.

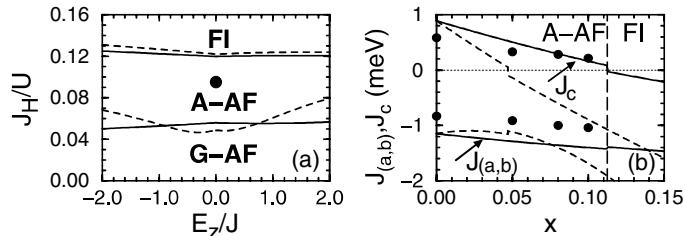


Fig. 1. (a) Mean-field phase diagram of LaMnO_3 obtained using SE interactions H_J^c and H_J^t (dashed lines), and both SE and cooperative JT effect H_{JT} (full lines); the parameters of LaMnO_3 [19] are indicated by a dot. (b) Exchange interactions $J_{(a,b)}$ and J_c as functions of doping x for the states with OO (full lines), and for orbital polarons (dashed lines), compared with experimental data for $\text{La}_{1-x}\text{Ca}_x\text{MnO}_3$ (dots) [21].

2 Stoner Instability in the Orbital Model

As described in the previous Section, the DE induces a transition to a FM metallic phase in doped manganites. This transition occurs typically around $x \simeq 0.17$, and its mechanism is one of the outstanding questions in the theory of the CMR phenomenon [1]. We will not consider it here, but instead investigate which orbital state might be realized in this phase. In particular the question *whether the orbitals order or not* is both of fundamental nature, and of great interest for the magnetic properties of the FM manganites.

Therefore, we consider in this Section a generic model of electrons with polarized spins, as in FM metallic manganites, which move within an e_g band on a cubic lattice in the presence of local Coulomb repulsion U . Thus, we neglect the spin index of the fermion operators, and investigate a spinless orbital-Hubbard model with kinetic energy for a three-dimensional (3D) cubic lattice,

$$H_t = -t \sum_{\langle ij \rangle} c_{i\zeta}^\dagger c_{j\zeta}, \quad (7)$$

where hopping occurs only between the orbitals $|\zeta\rangle$ oriented along the bond $\langle ij \rangle$, as explained in Sec. 1. However, to describe the electron interactions it is more convenient to introduce a fixed orthogonal basis for the two orbital flavours of the e_g electrons. In analogy to the spin case described by the standard single-band Hubbard model, they are usually labelled as x and z , thus taking the real eigenstates of the σ^z Pauli matrix, $|x\rangle$ and $|z\rangle$, as a basis. The kinetic energy (7) is then given as (with $\langle ij \rangle$ either within the (a, b) planes or along the c axis),

$$H_t = -\frac{1}{4}t \sum_{\langle ij \rangle \parallel (a,b)} \left[3c_{ix}^\dagger c_{jx} + c_{iz}^\dagger c_{jz} \pm \sqrt{3}(c_{ix}^\dagger c_{jz} + c_{iz}^\dagger c_{jx}) \right] - t \sum_{\langle ij \rangle \parallel c} c_{iz}^\dagger c_{jz}. \quad (8)$$

The electrons interact by the local Coulomb interaction, $H_U = U \sum_i n_{ix} n_{iz}$, and are thus prone to instabilities towards OO, similar to those towards magnetic order in the standard Hubbard model, induced by the interaction between electrons with spins up and down.

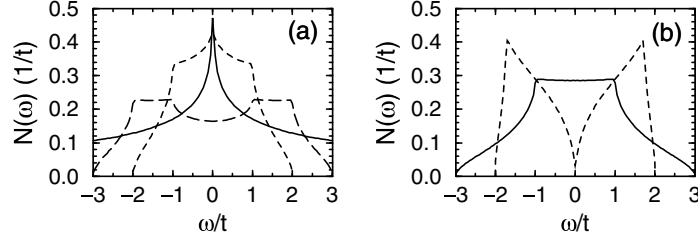


Fig. 2. Density of states $N(\omega)$ for: (a) FO $|\Phi_x\rangle$ (full line) and $|\Phi_z\rangle$ (long-dashed line) states (9), and for $(|x\rangle + |z\rangle)/(|x\rangle - |z\rangle)$ AO state (dashed line); (b) FO $|\Phi_{FO}\rangle$ (full line) and AO $|\Phi_{AO}\rangle$ (dashed line) states (18) with complex orbitals.

The simplest possibility to avoid double occupancies and reduce the interaction energy $\propto U$ would be to polarize the system completely. Using the above basis, one has two fully polarized orbital [*ferro orbital* (FO)] states at $n = 1$:

$$|\Phi_x\rangle = \prod_i c_{ix}^\dagger |0\rangle, \quad |\Phi_z\rangle = \prod_i c_{iz}^\dagger |0\rangle. \quad (9)$$

They would correspond in the spin problem to two (equivalent) fully polarized FM states with opposite magnetization, obtained as the ground state for large U at all values of n in the HF approximation, and in a more restricted range of n when the problem is investigated by more sophisticated methods which include electron correlations by means of variational wave functions [23,24]. However, these variational studies were carried out for a square lattice only, and we are not aware of similar results for a cubic lattice which is of interest for the manganites.

We investigate the FO states (9) first using a slave-fermion approach, where the electrons are represented by orbital bosons $b_{i\alpha}^\dagger$ ($\alpha = x, z$), and a slave-fermion (hole) operator f_i^\dagger , such that $c_{i\alpha}^\dagger = b_{i\alpha}^\dagger f_i^\dagger$, with a local constraint,

$$b_{ix}^\dagger b_{ix} + b_{iz}^\dagger b_{iz} + f_i^\dagger f_i = 1. \quad (10)$$

This approach is well suited to investigate the kinetic energy $E_{\text{kin}} = \langle H_t \rangle$ for the orbital ordered states [22]. At half filling, as no holes are present, it vanishes by construction (10). If the band is partly filled with $n < 1$, the states (9) must be modified to involve a coherent mixture of occupied and empty sites, and the kinetic energy is finite. In this case one has to choose the type of occupied orbitals $|i\mu\rangle$, given in general by a linear combination of $\{|z\rangle, |x\rangle\}$ orbitals, and defined by a basis transformation with the same angle θ at each site,

$$\begin{pmatrix} |i\mu\rangle \\ |i\nu\rangle \end{pmatrix} = \begin{pmatrix} \cos \theta & \sin \theta \\ -\sin \theta & \cos \theta \end{pmatrix} \begin{pmatrix} |iz\rangle \\ |ix\rangle \end{pmatrix}. \quad (11)$$

The states $|\Phi_x\rangle$ and $|\Phi_z\rangle$ are realized for $\theta = \pi/2$ and $\theta = 0$, respectively. The fermionic band is obtained by averaging over the boson operators, and one finds a dispersion which depends on the orbital order,

$$\varepsilon_{\mathbf{k}}^{\text{FO}}(\theta) = t[2 - \cos(2\theta)]\gamma_+(\mathbf{k}) + \sqrt{3}t \sin(2\theta)\gamma_-(\mathbf{k}) + t[1 + \cos(2\theta)]\gamma_z(\mathbf{k}), \quad (12)$$

with $\gamma_{\pm}(\mathbf{k}) = \frac{1}{2}(\cos k_x \pm \cos k_y)$, and $\gamma_z(\mathbf{k}) = \cos k_z$. One can now investigate the energy as a function of the angle θ . At low doping x the kinetic energy is only weakly dependent on θ as the band has the full width of $6t$, with the minimum of $\varepsilon_{\mathbf{k}}^{\text{FO}}(\theta)$ at $\omega = -3t$, independent of the value of θ . It is an important feature of all FO states that the cubic symmetry is broken and the properties of the system are *highly anisotropic*. This follows from the effective reduction of the dimensionality, exemplified by the two-dimensional (2D) $|\Phi_x\rangle$ state and the quasi-one-dimensional $|\Phi_z\rangle$ state. The corresponding densities of states $N(\omega)$ have therefore appreciable spectral weights close to the band edges [Fig. 2(a)].

As a characteristic consequence of the OO, lattice distortions are induced due to the coupling to the lattice. We have shown in Sec. 1 that the JT interaction together with the SE interactions induce orbital alternation within the (a, b) planes, with angle alternating between $+\theta$ and $-\theta$, and such *alternating orbital* (AO) order competes with the polarized FO states described above. The kinetic energy in the AO states follows from the fermionic band determined in a similar way,

$$\varepsilon_{\mathbf{k}}^{\text{AO}}(\theta) = t[2 \cos(2\theta) - 1]\gamma_+(\mathbf{k}) + t[1 + \cos(2\theta)]\gamma_z(\mathbf{k}). \quad (13)$$

In contrast to the FO case, the width of this band depends on the angle θ , and amounts to $4t$ for the alternating $(|x\rangle + |z\rangle)/(|x\rangle - |z\rangle)$ orbitals found at $\theta = \pi/4$ [Fig. 2(a)], the angle favored at $n = 1$ by the cooperative JT effect. Therefore, the kinetic energy is in general worse in the AO than in the FO states.

A more general approach to investigate the kinetic energy in a partly filled e_g band is to introduce the *complex orbitals* which are the eigenstates of the σ^y Pauli matrix with eigenvalues $\lambda_{\pm} = \pm 1$,

$$c_{i+}^{\dagger} = \frac{1}{\sqrt{2}}(c_{iz}^{\dagger} - ic_{ix}^{\dagger}), \quad c_{i-}^{\dagger} = \frac{1}{\sqrt{2}}(c_{iz}^{\dagger} + ic_{ix}^{\dagger}). \quad (14)$$

Using these as a basis gives the kinetic energy H_t a more symmetric form,

$$H = -\frac{t}{2} \sum_{\langle ij \rangle} \left[c_{i+}^{\dagger} c_{j+} + c_{i-}^{\dagger} c_{j-} + \gamma \left(e^{i\chi_{\alpha}} c_{i+}^{\dagger} c_{j-} + e^{-i\chi_{\alpha}} c_{i-}^{\dagger} c_{j+} \right) \right] + U \sum_i n_{i+} n_{i-}. \quad (15)$$

Here the phase factors χ_{α} depend on the bond direction: $\chi_{\alpha} = \pm 2\pi/3$ for $\alpha = a, b$, and $\chi_{\alpha} = 0$ for $\alpha = c$. The representation (15) displays manifestly the difference between the spin case and the orbital case, and in fact allowed us to introduce a parameter γ to treat a more general case which interpolates between the spin-Hubbard model ($\gamma = 0$) and the e_g band orbital-Hubbard model ($\gamma = 1$). Due to the terms $\propto c_{i\pm}^{\dagger} c_{j\mp}$ the pseudospin quantum number is not conserved, and qualitatively one expects the kinetic energy to decrease with increasing $\gamma \rightarrow 1$.

The coherent orbital state at site l may be now written in the general form,

$$|\Omega_l\rangle = \cos(\psi_l/2) e^{-i\theta_l} |l+\rangle + \sin(\psi_l/2) e^{+i\theta_l} |l-\rangle. \quad (16)$$

It determines the values of the SE (1) and JT (5) interactions, described by:

$$\langle \sigma_l^x \rangle = -\sin \psi_l \sin(2\theta_l), \quad \langle \sigma_l^z \rangle = -\sin \psi_l \cos(2\theta_l). \quad (17)$$

Hence, one finds that $\langle \sigma_l^z \rangle = \langle \sigma_l^x \rangle = 0$, if either $\psi_l = 0$ or $\psi_l = \pi$. This choice corresponds to either $|l+\rangle$ or $|l-\rangle$ local states, respectively. Therefore, FO or AO states built from complex orbitals,

$$|\Phi_{\text{FO}}\rangle = \prod_i c_{i+}^\dagger |0\rangle, \quad |\Phi_{\text{AO}}\rangle = \prod_{i \in A} c_{i+}^\dagger \prod_{j \in B} c_{j-}^\dagger |0\rangle, \quad (18)$$

where A and B are two interpenetrating sublattices, will manifestly retain cubic symmetry and will cause no lattice distortion. Such states have been proposed as weak-coupling instabilities of the e_g band by Khomskii [25] (FO state) and by Takahashi and Shiba (AO state) [26]. The kinetic energy in these states,

$$\varepsilon_{\mathbf{k}}^{\text{FO}} = t[2\gamma_+(\mathbf{k}) + \gamma_z(\mathbf{k})], \quad (19)$$

$$\varepsilon_{\mathbf{k}}^{\text{AO}} = \pm t[(\gamma_+(\mathbf{k}) - \gamma_z(\mathbf{k}))^2 + 3\gamma_-^2(\mathbf{k})]^{1/2}, \quad (20)$$

is cubic symmetric and thus the physical properties are expected to be *isotropic*. In the case of the FO state, it has the same minimum $\varepsilon_0^{\text{FO}} = -3t$ as found before for the $|\Phi_x\rangle$ and $|\Phi_z\rangle$ states. However, the density of states (DOS) $N(\omega)$ is just the same as for a tight-binding problem in a simple cubic lattice, with hopping amplitude $\frac{1}{2}t$ [Fig. 2(b)]. Therefore, $|\Phi_{\text{FO}}\rangle$ is *unstable* against $|\Phi_x\rangle$ and $|\Phi_z\rangle$ at all doping concentrations x . We note also that, in contrast to the corresponding spin model, the orbital polarized state $|\Phi_{\text{FO}}\rangle$ is *not* an eigenstate of H_t .

The two-sublattice state $|\Phi_{\text{AO}}\rangle$ has also an isotropic band structure (20), but has bandwidth $4t$, the same as the $(|x\rangle + |z\rangle)/(|x\rangle - |z\rangle)$ AO state. Surprisingly, this state has a DOS with distinct maxima close to the band edges [Fig. 2(b)], and could thus be stable near quarter filling [26]. This band mechanism is different from the spin model, where AF states follow either from the Fermi surface instability at weak coupling, or from the SE at large U .

As expected, the orbital model (15) gives symmetry-broken ground states at finite U when the HF approximation, $Un_{i+}n_{i-} \simeq U(\langle n_{i+} \rangle n_{i-} + n_{i+} \langle n_{i-} \rangle)$, is used [26]. At $\gamma = 0$ (spin model) one recovers the usual Stoner criterion $U_c N(E_F) = 1$ for the magnetic order, where E_F is the Fermi energy, with $U_c \simeq 3.4t$ in a broad range of $0.42 < n < 1.58$. The saturated FM state is obtained at a somewhat higher value of U ; for instance at $n = 1$ it is found at $U > 4.9t$ [see Fig. 3(a)]. The Stoner instability disappears close to the band edges (at $|n - 1| \simeq 1$) due to the low values of $N(\omega)$, and is then replaced by a first order transition to the saturated FM states at $U \simeq 12t$. In contrast, at $\gamma \neq 0$ the FO states appear not as a Fermi surface instability, but as a global property of the band, and the band structure changes. This instability occurs more easily near $n = 1$, and is not related to the DOS at the Fermi energy $N(E_F)$ [Fig. 3(b)]. The FO states at $\gamma = 1$ are similar to the AF states in the $\gamma = 0$ spin-Hubbard model at large U , with fully polarized FO states found *only* in the limit $U = \infty$. At finite but large U , the orbital moments are reduced in lowest order by terms $\propto (\gamma t/U)^2$. This shows that indeed the orbital model (15) with $\gamma \neq 0$ is qualitatively different from the spin problem at $\gamma = 0$.

Nagaoka has shown that FM states are realized for a single hole/electron in a half-filled band, described by the Hubbard model at $U = \infty$ [27]. Indeed, also

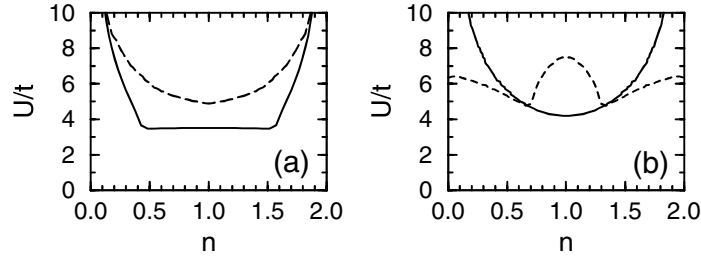


Fig. 3. Instabilities towards weakly polarized states (full lines) in the orbital model (15) for: (a) $\gamma = 0$, and (b) $\gamma = 1$. Fully polarized states occur above the long-dashed line in case (a). The dashed line in (b) shows the Stoner condition given by $N^{-1}(\omega)$.

for a square filled by $N = 3$ electrons, the Nagaoka theorem is fulfilled, and a ground state with high spin $S = \frac{3}{2}$, and energy $E_{\square} = -t$ [assuming the hopping of $-\frac{1}{2}t$ and $\gamma = 0$ in Eq. (15)], is found. In contrast, the eigenstates of the orbital model at $\gamma > 0$ cannot be classified by a pseudospin quantum number, and the *Nagaoka theorem does not apply*. The ground state energy $E_{\square} = -(1 + \gamma)t$ [28] decreases with increasing γ , and is lower by a factor of two for e_g orbitals at $\gamma = 1$, when full advantage of all hopping terms is taken and the orbitals are disordered. This demonstrates a generic tendency towards an *orbital liquid* state promoted in the correlated e_g band by the orbital mixing terms $\propto c_{i\pm}^{\dagger} c_{j\mp}$.

The above result for the square suggests that the FO state $|\Phi_{\text{FO}}\rangle$ (18) may also be difficult to realize in the thermodynamic limit. The stability of this state can only be investigated reliably if the correlation energy in the unpolarized (orbital liquid) state is calculated with a comparable accuracy as the kinetic energy of the fully polarized states, where the electron interactions give no contribution. This problem is known to be notoriously difficult in itinerant ferromagnetism [29], but fortunately variational treatment similar to that in the Hubbard model [24] is possible. We will consider the $U \rightarrow \infty$ limit which is the only case where the fully polarized FO states might be realized at all, as we learned from the above HF study. This limit is also consistent with the t - J model introduced for the manganites [19,30], and studied in the following Section. At $U \rightarrow \infty$ the correlated space may be formally described by including slave bosons $\{b_{i+}^{\dagger}, b_{i-}^{\dagger}\}$ for the complex orbitals, and a slave boson e_i^{\dagger} for an empty site, with the basis defined by:

$$b_{i\pm}^{\dagger} f_{i\pm}^{\dagger} |vac\rangle = c_{i\pm}^{\dagger} |vac\rangle = |\pm\rangle, \quad e_i^{\dagger} |vac\rangle = |0\rangle. \quad (21)$$

The physical space is defined by the local constraint $b_{i+}^{\dagger} b_{i+} + b_{i-}^{\dagger} b_{i-} + e_i^{\dagger} e_i = 1$, and the condition that the numbers of respective bosons and fermions are equal: $b_{i\pm}^{\dagger} b_{i\pm} = f_{i\pm}^{\dagger} f_{i\pm}$. These conditions have to be included with the help of Lagrange multipliers when the kinetic energy E_{kin} is minimized.

The Hamiltonian (15) may now be written following Kotliar and Ruckenstein (KR) who introduced this approach for the Hubbard model [31]. A transition of an electron along a bond $\langle ij \rangle$ is accompanied by the respective change in the slave boson configuration. Therefore, the effective Hamiltonian in this limit operates in the restricted space without double occupancies, and contains

new operator expressions $z_{i\alpha}^\dagger z_{j\beta}$ ($\alpha, \beta \in \{+, -\}$) which multiply the fermionic expressions; for instance, the hopping between $|+\rangle$ orbitals is represented by $c_{i+}^\dagger c_{j+} = z_{i+}^\dagger f_{i+}^\dagger f_{j+} z_{j+}$, where the bosonic factors z_{i+}^\dagger and z_{i-} are selected to satisfy the limit of the uncorrelated band [31]. We have verified that this formulation fulfills U(1) symmetry, in contrast to a similar formalism which might be proposed for real orbitals $\{|x\rangle, |z\rangle\}$ [30].

As an example we consider explicitly an FO state, while a similar analysis can also be performed for an AO state. In the mean-field (MF) approximation one finds the renormalization Gutzwiller factors $\sqrt{q_\pm} = \langle z_{i\pm} \rangle = \sqrt{x/[1 - \langle b_{i\pm}^\dagger b_{i\pm} \rangle]}$ for the individual hopping processes, and the effective Hamiltonian,

$$H_t^{\text{MF}} = -\frac{t}{2} \sum_{\langle ij \rangle} \left[q_+ f_{i+}^\dagger f_{j+} + q_- f_{i-}^\dagger f_{j-} + \gamma \sqrt{q_+ q_-} \left(e^{i\chi_\alpha} f_{i+}^\dagger f_{j-} + e^{-i\chi_\alpha} f_{i-}^\dagger f_{j+} \right) \right] - \mu \sum_i n_i - \lambda \sum_i (n_{i+} - n_{i-}). \quad (22)$$

After minimizing the kinetic energy $E_{\text{kin}} = \langle H_t^{\text{MF}} \rangle$ one finds that for $\gamma = 1$ the minimum corresponds to an OL state with *equal* densities of fermions of each flavour, $\langle n_{i+} \rangle = \langle n_{i-} \rangle = \frac{1}{2}(1 - x)$, and the same renormalization factor $q(x) = q_{i\pm}(x) = 2x/(1 + x)$ for both complex orbitals. This OL state is qualitatively different from the statistical average over regions of polarized states proposed earlier by Nagaosa *et al.* [32]. The bands in this correlated disordered state,

$$\varepsilon_\pm(\mathbf{k}) = -tq(x) \left\{ 2\gamma_+(\mathbf{k}) + \gamma_z(\mathbf{k}) \pm [(\gamma_+(\mathbf{k}) - \gamma_z(\mathbf{k}))^2 + 3\gamma_-^2(\mathbf{k})]^{1/2} \right\}, \quad (23)$$

are isotropic and interpolate correctly between the limit of empty band ($x \rightarrow 1$), where the electron correlations disappear, and the half-filled band ($x \rightarrow 0$), where the electrons localize in a Mott insulator. The above band structure represents a superposition of two different channels: diagonal hopping $\propto f_{i\pm}^\dagger f_{j\pm}$, which determines the dispersion in the FO states (19), and off-diagonal hopping $\propto f_{i\pm}^\dagger f_{j\mp}$, responsible for the dispersion in the AO states (20).

The FO states considered before in the slave-fermion approach, $|\Phi_x\rangle$, $|\Phi_z\rangle$, and $|\Phi_{\text{FO}}\rangle$, can also be obtained within the present KR slave-boson formalism by an appropriate choice of the Lagrange multipliers. For instance, the $|\Phi_{\text{FO}}\rangle$ state (18) is obtained by choosing $\mu + \lambda = 0$ and $\mu - \lambda \rightarrow \infty$ in Eq. (22). In this way one finds results equivalent to those discussed above, which demonstrates that a single slave-fermion approach represents accurately the OO states. Comparing for $\gamma = 0$ the energy of the FM state with the spin liquid we have found that the polarized states are stable close to half filling, $0.67 < n < 1.33$. Thus, the range of stability of ferromagnetism in the Hubbard model on a 3D cubic lattice is much restricted, and large corrections occur to the results obtained in HF approximation (Fig. 3). It is believed that the present method gives results close to rigorous answers, as for a 2D Hubbard model at $U = \infty$ it predicts that the FM state is unstable for $x > 0.33$ [24], which is indeed very close to $x > 0.29$, given by a more sophisticated variational wave function [23]. It is thus

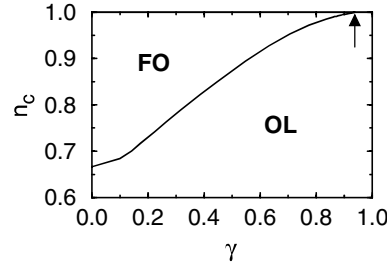


Fig. 4. Phase diagram of the orbital model (15) at $U = \infty$ – the FO state (FO) is more stable than the orbital liquid state (OL) in a range $n_c < n < 2 - n_c$.

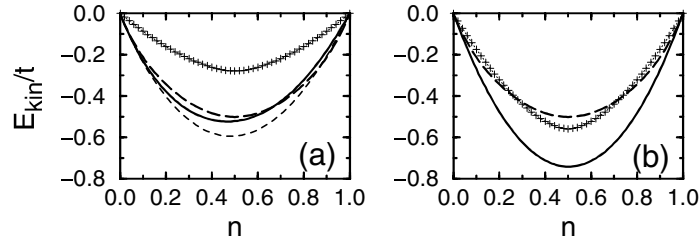


Fig. 5. Kinetic energy in the orbital model (15) as obtained for the FO state (long-dashed lines) and for OL states (full lines) for: (a) $\gamma = 0$, and (b) $\gamma = 1$. The AO states are shown by pluses for: (a) $\gamma = 0.5$, and (b) $\gamma = 1$, while the OL state for $\gamma = 0.5$ is shown in (a) by the dashed line.

very interesting to observe, that the range of stability of FO states shrinks with increasing γ (Fig. 4), and FO order is unstable for all values of n , if $\gamma > 0.92$.

The suppression of FO states by increasing orbital mixing terms $\propto \gamma$ is easy to understand by investigating the kinetic energy of the correlated states. In the spin model ($\gamma = 0$) the kinetic energies of the FM and paramagnetic states are very close to each other [Fig. 5(a)]. While the energy of the polarized FO states does not change when γ is increased, energy is gained in the OL states with increasing γ , similar to the case of three electrons moving on a square discussed above. In the case of e_g orbitals ($\gamma = 1$) the extra energy gain is close to 50% of the energy found in the spin case (Fig. 5), and thus the OL state is more stable. The kinetic energy of the AO states is also lowered with increasing γ , but at $\gamma = 1$ is finally in the same range as that of the FO states, not quite enough to stabilize the AO states either. We have also checked that other states such as $|\Phi_x\rangle$, $|\Phi_z\rangle$, or the disordered state with real orbitals occupied [$\psi = \pi/2$ in Eq. (16)], are unstable. Therefore, we conclude that the OL state is the ground state of the orbital-Hubbard model in the entire range of U and n .

3 Double Exchange in the Correlated e_g Band

The total energy in the doped manganites is described by the manganite t - J model, where the SE interactions H_J^e and H_J^t involve either spins $S = 2$ or

$S = \frac{3}{2}$, as explained in Sec. 1, and the hopping H_t which occurs in the correlated e_g orbitals. Adopting again the MF slave-boson approach, the energy follows from the t - J Hamiltonian,

$$\mathcal{H}_{tJ} = H_t^{\text{MF}} + H_J^e + H_J^t + H_{\text{JT}}. \quad (24)$$

As explained, the kinetic energy $E_{\text{kin}} = \langle H_t^{\text{MF}} \rangle$ alone favors the OL state in the doped manganites [Fig. 6(a)]. It is expected that this term wins if the doping is high enough, and this explains why the doped manganites are FM. The advantage of the OL state and also of polarized FO and AO states built from complex orbitals (18) is that the electrons do not couple to the lattice as $\langle \sigma_l^z \rangle = \langle \sigma_l^x \rangle = 0$ [see Eq. (17)], and thus $\langle H_{\text{JT}} \rangle = 0$. Therefore, such states give isotropic magnetic properties, as observed in FM metallic manganites [15].

It is important to realize that the SE and JT terms favor instead OO with *alternating* orbitals at small doping, and thus a competition between the OO and OL states occurs. In order to gain also the energy from the lattice distortions, the respective OO states are built by real orbitals ($\psi_i = \pi/2$). By contrast, the real FO states such as $|\Phi_x\rangle$ or $|\Phi_z\rangle$ are unfavorable for the JT interactions, as the energy increases when the orbitals are uniformly polarized. Therefore, the ground state exhibits AO order at low x . For the realistic parameters we have found that two polaronic phases are stable: the A-AF phase for $x < 0.11$, and the FI phase in the intermediate regime of $0.11 < x < 0.15$, while the ground state changes abruptly to a metallic FM phase with disordered orbitals around $x > 0.15$ [Fig. 6(b)].

The correlated hopping in the e_g band (15) is responsible for the DE interactions. They may be derived using the first order terms in Schwinger bosons $a_{i\sigma}^\dagger$. First, the kinetic energy H_t has to be written for both spins, using the decomposition of electron operators into Schwinger bosons, orbital bosons, and fermion operators: $c_{i\pm,\sigma}^\dagger = a_{i\sigma}^\dagger z_{i\pm}^\dagger f_{i\pm}^\dagger$ [30]. This allows to separate the charge and orbital dynamics from the spin dynamics, and to expand the Schwinger boson terms around the \uparrow -spin FM ground state. The physical space is defined by the constraint $\sum_\sigma a_{i\sigma}^\dagger a_{i\sigma} + b_i^\dagger b_i = 2S$, with $S = 2$, which gives $a_{i\uparrow} \simeq \sqrt{2\bar{S}} \sqrt{1 - a_{i\downarrow}^\dagger a_{i\downarrow}/2\bar{S}}$ and leads then to

$$a_{i\uparrow}^\dagger a_{j\uparrow} + a_{i\downarrow}^\dagger a_{j\downarrow} \simeq 2\bar{S} - \frac{1}{2} \left(a_{i\downarrow}^\dagger a_{i\downarrow} + a_{j\downarrow}^\dagger a_{j\downarrow} - 2a_{i\downarrow}^\dagger a_{j\downarrow} \right), \quad (25)$$

with $2\bar{S} = 4 - x$ standing for the average number of Schwinger bosons in the doped system. After inserting Eq. (25) into the hopping Hamiltonian H_t , one finds from the zeroth order term $H_t^{(0)} \propto 2\bar{S}$ the kinetic energy E_{kin} considered above, while the first order term gives the magnon excitations, with the energies $\omega_{\mathbf{q}} = 2J_{\text{DE}}\bar{S}[3 - 2\gamma_+(\mathbf{q}) - \gamma_z(\mathbf{q})]$, with $J_{\text{DE}} = \langle H_t^{(0)} \rangle / 2z\bar{S}^2$, and $z = 6$. Thus, the DE contribution to the magnon bandwidth $W_{\text{DE}} = 2J_{\text{DE}}z\bar{S} = \langle H_t^{(0)} \rangle / \bar{S}$ vanishes in the $x \rightarrow 0$ limit, and *increases with increasing x* [Fig. 7(a)]. The increase of W was observed experimentally in doped manganites [15,33]. We emphasize that this result is reproduced *only* when the theory includes the local

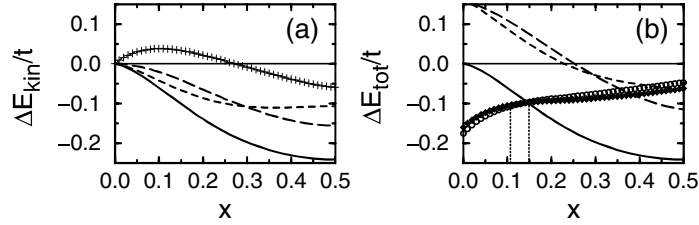


Fig. 6. Energy gain for various phases with respect to the FO state with complex orbitals (18) versus hole doping x : (a) kinetic energy $\Delta E_{\text{kin}}/t$, and (b) total energy $\Delta E_{\text{tot}}/t$. Here $|\Phi_x\rangle$, $|\Phi_z\rangle$ (9), AO state with complex orbitals (18), and OL state, are shown by dashed lines, long-dashed lines, pluses, and full lines, respectively. The AO states with A-AF (circles) and FI (diamonds) order [part (b)] are more stable than the OL state at low doping x ; two phase transitions are indicated by vertical dotted lines.

correlations between e_g electrons, while the *opposite* and incorrect result with the strongest FM DE interactions at $x = 0$ [34] follows from electronic structure calculations that ignore local electron correlations altogether.

The magnon width W which follows from the manganite t - J model contains also SE contributions. The situation is here different than when the ground state energy is studied, which contains only the energy contribution from the excitations of high-spin 6A_1 states. Using again an expansion in terms of Schwinger bosons around the FM state, both FM and AF terms in the SE Hamiltonian, H_J^e and H_J^t , contribute to the magnon dispersion. The t_{2g} SE gives a large AF term which reduces the magnon dispersion obtained from the DE mechanism. Further terms follow from the e_g SE interactions: the interactions between the Mn^{3+} - Mn^{3+} pairs described by H_J^e (1), and the AF interactions between the Mn^{3+} - Mn^{4+} pairs, which arise in addition due to excitations to the low-spin 3E states when the system is doped, $\propto \frac{1}{3}\bar{J}_e(1 - n_i)n_j(\mathbf{S}_i \cdot \mathbf{S}_j - 3)P_{j\zeta}$, with $\bar{J}_e = 22.7$ meV. As the orbital operators are isotropic in the OL state, with $\langle \mathcal{P}_{ij}^{\zeta\zeta} \rangle = \langle \mathcal{P}_{ij}^{\zeta\zeta} \rangle = \frac{1}{2}$, the SE contribution evaluated from H_J^e is isotropic and weakly AF, taking the realistic parameters [5]. The second contribution $\propto \bar{J}_e$ term is larger and is mainly responsible for the additional reduction of $W = W_{\text{DE}} + W_{\text{SE}}$, shown in Fig. 7(a).

The total magnon dispersion is thus isotropic and determined by a combination of DE and SE terms, $J_{\text{eff}} = J_{\text{DE}} + J_{\text{SE}}$, with $J_{\text{SE}} < 0$. The DE term dominates and the magnon width W increases with x in the FM metallic phase and almost saturates close to $x = 0.5$. The calculated values lie somewhat below the experimental points, but reproduce well the observed increase of W [33] with increasing x in the FM metallic regime of $x > 0.15$ [Fig. 7(a)]. At small doping $x \leq 0.15$ we show instead W obtained for two polaronic phases: A-AF and FI. The magnon width *decreases* somewhat with increasing x within the A-AF phase which agrees qualitatively with the observed decrease of the Néel temperature under doping in $\text{La}_{1-x}\text{Ca}_x\text{MnO}_3$ [21]. As seen in Fig. 7(b), the magnon dispersion found at $x = 0.3$, with $J_{\text{eff}}\bar{S} = 7.10$ meV, is *isotropic* and reproduces well the experimental points for $\text{La}_{0.7}\text{Pb}_{0.3}\text{MnO}_3$, and the experimental exchange

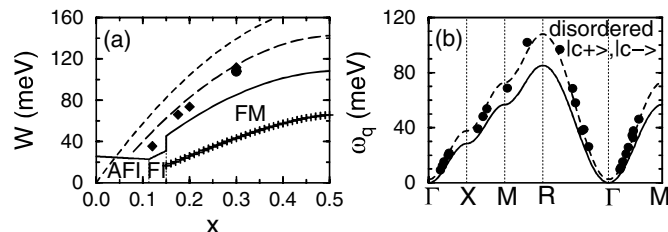


Fig. 7. Magnons as obtained in the FM metallic OL state. Part (a) shows the total width W of the magnon band as a function of hole doping x (full line), its DE part (dashed line), and DE together with SE contribution due to t_{2g} electrons only (long-dashed line); experimental points correspond to: $\text{La}_{1-x}\text{Sr}_x\text{MnO}_3$ [33] (diamonds) and $\text{La}_{0.7}\text{Pb}_{0.3}\text{MnO}_3$ [35] (filled circle). The result found with a two-sublattice $|c+\rangle/|c-\rangle$ AO state is shown by pluses. Part (b) shows the magnon dispersion at $x = 0.30$ (full line) and the experimental points for $\text{La}_{0.7}\text{Pb}_{0.3}\text{MnO}_3$ (circles and dashed line) [35].

constant $J_{\text{exp}}\bar{S} = 8.79$ meV deduced by Perring *et al.* [35]. This agreement is very encouraging indeed as no fit was used, and all the parameters were obtained from the spectroscopic data. Note that the FO $|\Phi_x\rangle$ (or $|\Phi_z\rangle$) states, obtained instead in the slave-fermion approach, require a statistical average over the three cubic axes, and give too small values of $J_{\text{eff}}\bar{S} \simeq 4.0$ meV [36].

4 Summary and Conclusions

In conclusion, we have demonstrated a generic competition between orbital order and orbital liquid states in doped manganites. The SE interactions dominate at low doping and explain well the anisotropic A-AF state observed in LaMnO_3 . We have verified that the derived SE interactions (1) and (4) reproduce rather well the experimental Néel temperatures T_N of 136, 122, and 110 K for LaMnO_3 , $\text{La}_{0.92}\text{Ca}_{0.08}\text{MnO}_3$, and CaMnO_3 , respectively, as they give the values 106, 95, and 124 K, using mean-field theory and the appropriate reduction due to quantum fluctuations.

The orbital model which describes the correlated e_g band is qualitatively different from the spin problem, and the instabilities towards orbital order are suppressed by the structure of the hopping. Therefore, an orbital liquid state is stabilized in FM manganites which provides a natural explanation of their isotropic magnetic properties. The electron correlations play a crucial role in this phase and are directly measurable by the magnon dispersion (or stiffness) which is proportional to the doping x , and thus to the Gutzwiller factor $q(x)$ representing the correlation effect.

Acknowledgment

This work was supported by the Committee of Scientific Research (KBN) of Poland, Project No. 2 P03B 055 20.

References

1. M. Imada, A. Fujimori, Y. Tokura: Rev. Mod. Phys. **70**, 1039 (1998)
2. K.I. Kugel, D.I. Khomskii: Sov. Phys. Usp. **25**, 232 (1982); A.M. Oleś, L.F. Feiner, J. Zaanen: Phys. Rev. B **61**, 6257 (2000)
3. Y. Tokura, N. Nagaosa: Science **288**, 462 (2000)
4. A.M. Oleś, M. Cuoco, N.B. Perkins: in: *Lectures on the Physics of Highly Correlated Electron Systems IV*, edited by F. Mancini, AIP Conference Proceedings Vol. **527** (New York, 2000), pp. 226-380
5. L.F. Feiner and A.M. Oleś: Phys. Rev. B **59**, 3295 (1999)
6. R. Shiina, T. Nishitani, H. Shiba: J. Phys. Soc. Jpn. **66**, 3159 (1997)
7. L.F. Feiner, A.M. Oleś, J. Zaanen: Phys. Rev. Lett. **78**, 2799 (1997)
8. P.W. Anderson, H. Hasegawa: Phys. Rev. **100**, 675 (1955); P.-G. de Gennes: Phys. Rev. **118**, 141 (1960)
9. N. Furukawa: J. Phys. Soc. Jpn. **65**, 1174 (1996)
10. Y. Okimoto, T. Katsufuji, T. Ishikawa, T. Arima, Y. Tokura: Phys. Rev. B **55**, 4506 (1997)
11. A.J. Millis, P.B. Littlewood, B.I. Shraiman: Phys. Rev. Lett. **74**, 5144 (1995)
12. Y. Murakami, J.P. Hill, D. Gibbs, M. Blume, I. Koyama, M. Tanaka, H. Kawabata, T. Arima, Y. Tokura, K. Hirota, Y. Endoh: Phys. Rev. Lett. **81**, 582 (1998)
13. M. Capone, D. Feinberg, M. Grilli: Eur. Phys. J. B **17**, 103 (2000)
14. A.I. Liechtenstein, V.I. Anisimov, J. Zaanen: Phys. Rev. B **52**, R5467 (1995)
15. J.A. Fernandez-Baca, P. Dai, H. Hwang, C. Kloc, S.-W. Cheong: Phys. Rev. Lett. **80**, 4012 (1998)
16. S. Maezono, S. Ishihara, N. Nagaosa: Phys. Rev. B **58**, 11583 (1998)
17. S. Okamoto, S. Ishihara, S. Maekawa: Phys. Rev. B **61**, 451 (2000)
18. T. Mizokawa and A. Fujimori: Phys. Rev. B **54**, 5368 (1996)
19. L.F. Feiner, A.M. Oleś: Physica B **259-261**, 796 (1999)
20. A. J. Millis: Phys. Rev. B **53**, 8434 (1996)
21. F. Moussa, M. Hennion, G. Biotteau, J. Rodríguez-Carvajal, L. Pinsard, A. Revcolevschi: Phys. Rev. B **60**, 12299 (1999)
22. R. Kilian, G. Khaliullin: Phys. Rev. B **60**, 13458 (1999)
23. W. von der Linden, D. Edwards: J. Phys.: Condens. Matter **3**, 4917 (1991)
24. B. Möller, K. Doll, R. Frésard: J. Phys.: Condens. Matter **5**, 4847 (1993)
25. D.I. Khomskii: private communication (2000)
26. A. Takahashi, H. Shiba: J. Phys. Soc. Jpn., in press (2000)
27. Y. Nagaoka: Phys. Rev. **147**, 392 (1966)
28. K. Rościszewski: private communication (2000)
29. A.M. Oleś: Phys. Rev. B **28**, 327 (1983); A.M. Oleś, G. Stollhoff: Phys. Rev. B **29**, 314 (1984); G. Stollhoff, A.M. Oleś, V. Heine: Phys. Rev. B **41**, 7028 (1990)
30. A.M. Oleś, L.F. Feiner: Acta Phys. Polon. A **97**, 193 (2000)
31. G. Kotliar, A.E. Ruckenstein: Phys. Rev. Lett. **57**, 1362 (1986)
32. S. Ishihara, M. Yamanaka, N. Nagaosa: Phys. Rev. B **56**, 686 (1997)
33. Y. Endoh, K. Hirota: J. Phys. Soc. Jpn. **66**, 2264 (1997)
34. I.V. Solov'yev, K. Terakura: Phys. Rev. Lett. **82**, 2959 (1999)
35. T.G. Perring, G. Aeppli, S.M. Hayden, S.A. Carter, J.P. Remeika, S.-W. Cheong: Phys. Rev. Lett. **77**, 711 (1996)
36. S. Maezono, N. Nagaosa: Phys. Rev. B **61**, 1189 (2000)

First Principles Theory of Magnetism for Materials with Reduced Dimensionality

Olle Eriksson

Department of Physics, Uppsala University, Box 530, S-75112 Uppsala, Sweden

Abstract. Theoretical work on thin film and bulk magnetism is reported. The calculation of spin and orbital moments are demonstrated to reproduce experiment within a few percent, whereas the magneto crystalline anisotropy (MAE) and magneto striction coefficients are hard to reproduce with similar accuracy. The correct easy axis is, with a few exceptions, always reproduced by first principles theory, and the size of the MAE and the related magnetostriction is always of the correct order of magnitude. However, examples are given when the size of the MAE and magneto striction differ from experiment with a factor 2-3, suggesting a need for improved density functionals.

1 Introduction

The magnetic moment of a material, whether it is ferro, ferri, or anti ferromagnetically coupled to its neighbors, is composed of a spin, S_z , and an orbital moment, L_z . In order for an orbital moment to develop one needs to consider relativistic effects in parallel to the exchange splitting, and this may be done by solving the spin polarized Dirac equation or by diagonalizing a Hamiltonian that includes the relevant relativistic effects, most notably the spin-orbit coupling, using products of scalar relativistic basis functions and spinor functions as basis functions. The latter approach is often used either in a direct way[1] or by use of the so called second variational approach[2]. Results from the different approaches give similar anisotropic magnetic properties [3]. Irrespective of calculational method one ends up considering a Hamiltonian that includes relativistic effects and as a result of this the only angular momentum states that commute with the Hamiltonian are $\mathbf{J}^2, J_z, \mathbf{L}^2, \mathbf{S}^2$, hence only these angular momenta are constants of the motion. Since S_z and L_z are not, one may ask whether it is possible at all to calculate them. However, one may still calculate the average of the spin operator, S_z , (and L_z) and below we illustrate this with a simple example from atomic physics. In order to do this we show in Fig.1 the vector model (which is justified by the Wigner-Eckart theorem[4]) for an LS coupled state, under the influence of a tiny external magnetic field \mathbf{B} . In this figure \mathbf{J} , \mathbf{L} and \mathbf{S} are treated as vector quantities. They are not static but drawn at an arbitrary time. \mathbf{J} is precessing relatively slowly around \mathbf{k} (the direction where \mathbf{B} is pointing) and \mathbf{L} and \mathbf{S} precess rapidly around \mathbf{J} with a frequency proportional to the strength of the spin-orbit coupling. The mean of S_z can be calculated by first forming the vector \mathbf{S}_J , i.e. the component of \mathbf{S} along \mathbf{J} , and secondly calculating $\mathbf{S}_J \cdot \mathbf{k}$. The magnitude of \mathbf{S}_J is $S_J = \frac{\mathbf{S} \cdot \mathbf{J}}{J}$ and \mathbf{S}_J can hence be written as $\mathbf{S}_J = \frac{\mathbf{S} \cdot \mathbf{J}}{J} \frac{\mathbf{J}}{J}$. S_z can

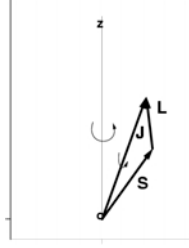


Fig. 1. LS-coupling of Angular momenta J , L and S . A small magnetic field, B , is pointing along the k -direction (from o to z).

be calculated as the projection of \mathbf{S}_J along \mathbf{k} , using $S_z = \mathbf{S}_J \cdot \mathbf{k} = \frac{\mathbf{S} \cdot \mathbf{J}}{J^2} J_z$. Since $\mathbf{S} \cdot \mathbf{J} = (J^2 - L^2 + S^2)/2$ we obtain $S_z = \frac{(J^2 - L^2 + S^2)J_z}{2J^2}$. Using similar arguments for \mathbf{L} we arrive at $L_z = \frac{(J^2 + L^2 - S^2)J_z}{2J^2}$. Replacing the vectors (J^2 , L^2 and S^2) for operators we can now calculate the average of S_z and L_z , using in the calculation operators that commute with the Hamiltonian. In relativistic electronic structure calculations one goes about the calculation of spin and orbital moments somewhat differently and calculates the expectation values of these operators directly from the eigenfunctions of the crystal Hamiltonian.

From the analysis above it becomes clear that the projection of S_z and L_z onto J_z can indeed be both calculated and measured and this chapter deals mostly with theoretical attempts to calculate S_z and L_z of thin film materials and multilayer systems, although a few examples of bulk magnetism are also given. In particular a few examples of calculated spin and orbital moments of thin film magnets will be given as well as theoretical values of the magneto crystalline anisotropy (MAE). The possibility to sometimes relate the MAE and orbital magnetism to each other will be analyzed as well. Results in theoretical work on magnetostriction coefficients will also be given, with an example of a recent work on alloys between Fe, Co and Ni[5].

2 MAE, Magnetostriction and Magneto-elastic Coupling

In this section we define some of the magnetic properties that are of interest to us in this chapter. An important fact for use of magnetism is that it is a vector quantity, both with a magnitude and a directionality. The preferred orientation of the magnetization in a crystalline structure is called the easy magnetization axis and the energy required to rotate the magnetization to another direction is named the magneto crystalline anisotropy (MAE). A large MAE is important in fabricating magneto optical devices since a well characterized out of plane magnetization is desired. Other applications require a small MAE, since so called soft magnetic materials are used in many applications, such as in transformers and generators, to mention a few examples.

For strains close to the cubic phase, bcc and fcc, the change in the MAE is linearly dependent on the strain, ϵ ($\epsilon=c/a-1$), and as will be clear below this is an important ingredient for understanding the magnetostriction (normally symbolized as λ). Using arguments from magneto-elastic theory, the MAE of small tetragonal distortions can be used to calculate the magnetostriction coefficient, e.g. λ_{001} , as illustrated in Ref.[6] for fcc Ni. The total energy can be written as the sum of an elastic and a magneto-elastic energy (E_{el} and E_{me}) which are assumed to be quadratic respectively linear in small distortions,

$$\begin{aligned} E_{el} &= C\epsilon^2 \\ E_{me} &= \alpha B\epsilon. \end{aligned} \quad (1)$$

Here ϵ is a volume conserving tetragonal distortion ($\epsilon \approx 2(c/a - 1)/3$), α is a constant which takes the value 1 for magnetization parallel to the tetragonal axis and $-1/2$ for a perpendicular direction, and B and C are the magneto-elastic and elastic coefficients, respectively. The latter is related to the regular elastic constants as $C = 3V_0(C_{11} - C_{12})/4$, where V_0 is the volume of the unit cell. The magnetostriction coefficient is, when the magnetization is along the [001] direction, written as λ_{001} , and is defined as the equilibrium distortion, i.e. when the total energy, $E_{el} + E_{me}$, has its minimum. By differentiation of the total energy and setting the expression equal to zero, we obtain

$$\lambda_{001} = \frac{-B}{2C}. \quad (2)$$

From this equation we observe that the magneto elastic coupling and magnetostriction are intimately connected to each other.

3 Theoretical Method

The theoretical method used in this work is the so called FP-LMTO method[7] and we will below describe this method in some detail. Before doing this we describe it shortly in simple terms. The method adopts a base geometry which consists of muffin-tin spheres and an interstitial region. Inside the muffin-tins the density and potential are expanded by means of spherical harmonic functions times a radial component. In the interstitial region the expansion of the density and potential makes use of a Fourier series. The interstitial basis function is a Bloch sum of Neumann and Hankel functions. Each Neumann or Hankel function is then augmented (replaced) by a numerical basis function inside the muffin-tin spheres, in the standard way of the linear muffin-tin orbital method[1]. Since a Bloch sum of atomically centered Hankel or Neumann functions involves an object which has the periodicity of the underlying lattice one may expand the periodic part in a Fourier series, which is done in the present method[7]. Evaluating matrix elements of the Hamiltonian the interstitial region thus involves relatively simple analytical functions: plane waves. The exchange-correlation term is approximated by the generalized gradient approximation (GGA) according to

Perdew and Wang[8] and by the local density approximation (LDA) according to Hedin-Lundqvist[9].

Let us now proceed with a somewhat more detailed description of the theory, and how the Kohn-Sham equation (the Schrödinger like equation that is central to all first principles calculations) is solved. First of all one normally assumes in a bulk material that the potential which enters the Kohn-Sham equation is periodic, i.e. $V_{eff}^{\uparrow(\downarrow)}(\mathbf{r}) = V_{eff}^{\uparrow(\downarrow)}(\mathbf{r} + \mathbf{R})$, where \mathbf{R} is a translation vector (a Bravais lattice vector) of the solid. This periodic boundary condition leads to Bloch's theorem[10] which states that as an effect of the periodicity of the bulk material the one-electron wave function must obey the following condition,

$$\psi_{i,\mathbf{k}}^{\uparrow(\downarrow)}(\mathbf{r} + \mathbf{R}) = e^{i\mathbf{k}\cdot\mathbf{R}}\psi_{i,\mathbf{k}}^{\uparrow(\downarrow)}(\mathbf{r}), \quad (3)$$

and we note that a vector of reciprocal space, \mathbf{k} , has been introduced. In addition one can solve the Kohn-Sham equations for each \mathbf{k} -vector being separate and independent of the others. However, the dependence of the one-electron wave function on \mathbf{k} makes the calculation of the one-electron density somewhat more complex since we have to include a sum over all possible \mathbf{k} -vectors, and the density is calculated from,

$$\rho_{op}^{\uparrow(\downarrow)}(\mathbf{r}) = \sum_i \sum_{\mathbf{k}} |\psi_{i,\mathbf{k}}^{\uparrow(\downarrow)}(\mathbf{r})|^2. \quad (4)$$

In a similar way one often needs to sum all the possible Kohn-Sham eigenvalues E_i to be used for calculating the total energy. The sum of the eigenvalues, E_{sum} , is often referred to as the eigenvalue sum and it is calculated from

$$E_{sum} = \sum_i \sum_{\mathbf{k}} E_{i,\mathbf{k}}. \quad (5)$$

3.1 Different Types of k-Space Integration

Having defined the eigenvalue sum, in Eqn.5 we are now ready to discuss different ways to approximate the integral over the Brillouin zone (BZ), which is necessary in numerical methods where one does not have an analytical expression of $E_{i\mathbf{k}}$. This is actually very important for calculating anisotropic magnetic properties, since the sum in Eqn5. converges very slowly as function of increasing k-mesh density. Below we will discuss three different BZI schemes to compare their merits. In all three cases a uniform mesh of k-points is used, distributed as to fulfill the symmetry of the space-group. The BZI can in all three cases be written as weighted sums over the bands, i , and the discrete set of sampled k-points, \mathbf{k}_j , with weight functions, w_{ji} . In the so-called linear tetrahedron method[11], LTM, the uniform mesh is divided into corner-sharing tetrahedra. A linear interpolation of the eigenvalues is performed between the k-points belonging to one tetrahedron, resulting in a weight function w_{ji} . The step function is used directly by using E_F as an upper limit in the energy integration. A modification of the linear tetrahedron method, MTM, was suggested by Blöchl et al.[12] In the MTM the

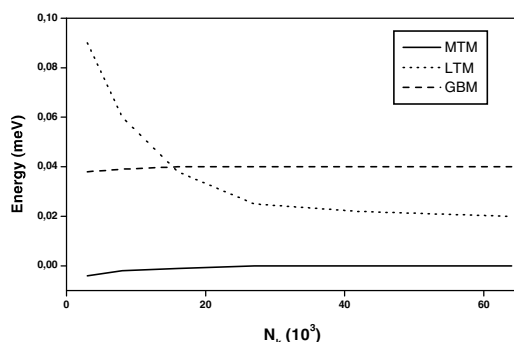


Fig. 2. Calculated total energy of fct Ni (normalized to zero) for three different k-space samplings (LTM, MTM and GBM). For details see text.

linear weights, w_{ji} , are corrected by, $dw_{ij} = \sum_T \frac{1}{40} D_T(E_F) \sum_l^4 (E_{il} - E_{ij})$, where T is an index for the tetrahedra and l is an index for the \mathbf{k} -points at the corners of the tetrahedron T . $D_T(E_F)$ is the contribution to the density of states from the tetrahedron T at the Fermi level and E_{ij} is the i^{th} eigenvalue of the j^{th} \mathbf{k} -point belonging to the tetrahedron T . The MTM corrects approximately the curvature of the energy band to leading order. Another way to perform the BZI is to use a Gaussian broadening method, GBM, which convolute each discrete eigenvalue with a Gaussian function of width W . This method and the related Fermi-Dirac broadening method are very popular in total energy methods since they lead to a fast and stable convergence of the charge and spin densities. The GBM can be seen as a truncation of a complete series expansion of a δ -function in terms of Hermite polynomials, H_n , with a Gaussian weight function [13].

An example of how the different BZ integration methods work is shown in Fig. 2 where the total energy of fct Ni (c/a ratio of 0.945) is presented as a function of the number of \mathbf{k} -points in the irreducible wedge of the BZ [6]. The calculations were based on a full potential linear muffin-tin orbital method, described in the next section. Note from Fig. 2 that the LTM converges much slower than the MTM and GBM. Notice also that the GBM does not converge to the same value as the other two methods which seem to converge to the same value. This is due to the fact that in the GBM the sum over Hermite polynomials is truncated, resulting in an approximate step function. However, the error in the energy difference is much smaller [6][14].

3.2 The FP-LMTO Method

Let us now describe the theoretical method used in this work, the FP-LMTO method of Wills [7]. The approach is to expand the (unknown) one-electron wave function in a set of (known) basis functions as,

$$\psi_{i,\mathbf{k}}(\mathbf{r}) = \sum_l^{l_{\max}} c_{li\mathbf{k}} \chi_{li\mathbf{k}}(\mathbf{r}). \quad (6)$$

The sum in the equation above is truncated after sufficiently many basis functions have been included and the coefficients $c_{li\mathbf{k}}$ are, via the Rayleigh-Ritz principle[15], determined from the following secular equation,

$$\sum_l^{l_{\max}} [H_{ll'} - E_{i\mathbf{k}} O_{ll'}] c_{li\mathbf{k}} = 0, \quad (7)$$

where

$$H_{ll'} = \int_{U_c} \chi_{l\mathbf{k}}(\mathbf{r}) \left[\frac{-\nabla^2}{2} + V_{eff}^{\uparrow(l)} \right] \chi_{l'\mathbf{k}}(\mathbf{r}) d^3r \equiv \int_{U_c} \chi_{l\mathbf{k}}(\mathbf{r}) h_{eff} \chi_{l'\mathbf{k}}(\mathbf{r}) d^3r \quad (8)$$

and

$$O_{ll'} = \int_{U_c} \chi_{l\mathbf{k}}(\mathbf{r}) \chi_{l'\mathbf{k}}(\mathbf{r}) d^3r, \quad (9)$$

where the integral is over the unit cell (U_c). Once $H_{ll'}$ and $O_{ll'}$ have been evaluated the eigenvalues, $E_{i\mathbf{k}}$ ($i=1-l_{\max}$), are determined by [15]

$$\det |H_{ll'} - E_{i\mathbf{k}} O_{ll'}| = 0, \quad (10)$$

a standard numerical problem, which may be solved by existing software.

3.3 Defining the LMTO Basis Functions

The difficulty is now to choose a basis set which is flexible and converges fast, i.e. as few basis functions as possible are needed to represent with sufficient accuracy a given eigenfunction, $\psi_{i,\mathbf{k}}(\mathbf{r})$. One efficient basis set is comprised of so called linear muffin-tin orbitals [1], which may be used in a full potential mode, as described by Wills[7] or with the use of the atomic sphere approximation [1]. Both these methods are reviewed elsewhere and the theory presented here is based on these works, but the presentation differs somewhat.

Let us note here that the FP-LMTO method is defined using a base geometry, which is the usual construction of muffin-tin spheres centered around the atoms and a region outside these spheres, called the interstitial region. In the muffin tins, the basis functions, electron density, and potential are expanded in spherical waves, whereas in the interstitial, the basis functions, electron density, and potential are expanded in Fourier series. The calculation of the Hamiltonian and overlap matrix elements thus involves replacing the integrals in Eqns.8 and 9 with two parts, one coming from the muffin-tins (MT) and one coming from the interstitial (Int). To be specific one breaks up integrals of $f(\mathbf{r})$ as $\int_{U_c} f(\mathbf{r}) d^3r = \int_{MT} f(\mathbf{r}) d^3r + \int_{Int} f(\mathbf{r}) d^3r$.

Let us now proceed and define some of the mathematical functions and special symbols that will be used below.

Spherical harmonics: $\mathcal{Y}_{\ell m}(\hat{\mathbf{r}}) \equiv i^l Y_{\ell m}(\hat{\mathbf{r}})$; $C_{lm}(\hat{\mathbf{r}}) \equiv \sqrt{\frac{4\pi}{2l+1}} Y_{\ell m}(\hat{\mathbf{r}})$;
 $\mathcal{C}_{lm}(\hat{\mathbf{r}}) \equiv i^l C_{lm}(\hat{\mathbf{r}})$, where $Y_{\ell m}$ is a spherical harmonic.

Bessel functions:

$$\mathcal{K}_l(\kappa, r) \equiv -\kappa^{l+1} \begin{cases} n_l(\kappa r) - i j_l(\kappa r) & \kappa^2 < 0 \\ n_l(\kappa r) & \kappa^2 > 0 \end{cases} \quad (11)$$

$\mathcal{K}_L(\kappa, \mathbf{r}) \equiv \mathcal{K}_l(\kappa, r) \mathcal{Y}_L(\hat{\mathbf{r}})$; $\mathcal{J}_l(\kappa, r) \equiv \frac{j_l(\kappa r)}{\kappa^l}$; $\mathcal{J}_L(\kappa, \mathbf{r}) \equiv J_L(\kappa, r) \mathcal{Y}_L(\hat{\mathbf{r}})$, where L denotes lm and n_l and j_l are spherical Neuman and Bessel functions, respectively.

Symmetric functions: Within the muffin-tin, functions invariant under the space group are expressed in harmonic series. This is motivated by the fact that around the atomic nuclei in the lattice most properties are atomic like and hence an expansion in spherical harmonics is efficient and converges fast. If $f(\mathbf{r})$ is such a function, at atomic site τ , the expansion may be written as,

$$f(\mathbf{r})|_{r_\tau < s_\tau} = \sum_{h_\tau} f_{h_\tau}(r_\tau) D_{h_\tau}(\mathcal{D}_\tau \hat{\mathbf{r}}_\tau) \quad (12)$$

where $D_{h_\tau}(\hat{\mathbf{r}}) = \sum_m \alpha_{h_\tau}(m) \mathcal{C}_{\ell_h m}(\hat{\mathbf{r}})$.

In Equation 12 \mathcal{D}_τ is a transformation to local coordinate system of site τ ; the local coordinates of sites of the same type are related by an element of the crystal point group that takes one site into another. Expressed in this way, the functional form of D_{h_τ} depends only on local symmetry of the atomic site in question.

In the interstitial, symmetric functions, which we again symbolize with the function $f(\mathbf{r})$, are expressed in a Fourier series: $f(\mathbf{r})|_{\mathbf{r} \in \mathbf{I}} = \sum_s f(s) \sum_{g \in s} e^{i\mathbf{g} \cdot \mathbf{r}}$, since the functions in this region vary smoothly. The sum is over symmetry stars, s , of the reciprocal lattice and $\mathbf{r} \in \mathbf{I}$ indicates the interstitial region.

Basis set. In the interstitial region (again symbolically denoted by I), a basis function, labeled i , is a Bloch sum of spherical Hankel or Neumann functions:

$$\psi_i(\mathbf{k}, \mathbf{r})|_{\mathbf{r} \in I} = \sum_{\mathbf{R}} e^{i\mathbf{k} \cdot \mathbf{R}} \mathcal{K}_{\ell i}(\kappa_i, |\mathbf{r} - \tau_i - \mathbf{R}|) \mathcal{Y}_{\ell i m_i}(\mathcal{D}_{\tau_i}(\mathbf{r} - \tau_i - \mathbf{R})). \quad (13)$$

The rotation \mathcal{D}_{τ_i} in Eqn.13 takes the argument into a coordinate system local to each site τ . The purpose of this will be made evident below. The function on the right hand side of Equation 13 is sometimes called the envelope function. Notice the parameters, specifying a basis function, inherent in this definition. There are the site τ in the unit cell on which the spherical wave is based, the angular momentum parameters ℓ and m of the spherical wave with respect to its parent cell, and the kinetic energy κ^2 of the basis in the interstitial. The angular momentum parameters specifying the basis set are chosen to represent the atomic states from which crystal eigenstates are derived. In the method described here it is usual to use “multiple κ ” basis sets, bases having all parameters except the tail parameter the same. Hence the method described is not a minimal basis set method, as opposed to the LMTO-ASA method.

Muffin tins spheres. In the muffin tin spheres, a basis function is a linear combination of spherical waves, that match continuously and differentially to an envelope function at the muffin-tin sphere. An envelope function \mathcal{K} may be expanded in a series of spherical Bessel functions about any atomic site, except the atomic site that it is centered on. A basis function on a muffin-tin sphere in the unit cell at $\mathbf{R} = 0$ is therefore

$$\begin{aligned}\psi_i(\mathbf{k}, \mathbf{r})_{r_\tau=s_\tau} &= \sum_{\mathbf{R}} e^{i\mathbf{k}\cdot\mathbf{R}} \sum_L \mathcal{Y}_L(\mathcal{D}_\tau \hat{\mathbf{r}}_\tau) (\mathcal{K}_l(\kappa_i, s_\tau) \delta(R, 0) \delta(\tau, \tau_i) \delta(L, L_i) \\ &\quad + \mathcal{J}_L(\kappa, s_\tau) B_{L, L_i}(\kappa_i, \tau - \tau' - \mathbf{R})) \\ &= \sum_L \mathcal{Y}_L(\mathcal{D}_\tau \hat{\mathbf{r}}_\tau) (\mathcal{K}_l(\kappa_i, s_\tau) \delta(\tau, \tau_i) \delta(L, L_i) \\ &\quad + \mathcal{J}_L(\kappa, s_\tau) B_{L, L_i}(\kappa_i, \tau - \tau', \mathbf{k})),\end{aligned}\quad (14)$$

where $\hat{\mathbf{r}}_\tau \equiv \widehat{\mathbf{r} - \tau}$ and B is unitarily equivalent to the KKR structure constant. Equation 14 is compactly expressed by defining a two-component row vector K so that $K_l(\kappa, r) = (\mathcal{K}_l(\kappa, r), \mathcal{J}_l(\kappa, r))$, and a two component column vector S so that

$$S_{L, L'}(\kappa, \tau - \tau', \mathbf{k}) = \begin{pmatrix} \delta(\tau, \tau') \delta(L, L') \\ B_{L, L'}(\kappa, \tau - \tau', \mathbf{k}) \end{pmatrix}. \quad (15)$$

Then the value of a basis function inside a muffin-tin sphere is a linear combination of atomic like functions, ϕ , and their energy derivatives, $\dot{\phi}$, matching continuously and differentially to the radial function K . Collecting ϕ and $\dot{\phi}$ in a row vector, $U(r) \equiv (\phi(r), \dot{\phi}(r))$, a simple case of this matching condition may be expressed as $U(r)\Omega(\kappa) = K(\kappa, s)$ and $U'(r)\Omega(\kappa) = K'(\kappa, s)$, where $\Omega(\kappa)$ is a matrix of order 2, to be described below.

A basis function in a muffin tin sphere is therefore

$$\psi_i(\mathbf{k}, \mathbf{r})|_{r_\tau < s_t} = \sum_{L, \ell}^{\ell \leq \ell_m} U_{tL}(e_i, \mathcal{D}_\tau \mathbf{r}_\tau) \Omega_{t\ell}(e_i, \kappa_i) S_{L, L_i}(\kappa_i, \tau - \tau', \mathbf{k}) \quad (16)$$

and $U_{tL}(e, \mathbf{r}) \equiv \mathcal{Y}_L(\hat{\mathbf{r}}) U_{t\ell}(e, r)$. The necessary cutoff in angular momentum has now been made explicit. The 2×2 matrix Ω matches U to K continuously and differentially at the muffin-tin radius. Specifically, Ω is specified by

$$\begin{pmatrix} \phi_{tL}(e, s_t), \dot{\phi}_{tL}(e, s_t) \\ \phi'_{tL}(e, s_t), \dot{\phi}'_{tL}(e, s_t) \end{pmatrix} \Omega_{t\ell}(e, \kappa) = \begin{pmatrix} \mathcal{K}_l(\kappa, s_t), \mathcal{J}_l(\kappa, s_t) \\ \mathcal{K}'_l(\kappa, s_t), \mathcal{J}'_l(\kappa, s_t) \end{pmatrix}. \quad (17)$$

3.4 Calculating the Matrix Elements

Muffin-Tin contribution. The potential in a muffin-tin at τ has an expansion in linear combinations of spherical harmonics invariant under that part of the point group leaving τ invariant:

$$V(\mathbf{r})|_{r_\tau < s_t} = \sum_{h_\tau} v_{h_\tau}(r_\tau) D_{h_\tau}(\mathcal{D}_\tau \hat{\mathbf{r}}_\tau), \quad (18)$$

where \mathcal{D}_{h_τ} is defined above. The utility of referring bases and potentials in muffin tins to site-local coordinates is apparent in 18. Combining Eqns.16 and 18 the potential matrix element $\langle \psi_i | V | \psi_j \rangle |_{mt}$ may be calculated.

Interstitial contribution. A Fourier transform of the basis functions described in Eqn.16 would be too poorly convergent for practical use. However, the evaluation of the interstitial potential matrix only requires a correct treatment of basis functions (and potential) in the interstitial, and this freedom can be used to design “pseudo bases”, equal to the true bases in the interstitial although not in the muffin-tins, which have a Fourier transform which converges rapidly enough for practical use. We define these pseudo bases by

$$\tilde{\psi}_i(\mathbf{k}, \mathbf{r}) = \sum_{\mathbf{R}} e^{i\mathbf{k} \cdot \mathbf{R}} \tilde{\mathcal{K}}_{l_i}(\kappa_i, |\mathbf{r} - \tau_i - \mathbf{R}|) i^l Y_{l_i m_i}(\widehat{\mathbf{r} - \tau_i - \mathbf{R}}), \quad (19)$$

where $\tilde{\mathcal{K}}_l(\kappa, r) \equiv \mathcal{K}_l(\kappa, r)$, $r > s$, where s is the radius of a sphere such that $s \leq s_\tau$. Inside a sphere with radius s , the form of the pseudo basis is unimportant since in this region the basis function to be used is given by Eqn. 16 and instead the form of the pseudo basis is determined to give an optimally convergent Fourier series.

The potential in the interstitial is similarly obtained from a “pseudo-potential” that equals the true potential in the interstitial and has rapidly converging Fourier coefficients:

$$V(\mathbf{r})|_I = \tilde{V}(\mathbf{r})|_I = \sum_s \tilde{V}(s) \sum_{g \in s} e^{i\mathbf{g} \cdot \mathbf{r}}, \quad (20)$$

The sum in Equation (20) is over stars \mathcal{S} of the reciprocal lattice.

Integrals over the interstitial are performed by convoluting the potential with an interstitial step function and integrating over the unit cell:

$$\langle \psi_i | V | \psi_j \rangle_I = \left\langle \tilde{\psi}_i \left| \tilde{V} \right| \tilde{\psi}_j \right\rangle_I = \left\langle \tilde{\psi}_i \left| \theta_I \tilde{V} \right| \tilde{\psi}_j \right\rangle_{U_c}.$$

3.5 Surface Slab Calculations

Since we will describe here results of spin and orbital moments of surfaces we describe how the above bulk method has been extended in Ref. [16] to a surface, slab method. As mentioned the present method uses a slab geometry, where three different regions are defined; muffin-tin regions, an interstitial region (outside the spheres and in-between the boundaries of the slab in the positive and negative z -direction, z_1 and $-z_2$, respectively), and two vacuum regions (for z -values greater than z_1 and less than $-z_2$). The slab is built up of sufficiently many atomic layers so that bulk behavior is found for the center layer. Normally 7-13 atomic layers are necessary to achieve this.

Inside the muffin-tins the treatment is the same as in the bulk method. The interstitial region is likewise described in a similar way as for bulk calculations,

i.e. the basis function is represented as a Fourier series. However, here one must consider a smaller modification as compared to the bulk calculation, since the slab only has periodic boundary conditions perpendicular to the slab normal. In order to do this we repeat the slab in the perpendicular direction, with a spacing R_z between the slabs, and all properties of the slab have periodic boundary conditions which enables a representation using a Fourier series. Hence, we can define a reciprocal vector also in the z-directions, i.e. $g_z = \frac{2\pi}{R_z}$. The basis functions inside the slab can then be represented as a Fourier series using a three dimensional g-vector, $\mathbf{g} = \mathbf{g}_{||} + \hat{z}g_z$. It is desirable to ensure that the overlap of the wavefunctions coming from different slabs is zero. Therefore, in calculating the Fourier coefficients used for the plane wave expansion we use a basis function which is truncated outside z_1 and $-z_2$ (see below). As a consequence the basis function inside the central slab has only contributions from muffin-tin spheres inside the slab. The basis function inside the slab is then matched on to a vacuum basis function, in a continuous and differentiable way. The vacuum basis function closely resembles a basis function inside a muffin-tin sphere (see below), since it is a numerical function (calculated using the planar averaged vacuum potential). The resulting wave function is continuous and has a continuous first derivative everywhere.

Let us now describe the form of a basis function in the interstitial region, and consider a Bloch sum of the 'pseudo' basis functions, written as

$$\tilde{\psi}_i(\mathbf{k}, \mathbf{r}) = \sum_{\mathbf{R}_{||}} e^{i\mathbf{k} \cdot \mathbf{R}_{||}} f(\mathbf{r} - \mathbf{t} - \mathbf{R}_{||}). \quad (21)$$

For a single slab we have only translation symmetry in two dimensions, and the two dimensional Bravais lattice is represented by $\mathbf{R}_{||}$ and f is defined in Eqn.19. A three dimensional Fourier representation can, as mentioned, be obtained by repeating the slab in the z-direction. The wavefunctions centered inside a given slab has to be truncated outside that slab, and by doing this one ensures that there is no overlap between wavefunctions coming from different slabs. The Fourier representation of the interstitial wavefunction (truncated outside the slab) can then be written as,

$$\tilde{\psi}_i(\mathbf{k}, \mathbf{r}) = \sum_{\mathbf{G}_{||}, \mathbf{G}_{\perp}} F_i(\mathbf{k} + \mathbf{G}_{||}, \mathbf{G}_{\perp}) e^{i(\mathbf{k} + \mathbf{G}_{||} + \mathbf{G}_{\perp}) \cdot \mathbf{r}}. \quad (22)$$

The expression for the Fourier coefficients, F , in Eqn.(22) are similar to the expression for the bulk coefficients. Since the potential in the interstitial region is also expressed as a Fourier series, the Hamiltonian and overlap matrix elements can be evaluated as simple reciprocal lattice sums, convoluted with a step function that is one in the interstitial region and zero everywhere else. It now remains to specify the basis function in the vacuum region. The requirement of the basis function in the vacuum is that it should decay asymptotically in the z-direction and be continuous and differentiable at the interface between vacuum and interface regions. This can be achieved by augmenting the basis functions centered at the atoms inside the slab, with a numerical solution to the Schrödinger equation

in the vacuum region. As mentioned, the wavefunction in the vacuum must have the same magnitude and first derivative (and therefore the same logarithmic derivative) as the wavefunction defined inside the slab. We therefore need first to evaluate the interstitial wavefunction (Eq.22) and its logarithmic derivative at z_1 (and $-z_2$). The value of the interstitial wave function at the upper plane, $\mathbf{r} = \mathbf{r}_{||} + \hat{z}z_1$, is (using Eqn.22)

$$\tilde{\psi}_i(\mathbf{k}, \mathbf{r}_{||} + \hat{z}z_1) = \sum_{\mathbf{G}_{||}, \mathbf{G}_{\perp}} F_i(\mathbf{k} + \mathbf{G}_{||}, \mathbf{G}_{\perp}) e^{i((\mathbf{k} + \mathbf{G}_{||}) \cdot \mathbf{r}_{||} + \mathbf{G}_{\perp} \cdot z_1)}. \quad (23)$$

However, in this case we are only interested of the wavefunction, and its derivative at the boundaries of the slab, namely at z_1 and $-z_2$. We can achieve this by considering pseudo wavefunctions which are not truncated, but with a spacing between different slabs (normally R_z) which goes to infinity. The summation over \mathbf{G}_{\perp} is then replaced by an integral $\int d\mathbf{G}_{\perp}$. The wavefunction at the upper plane, z_1 , is:

$$\begin{aligned} \tilde{\psi}_i(\mathbf{k}, \mathbf{r}_{||} + \hat{z}z_1) &= \sum_{\mathbf{G}_{||}} e^{i((\mathbf{k} + \mathbf{G}_{||}) \cdot \mathbf{r}_{||})} \int_{\mathbf{G}_{\perp}} F_i(\mathbf{k} + \mathbf{G}_{||}, \mathbf{G}_{\perp}) e^{i\mathbf{G}_{\perp} \cdot z_1} \\ &= \sum_{\mathbf{G}_{||}} e^{i((\mathbf{k} + \mathbf{G}_{||}) \cdot \mathbf{r}_{||})} \hat{P}_{\mathbf{G}_{||}}^{uv}, \end{aligned} \quad (24)$$

and the logarithmic derivative ($\frac{1}{\psi} \frac{d\psi}{dz}$) of this function is

$$D_{\mathbf{G}_{||}}^{uv} = z_1 \frac{\int_{\mathbf{G}_{\perp}} i\mathbf{G}_{\perp} F_i(\mathbf{k} + \mathbf{G}_{||}, \mathbf{G}_{\perp}) e^{i\mathbf{G}_{\perp} \cdot z_1}}{\int_{\mathbf{G}_{\perp}} F_i(\mathbf{k} + \mathbf{G}_{||}, \mathbf{G}_{\perp}) e^{i\mathbf{G}_{\perp} \cdot z_1}}. \quad (25)$$

We can now specify the wave function in the vacuum region as a linear combination of the solution to the Schrödinger equation, and its first energy derivative, in the vacuum region. This linear combination must have the same amplitude and logarithmic derivative as the interstitial wavefunction (for each $\mathbf{G}_{||}$). To be specific, the wave function in the upper vacuum region is defined as,

$$\psi_i^{uv, \mathbf{k}}(\mathbf{r}) = \sum_{\mathbf{G}_{||}} \hat{P}_{\mathbf{G}_{||}}^{uv} e^{i(\mathbf{G}_{||} + \mathbf{k}) \cdot \mathbf{r}_{||}} \frac{\Phi(\epsilon, D_{\mathbf{G}_{||}}^{uv}, z)}{\Phi(\epsilon, D_{\mathbf{G}_{||}}^{uv}, z_1)} \quad (26)$$

where uv denotes the upper vacuum. Due to the augmentation of the vacuum wave function with $\Phi(\epsilon, D_{t, \kappa, \mathbf{G}_{||}}^{uv}, z)$, the correct asymptotic behavior in the vacuum is ensured (exponentially decaying wavefunctions). Also, $\hat{P}_{\mathbf{G}_{||}}^{uv}$ can be calculated once and for all, given the geometry, and stored. With the use of the above specified vacuum wavefunction we can now derive the contribution to the Hamiltonian and overlap from the vacuum region. This is done by first considering the planar averaged contribution to the Hamiltonian, and then the non-spherical, warping terms, *i.e.*, $\langle \psi_{p'}^{uv, \mathbf{k}}(\mathbf{r}) | H | \psi_p^{uv, \mathbf{k}}(\mathbf{r}) \rangle = \langle \psi_{p'}^{uv, \mathbf{k}}(\mathbf{r}) | H_{planar} | \psi_p^{uv, \mathbf{k}}(\mathbf{r}) \rangle +$

$\langle \psi_{p'}^{uv,\mathbf{k}}(\mathbf{r}) | v_{nonspher} | \psi_p^{uv,\mathbf{k}}(\mathbf{r}) \rangle$. First, we consider the planar averaged Hamiltonian matrix elements, and much of the formalism and derivation is analogous to the spherical contribution from inside the muffin-tin spheres. [1] We thus get:

$$\begin{aligned} \langle \psi_{i'}^{uv,\mathbf{k}}(\mathbf{r}) | H_{planar} | \psi_i^{uv,\mathbf{k}}(\mathbf{r}) \rangle = & \quad (27) \\ & A_c \sum_{\mathbf{G}_{||}} \frac{\hat{P}_{\mathbf{G}_{||},i'}^{uv*} \hat{P}_{\mathbf{G}_{||},i}^{uv}}{\Phi^*(\epsilon, D_{i',\mathbf{G}_{||}}^{uv}, z_1) \Phi(\epsilon, D_{i,\mathbf{G}_{||}}^{uv}, z_1)} \\ & (\omega(D_{i,\mathbf{G}_{||}}^{uv}) + [E_\nu - G_x^2 - G_y^2 + K_x^2 + K_y^2] \\ & [1 + \omega^*(D_{i',\mathbf{G}_{||}}^{uv}) \omega(D_{i,\mathbf{G}_{||}}^{uv}) < \dot{\phi}^2 >]) \end{aligned}$$

and the overlap is

$$\begin{aligned} \langle \psi_{i'}^{uv,\mathbf{k}}(\mathbf{r}) | \psi_i^{uv,\mathbf{k}}(\mathbf{r}) \rangle = & A_c \sum_{\mathbf{G}_{||}} \frac{\hat{P}_{\mathbf{G}_{||},i'}^{uv*} \hat{P}_{\mathbf{G}_{||},i}^{uv}}{\Phi^*(\epsilon, D_{i',\mathbf{G}_{||}}^{uv}, z_1) \Phi(\epsilon, D_{i,\mathbf{G}_{||}}^{uv}, z_1)} \quad (28) \\ & (1 + \omega^*(D_{i',\mathbf{G}_{||}}^{uv}) \omega(D_{i,\mathbf{G}_{||}}^{uv}) < \dot{\phi}^2 >). \end{aligned}$$

Here A_C is the area of the surface unit cell, and $K_x = G_x + k_x$.

The non-spherical part of the potential in the vacuum region is represented as a Fourier series, *i.e.*, $v_{warp}(\mathbf{r}) = \sum_{\mathbf{G}_{||}'' \neq 0} V_{\mathbf{G}_{||}}''(z) e^{i\mathbf{G}_{||}'' \cdot \mathbf{r}}$, and the matrix elements for this part of the potential are,

$$\begin{aligned} \langle \psi_{i'}^{uv,\mathbf{k}}(\mathbf{r}) | v_{nonspher}(\mathbf{r}) | \psi_i^{uv,\mathbf{k}}(\mathbf{r}) \rangle = & A_c \sum_{\mathbf{G}_{||}} \sum_{\mathbf{G}_{||}'' \neq 0} \sum_{\mathbf{G}_{||}} \delta_{\mathbf{G}_{||}'' + \mathbf{G}_{||}, \mathbf{G}'} \quad (29) \\ & \frac{\hat{P}_{\mathbf{G}_{||},i'}^{uv*} \hat{P}_{\mathbf{G}_{||},i}^{uv}}{\Phi^*(\epsilon', D_{i',\mathbf{G}_{||}}^{uv}, z_1) \Phi(\epsilon, D_{i,\mathbf{G}_{||}}^{uv}, z_1)} \\ & \int_{z_1}^{\infty} \Phi^*(\epsilon', D_{i',\mathbf{G}_{||}}^{uv}, z) V_{\mathbf{G}_{||}}''(z) \Phi(\epsilon, D_{i,\mathbf{G}_{||}}^{uv}, z) dz. \end{aligned}$$

Equations similar to the ones described above, can be derived for the lower vacuum, and these two contributions are added to the total Hamiltonian and overlap matrices for the slab system[16].

4 Spin and Orbital Pairing

In the sections above theoretical methods for calculating the electronic structure of bulk and surfaces were described. We will now proceed with an analysis of how the effective potential and total energy expression can be improved upon. Since the spin-polarization (spin pairing) is treated via a spin-dependent effective potential, such as Eqn.8, and the relativistic spin-orbit interaction is also treated explicitly, the physical mechanisms behind Hund's first and third rules,

respectively, are (at least approximately) included. One can at this stage ask the question why total energy calculations based on different approximations to DFT ignore Hund's second rule. The answer to this question is of course that to day an exact, practical formalism for including effects responsible for Hund's second rule is lacking. However, it has been pointed out[17] that an approximate way to incorporate Hund's second rule in total energy calculations, using DFT, is to add to the LDA (or GGA) energy functional a term,

$$E_{OP} = -\frac{1}{2} \sum_{\sigma} E_{\sigma}^3 L_{\sigma}^2. \quad (30)$$

In this equation E_{σ}^3 is the so called Racah parameter (note that this parameter is normally denoted B for d-electrons and E^3 for f-electrons), which may be calculated from Slater integrals; F^2, F^4 and F^6 [18][19]. The correction in Eqn.30 is normally referred to as the orbital polarization (OP) correction. This form for including electron-electron interactions comes from the finding that a vector model, involving interactions of the form $l_i \cdot l_j$ between electron pairs[20][21], can be used to calculate the lowest energy multiplet. In fact an explicit expression for electron-electron interactions of a d-shell, in a cubic crystal field, having a form $l_i \cdot l_j$, is quoted by Ballhausen[21]. This form of the electron-electron interaction was used by Norman et al.[22] to give a correction term which is very similar to the form in Eqn.30. Summing the interaction, $l_i \cdot l_j$ over electron pairs as well as replacing the average of this interaction with the sum over average interactions, $l_{zi}l_{zj}$, gives rise to a form which is slightly different from Eqn.30[17]. The approximation of replacing $l_i \cdot l_j$ with the average is in the spirit of replacing the spin pairing energy, $\sum_{i \neq j} s_i \cdot s_j$, with a Stoner expression $\sum_i s_{zi} \sum_j s_{zj} = S_z^2$. Since this form of the energy is absent in the LDA or GGA energy functionals one must add the energy of Eqn.30 to these total energy functionals. The interactions which are responsible for Hund's second rule, which in a physical language are a reflection of that different angular momentum states have different angular dependence - and hence a different Coulombic interaction, are now in an approximate way included in the energy functional.

To illustrate the importance of Eqn.30 we show in Fig.3 the energy correction corresponding to Eqn.30 for the 4f electrons of the lanthanide atoms (or ions). To be specific Fig.3 shows Eqn.30 neglecting the effect of E^3 , hence illustrating only the angular behavior of the correction. The correction in Eqn.30 is compared to the exact values[23], which are calculated from the energy difference between the lowest atomic multiplet of the f^n configurations and those corresponding to the Grand Barry Centre (an average of the multiplets). This energy difference involves of course also spin-pairing energy and spin-orbit interaction, but shown in Fig.3 is only the part which depends on the orbital angular momentum.

To illustrate the importance of the OP correction we show in Figs.4 and 5 the calculated spin and orbital moments[24] of Fe, Co and Ni alloys, respectively. The calculations of the orbital magnetism was made using a standard LSDA calculation (with spin-orbit interaction), as well as from a calculation which incorporates the correction in Eqn.30. In Figure 5 experimental values are also

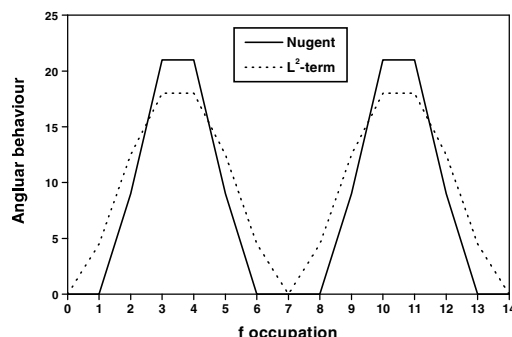


Fig. 3. Tetrad effect according to Nugent[23] compared to the orbital polarization term described in the text. Data evaluated for the lanthanides and scaled with the Racah parameter.

shown, and we note that an improved agreement between theory and experiment is consistently found for the orbital moment, when the OP correction is used. This is encouraging as well as reasonable, since the correction is supposed to include an interaction which is present in an interacting electron system. In addition we also observe that the orbital moments show a rather irregular behavior and as discussed by Söderlind [24] this is due to band filling effects. Since the size of the orbital moment is to a large degree caused by a redistribution of electron states around the Fermi level,[25][26] it generally scales to some degree with the value of the DOS at E_F . Hence a large DOS at E_F normally results in a larger orbital moment and the irregular behavior of the orbital moment is to some degree a reflection of an irregular behavior of the DOS at E_F , for these alloys. In addition the crystal symmetry is important since hcp Co is found to have the largest orbital moment. It can be argued from perturbation theory that for a cubic material the influence of the spin-orbit coupling strength, ξ , enters as ξ^4 . For non-cubic materials the dependence is stronger, and generally this results in larger orbital moments.

5 Force Theorem and MAE

In the sections above we have defined the anisotropic magnetic properties we are interested in and we are now ready to give examples of materials with interesting properties. First, we note that in the different approximations to density functional theory an explicit expression for the total energy is obtained, involving different terms such as the kinetic energy of effective one-electron states, the Hartree interaction and the exchange and correlation potential. This expression has been demonstrated to be very useful for theoretical studies of a vast variety of problems in physics and chemistry. For certain theoretical calculations it has been found that short-cuts may be made to reduce the computational effort appreciably, such as the so called force theorem[1,27,28]. The force theo-

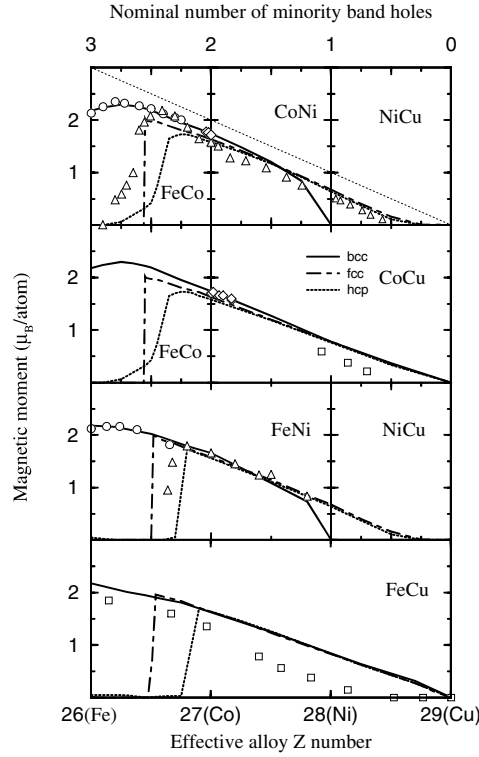


Fig. 4. Calculated average spin moments[14] of the FeCo, FeNi, FeCu, NiCu, CoCu and CoNi alloys, using the CPA method.

rem states that the energy difference between two crystal structures or between two magnetization directions of a crystal may simply be calculated as the difference in sum of occupied eigenvalues between the two structures or between the two magnetization directions, provided that the same effective potential in the Kohn-Sham equation is used [27]. This has the great advantage that only one self consistent calculation must be done, then the energy of the other configuration (crystal structure or magnetization direction) is obtained by one additional (non-self consistent) calculation.

We now compare the two different approaches to calculate the MAE, called the total energy approach (TE) and the force theorem approach (FT). In order to be able to subtract out a small number (e.g. the MAE) from two very large numbers (e.g. the total energies) extremely careful calculations are needed. Typically the total energies are required to be converged within $0.01 - 0.5 \mu eV$, depending on the magnitude of the calculated MAE. In the FT the effect of introducing the spin-orbit coupling is treated in the following way: A potential with a reduced symmetry and without the spin-orbit coupling is calculated self-consistently. From this potential two extra iterations are performed including

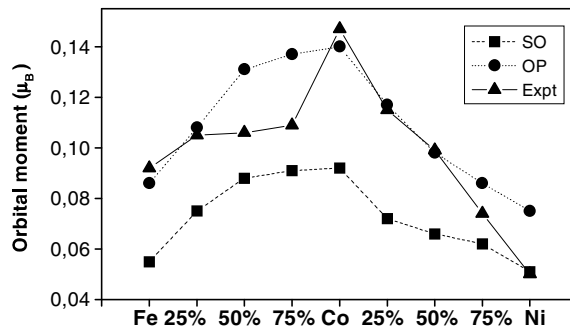


Fig. 5. Calculated and experimental orbital moments of Fe, Co and Ni, including their alloys, according to Ref.[24]. Data with and without orbital polarization shown.

the spin-orbit coupling and with the magnetization in different directions. The most straightforward way to perform FT calculations, and done here, is to reduce the symmetry and use only those point group symmetry operations that are common for both spin directions. The \mathbf{k} -point convergence of the self-consistent potential is not very crucial. Using a potential converged with a \mathbf{k} -point set of 13500 \mathbf{k} -points or with a set of 32000 \mathbf{k} -points yields only a shift in the MAE of 2%. Furthermore, the convergence of the total energy of the self-consistent potential does not at all need to be in the same range as the finally predicted value of the MAE, as is the case for the total energies in the TE. The orbital polarization term is not included in these calculations.

The results of the comparison are shown for bcc Fe and fcc Ni in Fig. 6. The MAE is, in all these figures, plotted as a function of number of \mathbf{k} -points. One can note that the total energy results and the data from the force theorem acquire the same easy axis direction for both elements and all \mathbf{k} -point sets. In addition, the differences of the converged MAE values between FT and TE are smaller than what can be resolved by the TE calculations. The good agreement between the TE and FT approach is quite encouraging and suggests that FT calculations of the MAE are quite accurate and may also be applied to other systems, such as alloys, surfaces, interfaces etc.

In Fig.7 the magneto crystalline energy obtained from the FT approach is compared to experimental data on bcc Fe[14]. Here the energy as a function of angle between the magnetization direction and the 001 axis is plotted, and it may be seen that overall there is good agreement between experiment and theory, both in the general shape of the curves as well as the relative ordering of the 001, 111 and 110 directions.

6 Thin Film Magnetism

Above it was argued that enhancement of relativistic effects may be found for materials with reduced symmetry or with a large value of the DOS around the

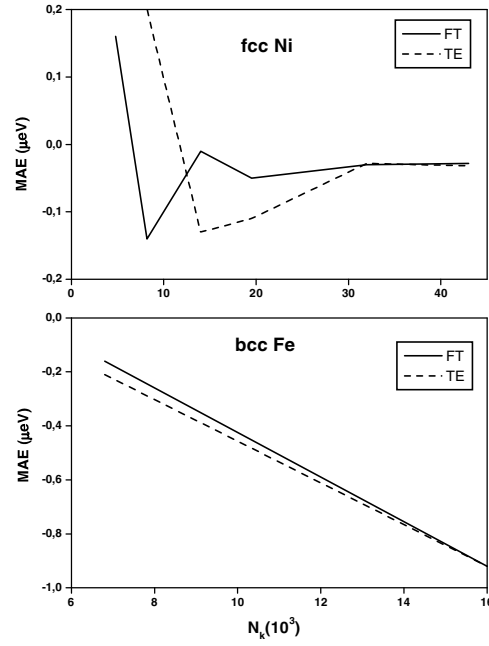


Fig. 6. MAE (comparing 100 with 111) of fcc Ni and bcc Fe using the FT (solid lines) and TE (dashed lines) approach (see text for details).

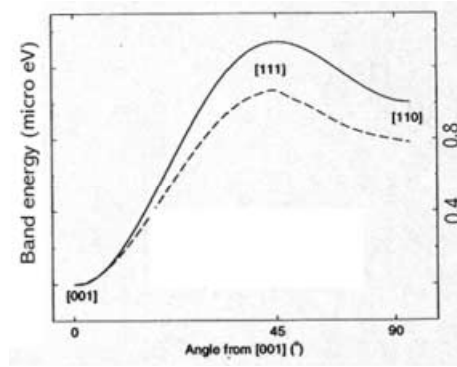


Fig. 7. Calculated MAE (using FT-dashed line) of bcc Fe as function of angle of the magnetization direction away from 001, compared to experimental data (full line).

Fermi level. One way to achieve this in practice is to fabricate thin films of a magnetic material, since both the symmetry is reduced and, due to the reduced coordination number, the band width is smaller. A good example of this is the growth of fcc Co on Cu (001), a system known to have several layers of Co grown epitaxially on the Cu substrate. Up to 50 atomic layers can be grown.[29] By

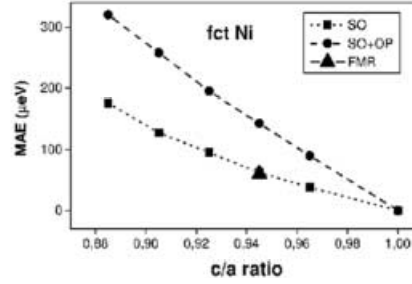


Fig. 8. Calculated and measured (filled triangle) values of the MAE (in plane minus out-of-plane) of bulk fct Ni. The calculations were made as a function of c/a ratio, with and without the orbital polarization correction. Positive numbers indicate the 001 direction as the easy axis.

means of x-ray magnetic circular dichroism the ratio of spin and orbital moments were detected and for thin film thicknesses, where the surface contribution becomes increasingly important, the ratio increases dramatically. First principles calculations[29] reproduced this behavior, and showed that the origin lies in an enhanced orbital moment of the surface. As a matter of fact the calculations showed that both the spin and orbital moments are enhanced at the surface, but that the orbital enhancement is substantially larger. This behavior was actually predicted [30] prior to the experimental work and subsequent experimental work have been reported[31].

Other systems of large interest are Ni films epitaxially grown on Cu, [32,33] which are known to have an out of plane magnetization for film thicknesses *above* ~ 7 atomic monolayers and an in plane magnetization for thinner thicknesses.[34] This is a rather unusual behavior since in most systems the shape anisotropy will be the dominating term in the thick limit and it always favors the in plane magnetization. In a previous work[32] it was speculated that this unusual behavior is driven by a large and positive volume contribution, K_v , to the magnetic anisotropy energy in the Ni film which occurs due to the tetragonal distortion of Ni grown on a Cu(001) substrate, in combination with a negative surface contribution, K_s .

Using the theoretical method presented above we have calculated K_v for Ni in a face centered tetragonal, fct, structure. K_v is defined as the difference in total energy, between the [110] and [001] magnetization directions, per atom. In figure 8 K_v is plotted as a function of c/a for an fct crystal assuming a constant in plane parameter, a_{ip} (i.e. this distortion is not volume conserving). The in plane lattice parameter, a_{ip} , is chosen to be 3.58 Å which is the same as the value measured by LEED for thin Ni films on Cu.[35] The experimental lattice parameter of bulk fcc Ni is 3.52 Å. This means that at $c/a=1.0$ we will for the fct crystal have a volume which is larger than the volume of bulk fcc Ni. For comparison both the calculated K_v with and without orbital polarization is shown. Note the large increase of K_v due to the orbital polarization. It is

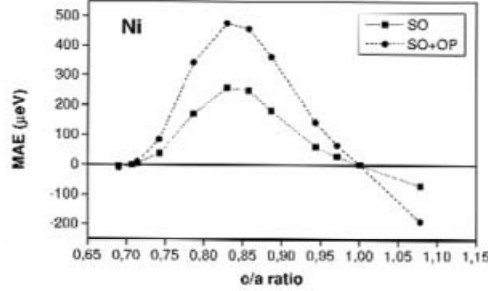


Fig. 9. Calculated values of the MAE (in plane minus out-of-plane) of bulk fct Ni. The calculations were made as a function of c/a ratio along the Bains path. Positive numbers indicate the 001 direction as the easy axis.

found that the [001] direction is the easy direction for all $c/a < 1.0$. Also one experimental point is shown in fig 8, and the agreement between experiment and theory is rather good (a more detailed analysis of the comparison between experiment and theory is given in the chapter by K.Baberschke in this volume).

We have performed calculations of K_v as a function of c/a when going from the fcc structure ($c/a=1.0$) to the bcc structure ($c/a=\frac{1}{\sqrt{2}}$), i.e. along the Bain path. These calculations are done in such a way that the volume is the same for all different c/a ratios. The results are shown in figure 9. For c/a close to fcc or bcc we see an almost linear behavior as expected from magneto-elastic arguments. Since both fcc and bcc are cubic structures, and have magnetic anisotropy constants that scale approximately with the spin-orbit constant to 4th order, and since the spin-orbit coupling is rather weak for these elements K_v has to be small for c/a close to 1.0 and $\frac{1}{\sqrt{2}}$. Therefore the K_v curve has to deviate from the linear behavior at some intermediate c/a ratio. In fig 9 it is seen that this happens when c/a is between 0.8 and 0.9. Further we notice that K_v is positive in the interval $\frac{1}{\sqrt{2}} < c/a < 1.0$ and negative for $c/a > 1.0$ and $c/a < \frac{1}{\sqrt{2}}$. It seems likely that this information can serve as a prediction of the volume contribution to the MAE, K_v , of pseudomorphically grown tetragonal Ni films on any substrate (if possible to fabricate). Due to the elasticity the volume of fct Ni will never deviate much from the volume of fcc Ni, and the curve in Fig. 9 should resemble the experimental reality. Of course it will be possible to repeat this procedure for any magnetic material which may possibly grow in an fct structure.

7 Magnetostriction of Fe, Co and Ni

Let us now return to the question of magnetostriction for a cubic system and its relation to the MAE of distorted structures (in our case fct), to see how well our first principles calculations compare to the magneto-elastic theory. First we will

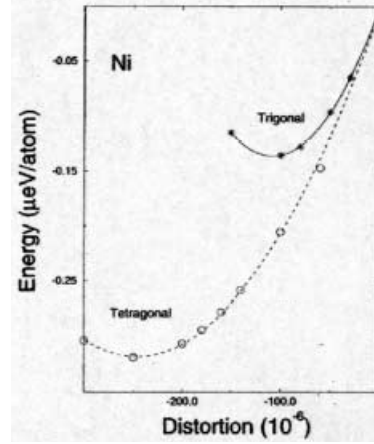


Fig. 10. Calculated magnetostriction λ_{111} and λ_{001} for Ni, using the total energy approach (circles and asterisks) and Eqn.2 (full and dashed lines).

use Eqn.2 in order to obtain, λ_{001} . In a previous work [36] the elastic constants C_{11} and C_{12} were calculated for fcc Ni using the same first principles method as in the present work. The deviation between these theoretical results and experimental values is less than 10 % and is not crucial for our discussion. Using these theoretical values of C_{11} and C_{12} and our calculated MAE, K_v , for a given strain (ϵ_1 and ϵ_2) we can calculate λ_{001} , using Eqn.2. This procedure gives $\lambda_{001} = -270 \cdot 10^{-6}$ [5,14]. A similar approach has previously been used by Wu et al. [37] for fcc Co in bulk and Co based multilayers. For comparison we show λ_{001} calculated directly from first principles by performing total energy calculations (including spin-orbit as well as orbital polarization), as a function of small (10^{-5} - 10^{-4}) tetragonal distortions [14]. The result is shown in figure 10. Notice the small energy scale on the y-axis ($\sim 0.1 \mu\text{eV}$) and how well the calculated energies fit to a parabola, which serves as a good illustration of the high accuracy of in the numerical procedure. From these total energy calculations one obtains $\lambda_{001} = -245 \cdot 10^{-6}$ [14], which agrees well with the value we obtained from magneto-elastic theory, quoted above. For completeness we show λ_{111} calculated using the total energy. This magnetostriction constant corresponds to a trigonal distortion (i.e. a length change in the [111] direction). The result is also shown in figure 10. From this one obtains the theoretical value of λ_{111} to be $-107 \cdot 10^{-6}$ [14]. In the literature [38,39,40] we have found from low temperature measurements of $\lambda_{001} = (-71 \pm 3) \cdot 10^{-6}$ and $\lambda_{111} = (-39 \pm 3) \cdot 10^{-6}$. The deviation between theory and experiment is close to a factor of three in both cases.

In order to discuss further the dependence of the MAE on crystal structure we refer to the work by James [14] who calculated the MAE as a function of strain (or c/a ratio of the tetragonal distortions) of Fe, Co and Ni. In this work the MAE was calculated for a range of c/a ratios which, via the Bain transformation path, connects the bcc and fcc structures. It is interesting to note that the size of the

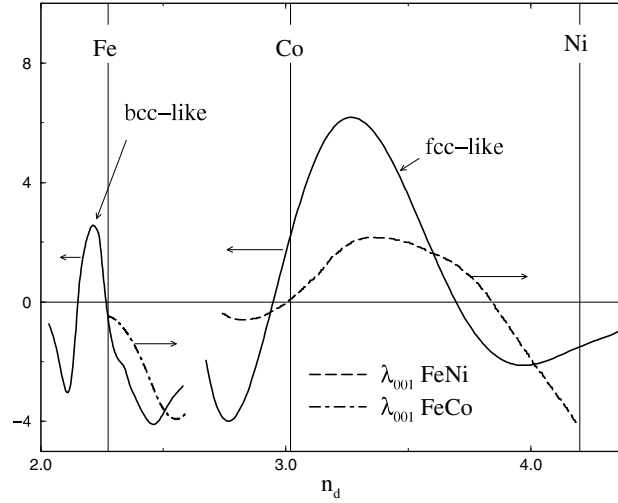


Fig. 11. Calculated values (full lines) of the magneto striction (or rather OMA see text) compared to experimental data (dashed lines and dashed-dotted lines) for FeNi and FeCo alloys.

MAE explodes in magnitude when the cubic symmetry is broken. In a work by Engel et al. the volume contribution to the MAE of fct Co in a Co/Pd multilayer was measured to be $-220 \mu\text{eV}/\text{atom}$. The c/a ratio of this film was 0.84. The calculations of James[14] shows that the values of fct Co are in good agreement with experiment. James[14] also compared the difference in the orbital moment between the two different magnetization directions, $L_z^{110} - L_z^{001}$, a property we will call the orbital moment anisotropy (OMA), to the MAE, and he found that there is a direct relationship between the MAE and OMA, as has been suggested from analysis based on perturbation theory.[41] Assuming that the exchange splitting is larger than the bandwidth (which indeed is not true in our case) Bruno[41] showed that the magnetic anisotropy energy for a uniaxial system can be written, in first order perturbation theory, as $K^U = \frac{\xi}{4\mu_B} (m_l^{\parallel} - m_l^{\perp})$, where ξ is the spin-orbit coupling parameter and m_l^{\parallel} and m_l^{\perp} is the total orbital moment assuming a magnetization axis parallel and perpendicular to the symmetry axis, respectively.

If there is a linear relationship between the OMA and MAE and since there is, via the magneto elastic theory, a linear relationship between the MAE and λ , there will be a linear relationship between the OMA and λ . Hence, in order to study trends in the MAE as a function of for instance alloy concentration one may as an alternative study experimental trends in λ or the OMA, and this is something we will do next. In Fig.11 we compare the calculated OMA of bcc Fe and fcc Co to the corresponding experimental magneto striction coefficients, λ . Note that the theoretical calculations reproduce the experimental trends very well. For the FeCo alloy (bcc) theory reproduces the drop in λ with increasing Co concentration and the dip at a Co concentration corresponding to ~ 2.5 spin down d-electrons. The trends in λ of the FeNi (fcc) alloys is somewhat more

intricate where λ changes sign two times as a function of alloy concentration. The theoretical curves reproduce this behavior and the concentrations where a small respectively large λ is observed are reproduced by theory.

8 Summary and Conclusion

Different aspects of magnetism of materials with reduced dimensionality have been discussed with special emphasis on spin and orbital moments, the magneto crystalline anisotropy, the magneto elastic coupling and magneto striction. The work presented shows that most materials are described rather well with first principles theory, where especially the spin and orbital moments typically agree within a few percent from experiment. The magneto crystalline anisotropy is normally harder to calculate due to that for most materials it is very small. For most bulk materials the reason for this is that the cubic symmetry reduces the influence of the spin-orbit coupling, and hence the MAE becomes quite small. By epitaxial growth techniques, thin films of e.g. Co on Cu can be fabricated and due to the lattice miss-match a structure of reduced symmetry is often found. This enhances the influence of the spin-orbit coupling and this together with the band narrowing for the surface of e.g. the surface Co atoms help produce a large enhancement of the orbital magnetism. Another example of the where the reduced symmetry is important has been given, i.e. fct Ni grown on Cu (001). Calculations of the orbital moment has been shown to give better agreement with experimental data when the orbital polarization correction is considered, whereas concerning the MAE the situation is less encouraging. The magneto striction coefficients have been evaluated for FeNi and FeCo alloys and although it seems that the absolute size of the magneto striction sometimes is difficult to calculate its trends as function of alloying (or band filling) as reproduced rather well by theory.

Although it seems that in many cases first principles theory have predictive power for thin film (and bulk) magnetism, there is certainly need for improvements. For instance, other versions of the orbital polarization correction should be tried, improvements of mean field approximations to Hubbard like correlation[42] [43][44][45][46] should be explored, as well as the exploration of different approximations for calculating the self energy. For more localized electron systems recent work on the strong coupling limit[47] have been encouraging.

Acknowledgments

The support from The Swedish Foundation for Strategic Research (SSF), NFR and TFR is acknowledged. All theoretical results presented here have been obtained in collaboration with I. Abrikosov, M. Alouani, M. S. S. Brooks, H. Dreyse, I. Galanakis, O. Hjortstam, P. James, B. Johansson, L. Nordström, J. M. Wills, P. Söderlind, A. Taga, J. Trygg and J. M. Wills.

References

1. O. K. Andersen, H. L. Skriver and B. Johansson, *Pure Appl. Chem.* **52**, 93 (1979); A. R. Mackintosh and O. K. Andersen, in *Electrons at the Fermi Surface*, edited by M. Springford (Cambridge University Press, Cambridge, 1980); O. K. Andersen, *Phys.Rev.B* **12**, 3060, 1975; H. L. Skriver "The LMTO Method", (Springer, Berlin, 1984).
2. C.Li, A.J.Freeman, H.J.F.Jansen, and C.L.Fu, *Phys. Rev. B* **42**, 869 (1990).
3. Compare for instance the orbital moments of the two methods in P. Söderlind et al. *Phys. Rev. B* **45**, 12911 (1992) and P. Strange, H. Ebert, J. B. Staunton, and B. L. Györfy, *J. Phys.: Condens. Matter* **1**, 3947 (1989); P. Strange, J. B. Staunton, and B. L. Györfy, and H. Ebert, *Physica B* **172**, 51 (1991)
4. See e.g. A. R. Edmonds, "Angular Momentum in Quantum Mechanics", Princeton University Press, 1974.
5. P.James, O.Eriksson, Olof Hjortstam, B.Johansson, and L.Nordström, *J.Appl.Phys.*(in press).
6. O.Hjortstam, K.Baberschke, J.M.Wills, B.Johansson, and O.Eriksson, *Phys. Rev. B* **55**, 15026 (1997).
7. J M. Wills (unpublished); J.M.Wills, O.Eriksson, and M.Alouani, "Full-Potential LMTO Total Energy and Force Calculations" in "Electronic structure and physical properties of solids" Ed. Hugues Dreyse, (Springer Verlag, Berlin, 2000) p.148.
8. J. P. Perdew and Y. Wang, *Phys. Rev. B* **45**, 13244 (1992).
9. L. Hedin and B.I. Lundquist, *J. Phys. C* **4**, 2064 (1971).
10. N. Ashcroft and D. Mermin, *Solid State Physics* (Holt-Saunders International Editions, Philadelphia, 1981).
11. O.Jepsen and O.K.Andersen, *Solid State Commun.* **9**, 1763 (1971).
12. P.E.Bloch, O.Jepsen, and O.K.Andersen, *Phys. Rev. B* **49**, 16223 (1994).
13. M.Methfessel and T.Paxton, *Phys. Rev. B* **40**, 3616 (1989).
14. P.James (Thesis, Uppsala University, 1999).
15. P.W.Atkins, "Molecular Quantum Mechanics", Oxford University Press, Oxford, (1983).
16. J.M.Wills and O.Eriksson (unpublished).
17. O. Eriksson, B. Johansson, and M.S.S. Brooks, *Phys. Rev. B* **41**, 7311, (1990).
18. G.Racah, *Phys. Rev.* **61**, 186 (1949).
19. J.K.Jorgensen, "Electrons in Atoms and Molecules" (Academic Press, London, 1962).
20. J.H.van Vleck, *Phys. Rev. B* **52**, 1178 (1937).
21. C.J.Ballhausen, "Crystal Field Theory", McGraw-Hill, New York, (1962).
22. M.Norman, *Phys. Rev. Lett.* **64**, 1162 (1990).
23. L.J.Nuget, *J.Inorg. Nucl. Chem.* **32**, 3485 (1970).
24. P.Söderlind, O.Eriksson, R.C.Albers., A.M.Boring, and B.Johansson, *Phys. Rev. B* **45**, 12911 (1992).
25. O. Eriksson, B. Johansson, R.C. Albers, A.M. Boring, and M.S.S. Brooks, *Phys. Rev. B* **42**, 2702, (1990).
26. H.Ebert et al.,*J.Appl. Phys.* **67**, 4576 (1990).
27. X.Wang, D.-S.Wang, R.Wu and A.J.Freeman, *J.Magn.Mag.Mat.* **159**, 337 (1996).
28. R.Wu, L.Chen, A.J.Freeman, *J.Magn.Magn.Mater.* **170**, 103 (1997).
29. M.Tischer, O.Hjortstam, D.Arvanitis, J.Hunter Dunn, F.May, K.Baberschke, J.Trygg, J.M.Wills, B.Johansson and O.Eriksson, *Phys. Rev. Lett.* **75**, 1602 (1995).

30. O.Eriksson, G.W. Fernando, R.C.Albers, and A.M.Boring, Solid State Commun **78**, 801 (1991).
31. D. Weller, Y. Wu, J. Stöhr, G. Samant, B. D. Hermsmeier, C. Chappert, Phys. Rev. B **49**, 12888 (1994); D. Weller, J. Stöhr, R. Nakajima, A. Carl, M. G. Samant, C. Chappert, R. Mégy, P. Beauville, P. Veillet, and G. A. Held, Phys. Rev. Lett. **75**, 3752 (1995).
32. B. Schulz and K. Baberschke, Phys. Rev. B **50**, 13467 (1994).
33. K. Baberschke, Appl. Phys. A **62**, 417 (1996).
34. U. Gradmann, Ann. Phys. **17**, 91 (1966).
35. S. Muller, B. Schulz, G. Kostka, M. Farle, K. Heinz, and K.Baberschke, Surf. Sci. **364**, 235 (1996).
36. J.M.Wills, O.Eriksson, P.Söderlind and A.M.Boring, Phys. Rev. Lett.**68**, 2802 (1992).
37. R. Wu and A.J. Freeman, J. Appl. Phys. **79**, 6209 (1996).;R. Wu, L. Chen, A.J. Freeman, J. Magn. Magn. Mater. **170**, 103 (1997).D. Wang, R. Wu, A. J. Freeman, Phys. Rev. B **47**, 14932 (1993)
38. D. Bonnenberg, K.A. Hempel, and H.P.J. Wijn, in "Landolt-Börnstein, Numerical Dataand Functional Relationships in Science and Technology", edited by H.P.J Wijn (Springer-Verlag, Berlin, 1986), Group 3, Vol. 19a.
39. E.W. Lee and M.A. Asgar, Proc. R. Soc. London Ser. A **326**,73 (1971).
40. D.I.Bower, Proc. R. Soc. London Ser. A **326**, 87 (1971).
41. P. Bruno, Phys. Rev. B **39**, 865 (1989).
(1990)
42. L.Falicov and Viktoria, Phys. Rev. B **20**, 4637 (1979).
43. S.Balle, J.Costa-Quintana, and F.Lopez-Auiliar, J.Phys. C **20**, L223 (1987); F.Lopez-Auiliar, S.Balle, and J.Costa-Quintana, Phys. Rev. B **38**, 163 (1988).
44. B.Brandow, Adv. Phys. **26**, 651 (1977).
45. A.M.Boring, R.C.Albers, O.Eriksson, and D.D.Koelling, Phys. Rev. Lett. **68**, 2652 (1992).
46. V. Anisimov, J. Zaanen and O. K. Andersen, Phys. Rev. B **44** (1991) 943.
47. U.Lundin, I.Sandalov, and O.Eriksson, Solid State Commun.**115**, 7 (2000).

Surface Electronic Structure of Band Ferromagnets

Markus Donath

Physikalisches Institut, Westfälische Wilhelms-Universität Münster,
Wilhelm-Klemm-Str. 10, D-48149 Münster, Germany

Abstract. Modern research on band ferromagnetism aims at its understanding on a microscopic level, i.e. on the basis of the spin-dependent electronic structure. The discovery of novel magnetic phenomena in systems of reduced dimension adds new challenges for experimentalists as well as theoreticians to describe the important surface and interface effects in these systems. This contribution presents a status report on our current understanding of surface-derived electronic states in 3d ferromagnets.

1 Dimension-Reduced Band Ferromagnets

Ferromagnetism is known as a state of collective order in three-dimensional solids. In most elements, the magnetic moments per atom as a consequence of non-completely filled electronic shells lead to a paramagnetic answer of the system to an applied external magnetic field. In only a few cases, most-known for iron, cobalt, and nickel, the magnetic moments are found to be spontaneously ordered below a critical temperature, the Curie temperature T_C . This state of ferromagnetic order is caused by the so-called exchange interaction, which is understood as the result of the Coulomb interaction in combination with the Pauli exclusion principle. Ferromagnetism is, therefore, a many-body effect of quantum-mechanical nature. It depends critically upon the overlap of electron wave-functions of adjacent atoms. As a consequence, magnetic properties respond sensitively to a changed number of neighbouring atoms, an altered crystal structure and an enhanced or reduced lattice parameter.

The development of smaller and smaller magnetic devices for data storage and retrieval demands for studying the influence of the reduced dimensionality on the magnetic properties. Ultrathin films as quasi two-dimensional systems are grown and characterized by state-of-the-art surface-science techniques under ultra-high vacuum conditions. Rows of atoms as realization of quantum wires and clusters as quantum dots are deposited on carefully selected substrates. The growth conditions and the morphology of these nanometer-scale structures are controlled with high precision. Novel magnetic phenomena have been discovered to be used in a wide spectrum of possible and already commercially available products for application in daily life. A famous example is the giant magnetoresistance (GMR) discovered in exchange-coupled layered structures, but now realized in a variety of spin valve structures. The GMR effect has already revolutionized the data storage and sensor technology [1].

From a fundamental physics point of view, finite-size effects, i.e. the influence of the reduced dimensionality, altered crystal structure, and modified lattice parameter on the magnetic properties, have to be understood. Primary magnetic properties like the Curie temperature, the spin and orbital magnetic moments per atom, and the magnetic anisotropy have to be explained as well as the electronic states with their spin dependence that underlie the primary magnetic properties. Electron wave functions no longer extend to infinity as in a three-dimensional solid, they are confined by the presence of surfaces and/or interfaces.

In this contribution, surface magnetic effects are discussed in relation to the surface electronic structure. It is predicted from theory and confirmed by experiments that surfaces of ferromagnets exhibit an enhanced spin magnetic moment compared with the bulk. In the studied cases, this is explained by the lowered symmetry and the reduced coordination number at the surface. For Ni(111) the enhancement is expected to be between +9% [2] and +11% [3]. A spin-polarized low-energy-electron diffraction (SPLEED) experiment reports on a magnetic moment “comparable to, or possibly slightly larger than, the bulk” [4]. For Co(0001) and Fe(110), the enhancement was calculated to be +7% and +19%, respectively [2]. Experimentally, an enhancement of the surface spin magnetic moment of Fe(110) was determined as +38% by SPLEED [5]. This result became unclear after a careful reanalysis [6] but was later confirmed (+39%) by torsion oscillation magnetometry (TOM) [7] as well as by spin-resolved appearance potential spectroscopy [8].

The key question we want to address is the following: Are surface magnetic effects reflected in the surface electronic states? In section 2 bulk-derived electronic states are briefly discussed. Surface-derived electronic states are introduced in section 3. Section 4 describes the experimental access to surface states and the characteristics of surface-state spectroscopy. A comparative study of the closed-packed surfaces of Ni, Co, and Fe is presented in section 5. A conclusion is given in section 6.

2 Bulk-Derived Electronic States

In ferromagnets, the electronic states are no longer degenerate with respect to the spin quantum number. The electronic bands split into two subsets of bands for electrons with spin magnetic moment parallel (\uparrow , spin up) and antiparallel (\downarrow , spin down) to the magnetization direction, which is the quantization axis. The two subsets of bands are energetically separated by the so-called exchange splitting with the spin-up states usually lower in energy than the spin-down states. This energy splitting is not at all rigid, its value depends on the energy, the electron wave vector \mathbf{k} , the band character, and the temperature. Owing to electron correlation effects, even the band widths become spin dependent which may give rise to an “inverse exchange splitting” at certain points in \mathbf{k} space [9]. Since all bands are occupied up to the Fermi energy E_F , more spin-up states are occupied than spin-down states, therefore called majority and minority states, respectively. This imbalance in band occupation causes the net magnetic moment

per atom with non-integer numbers of Bohr magnetons for the $3d$ ferromagnets Fe, Co, and Ni. They are called itinerant or band ferromagnets because the $3d$ conduction electrons are responsible for the magnetic properties. In Ni all d bands are occupied except the uppermost minority d band, while in Co more than one d band contributes to the magnetic properties [10]. Both are called strong ferromagnets because all majority d bands are occupied. In contrast, Fe is called a weak ferromagnet because the majority d states are not completely filled. It should be noted, however, that this strict classification is somewhat artificial owing to hybridization effects between d , p , and s states, leading to considerable d contributions in bands well above the Fermi energy. In addition, the spin is only a good quantum number in systems with small spin-orbit interaction. On the one hand, this is true for the $3d$ elements Fe, Co, and Ni. On the other hand, the spin-orbit coupling causes magnetic anisotropy effects, especially at interfaces. These effects determine the directions of easy magnetization, which are essential from an applications point of view.

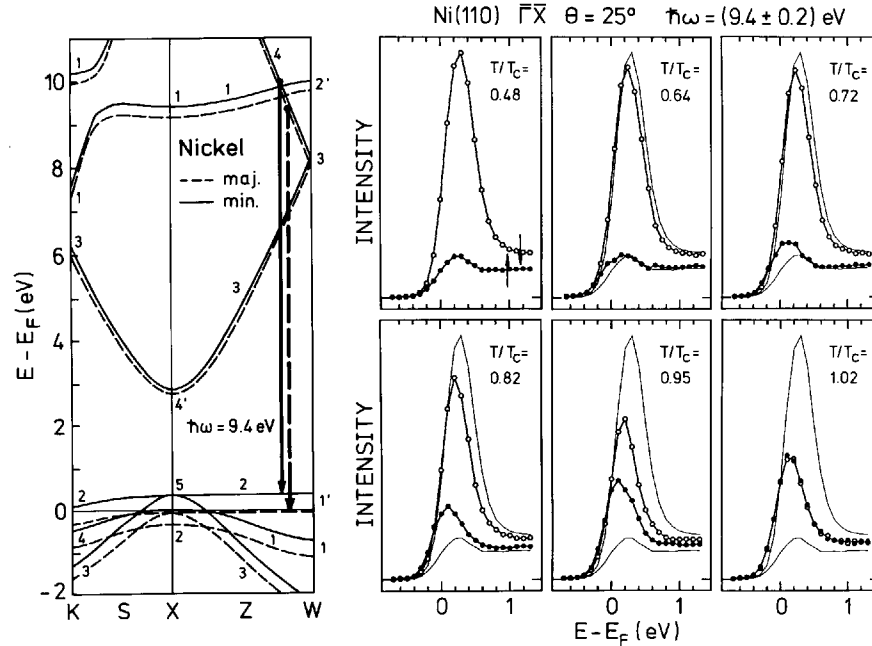


Fig. 1. (left) Spin-dependent bulk band structure of nickel at $T = 0$ along $K - (S) - X - (Z) - W$ [11]. Majority and minority bands are shown as dashed and solid lines, respectively. A direct transition into the magnetic Z_2 band is marked by a vertical arrow. (right) Spin-resolved inverse-photoemission spectra for transition $Z_4 \rightarrow Z_2$ for six different temperatures. The room temperature data ($T/T_c = 0.48$) are included as thin solid lines for reasons of reference (from Ref. [12])

The left part of Fig. 1 gives an example of a spin-dependent band structure $E(\mathbf{k})$ of a ferromagnet. A calculated band structure of Ni for $T = 0$ along some high-symmetry directions of the bulk Brillouin zone is shown as dashed and solid lines for majority and minority states, respectively [11]. The diagram clearly shows the majority d states completely below the Fermi energy and the uppermost minority d band partially unoccupied. A direct transition between the Z_4 and Z_2 bands with energy $\hbar\omega = 9.4$ eV is indicated by arrows. An inverse-photoemission experiment is expected to observe the transition into the unoccupied minority part of the Z_2 band, but not into the occupied majority part. The result of this experiment is shown in the right part of Fig. 1 for six different temperatures [12]. The room-temperature result ($T/T_C = 0.48$), which corresponds to about 95% of the magnetization at $T = 0$, confirms the expectation: high spectral intensity just above the Fermi energy for spin-down electrons and low intensity for spin-up electrons. The experiment clearly detects the magnetic band which carries the magnetization in Ni.

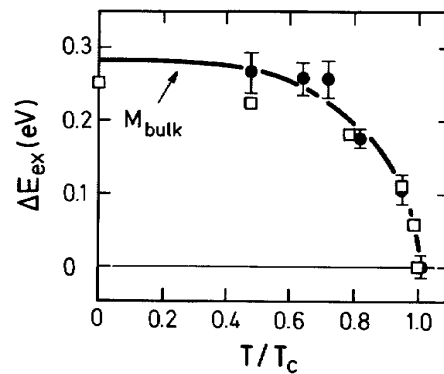


Fig. 2. Experimental exchange splitting ΔE_{ex} of the Z_2 band in nickel as a function of temperature (solid circles with error bars) obtained from the spin-resolved inverse-photoemission spectra of Fig. 1. The true spectral densities were extracted from the data by means of the maximum-entropy regularization, removing the influence of the Fermi function cutoff and apparatus function [14]. Open squares represent theoretical results (no scaling factor used) [16]. The full line is the experimental bulk magnetization M_{bulk} of nickel [15] rescaled to fit the ΔE_{ex} data (from Ref. [13])

The temperature dependence of the exchange splitting has been extensively discussed in the literature for about twenty years. It is clear that the spin dependence disappears with vanishing long-range magnetic order at the Curie temperature. What, however, happens with the spin-split bands upon approaching T_C ? Will they collapse to one band in the paramagnetic state as expected from a simple Stoner picture? Or will the spin-dependent intensities be redistributed in such a way that the energetic splitting persists at T_C while only the spin polarization vanishes? This so-called spin-mixing scenario is expected from model

calculations which assume short-range magnetic order even above the Curie temperature. From the experimental data obtained so far, the bands in Ni with their exchange splitting of up to ≈ 0.3 eV tend to show collapsing band behavior, while the bands in Fe with a splitting of up to ≈ 2.2 eV show spin-mixing and collapsing band behavior depending on the wave vector \mathbf{k} . An example of the magnetic band in Ni is presented in the right part of Fig. 1. With increasing temperature the majority Z_2 band becomes partially unoccupied while the minority band disappears partially below the Fermi energy [12,13]. A detailed data analysis using the maximum entropy method recovered the spectral densities undistorted by the Fermi distribution and apparatus function [14]. The experimental exchange splitting of the magnetic Z_2 band is shown as solid circles in Fig. 2. The data follow nicely the rescaled experimental bulk magnetization curve of Ni [15]. The often made assumption that spin-mixing behavior reflects local moments while collapsing band behavior indicates delocalized moments does not hold in view of a thorough analysis. In the case of Ni, for example, local moments above T_C and collapsing band behavior have been detected. More sophisticated models are needed to evaluate the experimental results. One example is the multi-band Hubbard model whose results are in excellent agreement with the experiment and are included in Fig. 2 as open squares [16]. On the other hand, more high-resolution photoemission and inverse photoemission results are needed to provide a reliable data basis for a detailed comparison between theory and experiment. The reader is referred to theoretical [9,17] and experimental contributions [18,19] in this volume dealing with this issue in more detail.

3 Surface-Derived Electronic States

With the information about bulk-derived electronic states in mind, we now focus on electronic states which are caused by the broken symmetry at the surface. They are located predominantly in energy gaps of the projected bulk band structure and their wave functions are peaked at the very surface and exponentially damped towards the vacuum and the crystal [20]. A detailed understanding of the surface potential, which connects the bulk potential with the vacuum level, is necessary for explaining and modeling the various kinds of surface states. Basically, one distinguishes two types of surface states: image-potential-induced and crystal-induced surface states. The first class is caused by the Coulomb-like tail of the surface potential towards the vacuum. A Rydberg-like series of states is formed within less than 1 eV below the vacuum level. They are totally unoccupied, pinned to the vacuum level, and concentrated with their wave functions in front of the outermost atomic layer. This kind of states appear in front of every conducting surface provided an energy gap of the bulk bands supplies the necessary confinement between crystal and vacuum barrier. They form a quasi two-dimensional electron gas in front of the surface with almost free-electron-like dispersion as a function of \mathbf{k}_{\parallel} . The second class depends on the specific band structure of the material. Crystal-induced surface states are derived from bulk bands and can, therefore, have distinct band character. They may be more lo-

calized like d states or more delocalized like sp states. The penetration depth of their wave functions towards the crystal depends on their position within the bulk-band gap. They may even become surface resonances characterized by periodic wave functions within the bulk but with a resonance-like enhancement of their amplitude towards the surface. While the energies and dispersion behavior of image-potential-induced surface states provide unique information about the Coulomb-like tail of the surface potential far away from the surface, the $E(\mathbf{k}_{\parallel})$ data of crystal-induced surface states tell about the shape of the potential close to the outermost atomic layer. Systematic studies on mostly noble metal surfaces have given us a comprehensive knowledge about surface states [20].

Surface states at ferromagnets are of particular importance because of the additional parameter spin, which carries information about the magnetic properties at the very surface as well as the spin dependence of the surface potential. In the vicinity of the Fermi energy, the exchange splitting leads to a spin-dependent occupation, evidence of a direct contribution to the surface magnetic moment. The shape of the spectral densities and their linewidths tell about a spin-dependent relaxation dynamics and an interaction with bulk states. However, ferromagnets are not free-electron-like metals, which adds considerable complexity to the problem.

Image-potential states have been thoroughly investigated by inverse photoemission and two-photon photoemission [21]. Their exchange splitting is influenced by the spin-dependent band-gap boundaries at the crystal side as well as a spin-dependent barrier potential at the vacuum side. Spin-resolved inverse photoemission succeeded in detecting exchange splittings for the $n = 1$ members of the Rydberg series for various magnetic surfaces. Even spin-dependent linewidths were measured for Fe(110) [22,23]. Image-potential states are important for understanding details of the surface potential but do not contribute to the surface magnetic moment. Therefore, they are not discussed further in this contribution. Crystal-induced surface states at ferromagnets will be described in the following sections with respect to their possible relevance for surface magnetism.

4 Surface-State Spectroscopy

The most direct experimental access to surface electronic states is given by photoemission (PE) and inverse photoemission (IPE) for the occupied and the unoccupied states, respectively. Two-photon photoemission with its superior energy resolution is an alternative for the study of unoccupied states, but without spin resolution so far. However, experiments with polarization-dependent excitation give indirect access to exchange-split states [24]. Since wide energy gaps open predominantly above the d bands in the unoccupied band region, most of the clear-cut case studies on magnetic surface states have been performed with spin-resolved inverse photoemission. The probing depth of electron spectroscopies is given by the inelastic mean free path of the incoming/emitted electrons, which is a few atomic layers in the 10 to 20 eV energy range. As a consequence, the

spectroscopic signal contains both bulk-derived and surface-derived states. To distinguish between bulk and surface contributions, the following criteria may be used: (i) sensitivity to surface contamination, (ii) (non)dependence on \mathbf{k}_\perp , (iii) appearance within a gap of the projected bulk band structure, (iv) comparison with theoretical studies. First, surface states are sensitive to adatoms. The reaction to it, however, depends on the particular state and the kind of adatoms. Image-potential states shift according to the work-function change, because they are pinned to the vacuum level, and their intensities are reduced with increasing surface disorder. Crystal-induced states may be quenched, altered or just shifted in energy. Second, true surface states are two dimensional and, therefore, do not depend on \mathbf{k}_\perp . To test this, one needs an experiment with variable photon energy. Third, surface states appear in gaps of the projected bulk band structure. A gap of bands with the same symmetry as the surface state is sufficient to generate it. However, criteria (ii) and (iii) do not hold for surface resonances. In many cases, a detailed comparison with calculations is necessary to uniquely identify a surface state.

Provided a surface state is identified, the experiment is sensitive to the very surface. The information depth for this particular spectral feature is not given by the electron inelastic mean free path but only by the penetration length of the surface-state wave function. This gives surface-state spectroscopy a surface-layer sensitivity. By detecting different exchange-split electronic states, e.g. a bulk-derived state and a surface state, conclusions can be drawn about a magnetic depth profile. This was shown for 6 monolayers (ML) of fcc-(face centered cubic)-like Fe on Cu(001), where the surface has an enhanced magnetization compared with the sublayers [25,26]. In addition, surface-state spectroscopy is structure selective because the position of energy gaps in $E(\mathbf{k})$ space and, as a consequence, the appearance of surface states depends on the crystal structure. The detection of a particular surface state can help to identify the crystal symmetry as it was demonstrated for fcc Fe on Cu(001). This advantage as a result of the experimental \mathbf{k} resolution turns into a disadvantage for the determination of magnetic moments. Magnetic moments result from the imbalance between spin-up and spin-down states, integrated over the whole Brillouin zone. As a consequence, \mathbf{k} -resolved investigations cannot measure magnetic moments.

One more issue has to be addressed. Provided, a truly magnetic surface band is detected. What is the contribution of this band to the surface magnetic moment? This depends very much on the character of the band. *sp*-derived surface bands with free-electron-like dispersion in 3d ferromagnets do only contribute a few percent to the magnetic moment, which is dominated by the more localized *d* contributions [27,28]. The situation is more favorable for *d*-derived surface states with their smaller group velocity. Independent of their actual contribution to the surface magnetic moment, the study of magnetic surface states offers unique access to surface magnetic properties. The same is true for interfaces and quantum-well structures, which also give rise to specific electronic states.

5 The Closed-Packed Surfaces of Fe, Co, and Ni

In this section, we will discuss crystal-induced surface states close to the Fermi energy at the closed-packed surfaces of the classical $3d$ ferromagnets: bcc (body centered cubic) Fe (110), hcp (hexagonal closed packed) Co(0001), and fcc (face centered cubic) Ni(111). Co(0001) and Ni(111) exhibit the same six-fold surface symmetry, Fe(110) shows a distorted hexagonal surface geometry with only two-fold symmetry. The bulk bands perpendicular to the surface, calculated with the tight-binding linear muffin-tin orbital (TB-LMTO) method [29], are shown in Fig. 3. Although the calculation overestimates the exchange splitting, the main similarities and differences between the three cases are evident. Co and Ni are strong ferromagnets with all majority d states occupied, while Fe exhibits

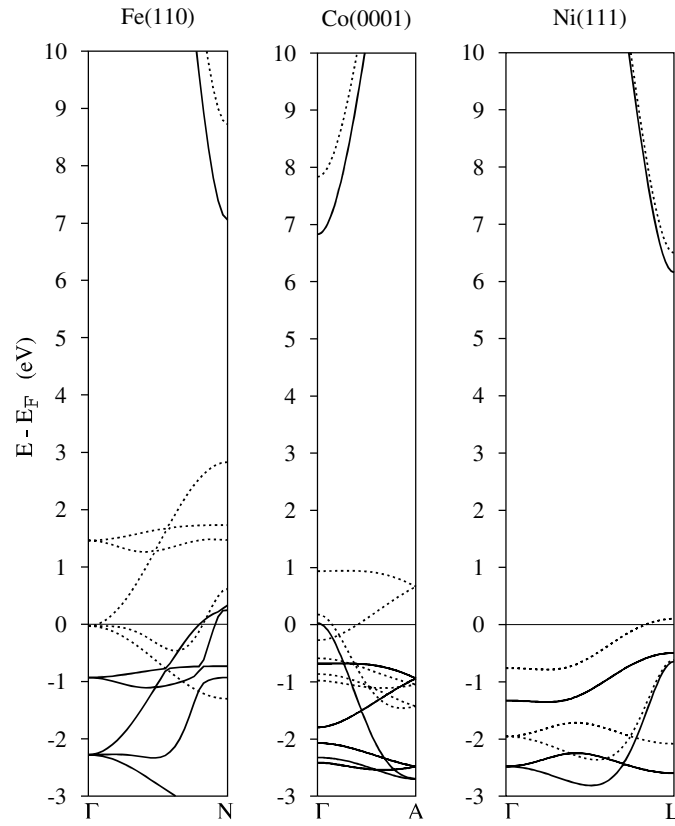


Fig. 3. Spin-dependent bulk band structure along [110] for iron, [0001] for cobalt, and [111] for nickel [29]. This represents electronic states accessible by photoemission and inverse-photoemission experiments with normal electron emission and incidence, respectively, on the (110) surface of iron, the (0001) surface of cobalt, and the (111) surface of nickel. Majority bands are shown as solid lines, minority bands as dotted lines.

unoccupied majority d states. The energy separation between spin-up and spin-down bands increases from Ni to Fe. In all three cases, wide sp -derived energy gaps open from close to the Fermi energy to some eV above it. Since the lower and upper gap boundaries have p and s character, respectively, the gaps are called Shockley-inverted. The gaps are traversed by d bands in an increasingly complex way from Ni to Fe. In particular, for Fe the band order at the N point differs significantly in the two spin subsystems. For the minority system, the p -derived lower band gap boundary lies below three d bands. For the majority system, it reaches the N point above them. Only for Ni, the gap starts well below the Fermi energy which may give rise to a surface state with different occupation in the two spin bands.

We have studied the three surfaces with spin-resolved IPE. Spin-polarized electrons emitted from a GaAs photocathode impinge with variable energy on the well-prepared surfaces with a defined angle of incidence, in the presented study mostly along the surface normal. Radiative transitions to lower-lying electronic states in the sample are detected via emitted photons of energy $\hbar\omega = 9.4$ eV at a photon take-off angle of 35° . Details about the measurements are described elsewhere [30,31,13]. The samples are remanently magnetized in a one-domain state with the magnetization direction collinear to the electron spin polarization. The presented spectra have been normalized to 100 % spin polarization of the incoming electrons. Consequently, the partial spin spectra represent transitions between majority and minority states separately. This is true as long as the spin is a good quantum number. The spectra are recorded at room temperature which corresponds almost to the magnetic ground state. Measurements of the surface states under consideration upon approaching the Curie temperature have not been reported so far. The Ni(111) surface was prepared on a picture-frame bulk crystal, while the Co(0001) and Fe(110) surfaces were prepared as thin films on a W(110) substrate with thicknesses of 10 ML and 20 ML, respectively. The film thickness was chosen in such a way that the surface electronic structure did no longer exhibit thickness-dependent changes due to film-growth effects caused by the lattice mismatch between substrate and overlayer.

5.1 Ni(111)

Crystal-induced surface states on (111) surfaces of fcc metals form at the bottom of the $L_{2'} - L_1$ sp -band gap and, depending on the material, they are either occupied (Cu, Ag, Au) or empty (Pd) at the center of the surface Brillouin zone $\bar{\Gamma}$. With increasing \mathbf{k}_{\parallel} , they disperse to higher energy and, in the event of overlap with bulk bands of the same symmetry, they become surface resonances. For Ni the situation is more complicated owing to the uppermost d band traversing the sp gap (see Fig. 3). An sp -like occupied surface state at 0.25 eV below E_F with downward energy dispersion as a function of \mathbf{k}_{\parallel} was detected by PE [32]. Fig. 4 shows spin-resolved IPE results for normal and off-normal ($\Theta = -12^\circ$) electron incidence on Ni(111) [33]. The spectra of the clean surface exhibit a prominent feature just above E_F with spin-dependent intensity. The minority intensity may be attributed to transitions into empty bulk d states, but there are no empty

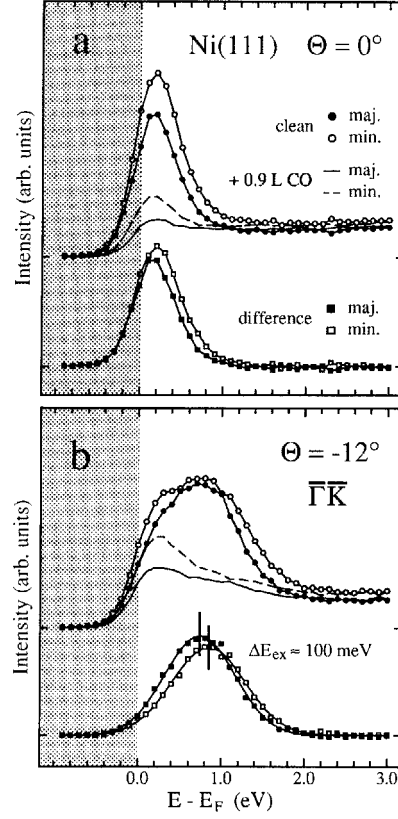


Fig. 4. Spin-resolved inverse-photoemission spectra of Ni(111) for normal electron incidence (a) and $\Theta = -12^\circ$ (b): clean surface (open and closed circles), surface exposed to 0.9 L of CO (dashed and solid lines) and difference spectra (open and closed squares). The spectra have been normalized to equal background intensity (from Ref. [33])

majority d states available in Ni. To test the surface sensitivity, the surface was exposed to 0.9 L ($1\text{L} = 1.33 \times 10^{-4} \text{ Pa} \cdot \text{s}$) of CO. Most of the intensity is quenched by the adsorbate. The remaining feature of the contaminated surface exhibits high spin asymmetry and is, therefore, interpreted as originating from indirect transitions into minority d states, which are known to be not very surface sensitive. The spin-resolved difference spectra reveal a surface-sensitive feature which is spin-split at the high-energy, but identical at the low-energy flank. This result is interpreted as a surface-state emission which is cut off by the Fermi function at least for the majority part. Consequently, the surface state is only partially occupied. The exchange splitting of about 100 meV is determined from off-normal measurements, where the state appears completely above the Fermi level in both spin channels. This splitting resembles the splitting of the p -like lower band-gap boundary, which the surface state is derived from.

Ni(111) exhibits an exchange-split magnetic surface state at the center of the surface Brillouin zone. Its contribution to the surface spin magnetic moment, however, was estimated to be at most a few percent [27]. The oxygen-induced reduction of the surface magnetic moment observed by TOM [34] is reflected in the electronic structure by a depopulation of the surface state as well as a reduction of its exchange splitting [35]. This adsorbate-induced modification of the surface state, however, cannot account for the significant reduction of the surface magnetic moment. The magnetic moment is carried predominantly by the d bands, and no modification of the d bands has been observed so far. Nevertheless, the surface state has been proven to be a unique sensor of surface magnetic properties. It should be noted that the appearance of the occupied surface state at $\bar{\Gamma}$ mentioned above is not yet understood [36,37] and its spin dependence is not known at present.

5.2 Co(0001)

The (0001) surface of hcp Co and the (111) surface of fcc Ni are quite similar with respect to their surface geometry and projected electronic bulk band structure. As for Ni(111), an occupied surface state was found by PE at 0.3 eV below the Fermi energy [38,39]. In contrast to these findings, a spin-resolved PE study did not support the existence of an occupied surface state [40]. A recent high-resolution PE study, however, finds again evidence of an occupied surface state below E_F [41]. In spin-averaged IPE work, depending on the photon energy, a one-peak or a two-peak structure was observed just above E_F [42,43,44]. Based on measurements without spin resolution, most of the intensity was ascribed to a minority d band, while a shoulder on the low-energy side was interpreted as the tail of the occupied state found by PE [43].

With this unclear situation in mind, we performed spin-resolved IPE measurements on Co(0001) shown in Fig. 5 [45]. The observed minority peak at 0.75 eV above the Fermi level may be easily attributed to transitions into empty minority d states. Surprisingly, a peak at 0.25 eV shows majority character, even though no majority bulk bands are expected to appear above E_F . As in the case of Ni(111), exposure to 1 L of CO causes a significant effect: The majority peak is completely quenched, while the minority peak is partially quenched, preferably at the high-energy flank. The remaining minority intensity is ascribed to empty minority d states. The difference spectra, presented in the lower part of Fig. 5, are interpreted as unoccupied surface states with an exchange splitting of 0.65 eV. This assumption is supported by calculations within the fully relativistic one-step model, which find a surface state, exchange-split by 0.75 eV, with both components above E_F at $\bar{\Gamma}$ and a transition into a minority bulk band at 0.8 eV [45]. It should be noted that both in experiment and in theory the surface state shows a positive dispersion as a function of \mathbf{k}_{\parallel} .

In contrast to the surface state on Ni(111), the surface state on Co(0001) does not contribute to the surface magnetic moment. Similar to the case of Ni(111), the role of the occupied surface state observed in PE is not clear at present. The size of the exchange splitting is unexpectedly large compared with the exchange

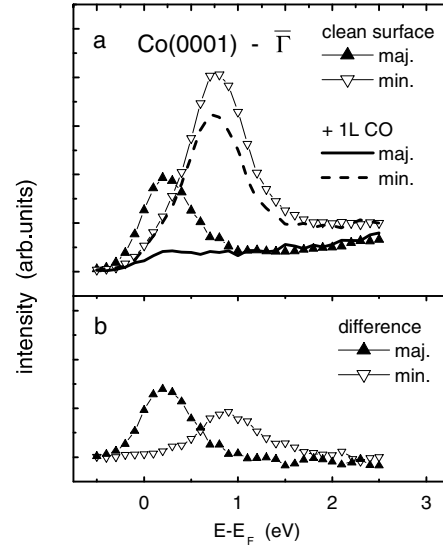


Fig. 5. Spin-resolved inverse-photoemission spectra for normal electron incidence on Co(0001). (a) Spectra of clean surface and surface exposed to 1 L of CO. (b) Difference spectra (from Ref. [45])

splitting of the p -like lower band-gap boundary. Future experimental as well as theoretical studies have to clarify this question.

5.3 Fe(110)

The (110) surface of bcc crystals is not too different from the hexagonal fcc(111) and hcp(0001) surfaces discussed so far. Therefore, for a comparative study between the prototype band ferromagnets Fe, Co, and Ni, Fe(110) is chosen to be compared with Ni(111) and Co(0001). The energy gap between sp bands is an absolute gap in the majority system, but it is traversed by d bands in the minority system. One band has even the same symmetry as the sp bands confining the gap. Therefore one might expect a different surface-state behavior in the two spin systems.

The experiments reported so far are not very conclusive with respect to surface states. Apart from very few exceptions, the measurements are successfully interpreted on the basis of bulk-band transitions alone. One spin-integrated PE study, however, reports a surface state at 0.15 eV below E_F at $\bar{\Gamma}$ [46]. In another PE investigation with spin resolution, a minority surface feature was observed at 0.3 eV below E_F at $0.5 \bar{\Gamma} \bar{H}$ [47], which was predicted by a tight-binding calculation [48]. In the calculations, the surface state starts from 0.4 eV above the Fermi level at $\bar{\Gamma}$ and disperses to lower energies along the $\bar{\Gamma} \bar{H}$ direction. Although the corresponding majority partner was predicted as well, it was not observed experimentally. Calculations within the one-step model of photoemission support

the existence of a minority surface state, whose appearance depends critically on the particular shape of the chosen surface potential [49]. In IPE measurements [50,51] and calculations [52] no evidence of a surface-state emission close to E_F was found. The identification of surface states for Fe is definitely hindered by the various d bands.

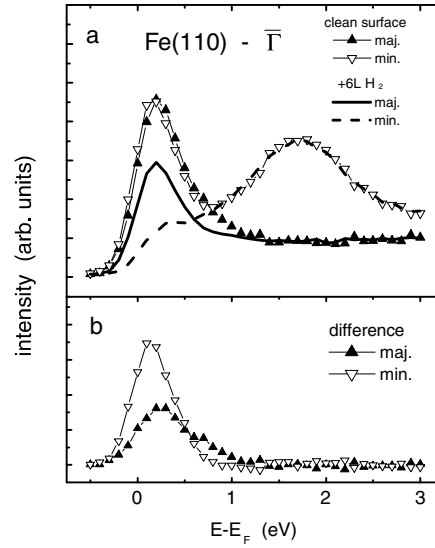


Fig. 6. Spin-resolved inverse-photoemission spectra for normal electron incidence on Fe(110). (a) Spectra of clean surface and surface exposed to 6 L of H₂. (b) Difference spectra (from Ref. [53])

Spin-resolved IPE spectra for Fe(110) are shown in Fig. 6 [53]. The data reveal three spectral features, two of them just above the Fermi energy with almost equal intensities in both spin channels and one minority structure at 1.8 eV above E_F . The latter is easily explained as minority d -band emission. The features close to the Fermi level appear at slightly different energies for spin-up and spin-down electrons. Their origin is investigated by exposing the surface to hydrogen. CO turned out not to be a suitable test adsorbate because, in contrast to the Ni(111) and Co(0001) surfaces discussed above, it quenches the bulk d -band emissions as well. 6 L of H₂ do not affect the minority bulk emission but influence the features close to E_F in an elucidating way. The minority peak disappears completely while the majority peak is only partially quenched. The remaining majority feature is attributed to majority bulk bands, i.e. the spin partner of the minority feature at 1.8 eV. The difference spectra in Fig. 6 show a minority structure and a smaller majority peak with peculiar asymmetric lineshape. The majority peak maximum appears at slightly higher energy than the maximum

of the minority peak. Is this result evidence of an inverse exchange splitting of a surface state?

A detailed theoretical analysis within the one-step model of inverse photoemission revealed the following unexpected situation [53]. There is a minority surface state just above the Fermi level which disperses slightly to lower energies with increasing \mathbf{k}_{\parallel} . There is also a majority surface state, lower in energy at $\bar{\Gamma}$, which, however, disperses to higher energies while losing spectral weight. This dispersion behavior is consistent with IPE data for off-normal electron incidence [54]. According to theory, the majority state even splits into two states with different dispersion behavior in certain directions of the surface Brillouin zone. The expected scenario with one pair of spin states is not valid for Fe with its large spin splitting compared with the band width. Hybridization between s , p , and d states with their different spin splittings results in a band order which is different for the two spin systems – and so are the conditions for surface states to form. With the assumption of a small, but finite angular distribution of the incoming electrons, the high-energy wing of the observed majority spectral feature is explained as caused by the positive dispersion behavior of the surface state. Due to the spin-dependent band order in Fe, the two surface features have quite different band character and cannot be viewed as spin partners any more. It is no longer possible to define an exchange splitting between the two surface features of different spin. The Stoner picture, we often have in mind, with two sets of bands separated in energy by a rigid shift, called exchange splitting, is too simple to describe band ferromagnetism. It is even more difficult now to get an idea about the surface-state contribution to the magnetic moment. Layer-dependent spin-density calculations may shed more light on this issue. However, this kind of calculations do not include a realistic surface potential yet, which is essential to describe the observed surface states. In this study on Fe(110), we have identified an unexpected and complex surface-state behavior at a magnetic surface. Combined investigations below and above the Fermi level are needed to learn more about the impact of surface states on the magnetic behavior of surfaces.

6 Conclusion

For a microscopic picture about band ferromagnetism we need to understand the spin-dependent electronic structure and their relation to the primary magnetic quantities. The spin-dependent electronic structure below and above the Fermi level can be determined by photoemission and inverse photoemission. The experiments provide combined information about bulk-derived and surface-derived states, which has to be separated with due care. Surface states of various kinds and their spin dependences have been revealed for a number of ferromagnets. Sophisticated theoretical analyses help to interpret the often complex experimental spectra. Surface-state spectroscopy has been proven to be an excellent surface-layer sensitive tool to improve our knowledge about surface magnetism.

What is our current knowledge about the correlation between the primary magnetic quantities and the spin-dependent electronic structure for ferromagnetic surfaces? Surface magnetic moments, enhanced compared with the bulk, have been measured by magnetometry techniques and are theoretically understood. Surface electronic states have been identified but their contribution to the surface magnetic moment is small in many cases. At present, it is not possible to quantify changes of the surface magnetic moment from measurements of the electronic structure. A systematic study on the closed-packed surfaces of the prototype band ferromagnets Fe, Co, and Ni was presented in this contribution. It is a status report which leaves us with the impression that we are still on the way to explore experimentally the correlation between magnetic order and electronic states at ferromagnetic surfaces.

Acknowledgments

It is a pleasure to thank Ch. Math and J. Braun for their enjoyable collaboration and W. Nolting for stimulating discussions and a critical reading of the manuscript. Financial support by the Deutsche Forschungsgemeinschaft is gratefully acknowledged.

References

1. *Magnetism Beyond 2000*, ed. by A.J. Freeman, S.D. Bader: J. Magn. Magn. Mater. **200** (1999)
2. A.J. Freeman, R. Wu: J. Magn. Magn. Mater. **100**, 497 (1991)
3. F. Mittendorfer, A. Eichler, J. Hafner: Surf. Sci. **423**, 1 (1999)
4. G.A. Mulhollan, A.R. Köymen, D.M. Lind, F.B. Dunning, G.K. Walters, E. Tamura, R. Feder: Surf. Sci. **204**, 503 (1988)
5. E. Tamura, R. Feder, G. Waller, U. Gradmann: Phys. Stat. Solidi (b) **157**, 627 (1990)
6. A. Ormeci, B.M. Halls, D.L. Mills: Phys. Rev. B **44**, 12369 (1991)
7. K. Wagner, N. Weber, H.J. Elmers, U. Gradmann: J. Magn. Magn. Mater. **167**, 21 (1997)
8. G. Rangelov, H. D. Kang, J. Reinmuth, M. Donath: Phys. Rev. B **61**, 549 (2000)
9. W. Nolting: this volume
10. A. Vega, W. Nolting: Phys. Stat. Solidi (b) **193**, 177 (1996)
11. H. Eckardt, L. Fritsche: J. Phys. F **17**, 925 (1987)
12. M. Donath, V. Dose: Europhys. Lett. **9**, 821 (1989)
13. M. Donath: Surf. Sci. Rep. **20**, 251 (1994)
14. W. von der Linden, M. Donath, V. Dose: Phys. Rev. Lett. **71**, 899 (1993)
15. P. Weiss, R. Forrer: Ann. Phys. **5**, 153 (1926)
16. W. Borgiel, W. Nolting, M. Donath: Solid State Commun. **72**, 825 (1989) W. Nolting, W. Borgiel, V. Dose, Th. Fauster: Phys. Rev. B **40**, 5015 (1989)
17. M. Potthoff: this volume
18. Th. Greber: this volume
19. A. Kakizaki: this volume
20. *Electronic Surface and Interface States on Metallic Systems*, ed. by E. Bertel, M. Donath (World Scientific, Singapore 1995)

21. Th. Fauster, W. Steinmann: In: *Electromagnetic Waves: Recent Developments in Research*, ed. by P. Halovi (North-Holland, Amsterdam 1995), Vol. 2, Chap. 8, p. 347
22. F. Passek, M. Donath, K. Ertl, V. Dose: Phys. Rev. Lett. **75**, 2547 (1995)
23. M. Donath: 'Magnetic Surface States of 3d Ferromagnets'. In: *Electronic Surface and Interface States on Metallic Systems*, ed. by E. Bertel, M. Donath (World Scientific, Singapore 1995), p. 233
24. U. Thomann, Ch. Reuß, Th. Fauster, F. Passek, M. Donath: Phys. Rev. **61**, 16 163 (2000)
25. B. Gubanka, M. Donath, F. Passek: J. Magn. Magn. Mater. **161**, L11 (1996)
26. B. Gubanka, M. Donath, F. Passek: Phys. Rev. B **54**, R11 153 (1996)
27. N. Memmel: Phys. Rev. B **55**, 5634 (1997)
28. N. Memmel: Surf. Sci. Rep. **32**, 91 (1998)
29. J. Braun: private communication
30. U. Kolac, M. Donath, K. Ertl, H. Liebl, V. Dose: Rev. Sci. Instrum. **59**, 1933 (1988)
31. M. Donath: Appl. Phys. A **49**, 351 (1989)
32. F.J. Himpsel, D.E. Eastman: Phys. Rev. Lett. **41**, 507 (1981)
33. M. Donath, F. Passek, V. Dose: Phys. Rev. Lett. **70**, 2802 (1993)
34. H.J. Elmers, U. Gradmann: Surf. Sci. **193**, 94 (1988)
35. F. Passek, M. Donath: Phys. Rev. Lett. **71**, 2122 (1993)
36. G. Borstel, G. Thörner, M. Donath, V. Dose, A. Goldmann: Solid State Commun. **55**, 469 (1995)
37. J. Kutzner, R. Pauksch, C. Jabs, H. Zacharias, J. Braun: Phys. Rev. B **56**, 16 003 (1997)
38. F.J. Himpsel, D.E. Eastman: Phys. Rev. B **20**, 3217 (1979)
39. F.J. Himpsel, D.E. Eastman: Phys. Rev. B **21**, 3207 (1980)
40. M. Getzlaff, J. Bansmann, J. Braun, G. Schönhense: J. Magn. Magn. Mater. **161**, 70 (1996)
41. E. Wetli, T.J. Kreutz, H. Schmid, T. Greber, J. Osterwalder, M. Hochstrasser: Surf. Sci. **402-404**, 551 (1998)
42. F.J. Himpsel, Th. Fauster: Phys. Rev. B **26**, 2679 (1982)
43. G.J. Mankey, R.F. Willis, F.J. Himpsel: Phys. Rev. B **47**, 190 (1993)
44. S. Bode: Doctoral Thesis, Freie Universität Berlin (1997)
45. Ch. Math, J. Braun, M. Donath: Surf. Sci., in press (2001)
46. Y. Sakisaka, Th. Rhodin, D. Mueller: Solid State Commun. **53**, 793 (1985)
47. E. Vescovo, C. Carbone, W. Eberhardt: Phys. Rev. B **48**, 285 (1993)
48. D.G. Dempsey, L. Kleinman, E. Caruthers: Phys. Rev. B **13**, 1489 (1975)
49. J. Redinger, C.L. Fu, A.J. Freeman, U. König, P. Weinberger: Phys. Rev. B **38**, 5203 (1988)
50. H. Scheidt, M. Glöbl, V. Dose: Phys. Rev. Lett. **51**, 1688 (1983) V. Dose, M. Glöbl: In: *Polarized Electrons in Surface Physics, Advanced Series in Surface Science*, ed. by R. Feder (World Scientific, Singapore 1985), p. 547
51. A. Santoni, F.J. Himpsel: Phys. Rev. B **43**, 1305 (1991)
52. R. Feder, A. Rodriguez: Solid State Commun. **50**, 1033 (1984)
53. Ch. Math, J. Braun, M. Donath: to be published
54. F. Passek: Doctoral Thesis, Universität Bayreuth (1994)

Phase Transitions in Coupled Two-Dimensional Ferromagnetic Layers

P. Pouloupoulos and K. Baberschke

Institut für Experimentalphysik, Freie Universität Berlin,
Arnimallee 14, D-14195 Berlin, Germany

Abstract. The focal point of this work is the problem of phase transitions in two dimensional (2D) magnetic films which interact through a non-ferromagnetic spacer via the interlayer-exchange coupling J_{inter} . By means of an element-specific technique, this is the x-ray magnetic circular dichroism, we probe temperature dependent magnetization curves for Co and Ni in prototype Co/Cu/Ni/Cu(001) trilayers with 2D Co and Ni layers. Co and Ni while coupled they have onsets of ferromagnetic order at separate temperatures. The interlayer exchange coupling enhances the lower ordering temperature. However, no 'tail' in the magnetization curve occurs, suggesting that interlayer exchange coupling fades away near the lower ordering temperature. We show that such types of experiments can not be done in bulk, but only in 2D magnetic layers.

1 Introduction

The development of experimental techniques with monolayer sensitivity and element specificity provides new opportunities to reveal and study astonishing effects in the ultrathin film magnetism that were never realized in the bulk [1,2,3]. Among these techniques the X-ray magnetic circular dichroism (XMCD) has been proven to be an ideal method for studying systems where more than one element are involved [4]. It is a novel powerful technique which is based on the difference in the absorption coefficient for right and left circularly polarized X-rays in a magnetic medium (the Kerr-Faraday effect at x-rays). The possibility to perform temperature-dependent measurements on well-characterized systems allows us to give a new input to general and eternal problems of physics like magnetic phase transitions and related topics. Magnetic phase transitions have attracted a lot of interest in the 50's and 60's and solid experimental and theoretical work was done in their study, see as a review [5,6,7,8]. In this contribution we are not going to deal with phase transitions of three-dimensional (3D) systems of many elements like, for example, alloys or compounds. We will deal with phase transitions in ultrathin magnetic layers, each of them consisting of a pure element, in a geometry of two dimensions (2D). The purity of the element guarantees that, unlike in the case of alloys, the electronic structure is not altered. Therefore, one can take as an input the magnetic and electronic information given for the ultrathin layers and focus on the effects of a link, of an exchange interaction between them, on the magnetic properties. A lot of effort was put on the study and optimization of technologically important properties originating from the exchange interaction in layered magnetic structures (interlayer exchange coupling J_{inter}) at room temperature [9]. However, few attention

was paid on the influence of J_{inter} on temperature-dependent fundamental magnetic observables and magnetic phase transitions. This will be the focal point of our work.

For a ferro- to paramagnetic phase transition of a ferromagnetic material the spontaneous magnetization M_{sp} is the order parameter and the temperature at which M_{sp} vanishes defines the Curie temperature (T_C) of the magnetic system. M_{sp} vanishes continuously while its first derivative, the magnetic susceptibility $\chi'(T)$, presents a discontinuous behavior, a singularity, at T_C . This behavior is consistent with a second-order phase transition [6]. From theoretical point of view a phase transition demands an infinite sample, because only then $\chi'(T)$ diverges and the correlation length ξ tends to infinite at T_C . However, one may ask if real materials, i.e. ones with a finite size, undergo phase transitions. In an experiment, while the internal susceptibility equals $\chi'_{\text{int}} = \partial M / \partial H_{\text{int}}$, the measured susceptibility χ'_{exp} is given as:

$$\chi'_{\text{exp}} = \frac{1}{\frac{1}{\chi'_{\text{int}}} + N} \quad (1)$$

where N is the demagnetizing factor determined by the finite size and shape of the sample [10]. Taking into account that χ'_{int} should diverge at T_C , Equation (1) determines the measured susceptibility to be $\chi'_{\text{exp}} \leq 1/N$. For a bulk sphere, where $N = 1/3$, this means that $\chi'_{\text{exp}} \leq 3$ S.I. units! That is, in real world one measures a phase transition which is always suppressed. In the following, we will not discriminate between a theoretical, i.e. idealized T_C , and an effective T_C realized in experiments. This will allow us to give an intuitive experimental input to the problem of phase transitions in the presence of an exchange interaction.

In our presentation we will deal with in-plane magnetized ultrathin films. These provide a prototype of geometrical 2D systems. How the picture of phase transitions is transferred in this case? M_{sp} corresponds to the remanent magnetization M_{rem} recorded along an easy-axis. This choice has been shown to be the proper one because in-plane magnetized films stay in a single-domain state up to T_C [11]. For two magnetic layers A and B the situation becomes more complicated. There are two trivial limits: (i) two ultrathin films directly coupled. This case is similar to a disordered CoNi alloy. The order parameter is the average magnetization vanishing at the common T_C as was shown previously for ultrathin Co/Ni bilayers on Cu(001) [12]. (ii) The other trivial case is encountered at the decoupled limit. There, one may define two order parameters M_{sp}^A and M_{sp}^B and two well-defined Curie temperatures T_C^A (lower) and T_C^B (higher). From here and on these will be denoted as T_C^{low} and T_C^{high} . This situation resembles a powder of sufficiently large Co and Ni grains. What about the intermediate case, i.e. the one where there is sufficient exchange but not enough to create a common T_C ? We will show interesting effects for basic physics and technology that may be observed in the latter case only. We will describe this case starting from the decoupled limit, i.e. considering by definition two order parameters and we will actually test how valid is this approach.

This work is organized in the following way: In Section 2 the experimental details which include a brief description of the XMCD technique and structural and magnetic information for our samples will be given. Section 3 presents the main experimental results, i.e. the effects of the interlayer coupling on the fundamental magnetic observables near the ordering temperature. Finally, we will develop a qualitative discussion on our results and on the problem of phase transition in coupled 2D magnetic layers.

2 Experimental Details

For the realization of a prototype system to study magnetic phase transitions in 2D coupled layers we select Co/Cu/Ni trilayers grown on a single-crystalline Cu(001) substrate under ultrahigh vacuum conditions (base pressure $p \leq 2 \times 10^{-10}$ mbar). The Ni thickness is chosen to be 3-5 monolayers (ML). In this thickness range Ni grows pseudoepitaxially on Cu(001) [13] with minor problems of interdiffusion [14] or roughness [15,16]. The layers are thin enough to be still in the 2D range. Indeed, for ultrathin Ni/W(110) the transition between 2D-3D was shown to occur at 5-7 ML [17]. The T_C of Ni at this thickness range is between 150-300 K [18], i.e. in an ideal temperature range for measurements without facing problems of interdiffusion. Extensive characterization of Ni/Cu(001) ultrathin films is available [2,19,20] leading to a detailed knowledge of their magnetic properties which is a demand for the purposes of this work. On the top of the Ni film a Cu spacer in the thickness range $d = 2-5$ ML was grown in order (i) to keep the surface roughness at a minimum level and (ii) to maintain considerable values of J_{inter} , since the latter is known to decrease with $1/d^2$, see e.g. [9]. On top of Cu, a 1-2 ML thick Co film was grown. As for Ni, the temperature range for the Co T_C (100-400 K) was the main reason for this thickness selection. Finally, for Co/Cu(001) a detailed data base of information is available which facilitates the selection of growth parameters and the understanding of its magnetic behavior, see e.g. [21,22,23,24,25,26].

Temperature-dependent magnetic measurements on the Co/Cu/Ni/Cu(001) trilayers were carried out by means of several techniques like XMCD, magneto-optic Kerr effect (MOKE), ac-susceptibility and ferromagnetic resonance (FMR). Here we will deal in detail with the XMCD technique which gives us the possibility to be element-specific and, consequently, has the most important input to this work. For details on the other techniques see [2].

The XMCD measurements were performed at the SX 700 monochromator beamlines at BESSY I, the synchrotron facility in Berlin. By scanning the energy range between 700-900 eV one will encounter successively the strong absorption resonances of the incident beam at the $L_{2,3}$ edges of Co and Ni (Fig. 1). For example, at 778 (853) eV the L_3 edge of Co (Ni) is placed where x-rays are absorbed because of $2p^{3/2}$ - $3d$ transitions. By using circularly polarized x-rays one may record the difference in the absorption spectra, shown in Fig. 1, between left and right circularly polarized x-rays. This difference, the so-called XMCD signal is a measure of the magnetization. After proper analysis by means of the

sum rules the magnetic moments of the elements and a separation into spin and orbital moments is possible [4]. In this process the polarization degree of the x-rays ($P_c=0.7$, in our case) and the number n_h of the d-holes for Ni and Co are necessary inputs. XMCD is a relative technique. This means that for the proper determination of the magnetic moments a sample with a well-known magnetic moment like, for example, a bulk sample, is necessary. In our measurements we used the electron yield detection mode. A short electrical pulse in a coil saturated the samples and the measurements were carried out at magnetic remanence. More technical details about our measurements may be found, for example, in Ref. [27].

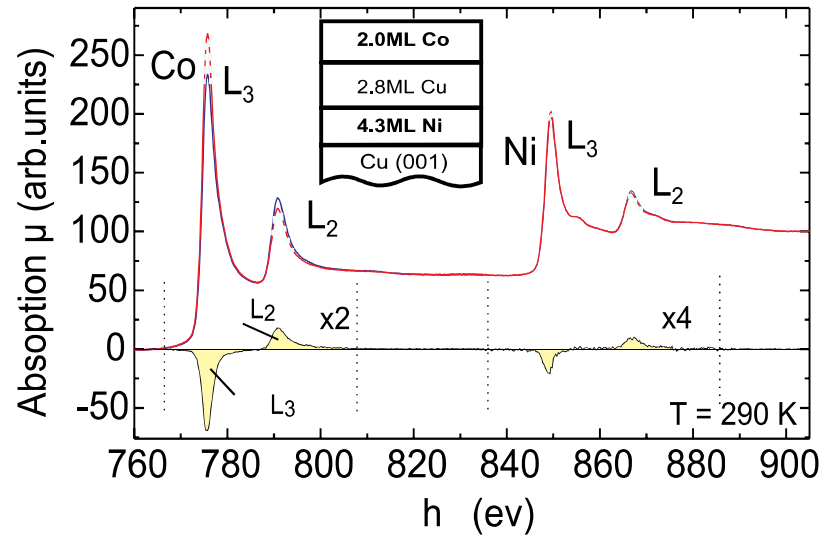


Fig. 1. The beauty of the XMCD technique is the element specificity. By varying the energy of the incident x-ray beam on one trilayer (inset) one encounters the strong absorption of photons at the Co and Ni L-edges, as denoted. The difference $\Delta\mu$ of the absorption coefficient μ for left (dashed) and right (solid line) circularly polarized light is the XMCD signal which is proportional to the magnetization (shaded areas). The parallel order of the XMCD spectra for Co and Ni suggests ferromagnetic coupling.

3 Results and Discussion

We will attempt to give a physical insight to the interesting problem of phase transitions in coupled 2D layers starting the discussion from the most representative of our experiments, as shown in Fig. 2. 4.8 ML Ni are grown on Cu(001) and capped by 2.8 ML Cu(001). The magnetization of Ni is measured by XMCD (open circles). It vanishes at about 275 K. As discussed in the introduction for

single layers, this temperature is the T_C of our film. Successively, we evaporate 2.8 ML of Co on the top of the Cu/Ni/Cu(001) bilayer. First, we will discuss the effects of J_{inter} on the T_C of Ni:

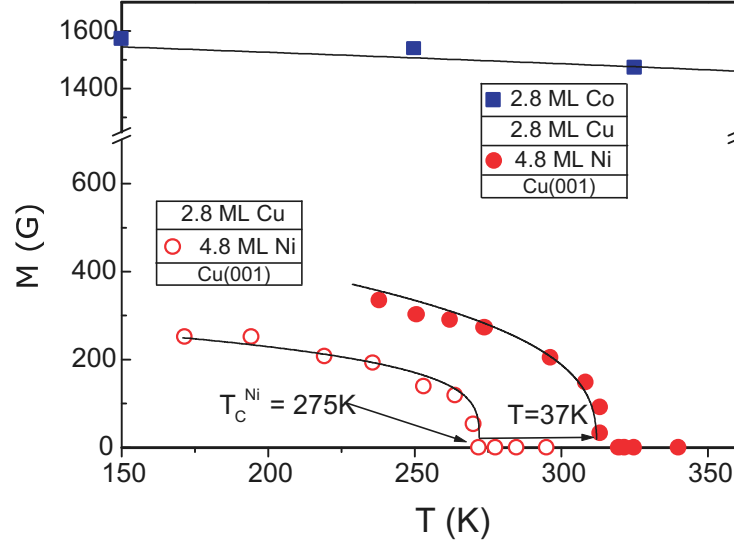


Fig. 2. The Ni magnetization in the trilayer vanishes at 312 K. At this temperature Co is clearly still ferromagnetically ordered. The increase of the ordering temperature of Ni by an amount $\Delta T_{\text{Ni}}=37$ K compared to the Cu/Ni bilayer proves the presence of J_{inter} .

The Ni magnetization vanishes at 312 K (full circles). The Co film at this and at higher temperatures remains ferromagnetic [28]. If the system was decoupled this observation would be trivial. Consequently, one may ask if we have any evidence for the presence of an interlayer interaction. The witness of the presence of J_{inter} is the change in the temperature where the Ni magnetization vanishes in the trilayer with respect to the bilayer. Indeed, an increase of $\Delta T_{\text{Ni}}=37$ K in the temperature where the Ni magnetization vanishes is observed after evaporating Co. The energy accompanying J_{inter} is written according to the following simple formula [9]:

$$E_{\text{inter}} = -J_{\text{inter}} \cos(\Delta\theta) \quad (2)$$

where $\Delta\theta$ is the angle between the Co and Ni magnetizations. Equation (2) reveals that the energy E_{inter} has always the same sign, irrespective of the sign of J_{inter} (positive J_{inter} for ferromagnetic-FM and negative for antiferromagnetic-AFM coupling). Therefore, an increase ΔT_{Ni} may be understood by regarding that the energy due to J_{inter} is added to the intralayer exchange coupling energy and, therefore, it helps Ni to order at higher temperatures than in the

Cu/Ni/Cu(001) bilayer [29]. This argument has been verified by all our experiments. While this picture in terms of the molecular field theory gives a nice qualitative description of the effect, it fails to give reasonable values of J_{inter} .

As a next step, since J_{inter} is known to oscillate with d [9], one would expect ΔT_{Ni} to show a similar behavior, as was suggested by Bayreuther et al. [30]. In Fig. 3 we plot ΔT_{Ni} (full squares) as a function of the spacer thickness d . Note that, as mentioned above, ΔT_{Ni} is always positive. Our motivation to give a more illustrative presentation in Fig. 3 led us to plot results for FM coupling above the $Y=0$ line and results for AFM coupling below. With this presentation it is easier to identify an oscillatory-like dependence of ΔT_{Ni} on d . The full line in Fig. 3 is the result of a simple Ruderman-Kittel-Kasuya-Yoshida (RKKY) approach to the interlayer exchange coupling, see e.g. [9]:

$$J_{\text{inter}}(d) = \frac{1}{d^2} \{A_1 \sin(2\pi d/\Lambda_1 + \Phi_1) + A_2 \sin(2\pi d/\Lambda_2 + \Phi_2)\} \quad (3)$$

In this formula, the symmetry of the Fermi surface of Cu(001) results in the existence of two periods Λ_1 and Λ_2 of $J_{\text{inter}}(d)$. The full line is produced by taking all parameters entering Equation (3) from theory [31]. Since theory can not give reasonable values for the amplitudes A_1 and A_2 , we borrowed these numbers from an experiment on similar trilayers with Cu(001) spacers [32]. An excellent agreement is observed between experiment and theory without using any fit parameters [33]. One has to note that the maximum in ΔT_{Ni} is observed for $d=2.8$ ML, exactly at the thickness where quantum-well states have been observed in trilayers with Cu(001) spacers [34]. Figure 3 offers the possibility to manipulate T_C in layered structures by varying the spacer thickness and, therefore, it is interesting for applications. As a final remark, the presence of AFM coupling in our films with very thin spacers guarantees that problems of 'pinholes' [35], i.e. bridges of direct coupling between Ni and Co, are negligible. Therefore, the physical mechanisms we discuss are dominated by the interlayer exchanging coupling.

A more rigorous theoretical description of the effects of J_{inter} on ΔT_{Ni} was recently given taking into account the 2D nature of the coupled layers [36]. Within a many-body Green's function approach, and using the Tyablicov's approximation, the collective excitations (spin waves, magnons) were incorporated in the calculations. As it is well known a 2D system is not ferromagnetic at any finite temperature [37]. This occurs because a positive feedback is encountered for any thermal fluctuation of the spins. However, real films with a 2D geometry have been shown from numerous experiments to order ferromagnetically. To bridge the inconsistency between theory and experiment, it was suggested that anisotropy stabilizes ferromagnetism at finite temperatures [38]. In the same sense, any internal or external field may stabilize ferromagnetic order at higher temperatures as was shown, for example, in Ref. [11] following a theoretical approach by Pokrovskii [39]. In a similar way, the spin-waves which tend to disorder the ferromagnetic layer near T_C are suppressed due to J_{inter} . Therefore, J_{inter} will always introduce ferromagnetic order at higher temperatures. Figure 4 shows together experimental data and theoretical curves produced for various reasonable

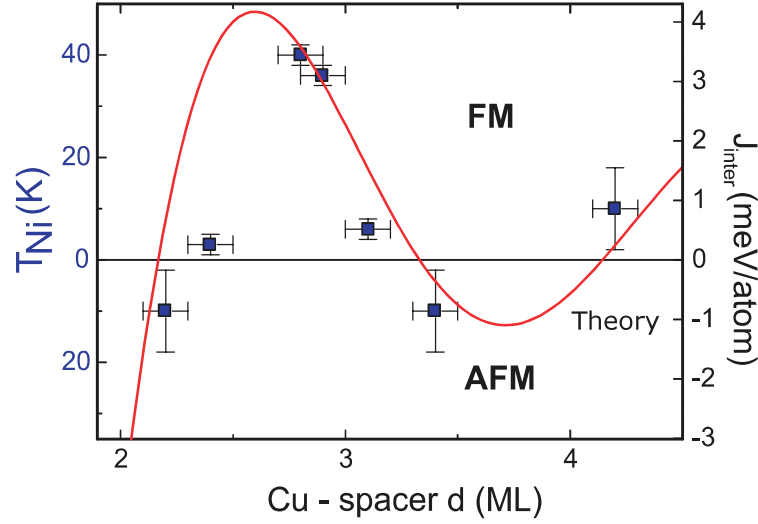


Fig. 3. The increase ΔT_{Ni} follows an oscillatory dependence on the Cu-spacer thickness similar to J_{inter} . The solid line is the result of theoretical calculations as explained in the text. The right side of the Y-axis is scaled to coupling values deduced via a simple molecular-field approach. This approach overestimates the values of J_{inter} .

values of J_{inter} [9] (note that 1K corresponds to about 10000 G in exchange field units). Figure 5 presents theoretical results for ΔT_{Ni} in a reduced temperature scale as a function of the Ni thickness. For comparison, the results predicted by the molecular field theory (MFT) are shown. In the inset the calculations are compared to experimental results. One may see that (i) ΔT is increasing by decreasing the film thickness and (ii) MFT can not describe properly the experiment. Both conclusions show that this type of experiment can be realized only in 2D ferromagnets [40].

Now one may turn to the crucial question if and to what extent the lower ordering temperature which was denoted as $T_{\text{C}}^{\text{low}}$ may be considered as a phase transition temperature. Theory provides calculations for infinite samples and predicts phase transitions only at the absence of any internal field. As discussed in the introduction, this is not the case in the experimental world. In the presence of an exchange interaction Equation (1) may be written as [41]:

$$\chi'_{\text{exp}} = \frac{1}{\frac{1}{\chi'_{\text{int}}} + N + \frac{H_{\text{exch}}}{M}} \quad (4)$$

where, for trilayers, [9]:

$$H_{\text{exch}} = \frac{2J_{\text{inter}}}{d \cdot M} \quad (5)$$

In the same way with the demagnetizing factor N , H_{exch} will limit the measured susceptibility in an experiment. Taking into account that ultrathin films

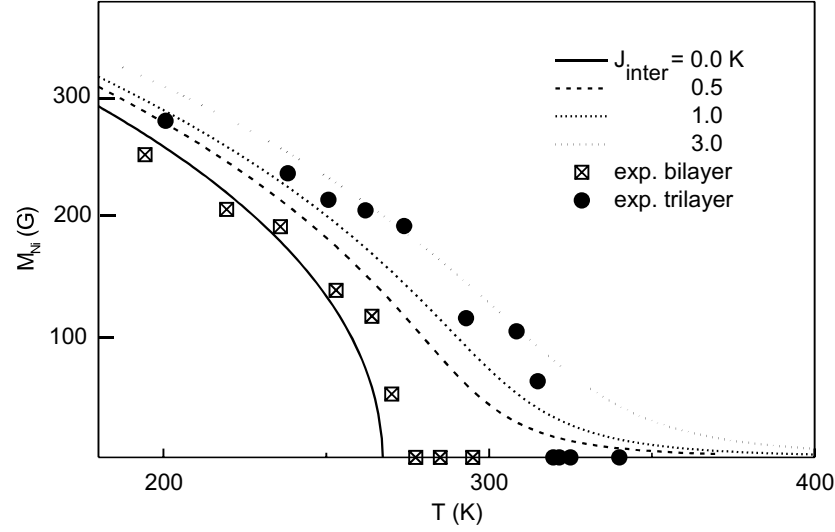


Fig. 4. Experimental data points for the Ni magnetization in the bilayer and the trilayer of Fig. 2 and theoretical curves for various values of J_{inter} , as indicated. The curves were deduced via a many-body Green's function approach which allows for the manifestation of effects related to the reduced dimensionality of the magnetic layers [36].

have a small mass and therefore they give small signals compared to bulk samples, susceptibility signals will be undetectable in the presence of even a small J_{inter} . Indeed, the only experimental results up to now concern a case with $d = 25$ ML [29], Fig. 6(a), where according to Equation (3) J_{inter} should be very small and a second case where $d = 5$ ML [42]. The latter thickness was near a d -dependent crossover from FM to AFM coupling and H_{exch} was measured to be in the order of 10 G near T_C^{low} [42]. The strong suppression of the susceptibility near T_C^{low} is in agreement with all previous calculations for the susceptibility in the presence of an exchange interaction [36,43,44], see also Fig. 6(b).

While the susceptibility data are well-understood it still remains a question arising from a careful inspection of Fig. 4: By all theories [36,43,44] a magnetization 'tail' is calculated in the layered structure above T_C^{low} , see the lines in Fig. 4. This was never observed in our experiment [45]. As an illustrative example, we plot in Fig. 7 in reduced temperature and magnetization units the results from Ni magnetization curves in seven different trilayers. All data points follow a rather abrupt path near T_C^{low} . Within our experimental sensitivity, no signal is observed above $t=1.0$. Another evidence for the absence of a magnetization 'tail' comes from Fig. 8. There we plot the remanent magnetization curves for a 1.3 ML Co/2.1 ML Cu/4 ML Ni/Cu(001). In this trilayer, unlike all the previous ones, we select a very thin Co film with a T_C which is placed below the one of

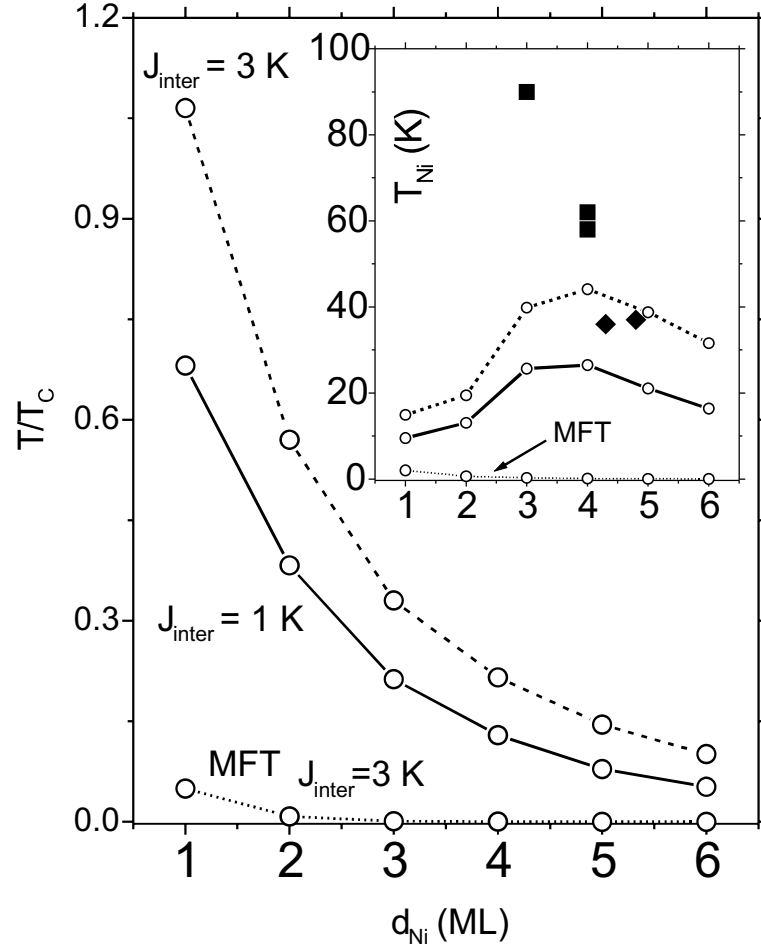


Fig. 5. Coupling-induced increase ΔT_{Ni} , plotted in a reduced temperature scale, as a function of the number of Ni layers with J_{inter} as a parameter. In the inset calculations are compared to experimental data points. The calculations based on a mean-field theory (MFT) can not describe properly the experiment [36]. In other words, these experiments can not be realized in the bulk, but only in 2D magnets.

Ni. Therefore, we may probe the magnetization curve of Co vanishing under the influence of J_{inter} . Like the ones of Ni, the magnetization curve of Co shows no 'tail'.

Reference [36] suggested that might be the formation of domains near T_C^{low} that inhibits the observation of a 'tail'. At first place, domains are inconsistent with in-plane magnetized ultrathin films [46]. One may, however, ask what will be the situation in trilayers having spacers with non-integer numbers of layers.

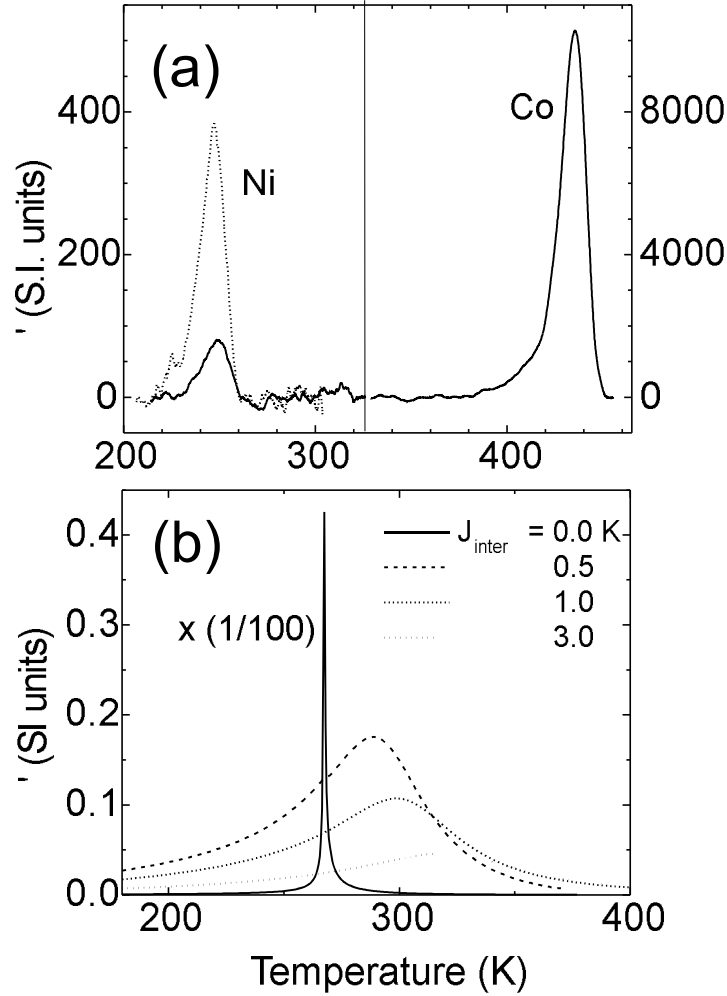


Fig. 6. (a) Experimental susceptibility peaks in the Cu/Ni bilayer (dotted) and the Co/Cu/Ni trilayer (solid line) [29]. Even small values of J_{inter} , as for this trilayer, suppress the Ni peak and shift it to higher temperatures, see also [42] (b) The susceptibility is calculated within the Green's function approach [36] by considering large values of J_{inter} like the ones of the trilayer of Fig. 2. We see a very strong suppression of the susceptibility which justifies the lack of an experimental detection of the susceptibility in trilayers with large J_{inter} .

For example, for 3.5 ML Cu half of the spacer will consist of 3 ML and another half of 4 ML. If we suppose that the one thickness favors AFM coupling and the other FM, could the Ni layer break up into domains near T_C^{low} ? To answer this question one has to take into account the diffusion length which for Ni, Co, Cu

on Cu(001) is only about 3-4 nm [47]. This determines the lateral dimensions of the 3 and 4 ML areas, in the previous example. Minimization of the intra- and interlayer exchange energies will result in domain-wall thicknesses which are much larger than this length scale of 3-4 nm. Therefore, the formation of such domains is energetically unfavorable.

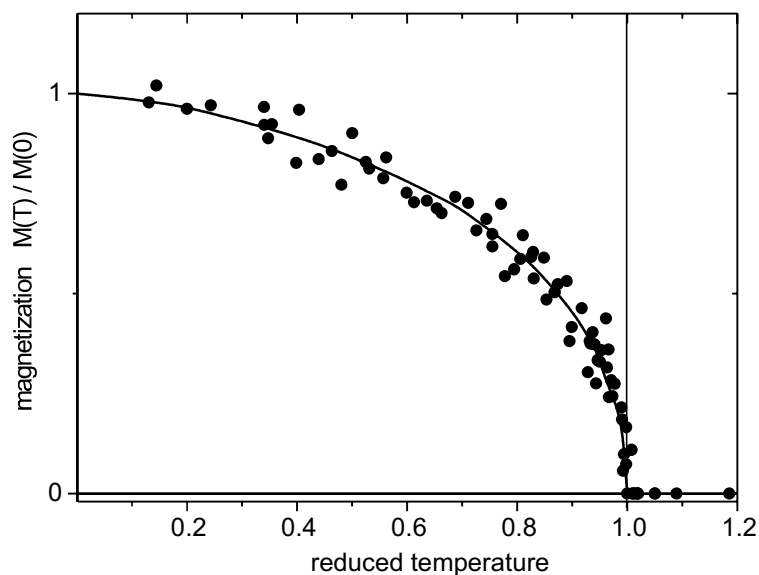


Fig. 7. Reduced magnetization of Ni as a function of reduced temperature. The data were collected from seven different trilayers. Contrary to all theoretical calculations a magnetization 'tail' is not observed in the experiments. The line serves only as a guide to the eye.

While we can not give a definite answer to the question of why we do not observe a 'tail' in our experiments, a possible suggestion is the strong temperature dependence of J_{inter} near $T_{\text{C}}^{\text{low}}$. J_{inter} has two origins of temperature dependence [48]. The one is intrinsic and has to do with the approach to the Fermi temperature. Since the Fermi temperature of metals is much higher than T_{C} , this dependence is of minor importance. The second one derives from the disordering of the magnetic moments due to spin-waves [48,49]. This is very strong near the interfaces. We think that since J_{inter} is an interface effect a very strong temperature dependence should be expected near $T_{\text{C}}^{\text{low}}$. Simple estimates can show that in the presence of a vanishing J_{inter} , no 'tail' will be observed in the magnetization curves, while the susceptibility will still be suppressed below the experimental sensitivity. Unfortunately [48,49] provide calculations at relatively low reduced temperatures. It would be of interest to see such calculations near $T_{\text{C}}^{\text{low}}$.

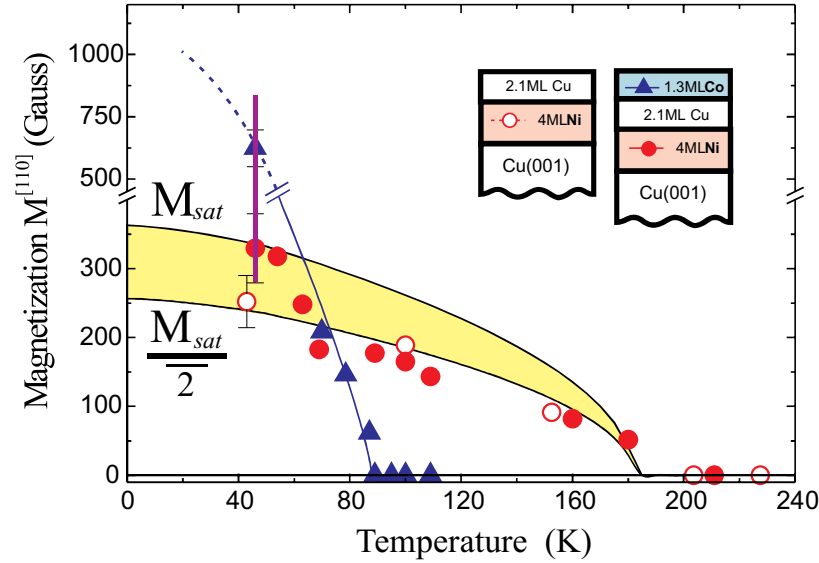


Fig. 8. Magnetization curves for Ni in the bilayer (open) and in the trilayer (closed circles) and for Co (triangles). Co has a larger magnetization, but lower T_C than Ni. Therefore, the magnetization curves of Ni and Co cross each other. The unusual shape of the Ni magnetization curve in the trilayer indicates a coupling-induced reorientation from the [110] (easy-axis of Co) to the [100] (easy-axis of Ni). The root-square-two relation between the two curves suggests that Ni stays always in a single-domain state.

4 Summary

Magnetic layers of reduced dimensionality coupled via a non-magnetic spacer are shown to have separate onset of ferromagnetism. Interlayer exchange coupling shifts the lower ordering temperature to higher temperatures. This phenomenon can be described properly only by taking into account the 2D nature of the layers. It can be used to manipulate T_C in layered magnetic structures, as it is a demand for technological purposes. The lower ordering temperature can be treated, from an experimental point of view, as a temperature of a phase transition. Therefore, we suggest that the 2D coupled magnetic layers present two phase transitions within the same conventions posed when measuring phase transitions in a real experiment.

Acknowledgments

We gratefully acknowledge F. Wilhelm, A. Ney, A. Scherz, U. Bovensiepen and P. Srivastava for the experiments, M. Farle and H. Wende for discussions and M. Tischer and F. May for the initialization of this work. Work supported by the BMBF(05 SC8 KEA3) and the DFG Sfb290.

References

1. a. A. J. Freeman, S. D. Bader: *Magnetism beyond 2000*, (Elsevier, Amsterdam, Lausanne, New York, Oxford, Shannon, Singapore, Tokyo 1999); b. J.A.C. Bland, B. Heinrich: *Ultrathin Magnetic Structures*, (Springer, Berlin 1994) Vol. I and II.
2. P. Pouloupoulos, K. Baberschke: J. Phys.: Cond. Matter **11**, 9495 (1999)
3. F.J. Himpsel, J.E. Ortega, G.J. Mankey, R.F. Willis: Adv. in Phys. **47**, 511 (1998) and references therein.
4. G. Schütz, H. Ebert: *Spin-Orbit-Influenced Spectroscopies of Magnetic Solids*, (Springer-Verlag, Berlin 1996) Vol. **466**.
5. L.P. Kadanoff, W. Gotze, D. Hamblen, R. Hecht, E.A.S. Lewis, V.V. Palciauskas, M. Rayl, J. Swift, D. Aspnes, J. Kane: Rev. Mod. Phys. **39**, 395 (1967)
6. H.E. Stanley: *Introduction to Phase Transitions and Critical Phenomena*, (Clarendon Press, Oxford 1971)
7. C.N.R. Rao, K.J. Rao: *Phase Transitions in Solids*, (McGraw-Hill Inc., New York 1978)
8. S.N. Kaul: J. Magn. Magn. Mater. **53**, 5 (1985)
9. A. Fert, P. Grünberg, A. Barthelémy, F. Petroff, W. Zinn: J. Magn. Magn. Mater. **140-144**, 1 (1995) and references therein.
10. C. Kittel: *Introduction to Solid State Physics*, (Wiley and Sons, New York 1976).
11. D. Kerkmann, D. Pescia, A. Allenspach: Phys. Rev. Lett. **68**, 686 (1992)
12. A. Aspelmeier, M. Tischer, M. Farle, M. Russo, K. Baberschke, D. Arvanitis: J. Magn. Magn. Mater. **146**, 256 (1995)
13. W. Platow, U. Bovensiepen, P. Pouloupoulos, M. Farle, K. Baberschke, L. Hammer, S. Walter, S. Müller, K. Heinz: Phys. Rev. B **59**, 12641 (1999)
14. J. Lindner, P. Pouloupoulos, F. Wilhelm, M. Farle, K. Baberschke: Phys. Rev. B **62**, 10431 (2000)
15. J. Shen, J. Giergiel, J. Kirschner: Phys. Rev. B **52**, 8454 (1995)
16. P. Pouloupoulos, J. Lindner, M. Farle, K. Baberschke: Surf. Sci. **437**, 277 (1999)
17. Yi Li, K. Baberschke: Phys. Rev. Lett. **68**, 1208 (1992)
18. U. Bovensiepen, P. Pouloupoulos, M. Farle, K. Baberschke: Surf. Sci. **402-404**, 396 (1998)
19. K. Baberschke, M. Farle: J. Appl. Phys. **81**, 5038 (1997)
20. M. Farle: Rep. Prog. Phys. **61**, 755 (1998)
21. C.M. Schneider, P. Bressler, P. Schuster, J. Kirschner, J.J. de Miguel, R. Miranda: Phys. Rev. Lett. **64**, 1059 (1990)
22. A.K. Schmidt, J. Kirschner: Ultramicroscopy **42-44**, 483 (1992)
23. P. Krams, F. Lauks, R.L. Stamps, B. Hillebrands, G. Güntherodt: Phys. Rev. Lett. **69**, 3674 (1992)
24. J.R. Cerda, P.L. de Andres, A. Cebollada, R. Miranda, E. Navas, P. Schuster, C.M. Schneider, J. Kirschner: J. Phys.: Cond. Matter **5**, 2055 (1993)
25. U. Bovensiepen, P. Pouloupoulos, W. Platow, M. Farle, K. Baberschke: J. Magn. Magn. Mater. **192**, L386 (1999)
26. J. Fassbender, R. Allenspach, U. Dürig: Surf. Sci. **383**, L742 (1997)
27. P. Srivastava, F. Wilhelm, A. Ney, M. Farle, H. Wende, N. Haack, G. Ceballos, K. Baberschke: Phys. Rev. B **58**, 5701 (1998)
28. We did not measure at temperatures higher than 350 K to avoid problems of intermixing
29. U. Bovensiepen, F. Wilhelm, P. Srivastava, P. Pouloupoulos, M. Farle, A. Ney, K. Baberschke: Phys. Rev. Lett. **81**, 2368 (1998)

30. G. Bayreuther, F. Bensch, V. Kottler: J. Appl. Phys. **79**, 4509 (1996)
31. P. Bruno, C. Chappert: Phys. Rev. Lett. **67**, 1602 (1991)
32. W. Weber, R. Allenspach, A. Bischof: Europhys. Lett. **31**, 491 (1995)
33. A. Ney, F. Wilhelm, M. Farle, P. Pouloupoulos, P. Srivastava, K. Baberschke: Phys. Rev. B **59**, R3938 (1999)
34. P. Segovia, E.G. Michel, J.E. Ortega: Phys. Rev. Lett. **77**, 3455 (1996)
35. J.F. Bobo, M. Piecuch, E. Snoeck: J. Magn. Magn. Mater. **126**, 440 (1993)
36. P.J. Jensen, K.H. Bennemann, P. Pouloupoulos, M. Farle, F. Wilhelm, K. Baberschke: Phys. Rev. B **60**, R14994 (1999); P.J. Jensen, K.H. Bennemann, K. Baberschke, P. Pouloupoulos, M. Farle: J. Appl. Phys. **87**, 6692 (2000)
37. N.D. Mermin, H. Wagner: Phys. Rev. Lett. **17**, 1133 (1966)
38. D.L. Mills in [1]b, Vol. I, pp. 90-121 and references therein
39. V. Pokrovskii: Adv. Phys. **28**, 595 (1979)
40. In a recent work, the Green's function method in the Tyablicov's approximation was combined with first principles tight-binding linear muffin-tin orbital calculations to predict oscillations of the Curie temperature of two-dimensional ferromagnets as a function of Cu-capping, M. Pajda, J. Kudrnovsky, I. Turek, V. Drchal, P. Bruno: (unpublished). The theoretical method used in that Reference (which is similar to ours [36]) and the consistency of their predictions with the RKKY approach supports fully our work.
41. For a detailed discussion see U. Bovensiepen: : *Phasenübergänge in magnetischen Monolagen und austauschgekoppelten Schichten*, (Shaker Verlag, Berlin 2000)
42. P. Pouloupoulos, U. Bovensiepen, M. Farle, K. Baberschke: J. Magn. Magn. Mater. **212**, 17 (2000)
43. R.W. Wang, D.L. Mills: Phys. Rev. B **46**, 11681 (1992)
44. J.H. Wu, T. Herrmann, M. Potthoff, W. Nolting: J. Phys.: Cond. Matter **12**, 2847 (2000)
45. In a pioneer experiment to demonstrate the effects of J_{inter} on the magnetization near the T_C^{low} the existence of magnetization 'tails' was reported (M. Donath, D. Scholl, H.C. Siegmann, E. Kay: Phys. Rev. B **43**, 3164 (1991)). From the raw data presented in that Ref., the observation of such 'tails' may be questioned.
46. R. Allenspach: J. Magn. Magn. Mater. **129**, 160 (1994)
47. J. Lindner, P. Pouloupoulos, M. Farle, K. Baberschke: J. Magn. Magn. Mater. **218**, 10 (2000) and references therein
48. K. Hathaway in [1]b, Vol. II, pp. 45-81 and references therein
49. N.S. Almeida, D.L. Mills, M. Teitelman: Phys. Rev. Lett. **75**, 733 (1995)

Theory of Spin Excitations and the Microwave Response of Cylindrical Ferromagnetic Nanowires

Doug Mills

University of California, Irvine, Irvine, CA, USA

Abstract. We develop the theory of exchange/dipole spin wave excitations of ferromagnetic nanowires of cylindrical cross section, where the magnetization is parallel to the axis of the wire. In addition, we provide the theory of the microwave response of such structures, for the case where the nanowire is also a conductor. We present explicit calculations of both the mode structure of nanowires, and also their ferromagnetic resonance spectrum, with attention to recent experimental studies. We compare differences between the physical picture appropriate for the cylinder, with the well studied case of the ferromagnetic film.

1 Introduction

In recent years, very considerable attention has been devoted to the study of ultrathin ferromagnetic films, and magnetic multilayers formed from such films. Such systems have unique physical properties, by virtue of the fact that a large fraction of the magnetic ions reside in low symmetry sites at the film surfaces, thus providing strong anisotropies not found in bulk magnetic matter constructed from the same ions. Also, in multilayers, exchange couplings between nearest neighbor films provide for diverse magnetic phases, spin reorientation transitions induced by very modest applied magnetic fields, and other phenomena as well. Finally, important applications of magnetic multilayers have been realized, and more are envisioned.

Other forms of magnetic nanostructures can be fabricated and studied as well. For example, Ebels and Wigen [1] have created arrays of very long ferromagnetic nanowires of Ni, permalloy and Co, with diameters in the range of 30 to 500 nm. These are very uniform in cross section, with lengths in the range of 20 microns. They thus are realizations of nanowires one can reasonably view as infinite in length, to excellent approximation. These authors have carried out ferromagnetic resonance studies of their samples, which consist of nanowire arrays, with individual entities accurately parallel to each other, but arranged randomly over a plane.

The diameter range explored in these studies is such that when one considers the spin wave modes of an isolated nanowire, it is necessary to include both exchange and dipolar contributions to their excitation energy. The present paper presents the theory of such dipole/exchange spin wave modes of isolated ferromagnetic nanowires of circular cross section, for the case where the magnetization is parallel to the symmetry axis of the wire. In addition, we provide

a description of the ferromagnetic resonance absorption spectrum, for the case where, as in the samples discussed above, the materials are metallic in nature. It is thus important to take into account the influence of the finite skin depth, particularly for the larger diameters explored in these particular studies.

There is a long history of the study of the magnetostatic spin wave modes of uniformly magnetized ferromagnets of various shapes [2], with explicit attention to cylindrical samples [3]. However, little attention has been devoted to the inclusion of exchange, since these early studies were motivated by applications to ferrite samples of rather large dimensions. The structure of the spin wave modes accessible to microwave excitation in such samples are influenced little by exchange. In the particular case of samples of cylindrical shape, one study of the exchange dipole modes has appeared [4]; so far as we know, the text is not available in English, so its content is of limited accessibility.

There are two interesting implications of the mode structure of the ferromagnetic nanowires. First, as we shall see below, at long wavelengths, the dispersion is controlled by the long ranged dipolar fields. While details are different, very much as in ultrathin films [5], [6], the dipolar contribution can produce downward curvature in the dispersion relation at long wavelengths. At larger wave vectors, the curvature is always positive, as a consequence of the presence of exchange. Thus, one realizes short wavelength spin wave modes degenerate in frequency with the uniform mode of the cylinder excited in ferromagnetic resonance. If the cylinder surfaces are not perfectly smooth, the two magnon dipolar mechanism operative in ultrathin films [6], [7] should then also be "active" in the ferromagnetic nanowires. This will lead to extrinsic contributions to the ferromagnetic resonance linewidth similar to those demonstrated to be substantial in ultrathin ferromagnetic films [7].

Also, when the ferromagnetic resonance mode of the nanowire is excited, the precession of the magnetization leads to large magnetic fields outside the sample, in contrast to the case of thin films, where the field is confined to the film interior. There should then be strong interactions between nanowires, in dense arrays such as those explored by Ebels and Wigen [1]. The consequence of these interactions is not explored here, though our formal structure can be used for this purpose.

In the discussion above, we have discussed on the experimental studies of Ebels and Wigen [1]. It should be remarked that Demokritov and Hillebrands [8] have carried out extensive studies of nanowire arrays. Their nanowires have rectangular cross section, however. It would be highly desirable to develop a theory of the dipole/exchange modes of such entities. We shall address such questions in future studies.

The outline of this paper is as follows. In section II, we present the theory of the exchange/dipole spin wave modes, and in section III we provide numerical studies of the spin wave dispersion and ferromagnetic resonance response. We also discuss differences between the mode structure and response characteristics of the nanowire, and the well known case of the thin film. In regard to the microwave response, for the case where the sample is made of conducting

material, there are very substantial differences between the two cases. Section IV is devoted to concluding remarks.

2 Theoretical Discussion

In this section, we first present the theory of the spin wave excitations of a long ferromagnetic nanowire with circular cross section, and magnetization parallel to its axis. Then we turn to a description of its response to a spatially uniform microwave field, appropriate to a ferromagnetic resonance experiment. Throughout this section, the magnetization is assumed parallel to the z axis, which is also parallel to the symmetry axis of the nanowire.

As mentioned in Section I, we develop here the theory of the spin waves of the nanowire, with emphasis on the regime where both exchange and dipolar couplings between the spins are comparable in magnitude. However, before we turn to this general analysis, it will be useful for what follows to have in hand a summary of the theory of dipolar spin waves, in the absence of exchange. This will serve also to introduce notation used throughout the paper.

In the linearized version of spin wave theory, when a mode is excited the magnetization of the sample is given by

$$\mathbf{M}(\mathbf{r}, t) = \hat{z}M_S + \hat{x}m_x(\mathbf{r})\exp(-i\Omega t) + \hat{y}m_y(\mathbf{r})\exp(-i\Omega t), \quad (1)$$

where for any nanowire of uniform cross section, $m_\alpha(x, y, z) = m_\alpha(x, y)\exp(ikz)$ where k is the wave vector of the mode, in the direction parallel to the axis of symmetry. The precession of the magnetization generates a magnetic field of dipolar origin, with frequency Ω . We call this \mathbf{h}^d . The dependence of the dipolar field on z is the same as that given above. In the absence of exchange, the components of the dipolar field and those of the transverse magnetization are linked by the constitutive relations, suppressing explicit reference to time dependence for brevity,

$$m_x(x, y) = \chi_1(\Omega)h_x^d(x, y) + i\chi_2(\Omega)h_y^d(x, y) \quad (2)$$

and

$$m_y(x, y) = \chi_1(\Omega)h_y^d(x, y) - i\chi_2(\Omega)h_x^d(x, y),$$

where for a ferromagnet, $\chi_1(\Omega) = \Omega_H\Omega_M/(\Omega_H^2 - \Omega^2)$ and $\chi_2(\Omega) = \Omega\Omega_H/(\Omega_H^2 - \Omega^2)$. If γ is the gyromagnetic ratio and H_0 an applied DC magnetic field parallel to the magnetization, we have introduced $\Omega_H = \gamma H_0$ and $\Omega_M = \gamma M_S$. Within the magnetostatic approximation, the dipole field may be expressed as the gradient of the magnetic potential,

$$\mathbf{h}^d(\mathbf{r}) = -\nabla\Phi_M(\mathbf{r}), \quad (3)$$

where again $\Phi_M(\mathbf{r}) = \Phi_M(x, y)\exp(ikz)$. Inside the nanowire, the induction $\mathbf{b} = \mathbf{h}^d + 4\pi\mathbf{m}$, while outside $\mathbf{b} = \mathbf{h}^d$. The magnetostatic theory of spin waves,

with exchange ignored, follows by exploring the solutions of $\nabla \cdot \mathbf{b} = 0$ everywhere, with the solution subject to the condition that the normal (radial, in this case) component of \mathbf{b} be continuous across the surface, while tangential (azimuthal, z) components of \mathbf{h}^d are continuous. Inside the cylinder, the magnetic potential satisfies Walker's equation [2]

$$(1 + 4\pi\chi_1(\Omega))\left(\frac{\partial^2}{\partial x^2} + \frac{\partial^2}{\partial y^2}\right)\Phi_M(x, y) - k^2\Phi_M(x, y) = 0 \quad (4)$$

while outside, one sets $\chi_1(\Omega)$ to zero. We let $\mu_1(\Omega) = 1 + 4\pi\chi_1(\Omega)$ and $\mu_2(\Omega) = 4\pi\chi_2(\Omega)$ in what follows.

For the problem of interest, we use cylindrical coordinates, and seek solutions for which the magnetic potential has the form $\Phi_M(\rho, \phi) = f_m(\rho)\exp(im\phi)$. We shall focus our attention here on the frequency regime where $\mu_1(\Omega)$ is positive. Then inside the nanowire, one has $f_m^<(\rho) = AI_m(k\rho/\mu_1(\Omega)^{\frac{1}{2}})$ while outside one has $f_m^>(\rho) = BK_m(k\rho)$, where I_m and K_m are the modified Bessel functions.

Application of the boundary conditions described above at the surface of the nanowire, where $\rho = R$, leads one to the implicit dispersion relation from which the frequency of the magnetostatic modes are found:

$$\mu_1^{\frac{1}{2}} \left\{ \frac{I'_m(kR/\mu_1^{\frac{1}{2}})}{I_m(kR/\mu_1^{\frac{1}{2}})} \right\} - \frac{m\mu_2}{kR} = \frac{K'_m(kR)}{K_m(kR)} \quad (5)$$

In this expression, I'_m and K'_m are derivatives of the modified Bessel functions with respect to their argument.

For what follows, our interest will reside in the behavior of the magnetostatic modes at very long wavelengths, in the regime $kR \ll 1$. Through use of the appropriate series expansions for the modified Bessel functions in Eq. (2.5), one may obtain analytic expressions for the frequencies of the various modes. We denote, for a given choice of the wave vector k and the azimuthal quantum number m the frequency of the mode by $\Omega_m(k)$. One then has

$$|\Omega_1(k)| = -\Omega_1(k) = H_0 + 2\pi M_S - \pi M_S(kR)^2 \ln\left(\frac{2}{kR}\right) + \dots \quad (6)$$

while for $m > 1$

$$|\Omega_m(k)| = -\Omega_m(k) = H_0 + 2\pi M_S - \frac{\pi M_S}{(m^2 - 1)}(kR)^2 + \dots$$

These results require some comment. First of all, when the azimuthal quantum number is positive, as assumed in deriving Eqs.(2.6), the frequencies are all negative, as one sees from these results. These modes all describe a circulation of energy in the counterclockwise sense around the cylinder, as one looks down the magnetization. If we had chosen the azimuthal quantum number negative, the frequencies would have all been positive; the frequency is an odd function of m as one can appreciate from the structure of Eq.(2.5). Thus the entire spectrum of

magnetostatic modes describes a circulation of energy around the magnetization, with the counterclockwise sense.

As the wave vector $k \rightarrow 0$, all the magnetostatic modes approach the frequency $H_0 + 2\pi M_S$. This is the ferromagnetic resonance frequency of the cylindrical nanowire. When this uniform ferromagnetic resonance mode is excited, the transverse magnetization engages in circular precession about the static magnetization, and generates an internal, spatially uniform demagnetizing field of strength $2\pi M_S$ as it does so. As we move off to finite wave vectors, the magnetic dipole interactions produce a negative dispersion initially, so the frequency of the spin wave modes drops below that of the ferromagnetic resonance mode. We will see below that when exchange is added, a positive contribution to the dispersion is produced for many of the modes, so the minimum frequency can lie away from $k = 0$.

A complete description of the spin wave modes of the cylinder requires us to include the influence of exchange. We now turn to this question.

In the macroscopic description of the spin excitations, the magnetic field \mathbf{h}^d inside and outside the cylinder is still described through introduction of a magnetic potential as in Eq.(2.3), and we still require that $\nabla \cdot \mathbf{b} = 0$ everywhere, just as before. However, we no longer can utilize Eqs.(2.2) to relate the transverse magnetization components to the dipolar field. We must resort to the Landau-Lifshitz equation of motion instead, and in this one incorporates the exchange field a given spin experiences from its neighbors. This may be done by replacing the spatially uniform DC magnetic field by the effective field $\hat{z}(H_0 - D\nabla^2)$, where D is the exchange stiffness. This leads us to the following relations:

$$i\Omega m_x = (H_0 - D\nabla^2)m_y + M_S \frac{\partial \Phi_M}{\partial y} \quad (7)$$

$$-i\Omega m_y = (H_0 - D\nabla^2)m_x - M_S \frac{\partial \Phi_M}{\partial x}$$

while inside the material, the $\nabla \cdot \mathbf{b} = 0$ condition becomes

$$\nabla^2 \Phi_M - 4\pi \left(\frac{\partial m_x}{\partial x} + \frac{\partial m_y}{\partial y} \right) = 0.$$

Outside the material, the magnetic potential satisfies Laplace's equation. Of course, when the exchange stiffness is set to zero, Eq. (2.7a) and Eq.(2.7b) produce results equivalent to those in Eqs. (2.2).

Some manipulation is required to cast Eqs. (2.7) into a form where one may extract the structure of the solution, for the geometry of present interest. We first rewrite the equations, to express them in terms of the right and left circularly polarized variables $m_{+,-} = m_x \pm im_y$, and similarly for the dipole field components. Then Eqs. (2.7) are replaced by

$$(\Omega + H_0 - D\nabla^2)m_+ = M_S h_+^d, \quad (8)$$

$$(\Omega - H_0 + D\nabla^2)m_- = -M_S h_-^d,$$

and

$$\nabla^2 \Phi_M - 2\pi \left[\left(\frac{\partial}{\partial x} - i \frac{\partial}{\partial y} \right) m_+ + \left(\frac{\partial}{\partial x} + i \frac{\partial}{\partial y} \right) m_- \right] = 0.$$

In what follows, we shall utilize the identities

$$\left(\frac{\partial}{\partial x} - i \frac{\partial}{\partial y} \right) h_+^d = \left(\frac{\partial}{\partial x} + i \frac{\partial}{\partial y} \right) h_-^d = -\nabla_\perp^2 \Phi_M, \quad (9)$$

where $\nabla_\perp^2 = (\partial^2/\partial x^2 + \partial^2/\partial y^2)$. We next introduce the auxiliary quantities

$$f_+ = \left(\frac{\partial}{\partial x} - i \frac{\partial}{\partial y} \right) m_+ \quad (10)$$

and

$$f_- = \left(\frac{\partial}{\partial x} + i \frac{\partial}{\partial y} \right) m_-.$$

Then one may rewrite Eq. (2.8c) to read

$$f_+ + f_- = \frac{1}{2\pi} \nabla^2 \Phi_M, \quad (11)$$

while Eq. (2.8a) and Eq. (2.8b) may be rearranged to state

$$\Omega(f_+ + f_-) + (H_0 - D\nabla^2)(f_+ - f_-) = 0, \quad (12)$$

and

$$\Omega(f_+ - f_-) + (H_0 - D\nabla^2)(f_+ + f_-) = -2M_S \nabla_\perp^2 \Phi_M.$$

Upon combining Eq. (2.12a) with Eq. (2.12b), one may relate $(f_+ - f_-)$ to the potential Φ_M . When this statement and Eq. (2.11) are substituted into Eq. (2.21a), we obtain a homogeneous equation that must be satisfied by the magnetic potential:

$$[(D\nabla^2 - H_0)(D\nabla^2 - B_0)] \nabla^2 \Phi_M + 4\pi M_S (D\nabla^2 - H_0) \frac{\partial^2}{\partial z^2} \Phi_M = 0. \quad (13)$$

In Eq.(2.13), we introduce $B_0 = H_0 + 4\pi M_S$.

One finds that Eq. (2.13) admits solutions of the form

$$\Phi_M(\rho, \phi, z) = J_m(\kappa\rho) \exp(im\phi + ikz) \quad (14)$$

If Eq.(2.14) is inserted into Eq.(2.13), and one notes that

$$\left(\frac{1}{\rho} \frac{d}{d\rho} \rho \frac{d}{d\rho} + \left(\kappa^2 - \frac{m^2}{\rho^2} \right) \right) J_m(\kappa\rho) = 0, \quad (15)$$

then for Eq.(2.14) to be a solution of Eq. (2.13), κ must be a root of

$$D^2(\kappa^2 + k^2)^3 + D(H_0 + B_0)(\kappa^2 + k^2)^2 + (H_0 B_0 - \Omega^2 - 4\pi M_S D k^2)(\kappa^2 + k^2) - 4\pi M_S H_0 k^2 = 0 \quad (16)$$

Since Eq. (2.16) is a cubic equation in κ^2 , for each choice of m and k , there are three linearly independent solutions of Eq. (2.14). Thus, we write the magnetic potential inside the material in the form

$$\Phi_M(\rho, \phi, z) = \sum_{i=1}^3 A_i J_m(\kappa_i \rho) \exp(im\phi + ikz). \quad (17)$$

Outside the cylinder, the magnetic potential satisfies Laplace's equation precisely as in the magnetostatic theory, so once again for $\rho > R$ we have

$$\Phi_M(\rho, \phi, z) = B K_m(k\rho) \exp(im\phi + ikz) \quad (18)$$

To find the dispersion relation of the spin waves, through application of the boundary conditions, we shall obtain four homogeneous equations for the four coefficients in the magnetic potential, as displayed in Eq. (2.17) and Eq.(2.18). Two of the boundary conditions are continuity of the magnetic potential (this assures continuity of tangential components of \mathbf{h}^d) and continuity of b_ρ . We shall have two other boundary conditions on the transverse components of magnetization, stated below. To apply the boundary conditions, within the material we need explicit expressions for the radial and azimuthal components of the transverse magnetization. To obtain these, we expand these components in a Bessel function series and use Eq. (2.8a) and Eq. (2.8b), noting Eq.(2.15). The following operator identities are useful:

$$\frac{\partial}{\partial x} + i \frac{\partial}{\partial y} = e^{i\phi} \left(\frac{\partial}{\partial \rho} - \frac{i}{\rho} \frac{\partial}{\partial \phi} \right) \quad (19)$$

and

$$\frac{\partial}{\partial x} - i \frac{\partial}{\partial y} = e^{-i\phi} \left(\frac{\partial}{\partial \rho} + \frac{i}{\rho} \frac{\partial}{\partial \phi} \right).$$

One finds the following expressions for the two components of magnetization:

$$m_+(\rho, \phi, z) = -\frac{M_S}{4\pi} \left(\sum_{i=1}^3 \frac{\kappa_i A_i J_{m+1}(\kappa_i \rho)}{[D(\kappa_i^2 + k^2) + H_0 + \Omega]} \right) \exp(i(m+1)\phi + ikz). \quad (20)$$

and

$$m_-(\rho, \phi, z) = -\frac{M_S}{4\pi} \left(\sum_{i=1}^3 \frac{\kappa_i A_i J_{m-1}(\kappa_i \rho)}{[D(\kappa_i^2 + k^2) + H_0 - \Omega]} \right) \exp(i(m-1)\phi + ikz).$$

The two boundary conditions which supplement those of magnetostatics refer to the behavior of the magnetization at the cylinder surface. If one considers

an idealized Heisenberg ferromagnet, and examines the behavior of the spin wave eigenfunction at the sample surface, in the long wave length limit, it is well known that one must require that the normal derivative of the transverse components of magnetization vanish there. We wish to consider the possibility that surface anisotropy is present on the cylinder surface; its presence influences the boundary condition. We assume that the surface anisotropy contributes a term to the surface energy of our cylinder in the form $-K_S(m_\rho/M_S)^2$, where the units of K_S is *ergs/cm²*. When K_S is positive, the normal to the surface is an easy axis, and when it is negative, the normal to the surface is a hard axis. In terms of the standardly defined exchange stiffness used often in the literature on ferromagnetism, then the boundary conditions for the transverse magnetization become

$$\left(\frac{\partial m_\phi}{\partial \rho}\right)_{\rho=R} = 0, \quad (21)$$

$$A\left(\frac{\partial m_\rho}{\partial \rho}\right)_{\rho=R} - \left(\frac{2K_S}{M_S}\right)m_\rho|_{\rho=R} = 0$$

The exchange stiffness D in our formulae has units of *gauss/cm²*. It is proportional to A , and in fact $D = 2A/\mu_B M_S$, where μ_B is the Bohr magneton.

This completes our discussion of the formalism for the description of the exchange/dipole spin wave excitations of a ferromagnetic nanowire of cylindrical cross section. We describe numerical calculations based on this description in section III. We turn next to the theory of the microwave response of a conducting ferromagnetic nanowire, before we present the numerical results.

2.1 The Microwave Response of an Isolated Ferromagnetic Nanowire

In this section, we present the theory of the microwave response of the nanowire considered above, with exchange and the presence of surface anisotropy included. The geometry is the same as that considered in the previous section. We have a nanowire, whose saturation magnetization is directed parallel to its symmetry axis. It is the case as well that the samples employed in the experiments which motivated this study are metallic in nature, so we wish to include the influence of the conductivity of the wire on its response. In essence, the microwave fields to which the wire is exposed create eddy currents which produce a finite skin depth. This influences the spatial profile of the exciting field within the sample, though the discussion presented in section III will show that the influence of the skin depth is much more modest for the cylindrical geometry, compared to the ultrathin film.

In what follows, it is assumed that the microwave magnetic field of interest is spatially uniform far from the wire, and is parallel to the x direction. All quantities will be assumed independent of z in what follows. Such a microwave field

excites the magnetization of the sample, of course, so the field is inhomogeneous near the wire, but always in the plane, and independent of z . By Faraday's Law, the time varying magnetic field generates an electric field, parallel to z . It is this electric field which is responsible for the eddy currents in the conducting material that lead to the skin effect.

We may describe these fields by introducing the vector potential

$$\mathbf{A}(x, y; t) = \hat{z}A(x, y)\exp(-i\Omega t). \quad (22)$$

Then, upon dropping explicit reference to the time dependence of various quantities once again, the electric field is given by

$$\mathbf{e}(x, y) = i\frac{\Omega}{c}\hat{z}A(x, y). \quad (23)$$

The magnetic field \mathbf{h} is linked to the electric field via

$$\nabla \times \mathbf{h} = \frac{4\pi}{c}\mathbf{j} = \frac{4\pi\sigma}{c}\hat{z}e = \frac{2i}{\delta_0^2}\hat{z}A, \quad (24)$$

where σ is the conductivity of the material. We have introduced the classical skin depth $\delta_0 = c/(2\pi\sigma\Omega)^{\frac{1}{2}}$. In Eq. (2.24), we ignore the displacement current term in the Maxwell equation. If this were to be included, its influence can be absorbed into a correction to the formula for the skin depth. The correction is of no quantitative importance at microwave frequencies, for typical metals.

The magnetic induction $\mathbf{b} = \nabla \times \mathbf{A}$, and of course $\mathbf{h} = \mathbf{b} - 4\pi\mathbf{m}$. When these statements are combined with Eq.(2.24), and it is noted that all quantities are independent of z , we find

$$[\nabla_{\perp}^2 + \frac{2i}{\delta_0^2}]A = 4\pi[\frac{\partial m_x}{\partial y} - \frac{\partial m_y}{\partial x}], \quad (25)$$

where the operator ∇_{\perp}^2 is introduced just after Eq. (2.9). Additional relations between the magnetization and the vector potential follow from the Landau Lifshitz equations. We use analogs of Eqs.(2.7), where now the field $\mathbf{h} = \nabla \times \mathbf{A} - 4\pi\mathbf{m}$, rather than $-\nabla\phi_M$ as earlier, and we also add to the right hand side the damping term $(G/M_S^2)(\mathbf{M} \times d\mathbf{M}/dt)$, with G the Gilbert damping factor. We then find, with all quantities once again expressed in magnetic field units,

$$i\Omega m_x = [\tilde{B}_0 - D\nabla_{\perp}^2]m_y + M_S\frac{\partial A}{\partial x} \quad (26)$$

and

$$i\Omega m_y = -[\tilde{B}_0 - D\nabla_{\perp}^2]m_x + M_S\frac{\partial A}{\partial y}$$

We have introduced $\tilde{B}_0 = H_0 + 4\pi M_S + ig\Omega$, where $g = G/\gamma M_S$. After a bit of manipulation, from Eqs. (2.26), we may obtain the statement that

$$[(\tilde{B}_0 - D\nabla_{\perp}^2)^2 - \Omega^2](\frac{\partial m_x}{\partial y} - \frac{\partial m_y}{\partial x}) - M_S(\tilde{B}_0 - D\nabla_{\perp}^2)\nabla_{\perp}^2 A = 0, \quad (27)$$

which when combined with Eq. (2.25) provides us with two equations that link the vector potential with the quantity

$$F(x, y) = \frac{\partial m_x}{\partial y} - \frac{\partial m_y}{\partial x}. \quad (28)$$

For constructing explicit expressions for the components of transverse magnetization, it is useful to note the relation

$$i\Omega\left(\frac{\partial m_x}{\partial x} + \frac{\partial m_y}{\partial y}\right) = \left[\tilde{B}_0 - D\nabla_\perp^2\right] F + M_S \nabla_\perp^2 A \quad (29)$$

The combination of Eq. (2.25) and Eq.(2.27) admit solutions of the form

$$A = aJ_m(\kappa\rho)\exp(im\phi) \quad (30)$$

and

$$F = bJ_m(\kappa\rho)\exp(im\phi)$$

When these forms are substituted into the two equations, we find that κ satisfies

$$\begin{aligned} D^2\kappa^6 + \left[2(\tilde{H}_0 + 2\pi M_S)D - \frac{2iD^2}{\delta_0^2}\right]\kappa^4 + \left[\tilde{B}_0\tilde{H}_0 - \frac{4iD\tilde{B}_0}{\delta_0^2} - \Omega^2\right]\kappa^2 \\ - \frac{2i}{\delta_0^2}\left[\tilde{B}_0^2 - \Omega^2\right] = 0. \end{aligned} \quad (31)$$

Here we have $\tilde{H}_0 = H_0 + ig\Omega$. Notice in the limit that the skin depth is allowed to become infinite and also when damping is ignored, Eq.(2.31) reduces to Eq.(2.13) if there we set k equal to zero.

There are three independent solutions of Eq. (2.31) for κ . Thus, the most general solution for the vector potential in the medium, with the azimuthal variation as given in Eq. (2.30a), is

$$A(\rho, \phi) = \sum_{i=1}^3 a_i J_m(\kappa_i \rho) \exp(im\phi). \quad (32)$$

For the purpose of applying boundary conditions at the surface of the cylinder, we require explicit expressions for the magnetization, and for the components of magnetic field generated by the motion of the magnetization. It is most convenient for these to be expressed in cylindrical components. After some algebra which employs standard Bessel function identities, we find

$$m_\rho(\rho, \phi) = i\frac{M_S}{2} \sum_{i=1}^3 a_i \kappa_i \left\{ \frac{J_{m+1}(\kappa_i \rho)}{\tilde{B}_0 + D\kappa_i^2 + \Omega} + \frac{J_{m-1}(\kappa_i \rho)}{\tilde{B}_0 + D\kappa_i^2 - \Omega} \right\} \exp(im\phi), \quad (33)$$

$$m_\phi(\rho, \phi) = i \frac{M_S}{2} \sum_{i=1}^3 a_i \kappa_i \left\{ \frac{J_{m+1}(\kappa_i \rho)}{\tilde{B}_0 + D\kappa_i^2 + \Omega} - \frac{J_{m-1}(\kappa_i \rho)}{\tilde{B}_0 + D\kappa_i^2 - \Omega} \right\} \exp(im\phi),$$

$$b_\rho(\rho, \phi) = \frac{im}{\rho} \sum_{i=1}^3 a_i J_m(\kappa_i \rho) \exp(im\phi), \quad (34)$$

$$b_\phi(\rho, \phi) = -\frac{1}{2} \sum_{i=1}^3 a_i \kappa_i \{J_{m+1}(\kappa_i \rho) - J_{m-1}(\kappa_i \rho)\} \exp(im\phi) \quad (35)$$

and the electric field is given in Eq.(2.23). We now need to match the interior solutions just described to the fields outside the cylindrical nanowire. It is a simple matter to generate expressions for the magnetic and electric field in the vacuum outside, following a simplified version of the method just given. One may generate an expression for the vector potential in spherical coordinates through the wave equation in vacuum, then use this to find the components of the various fields. We do this assuming the limit $\Omega R/c \ll 1$ applies for the nanostructures of interest; in the near vicinity of the nanowire, the incident microwave field is viewed as spatially uniform, with magnitude h_0 , and also parallel to the x axis. We have outside the cylinder the incident field, supplemented by that generated by the motion of the magnetization in the nanowire; the latter will vary with the azimuthal angle as $\exp(\pm i\phi)$ in the limit the incident field is approximated as spatially uniform outside the wire. Then for the fields outside we find

$$h_\rho^>(\rho, \phi) = h_0 \cos(\phi) + i \frac{b_+}{\rho^2} \exp(i\phi) + i \frac{b_-}{\rho^2} \exp(-i\phi) \quad (36)$$

$$h_\phi^>(\rho, \phi) = h_0 \sin(\phi) + \frac{b_+}{\rho^2} \exp(i\phi) + \frac{b_-}{\rho^2} \exp(-i\phi)$$

and for the magnitude of the electric field, we have

$$e(\rho, \phi) = i \frac{\Omega}{c} \left\{ h_0 \rho \sin(\phi) + \frac{b_+}{\rho} \exp(i\phi) + \frac{b_-}{\rho} \exp(-i\phi) \right\}.$$

Our next task is to apply the boundary conditions. The solutions inside the medium are formed by superimposing the $m = +1$ and $m = -1$ forms given above. Thus, we have six unknown amplitudes associated with the solution in the interior of the wire, and as one sees from Eqs. (2.36) there are two more associated with the fields outside, for a total of eight. The boundary conditions on the fields are of course that the magnitude of the (tangential) electric field be conserved across the boundary, along with continuity of b_ρ and h_ϕ . The conservation of b_ρ and tangential electric field yield identical constraints, so from the field conservation conditions, we have two independent statements. We also apply the boundary conditions on the magnetization given in Eqs. (2.21). When

these four statements are broken down, with components proportional to and components proportional to $\exp(+i\phi)$ separated, we obtain eight inhomogeneous equations from which the unknown amplitudes may be expressed in terms of h_0 . We will not quote the explicit form of these statements here, since they may be derived readily from the information given above.

As remarked earlier, in section III, we present a series of numerical studies based on the formalism just given.

3 Numerical Studies of the Exchange/Dipole Spin Wave Modes and the Microwave Response of Ferromagnetic Nanowires

3.1 The Nature of the Spin Wave Modes

First, we begin with some general remarks. An interesting question is the initial behavior of the spin wave dispersion curves in the limit of small wave vector k . If initially, there is downward curvature, then the minimum frequency of a given branch will be at a finite, non-zero wave vector, since we can expect exchange to dominate at large values of the wave vector. Conversely, if the initial curvature is positive, then we may expect the minimum to reside at zero wave vector.

To examine this behavior, as one sees from Eqs. (2.6), we need to consider the case $m = 1$ separately from the case where $m > 1$. As we have seen from section II(b), the zero wave vector modes with $m = 1$ are the modes excited by a spatially uniform microwave field.

We may expect exchange to add a term to the dispersion relation proportional to Dk^2 , of course. If we then examine Eq. (2.6a), we see that by virtue of the logarithmic term, in the long wavelength limit, the negative dispersion from the dipolar contribution will always dominate that from exchange. However, since the prefactor of the logarithm is proportional to $(kR)^2$, for nanowires of small radii the dipolar term will assert itself only at very small values of the wave vector. One sees easily that the dipolar term will dominate the long wavelength form of the dispersion relation only when $k < (2/R)\exp(-D/\pi M_S R^2)$. Thus, while for $m = 1$, we expect the minimum frequency of the magnetostatic mode to always lie away from zero wave vector, but in numerical calculations for nanowires of small radii, the initial negative dispersion will be a subtle feature. At larger values of the radius, we will see the negative dispersion clearly.

For the modes with $m > 2$, from Eq.(2.6b), we see that the dipolar contributions to the dispersion provide negative dispersion in the form of a term quadratic in the wave vector, with prefactor scaling also as R^2 . Since an exchange contribution Dk^2 is independent of radius, we expect to see positive dispersion in these modes for nanowires of small radii, and then for nanowires of larger radii, we will realize negative dispersion initially, with the minimum frequency of a given branch shifted away from zero wave vector.

One may cast the discussion of the spin wave dispersion relation in terms of two dimensionless parameters, $h = H_0/4\pi M_S$, and $p = l/R$, and , where

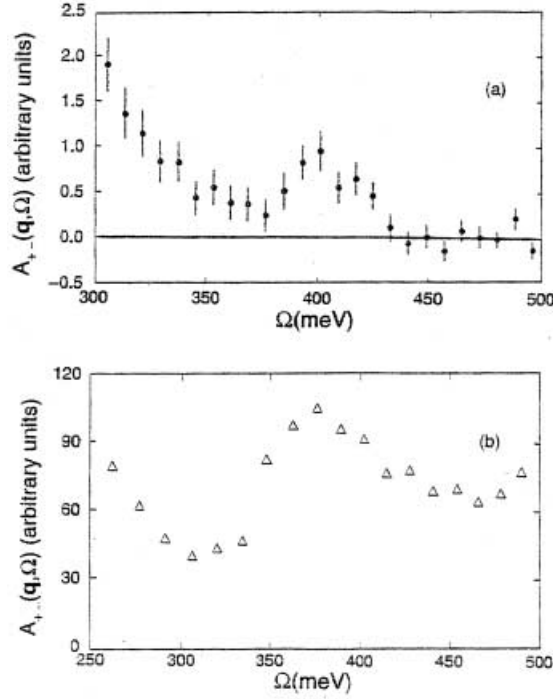


Fig. 1. For the case where $m = 1$, and for $h = H_0/4\pi M_S = .19$, we show the spin wave frequencies plotted as a function of $\log(kR)$ for (a) $p = 2$, and (b) $p = .2$, where p is the ratio of the exchange length defined in the text and the radius of the nanowire.

$l = (D/4\pi M_S)^{\frac{1}{2}}$ is an exchange length. For Ni, the exchange length is roughly 58 Å, while for Fe it is 35 Å. In what follows, we use the reduced frequency $\omega = \Omega/4\pi M_S$, and the frequencies will be plotted against the logarithm of kR .

In Fig. (1a), for $m = 1$ and for $h = .19$ (this corresponds to an applied DC field of 4 kgauss for Fe), we show the spin wave dispersion for the case where $p = 2$. Within the range of frequencies displayed, there is one mode only, which in the limit of zero wave vector approaches the FMR frequency, which in our dimensionless units has the frequency $h + \frac{1}{2}$. The negative dispersion at small wave vectors discussed above does not show, on the scale of this plot. Clearly, by the time the parameter kR approaches unity, the excitation energy of the spin wave is dominated by exchange for nanowires of such small radius. In Fig.(1b), for the same applied magnetic field, and again for $m = 1$, we show dispersion curves for nanowires of much larger radius, where $p = 0.2$. We now see several standing wave exchange branches, whose frequency at zero wave vector is above that of the FMR mode. Also, at these larger radii, for the mode that approaches the FMR frequency at long wavelengths, the negative dispersion at small wave vectors is now evident in the plot.

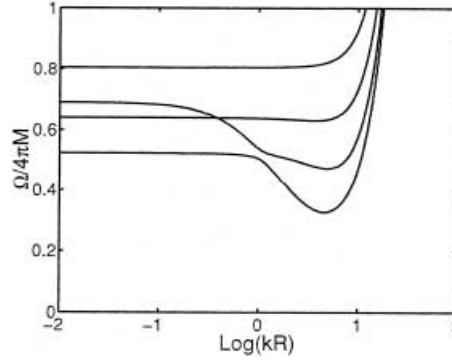


Fig. 2. For $m = 1$, $h = .19$ and $p = .05$, we show the spin wave frequencies of the nanowire plotted as a function of $\log(kR)$.

We find very interesting behavior at much larger radii, as illustrated in Fig. 2. These calculations again are for $m = 1$, and $h = .19$, but now we have $p = 0.05$. In the case of Ni, this would describe a nanowire whose radius is a bit under 1200 Å. We now have a larger number of more closely spaced exchange branches, as expected, but now notice that there are two exchange modes which lie below the ferromagnetic resonance frequency, in the limit of zero wave vector. The magnetostatic mode that approaches the FMR frequency as $k \rightarrow 0$ shows large negative dispersion at small wave vectors, until exchange takes over, and in fact we see that the magnetostatic mode hybridizes with the low frequency exchange modes, as the wave vector increases.

This set of dispersion curves, and the comparison between Fig. 2 and Fig. 1(b) requires some comment. Let us consider the basic solutions we encounter in the limit the wave vector k is zero. If we think of infinitely extended ferromagnetic matter for the moment, then we shall have spin waves that propagate within the xy plane, whose frequency is given by the well known expression $\Omega(\kappa) = [(H_0 + D\kappa^2)(H_0 + 4\pi M_S + D\kappa^2)]^{\frac{1}{2}}$, where we denote the in plane wave vector as κ . When such a wave is confined to within a cylinder of finite radius R , κ will obtain quantized values in the range of $\kappa = \kappa_n = n\pi/R$, where the lowest standing mode has $n = 1$. There is in addition a uniform mode of the cylinder, wherein the magnetization engages in perfectly circularly polarized precession at the FMR frequency $H_0 + 2\pi M_S$, which, it will be noted, lies higher in frequency than $\Omega(\kappa = 0)$. In the cylinder, in the presence of the boundaries, the boundary conditions mix the uniform FMR mode with the standing wave exchange modes, so to speak. Now if the radius of the nanowire is so small that $\Omega(\kappa = \pi/R)$ lies above the FMR frequency, we have a situation where one of the modes, which we have referred to above as the magnetostatic mode, approaches the FMR frequency as $k \rightarrow 0$, while all the standing wave exchange modes lie above this frequency. This is the case for the example given in Fig. 1(b). Now as the radius of the cylinder is increased, one or more of the modes of frequency $\Omega(\kappa_n)$ will

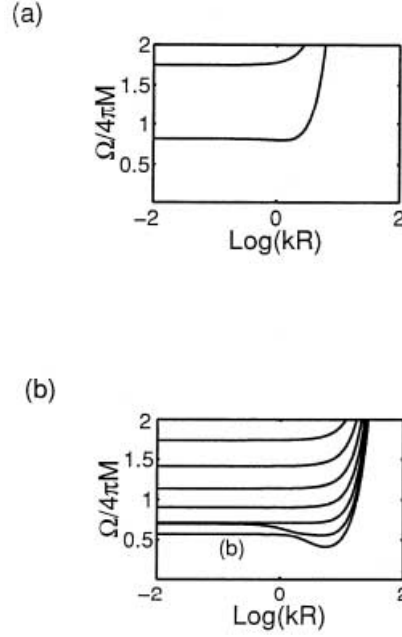


Fig. 3. For $m = 2$, $h = .19$ and (a) $p = .2$, and (b) $p = .05$, we show the spin wave frequencies plotted as a function of $\log(kR)$.

drop below the FMR frequency. In the limit $k \rightarrow 0$, we thus have standing wave exchange modes which lie below the FMR frequency. This is the case for the example in Fig. 2. The magnetostatic mode, which approaches the FMR frequency in this limit, exhibits negative dispersion at small wave vectors as expected from Eq. (2.6a), and the boundary conditions lead to the hybridization with the exchange modes evident in Fig. 2.

The situation just described is very different than realized in the much studied case of the thin film magnetized parallel to its surfaces. We still have the in plane standing wave exchange modes, with the frequency $\Omega(\kappa)$ just as above, but now the uniform mode that mixes with these is elliptically polarized, with frequency $[H_0(H_0 + 4\pi M_S)]^{\frac{1}{2}} \equiv \Omega(0)$. The standing wave spin waves always lie above the ferromagnetic resonance frequency.

These comments have implications for ferromagnetic resonance studies for nanowires, where the response of the sample is probed at fixed frequency, and the external DC magnetic field is swept. In the thin film, the standing wave exchange resonances are always found at resonance fields below the main FMR resonance field (provided, of course, there are no perturbations at the boundary so large as to produce spin waves tightly bound to the surface). It will be the case as well that in nanowires of small radius, the standing wave resonances will lie lower in field than the main FMR line. However as the radius of the nanowire is increased, one reaches a point where one may find standing wave resonances

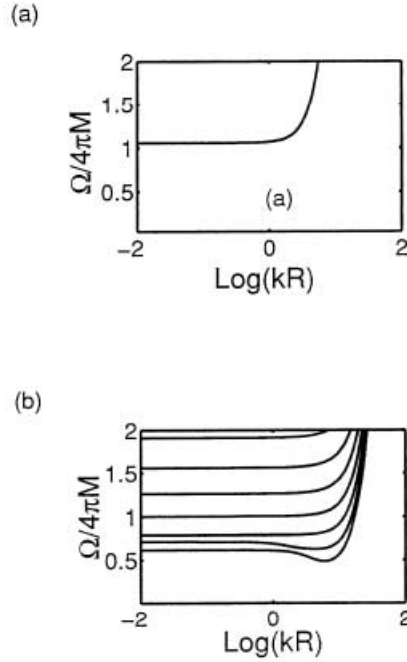


Fig. 4. For $m = 3$, $h = .19$, and (a) $p = .2$ and (b) $p = .05$, we show the spin wave frequencies plotted as a function of $\log(kR)$.

of the structure at fields above the FMR field; such lines will be produced by the exchange modes that have dropped below the FMR frequency.

In Fig. (3) and in Fig. (4), we show dispersion curves for modes with $m = 2$ and $m = 3$, respectively. One sees that for the samples of small diameter, the dispersion is positive at long wavelengths, whereas one sees negative dispersion at larger radii, as expected from the discussion above.

3.2 The Microwave Response of Conducting Ferromagnetic Nanowires

We next turn to studies of the microwave response of ferromagnetic nanowires, utilizing the formalism given in Section II(b). All computations below use parameters appropriate to Ni at room temperature, with the experiments of ref. [1] in mind. We take $M_S = 480 \text{ gauss}$, the g factor to be 2.15, the spin wave exchange stiffness as $D = 2 \times 10^{-9} \text{ gauss/cm}^2$ and for the purposes of including the influence of the skin depth on the response, the electrical resistivity is 7 micro ohm-cm. This gives a classical skin depth in the range of a micron at 10 GHz, which is very much larger than the radii of the nanowires considered here.

For the purposes of calculating the FMR spectra, we consider a quantity Γ defined as follows. As we have seen in section II(b), the precessing magneti-

zation of the wire creates a strong magnetic field outside the wire, which falls off inversely with the square of the distance from the axis of symmetry, as we see from Eq. (2.36a) and Eq.(2.36b). The coupling of the nanowire to a detector will scale as the square of the strength of this field. We define Γ to be $\Gamma = \langle (h_\rho)^2 + (h_\phi)^2 \rangle_{p=R+} / h_0^2$, where the angular brackets denote an average over the circumference of the wire.

Before we present our results, we comment on the role of the spin depth in the present analysis. Our point is that it differs qualitatively for nanowires from the case of the thin film. First of all, in a conducting magnetic medium, the skin depth is influenced not only by the conductivity of the material, but by its magnetization as well. To good approximation [9], in place of the classical skin depth $\delta_0 = c/(2\pi\omega\sigma)^{1/2}$, penetration of microwave fields is controlled by $\delta_M = c/(2\pi\omega\sigma\mu_V)^{1/2}$, where $\mu_V = (\mu_1^2 - \mu_2^2)/\mu_1$ is the Voigt susceptibility. Here $\mu_1 = 1 + 4\pi\chi_1$, and $\mu_2 = 4\pi\chi_2$, with χ_1 and χ_2 the dynamic susceptibilities defined in Eqs. (2.2). For the picture used here in section II(a), one has $\mu_V = (B_0^2 - \Omega^2)/(H_0B_0 - \Omega^2)$.

Now if we wish to consider the ferromagnetic resonance response of thin films, note that their resonance frequency is $(H_0B_0)^{1/2}$. At precisely this frequency, the Voigt susceptibility diverges, if we examine the simple expression above. A consequence is the skin depth collapses to zero. Of course, dissipative effects not included in the simple expression just given limit the divergence, but it is the case that the skin depth collapses to a small value, as one scans through resonance. In a high quality ferromagnetic metal such as Fe, the effective skin depth on resonance can be as small as 500 Angstroms, in the 10 GHz frequency range. The very strong frequency dependence of the skin depth as one scans through resonance means it is essential to include its role, in the discussion of microwave response of thin, conducting ferromagnetic films. In ref. [9], and earlier references cited therein, one sees strong influences of the frequency dependence of the skin depth, including the "window" near B_0 where the skin depth becomes very large.

In the ferromagnetic nanowires, we are concerned with much higher frequencies, near $H_0 + 2\pi M_S$, where there is no particular resonance or strong frequency dependence in the Voigt susceptibility. The penetration depth of the fields differs only nominally for that expected in the absence of the magnetic response. Thus, for nanowires with radius small compared to the classical skin depth, their finite, metallic conductivity has at most a modest influence on their response.

Further comments along these lines are of interest. To return to the case of the thin metallic film, if the film has thickness small compared to the renormalized skin depth on resonance, a situation encountered commonly in the study of the FMR of ultrathin films, one might suppose that within the film, the microwave exciting field is uniform to excellent approximation. This is not the case, if the film is illuminated by a microwave field incident from one side. In such a case, it is an elementary matter to see that within the film, if its thickness d is thin compared to the skin depth, and also the skin depth is thin compared to a vacuum wavelength, the spatial variation $h(z)$ of the microwave magnetic field

within the films is well approximated by, with $k_0 = \Omega/c$,

$$h(z) = 2h_0 \frac{(1 - z/d) + k_0 \delta_M^2 / 2d}{1 + k_0 \delta_M^2 / d}. \quad (2.37)$$

Thus, even if the film is very thin compared to the skin depth, the field drops linearly from a value very close to $2h_0$ at the surface exposed to the microwaves, to $h_0 k_0 \delta_M^2 / d$ at the back surface; the field is highly non uniform within the film, until one reaches thicknesses where $k_0 \delta_M^2 / d$ is of order unity.

The physical origin of the highly non uniform magnetic field distribution within a film illuminated from one side, even though its thickness may be small compared to the skin depth, is the poor impedance mismatch between the electromagnetic disturbance within the film, and the transmitted wave on the output surface. The magnetic field thus drops from a value roughly twice that of the incident field on the illuminated surface, to a very small value on the backside of the film. Quite in contrast to this, our conducting nanowire is embedded in a spatially uniform magnetic field, so the profile within the wire is not influenced by such considerations. If the wire radius is small compared to the classical skin depth, the exciting field the wire will be rather uniform in character.

We now present a summary of our studies of the microwave response. The principal conclusions can be summarized quite briefly.

First of all, we have seen that the nanowire admits a rich spectrum of exchange dipole modes in the vicinity of $k = 0$ for the modes with azimuthal quantum number $m = 1$. We have modes both above and below that of the ferromagnetic resonance frequency, for nanowire diameters in the range of a few hundred Angstroms or more. However, if we assume that the surface anisotropy K_S vanishes, then the only mode we see in the calculated spectrum is the main ferromagnetic resonance mode itself. We have searched even for weak structures from exchange/dipole modes removed from the main FMR mode, to find no evidence of absorption features. It is very much as if there is a hidden theorem we have not been able to prove analytically which forbids all modes other than the FMR mode to be active in microwave excitation when $K_S = 0$. It is well known that in the elementary Heisenberg ferromagnet, the standing spin wave resonances are "silent" in the absence of surface spin pinning produced by surface anisotropy, in the limit the microwave exciting field may be viewed as uniform within the film. We were surprised to see the complete absence of all modes except the main FMR mode in our numerical studies of the ideal nanowire, with surface anisotropy absent. In our minds, the existence of a selection rule is not obvious.

We illustrate these remarks in Fig. 5, which shows a portion of the low field wing of the main FMR line of a Ni nanowire 1000 Angstroms in diameter. We have assumed the frequency is 34.4 GHz, as utilized in ref. [1]. Thus, the resonance field is a bit above 8kG, for our parameters. In Fig. 5(a), we show a region of the low frequency wing, calculated for the case where surface anisotropy is absent. One can perceive no structure whatsoever from exchange/dipole modes. Yet modes exist in this field regime, and illustrated in the inset, where we plot

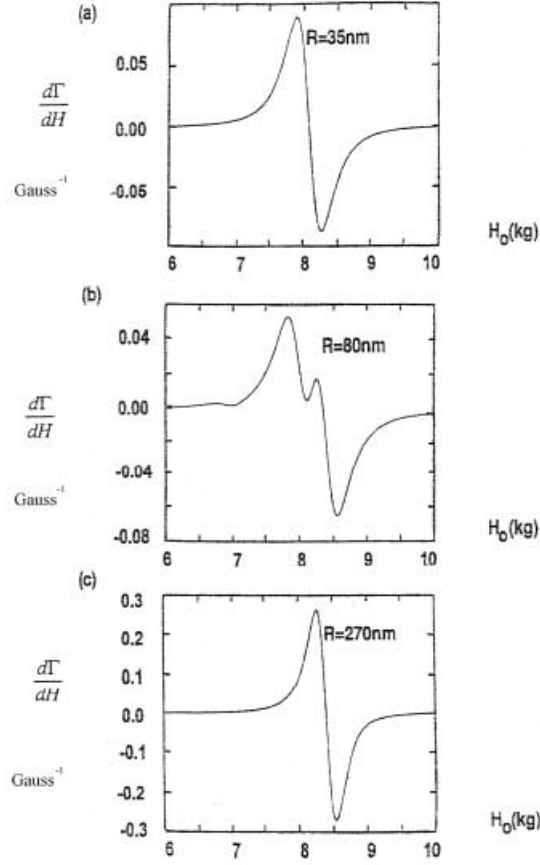


Fig. 5. We illustrate the role of surface anisotropy in activating the standing wave exchange/dipole satellite modes in the ferromagnetic resonance spectrum of the nanowire. The calculations are for a Ni nanowire with radius 1000 Angstroms, and focus on the low field wing of the absorption line. We calculate the derivative with respect to DC field of the ratio Γ defined in the text for (a) the case where the surface anisotropy is zero, and (b) where $K_S = -0.3 \text{ ergs/cm}^2$. The two insets show the inverse of the determinant of the matrix that must be inverted to solve for the magnetization amplitude. The peaks are the positions of the spin wave normal modes. We have used the rather small value $G = .5 \times 10^8 \text{ sec}^{-1}$ for the Gilbert damping function, to enhance the satellite features.

the inverse of the determinant that must be evaluated to find the various field amplitudes in section II(b). This determinant has a peak at the field where an exchange dipole mode occurs.

If surface anisotropy is introduced, then the exchange dipole modes "light up" as illustrated in Fig. 5(b). The results displayed here are for the choice $K_S = -0.3 \text{ ergs/cm}^2$, which is a substantial value of the surface anisotropy. Spin

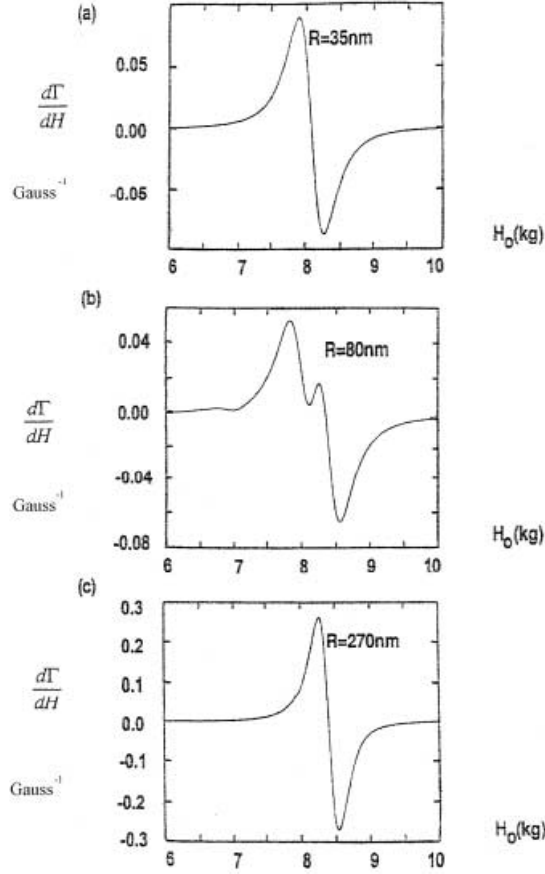


Fig. 6. For three values of the radius of Ni nanowires, (a) 350 Angstroms, (b) 800 Angstroms, and (c) 2700 Angstroms, we show calculated ferromagnetic resonance spectra. The calculations employ $G = 2.5 \times 10^8 \text{ sec}^{-1}$ which is a realistic value for Ni, and we have taken $K_S = -0.85 \text{ ergs/cm}^2$.

pinning to this degree may be realized at the surface if, for example, an oxide layer is present. The principal satellite at the higher field has an intensity of about 1% of that of the main FMR line.

In situations where the nanowire radius is such that an exchange/dipole mode lies quite close in frequency to the FMR mode, the mixing of the two by the boundary conditions can endow the satellite with appreciable integrated strength. This is illustrated in spectra taken by Ebels and Wigen [1]. These authors explore the FMR spectra of Ni nanowires with radius 350, 800, 2700 and 5000 Angstroms. With the exception of the 800 Angstrom sample, a single absorption line is observed. However, for the 800 Angstrom sample, there is a clear doublet. In Fig. 6, we show calculations of the spectrum for three of the

sample radii, and indeed we find a doublet very similar in character to that observed. The relative oscillator strength of the two modes is given nicely, when theory is compared to experiment. Not displayed is the calculation for the 5000 Angstrom case, which also shows a single feature as in the data. The calculations in Fig. (6) use $K_S = -0.85 \text{ ergs/cm}^2$, corresponding to a hard axis normal to the nanowire surface. This is again a large value of the surface anisotropy, appropriate to a case where oxide is present on the surface.

4 Concluding Remarks

We have developed the theory of the exchange/dipole spin wave modes of ferromagnetic nanowires of circular cross section, along with that of their response to spatially uniform microwave exciting fields. We also have presented studies of both the excitations in and the microwave response of samples quite similar to those explored in ref. [1], and compared the differences between the wire and the well know case of the thin film. We conclude with some additional remarks.

The origin of the linewidth in such samples is of interest. Of course, there is the intrinsic linewidth, described in our phenomenology by the damping term in the Landau Lifshitz equation of motion. In addition, there will be extrinsic mechanisms operative as well. For the case of ultrathin ferromagnetic films, in recent work we have shown [6] that the two magnon mechanism considered many years ago as the source of extrinsic linewidth in the garnets [9] can operate in the ultrathin films as well, by virtue of the fact that in two dimensions, the long ranged dipolar interaction in combination with exchange produces an off center minimum in the spin wave dispersion relation, for a range of propagation directions. This leads to spin wave modes of finite, non-zero wave vector degenerate with the zero wave vector FMR mode. Surface defects (or defects of any other sort) may then scatter energy from the FMR mode to the finite wave vector modes, producing a dephasing contribution to the linewidth. Our predictions seem confirmed by recent experiments [7]. One can inquire if the two magnon mechanism is operative in nanowires as well.

In principle, this mechanism should be operative. First suppose we have a nanowire with undulating surfaces of such character that the wire is still form invariant under rotations about the z axis. Then from symmetry considerations, there will be a non-zero matrix element for scattering energy from the zero wave vector FMR mode of $m = 1$ character, to $m = 1$ modes of finite wave vector on the FMR branch which are degenerate with the FMR mode. We see when Eq. (2.6a) is supplemented by an exchange term that scales as Dk^2 , there is always a minimum in the dispersion relation of $m = 1$ spin waves away from zero wave vector, and thus there always will be finite wave vector modes degenerate with the FMR mode. However, when $R < R_C = (D/\pi M_S)^{1/2}$, from the structure of the dispersion curve the minimum will lie quite near zero wave vector, and the number of degenerate modes will be rather small. When $R > R_C$, the minimum will be in the vicinity of $k = 1/R$, and we expect the mechanism to be more

efficient. For Ni, R_C is roughly 100 Angstroms, and for Fe, perhaps a factor of two shorter.

If the surface has, say, roughness of random character, so that azimuthal symmetry is no longer present, then the matrix element for scattering energy from the $m = 1$ FMR mode to modes with $m > 1$ is non-zero. The criterion $R > R_C$ remains relevant, in that it is for these larger radii that the dispersion relation for the $m > 1$ magnetostatic modes (those which approach the FMR frequency as the wave vector vanishes) has an off center minimum. Also, this is a crude criterion for the appearance of zero wave vector modes below the FMR frequency of the cylinder, which is another source of finite wave vector modes degenerate with the FMR mode.

The above discussion suggests that the two magnon mechanism should be relatively inefficient in very small radius nanowires with $R < R_C$, but for larger nanowires we suggest it should be quite efficient. A detailed theory, beyond the scope of the present paper, will be required to explore this question further.

Another aspect of the geometry considered here is the large microwave magnetic field created outside the wire, by the precession of the magnetization. We see from Eq.(2.18) that for a spin wave with finite wave k , we have a field that falls off as $\exp(-\kappa\rho)/\rho^{\frac{1}{2}}$ far from the wire. For long wavelength modes, this field has a very long range. In the limit of zero wave vector, we see from Eqs.(2.36) that the field created by the precession of the magnetization falls off inversely with the square of the distance from the center of the wire. The existence of this large field outside the nanowire is a substantial difference that the situation with thin films. If, for the thin film, we consider the uniform precession mode excited in an FMR experiment, the macroscopic magnetic field created by precession of the magnetization is completely confined to within the film. There are "magnetic poles" on the film surfaces associated with the precessing magnetization, but the field generated by these is confined to within the film itself, as in a condenser plate problem. If we consider a spin wave whose wave vector parallel to the film surfaces is k , there is a macroscopic field outside with the spatial variation $\exp(-kz)$ if the film surfaces are parallel to the xy plane, but the prefactor which controls the strength of this field scales as $4\pi M_S(kd)$, where d is the film thickness. This field is thus very weak in the thin film limit, or whenever the wavelength of the spin wave is large compared to the film thickness.

The existence of these large fields outside the nanowire have interesting implication for samples such as those explored by the authors of ref. [1]. We have long ranged interactions between the nanowires, so one is led to explore the collective excitations of the nanowire array. In the particular case of the samples used by Ebels and Wigen, the nanowires are accurately parallel to each other, but randomly arrayed over a plane. We thus have a random 2D system with long ranged interactions. Indeed, if one were to excite spin waves of variable wavelength k , as in a light scattering experiment, then the ratio of the average interwire separation to the range of interaction can be varied. There is an analogy between this system, and the vortex glass state of 2D superconductors, where here the average vortex separation can be varied, but the range of the

interaction if fixed as the London penetration depth. In the case of nanowire arrays, the nature of their collective excitations will be a most interesting topic, for ordered and disordered arrays.

Acknowledgments

This research was stimulated by conversations with Dr. Ursula Ebels, and Prof. P. E. Wigen. Support was provided by the U. S. Army Research Office (Durham), under Contract No. CS0001028.

References

1. U. Ebels and P. E. Wigen (to be published).
2. See the discussion that begins on p. 348 of the chapter by L. R. Walker, in *Magnetism*, Vol. 1, edited by G. Rado and H. Suhl (Academic Press, N.Y., 1963).
3. B. C. Fletcher and C. Kittel, *Phys. Rev.* **120**, 2004(1960).
4. Lai Wu-Yan, Wang Ding-Sheng, and Pu Fu-Cho, *Acta. Phys. Sinica*, **26**, 285 (1977).
5. R. P. Erickson and D. L. Mills, *Phys. Rev.* **B43**, 10715(1991).
6. Rodrigo Arias and D. L. Mills, *Phys. Rev.* **B60**, 7395(1999).
7. A. Azevedo, A. B. Olivera, F. M. de Aguiar, and S. M. Rezende, *Phys. Rev.* **B62**, 5331 (2000).
8. S.O. Demokritov and B. Hillebrands, *J. Magn. Mat.* **200**, 706 (1999).
9. For a recent discussion of this effect, and its influence on the response characteristics of device structures, see R. E. Camley and D. L. Mills, *J. Appl. Phys.* **82**, 3082(1997).

Transmission of Electron Beams Through Thin Magnetic Films

W. Weber, S. Riesen, and H.C. Siegmann

Laboratorium für Festkörperphysik, ETH Zürich, CH-8093 Zürich, Switzerland

Abstract. Electrons with the spin polarization vector perpendicular to the magnetization are spin analyzed after transmission through ferromagnetic layers. Due to the exchange energy and the inelastic spin-dependent scattering in the ferromagnet, two types of motion of the spin polarization vector occur: a precession around the magnetization and a rotation towards it. This spin motion is measured as a function of the thickness of the ferromagnetic film and of the electron energy for Fe, Co, and Ni. It is shown how the torque generated on the magnetization by the injection of picosecond pulses of spin-polarized electrons is sufficient to induce precessional magnetization reversal in nanosized magnetic samples. Spin injection establishes a new concept of writing magnetic bits which is extremely fast and requires far less energy compared to the conventional recording employing miniature electromagnets.

1 Introduction

If an electron beam traverses a ferromagnetic material, there is spin-dependent scattering as well as exchange interaction between the electrons in the beam and the electrons establishing the magnetization. In both processes, angular momentum may be transferred from the beam to the magnetization leading to excitations of the magnetization [1,2,3]. By injecting currents of high density through nanocontacts, these excitations have been observed via the occurrence of spin waves, permanent changes of the micromagnetic structure, or even a reversal of the magnetization direction [4,5,6,7,8]. All of these phenomena may occur together, and additionally, there may also be an effect of the magnetic field surrounding the injected beam of electrons. Hence it is difficult if not impossible to understand and interpret most of the current experiments in terms of specific elementary processes. It is the purpose here to show that the torque acting on the magnetization by the injection of spin-polarized electrons can be determined experimentally without any further assumptions. This torque is surprisingly large and may be used to induce precessional magnetization reversal at minimal energy cost, leading to a new concept of writing magnetic bits in nanosized ferromagnetic materials.

What is actually observed in this work is the spin motion of electrons travelling through a thin ferromagnetic layer. The spin polarization vector of both the incident and the outgoing electron beam is measured in our experiment. We observe a precession of the spin polarization about the magnetization direction. From this, the torque acting on the injected electrons by the magnetization \mathbf{M} is

determined. By virtue of Newtons *actio = reactio*, the same torque is also exercised in turn by the spin-polarized electrons on \mathbf{M} . We will show that this torque leads to significant precession of \mathbf{M} at experimental current densities. With beam radii below 100 nm this exchange-induced precession is larger compared to the precession induced by the circular magnetic field of the injected current. Therefore, precessional magnetization reversal by injection of spin-polarized electrons is the method of choice for reversing \mathbf{M} in magnetic bits such as used in magnetic random access memories for instance. In fact, we are proposing to technologically exploit the huge exchange fields present in ferromagnetic materials to switch the magnetization. It turns out that this concept may be applied to many magnetic materials because there is no significant difference in the exchange field per Bohr magneton in the elemental 3d ferromagnets Fe, Co, and Ni.

2 Theoretical Background

2.1 Spin Motion of the Electron Beam

When the interaction of spin-polarized electrons with a ferromagnetic material was investigated in the past, the spin polarization vector \mathbf{P}_0 of the incident electron current was mostly oriented parallel or antiparallel to the magnetization \mathbf{M} (in this paper the direction of \mathbf{M} is defined as the direction of the majority spin); a configuration, in which a motion of the spin polarization vector cannot be observed. However, in order to fully understand the transmission of spin-polarized electrons through a ferromagnet it is important to observe the motion of the spin polarization vector as well. For this purpose electrons with \mathbf{P}_0 perpendicular to \mathbf{M} are spin-analyzed after transmission through a ferromagnetic film.

A general spin state of an electron is described by the wave function

$$\psi = c_1 \xi_1 + c_2 \xi_2 ,$$

in which ξ_1 and ξ_2 are two orthogonal wave functions corresponding to the two opposite spin orientations of the ferromagnet; c_1 and c_2 are complex numbers. For an ensemble of electrons the spin polarization vector \mathbf{P} is given by the expectation values of the Pauli matrices σ_i ($i = x, y, z$):

$$\mathbf{P} = \begin{pmatrix} \langle \sigma_x \rangle_\psi \\ \langle \sigma_y \rangle_\psi \\ \langle \sigma_z \rangle_\psi \end{pmatrix} .$$

We now consider a completely polarized electron beam propagating along the x -axis through a ferromagnetic material that is magnetized along the z -axis. As we can restrict our discussion to nonrelativistic electrons, the relative orientation of \mathbf{P}_0 with respect to the propagation direction is actually of no importance, yet we choose the initial spin polarization \mathbf{P}_0 along the direction of propagation, i.e. parallel to the x -axis. The incident spin wave function, which in this particular case is an eigenstate of the σ_x operator, is represented by a

coherent superposition of a majority-spin wave function $\xi_1 = \begin{pmatrix} 1 \\ 0 \end{pmatrix}$ (spin parallel to \mathbf{M}) and a minority-spin wave function $\xi_2 = \begin{pmatrix} 0 \\ 1 \end{pmatrix}$ (spin antiparallel to \mathbf{M}):

$$\psi_0 = \frac{1}{\sqrt{2}} (\xi_1 + \xi_2) = \frac{1}{\sqrt{2}} \begin{pmatrix} 1 \\ 1 \end{pmatrix}.$$

Then a phase difference ϵ between the two spin functions develops as well as a spin-dependent attenuation of the amplitudes, while the electrons spend a time t within the ferromagnet. Therefore, the spin wave function representing the electrons leaving the ferromagnet is [9]:

$$\psi = \frac{1}{\sqrt{2}} \left(\sqrt{1+A} \cdot e^{-i\epsilon/2} \cdot \xi_1 + \sqrt{1-A} \cdot e^{+i\epsilon/2} \cdot \xi_2 \right)$$

with the intensity asymmetry $A = (I^+ - I^-)/(I^+ + I^-)$, which is measured by measuring the transmitted current with \mathbf{P}_0 parallel to \mathbf{M} (I^+) and antiparallel to \mathbf{M} (I^-) [9]. Hence, the spin polarization vector of the transmitted electrons is:

$$\mathbf{P} = \begin{pmatrix} \sqrt{1-A^2} \cos \epsilon \\ \sqrt{1-A^2} \sin \epsilon \\ A \end{pmatrix}.$$

This corresponds to a decrease of the angle ϑ enclosed by \mathbf{P} and \mathbf{M} and to a precession of \mathbf{P} around \mathbf{M} by an angle ϵ (see Fig. 1). The angle ϑ is calculated from the intensity asymmetry A :

$$\vartheta = \arctan \left(\frac{\sqrt{1-A^2}}{A} \right) \quad (1)$$

and thus its changes are caused by the spin-dependent scattering in the ferromagnet. Because the minority-spin component of the spin wave function is preferentially attenuated, ϑ decreases with t and the spin polarization vector rotates into the direction of \mathbf{M} . The precession angle ϵ , on the other hand, is determined by the difference $\Delta E_{ex} = E_2 - E_1$ between the energies of the minority-spin (E_2) and the majority-spin function (E_1), the so-called exchange energy. ϵ increases with t according to $\epsilon = \Delta E_{ex} \cdot t/\hbar$ (\hbar : Planck constant). Neglecting quantum resonance effects t is simply given by $t = d/v$ [10], with d the thickness of the ferromagnetic film and v the group velocity of the electrons [11]. The precession angle ϵ is thus given by [12]

$$\epsilon = \frac{\Delta E_{ex} \cdot d}{\hbar \cdot v}. \quad (2)$$

The specific precession angle $\tilde{\epsilon}$ is the precession angle per unit film thickness. This yields $\epsilon = \tilde{\epsilon} \cdot d$.

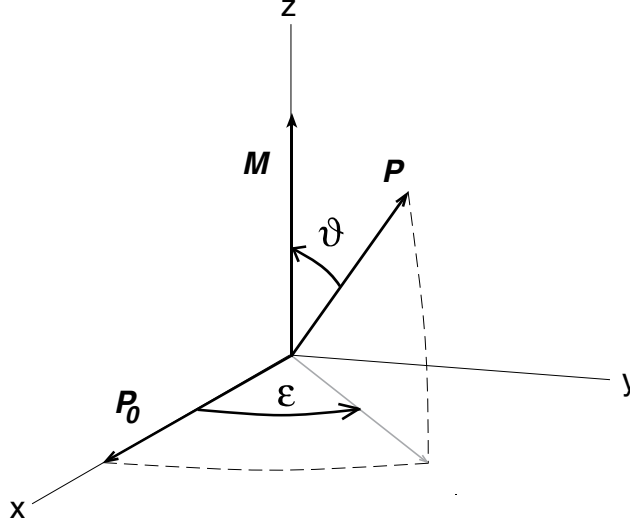


Fig. 1. Schematic drawing of the two types of movement of the spin polarization vector for $|P_0| = 1$ (pure spin state). Due to the difference in the amplitude of the majority-spin and the minority-spin wave function, the spin polarization vector rotates towards the sample magnetization \mathbf{M} , i.e., the angle ϑ decreases. The difference in the phase factors, on the other hand, causes the spin polarization vector to precess around \mathbf{M} by an angle of ϵ

The case of an incompletely spin-polarized electron beam ($|P_0| < 1$) is treated with the density matrix [13]. The spin polarization vector of the transmitted electrons is then given by

$$\mathbf{P} = \begin{pmatrix} P_0 \sqrt{1 - A^2} \cos \epsilon \\ P_0 \sqrt{1 - A^2} \sin \epsilon \\ A \end{pmatrix} \quad (3)$$

where \mathbf{P}_0 is parallel to the x -axis.

2.2 The Torque Acting on the Magnetization by Spin Injection

In the mean field approximation, the magnetization \mathbf{M} of a ferromagnet produces a molecular field or Weiss field given by $\mathbf{W} = \alpha \mathbf{M}$ where α is the molecular field constant. The Weiss field is a function of both the electron energy and the linear momentum, and it is an axial field parallel to \mathbf{M} . \mathbf{W} exercises a torque $\boldsymbol{\tau}_e$ on any electron introduced into the ferromagnet with a component of its magnetic moment $\boldsymbol{\mu}_e$ perpendicular to \mathbf{M} . This torque is given by

$$\boldsymbol{\tau}_e = \boldsymbol{\mu}_e \times \mathbf{W} = -(g\mu_B/\hbar) \mathbf{s} \times \mathbf{W}$$

with g the gyromagnetic factor, which is assumed in the following to be exactly 2 as reasonable for nonrelativistic electrons, μ_B the Bohr magneton and \mathbf{s} the injected electron spin. $\boldsymbol{\tau}_e$ leads to precession of \mathbf{s} around \mathbf{W} with a frequency $\omega_e = (e/m)W$ (e : elementary charge, m : mass of electron). Such spin or Larmor precession occurs also when a regular magnetic field is applied. However, \mathbf{W} is by no means equivalent to a magnetic field as it produces no Lorentz force on the electrons, and as its changes with time do not induce eddy currents. It is precisely this difference to a magnetic field and the huge magnitude of W encountered in the 3d ferromagnets that make the technological application of the Weiss field extremely interesting.

Once an electron has crossed the surface barrier potential and is inside the ferromagnet, we have a closed system with no external forces. Hence the total angular momentum \mathbf{L} consisting of the angular momentum of the magnetization and the one of the injected spins must be conserved by virtue of Newtons *actio* = *reactio*, i.e., the total torque $\mathbf{T} = d\mathbf{L}/dt = 0$. Therefore

$$\mathbf{T}_e + \mathbf{T}_M = 0$$

where \mathbf{T}_e is the torque acting on the ensemble of injected spin-polarized electrons and \mathbf{T}_M is the torque exercised in turn on the magnetization. Consequently, by determining experimentally \mathbf{T}_e , we have also measured \mathbf{T}_M . From \mathbf{T}_M , we can then calculate the precession frequency ω_M of the magnetization, and determine the conditions for precessional magnetization reversal. It turns out, that writing bits in magnetic recording by injection of spin-polarized electrons is much simpler and consumes many orders of magnitude less energy compared to traditional magnetic recording in which the electrons have to move through a coil producing a regular magnetic field.

What is observed experimentally in the experiments is the angle ϵ by which the spin polarization vector of the ensemble of injected electrons has precessed on traversing the ferromagnetic film of thickness d without losing energy. According to the discussion in the preceding chapter a linear thickness dependence of the precession angle is expected: $\epsilon(d) = \tilde{\epsilon} \cdot d$. This is indeed observed as shown later in paragraph 4. With the precession frequency $\omega_e = \tilde{\epsilon} \cdot v$ and the current density $j = n_e \cdot e \cdot v$ of the injected electrons where n_e is the electron density, the torque (per unit volume) acting on the injected spins is $T_e = |\boldsymbol{\omega}_e \times \mathbf{L}_e| = P_0 \cdot n_e \cdot \omega_e \cdot (\hbar/2) \cdot \sin \vartheta = (\hbar/2e) \cdot P_0 \cdot j \cdot \tilde{\epsilon} \cdot \sin \vartheta$. All quantities determining T_e are thus determined by the experiment without any further assumptions. On the other hand, the torque (per unit volume) acting on the magnetization is $T_M = |\boldsymbol{\omega}_M \times \mathbf{L}_M| = \omega_M \cdot L_M \cdot \sin \vartheta$. With $T_M = T_e$, the precession frequency of \mathbf{M} is then obtained from:

$$\omega_M = \frac{P_0 \cdot j \cdot \tilde{\epsilon}}{e \cdot n_M \cdot n_B} \quad (4)$$

where n_B is the number of Bohr magnetons per atom and n_M the density of the atoms in the ferromagnet. For simplicity, we have neglected the orbital contribution to the magnetization by putting the angular momentum (per unit volume)

$L_M = n_B \cdot n_M \cdot \hbar/2$. Again, all quantities entering eq. (4) can be measured directly.

The spin polarization vector \mathbf{P} relaxes into the direction of \mathbf{M} . This relaxation is characterized by the spin asymmetry A of the absorption of electrons in the ferromagnet as discussed in the preceding chapter. The relaxation generates a component P_{\parallel} of the spin polarization vector parallel to \mathbf{M} . There is no torque generated in this process. But as P_{\parallel} increases, M must decrease to conserve the magnitude of the total angular momentum. The subsequent re-installment of the magnitude of M to its thermodynamic equilibrium involves localized and travelling spin waves and is not considered here. It is these spin waves that are commonly observed in the experiments. Note that they occur also with an initially unpolarized injected electron beam, as opposed to the spin waves excited by the precession of \mathbf{M} .

The axis of precession of \mathbf{M} also changes direction in space as the injected electrons travel through the ferromagnet. This arises, because the torque $\mathbf{T}_e = -\mathbf{T}_M$ is always perpendicular to \mathbf{M} and \mathbf{P} , hence the axis of precession changes direction with the precession of \mathbf{P} . Yet, to use the torque \mathbf{T}_M for precessional magnetization reversal, there has to be a preferred direction in the crystal lattice about which the magnetization must precess. This can be achieved by making the ferromagnetic film thin compared to the pathlength on which \mathbf{P} precesses by π . The experiments described in paragraph 4 show that the precession of \mathbf{P} may be neglected altogether even in the most critical case of Fe if the ferromagnetic film is 1 nm thick.

3 Experiment

3.1 Experimental Setup

In order to investigate the spin motion of electrons upon transmission across ferromagnets, a “complete” spin-polarized electron scattering experiment must be set up. The experiment is sketched in Fig. 2. An electron source of the GaAs-type produces a spin-polarized electron beam with a degree of spin polarization $|\mathbf{P}_0| = 25\%$ by means of optical pumping with circularly polarized light (wavelength: 785 nm). By switching from right- to left-circularly polarized light for excitation of the photoelectrons, we can invert the spin polarization vector \mathbf{P}_0 . It is also possible to produce an unpolarized electron beam by using linearly polarized light. By applying a combination of electric and magnetic fields to the electron beam, \mathbf{P}_0 can be rotated into any desired direction in space. For this purpose two solenoids are used, one to rotate the spin polarization around the x -axis and the other one to rotate it around the y -axis. The electron beam impinges normally onto a ferromagnetic film of varying thickness sandwiched between Au layers, which serve both as support and protection layers. The transmitted electrons are energy analyzed by a retarding field with an energy resolution of 0.5 eV (FWHM). The electrons are subsequently accelerated to an energy of 100 keV to determine the components of the spin polarization vector perpendicular to the x -axis, which is the propagation direction of the electrons, via Mott scattering.

Since the x -component of the spin polarization vector cannot be measured with our set-up, the determination of the precession angle ϵ is made in the following way. In a first experiment the spin polarization \mathbf{P}_0 of the incident electrons is rotated until $P_{0y} = P_{0z} = 0$. Consequently, \mathbf{P}_0 must be aligned parallel to the x -axis. The spin polarization $\mathbf{P}(\mathbf{P}_0||x)$ of the transmitted electrons is then given by eq. (3). In a second experiment \mathbf{P}_0 is aligned parallel to the y -axis, resulting in

$$\mathbf{P}(\mathbf{P}_0||y) = \begin{pmatrix} -P_0\sqrt{1-A^2}\sin\epsilon \\ P_0\sqrt{1-A^2}\cos\epsilon \\ A \end{pmatrix}.$$

Thus, the angle of precession ϵ is obtained by measuring P_y with \mathbf{P}_0 parallel to the x -axis and parallel to the y -axis:

$$\epsilon = \arctan\left(\frac{P_y(\mathbf{P}_0||x)}{P_y(\mathbf{P}_0||y)}\right).$$

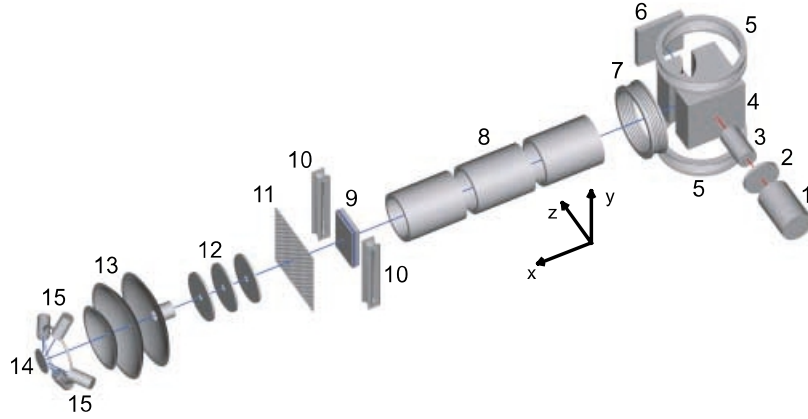


Fig. 2. Scheme of the experiment. 1: Laser; 2: Polarizer; 3: Pockels cell (to change helicity of the circularly polarized light); 4: Electrostatic 90°-deflector; 5: Solenoids (to rotate \mathbf{P}_0 around the y -axis); 6: GaAs crystal; 7: Solenoid (to rotate \mathbf{P}_0 around the x -axis); 8: Transfer electron optics; 9: Sample; 10: Solenoids (to remanently magnetize the sample along the z -axis); 11: Retarding field grid (as energy analyzer); 12: Transfer electron optics; 13-15: Spin detector (13: Accelerator; 14: Au-foil (for Mott scattering); 15: Detectors)

It is important to note that in our set-up, where electrons impinge normally onto the film and are collected within a symmetric cone of $\pm 5^\circ$ after transmission,

spin-orbit interaction in the heavy element Au cannot produce any additional spin polarization. This is proven by measuring the spin polarization of electrons which pass through a pure Au film. Figure 3 shows that the spin polarization of the elastic electrons is not altered on passing through the Au film. Secondary electrons, on the other hand, which have suffered collisions, have a lower spin polarization due to admixture of unpolarized electrons excited from below the Fermi energy of the nonmagnetic Au.

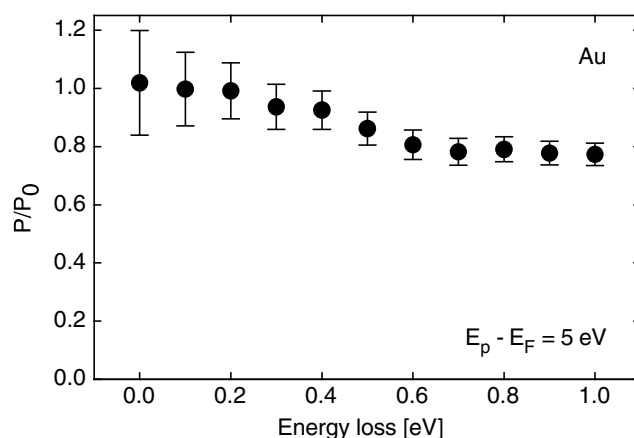


Fig. 3. The degree of relative spin polarization P/P_0 after the electron beam has traversed a pure Au-film is shown as a function of energy loss. P_0 is the degree of spin polarization delivered by the electron source. The primary energy E_p of the incident electron beam is 5 eV above the Fermi energy E_F

3.2 Samples

In order to study the transport of electrons through a ferromagnetic sample, a film must be prepared through which at least an observable portion of a spin-polarized electron beam can penetrate. Since electron-electron scattering produces inelastic mean free paths of the order of one nm or even less in transition metals [14], the film has to be extremely thin to observe the emerging electron beam. In fact, the experiment cannot be done with a self-supporting film of a transition metal. Rather, one has to make use of the fact that electron scattering is reduced in noble metals like Au. An Au-film of about 20 nm thickness as a substrate for the ferromagnetic transition metal attenuates low-energy electron beams by only $10^{-4} - 10^{-5}$ making it still possible to observe the transmitted electrons and to measure their spin polarization. Finally, the ferromagnetic Fe-, Co-, or Ni-films are capped with a protecting Au-layer of 2 nm thickness to prevent corrosion. The ferromagnetic films produced here are polycrystalline as probed by electron diffraction.

The trilayers are made in a separate UHV chamber on a substrate consisting of a film of nitrocellulose supported by a Si-wafer with a number of 0.5 mm wide apertures. All metals are deposited by electron beam bombardment (Au: 0.4 nm/min; Fe, Co, Ni: 0.2 nm/min). Their thicknesses are measured by a quartz microbalance, which was calibrated by profilometry. As magnetic in-situ characterization the magneto-optic Kerr effect is used. Along the easy direction of magnetization induced by the oblique incidence of the atom beam during deposition, the hysteresis loops exhibit full magnetic remanence in zero external field. After the magnetic tests are completed, the complete sample is let to air and the nitrocellulose on the apertures is removed by putting the sample into acetone. The sample is then introduced through a load-lock system into the chamber with the spin-polarized electron source. There, the sample is sputtered to thin the supporting Au-layer until low-energy electrons are transmitted at an attenuation of 10^{-5} – 10^{-6} . The Kerr hysteresis loops taken later show no obvious difference to the loops obtained just after deposition of the complete trilayers. If the supporting Au-layer is excessively thinned, the sandwiched magnetic film is attacked resulting in a reduction of the magnetization.

Of crucial importance for the transmission experiments is the preparation of pinhole-free self-supporting trilayers. The easiest method to check for the existence of pinholes is to investigate the energy dependence of the transmitted elastic intensity. For primary electron energies around 30 eV the inelastic mean free path in Au is smallest [15]. In this case, electrons cannot penetrate unless they loose energy. Hence pinholes are not present if elastic electrons of energy 30 eV are not observed. If there is the tiniest pinhole, the main part of the elastic signal observed at the backside of the trilayer is caused by electrons that have passed through the pinhole.

4 Experimental Results for Fe, Co and Ni

In fact, the precession of the electron spin polarization in the exchange field has been detected previously [9,12]. We now present comprehensive results for all three 3d elemental ferromagnets. Figure 4 shows the experimental precession angle ϵ for Fe-, Co-, and Ni-films of different thicknesses at a primary electron energy $E - E_F = 7$ eV. If and inasmuch the precession is a bulk property of the ferromagnets, we expect a linear increase of the precession angle ϵ with film thickness d according to eq. (2). We see that indeed a linear fit to the data describes the observations on all three ferromagnets very well, yielding their specific precession angle $\tilde{\epsilon}$ as the slope of the fit. However, the $\epsilon(d)$ -lines intercept $\epsilon = 0$ at film thicknesses $d_0 > 0$. The magneto-optic Kerr effect plotted vs. d on the same samples showed a nonzero intercept of similar magnitude. This means that the two interface regions of the ferromagnetic film with joint thickness d_0 do not contribute to the precession nor to the magnetization. Possible reasons for this include the absence or weakening of the magnetization by interdiffusion and/or roughness of the polycrystalline Au substrate. We will not discuss the reasons for the occurrence of d_0 in more depth as this paper is only concerned

with bulk effects. These are extracted by plotting the rate of increase of ϵ with increasing thickness d .

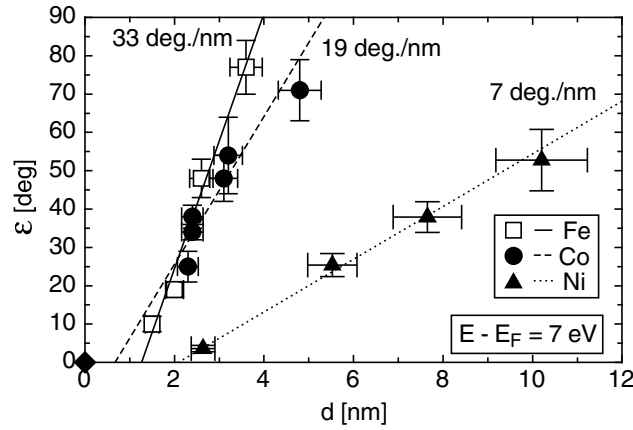


Fig. 4. The spin precession angle ϵ as a function of the ferromagnetic film thickness for Fe, Co, and Ni, measured with elastic electrons of energy $(E - E_F) = 7$ eV. The point at zero thickness was measured with a pure Au-film of 20 nm thickness. The straight lines through the data points represent linear fits. The values of the slope, i.e., the specific precession angle $\tilde{\epsilon}$, are summarized in tab. 1

The angle ϑ enclosed by \mathbf{P} and \mathbf{M} as it depends on film thickness d is shown in Fig. 5. For all three ferromagnets ϑ decreases with increasing film thickness, i.e., the spin polarization vector turns increasingly into the direction of \mathbf{M} with increasing thickness as expected. Following paragraph 2, this rotation of \mathbf{P} into \mathbf{M} is due to the spin-dependent absorption of electrons in the ferromagnetic metal, commonly called the spin-filter effect. It is evident that the strength of spin filtering in Fe and Co is quite similar, while spin filtering is much less effective in Ni. The curves through the data points represent fits on the basis of what is expected from a number of previous, quite different spin-filter experiments [14,16]. From the measurement of $\vartheta(d)$, $A(d)$ is obtained and vice versa, and knowing $A(d)$, one can also evaluate $\sigma^- - \sigma^+$, the difference in the electron absorption coefficient for minority and majority spins, respectively. These parameters are summarized in tab. 1. Like in the case of the linear fits to the $\epsilon(d)$ data in Fig. 4, the $\vartheta(d)$ curves intercept $\vartheta = \pi/2$ at $d_0 > 0$. In fact, the d_0 values representing the film thicknesses at which no spin-dependent absorption of electrons occurs are much the same as for the case of the absence of precession. This makes an interpretation of this phenomenon on the basis of reduced or absent magnetization in the interfaces most likely.

The energy dependence of ϵ for all three ferromagnets is shown in Fig. 6. In the case of Co and Ni, the variation of ϵ in the energy range of 5-14 eV above E_F is weak; ϵ decreases somewhat in agreement with $\epsilon = \Delta E \cdot t/\hbar$ due to the

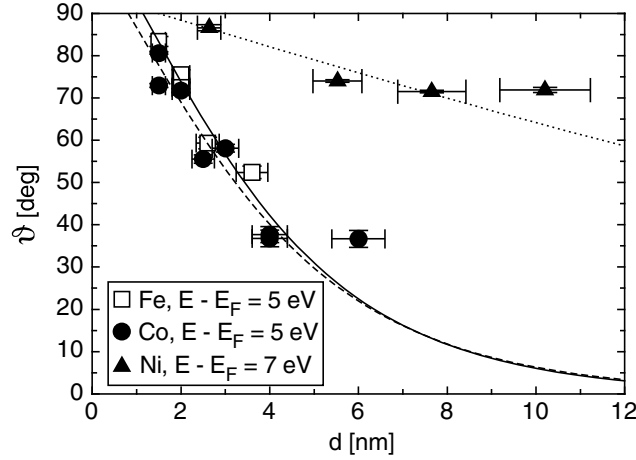


Fig. 5. The angle ϑ enclosed by \mathbf{P} and \mathbf{M} as a function of the ferromagnetic film thickness for Fe, Co, and Ni, measured with elastic electrons of energy $(E - E_F) = 5$ and 7 eV. We note that the values of the angle ϑ are normalized to $P_0 = 1$ (pure spin state). The curves through the data points represent fits which are based on results obtained in a number of different spin-filter experiments [14,16] (Fe: continuous line, Co: dashed line, Ni: dotted line). The values extracted from ϑ for the difference $\sigma^- - \sigma^+$ between the spin-dependent absorption coefficients are summarized in tab. 1

fact that the time t spent by the electrons within the ferromagnet decreases with $1/\sqrt{E}$ (assuming a free-electron behavior). Thus the exchange energy ΔE in the polycrystalline samples is quite constant extending to surprisingly high electron energies. This finding agrees with predictions from band structure calculations [17]. In the case of Fe, ϵ exhibits a much stronger dependence on electron energy with a maximum at 9 eV above E_F [18]. This agrees well with the band structure showing flattening of the bands at this energy and thus a decrease of the group velocity of the electrons [19].

In the case of Fe and Co we also investigated the spin precession at much higher energies (see insets in Fig. 6), where the larger inelastic mean free path in the Au support permits again transmission experiments. In both cases small but significant precession angles of a few degrees are found up to several 100 eV electron energy. One might ask if these nonvanishing values of ϵ are actually due to a nonvanishing exchange energy. Can the stray field of the ferromagnetic sample cause such small precession angles? It might. However, the direction of the stray field outside the ferromagnet is opposite to the magnetization direction and should therefore result in a negative value of ϵ , whereas positive values are found in the experiment.

Going back to eq. (2), we see that ϵ is proportional to $\Delta E_{ex}/v$. From the data we readily recognize that the increase of the group velocity (roughly by a factor of 3) by going from the low energy to the high energy regime, can only partly explain the observed reduction of ϵ . Thus, there must be a significant decrease of

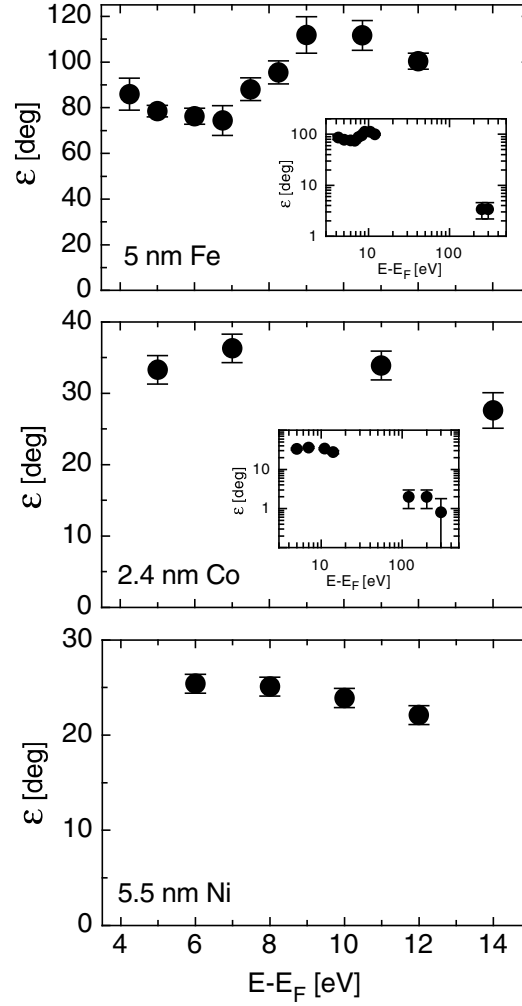


Fig. 6. The spin precession angle ϵ at constant film thickness as a function of the electron energy for Fe (top), Co (middle), and Ni (bottom). The insets show ϵ over a larger energy range. Note the double-logarithmic plot

the exchange energy with increasing energy as well. This is in accordance with calculations showing a decrease of ΔE_{ex} with increasing energy [20]. The higher the energy, the weaker the exchange interaction between the quasi-free injected electrons and the d-electrons below the Fermi level.

A similar precession of the electron-spin polarization has been proposed by Byrne and Farago [21] in electron-atom scattering and is caused by exchange scattering. According to [22] the precession angle due to exchange scattering ϵ_{ex}

Table 1. Parameters of the ferromagnets (FM) Fe, Co, and Ni. n_B : number of Bohr magnetons; $\tilde{\epsilon}$: specific precession angle; v : group velocity of the electrons at the energy $E - E_F = 7$ eV (see [11]); ω_e : Larmor precession frequency of the injected electron spins; W : Weiss field of the ferromagnet; ω_M : Larmor precession frequency of the magnetization; P_0 : initial degree of the spin polarization of the injected electrons; j : current density of the injected current; σ^- , σ^+ : absorption coefficient for minority-spin and majority-spin electrons, respectively [16]

FM	n_B	$\tilde{\epsilon}$ [deg./nm]	v [10^6 ms $^{-1}$]	ω_e [10^{14} s $^{-1}$]	W [T]	ω_M/P_0j [10^{-2} s $^{-1}$ /Am $^{-2}$]	$\sigma^- - \sigma^+$ [nm $^{-1}$]
Fe	2.2	33	2.5	14.4	8200	1.94	0.67
Co	1.7	19	2.5	8.3	4700	1.35	0.63
Ni	0.6	7	2.3	2.8	1600	1.40	0.11

is given by:

$$\tan \epsilon_{ex} = \frac{i(fg^* - f^*g)}{2|f|^2 - (fg^* + f^*g)}$$

with f the direct, g the exchange scattering amplitude (f^* and g^* are the corresponding complex conjugated quantities), and i the imaginary unit. If we can show that $g = 0$, an exchange induced contribution to the observed precession angle is excluded.

The test on the contribution of the elastic exchange of electrons consists of two parts:

1) An unpolarized electron beam passes through the ferromagnet. This produces a spin polarization P which consists of two parts:

$$P = P' + \Delta P.$$

P' is the transport polarization generated by spin-selective scattering into the holes of the d-band [14], while ΔP is the additional spin polarization generated by elastic exchange scattering.

2) An electron beam of initial polarization P_0 passes through the ferromagnet. The intensity asymmetry A (normalized to $P_0 = 1$) is given by:

$$A = A' - \Delta A$$

where A' is the asymmetry due to inelastic spin-selective absorption [9] and ΔA is the reduction of this asymmetry because some electrons have flipped their spin in elastic exchange collisions and thus avoided spin-dependent absorption. We find within the experimental uncertainty that $P = A$ (see Fig. 7) [18]. Since a polarizing spin filter must be equal to an analyzing spin filter in the absence of spin-productive scattering such as exchange scattering, i.e. $P' = A'$, both ΔP and ΔA must be zero. Thus, elastic exchange scattering is not important in this experiment.

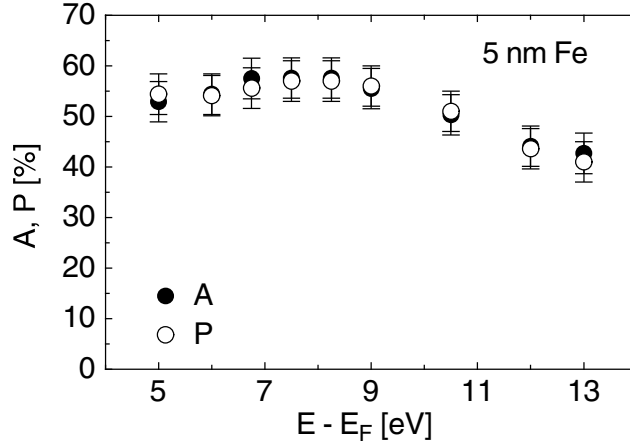


Fig. 7. The intensity asymmetry A (measured with a polarized incident electron beam and normalized to $P_0 = 1$) and the degree of spin polarization P (measured with an unpolarized incident electron beam) of elastic electrons are shown as a function of the primary electron energy [18]. This shows that the analyzing power of a ferromagnetic spin filter is equal to the polarizing power within the experimental uncertainty

5 Precessional Magnetization Reversal Induced by a Spin-Polarized Current

Very recently it was shown that ultrafast magnetic field pulses of a few picoseconds ($\hat{=} 10^{-12}$ s) duration and surprisingly small amplitudes are able to induce magnetization reversal in in-plane magnetized, uniaxial films [23]. Of crucial importance is the fact that the external magnetic field pulse \mathbf{B}_{ext} is applied in the plane of the film at a right angle to \mathbf{M} . In this way maximum torque is exerted on the magnetic moments of the ferromagnet and \mathbf{M} precesses around \mathbf{B}_{ext} out of the plane of the film. As \mathbf{M} leaves the plane of the film, the demagnetizing field comes into play. When the external magnetic field pulse is terminated, the demagnetizing field persists, and the precession of \mathbf{M} around the demagnetizing field (plus the anisotropy field) completes the reversal. Thus, in order to induce precessional magnetization reversal in in-plane magnetized films the magnetization must precess out of plane by a certain angle, which is determined by the demagnetizing field, the anisotropy field and the damping constant. Using typical values for these parameters [23] a precession angle $\epsilon_M \approx 20^\circ$ of the magnetization is needed.

Can a spin polarized current produce such a precession angle? To answer this question eq. (4) has to be considered. The values of the ratio $\omega_M/P_0 j$ are listed in tab. 1. Assuming an electron current which is completely spin polarized perpendicular to \mathbf{M} ($P_0 = 1$) and a current density of $j = 10^{13}$ Am⁻² we find that pulse durations $t_{pulse} = \epsilon_M/\omega_M$ of ~ 2 picoseconds are sufficient to trigger precessional magnetization reversal. Injection of such a pulse of spin-polarized

electrons is equivalent to applying a 2 picosecond magnetic field pulse of an amplitude of 1.1, 0.76, 0.79 T in Fe, Co, and Ni, respectively. Such field pulses have so far only been achieved with the 50 GeV electron bunches of the Stanford linear accelerator [24]. We emphasize that the choice of a smaller j and hence smaller ω_M can be compensated for by a larger t_{pulse} value, yet only as long as this latter value remains much smaller than the spin-lattice relaxation time, which lies in the realm of 100 picoseconds [25,26].

We note that even higher current densities of $5 \cdot 10^{13} \text{ Am}^{-2}$ have been realized in ballistic injection of electrons [27]. In the case of transport electrons ($E = E_F$) current densities of $0.75 \cdot 10^{13} \text{ Am}^{-2}$ have been reported [4]. Moreover, the exchange energy and hence $\tilde{\epsilon}$ is expected to be larger at E_F . However, the spin polarization P_0 of the injected electrons is not expected to be 1 with ferromagnets as emitters. In practice values of $P_0 = 0.3$ can be achieved routinely.

Up to now we have not considered the effect of the circular magnetic field that is always induced by an electric current. This is exactly the type of magnetic field which was used to show that precessional magnetization reversal with in-plane magnetized films is possible with ultrafast field pulses [23]. Therefore the question arises: How can we distinguish between precession induced by the Oersted field and the Weiss field? Actually, this distinction has been made easy as it has been shown recently that the precession of the magnetization may be imaged using ultrafast laser pulses and the magneto-optic Kerr effect [28]. The Oersted field changes sign across the electron beam and the precession of \mathbf{M} will therefore proceed in different directions at the beam edges, while the Weiss field always has the direction of the magnetization. A simple calculation proves that the precession due to the Weiss field is always faster compared to the one of the Oersted field as soon as one injects the current through a nanocontact. The maximum field strength B_{max} of a current flowing across a circular area with radius r is given by $B_{max} = \mu_0 \cdot j \cdot r/2$ (μ_0 : vacuum permeability) and induces a precessional motion of the magnetization with the frequency $\omega_{max} = (e/m)B_{max}$. Hence the Weiss field precession dominates over the precession induced by the Oersted field, if

$$\frac{\omega_{max}}{\omega_M} = \frac{\mu_0 \cdot e^2}{2m} \cdot \frac{n_M \cdot n_B \cdot r}{P_0 \cdot \tilde{\epsilon}} < 1.$$

Given the fact that $\tilde{\epsilon}/n_B$ as well as n_M is not varying much with the different 3d-ferromagnets this situation is realized if the radius r of the current carrying filament is smaller than 100 nm. Thus, in nanocontacts with $r < 100 \text{ nm}$, the Weiss field is always more effective for switching the magnetization than the Oersted field.

6 Further Experiments to Determine the Precession Angle

6.1 Transmission Measurements at Energies Below the Vacuum Level

In order to study spin precession at energies below the vacuum level down to the Fermi energy, measurements with free-electron beams are not anymore possible. In this case it is necessary to have the spin polarized electron source, the ferromagnetic film, and the spin analyzer in one solid. Such type of experiment has been proposed by L. Berger [29]. The proposed film system consists of three ferromagnetic layers which are separated by nonmagnetic metallic spacer layers. The first ferromagnetic film is used as spin-polarized electron source, the second one, in which the spin precession occurs, is magnetized perpendicular to the first one, and the third one serves as spin analyzer. Depending on the angle between the spin direction of the electrons leaving the second ferromagnet and the magnetization direction of the (analyzing) third ferromagnet, different resistances should be observed if a current is drawn across the film system. This would permit to measure the spin precession at the Fermi level. Measurements at energies above the Fermi energy, on the other hand, may become feasible by replacing the nonmagnetic metallic spacer by a nonmagnetic insulating material.

6.2 Measurements in Reflection Geometry

The most obvious modification of our transmission experiment can be done by changing from transmission to reflection geometry. This would be of advantage for the following reasons. Firstly, one would not further rely on self-supporting samples. The ferromagnetic films could be grown on any type of substrate. In particular, single crystalline films can be prepared, while the self-supporting films grown on the nitrocellulose are polycrystalline. Secondly and most importantly, there is no “intensity-problem” in the reflection geometry, because the electrons do not have to pass through a thick layer of Au or any other supporting material. Thus, the entire electron energy range can be investigated, whereas the intermediate energy range of 15 - 100 eV is not accessible with our present transmission geometry.

In contrast to the transmission experiment, where a linear relationship between ϵ and the thickness of the ferromagnetic film is found (see Fig. 4), ϵ will saturate at large thicknesses in the reflection experiment. This saturation value can easily be estimated by using the experimentally determined values of the specific precession angle $\tilde{\epsilon}$ in the transmission experiment (tab. 1) and of the inelastic mean free path λ [14]. For instance, in the case of Co (at $E - E_F = 7$ eV) we expect a saturation value of $\epsilon = \tilde{\epsilon} \cdot \lambda \approx 15^\circ$. This estimate, however, holds only as long as interface and surface effects are not considered. As shown in paragraph 4 interface effects can be significant, resulting in a nonzero d_0 value. At any rate, the reflection experiment will give insight into the behavior of the topmost atomic layers of a ferromagnet, and will thus represent a technique that is complementary to our present transmission experiment.

7 Conclusion

The transport of spin-polarized electrons through self-supporting ferromagnetic layers is investigated by means of a “complete” spin-polarized electron scattering experiment. In order to study the spin motion of electrons, the spin polarization vector of the incident free-electron beam is chosen perpendicular to the magnetization direction. A spin precession around the magnetization direction is found with all three elemental 3d ferromagnets. It is caused by different phase factors of the majority- and minority-spin wave functions, having their origin in the exchange energy of the ferromagnetic film. Because of angular momentum conservation the precession frequency of the sample magnetization can be inferred without further assumptions. Injecting pulses of spin-polarized electrons through nanocontacts at experimental current densities into ferromagnetic films of a few atomic layers thickness is equivalent to applying a magnetic field pulse of the order of 1 T. It can be foreseen that this is the method of choice for reversing the magnetization in magnetic bits by precessional magnetization reversal thus decreasing the energy and time needed to write information into a magnetic medium by many orders of magnitude.

Acknowledgment

We thank Jürg Fröhlich at ETH and Peter Farago at the University of Edinburgh for many illuminating discussions. We gratefully acknowledge financial support by the Swiss National Science Foundation.

References

1. J.C. Slonczewski, J. of Magn. Magn. Mater. **159**, L1 (1996)
2. L. Berger, Phys. Rev. B **54**, 9353 (1996)
3. Ya.B. Bazaliy, B.A. Jones, and Shou-Cheng Zhang, Phys. Rev. B **57**, R3213 (1998)
4. M. Tsoi, A.G.M. Jansen, J. Bass, W.-C. Chiang, M. Seck, V. Tsoi, and P. Wyder, Phys. Rev. Lett. **80**, 4281 (1998)
5. E.B. Myers, D.C. Ralph, J.A. Katine, R.N. Louie, and R.A. Buhrman, Science **285**, 867 (1999)
6. J.Z. Sun, J. of Magn. Magn. Mater. **202**, 157 (1999)
7. J.-E. Wegrowe, D. Kelly, Y. Jaccard, Ph. Guittienne, and J.-Ph. Ansermet, Europhys. Lett. **45**, 626 (1999)
8. M. Tsoi, A.G.M. Jansen, J. Bass, W.-C. Chiang, V. Tsoi, and P. Wyder, Nature **406**, 46 (2000)
9. D. Oberli, R. Burgermeister, S. Riesen, and H.C. Siegmann, Phys. Rev. Lett. **81**, 4228 (1998)
10. One understands that the time spent by the electrons within the ferromagnet is in general not simply given by d/v . One expects corrections at energies where the electrons can form quantum well states in the ferromagnetic film. However, this requires single crystalline samples of uniform thickness and could not be observed with the present polycrystalline films.

11. The group velocities of the electrons are determined by assuming free-electron behavior and taking literature values of the inner potential in Fe (14.5 eV, E. Tamura *et al.*, Solid State Comm. **55**, 543 (1985)), Co (16 eV, B.W. Lee *et al.*, Phys. Rev. B **17**, 1510 (1978)), and Ni (~ 12 eV, W.N. Unertl and M.B. Webb, Surf. Sci. **59**, 373 (1976))
12. W. Weber, D. Oberli, S. Riesen, and H.C. Siegmann, New J. of Phys. **1**, 9.1 (1999)
13. H.A. Tolhoek, Review of Modern Physics **28**, 277 (1956)
14. G. Schönhense and H.C. Siegmann, Ann. Physik **2**, 465 (1993)
15. O. Paul, Dissertation ETH Zürich No. 9210 (1990)
16. The intensity asymmetry $A(d)$ (normalized to $P_0 = 1$), which enters the expression for $\vartheta(d)$ (see eq. (1)), is given by $A(d) = (\exp((\sigma^- - \sigma^+)d) - 1) / (\exp((\sigma^- - \sigma^+)d) + 1)$ with σ^- and σ^+ the absorption coefficient for minority-spin and majority-spin electrons, respectively
17. V.I. Anisimov and A. Shorikov, private communication
18. We note that the Au/5 nm Fe/Au trilayer, which was used for the energy-dependent measurements, was subject to excessive sputtering, leading to a reduction of the magnetization. This was necessary in order to enable measurements of the spin polarization up to electron energies of 12 eV above E_F . This is the reason why the data points close to $E - E_F = 7$ eV in Fig. 6 cannot be compared with the data set in Fig. 4. For the same reason the data in Fig. 7 (showing A) cannot be compared with the data set in Fig. 5 (showing ϑ)
19. E. Colavita, M. DeCrescenzi, L. Papagno, R. Scarmozzino, L.S. Caputi, R. Rosei, and E. Tosatti, Phys. Rev. B **25**, 2490 (1982)
20. R. Feder, J. Phys. C **14**, 2049 (1981)
21. J. Byrne and P.S. Farago, J. Phys. B **4**, 954 (1971)
22. J. Kessler, *Polarized Electrons* (Springer, New York, 1985), eq. (4.42)
23. C.H. Back, R. Allenspach, W. Weber, S.S.P. Parkin, D. Weller, E.L. Garwin, and H.C. Siegmann, Science **285**, 864 (1999)
24. H.C. Siegmann, E.L. Garwin, C.Y. Prescott, J. Heidmann, D. Mauri, D. Weller, R. Allenspach, and W. Weber, J. of Magn. Magn. Mater. **151**, L8 (1995)
25. A. Vaterlaus, T. Beutler, D. Guarisco, M. Lutz, and F. Meier, Phys. Rev. B **46**, 5280 (1992)
26. A. Scholl, L. Baumgarten, R. Jacquemin, and W. Eberhardt, Phys. Rev. Lett. **79**, 5146 (1997)
27. N. Garcia, H. Rohrer, I.G. Saveliev, and Y.-W. Zhao, Phys. Rev. Lett. **85**, 3053 (2000)
28. Y. Acremann, C.H. Back, M. Buess, O. Portmann, A. Vaterlaus, D. Pescia, and H. Melchior, Science **290**, 492 (2000)
29. L. Berger, IEEE Interact. of Magn. **31**, 3871 (1995)

New Developments in UPS and XPS from Ferromagnetic Materials

Jürgen Braun

Westfälische Wilhelms Universität Münster, Institute of Physics,
Wilhelm-Klemm Str. 10, 48149 Münster, Germany

Abstract. Recent theoretical developments concerning the simultaneous description of electronic correlations and relativistic effects in valence band and core-level spectroscopy serve as a point of major interest in this chapter. In the case where correlation effects are well described by a local potential this generalized approach to photoemission significantly enhances the applicability to ferromagnetic systems. Especially magnetic dichroic phenomena, which have attracted growing interest, turn out to be quantitatively interpretable in the framework of the new formalism.

1 Introduction

Not only due to their technological relevance magnetic materials have focused a high level of scientific activity over the last decades. In particular the new and fascinating properties which have been discovered in magnetic systems of reduced dimensionality seem to be very promising for further experimental and theoretical investigations. The occurrence of magnetism, of course, strongly depends on the geometric and electronic structure which should be known very precisely in order to achieve a detailed understanding of these phenomena. From the experimental point of view a well established method for studying the electronic structure can be found in the photoelectron spectroscopy [1,2,3], which has been developed into a powerful tool over the last thirty years. For example the experimental technique of angle- and spin resolved ultraviolet photoemission has been successfully applied to reveal the dispersion behaviour as well as the spin character of the valence bandstructure in magnetic bulk crystals, thin films and multilayers [4,5,6,7,8,9,10,11]. Increasing the photon energy by one or two orders of magnitude (e.g., entering the x-ray regime), the electronic and magnetic properties of low lying core states may be investigated as well [12,13,14,15,16,17]. In order to interpret the experimental data, it is often useful to have a quantitative comparison between experiment and theory. This demand has led to the development of various approaches for calculating the photocurrent, which ranges from sophisticated but numerically untractable many-body theories to one-electron formulations. For a deeper insight into these theories, the reader is referred to [18,19,20,21,22,23,24,25]. The first and most simple version of a one-electron approximation for the photocurrent has been given by Berglund and Spicer (1964), the so called three-step model of photoemission [26]. In the framework of this model the photoemission process is divided into three independent

steps, namely the excitation of the photoelectron, its transport through the crystal and its escape into the vacuum. Within this model, self-energy corrections, which give rise to damping processes and energetic shifts in the quasi-particle spectrum, are completely neglected. This means that the initial and final states in the photoemission process are assumed to be Bloch-states with an infinite lifetime. It should be mentioned that the assumption of an infinite electron lifetime does not allow for transitions into evanescent bandgap states, e.g. states, which decay exponentially into the solid. Similarly the assumption of an infinite lifetime for the initial state does in practice not allow to calculate photoemission spectra from surface states.

To overcome these deficiencies of the three-step model, a multiple scattering or dynamic approach has been suggested first for the final state by Liebsch (1974) and Spanjaard et al (1977) [27,28]. Later then multiple scattering effects were properly included for both, initial and final states by Pendry (1976), Hopkinson et al. (1980) and Pendry (1980), in order to treat self-energy corrections on equal footing [29,30,31]. In order to tackle the wide range of relativistic effects, visible in photoemission spectra, relativistic one-step models for pure elemental solids and compounds have been introduced in the following years by Thörner et al (1984), Ackermann et al (1985), Braun et al (1985, 1987 and 1993), Ginatempo et al (1989) and by Halilov et al (1993) [32,33,34,35,36,37,38,39].

A further generalization in the theory of photoemission concerns the so called magnetic dichroic effects, i.e. magnetic linear dichroism (MLD) and magnetic circular dichroism (MCD). Due to the interaction between spin-orbit coupling and exchange splitting in magnetic materials, the intensity distribution as well as the spin-polarization of the emitted photoelectrons becomes modified as a function of the macroscopic magnetization and the photon spin too. Herein, for example, can be found the origin of MLD and MCD. Since for the first time magnetic circular and linear dichroism have been observed in soft x-ray [40,41] and in valence band photoemission [42] these effects have been intensively used to study magnetic phenomena in the core level [43,44,45,46,47,48,49] and valence states [50,51,52,53,54,55,56,57,58,59,60,61] of bulk and low-dimensional systems. Most of these experiments have been performed at storage rings which open up the possibility to apply this method for photon energies ranging from the ultra-violet to the soft x-ray regime.

Nowadays so called one-step models are available, which allows for calculating spin-resolved valence band as well as core-level spectra from magnetic materials on a high level of accuracy [49,62,63]. Based on a fully relativistic description these theories quantitatively account for the simultaneous occurrence of spin-orbit coupling and exchange splitting in ferromagnetic metals and compounds. In the following section these theories will be outlined concentrating on the new and important aspects in the description of both UP- and XP-spectroscopy. As an example for magnetic linear dichroism in the valence band region spectroscopic data from Co(0001) will be discussed next. The last section of this chapter is devoted to actual results of core-level spectroscopy from the Fe_{3p}-

states, which will be quantitatively interpreted in terms of the fully relativistic theory of core-level photoemission.

2 One-Step Description of Photoemission Spectroscopy

The main idea of the one-step model is to describe the photoemission process as a single quantum-mechanically coherent process including all multiple-scattering events, which dominate the electron dynamics in the low-energy regime of typically 1-100 eV [64]. We start our considerations by a discussion of Pendry's formula for the photocurrent which defines the one-step model of photoemission [65]:

$$I \propto \text{Im} \langle \epsilon_f, \mathbf{k}_{\parallel} | G_2^+ \Delta G_1^+ \Delta^\dagger G_2^- | \epsilon_f, \mathbf{k}_{\parallel} \rangle. \quad (1)$$

The expression can be derived from Fermi's golden rule for the transition probability per unit time [66]. Consequently, I denotes the elastic part of the photocurrent. Vertex renormalizations are neglected. This excludes inelastic energy losses and corresponding quantum-mechanical interference terms [65,66,67]. Furthermore, the interaction of the outgoing photoelectron with the rest system is not taken into account. This "sudden approximation" is expected to be justified for not too small photon energies. We consider an energy-, angle- and spin-resolved photoemission experiment. The state of the photoelectron at the detector is written as $|\epsilon_f, \mathbf{k}_{\parallel}\rangle$, where \mathbf{k}_{\parallel} is the component of the wave vector parallel to the surface, and ϵ_f is the kinetic energy of the photoelectron. The spin state of the photoelectron is implicit in $|\epsilon_f, \mathbf{k}_{\parallel}\rangle$ which is understood as a four-component Dirac spinor. The advanced Green matrix G_2^- in Eq. (1) characterizes the scattering properties of the material at the final-state energy $E_2 \equiv \epsilon_f$. Via $|f\rangle = G_2^- |\epsilon_f, \mathbf{k}_{\parallel}\rangle$ all multiple-scattering corrections are formally included. Using standard full potential Korringa-Kohn-Rostocker (KKR) multiple scattering techniques [68,69,70] the final state $|f\rangle$ can be calculated as a (time-reversed) relativistic LEED state. Many-body effects are included only phenomenologically in the LEED calculation, i. e. by using a parametrized, weakly energy-dependent and complex inner potential $V_0(E_2) = V_{0r}(E_2) + iV_{02}(E_2)$ as usual [64]. This generalized inner potential also includes the (imaginary) optical potential, which takes into account inelastic corrections to the elastic photocurrent [66] as well as the actual (real) inner potential, which serves as a reference energy inside the solid with respect to the vacuum level [71]. Due to the finite imaginary part $iV_{02}(E_2)$, the flux of elastically scattered electrons is permanently reduced, and thus the amplitude of the high-energy wave field $|f\rangle$ can be neglected beyond a finite distance from the surface.

Δ in Eq. (1) is the dipole operator in the electric dipole approximation which is well justified in the ultraviolet and soft x-ray regime. It mediates the coupling of the high-energy final state with the low-energy initial states. The "low-energy" propagator G_1^+ in Eq. (1), i. e. the one-electron retarded Green matrix for the initial state in the operator representation, yields the "raw spectrum". It is directly related to the "bare" photocurrent and thereby represents the central physical quantity within the one-step model. $G_1^+ \equiv G_1^+(E_1)$ is to be evaluated

at the initial-state energy $E_1 \equiv \epsilon_f - \omega - \mu_0$, where ω is the photon energy (μ_0 stands for the chemical potential). It is advantageous to rewrite Eq. (1) into the space representation:

$$I(\epsilon_f, \mathbf{k}_{\parallel}) = -\frac{1}{\pi} \text{Im} \int d\mathbf{r} \int d\mathbf{r}' f^\dagger(\mathbf{r}) \Delta G_1^+(\mathbf{r}, \mathbf{r}') \Delta^\dagger f(\mathbf{r}') , \quad (2)$$

with

$$f(\mathbf{r}) = \langle \mathbf{r} | G_2^- | \epsilon_f, \mathbf{k}_{\parallel} \rangle . \quad (3)$$

A practical computation starts solving the spin-polarized Dirac equation for a single ion-core potential. The relativistic generalization of density functional theory (DFT) [72,73,74] introduced by Rajagopal and Callaway in 1973 [75] and Ramana and Rajagopal in 1983 [76] leaves us with the following one-particle Dirac equation ($\hbar = m = e = 1, c = 137.036$):

$$(-ic\boldsymbol{\alpha}\boldsymbol{\nabla} + \beta c^2 - c^2 + V_{\text{LDA}}(\mathbf{r}) + \beta\boldsymbol{\sigma}\mathbf{B}_{\text{LDA}}(\mathbf{r}))\Psi(\mathbf{r}) = E\Psi(\mathbf{r}) , \quad (4)$$

where $V_{\text{LDA}}(\mathbf{r}) = 0.5(V_{\text{LDA}}^\uparrow(\mathbf{r}) + V_{\text{LDA}}^\downarrow(\mathbf{r}))$ denotes the (effective) spin-independent potential, and $\mathbf{B}_{\text{LDA}}(\mathbf{r}) = 0.5(V_{\text{LDA}}^\uparrow(\mathbf{r}) - V_{\text{LDA}}^\downarrow(\mathbf{r}))$ is the (effective) magnetic field [77]. The constant unit vector \mathbf{b} determines the spatial direction of the (uniform) magnetization as well as the spin quantization axis. β denotes the usual 4×4 Dirac matrix with the nonzero diagonal elements $\beta_{11} = \beta_{22} = 1$ and $\beta_{33} = \beta_{44} = -1$, and the vector $\boldsymbol{\alpha}$ is given by its components $\alpha_k = \sigma_x \otimes \sigma_k$ ($k = x, y, z$) in terms of the 2×2 Pauli-matrices σ_k . As a consequence of the magnetic field the solutions of the Dirac equation do not have a unique spin-angular character. The reason can be found in a coupling of wavefunctions with different κ, μ -character, which is due to the following angular matrix elements $\mathbf{S} = \langle \chi_\kappa^\mu | \boldsymbol{\sigma} | \chi_{\kappa'}^{\mu'} \rangle$. Herein, χ_κ^μ denotes the spin-angular function given in the usual way by Pauli spinors, Clebsch-Gordan coefficients, and the spherical harmonics. Such an expression results from the effective magnetic field \mathbf{B} which appears in the spin-polarized Dirac equation via the term $\beta\boldsymbol{\sigma}\mathbf{B}$. In addition to the paramagnetic case with selection the rules $\delta_{\kappa, \kappa'} \delta_{\mu, \mu'}$ \mathbf{S} induces further types of couplings. For B_z one gets $((\delta_{\kappa, -\kappa' - 1}, \delta_{\kappa, -\kappa' + 1}) \delta_{\mu, \mu'})$ and for B_{xy} it follows $((\delta_{\kappa, \kappa'}, \delta_{\kappa, -\kappa' - 1}) \delta_{\mu, \mu' \pm 1})$. For example $\delta_{\kappa, -\kappa' - 1}$ corresponds to an $l \pm 1/2$ coupling and is caused by the z-component of the effective magnetic field. The second type concerns the quantum numbers μ and $\mu \pm 1$ and in distinction to the first one it is caused by the x- and y-components of the effective magnetic field. Furthermore, $\delta_{\kappa, -\kappa' + 1}$, connecting the quantum numbers $l+2$ and $l-2$ leads to an infinite number of coupled differential equations. Fortunately, it has been shown by Feder et al. [88] and Cortona et al. [89] that terms arising from this type of coupling are smaller by at least two orders of magnitude, and therefore may be neglected. Although the number of coupled differential equations can be reduced in taking advantage of the symmetry properties of the system, a maximum number of $(l_{\text{max}} + 1)^4$ coupled equations may appear. This, of course, tremendously increases the numerical expense compared to the paramagnetic case. An explicit derivation of the final state $|f\rangle$, which has been introduced before

as a so called time-reversed SPLEED-state defines the next step in a UV(XP)-photocurrent calculation. The single-site scattering solutions of the spin-polarized Dirac equation, which we need first, can be obtained by use of the generalized phase-functional ansatz of Calogero [78,79]. Having solved the system of coupled radial equations it is easy to define the atomic scattering matrix Γ for a single ion-core potential. The atomic scattering matrix Γ together with the crystal geometry determines the scattering matrix M for a single layer. By means of layer-doubling techniques [64] the so called bulk-reflection matrix can be calculated, which gives the scattering properties of a semi-infinite stack of layers. Finally applying the full-potential SPLEED-theory [80,81,82,83,84,85,86,87] it is straightforward to derive the final state $|f\rangle$ for a semi-infinite crystal.

To be able to calculate the photoemission matrix elements it is necessary to redefine the relativistic dipole operator. In the relativistic theory the dipole interaction of an electron with the electromagnetic field is given by the dipole operator $\Delta = -\boldsymbol{\alpha}\mathbf{A}_0$ where \mathbf{A}_0 is the spatially constant vector potential inside the crystal. In a typical photoemission matrix element $\langle\Psi_2|\Delta|\Psi_1\rangle$ between final $|\Psi_2\rangle$ and initial states $|\Psi_1\rangle$ with energies E_2 and E_1 , respectively, Δ can be written as:

$$\Delta = E_{21} \left(\boldsymbol{\nabla} + \frac{i\omega}{c} \boldsymbol{\alpha} \right) \mathbf{A}_0 V_{\text{LDA}} + E_{21} \left((\mathbf{A}_0 \boldsymbol{\nabla}) \beta \boldsymbol{\sigma} + \frac{\omega}{c} \beta \mathbf{A}_0 \times \boldsymbol{\sigma} \right) \mathbf{B}_{\text{LDA}}, \quad (5)$$

with $E_{21} = -2ic/[(E_2 + c^2)^2 - (E_1 + c^2)^2]$. The expression is derived by making use of commutator and anticommutator rules.

The remaining problem consists in the calculation of the propagator G_1^+ . For a single atomic cell this quantity may be constructed from the corresponding solutions of the spin-polarized Dirac equation (4). First we consider the excitation from core states labeled by the discrete eigenvalues E_{1m} . In this case the initial state propagator can be described by the following core-level Green matrix

$$G_1^+ = \sum_m |i_m\rangle \frac{V_{01}}{(E - E_{1m})^2 + V_{01}^2} \langle i_m|, \quad (6)$$

where $|i_m\rangle$ represents a core-level wavefunction with the relativistic indices $m = (\kappa_m, \mu_m)$. As it has been suggested for the final state, the optical potential V_{01} introduced in Eq. (6) accounts for inelastic processes in a phenomenological way. The core-level wavefunctions may be obtained by choosing the spin-quantization axis parallel to the z-axis. In this case one gets for the radial solution a set of four coupled Dirac equations which has to be solved by using normalization constraints. There are at least two technical strategies for solving the set of equations, i.e., finding the core level wavefunctions and the corresponding energies. First one has been suggested by Cortona et al. [89] and the other one is due to Ebert [90,91]. Because of the description of the core states by products of angular and radial parts an arbitrary direction of the magnetic field can be considered by rotational transformations of the spin angular functions[92]. It has to be mentioned that the couplings originated by the spin-dependent potential become more and more important for core states, in which the spin orbit splitting is of the same order of magnitude as the exchange splitting. This situation

for example is given in the 3p multiplet structure of ferromagnetic iron. At this stage we are in position to calculate the XP-photocurrent. Expanding the final state wavefield and the dipole operator in spherical waves around an arbitrary atom j located in the n 'th layer of the semi-infinite crystal, the evaluation of the core-level photocurrent results in:

$$I^{at}(\epsilon_f, \mathbf{k}_{\parallel}) \sim \sum_{jn} \sum_{\kappa\mu\kappa'\mu'} A_{2jn\kappa\mu} \mathcal{Z}_{jn\kappa\mu\kappa'\mu'}^{XP} A_{2jn\kappa'\mu'}^* , \quad (7)$$

where $A_{2jn\kappa\mu}$ denote the relativistic multiple scattering coefficients of the final state wavefield. The matrix \mathcal{Z}^{XP} is build up from integrals over products between the corresponding initial and final-state wavefunctions and the dipole operator. The calculational scheme for valence band photoemission turns out to be more complicated. This is due to the different physical behaviour of exponentially decaying core levels and delocalized valence states. Obviously we have to take care of this fact when calculating the initial state propagator for ultraviolet photoemission. According to Pendry [65] we proceed in the following way. First the atomic propagator for an isolated atomic potential should be derived from the single-site scattering solutions of the spin-polarized Dirac equation. The resulting, so called atomic contribution to the photocurrent, is quite similar to Eq. (7):

$$I^{at}(\epsilon_f, \mathbf{k}_{\parallel}) \sim \sum_{jn} \sum_{\kappa\mu\kappa'\mu'} A_{2jn\kappa\mu} \mathcal{Z}_{jn\kappa\mu\kappa'\mu'}^{UV1} A_{2jn\kappa'\mu'}^* . \quad (8)$$

As it is in the case of core-level photoemission the atomic contribution to the photocurrent is build up by a product between the Matrix \mathcal{Z}^{UV1} and the multiple scattering coefficients $A_{2jn\kappa\mu}$ of the final state. Again j denote the j th cell of the n th layer. For a numerical evaluation \mathcal{Z}^{UV1} it is advantageous to separate the angular matrix elements from the radial parts, which appear to be double radial integrals. A detailed description of the matrix \mathcal{Z}^{UV1} and of the multiple scattering coefficients $A_{2jn\kappa\mu}$ is given in [56]. The so called intra(inter)-layer contributions to the photocurrent describe the multiple scattering corrections of the initial state between and within the layers of the single crystal, and therefore take care of the dispersion behaviour of the valence states. They can be written in the following form:

$$I^{ia+ir}(\epsilon_f, \mathbf{k}_{\parallel}) \sim \sum_{jn} \sum_{\kappa\mu\kappa'\mu'} A_{2jn\kappa\mu} \mathcal{Z}_{jn\kappa\mu\kappa'\mu'}^{UV2} (B_{1jn\kappa'\mu'} + G_{1jn\kappa'\mu'}) . \quad (9)$$

Herein B and G denote the multiple scattering coefficients of the initial state within a layer and between different layers. For a detailed description of the matrix \mathcal{Z}^{UV2} and of the multiple scattering coefficients $B_{1jn\kappa\mu}$ and $G_{1jn\kappa\mu}$ the reader again is referred to [56]. Summation over these three contributions together with the surface contribution, which is considered in the usual way by a z-dependent surface barrier of Rundgren-Malmström type [93] leads to the relativistic full-potential UV-photocurrent for a magnetic system.

3 Results

3.1 MLD in Valence Band Photoemission from Co(0001)

Here we concentrate on Co(0001) valence band photoemission data taken at the storage ring BEESY I in the photon energy range between 20 and 31 eV with linearly polarized radiation from thin cobalt films on W(110) [61]. The experimental results will be discussed with respect to calculated spectra obtained by applying the new ferromagnetic one-step formalism. The measurements have been carried out in normal emission with an angular resolving electron spectrometer. The sample was remanently magnetized along the easy magnetization axis

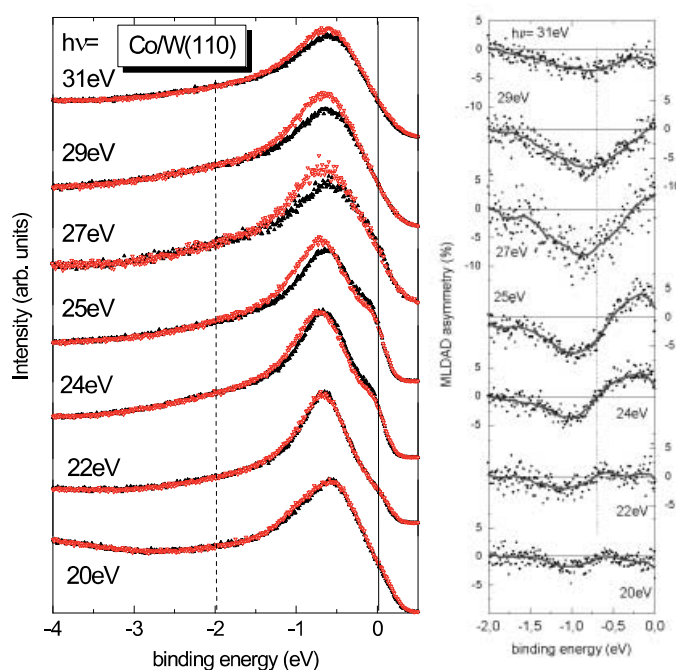


Fig. 1. Left part: valence band photoelectron spectra from a 7 ML thick hcp(0001) cobalt film on tungsten taken with linearly polarized radiation for opposite magnetization directions. Left part: corresponding asymmetry values for binding energies between -2 eV and E_F (cf. vertical lines in the left part).

for thin cobalt films, i.e. along the in-plane $W[1\bar{1}0]$ direction [94]. The photon beam incident under the angle $\Theta_i = 45^\circ$ with respect to the surface normal was linearly polarized parallel to the $W[001]$ direction, i.e. perpendicular to the magnetization direction. The experimental photoemission spectra displayed in the left part of Fig. 1 have been measured from a 7 ML thick cobalt film for opposite magnetization directions M^+ and M^- . All spectra show the Co-3d valence

band centered at about 1 eV below the Fermi level. Starting from 20 eV, the main peak disperses with increasing photon energy to higher binding energies. Moreover, the intensity difference also increases from 20 eV to a maximum value of 6-8% around a photon energy of 27 eV. This is seen in the right part of Fig. 1. In order to understand the origin of the observed intensity differences the exper-

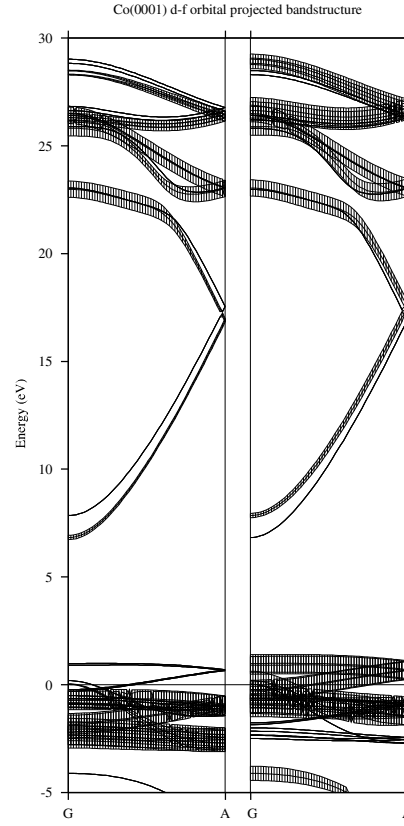


Fig. 2. Spin-polarized relativistic bandstructure of hcp cobalt along the Δ direction from Γ to A. Left part: orbital projected majority spin-character of d- and f-states represented by fat bands. Right part: projected minority spin-character of d- and f-states represented by fat bands.

imental results may be analysed in terms of bandstructure and photoemission calculations. Fig. 2 shows an orbital projected fully relativistic bandstructure for hcp cobalt along the Δ -direction from Γ to A. In the left (right) part the majority (minority) spin-character is visualized by so called “fat bands”. As it should be expected, the initial states are dominantly represented by Co-3d bands. On the other hand, it turns out from Fig. 2 that for excitation energies around 27

eV, where the maximum intensity asymmetry has been observed, mainly f-bands serve as possible candidates for the final states. The binding energy of the main peak in the Co 3d valence bands is almost constant at $E_{bin}=0.7$ eV from $h\nu=22$ up to $h\nu=31$ eV, and thus implies photoexcitation from a flat d-band. Such a flat band is visible indeed in Fig. 2 at $E_{bin}=0.7$ eV. Moreover, the observed MLD effect significantly depends on the excitation energy in the measured range of photon energies. The huge MLD can be ascribed to hybridization regions in the Co valence bands. In these regions, the spin character of the different d-bands

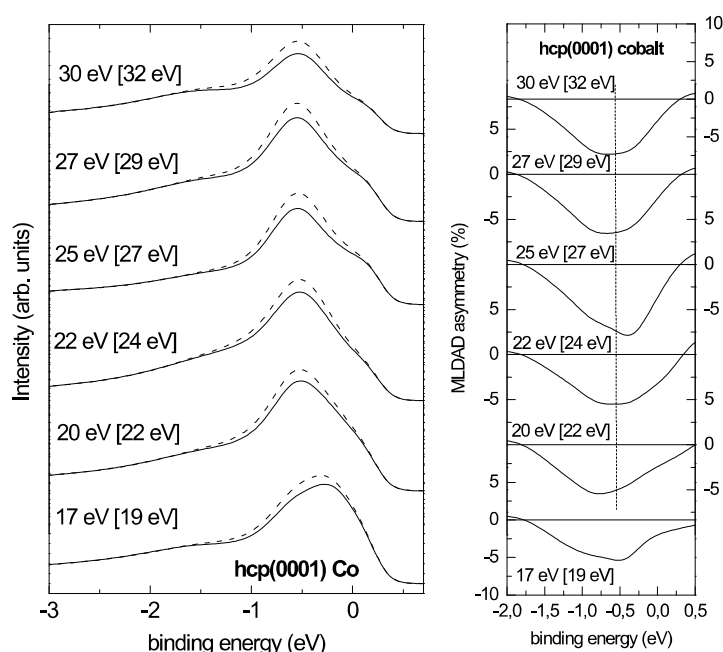


Fig. 3. calculated photoemission spectra (left part) and MLD asymmetry curves (right part) for hcp(0001) cobalt analogous to Fig 1.

is lifted off due to the combined interaction of spin-orbit coupling and exchange splitting. A quantitative description is given in terms of the generalized, B-dependent selection rules discussed in the previous section. The selection rules on the other hand define the orbital- and spin character of the initial (final)-state wave functions. In combination with the dipole selection rules, which occur due to the photoemission matrix elements, the energy- and B-dependent intensity variations can be understood in detail. In Fig. 3 calculated spectra and corresponding asymmetries for cobalt are shown. As it is indicated in Fig. 3 the calculated final states have been shifted in energy by approximately 2 eV to

higher energies in order to obtain a quantitative agreement between experiment and theory. This misfit in energy between measured and calculated final-state bands can be attributed to electron correlation effects beyond DFT(LDA). The energy values given in brackets denote the photon energies after correcting the final state energies by 2 eV with respect to the experiment. The right part of Fig. 3 displays the calculated MLD asymmetry analogously to Fig. 1. In contrast to the experimental findings the calculated asymmetry is found to be more pronounced and visible for all excitation energies. Nevertheless, a maximum of the asymmetry has been obtained at about $h\nu = 27$ eV, which agrees well with the measurements. Incoming light with a photon energy of about $h\nu = 27$ eV causes direct transitions from a hybridization region at $E_{bin} = 0.7$ eV into spin-split f-states, which disperses from 26 eV to 29 eV. Therefore, it is not surprisingly that the maximum value of the asymmetry just occurs for excitation energies around 27 eV.

3.2 Core-Level MCD from the Fe-3p States

By applying the method which has been introduced in Sec. 2 energy dependent core level spectra of Fe 3p have been calculated for right circularly polarized radiation. For the calculation of the core-level wavefunctions a parameter γ has been introduced, which is multiplied to the magnetic field $\mathbf{B}(r)$ in order to reproduce the experimental exchange splitting. A value of this parameter smaller than one results in a reduced exchange splitting. This procedure is necessary in order to get the experimentally observed exchange splitting. Such a reduction of the exchange splitting calculated from first principles has been theoretically explained by Liebsch[95]. In this calculation a value of 0.4 for γ seems to be the best choice. Since the spin-orbit interaction originates only from the coupling of the spin to the angular momentum the parameter γ has no effect on the spin-orbit induced splitting of the different core-states. The energy difference Δ is identified by the distance of the two centers of energy for the $p_{3/2}$ and $p_{1/2}$ states. The value of 1.2 eV has been found in good agreement with the one obtained by Tamura et al.[96]. The exchange splitting of the different j-states results in 0.20 eV between the $\mu = \pm\frac{1}{2}$ states and in 0.47, 0.24 and 0.26 eV between the states denoted by $\mu = \frac{3}{2}, \frac{1}{2}, -\frac{1}{2}, -\frac{3}{2}$. The core-hole lifetime, which is controlled by the parameter V_{01} has been chosen energy independent to 0.8 eV according to the experimental resolution. Fig. 4 shows measured photoelectron spectra for both magnetization directions (left part) and the asymmetry (right part; scale kept fixed to $\pm 25\%$ in all panels). In Fig. 5 the corresponding calculated spectra and asymmetries are presented. The calculated asymmetry values are about four times higher than the experimental ones without background subtraction, but correspond quite well with the experimental values after a Shirley background subtraction. The data of Fig. 5 display always a main peak with a more or less pronounced shoulder. The shape of the curves varies in detail with the photon energy and the magnetization state (full and dashed lines). Analogously to the experimental results the calculated intensities are clearly different when reversing the magnetization. Starting from 90 eV the MCD effect decreases until it

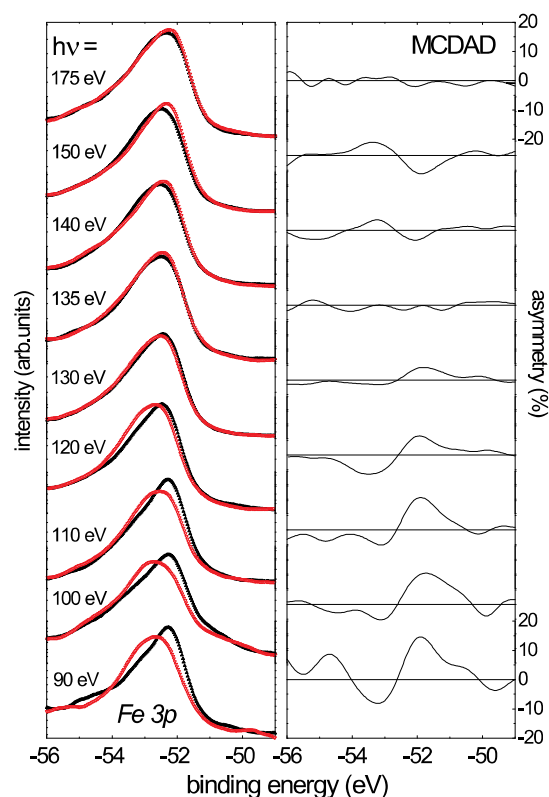


Fig. 4. Series of normal emission photoelectron spectra from the Fe 3p levels with Shirley background subtraction. The data have been taken with right circularly polarized radiation in the range between 90 eV and 175 eV, full and open triangles denote opposite magnetization states (left side). The full curves display the asymmetry results from a simple fitting procedure in order to guide the eye (right side).

vanishes at $h\nu=120$ eV. After changing its sign the MCD asymmetry increases to a maximum which is reached at a photon energy of around 160 eV. For photon energies below 140 eV, the calculated data agree qualitatively well with the experimental results. In order to explain the difference in the zero position of the asymmetry (120 eV vs. 135 eV) a more thorough calculation was performed in which the angular dependency was studied. It was found that the zero position could be shifted about one or two eV in both directions when the emission angle was taken to be within a cone of 20° around the surface normal. But there is no general tendency which would shift the zero position to the experimentally observed one. The insets in Fig. 5 indicate the energetic positions of the six Fe 3p sublevels (noted by 1 to 6) and the relative spectral intensities calculated

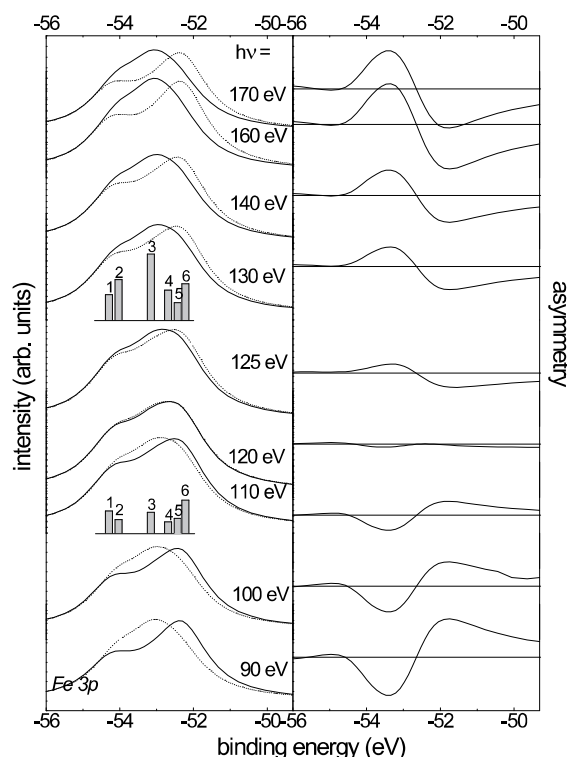


Fig. 5. Series of normal emission photoelectron spectra from the Fe 3p levels calculated for circularly polarized radiation in the range between 90 eV and 175 eV. Full and dashed lines denote opposite magnetization states (left side) and corresponding asymmetries (right side). The insets show the spectral intensities for one direction of the magnetic field for an energy resolution of 0.01 eV.

for this experimental geometry (parallel orientation of the magnetic field) with an energy broadening of 0.01 eV. It can be seen clearly that the reversal in the sign of the MCD signal is due to the change in these features of the core level. From 110 eV to 130 eV the following sublevels interchange their intensities, i.e. $1 \leftrightarrow 2$, $3 \leftrightarrow 6$ and $4 \leftrightarrow 5$. Since the core level wavefunctions are the same for all excitation energies the effect is only due to a change in the scattering properties of the final state.

4 Summary and Outlook

In this chapter new developments in the theory of core-level and valence band photoemission have been presented. It has been shown in Sec. 3 that relativistic

photoemission theory has reached a level that allows for a quantitative interpretation of magnetic dichroic phenomena in core-level as well as in valence band spectroscopy. Nevertheless, the rapidly growing range of applications in the area of photoemission implies a strong demand on further developments within the next years. For example, a fully relativistic photoemission theory for non-local potentials would be able to describe strong electronic correlations and relativistic effects on the same level of accuracy. Also the development of a spin-polarized relativistic one-step model for disordered materials and compounds would strongly enlarge the range of applicability of photoemission theory.

Acknowledgment

Financial support by the Deutsche Forschungsgemeinschaft DFG (contract no.: Br 1188/4-2, Schwerpunktprogramm 'Relativistische Effekte') is gratefully acknowledged.

References

1. B. Feuerbacher, B. Fitton, R.F. Willis: *Photoemission and the electronic Properties of Surfaces*, (Wiley&Sons, New York 1978)
2. M. Cardona, L. Ley: *Photoemission in Solids*, (Springer, Berlin 1979)
3. J. Kirschner In: *Polarized Electrons in Surface Physics*. ed. by R. Feder (World Scientific, Singapur 1985)
4. R. Clauberg, R. Feder In: *Polarized Electrons in Surface Physics*. ed. by R. Feder (World Scientific, Singapur 1985)
5. E. Kisker In: *Polarized Electrons in Surface Physics*. ed. by R. Feder (World Scientific, Singapur 1985)
6. C. Carbone, E. Kisker: Phys. Rev. B **36**, 1280 (1987)
7. K.P. Kämper, W. Schmitt, G. Güntherodt: Phys. Rev. B **42**, 10696 (1990)
8. J. Braun, G. Borstel, W. Nolting: Phys. Rev. B **46**, 3510 (1992)
9. M. Getzlaff, J. Bansmann, J. Braun, G. Schönhense: J. Mag. Mag. Matter **161**, 70 (1996)
10. M. Getzlaff, J. Bansmann, J. Braun, G. Schönhense: Z. Phys. B **104**, 11 (1997)
11. P.D. Johnson: Rep. Prog. Phys. **60**, 1217 (1997)
12. J.F. Van Acker, Z.M. Stadnik, J.C. Fuggle, H.J.W.M. Hoekstra, K.H.J. Bushow, G. Stroink: Phys. Rev. B **37**, 6827 (1988)
13. C. Carbone, E. Kisker: Solid State Commun. **65**, 1280 (1988)
14. B. Sinkovic, P.D. Johnson, N.B. Brookes, A. Clarke, N.V. Smith: Phys. Rev. Lett. **65**, 1647 (1990)
15. T. Cachel, C. Carbone, W. Gudat: Phys. Rev. B **47**, 15391 (1990)
16. L.E. Klebanoff, D.G. Van Campen, R.J. Pouliot: Phys. Rev. B **49**, 2047 (1994)
17. L. Hedin: J. Phys.: Condens. Matter **11**, R489 (1999)
18. I. Adawi: Phys. Rev. **134**, A788 (1964)
19. R. Kubo: J. Phys. Soc. Japan **12**, 570 (1957)
20. L.V. Keldysh: Sov. Phys. JETP **20**, 1018 (1965)
21. G.D. Mahan: Phys. Rev. B **2**, 4334 (1970)
22. W.L. Schaich, N.W. Ashcroft: Solid. St. Commun. **8**, 1959 (1970)
23. W.L. Schaich, N.W. Ashcroft: Phys. Rev B **3**, 2452 (1971)

24. C. Caroli, D. Lederer-Rozenblatt, B. Roulet, D. Saint-James: *Phys. Rev. B* **8**, 4552 (1973)
25. P.J. Feibelman, D.E. Eastman: *Phys. Rev. B* **10**, 4932 (1974)
26. C.N. Berglund, W.E. Spicer: *Phys. Rev.* **136A**, 1030 (1964)
27. A. Liebsch: *Phys. Rev. Lett.* **32**, 1202 (1974)
28. D.J. Spanjaard, D.W. Jepsen, P.M. Marcus: *Phys. Rev. B* **15**, 1728 (1977)
29. J.B. Pendry: *Surf. Sci.* **57**, 679 (1976)
30. J.F.L. Hopkinson, J.B. Pendry, D.J. Titterton: *Comput. Phys. Commun.* **5**, 599 (1980)
31. J.B. Pendry: *Phys. Rev. Lett.* **45**, 1381 (1980)
32. G. Thörner and G. Borstel: *Phys. Stat. Sol. (b)* **126**, 647 (1984)
33. B. Ackermann, R. Feder: *J. Phys. C* **18**, 1093 (1985)
34. J. Braun, G. Thörner, G. Borstel: *Phys. Stat. Sol. (b)* **130**, 643 (1985)
35. J. Braun, G. Thörner, G. Borstel: *Phys. Stat. Sol. (b)* **144**, 609 (1987)
36. B. Ginatempo, P.J. Durham, B.I. Gyorffy: *J. Phys. C* **17**, 6483 (1989)
37. S.V. Halilov, E. Tamura, D. Meinert, H. Gollisch, R. Feder: *J. Phys.: Condens. Matter* **5**, 3859 (1993)
38. S.V. Halilov, H. Gollisch, E. Tamura, R. Feder: *J. Phys.: Condens. Matter* **5**, 4711 (1993)
39. J. Braun, G. Borstel: *Phys. Rev. B* **48**, 14373 (1993)
40. L. Baumgarten, C.M. Schneider, H. Petersen, F. Schäfers, J. Kirschner: *Phys. Rev. Lett.* **65**, 492 (1990)
41. C. Roth, F.U. Hillebrecht, H. Rose, E. Kisker: *Phys. Rev. Lett.* **70**, 3479 (1993)
42. C.M. Schneider, M.S. Hammond, P. Schuster, A. Cebollada, R. Miranda, J. Kirschner: *Phys. Rev. B* **44**, 12066 (1991)
43. C.M. Schneider, D. Venus, J. Kirschner: *Phys. Rev. B* **45**, 5041 (1992)
44. E. Tamura, G.D. Waddill, J.G. Tobin, P.A. Sterne: *Phys. Rev. Lett.* **73**, 1533 (1994)
45. F.U. Hillebrecht, Ch. Roth, H.B. Rose, M. Finazzi, L. Braicovich: *Phys. Rev. B* **51**, 9333 (1995)
46. E. Arenholz, E. Navas, K. Starke, L. Baumgarten, G. Kaindel: *Phys. Rev. B* **51**, 8211 (1995)
47. F.U. Hillebrecht, Ch. Roth, H.B. Rose, W.G. Park, E. Kisker, N.A. Cherepkov: *Phys. Rev. B* **53**, 12182 (1996)
48. G. Rossi, G. Panaccione, F. Sirotti: *Phys. Rev. B* **55**, 11488 (1997)
49. J. Bansmann, L. Lu, K.H. Meiwes-Broer, T. Schlathölter, J. Braun: *Phys. Rev. B* **60**, 13860 (1999)
50. J. Bansmann, M. Getzlaff, C. Westphal, F. Fegel, G. Schönhense: *Surf. Sci.* **269/270**, 622 (1992)
51. J. Bansmann, C. Westphal, M. Getzlaff, G. Schönhense: *J. Magn. Mat.* **117**, 38 (1992)
52. K. Starke, E. Navas, L. Baumgarten, G. Kaindel: *Phys. Rev. B* **48**, 1329 (1993)
53. M. Getzlaff, Ch. Ostertag, G.H. Fecher, N.A. Cherepkov, G. Schönhense: *Phys. Rev. Lett.* **73**, 3030 (1994)
54. C.M. Schneider, J. Kirschner: *Critical Reviews in Solid State and Materials Science*, **20**, 179 (1995)
55. W. Kuch, A. Dittschar, K. Meinel, M. Zharnikov, C.M. Schneider, J. Kirschner: *Phys. Rev. B* **53**, 11621 (1996)
56. J. Braun: *Rep. Prog. Phys.* **59**, 1267 (1996)
57. K. Starke, E. Navas, E. Arenholz, Z. Hu, L. Baumgarten, G. van der Laan, C.T. Chen, G. Kaindel: *Phys. Rev. B* **55** (1997)

58. A. Rampe, G. Güntherodt, D. Hartmann, J. Henk, T. Scheunemann, R. Feder: Phys. Rev. B **57**, 14370 (1998)
59. J. Bansmann, L. Lu, M. Getzlaff, M. Fluchtmann, J. Braun, K. H. Meiwes-Broer: J. Mag. Mag. Matter **185**, 94 (1998)
60. G.H. Fecher, J. Braun, N.A. Cherepkov, L.V. Chernysheva, Th. Jentzsch, J. Morais, A. Oelsner, Ch. Ostertag, J. Paul, H. Ufer, G. Schönhense: Eur. Phys. J. B **11**, 161 (1999)
61. J. Bansmann, L. Lu, M. Getzlaff, M. Fluchtmann, J. Braun: Surf. Sci., **454-456**, 686 (2000)
62. M. Fluchtmann, M. Grass, J. Braun, G. Borstel: Phys. Rev. B **52**, 9564 (1995)
63. J. Henk, R. Feder: Phys. Rev. B **55**, 11476 (1997)
64. J.B. Pendry: *Low Energy Electron Diffraction*, (Academic, London 1974)
65. J.B. Pendry: Surf. Sci. **57**, 679 (1976)
66. G. Borstel: Appl. Phys. A **38**, 193 (1985)
67. C. Caroli, D. Lederer-Rozenblatt, B. Roulet, D. Saint-James: Phys. Rev. B **8**, 4552 (1973)
68. R. Feder: J. Phys. C **14**, 2049 (1981)
69. M. Graß, J. Braun, G. Borstel: Phys. Rev. B **47**, 15487 (1993)
70. M. Graß, J. Braun, G. Borstel: Phys. Rev. B **50**, 14827 (1994)
71. G. Hilgers, M. Potthoff, N. Müller, U. Heinzmann, L. Haunert, J. Braun, G. Borstel: Phys. Rev. B **52**, 14859 (1995)
72. P. Hohenberg, W. Kohn: Phys. Rev. **136**, 864 (1964)
73. W. Kohn, L.J. Sham: Phys. Rev. **140**, 1133 (1965)
74. L.J. Sham, W. Kohn: Phys. Rev. **145**, 561 (1966)
75. A.K. Rajagopal, J. Callaway: Phys. Rev. B **7**, 1912 (1973)
76. M.V. Ramana, A.K. Rajagopal: Adv. Chem. Phys. **54**, 231 (1983)
77. P. Strange, H. Ebert, B.L. Gyorffy: J. Phys.: Condens. Matter **1**, 2959 (1989)
78. F. Calogero: *Variable Phase Approach to Potential Scattering*, (Academic, New York, 1967)
79. A. Gonis: *Green functions for ordered and disordered systems*, Studies in Mathematical Physics **4**, (North Holland, Amsterdam, 1992)
80. W. Kohn, N. Rostoker: Phys. Rev. **94**, 1111 (1954)
81. A.R. Williams, J. van Morgan: J. Phys. C **7**, 37 (1974)
82. R.G. Brown, M. Ciftan: Phys. Rev. B **27**, 4564 (1983)
83. A. Gonis, X.G. Zhang, D.M. Nicholson: Phys. Rev. B **40**, 947 (1989)
84. X.G. Zhang, A. Gonis, J.M. MacLaren: Phys. Rev. B **40**, 3694 (1989)
85. W.H. Butler, R.K. Nesbet: Phys. Rev. B **42**, 1518 (1990)
86. R.K. Nesbet: Phys. Rev. B **41**, 4948 (1990)
87. W.H. Butler, A. Gonis, X.G. Zhang: Phys. Rev. B **45**, 11527 (1992)
88. R. Feder, F. Rosicky, B. Ackermann: Z. Phys. **B 52**, 31 (1983)
89. P. Cortona, S. Doniach, C. Sommers: Phys. Rev. A **31**, 2842 (1985)
90. H. Ebert: J. Phys.: Condens. Matter **1**, 9111 (1989)
91. H. Ebert: Rep. Prog. Phys. **59**, 1665 (1996)
92. M. Tinkham: *Group Theory and Quantum Mechanics*, (McGraw-Hill 1964)
93. G. Malmström, J. Rundgren: Comput. Phys. Commun. **19**, 263 (1980)
94. H. Pinkvos, H. Poppa, E. Bauer, J. Hurst: Ultramicroscopy, **47**, 339 (1992)
95. A. Liebsch: Phys. Rev. Lett. **43**, 1431 (1979)
96. E. Tamura, G. Waddill, J. Tobin, P. Sterne: Phys. Rev. Lett. **73**, 1533 (1994)

Theory of Electron Spectroscopies

Michael Potthoff

Institut für Physik, Humboldt-Universität zu Berlin, Germany

Abstract. The basic theory of photoemission, inverse photoemission, Auger-electron and appearance-potential spectroscopy is developed within a unified framework starting from Fermi's golden rule. The spin-resolved and temperature-dependent appearance-potential spectroscopy of band-ferromagnetic transition metals is studied in detail. It is shown that the consideration of electron correlations and orbitally resolved transition-matrix elements is essential for a quantitative agreement with experiments for Ni.

1 Basic Electron Spectroscopies

Electron spectroscopy [1,2,3,4,5,6] is one of the fundamental experimental techniques to investigate the electronic structure of transition metals. For a deeper understanding of the electronic properties, a meaningful interpretation of the measured spectra is necessary which is based on a reliable theory of spectroscopies. This is particularly important for the study of band ferromagnetism which is caused by a strong Coulomb interaction among the valence electrons. Due to the presence of strong electron correlations, simple explanations of spectral features within an independent-particle model may fail. Here we try to clarify what physical quantity is really measured and what ingredients are needed for a theoretical approach to find a satisfactory agreement with the experimental data. We are concerned with the theory of four basic types of electron spectroscopy (see Fig. 1 and the articles by Braun, Donath, Ebert, Greber and Kakizaki in this book): photoemission (PES), inverse photoemission (IPE), Auger-electron (AES) and appearance-potential spectroscopy (APS).

The spin-, angle- and energy-resolved (ultraviolet) valence-band photoemission (PES) more or less directly measures the occupied part of the band structure. Present theories of PES are mostly based on the so-called one-step model of photoemission [1,7,8,9] which treats the initial excitation step, the transport of the photoelectron to the surface and the scattering at the surface barrier as a single quantum-mechanically coherent process. The one-step model is essentially based on the independent-particle approximation. The valence electrons move independently in an effective potential as obtained from band-structure calculations within the local-density approximation (LDA) of density-functional theory (DFT) [10,11]. There are recent attempts [12,13] for a reformulation of the one-step model to include a non-local, complex and energy-dependent self-energy which accounts for electron correlations.

The one-step model also applies to inverse photoemission spectroscopy. IPE is complementary to PES and yields information on the unoccupied bands above

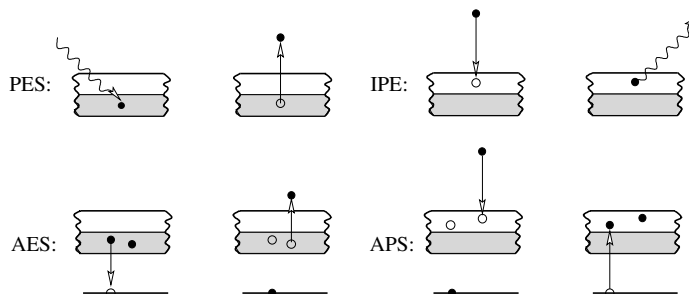


Fig. 1. Schematic picture of the initial and the final states for different electron spectroscopies. PES: photoemission spectroscopy ($s = 1$). IPE: inverse photoemission ($s = -1$). AES: Auger-electron spectroscopy ($s = 2$). APS: appearance-potential spectroscopy ($s = -2$). The grey region is the occupied part of the valence band

the Fermi energy [9]. For example, IPE can be used to determine the dispersions of the Rydberg-like series of surface states in the $1/z$ image potential in front of the surface [6].

The theory of CVV Auger-electron spectroscopy (AES) is more complicated compared to PES/IPE since there are two valence electrons participating in the transition. Due to core state involved additionally, AES is highly element specific. This feature is frequently exploited for surface characterization. Contrary to \mathbf{k} resolved (inverse) photoemission, the Auger transition is more or less localized in real space. High-resolution AES may thus yield valuable information on the local valence density of states (DOS). In the most simple theoretical approach suggested by Lander in 1953 [14], the Auger spectrum is given by the self-convolution of the occupied part of the DOS. Modern theories of AES also include the effect of transition-matrix elements [15]. Similar as the one-step model of PES and IPE, these approaches are based on the independent-electron approximation.

Finally, the appearance-potential spectroscopy (APS) is complementary to AES. Within Lander's independent-electron model [14] the AP line shape resulting from CVV transitions is given by the self-convolution of the unoccupied part of the DOS. Matrix elements are included in refined independent-particle theories [16]. Its comparatively simple experimental setup and its surface sensitivity qualifies APS to study surface magnetism, for example. For a ferromagnetic material, the spin dependence of the AP signal obtained by using a polarized electron beam gives an estimate of the surface magnetization as has been demonstrated for the transition metals Fe and Ni [17,18].

Common to all four spectroscopies are a number of fundamental concepts and approximation schemes used in the theoretical description. Therefore, it should be possible to develop the basic theory of PES, IPE, AES and APS within a unified framework. This is discussed in the following section 2. As a result of this basic theory of electron spectroscopies it found that in each case the intensity is essentially given in terms of a characteristic Green function.

The actual evaluation of the Green function is more specific and depends on the respective spectroscopy, on the material and the physical question to be investigated. In section 3 we will therefore pick up an example and give a more detailed discussion of APS for band ferro-magnets.

A notable quality of APS is its direct sensitivity to electron correlations: In the AP transition, two valence electrons are added to the system at a certain lattice site. These final-state electrons mutually experience the strong intra-atomic Coulomb interaction U . As a consequence the two-particle (AP) excitation spectrum is expected to show up a pronounced spectral-weight transfer or even a satellite with a characteristic energy of the order of U [19,20]. This is an important difference between the one- (PES, IPE) and the two-particle spectroscopies (AES, APS). To demonstrate this sensitivity to correlations in APS we consider the spin- and temperature-dependent AP spectra of ferromagnetic Nickel as a prototype of a strongly correlated and band-ferromagnetic material in section 4. The discussion of the calculations and the comparison with experimental results will show what presently can be achieved in the theory of electron spectroscopies. Some conclusions are given in section 5.

2 Theory

The basic theory starts from the Hamiltonian H which shall describe the electronic structure of the system within a certain energy range around the Fermi energy. In addition, we consider a perturbation V_s that mediates the respective transition. V_s is assumed to be small and will be treated in lowest-order perturbation theory. The index s distinguishes the different spectroscopies (see Fig. 1). $s = \pm 1, \pm 2$ stands for the difference between the number of valence electrons before and after the transition.

In the photoemission spectroscopy (PES, $s = +1$) a valence electron is excited into a high-energy scattering state by absorption of a photon. The photoelectron escapes into the vacuum and is captured by a detector depending on its spin, energy and angles relative to the crystal surface. Within the framework of second quantization, the perturbation can be written as:

$$V_{+1} = \sum_{\alpha\gamma} M_{\alpha\gamma} a_{\alpha}^{\dagger} c_{\gamma} + \text{h.c.} \quad (\text{PES}). \quad (1)$$

c_{γ} annihilates a valence electron with quantum numbers γ , and a_{α}^{\dagger} creates an electron in a high-energy scattering state α . The matrix element is calculated using the electric dipole approximation. This is well justified in the visible and ultraviolet spectral range. Neglecting the term quadratic in the field as usual and choosing the Coulomb gauge, one obtains:

$$M_{\alpha\gamma} = \langle \alpha | \mathbf{A}_0 \mathbf{p} | \gamma \rangle \quad (s = \pm 1). \quad (2)$$

Here \mathbf{p} is the momentum operator and \mathbf{A}_0 is the spatially constant vector potential inside the crystal. It can be determined from classical macroscopic dielectric theory. Note that we use atomic units with $e = m_e = \hbar = 1$.

In an inverse-photoemission experiment (IPE, $s = -1$) an electron beam characterized by quantum numbers α hits the crystal surface. An electron may be de-excited into an empty valence state γ above the Fermi energy by emission of a photon. The photon yield is measured as a function of α (the polarization, the energy and the angles of the incident electron beam). We have:

$$V_{-1} = \sum_{\gamma\alpha} M_{\gamma\alpha}^* c_{\gamma}^{\dagger} a_{\alpha} + \text{h.c.} \quad (\text{IPE}) . \quad (3)$$

Obviously, $V_{-1} = V_1$. Both, PES and IPE, are induced by the same electron-photon interaction.

In the case of the two-particle ($s = \pm 2$) spectroscopies AES and APS, the transitions are radiationless. Here the Coulomb interaction mediates between the initial and the final state. The initial state for AES ($s = +2$) is characterized by a hole in a core level (produced by a preceding core-electron excitation via x-ray absorption, for example). In the Auger transition the empty core state β is filled by an electron from a valence state γ . The energy difference is transferred to another valence electron in the state γ' which is excited into a high-energy scattering state α and detected. Thus,

$$V_{+2} = \sum_{\alpha\beta\gamma'\gamma} M_{\alpha\beta\gamma'\gamma} a_{\alpha}^{\dagger} b_{\beta}^{\dagger} c_{\gamma} c_{\gamma'} + \text{h.c.} \quad (\text{AES}) . \quad (4)$$

The creator b_{β}^{\dagger} refers to the core state.

Finally, an electron (α) approaching the crystal surface can excite a core electron (β) into a state of the unoccupied bands. Above a threshold energy both, the de-excited primary electron and the excited core electron occupy valence states (γ, γ') above the Fermi energy after the transition. The appearance-potential spectroscopy (APS, $s = -2$) monitors the intensity of this transition as a function of polarization, energy and momentum of the incoming electron beam by detecting the emitted x-rays or Auger electrons of the subsequent core-hole decay. The perturbation is:

$$V_{-2} = \sum_{\alpha\beta\gamma'\gamma} M_{\gamma'\gamma\alpha\beta}^* c_{\gamma'}^{\dagger} c_{\gamma}^{\dagger} b_{\beta} a_{\alpha} + \text{h.c.} \quad (\text{APS}) . \quad (5)$$

Again, $V_{-2} = V_2$. Since AES and APS are induced by the Coulomb interaction, the matrix element reads:

$$M_{\alpha\beta\gamma'\gamma} = {}^{(1)}\langle\alpha| {}^{(2)}\langle\beta| \frac{1}{|\mathbf{r}_1 - \mathbf{r}_2|} |\gamma'\rangle^{(1)} |\gamma\rangle^{(2)} \quad (s = \pm 2) . \quad (6)$$

To calculate the cross sections for the different spectroscopies, time-dependent perturbation theory with respect to the perturbation V_s is applied. Using Fermi's golden rule, the transition probability per unit time for a transition from the initial state $|E_i\rangle$ to the final state $|E_f\rangle$ is given by:

$$w_s = 2\pi |\langle E_f | V_s | E_i \rangle|^2 \delta(E_f - E_i - \omega_s) . \quad (7)$$

$|E_i\rangle$ and $|E_f\rangle$ are eigenstates of the grand-canonical Hamiltonian $H - \mu N$ with eigenenergies E_i and E_f . μ is the chemical potential and N the particle-number operator. Furthermore, $\omega_s = \pm\omega$ for $s = \pm 1$ where ω is the photon frequency. ($\omega_s = 0$ for $s = \pm 2$).

We proceed by applying the so-called sudden approximation which reads:

$$\begin{aligned} |E_f\rangle &= a_\alpha^\dagger |E_n\rangle, & E_f &= \epsilon_\alpha + E_n & (s = +1, +2), \\ |E_i\rangle &= a_\alpha^\dagger |E_n\rangle, & E_i &= \epsilon_\alpha + E_n & (s = -1, -2). \end{aligned} \quad (8)$$

At this point we have neglected the interaction of the high-energy electron with the rest system. The latter is left in the n -th excited state of H with eigenenergy E_n . ϵ_α is the one-particle energy of the high-energy scattering state. The electron and the rest system propagate independently in time but consistent with energy conservation. Generally, the sudden approximation is believed to hold well if ϵ_α is not too small. We can furthermore assume that

$$a_\alpha |E_i\rangle \simeq 0 \quad (s = +1, +2), \quad a_\alpha |E_f\rangle \simeq 0 \quad (s = -1, -2). \quad (9)$$

Hence,

$$\begin{aligned} \langle E_f | V_s | E_i \rangle &= \langle E_n | [a_\alpha, V_s]_- | E_i \rangle = \langle E_n | T_\alpha^{(s)} | E_i \rangle & (s = +1, +2), \\ \langle E_f | V_s | E_i \rangle &= \langle E_f | [V_s, a_\alpha^\dagger]_- | E_n \rangle = \langle E_n | T_\alpha^{(s)\dagger} | E_i \rangle & (s = -1, -2), \end{aligned} \quad (10)$$

where $[..., ...]_-$ denotes the commutator and

$$\begin{aligned} T_\alpha^{(s)} &\equiv [a_\alpha, V_s]_- = \sum_\gamma M_{\alpha\gamma} a_\alpha^\dagger c_\gamma & (s = \pm 1), \\ T_\alpha^{(s)} &\equiv [a_\alpha, V_s]_- = \sum_{\beta\gamma'\gamma} M_{\alpha\beta\gamma'\gamma} b_\beta^\dagger c_\gamma c_{\gamma'} & (s = \pm 2) \end{aligned} \quad (11)$$

the transition operator. The transition probability per unit time now reads:

$$\begin{aligned} w_s &= 2\pi |\langle E_n | T_\alpha^{(s)} | E_i \rangle|^2 \delta(E_n + \epsilon_\alpha - E_i - \omega_s) & (s = +1, +2), \\ w_s &= 2\pi |\langle E_f | T_\alpha^{(s)\dagger} | E_n \rangle|^2 \delta(E_f - E_n - \epsilon_\alpha - \omega_s) & (s = -1, -2). \end{aligned} \quad (12)$$

To get the intensity I_s we have to average over the possible initial states. Initially, the system is assumed to be in thermal equilibrium: At the temperature T ($\beta = 1/k_B T$) the system is found in the state $|E_i\rangle$ with the probability $W_i = Z^{-1} \exp(-\beta E_i)$. Here $Z = \sum_i \exp(-\beta E_i)$ is the grand canonical partition function. We consider an experiment that determines all quantum numbers α necessary for a complete measurement ($s = +1, +2$) or preparation ($s = -1, -2$) of the state of the high-energy electron. Consequently, all indices have to be summed over except for α . Eventually, this yields the intensity:

$$\begin{aligned} I_s(\alpha) &= \frac{2\pi}{Z} \sum_{i,n} e^{-\beta E_i} |\langle E_n | T_\alpha^{(s)} | E_i \rangle|^2 \delta(E_n + \epsilon_\alpha - E_i - \omega_s) & (s = +1, +2), \\ I_s(\alpha) &= \frac{2\pi}{Z} \sum_{f,n} e^{-\beta E_n} |\langle E_f | T_\alpha^{(s)\dagger} | E_n \rangle|^2 \delta(E_f - E_n - \epsilon_\alpha - \omega_s) & (s = -1, -2). \end{aligned} \quad (13)$$

These expressions can be written in a more compact form. For this purpose we define the Green function [21] as:

$$G_{\alpha\alpha'}(E) = \frac{1}{Z} \sum_{m,n} e^{-\beta E_n} (e^{\beta E} + 1) \frac{\langle E_n | T_{\alpha'}^{(s)\dagger} | E_m \rangle \langle E_m | T_{\alpha}^{(s)} | E_n \rangle}{E - (E_n - E_m)}, \quad (14)$$

which can also be written in the form $G_{\alpha\alpha'}(E) = \langle \langle T_{\alpha}^{(s)}; T_{\alpha'}^{(s)\dagger} \rangle \rangle$ to show the dependence on the transition operator. With the help of the Dirac identity $1/(E + i0^+) = \mathcal{P}(1/E) - i\pi\delta(E)$,

$$\begin{aligned} I_s(\alpha) &= -2 \frac{1}{e^{\beta E} + 1} \text{Im } G_{\alpha\alpha}(E + i0^+) \Big|_{E=\epsilon_\alpha - \omega_s} \quad (s = +1, +2), \\ I_s(\alpha) &= -2 \frac{e^{\beta E}}{e^{\beta E} + 1} \text{Im } G_{\alpha\alpha}(E + i0^+) \Big|_{E=\epsilon_\alpha - \omega_s} \quad (s = -1, -2). \end{aligned} \quad (15)$$

One recognizes the Fermi function $f(E) = 1/(\exp(\beta E) + 1)$ and the fact that both, the direct ($s > 0$) and the inverse spectroscopies ($s < 0$) are described by the same (Green) function. In fact, the following relations hold:

$$I_{+1}(E) = e^{-\beta E} I_{-1}(E), \quad I_{+2}(E) = e^{-\beta E} I_{-2}(E). \quad (16)$$

Eqs. (14) and (15) show that the intensity is given by a weighted sum of δ peaks at the excitation energies $E = E_n - E_m$. In the thermodynamic limit the energy spectrum will be continuous in general and thus the dependence $I_s(E)$ is smooth. The weight factors $\langle E_n | T_{\alpha'}^{(s)\dagger} | E_m \rangle \langle E_m | T_{\alpha}^{(s)} | E_n \rangle$ distinguish between the different spectroscopies.

The final equation (15) is the goal of our considerations so far. It relates the intensity to the Green function (14) which is a central quantity of many-body theory. It can be (approximately) calculated by standard diagrammatic methods such a perturbation theory with respect to the interaction strength or by methods involving infinite re-summations of diagrams [21]. This is an essential advantage compared with a direct evaluation of Eq. (13). The latter seems to be impossible since one would have to compute explicitly the eigenenergies E_n and eigenstates $|E_n\rangle$ of a system of interacting electrons.

3 APS for Band Ferromagnets

In the following we will concentrate on the appearance-potential spectroscopy to give an example how calculations can be performed in practice. Beforehand, however, some preparations are necessary.

Core-hole effects. A characteristic feature of APS is the formation of a core hole. The energy of core level ϵ_c involved in the transition determines the shallow energy: Energy conservation requires that the energy loss of the primary electron must be equal to or larger than $E_F - \epsilon_c$ where E_F is the Fermi energy. Besides

this static effect there are also dynamic core-hole effects originating from the scattering of valence electrons at the local core-hole potential in the final state for APS [22,23]. The dynamic core-hole effects are usually neglected assuming the Coulomb correlation between valence and core electrons to be small and not to affect the AP line shape significantly. This is an approximation which is difficult to justify and which has to be checked in each case separately.

It leads, however, to a substantial simplification of the problem. Similar to the sudden approximation discussed above, one can write:

$$|E_i\rangle = a_\alpha^\dagger b_\beta^\dagger |E_n\rangle', \quad E_i = \epsilon_\alpha + \epsilon_c + E_n', \quad b_\beta |E_f\rangle = 0. \quad (17)$$

With essentially the same steps as above one gets: $I_{\text{APS}} \propto (1 - f(E)) \text{Im}G(E + i0^+)$ where now $E = \epsilon_\alpha + \epsilon_c$ and where G is a two-particle Green function of the type $G = \langle\langle \sum M c_\gamma c_{\gamma'}; \sum M^* c_\gamma^\dagger c_{\gamma'}^\dagger \rangle\rangle$. Note that the core-electron creators are eliminated (cf. Eq. (11)). The only dynamic degrees of freedom left are those of the valence electrons (γ).

Hamiltonian. Characteristic for the valence electronic structure of the band-ferromagnetic 3d transition metals are the strongly correlated 3d bands around the Fermi energy which hybridize with essentially uncorrelated 4s and 4p bands. The band structure derives from a set of localized one-particle basis states $|\gamma\rangle$ with γ specified as $\gamma = (i, L, \sigma)$. Here $|iL\sigma\rangle$ is taken to be a localized (atomic-like) orbital centered at the site i of a lattice with cubic symmetry. $\sigma = \uparrow, \downarrow$ is the spin index. L is the orbital index running over the five 3d orbitals, the 4s and the three 4p orbitals. We also introduce an index m which labels the different d orbitals, namely the three-fold degenerate t_{2g} and the two-fold degenerate e_g orbitals. Using these notations the Hamiltonian H reads:

$$H = \sum_{ii'LL'\sigma} t_{ii'}^{LL'} c_{iL\sigma}^\dagger c_{i'L'\sigma} + \frac{1}{2} \sum_{i\sigma\sigma'} \sum_{m_1\dots m_4} U_{m_1m_2m_4m_3} c_{im_1\sigma}^\dagger c_{im_2\sigma'}^\dagger c_{im_3\sigma'} c_{im_4\sigma}. \quad (18)$$

This is a multi-band Hubbard-type model including a strongly screened on-site Coulomb interaction among the d electrons. The hopping term $\propto t_{ii'}^{LL'}$ = $\langle iL\sigma | H(U_{\dots} = 0) | i'L'\sigma \rangle$ describes the “free” (non-interacting) band structure which can be obtained by Fourier transformation to \mathbf{k} space $t_{ii'}^{LL'} \mapsto t^{LL'}(\mathbf{k})$ and subsequent diagonalization $t^{LL'}(\mathbf{k}) \mapsto \epsilon_r(\mathbf{k})$.

AP intensity. Having specified the one-particle basis and the Hamiltonian, we can write down the final expression for the AP intensity with all relevant dependencies made explicit:

$$I_{\sigma_c\sigma_i}(\mathbf{k}_\parallel, E) \propto \text{Im} \sum_{L_1L_2L'_1L'_2} M_{L_1L_2}^{\sigma_c\sigma_i}(\mathbf{k}_\parallel, E) \times \\ \times \langle\langle c_{iL_1\sigma_c} c_{iL_2\sigma_i}; c_{iL'_2\sigma_i}^\dagger c_{iL'_1\sigma_c}^\dagger \rangle\rangle_E (M_{L'_1L'_2}^{\sigma_c\sigma_i}(\mathbf{k}_\parallel, E))^*. \quad (19)$$

The intensity depends on the quantum numbers β of the core hole formed, particularly on the spin σ_c of the core state, and on the quantum numbers α of

the incoming electron, its energy E , its momentum parallel to the crystal surface \mathbf{k}_{\parallel} and its spin σ_i .

The AP line shape essentially results from intra-atomic transitions. Consequently, those transition-matrix elements M that lead to off-site contributions to the intensity are neglected in (19). The “raw spectrum” as given by the imaginary part of the Green function in Eq. (19) is therefore isotropic. Any angular (\mathbf{k}_{\parallel}) dependence is due to the angular dependence of the high-energy scattering state in the matrix element.

The energy dependence of the intensity, i. e. the actual AP line shape, is mainly determined by the two-particle Green function and reflects the energy-dependent probability for two-particle excitations. On the contrary, for typical kinetic energies of the primary electron of the order of keV the change of the matrix elements due to the energy dependence of the high-energy scattering states is expected to be weak over a few eV.

Spin dependence. The Coulomb interaction that induces the transition conserves the electron spin orientation. So the spin orientations of the incoming electron σ_i and of the core electron σ_c in the initial state determine the spin orientations of the two additional valence electrons in the final state. For an incoming electron with spin orientation σ_i one can distinguish between a “singlet” transition, i. e. excitation of a core electron with $\sigma_c = -\sigma_i$, and a “triplet” transition with $\sigma_c = \sigma_i$. It is important to note that the ratio between singlet and triplet transitions is regulated by the symmetry behavior of the transition-matrix elements under exchange of the orbital indices. Assume, for example, that the matrix element is symmetric: $M_{L_1 L_2} = M_{L_2 L_1}$. Then the transition operator for triplet transitions vanishes, $T_{\sigma_c \sigma_i} = \sum_{L_1 L_2} M_{L_1 L_2} c_{i L_1 \sigma_c} c_{i L_2 \sigma_i} = 0$ for $\sigma_i = \sigma_c$, since $c_{i L \sigma}^2 = 0$ (Pauli principle) and since $c_{i L_1 \sigma_c} c_{i L_2 \sigma_i}$ is antisymmetric with respect to $L_1 \leftrightarrow L_2$. Thus, a symmetric or even a constant matrix element (as is sometimes assumed for simplicity) completely excludes the triplet transitions.

Consider a paramagnetic material for a moment. The argument above shows that a symmetric $M_{L_1 L_2}$ would imply $\sigma_c = -\sigma_i$, i. e. a fully polarized primary electron beam leads to a full polarization of the core hole. Thus, any deviation from full core-hole polarization must be due to the antisymmetric part of the matrix element.

Below we will consider a ferromagnetic material and a situation where the spin state of the final core hole is not detected. Then, the intensities have to be summed incoherently: $I_{\sigma_i} \equiv I_{\sigma_c \sigma_i} + I_{-\sigma_c \sigma_i}$. For a ferromagnetic material one expects the intensity to be still dependent on the spin orientation of the primary electrons: $I_{\uparrow} \neq I_{\downarrow}$ (while $I_{\uparrow} = I_{\downarrow}$ above the Curie temperature). Let us assume again symmetric behavior: $M_{L_1 L_2} = M_{L_2 L_1}$. It has been argued above that this implies $I_{\sigma_c \sigma_i} = 0$ for $\sigma_i = \sigma_c$. Furthermore, it is easy to see that $T_{\uparrow \downarrow} = -T_{\downarrow \uparrow}$ which implies $I_{\downarrow \uparrow} = I_{\uparrow \downarrow}$. Hence, $I_{\uparrow} = I_{\downarrow}$. In conclusion, any spin asymmetry in the intensity is due to a non-vanishing antisymmetric part of the matrix elements. The AP intensity asymmetry is much more determined by the symmetry properties of the matrix elements with respect to their orbital indices as compared to their spin dependence.

Direct and indirect correlations. Any diagrammatic approach gives the two-particle Green function $\langle\langle c c; c^\dagger c^\dagger \rangle\rangle$ as a (complicated) functional \mathcal{F} of the one-particle Green function $\langle\langle c; c^\dagger \rangle\rangle$. One can thus distinguish between direct and indirect correlations [23]. As has been shown above, the one-particle Green function corresponds to the (inverse) photoemission spectrum. Indirect correlations in APS are those which originate from the renormalization of the free one-particle spectrum by the interaction term in (18). The direct correlations, on the other hand, are represented by the concrete form of the functional \mathcal{F} . Essentially, the direct correlations originate from the direct Coulomb interaction of the two additional valence electrons in the final state. Since both electrons are created at the same site, they are affected by the strong intra-atomic interaction. This may give rise to correlation-induced satellites in the AP spectrum as is demonstrated by the so-called Cini-Sawatzky theory [19,20].

When neglecting the direct correlations, the functional \mathcal{F} becomes a mere self-convolution of the one-particle Green functions. If furthermore the transition-matrix elements are taken to be constant, the AP spectrum is simply given by the self-convolution of the unoccupied part of the one-particle density of states $\propto \text{Im}\langle\langle c; c^\dagger \rangle\rangle$. This is the so-called Lander model [14] which is frequently employed for a rough interpretation of the spectra.

Within the framework of the self-convolution (Lander) model the two final-state electrons propagate independently. As a consequence one finds that only the direct term with $L_1 = L'_1$ and $L_2 = L'_2$ and the exchange term with $L_1 = L'_2$ and $L_2 = L'_1$ contribute to the sum over the orbital indices. Generally, however, the Green function in Eq. (19) depends on *four* orbital indices. This implies that the usual characterization of the final state with two quantum numbers (*d-d*, *s-d*, etc.) is no longer valid if the direct correlations are included. The orbital character may change by electron scattering.

4 Appearance-Potential Spectra of Nickel

The significance of electron-correlation effects in APS shall be elucidated in a more detailed discussion below. For this purpose we concentrate on ferromagnetic Nickel as a prototypical 3*d* band-ferromagnet and compare the results of the theoretical approach with experimental data.

Experiments. Experimental results are available for a Ni(110) single-crystal surface with in-plane magnetization [24,25]. In the setup a spin-polarized electron beam is used for excitation which is emitted from a GaAs source. To correct for the incomplete polarization of the electrons ($P \approx 30\%$), all data are rescaled to a 100% hypothetical beam polarization. The spin effect is maximized by alignment of the electron polarization and the sample magnetization vector. The core-hole decay is detected via soft-X-ray emission (SXAPS). To separate the signal from the otherwise overwhelming background, modulation of the sample potential by a peak-to-peak voltage of 2*V* together with lock-in technique is employed. Details of the experimental setup can be found in Refs. [24,18].

Fig. 2 shows the measured differential AP intensity as a function of the energy of primary electrons with polarization parallel (minority, \downarrow) or antiparallel (majority, \uparrow) to the target magnetization. The displayed energy range covers the emission from the L_{III} transition ($2p_{3/2}$ core state). The L_{II} ($2p_{1/2}$) emission would be seen at higher energies shifted by the $2p$ spin-orbit splitting of 17.2 eV.

For $T/T_C = 0.16$ ($T_C \approx 630$ K) the system is close to ferromagnetic saturation. The AP spectrum shows a strongly spin-asymmetric intensity ratio as well as a spin splitting of the main peak at $E = 852.3$ eV (indicated by the dotted line). Since Ni is a strong ferromagnet, there are only few unoccupied d states available in the majority spin channel, and thus $I_{\uparrow} < I_{\downarrow}$ holds for the (non-differential) intensities. This is the dominant spin effect. The intensity asymmetry in the main peak gradually diminishes with increasing T and vanishes at T_C .

The main peak is related to the high DOS at the Fermi energy. Within an independent-electron picture, one can thus characterize the main peak as originating from transitions with two final-state electrons of d - d character mainly. This is corroborated by calculations based on DFT-LDA [18,16]. Additional small s - d contributions are present in the secondary peak at $E \approx 859$ eV as has been concluded from the analysis of the transition-matrix elements. The secondary peak has been identified as resulting from a DOS discontinuity deriving from the L_7 critical point in the Brillouin zone [18]. No temperature dependence and spin asymmetry is detectable here.

Hamiltonian. To study the significance of electron correlations, we consider a nine-band Hubbard-type model $H = H_0 + H_1$ including correlated $3d$ and uncorrelated $4s/4p$ orbitals as given by Eq. (18). The first (“free”) term H_0 is obtained from a Slater-Koster fit to the paramagnetic LDA band structure for Ni [26]. Opposed to PES/IPE, this comparatively simple tight-binding parameterization appears to be sufficient in the case of APS since the two-particle spectrum does not crucially depend on the details of the one-particle DOS.

The on-site interaction among the $3d$ electrons is described by the second term H_1 . Exploiting atomic symmetries the Coulomb-interaction parameters which depend on the four orbital indices m_1, \dots, m_4 can essentially be expressed in terms of two independent parameters U and J . The numerical values for the direct and exchange interaction, $U = 2.47$ eV and $J = 0.5$ eV, are taken from Ref. [26] where they have been fitted to the ground-state magnetic properties of Ni. Residual interactions involving de-localized s and p states are assumed to be sufficiently accounted for by the LDA. Finally, a double-counting correction is applied to H since partially the interaction H_1 is already included in the LDA Hamiltonian H_0 (for details see Ref. [26]).

Green functions. The two-particle Green function in Eq. (19) is approximately calculated by using standard diagrammatic techniques. Because of the low density of $3d$ holes in the case of Ni, it appears to be reasonable to employ the so-called ladder approximation [27] which extrapolates from the exact (Cini-Sawatzky) solution for the limit of the completely filled valence band [19,20].

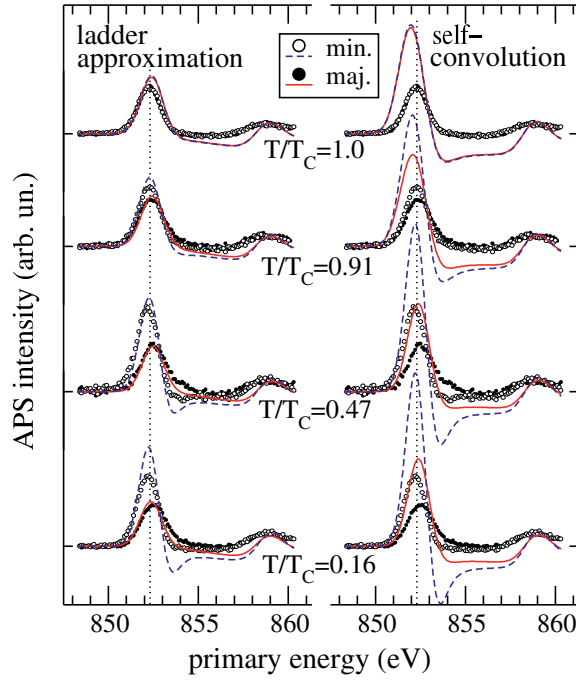


Fig. 2. (from Ref. [25]) Spin-resolved L_{III} Ni AP spectrum for different reduced temperatures T/T_C . *Data points:* measured differential intensity dI/dE as a function of the primary energy. For better comparison with theory the same data are shown twice (left and right panel). *Lines, left:* theory with direct and indirect correlations included (ladder approximation). *Lines, right:* indirect correlations included only (self-convolution)

For finite hole densities the ladder approximation gives the two-particle as a functional \mathcal{F} of the one-particle Green function (direct correlations).

The one-particle Green function, which describes the indirect correlations, is calculated self-consistently within second-order perturbation theory (SOPT) around the Hartree-Fock solution [26]. For a moderate U and a low hole density, a perturbational approach can be justified [28]. A re-summation of higher-order diagrams is important to describe bound states (“Ni 6 eV satellite”) [29] which, however, are relevant for AES only. Since spin-wave excitations are neglected in the approach, the calculated Curie temperature $T_C = 1655$ K is about a factor 2.6 too high. Using reduced temperatures T/T_C , however, the temperature trend of the magnetization is well reproduced [26].

Matrix elements. The transition-matrix elements in Eq. (19),

$$M_{L_1 L_2}^{\sigma_c \sigma_i}(\mathbf{k}_{\parallel}, E) = \langle 2p, \sigma_c | \langle \mathbf{k}_{\parallel} E \sigma_i | r_{12}^{-1} | iL_1 \sigma_c \rangle | iL_2 \sigma_i \rangle, \quad (20)$$

are calculated by assuming the transition to be intra-atomic as usual [5,15,16]. The different wave functions as well as the Coulomb operator $1/r_{12}$ are expanded

into spherical harmonics, the angular integrations are performed analytically, and the numerical radial integrations are cut at the Wigner-Seitz radius.

Surface effects enter the theory via the high-energy scattering state $|\mathbf{k}_{\parallel} E \sigma_i\rangle$. It is calculated as a conventional LEED state with $\mathbf{k}_{\parallel} = 0$ to describe the normally incident electron beam in the experimental setup. The (paramagnetic) LDA potential for Ni is determined by a self-consistent tight-binding linear muffin-tin orbitals (LMTO) calculation [30]. The $3d$, $4s$, and $4p$ valence orbitals $|iL\sigma\rangle$ are taken to be the muffin-tin orbitals. The four-fold degenerate $2p_{3/2}$ core state is obtained from the LDA core potential by solving the radial Dirac equation numerically. Its (relativistically) large component is decomposed into a (coherent) sum of Pauli spinors $|2p, \sigma_c\rangle$ with $\sigma_c = \uparrow, \downarrow$.

Results. The solid lines in Fig. 2 (left) show the spectra as calculated from Eq. (19) using the ladder approximation for the two-particle Green function. To account for apparatus broadening, the results have been folded with a Gaussian of width $\sigma = 0.6$ eV (see Ref. [16]). The calculated data are shifted by 852.3 eV such that onset of the un-broadened spectrum for $T/T_C = 0.16$ coincides with the maximum of L_{III} emission in the experiment (dotted line). Fig. 2 and also a more detailed inspection show that the secondary peak at $E \approx 859$ eV is not affected by correlations at all. This is consistent with observed temperature independence of the peak and with the fact that the DOS has mainly s - p character at the discontinuity deriving from the L_7 critical point. The maximum of the secondary peak is therefore used as a reference to normalize the measured spectra for each temperature.

What are the signatures of electron correlations? The indirect correlations manifest themselves as a renormalization of the one-particle DOS. Here, they are responsible in first place for the correct temperature dependence of the intensity asymmetry of the main peak in the AP spectrum. Details are discussed in Refs. [26,25]. The direct interaction between the two additional final-state electrons and thus the direct correlations are much more important for APS. To estimate this effect, Fig. 2 (right) also displays the results of the self-convolution model for comparison (still including matrix elements as well as the fully interacting one-particle DOS).

Looking at the results of the ladder approximation, the overall agreement with the measurements is rather satisfying. Except for the lowest temperature the intensity, the spin splitting and the spin asymmetry of the main peak are well reproduced and, consistent with the experiment, a negligibly small intensity asymmetry and spin splitting is predicted for the secondary peak. However, switching off the direct correlations (Fig. 2, right), results in a strong overestimation of the main peak structure.

A plausible qualitative explanation of this pronounced correlation effect can be given within the Cini-Sawatzky theory: For low hole density the main effect of the direct correlations is known to transfer spectral weight to lower energies inaccessible to APS. This weight shows up again in the (complementary) Auger spectrum (recall that APS and AES are described by the same Green function). Hypothetically, for $U \mapsto \infty$ all weight would be taken by a satellite split off at the

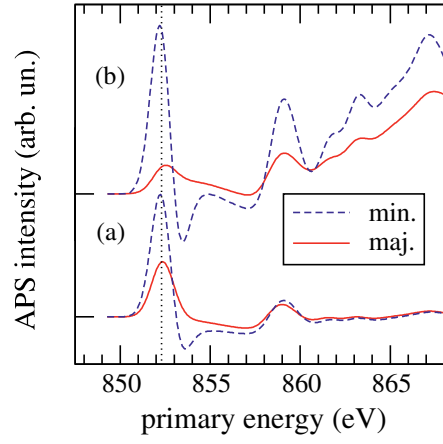


Fig. 3. (from Ref. [25]) Ni AP spectrum for $T = 0$. (a) full theory. (b) as (a) but matrix elements taken to be constant (see text)

lower boundary of the Auger spectrum [19,20]. A considerable weight transfer is in fact seen in AES [5,31].

Fig. 3 shows the effect of the transition-matrix elements. Their importance for a quantitative understanding of spin-resolved APS can be demonstrated by setting $M_{L_1 L_2}^{\sigma_c \sigma_i}(\mathbf{k}_{\parallel}, E) = \pm 1 = \text{const}$ for $L_1 \geq L_2$ or $L_1 < L_2$, respectively, (see below) and comparing with the results of the full theory. Their energy dependence (via the energy dependence of $|\mathbf{k}_{\parallel} E \sigma_i\rangle$) is weak over a few eV at energies of the order of keV and cannot explain the difference between (a) and (b) in Fig. 3. The main difference is rather a consequence of the fact that the radial $2p$ core wave function has a stronger overlap with the (more localized) $3d$ as compared to the (more de-localized) $4s/4p$ radial wave functions. This implies a suppression of the s - p contributions to the orbital sum in Eq. (19). The features above $E = 860$ eV originate from additional discontinuities of the s - p -like DOS (as for the peak at $E \approx 859$ eV).

For $T < T_C$ the spin asymmetry of the spectrum is mainly due to the spin dependence of the Green function in Eq. (19). If the calculation of the matrix elements (20) starts from the *spin-polarized* L(S)DA potential, an additional spin asymmetry is observed resulting from the spin dependence of the states in Eq. (20). This, however, is small and has practically no influence on the results.

On the other hand, Fig. 3 shows a strong suppression of the intensity asymmetry at high energies when taking matrix elements into account. This effect is controlled by the symmetry of the matrix $M_{L_1 L_2} \equiv M_{L_1 L_2}^{\sigma_c \sigma_i}(\mathbf{k}_{\parallel}, E)$. In the antisymmetric case, $M_{L_1 L_2} = -M_{L_2 L_1}$ ($L_1 \neq L_2$), there is a maximum spin asymmetry (Fig. 3) while, even for a ferromagnet, there is no spin asymmetry at all for the symmetric case, as discussed in section 3. The results of the full calculation along Eq. (20) are neither fully symmetric nor antisymmetric with respect to L_1, L_2 .

5 Conclusions

It has been shown that the basic theory of different electron spectroscopies, PES, IPE, AES and APS, can be developed within a unified framework. Starting from Fermi's golden rule and employing the sudden approximation, the intensity can be expressed in terms of a one- or two-particle Green function including electron-photon or Coulomb matrix elements, respectively. Citing APS from the typical band ferromagnet Ni as an example, it could be demonstrated that a quantitative agreement with spin-resolved and temperature-dependent measured spectra can be achieved when the basic spectroscopic formula is taken seriously and is evaluated by modern techniques of solid-state theory.

In particular, it has been shown that there are pronounced (direct) correlation effects in the AP line shape of Ni. While s - p derived features at higher energies appear to be sensitive to the geometrical structure only, the main peak is strongly affected by the direct interaction between the two additional final-state electrons. Consistent with the Cini-Sawatzky model and consistent with the well-known Ni Auger spectrum, there is a considerable spectral-weight transfer to energies below the threshold. For Co and Fe one can even expect stronger effects of d - d correlations on the AP line shape since the d -hole density is larger than in Ni. Simple self-convolution models neglecting the direct correlations must be questioned seriously.

It has also been demonstrated that a mere computation of the (two-particle) Green function is insufficient to describe spin-resolved APS. The spin asymmetry of the AP signal is found to be mainly determined by the orbital-dependent transition-matrix elements and their transformation behavior under exchange of the orbital quantum numbers.

Considering the temperature dependence of the spectra and the magnetic order resulting from strong (indirect) correlations in addition, one can state that the AP line shape of a typical ferromagnetic $3d$ transition metal is determined by a rather complex interplay of different factors.

Despite the fact that a reasonable understanding of APS from Ni has been achieved, there is much work to be done in the future: An open question concerns the importance of core-hole effects in APS, for example. For the present case there has been no need to consider scattering at the core-hole potential in the final state. This may likely be different for systems with a smaller $3d$ occupancy. Furthermore, one must recognize that even the determination of the valence-band Green function is a central problem of many-body theory. Recently much progress has been achieved to deal with single-band models [32]; for a quantitative interpretation of electron spectra from transition metals, however, one needs a theory that realistically includes orbital degeneracy and sp - d hybridization from the very beginning. Compared to perturbation theory or lowest-order re-summation of diagrams, as employed here, improvements are conceivable and necessary albeit not easily performed.

Acknowledgments

I would like to thank J. Braun, M. Donath (Universität Münster), W. Nolting, T. Wegner (Humboldt-Universität zu Berlin) and T. Schlathölter (Philips Hamburg) for stimulating discussions.

References

1. J. B. Pendry: *Low Energy Electron Diffraction* (Academic, London 1974)
2. R. L. Park, J. E. Houston: *J. Vac. Sci. Technol.* **11**, 1 (1974)
3. *Photoemission and the Electronic Properties of Surfaces*, ed. by B. Feuerbacher, B. Fitton, R. F. Willis (Wiley, New York 1978)
4. J. C. Fuggle: *Electron Spectroscopy: Theory, Techniques and Applications*, vol. 4 (Academic, London 1981) p. 85
5. D. E. Ramaker: *Crit. Rev. Solid State Mater.* **17**, 211 (1991)
6. M. Donath: *Surf. Sci. Rep.* **20**, 251 (1994)
7. J. B. Pendry: *Surf. Sci.* **57**, 679 (1976)
8. G. Borstel: *Appl. Phys. A* **38**, 193 (1985)
9. J. Braun: *Rep. Prog. Phys.* **59**, 1267 (1996)
10. P. Hohenberg, W. Kohn: *Phys. Rev.* **136**, 864 (1964)
11. W. Kohn, L. J. Sham: *Phys. Rev.* **140**, 1133 (1965)
12. M. Potthoff, J. Lachnitt, W. Nolting, J. Braun: *phys. stat. sol. (b)* **203**, 441 (1997)
13. C. Meyer, M. Potthoff, W. Nolting, G. Borstel, J. Braun: *phys. stat. sol. (b)* **216**, 1023 (1999)
14. J. J. Lander: *Phys. Rev.* **91**, 1382 (1953)
15. G. H \ddot{u} rmandinger, P. Weinberger, P. Marksteiner, J. Redinger: *Phys. Rev. B* **38**, 1040 (1988)
16. H. Ebert, V. Popescu: *Phys. Rev. B* **56**, 12884 (1997)
17. J. Kirschner: *Solid State Commun.* **49**, 39 (1984)
18. K. Ertl, M. Vonbank, V. Dose, J. Noffke: *Solid State Commun.* **88**, 557 (1993)
19. M. Cini: *Solid State Commun.* **24**, 681 (1977)
20. G. A. Sawatzky: *Phys. Rev. Lett.* **39**, 504 (1977)
21. A. A. Abrikosow, L. P. Gorkov, I. E. Dzyaloshinski: *Methods of Quantum Field Theory in Statistical Physics* (Prentice-Hall, New Jersey 1964).
22. M. Potthoff, J. Braun, W. Nolting, G. Borstel: *J. Phys.: Condens. Matter* **5**, 6879 (1993)
23. M. Potthoff, J. Braun, G. Borstel: *Z. Phys. B* **95**, 207 (1994)
24. M. Vonbank: *Spinaufgelöste Appearance Potential Spektroskopie an 3d-Übergangsmetallen*. PhD Thesis, TU Wien (1992)
25. M. Potthoff, T. Wegner, W. Nolting, T. Schlathölter, M. Vonbank, K. Ertl, J. Braun, M. Donath: *Phys. Rev. B* **63**, 165118 (2001)
26. T. Wegner, M. Potthoff, W. Nolting: *Phys. Rev. B* **61**, 1386 (2000)
27. W. Nolting: *Z. Phys. B* **80**, 73 (1990)
28. M. M. Steiner, R. C. Albers, L. J. Sham: *Phys. Rev. B* **45**, 13272 (1992)
29. A. Liebsch: *Phys. Rev. B* **23**, 5203 (1981)
30. O.K. Andersen, O. Jepsen: *Phys. Rev. Lett.* **53**, 2571 (1984)
31. P. A. Bennett, J. C. Fuggle, F. U. Hillebrecht, A. Lenselink, G. A. Sawatzky: *Phys. Rev. B* **27**, 2194 (1983)
32. A. Georges, G. Kotliar, W. Krauth, M. J. Rozenberg: *Rev. Mod. Phys.* **68**, 13 (1996)

Magnetic Dichroism in Electron Spectroscopy

H. Ebert, J. Minár, and V. Popescu

Univ. München, Phys. Chemie, Butenandtstr. 5–13, D-81377 München

Abstract. A simple scheme that is based on the Green's function formalism is introduced, that allows to investigate spin-orbit-induced properties in magnetic solids in a very transparent way. This is demonstrated by investigations on the orbital magnetic moments, on the Fano effect in angle-integrated valence band photoemission and on magnetic circular dichroism in X-ray absorption. Numerical results obtained by additional fully relativistic calculations are presented to support the various conclusions drawn from the analytical considerations. This applies in particular to the interpretation of the magnetic circular dichroism in X-ray absorption (MCXD) on the basis of the so-called sum rules, which relate the dichroic spectra to the spin and orbital magnetic moments of the absorbing atom.

1 Introduction

The simultaneous presence of magnetic ordering and spin-orbit coupling gives rise to many interesting phenomena that in several cases have important technological applications. Some examples for these are the magneto-crystalline anisotropy [1], the magnetostriction [2], the magneto-optical Kerr effect [3] and the galvano-magnetic effects [4] (see also the contributions of R. Wu and O. Eriksson *et al.* in this volume). The primary source for these phenomena is the reduction in symmetry of a system compared to its paramagnetic state that is caused by the interplay of magnetic ordering and spin-orbit coupling. A very detailed way to study the consequences of this reduction in symmetry is to apply various kinds of electron spectroscopy and to study the corresponding magnetic linear and circular dichroism, MLD and MCD, respectively. Results of corresponding theoretical studies are presented for the angle-integrated valence band photoemission and the X-ray absorption. These investigations are done by making use of a fully relativistic description of the underlying electronic structure within the framework of spin density functional theory. To allow the treatment of a wide range of different systems as ordered compounds, disordered alloys, surfaces as well as impurity systems, the fully relativistic Green's function formalism is used in connection with multiple scattering theory for this purpose. To achieve a more transparent description of the various complex dichroic phenomena a simplified approach is introduced that treats spin-orbit coupling as a perturbation. This approach provides in particular a simple access to the so-called MCXD sum rules that connect the spin and orbital magnetic moments of an absorbing atom and its circular dichroic X-ray absorption spectrum $\Delta\mu$.

2 Effective Single-Particle Hamiltonian for Magnetic Solids Including Spin-Orbit Coupling

One of the most satisfying and accurate way to study spin-orbit induced properties is to start from the Dirac Hamiltonian for spin-polarised solids, that is set up within the framework of spin-density functional theory [5]. This fully-relativistic approach supplies the basis for all calculations to be presented below. This also applies for the contribution of J. Braun to this volume, where a short description of this approach can be found. To allow for a more transparent discussion of the various spin-orbit-induced properties we will use in parallel in the following the modified Schrödinger Hamiltonian:

$$\hat{\mathcal{H}} = -\frac{\hbar^2}{2m}\nabla^2 + \bar{V}(\mathbf{r}) + \underbrace{\boldsymbol{\sigma} \cdot \mathbf{B}_{\text{xc}}(\mathbf{r})}_{\hat{\mathcal{H}}_{\text{xc}}} + \underbrace{\xi(\mathbf{r})\boldsymbol{\sigma} \cdot \mathbf{l}}_{\hat{\mathcal{H}}_{\text{SOC}}} . \quad (1)$$

Here, the spin-dependent exchange correlation term

$$\hat{\mathcal{H}}_{\text{xc}} = \boldsymbol{\sigma} \cdot \mathbf{B}_{\text{xc}}(\mathbf{r}) \quad (2)$$

accounts for the spin polarisation of the system. In the following we will restrict ourselves to collinear spin structures with the spin magnetisation aligned along the z-axis of the system. Accordingly, one can restrict the scalar product $\boldsymbol{\sigma} \cdot \mathbf{B}_{\text{xc}}$ to its zz-part $\sigma_z B_{\text{xc}}$.

There are now several different methods available to derive relativistic corrections to the Schrödinger Hamiltonian [6]. The most important of these corrections are the mass-velocity, the Darwin and the spin-orbit coupling terms [7]. The former two so-called scalar relativistic corrections are not of interest here, because they do not involve any of the Pauli spin matrices σ_i . In particular, because they transform like a scalar under symmetry operations, they do not introduce any anisotropy in the system. The remaining spin-orbit coupling term is usually written in the form [8]:

$$\begin{aligned} \hat{\mathcal{H}}_{\text{SOC}} &= \xi(\mathbf{r}) \frac{1}{2} \boldsymbol{\sigma} \cdot \mathbf{l} \\ &= \xi(\mathbf{r}) \frac{1}{2} [\sigma_z l_z + (\sigma_x l_x + \sigma_y l_y)] . \end{aligned} \quad (3)$$

Here we assumed that $\hat{\mathcal{H}}_{\text{SOC}}$ is derived from a spherically symmetric potential $V(\mathbf{r})$; i.e., $\xi(\mathbf{r})$ stands for $\frac{\hbar}{4m^2c^2} \frac{1}{r} \frac{d\bar{V}}{dr}$ [8]. In addition, we ignored a spin-dependence of the potential. The simple decomposition of the spin-orbit coupling operator in (3) shows immediately that only the first part of $\hat{\mathcal{H}}_{\text{SOC}}$ commutes with the spin-dependent term $\hat{\mathcal{H}}_{\text{xc}}$. As a consequence, if one performs band structure calculations, ignoring the other parts of $\hat{\mathcal{H}}_{\text{SOC}}$, spin is left as a good quantum number; i.e., the electronic states still have pure spin-up or spin-down character. This is demonstrated in the middle panel of Fig. 1, where results of a

corresponding calculation for fcc-Ni are shown. Compared to a non-relativistic calculation the spin-orbit coupling gives rise to a removal of degeneracies (e.g., at the Γ -point) and removes band crossings (e.g., at the positions E and F), but the spin character $\langle \Psi_{n\mathbf{k}} | \sigma_z | \Psi_{n\mathbf{k}} \rangle$ for any Bloch state $|\Psi_{n\mathbf{k}}\rangle$ is restricted to ± 1 . If, on the other hand, only the second part of the $\hat{\mathcal{H}}_{\text{SOC}}$ is kept, one notes that it gives rise to a mixing of states with different spin character (e.g., at positions C and D in the right panel of Fig. 1). For the most general case with the complete operator $\hat{\mathcal{H}}_{\text{SOC}}$ accounted for, all consequences of spin-orbit coupling - removal of degeneracies and mixing of states with and without the same spin character - are present at the same time (see left panel of Fig. 1). Fortunately, as it will be shown below, one does not have always to deal with this most general situation.

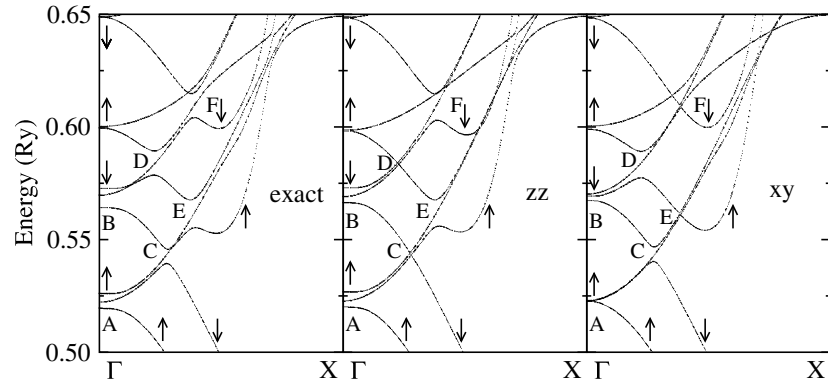


Fig. 1. Dispersion relation $E_{n\mathbf{k}}$ of fcc-Ni for the magnetisation \mathbf{M} and the wave vector \mathbf{k} along the [001] and [100] axis, respectively. The panels show from left to the right results based on the full Dirac equation and those obtained keeping only the zz and xy terms in (3)

3 Spin-Orbit-Induced Properties via Perturbation Theory

In the following, the spin-orbit coupling operator $\hat{\mathcal{H}}_{\text{SOC}}$ will be treated as a perturbation to the remaining part $\hat{\mathcal{H}}_0 = \hat{\mathcal{H}} - \hat{\mathcal{H}}_{\text{SOC}}$ of the Hamiltonian given in (1). The standard way to deal with this problem is to represent the electronic structure in terms of Bloch wave functions $\Psi_{n\mathbf{k}}(\mathbf{r})$ and the associated eigenvalues $E_{n\mathbf{k}}$ [9]. Instead of this, we use the retarded single-electron Green's function for this purpose, that is related to the Bloch wave functions $\Psi_{n\mathbf{k}\sigma}(\mathbf{r}, E_{n\mathbf{k}\sigma})$ and the energies $E_{n\mathbf{k}\sigma}$ by the corresponding spectral representation [10]:

$$G_0(\mathbf{r}, \mathbf{r}', E) = \lim_{\eta \rightarrow 0} \sum_{n\mathbf{k}\sigma} \frac{\Psi_{n\mathbf{k}\sigma}(\mathbf{r}, E_{n\mathbf{k}\sigma}) \Psi_{n\mathbf{k}\sigma}^\dagger(\mathbf{r}', E_{n\mathbf{k}\sigma})}{E - E_{n\mathbf{k}\sigma} + \eta i}. \quad (4)$$

Here we have added explicitly the spin index σ indicating that the wave functions are spinor functions. Accordingly, $G_0(\mathbf{r}, \mathbf{r}', E)$ is a 2×2 matrix function. Although (4) can be used to obtain $G_0(\mathbf{r}, \mathbf{r}', E)$ after calculating the wave functions $\Psi_{n\mathbf{k}\sigma}(\mathbf{r})$ and the energies $E_{n\mathbf{k}\sigma}$ [11], it is more convenient to use the multiple scattering theory representation for it [12]:

$$G_0(\mathbf{r}, \mathbf{r}', E) = \sum_{\mathcal{L}\mathcal{L}'} Z_{\mathcal{L}}^i(\mathbf{r}, E) \tau_{\mathcal{L}\mathcal{L}'}^{ij}(E) Z_{\mathcal{L}'}^{i\dagger}(\mathbf{r}', E) - \sum_{\mathcal{L}} Z_{\mathcal{L}}^i(\mathbf{r}_{<}, E) J_{\mathcal{L}}^{i\dagger}(\mathbf{r}_{>}, E) \delta_{ij} . \quad (5)$$

Here the wave functions $Z_{\mathcal{L}}^i(\mathbf{r}, E)$ and $J_{\mathcal{L}}^i(\mathbf{r}, E)$ are the regular and irregular, respectively, solutions to the single-site Schrödinger equation corresponding to $\hat{\mathcal{H}}_0$. These functions are again spinors of the form

$$Z_{\mathcal{L}}(\mathbf{r}, E) = Z_{l\sigma}(r, E) Y_L(\hat{\mathbf{r}}) \chi_{\sigma} , \quad (6)$$

where $Y_L(\hat{\mathbf{r}})$ is a complex spherical harmonic and χ_{σ} is a Pauli spinor. The indices \mathcal{L} and L stand for the quantum numbers (l, m, σ) and (l, m) , respectively. Finally, the quantity $\tau_{\mathcal{L}\mathcal{L}'}^{ij}$ is the scattering path operator that connects the lattice sites j and i , i.e., it transfers an incoming wave at site j with character \mathcal{L}' into an outgoing wave at site i with character \mathcal{L} . For the scattering path operator $\tau_{\mathcal{L}\mathcal{L}'}^{ij}$ based on the Hamiltonian $\hat{\mathcal{H}}_0$ there is no source for spin-flip scattering processes. Accordingly, $\tau_{\mathcal{L}\mathcal{L}'}^{ij}$ is diagonal with respect to the spin:

$$\tau_{\mathcal{L}\mathcal{L}'}^{ij}(E) = \tau_{LL'\sigma}^{ij}(E) . \quad (7)$$

As a consequence, the corresponding Green's function has the simple spin-diagonal form:

$$G_0 = \begin{pmatrix} G_0^{\uparrow\uparrow} & 0 \\ 0 & G_0^{\downarrow\downarrow} \end{pmatrix} , \quad (8)$$

where all arguments have been suppressed. If the spin-orbit coupling operator $\hat{\mathcal{H}}_{\text{SOC}}$ is included in the calculation of the Green's function, one will have the more general form:

$$G = \begin{pmatrix} G^{\uparrow\uparrow} & G^{\uparrow\downarrow} \\ G^{\downarrow\uparrow} & G^{\downarrow\downarrow} \end{pmatrix} . \quad (9)$$

The Green's function G can be related to the Green's function G_0 of the unperturbed system described by $\hat{\mathcal{H}}_0$ by the Dyson equation [10]:

$$G = G_0 + G_0 \hat{\mathcal{H}}_{\text{SOC}} G \quad (10)$$

$$= G_0 + G_0 \hat{\mathcal{H}}_{\text{SOC}} G_0 + G_0 \hat{\mathcal{H}}_{\text{SOC}} G_0 \hat{\mathcal{H}}_{\text{SOC}} G_0 + \dots \quad (11)$$

In the second equation we have expanded the second term by repeatedly inserting (10) into itself.

With the Green's function G available one can now calculate the expectation value of any operator $\hat{\mathcal{A}}$ [10]:

$$\langle \hat{\mathcal{A}} \rangle = -\frac{1}{\pi} \text{Trace Im } \hat{\mathcal{A}} G \quad (12)$$

$$= -\frac{1}{\pi} \text{Trace Im } \hat{\mathcal{A}} \left(G_0 + G_0 \hat{\mathcal{H}}_{\text{SOC}} G_0 + \dots \right) . \quad (13)$$

For the second equation, the expression for the Green's function as given by (11) has been used. Obviously, this allows one to study the source for any spin-orbit-induced property in detail.

In applying (13) one has to note that products like $G_0 \hat{\mathcal{H}}_{\text{SOC}} G_0$ correspond in practice to integrals with respect to the spatial variable \mathbf{r}'' of the form $\int d^3 r'' G_0(\mathbf{r}, \mathbf{r}'', E) \hat{\mathcal{H}}_{\text{SOC}}(\mathbf{r}'') G_0(\mathbf{r}'', \mathbf{r}', E)$ that extend over the whole space. Expressing the Green's function G_0 according to (5) this implies that one has terms like $\sum_j \tau_{LL''\sigma}^{ij}(E) \tau_{L'L'\sigma'}^{ji'}(E)$ with j running over all lattice sites; i.e., \mathbf{r}'' is restricted to the corresponding atomic cells centred at sites j . In addition, one has on-site contributions connected with the second term in (5). Because we are interested here only in a qualitative discussion of the consequences of $\hat{\mathcal{H}}_{\text{SOC}}$, we will ignore this term in the following. In addition, we will restrict the lattice summation to $j = i$; i.e., only products like $\tau_{LL''\sigma}^{ii}(E) \tau_{L'L'\sigma'}^{ii}(E)$ of the site-diagonal scattering path operator will occur.

4 Spin-Orbit-Induced Orbital Magnetic Moment

One of the most prominent consequences of $\hat{\mathcal{H}}_{\text{SOC}}$ is that the orbital angular momentum is no more quenched in a magnetic solid. This can be demonstrated straightforwardly using (13) to calculate the expectation value of the operator l_z :

$$\langle l_z \rangle = -\frac{1}{\pi} \text{Trace Im } l_z (G_0 + G_0 \hat{\mathcal{H}}_{\text{SOC}} G_0 + \dots) \quad (14)$$

$$\propto \text{Im} \int^{E_F} dE \sum_{\mathcal{L}_1 \mathcal{L}_2 \mathcal{L}_3 \mathcal{L}_4} \langle Z_{\mathcal{L}_4} | l_z | Z_{\mathcal{L}_1} \rangle \tau_{\mathcal{L}_1 \mathcal{L}_2} \langle Z_{\mathcal{L}_2} | \hat{\mathcal{H}}_{\text{SOC}} | Z_{\mathcal{L}_3} \rangle \tau_{\mathcal{L}_2 \mathcal{L}_3} \quad (15)$$

$$\propto \text{Im} \int^{E_F} dE \sum_{l\sigma} \sum_m m \sum_{l'm'} \sigma m' \xi_{l'\sigma} \tau_{lm l' m' \sigma} \tau_{l' m' l m \sigma} . \quad (16)$$

From this, the corresponding orbital magnetic moment μ_{orb} is simply obtained from $\mu_{\text{orb}} = \mu_B \langle l_z \rangle$.

In passing from (14) to (15) we made use of the fact that, without spin-orbit coupling, the orbital angular momentum is indeed quenched. This can be seen by evaluating the corresponding 0-th order term in (14) making use of the properties of the matrix elements $\langle Z_{\mathcal{L}} | l_z | Z_{\mathcal{L}'} \rangle = m \langle Z_l | Z_l \rangle \delta_{\mathcal{L} \mathcal{L}'}$ and of the scattering path

operator $\tau_{\mathcal{L}\mathcal{L}'} = \tau_{LL'\sigma}\delta_{\sigma\sigma'}$. This means that the first non-vanishing contribution to $\langle l_z \rangle$ or μ_{orb} , respectively, is 1-st order with respect to $\hat{\mathcal{H}}_{\text{SOC}}$. Because the matrix elements $\langle Z_{\mathcal{L}} | l_z | Z_{\mathcal{L}'} \rangle$ as well as $\tau_{\mathcal{L}\mathcal{L}'}$ are spin-diagonal, only the spin-diagonal matrix elements $\langle Z_{\mathcal{L}} | \hat{\mathcal{H}}_{\text{SOC}} | Z_{\mathcal{L}'} \rangle$ have to be considered in (15). This means that only the spin-diagonal zz-part of $\hat{\mathcal{H}}_{\text{SOC}}$ in (3) contributes to μ_{orb} .

Inspection of (16) immediately shows that μ_{orb} vanishes if there is no spin polarisation because in this case neither the radial spin-orbit matrix element $\xi_{l\sigma} = \langle Z_{l\sigma} | \xi(\mathbf{r}) | Z_{l\sigma} \rangle$ nor the scattering path operator $\tau_{LL'\sigma}$ depend on σ . Furthermore, one finds for the spin-polarised case that μ_{orb} is approximately given by the spin polarisation $n_{lm}^{\uparrow}(E_F) - n_{lm}^{\downarrow}(E_F)$ at the Fermi level E_F , where $n_{lm}^{\sigma}(E_F)$ is the (l, m, σ) -projected density of states (DOS) [13].

The properties of μ_{orb} derived from (14) - (16) can straightforwardly be demonstrated by corresponding calculations. An example for this is given in Fig. 2, where the spin-orbit-induced orbital magnetic moment of Fe in the disordered alloy $\text{Fe}_{0.2}\text{Ni}_{0.8}$ is shown as a function of the strength of the spin-orbit coupling [14]. These calculations have been done in a two-fold way. In a first set of

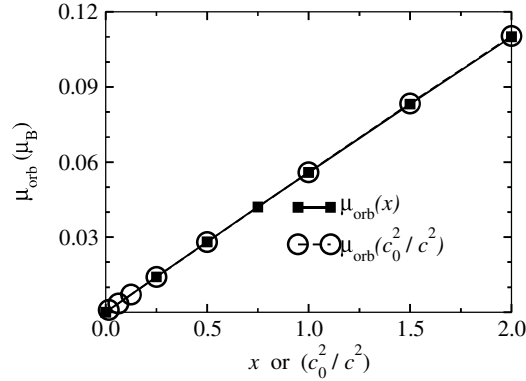


Fig. 2. Spin-orbit-induced orbital magnetic moments μ_{orb} of Fe in $\text{Fe}_{0.2}\text{Ni}_{0.8}$ as a function of the spin-orbit coupling strength scaling parameters x and c_0^2/c^2 , respectively (see text)

calculations the speed of light c has been varied. Because the leading relativistic corrections are proportional to $1/c^2$, μ_{orb} is plotted as a function of (c_0^2/c^2) with c_0 the proper speed of light. For the second set of calculations only the spin-orbit coupling has been manipulated by scaling the corresponding spin-orbit coupling strength with a factor x [14]. As one can see, in both cases μ_{orb} varies linearly over a wide range of the two parameters. For $x = 0$ or $(c_0^2/c^2) = 0$, respectively, i.e., in the non-relativistic limit, μ_{orb} vanishes. For x and (c_0^2/c^2) larger than 1 (the Dirac case) there is hardly a deviation from the linear behaviour. This is not a general rule, because for heavier elements deviations from the straight line can be quite pronounced. Finally, it should be mentioned that the coincidence of the

two data sets shown in Fig. 2 demonstrate that the so-called scalar relativistic corrections have not much influence on μ_{orb} and that they do not lead to a finite value for μ_{orb} if the spin-orbit coupling is suppressed (second data set for $x = 0$).

5 Fano Effect in Magnetic Dichroism Photoemission

Spin-orbit coupling gives rise to many interesting phenomena in the electron spectroscopy of magnetic solids. A rather straightforward access to the understanding of these phenomena is provided by the study of the Fano effect. This effect was predicted by Fano at the end of the sixties and denotes the fact that one obtains a spin-polarised photoelectron current even for paramagnetic systems if the excitation is done using circularly polarised light [15]. A theoretical description of the effect can be obtained by using the one-step model of photoemission [16], that enables one to express the photocurrent $I(E, \mathbf{k}, \sigma; \omega, \mathbf{q}, \lambda)$ for photons with frequency ω and polarisation λ in terms of the electronic Green's function:

$$I(E, \mathbf{k}, \sigma; \omega, \mathbf{q}, \lambda) \propto \int d^3 r \int d^3 r' \phi_{\mathbf{k}\sigma}^{\text{final}\dagger}(\mathbf{r}, E + \hbar\omega) \times \hat{\mathcal{H}}_\lambda \text{Im} G(\mathbf{r}, \mathbf{r}', E) \hat{\mathcal{H}}_\lambda^\dagger \phi_{\mathbf{k}\sigma}^{\text{final}}(\mathbf{r}', E + \hbar\omega). \quad (17)$$

Here the Green's function G represents the initial band-like states of the valence band, while the final states $\phi_{\mathbf{k}\sigma}^{\text{final}}$ with energy $E' = E + \hbar\omega$, wave vector \mathbf{k} and spin σ are given as a so-called time-reversed LEED state [17]:

$$\phi_{\mathbf{k}\sigma}^{\text{final}}(\mathbf{r}, E') = 4\pi \sum_L i^l Y_L^*(\hat{\mathbf{k}}) t_l(E') Z_l(r, E') Y_L(\hat{\mathbf{r}}) \chi_\sigma, \quad (18)$$

where t_l is the single-site scattering matrix [12].

For our present purpose it is again sufficient to treat spin-orbit coupling as a perturbation (for the fully relativistic counterpart see the contribution of J. Braun). This implies in particular that $\hat{\mathcal{H}}_\lambda$ is the standard non-relativistic electron-photon interaction operator [8]. Furthermore, the influence of the spin-orbit coupling on $\phi_{\mathbf{k}\sigma}^{\text{final}}$ can be ignored because the radial matrix elements $\langle Z_l | \xi(\mathbf{r}) | Z_l \rangle$ decay rapidly with increasing energy E' .

Inserting the expressions for G , $\phi_{\mathbf{k}\sigma}^{\text{final}}$ and $\hat{\mathcal{H}}_\lambda$ into (17) one gets a very general expression that allows to deal with the spin and angle-resolved photoemission of solids. Although the Fano effect can be studied in great detail also for the angle-resolved case, we are interested here only in the angle-integrated mode. This implies that one has to average the expression for $I(E, \mathbf{k}, \sigma; \omega, \mathbf{q}, \lambda)$ with respect to the wave vector \mathbf{k} of the photoelectron. For the spin-resolved photocurrent I_λ^σ of a paramagnetic solid one obtains that way:

$$I_\lambda^\sigma \propto \sum_l (\bar{R}_{l2})^2 (2l+1) \begin{pmatrix} l & 1 & 2 \\ 0 & 0 & 0 \end{pmatrix}^2 \sum_{m_1} \begin{pmatrix} l & 1 & 2 \\ -m & \lambda & m_1 \end{pmatrix}^2 \times \sum_{m_2} [N_2 \text{Im} \tau_{2m_1 2m_2} + \bar{\xi}_l m_2 \sigma N_2^2 \text{Im} (\tau_{2m_1 2m_2} \tau_{2m_2 2m_1})], \quad (19)$$

where $\bar{R}_{ll'}$ is a radial dipole matrix element with $\bar{R}_{ll'} = \langle Z_l | r | Z_{l'} \rangle / \sqrt{N_l}$ and the normalisation integral $N_l = \langle Z_l | Z_l \rangle$. Analogously, $\bar{\xi}_l = \xi_l / N_l$ is the normalised matrix element of the spin-orbit operator. In (19), one can identify the terms $N_l \text{Im } \tau_{lm lm}$ with the l, m -projected DOS. This leads to the conventional interpretation of angle-integrated valence band X-ray photoemission spectra (VB-XPS); i.e., their intensity reflects the sum over the matrix element weighted partial DOS. In writing down (19) use has been made of the fact that we are dealing with a paramagnetic solid; i.e., none of the matrix elements nor the scattering path operators depend on the spin character. Nevertheless, one may have a spin-polarised photocurrent that is obtained by calculating the corresponding spin-difference $\Delta I_\lambda = I_\lambda^\uparrow - I_\lambda^\downarrow$. As it can be easily seen from (19) the 0-th order term with respect to $\hat{\mathcal{H}}_{\text{SOC}}$ does not contribute to ΔI_λ . Restricting the l -character of the initial states to $l = 2$, i.e., d-electrons (see below), one ends up with the very simple expression:

$$\begin{aligned} \Delta I_\lambda &\propto (2l+1) \begin{pmatrix} l & 1 & 2 \\ 0 & 0 & 0 \end{pmatrix}^2 \sum_{m_1} \begin{pmatrix} l & 1 & 2 \\ -m & \lambda & m_1 \end{pmatrix}^2 \\ &\quad \times \sum_{m_2} m_2 \text{Im} (\tau_{2m_1 2m_2} \tau_{2m_2 2m_1}) \\ &\propto S_{l\lambda} \text{Im} [\tau_{t_{2g}} (4\tau_{e_g} + \tau_{t_{2g}})] . \end{aligned} \quad (20)$$

For the last step we assumed a cubic system. In that case only two different elements, $\tau_{t_{2g}}$ and τ_{e_g} of the scattering path operator matrix occur because of the high symmetry. The sign function $S_{l\lambda}$ in (20) has the simple properties for left (LCP) and right (RCP) circularly polarised light:

$$S_{l\lambda} = \begin{cases} +1 & \text{d} \rightarrow \text{p} & \lambda = +1 & (\text{LCP}) \\ -1 & \text{d} \rightarrow \text{f} & \lambda = +1 & (\text{LCP}) \\ -1 & \text{d} \rightarrow \text{p} & \lambda = -1 & (\text{RCP}) \\ +1 & \text{d} \rightarrow \text{f} & \lambda = -1 & (\text{RCP}) \end{cases} . \quad (21)$$

From this, one can see that the spin-difference for d→p and d→f transitions is just reversed in sign. In addition, one also can see that if the helicity of the radiation is reverted the spin-difference simply changes its sign. This implies in particular that if unpolarised radiation is used for excitation, i.e., an average with respect to left and right circularly polarised radiation is taken, the spin-difference vanishes exactly. Of course, this is what one would expect.

The scheme sketched above in short allows one to analyse corresponding experimental data in a very simple way. This is demonstrated in the following for the case of fcc-Cu that was investigated recently using left circularly polarised radiation ($\lambda = +1$) at 600 eV. The left panel of Fig. 3 shows the corresponding experimental spin-integrated spectrum in comparison with its theoretical counterpart. The latter was calculated in a fully relativistic way and appropriately broadened to account for experimental resolution and finite lifetime effects, leading to a very good agreement with experiment. A decomposition of the the-

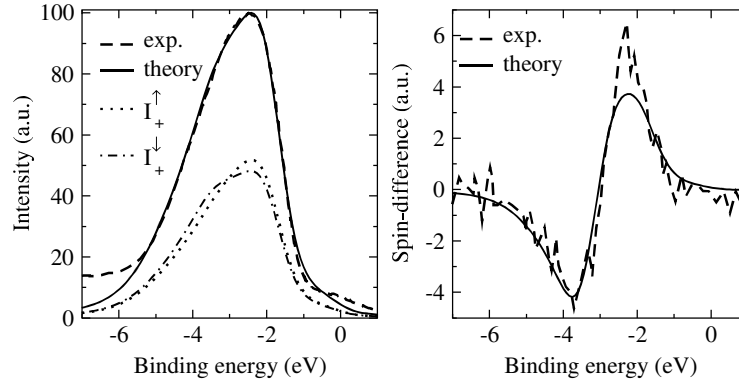


Fig. 3. Left: spin and angle-integrated VB-XPS spectrum of fcc-Cu for a photon energy of 600 eV. Right: spin-difference $\Delta I_+ = I_+^\uparrow - I_+^\downarrow$ of the photocurrent for excitation with left circularly polarised radiation. Theory (*full line*); experiment (*dashed line*) [18]. The left panel shows in addition the theoretical spin-resolved spectra $I_+^{\uparrow(\downarrow)}$

oretical spectrum according to the l -character of the initial state shows that the d-contribution is by far dominating and that the spectrum indeed maps the corresponding DOS. As it can be seen from Fig. 3 (left panel), the theoretical spin-resolved photoemission spectra I_+^σ differ slightly. The corresponding spin-difference $\Delta I_+ = I_+^\uparrow - I_+^\downarrow$ is shown in the right panel of Fig. 3. The fully relativistic calculations again reproduce the experimental data in a very satisfying way. As deduced from the above considerations, the spin-difference should be first order with respect to \hat{H}_{SOC} . This can be demonstrated by the fully relativistic calculations performing a scaling of the strength of the spin-orbit coupling. Figure 4 shows that this expectation is completely confirmed. By keeping only the spin-diagonal zz -part of \hat{H}_{SOC} during the calculation of the spectra, one can furthermore demonstrate that ΔI_λ is primarily due to the zz -part (see right panel of Fig. 4). This result is of course caused by the fact that ΔI_λ is a first order effect with respect to \hat{H}_{SOC} as follows from (19) - (20).

As mentioned above, reverting the helicity leads to a change in sign of the spin difference ΔI_λ . This implies in particular that there is no change in the total photocurrent or cross-section I_λ if the helicity is reverted. In other words, there is no circular dichroism for paramagnetic solids (this is not strictly true, because by going beyond the dipole approximation used here, there may be a natural circular dichroism [19]. However, this effect occurs only for crystals having a certain space group symmetry). For a magnetic solid, on the other hand, this balance may be broken and a magnetic circular dichroism may occur. This effect again can straightforwardly be deduced from the counterpart of (19) for the spin-polarised case and is demonstrated in Fig. 5. Obviously, a circular magnetic dichroism is present in spite of the angular average taken with respect to the photoelectron wave vector. So far corresponding experiments were done only for the angle-resolved case [20] and will be discussed in detail by J. Braun.

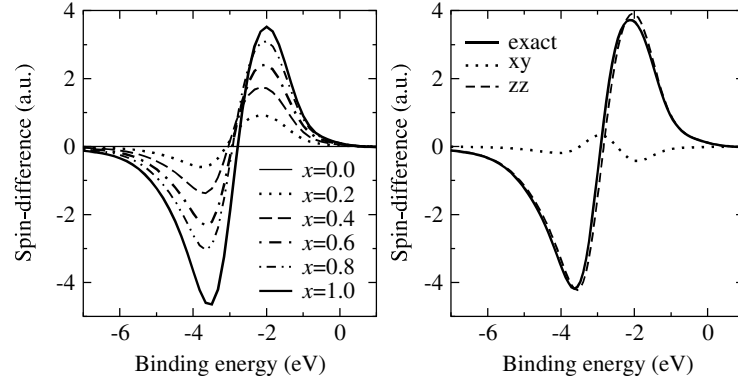


Fig. 4. The theoretical results for the spin-difference ΔI_+ obtained by model calculations. Left: the strength x of the spin-orbit coupling has been varied between 0 and 1. Right: only the spin-diagonal (zz) and only the spin-mixing (xy), respectively, part of the full spin-orbit coupling has been kept for the calculations

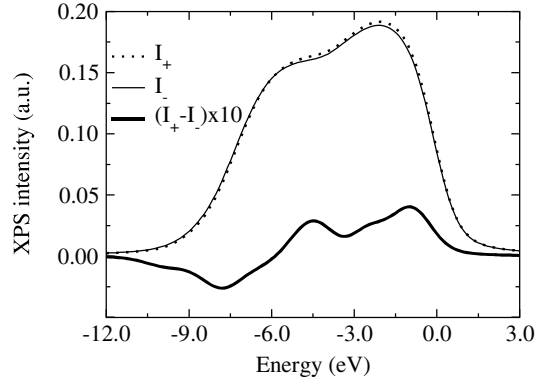


Fig. 5. Theoretical VB-XPS spectra of $\text{Co}_{0.6}\text{Pt}_{0.4}$ for left (I_+ , dotted line) and right (I_- , thin solid line) circularly polarised radiation and photon energy $\hbar\omega = 1253.6 \text{ eV}$, together with the difference in intensity for left and right circularly polarised radiation (thick solid line)

6 Magnetic Dichroism in X-Ray Absorption

X-ray absorption experiments allow one to probe the electronic structure of complex systems in an element specific way. Corresponding investigations of the magnetic circular X-ray dichroism (MCXD) give additional information on magnetic properties. This could first be demonstrated by measurements of Schütz and coworkers at the K-edge of bcc-Fe [21]. A description of this experiment can be obtained by expressing the X-ray absorption coefficient μ^λ for radiation with

polarisation λ by means of the electronic Green's function:

$$\mu^\lambda \propto \sum_{\Lambda_c} \sum_f |\langle \Phi_f | \hat{\mathcal{H}}_\lambda | \Phi_{\Lambda_c} \rangle|^2 \delta(E_f - E_{\Lambda_c} - \hbar\omega) \quad (22)$$

$$\propto \sum_{\Lambda_c} \langle \Phi_{\Lambda_c} | \hat{\mathcal{H}}_\lambda^\dagger | \text{Im } G(E) | \hat{\mathcal{H}}_\lambda | \Phi_{\Lambda_c} \rangle \quad (23)$$

$$\begin{aligned} &\propto \text{Im} \sum_{\Lambda_c} \sum_{\mathcal{L}_1 \mathcal{L}_2} \langle \Phi_{\Lambda_c} | \hat{\mathcal{H}}_\lambda^\dagger | Z_{\mathcal{L}_1} \rangle \tau_{\mathcal{L}_1 \mathcal{L}_2} \langle Z_{\mathcal{L}_2} | \hat{\mathcal{H}}_\lambda | \Phi_{\Lambda_c} \rangle \\ &\quad + \text{Im} \sum_{\Lambda_c} \sum_{\substack{\mathcal{L}_1 \mathcal{L}_2 \\ \mathcal{L}_3 \mathcal{L}_4}} \langle \Phi_{\Lambda_c} | \hat{\mathcal{H}}_\lambda^\dagger | Z_{\mathcal{L}_1} \rangle \tau_{\mathcal{L}_1 \mathcal{L}_2} \langle Z_{\mathcal{L}_2} | \hat{\mathcal{H}}_{\text{SOC}} | Z_{\mathcal{L}_3} \rangle \\ &\quad \times \tau_{\mathcal{L}_3 \mathcal{L}_4} \langle Z_{\mathcal{L}_4} | \hat{\mathcal{H}}_\lambda | \Phi_{\Lambda_c} \rangle, \end{aligned} \quad (24)$$

where Φ_{Λ_c} is a core state wave function labelled with the corresponding relativistic quantum numbers $\Lambda_c = (\kappa_c, \mu_c)$ [22] and Φ_f is a final band state.

Here we made again use of the expansion of Green's function given in (11) up to first order in $\hat{\mathcal{H}}_{\text{SOC}}$. Dealing with the special case of a K-edge, one can write the core state as $\Phi_{\Lambda_c}(\mathbf{r}) = \phi_{0\sigma}(r) Y_0^0(\hat{\mathbf{r}}) \chi_\sigma$. Because of the dipole selection rules the angular momentum of the final state is restricted to $l = 1$. Accordingly, one gets:

$$\begin{aligned} \mu_K^\lambda &\propto \text{Im} \sum_{\sigma} \langle Z_{1\sigma} | r | \phi_{0\sigma} \rangle^2 \langle Y_1^m | Y_1^\lambda | Y_0^0 \rangle^2 \tau_{1m 1m\sigma} \delta_{m\lambda} \\ &\quad + \text{Im} \sum_{\sigma} \langle Z_{1\sigma} | r | \phi_{0\sigma} \rangle^2 \langle Y_1^m | Y_1^\lambda | Y_0^0 \rangle^2 \\ &\quad \times \sum_{l'm'} \sigma m' \xi_{l'\sigma} \tau_{1m l'm'\sigma} \tau_{l'm' 1m\sigma} \delta_{m\lambda}, \end{aligned} \quad (25)$$

with the corresponding magnetic circular dichroism

$$\Delta\mu_K = \mu_K^+ - \mu_K^- \quad (26)$$

$$\begin{aligned} &\propto \text{Im} \sum_{\lambda=\pm 1} \lambda \sum_{\sigma} \langle Z_{1\sigma} | r | \phi_{0\sigma} \rangle^2 \langle Y_1^m | Y_1^\lambda | Y_0^0 \rangle^2 \tau_{1m 1m\sigma} \delta_{m\lambda} \\ &\quad + \text{Im} \sum_{\lambda=\pm 1} \lambda \sum_{\sigma} \langle Z_{1\sigma} | r | \phi_{0\sigma} \rangle^2 \langle Y_1^m | Y_1^\lambda | Y_0^0 \rangle^2 \\ &\quad \times \sum_{l'm'} \sigma m' \xi_{l'\sigma} \tau_{1m l'm'\sigma} \tau_{l'm' 1m\sigma} \delta_{m\lambda} \end{aligned} \quad (27)$$

$$\propto \text{Im} \sum_{\sigma} \langle Z_{1\sigma} | r | \phi_{0\sigma} \rangle^2 \sum_m m \sum_{l'm'} \sigma m' \xi_{l'\sigma} \tau_{1m l'm'\sigma} \tau_{l'm' 1m\sigma}. \quad (28)$$

The resulting expression clearly shows that $\Delta\mu_K$ is first order with respect to $\hat{\mathcal{H}}_{\text{SOC}}$. As a consequence, there are again only spin-diagonal contributions to $\Delta\mu_K$. A simple interpretation of the dichroic spectrum $\Delta\mu_K$ can be achieved by restricting the expression for spin-orbit-induced orbital angular momentum

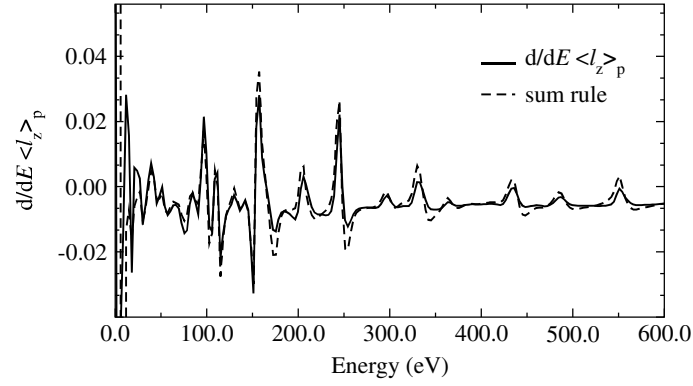


Fig. 6. Orbital polarisation $\frac{d}{dE}\langle l_z \rangle_p$ (solid line) corresponding to (29) for the p-states of fcc-Ni compared to the MCXD spectrum (dashed line) at the K-edge corresponding to (28)

given in (16) to p-like valence band states:

$$\langle l_z \rangle_p \propto \text{Im} \int^{E_F} dE \sum_{\sigma} \sum_m m \sum_{l'm'} \sigma m' \xi_{l'\sigma} \tau_{1m l' m' \sigma} \tau_{l' m' 1 m \sigma} . \quad (29)$$

Ignoring the spin and energy dependence of the occurring radial dipole matrix elements $\langle Z_{1\sigma} | r | \phi_{0\sigma} \rangle$ in (28) one finds that $\Delta\mu_K$ reflects the orbital polarisation $\frac{d}{dE}\langle l_z \rangle_p$ of the p-states.

Because the restriction to the site-diagonal terms $\tau_{LL''\sigma}^{ii} \tau_{L''L'\sigma}^{ii}$ (see the end of Sect. 3), only the spin-orbit coupling at the site of the absorbing atom is accounted for as a source of $\Delta\mu_K$ and μ_{orb} in (28) and (29). If this restriction is dropped, the spin-orbit coupling for the neighbouring sites may contribute as well in a rather substantial way. This has been demonstrated by corresponding model calculations [23,24,25]. Here it should be noted that an expression similar to that given in (24) and including the site-off-diagonal terms $\tau_{LL''\sigma}^{ij} \tau_{L''L'\sigma}^{ji}$ has been used by Brouder and coworkers to deal with the MCXD at the K-edge of pure Fe [26].

The results of the fully relativistic calculations shown in Fig. 6 demonstrate that the simple interpretation of the dichroic spectrum $\Delta\mu_K$ works very well over a wide range of energies. In particular it supports the interpretation of the dichroic spectrum $\Delta\mu_K$ on the basis of a simple rigid band model suggested by Brouder *et al.* [26] that assumes a rigid shift of the m -resolved p-like DOS curves due to the spin-orbit coupling. The relation of $\Delta\mu_K$ and $\frac{d}{dE}\langle l_z \rangle_p$ shown in Fig. 6 is the differential form of one of the so-called MCXD sum rules. For p-like final states the corresponding integral sum rule has first been derived by Igarashi and Hirai [23].

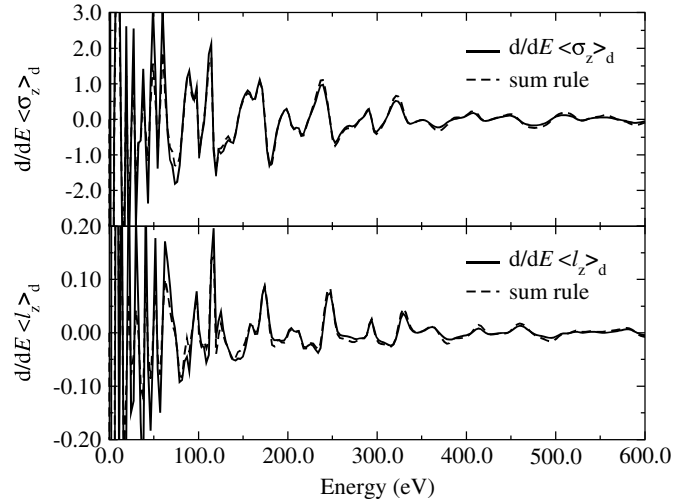


Fig. 7. Orbital polarisation $\frac{d}{dE}\langle l_z \rangle_d$ (solid line) for the d-states of Pt in Fe_3Pt compared to that derived from the MCXD spectra at the $L_{2,3}$ -edges (dashed line) using the differential sum rule in (31) (bottom). The upper panel gives the corresponding curves for the spin polarisation $\frac{d}{dE}\langle \sigma_z \rangle_d$. The small contribution $\frac{d}{dE}\langle T_z \rangle_d$ has been ignored

For the $L_{2,3}$ -edges the situation gets much more complex because spin-orbit coupling splits the initial core states into two sub-shells with $p_{1/2}$ - and $p_{3/2}$ -character. As a consequence, the resulting magnetic dichroic spectra do not reflect only the orbital polarisation of the final states. Nevertheless, one can derive corresponding sum rules that in their integral form have been first derived by Carra *et al.* [27] and Thole *et al.* [28]:

$$\int (\Delta\mu_{L_3} - 2\Delta\mu_{L_2}) dE = \frac{N}{3N_h} (\langle \sigma_z \rangle + 7\langle T_z \rangle) \quad (30)$$

$$\int (\Delta\mu_{L_3} + \Delta\mu_{L_2}) dE = \frac{N}{2N_h} \langle l_z \rangle, \quad (31)$$

where N is the integrated spectrum for unpolarised radiation and N_h is the number of unoccupied d-states, i.e., of d-holes. Finally, $T_z = \frac{1}{2} [\boldsymbol{\sigma} - 3\hat{\mathbf{r}}(\hat{\mathbf{r}} \cdot \boldsymbol{\sigma})]_z$ is the z-component of the magnetic dipole operator. As for the K-edge spectrum, a very stringent check of these rules can be made if they are used in their differential form [29]. Corresponding results for the $L_{2,3}$ -edges of Pt in Fe_3Pt are shown in Fig. 7. As one notes, the spin and orbital polarisation, $\frac{d}{dE}\langle \sigma_z \rangle_d$ and $\frac{d}{dE}\langle l_z \rangle_d$, respectively, for the d-states of Pt as determined directly from the band structure calculations are nearly identical to those derived from the calculated absorption spectra using the sum rules in (30) and (31). Here one should note that the term $\langle T_z \rangle_d$ in (30) has been ignored, because it was found to be much smaller than $\langle \sigma_z \rangle_d$. However, this does not have to be always the case because a finite value for $\langle T_z \rangle_d$ is caused by the presence of spin-orbit coupling as well

as a low symmetry of the system. If the latter source contributes to $\langle T_z \rangle_d$ this is in general no more negligible when applying the sum rules [30]. In spite of this problem and several additional ones [3], one can derive rather reliable estimates for the spin and orbital magnetic moments of an absorbing atom if the sum rules are carefully applied to spectroscopic data.

Acknowledgments

This work was supported by the German ministry for education and research (BMBF) under contract 05 SC8WMA 7 within the program *Zirkular polarisierte Synchrotronstrahlung: Dichroismus, Magnetismus und Spinorientierung*. One of the authors (H. E.) would like to thank Christian Brouder for stimulating discussions that triggered the considerations based on Sect. 3.

References

1. X. Wang, D. Wang, R. Wu, and A. J. Freeman, *J. Magn. Magn. Materials* **159**, 337 (1996).
2. A. B. Shick, D. L. Novikov, and A. J. Freeman, *Phys. Rev. B* **56**, R14259 (1997).
3. H. Ebert, *Rep. Prog. Phys.* **59**, 1665 (1996).
4. J. Banhart and H. Ebert, *Europhys. Lett.* **32**, 517 (1995).
5. A. H. MacDonald and S. H. Vosko, *J. Phys. C: Solid State Phys.* **12**, 2977 (1979).
6. H. Ebert, in *Electronic Structure and Physical Properties of Solids*, Vol. 535 of *Lecture Notes in Physics*, edited by H. Dreyssé (Springer, Berlin, 2000), p. 191.
7. D. D. Koelling and A. H. MacDonald, in *Relativistic Effects in Atoms, Molecules and Solids*, edited by G. L. Malli (Plenum Press, New York, 1979), p. 227.
8. G. K. Woodgate, *Elementary atomic structure* (McGraw-Hill, London, 1970).
9. D. S. Wang, R. Q. Wu, and A. J. Freeman, *Phys. Rev. B* **48**, 15886 (1993).
10. E. N. Economou, *Green's Functions in Quantum Physics* (Springer-Verlag, New York, 1990).
11. R. Zeller and P. H. Dederichs, *Phys. Rev. Letters* **42**, 1713 (197).
12. P. Weinberger, *Electron Scattering Theory for Ordered and Disordered Matter* (Oxford University Press, Oxford, 1990).
13. H. Ebert, R. Zeller, B. Drittler, and P. H. Dederichs, *J. Appl. Physics* **67**, 4576 (1990).
14. H. Ebert, H. Freyer, A. Vernes, and G.-Y. Guo, *Phys. Rev. B* **53**, 7721 (1996).
15. U. Fano, *Phys. Rev.* **184**, 250 (1969).
16. P. J. Feibelman and D. E. Eastman, *Phys. Rev. B* **10**, 4932 (1974).
17. P. J. Durham, *J. Phys. F: Met. Phys.* **11**, 2475 (1981).
18. G. Ghiringhelli, N. B. Brookes, O. Tjernberg, and L. H. Tjeng (unpublished).
19. C. R. Natoli *et al.*, *European Physical Journal B* **4**, 1 (1998).
20. R. Feder and J. Henk, in *Spin-orbit influenced spectroscopies of magnetic solids*, Vol. 466 of *Lecture Notes in Physics*, edited by H. Ebert and G. Schütz (Springer, Berlin, 1996), p. 85.
21. G. Schütz *et al.*, *Phys. Rev. Letters* **58**, 737 (1987).
22. M. E. Rose, *Relativistic Electron Theory* (Wiley, New York, 1961).
23. J. Igarashi and K. M. Hirai, *Phys. Rev. B* **50**, 17820 (1994).
24. H. Ebert, *Solid State Commun.* **100**, 677 (1996).

- 25. V. Popescu, Ph.D. thesis, University of Munich, 2000.
- 26. C. Brouder, M. Alouani, and K. H. Bennemann, *Phys. Rev. B* **54**, 7334 (1996).
- 27. P. Carra, B. T. Thole, M. Altarelli, and X. Wang, *Phys. Rev. Letters* **70**, 694 (1993).
- 28. B. T. Thole, P. Carra, F. Sette, and G. van der Laan, *Phys. Rev. Letters* **68**, 1943 (1992).
- 29. H. Ebert, V. Popescu, and D. Ahlers, *Phys. Rev. B* **60**, 7156 (1999).
- 30. G. Y. Guo, H. Ebert, W. M. Temmerman, and P. J. Durham, *Phys. Rev. B* **50**, 3861 (1994).

Neutrons as a Probe of the Magnetic Moment Stability in Itinerant Electron Ferromagnets

K.-U. Neumann and K.R.A. Ziebeck

Department of Physics, Loughborough University, Loughborough LE11 3TU, **UK**

Abstract. The size of the magnetic moment of itinerant electron ferromagnets depends, among other things, on the on-site Coulomb repulsion and the overlap of electronic wavefunctions between neighbouring atoms. Therefore a change of the electronic wavefunction overlap, arising from thermal vibrations of the atoms, will change the conditions for the formation of the magnetic moments. Neutron scattering is able to probe these changes by dynamic magnetic form factor measurements. In these experiments the magnetic signal is measured on a phonon. Such measurements yield information on the behaviour of the magnetic moment and its stability on a distorted lattice.

1 Introduction

For an itinerant electron ferromagnet the size of the magnetic moment and the interaction between neighbouring moments is determined by details of the band structure such as the size of the matrix element U (which describes the on-site Coulomb repulsion between electrons) and the band width W (which depends sensitively on the electronic overlap between wavefunctions centred on neighbouring atoms). While the Coulomb matrix element is not expected to vary as the nearest neighbour distances are changed the degree of overlap of the electronic wavefunction is modified and so is the width of the d-electron band. Thus as external or chemical pressure is applied to the system the magnetic characteristics of the itinerant electron ferromagnet are altered. The size of the magnetic moment and their interactions are renormalised as seen experimentally in a change of the saturation magnetisation at low temperatures or a shift of the magnetic transition temperature T_c . These changes are brought about by quasi-static constraints imposed onto the lattice system, which in turn determines the properties of the magnetic subsystem. However, the magnitude of the external field (pressure) required to bring about these changes are outside the experimentally accessible range, as may be seen from Hattox's calculation [1] for the moment formation in metallic vanadium. For other systems these changes can be brought about by chemical pressure e.g. the stability of the manganese moment in $REMn_2$ (for a review see Shiga [2]). In other systems such as those exhibiting an invar effect the role of the magnetic and lattice degrees of freedom is more subtle.

For these systems the coupling of magnetic and lattice degrees of freedom is believed to give rise to a low value of the thermal expansion coefficient at around room temperature [3]. A simple model which is able to account for these observations on a phenomenological basis is the 2-state model of Weiss [4]. Weiss

assumes that the magnetic moment of Fe in the fcc structure can exist in 2 different states: a state with larger volume and moment and an excited state with a smaller volume and magnetic moment. Using such a model and assuming an energy for the excited state of order $k_B 100\text{K}$ Weiss was able to reproduce the magnetic and lattice properties of $\text{Fe}_{65}\text{Ni}_{35}$ invar. Band structure calculations indicate the presence of at least 2 different electronic configurations for Fe on an fcc lattice [5]. However, intensive experimental work aimed at identifying these states and associate excitations on a microscopic level have failed to provide any supporting evidence. In particular extensive neutron scattering investigations [6], [7], [8], [9] have not been able to identify a transition within the thermal energy range. Recent spin polarised neutron experiments cast doubt on the validity of the 2-state model. Ishikawa [7] has compared the temperature dependence of the macroscopic magnetic moment as measured in magnetisation measurements with the temperature dependence as expected on the basis of the *measured* magnon dispersion curves. While good agreement is obtained for Fe, Ni and FeNi compounds away from the invar region, significant differences are observed for the invar compositions. Since the thermal population of spin waves can not account for the thermal variation of the magnetisation Ishikawa invoked the concept of *hidden excitations*. Recent polarised neutron measurements have shown that it is the coupling of the lattice and magnetic degrees of freedom which give rise to the anomalous variation of magnetisation [9] and it is therefore essential to understand how this coupling arises in a microscopic manner.

In the following the question of the experimental investigation of the magnetic moment stability, namely its variation with respect to a lattice deformation, will be discussed and related to the investigation of pure iron and fcc-iron containing compounds such as invar e.g. $\text{Fe}_{65}\text{Ni}_{35}$ and Fe_3Pt . The measurement idea is briefly described as follows: At finite temperatures the response of the system to small changes of the lattice is probed via the thermal excitation of lattice deformations. The phonons cause atoms to undergo small displacements from their equilibrium positions. It is argued that for an itinerant electron ferromagnet the change in atomic positions may modify the magnetic moment located on the atom. The magnitude of the magnetic moment on the dynamically deformed lattice can be measured by determining the dynamic magnetic form factor on a phonon.

The first measurements of this kind were carried out by Steinsvoll et al. [10] on bcc iron and Ni. The iron data is reproduced in figure 1. These measurements clearly show a small and systematic deviation of the dynamic magnetic form factor as compared to the static one. This variation is attributed to a change of the magnetic moment as a result of the lattice distortion.

For the interpretation of the results the simultaneous change of atomic positions and magnetic moments presents a very complicated problem. This problem, however, is made tractable by observing that the electronic and lattice subsystems approach their respective equilibrium configurations on significantly different time scales as discussed next.

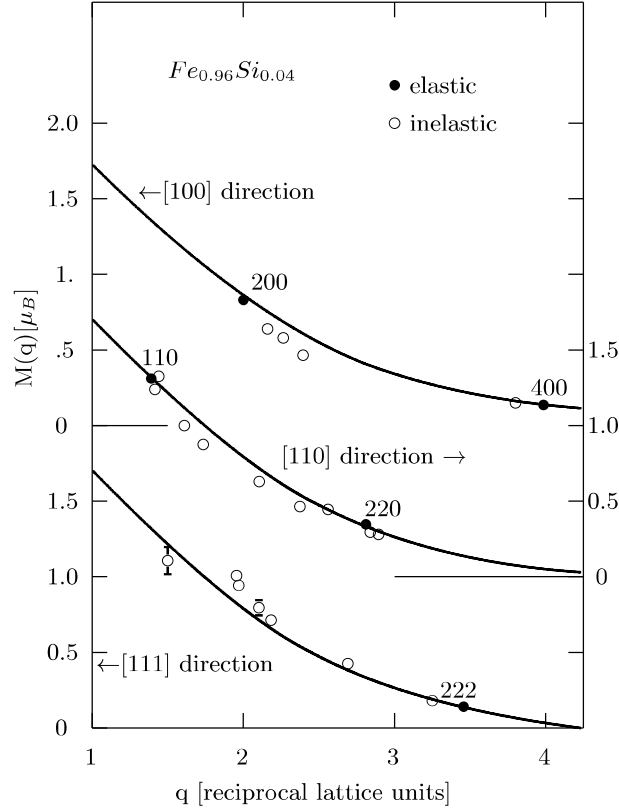


Fig. 1. Fourier transform of the magnetisation density $M(\mathbf{q})$ for bcc iron as measured on a phonon (hollow circles) and compared to the static magnetisation density (smooth curve) as measured on Bragg reflections. Full circles indicate an elastic measurement carried out on a Bragg reflection. Data taken from Steinsvoll et al. [10].

2 Time Scales for Lattice and Electronic Degrees of Freedom

For the lattice system a typical energy is defined by the Debye temperature Θ_D . According to Heisenberg's uncertainty principle, a time scale of order

$$\Delta t_{lattice} \approx \frac{\hbar}{k_B \Theta_D} \quad (1)$$

is associated with such an energy. Here k_B is the Boltzmann constant.

Similarly the electronic band width W has an associated time scale for electronic processes (such as electron hopping) of

$$\Delta t_{electronic} \approx \frac{\hbar}{W} \quad (2)$$

With typical electronic band widths of order of eV ($\approx 10^4 K$) and with Debye temperatures typically being of order $\Theta_D \approx 300 K$ the timescales for changes in

the electronic and lattice subsystems are different by several orders of magnitude with

$$\Delta t_{\text{electronic}} \ll \Delta t_{\text{lattice}} \quad (3)$$

With the much faster electronic processes it is reasonable to assume that on the scale of lattice vibrations the electronic subsystem instantly adopts its equilibrium configuration. This approximation is known as the adiabatic approximation. It is therefore admissible to treat the electronic subsystem by assuming that it adopts instantaneously and minimises the electronic energy for any given configuration of atomic positions. Thus if a lattice deformation causes a change of the magnetic moments such changes travel with the phonon and accompany the lattice deformation.

3 Neutron Scattering and Lattice Induced Magnetic Moment Modulation

Neutron scattering offers a means of measuring the changes of the magnetic moment on the dynamically deformed lattice. Such measurements are known as dynamic form factor measurements. In order to illustrate the physics of such measurements a description is developed first of the purely nuclear inelastic (phonon) scattering. This description is extended to include a magnetic scattering contribution and to demonstrate that a phonon in a ferromagnet has associated with it a magnetic scattering contribution. Finally the magnetic moment variation on the deformed lattice is considered. The argument is developed for small changes of the magnetic moment in terms of a Taylor series in the lattice deformation Δ .

In neutron scattering the nuclear contribution to the scattering cross section is determined by the Fourier transform in space and time of a nuclear density - nuclear density correlation function. The double differential neutron scattering cross section is given as

$$\left. \frac{d^2\sigma}{d\Omega d\omega} \right|_{\text{nuc.}} = \frac{k_f}{k_i} \frac{1}{2\pi\hbar} \int_{-\infty}^{\infty} dt e^{-i\omega t} \sum_{i,j} \langle \lambda | b_i^+ e^{-i\mathbf{q} \cdot \mathbf{R}_i(0)} b_j e^{i\mathbf{q} \cdot \mathbf{R}_j(t)} | \lambda \rangle \quad (4)$$

where k_i and k_f are the magnitudes of the initial and final neutron wavevectors and \mathbf{q} is the scattering vector. Ω is the solid angle and $\hbar\omega$ is the neutron energy change in the scattering process. b_i and b_j are the nuclear scattering lengths of the atoms located at lattice sites i and j with positions $\mathbf{R}_i(0)$ and $\mathbf{R}_j(t)$ at times $t=0$ and t , respectively. Here $|\lambda\rangle$ denotes the wavefunction of the system. If the sample is described by a superposition of states the matrix element $\langle \lambda | \dots | \lambda \rangle$ has to be replaced by $\sum_{\lambda} p_{\lambda} \langle \lambda | \dots | \lambda \rangle$ where p_{λ} is the probability with which the state $|\lambda\rangle$ occurs.

For the static lattice the atomic positions are time independent and fixed at their equilibrium positions $\mathbf{R}_i^{(0)}$ and $\mathbf{R}_j^{(0)}$. The Fourier transform in time

becomes a δ -function in energy transfer, resulting in elastic scattering.

$$\sum_{i,j} \frac{1}{2\pi\hbar} \int_{-\infty}^{\infty} dt e^{-i\omega t} e^{i\mathbf{q} \cdot (\mathbf{R}_i^{(0)} - \mathbf{R}_j^{(0)})} (b_i^+ b_j) \approx \delta(\hbar\omega) \sum_{\boldsymbol{\tau}} \delta(\mathbf{q} - \boldsymbol{\tau}) \quad (5)$$

Here $\boldsymbol{\tau}$ is a reciprocal lattice vector. This scattering is observed experimentally as Bragg scattering.

Now consider a small time and position dependent deviation from the equilibrium position as defined by

$$\boldsymbol{\Delta}_i(t) = \boldsymbol{\Delta}^{(0)} e^{i\mathbf{k} \cdot \mathbf{R}_i^{(0)}} e^{-i\bar{\omega}t} \quad (6)$$

with $\mathbf{R}_i(t) = \mathbf{R}_i^{(0)} + \boldsymbol{\Delta}_i(t)$. Here the amplitude $\boldsymbol{\Delta}^{(0)}$, the wavevector \mathbf{k} and the angular frequency $\bar{\omega}$ characterise the deformation. For the discussion here the deformation is taken to be externally generated. For the actual experiment the distortions are provided by the phonons of the system. For the phonon system the intensity of the scattering is determined by the Bose factor for the creation / annihilation of phonons in the scattering process. It is the ratio of magnetic to nuclear intensity which is determined. Therefore the factors determining the intensity are not included in the discussion.

Developing the exponential in (6) up to 2^{nd} order in $\boldsymbol{\Delta}$ yields

$$e^{i\mathbf{q} \cdot \mathbf{R}_i(t)} \approx e^{i\mathbf{q} \cdot \mathbf{R}_j^{(0)}} \left(1 + i\mathbf{q} \cdot \boldsymbol{\Delta}_i(t) - \frac{(\mathbf{q} \cdot \boldsymbol{\Delta}_i(t))^2}{2} \right) \quad (7)$$

The combination $1 - \frac{(\mathbf{q} \cdot \boldsymbol{\Delta}_i(t))^2}{2}$ has the same first 2 terms in the series expansion as $e^{-\frac{1}{2}(\mathbf{q} \cdot \boldsymbol{\Delta}_i(t))^2}$. This contribution is commonly known as the Debye-Waller factor and this contribution is denoted by $e^{-W(\mathbf{q})}$.

The deviations $\boldsymbol{\Delta}_i$ have zero mean. Therefore inserting this expression into the relevant part of equation (4) yields an elastic contribution of the form of (5), modified by the Debye-Waller factor $e^{-2W(\mathbf{q})}$, and an inelastic contribution given by

$$\sum_{i,j} \frac{1}{2\pi\hbar} \int_{-\infty}^{\infty} dt e^{-i\omega t} e^{-i\mathbf{q} \cdot (\mathbf{R}_i^{(0)} - \mathbf{R}_j^{(0)})} (b_i^+ b_j) < \lambda | (\boldsymbol{\Delta}_i(0) \cdot \mathbf{q}) (\boldsymbol{\Delta}_j(t) \cdot \mathbf{q}) | \lambda > \quad (8)$$

For the deformation as given in (6) the integration yields

$$\delta(\hbar\omega - \hbar\bar{\omega}) \sum_{\boldsymbol{\tau}} \delta(\mathbf{q} + \mathbf{k} - \boldsymbol{\tau}) \quad (9)$$

This result is essentially the convolution of the Fourier transform of the static lattice (given by $\delta(\hbar\omega)$ and $\sum_{\boldsymbol{\tau}} \delta(\mathbf{q} - \boldsymbol{\tau})$) with the Fourier transform of the deviation (which is characterised by δ -functions in frequency and propagation vector).

Now consider the purely magnetic scattering cross section.

$$\left. \frac{d^2\sigma}{d\Omega d\omega} \right|_{mag.} = r_0^2 \frac{k_f}{k_i} \left(\frac{1}{2} g f(\mathbf{q}) \right)^2 \sum_{\alpha, \beta} (\delta_{\alpha, \beta} - \hat{q}_\alpha \hat{q}_\beta) \frac{1}{2\pi\hbar} \int_{-\infty}^{\infty} dt e^{-i\omega t} \sum_{i,j} \langle \lambda | (\mathbf{M}_i^+)_{\alpha}(0) e^{-i\mathbf{q} \cdot \mathbf{R}_i(0)} (\mathbf{M}_j)_{\beta}(t) e^{i\mathbf{q} \cdot \mathbf{R}_j(t)} | \lambda \rangle \quad (10)$$

Here $r_0 = -0.5 \cdot 10^{-12}$ cm, g is the gyromagnetic ratio, $f(\mathbf{q})$ is the magnetic form factor, α and β denote the components of the (time dependent) magnetic moment \mathbf{M} . Due to the magnetisation being a vector quantity and spatially more extended than the nucleus the expressions are slightly more evolved compared to the case of nuclear scattering. A geometric restriction applies with the effect that only the component of the magnetisation which is oriented perpendicular to the scattering vector \mathbf{q} will give rise to magnetic scattering. For the experimental configurations of interest here this has been ensured by aligning the magnetic moments perpendicular to the scattering plane with an external magnetic field. This magnetisation component will be denoted by M^\perp or simply M . The finite size of the magnetisation distribution gives rise to a magnetic form factor $f(\mathbf{q})$ which describes the decrease of the magnetic scattering contribution with increasing scattering vector. With this simplification the correlation function takes the form

$$\sum_{i,j} \left(\frac{g}{2} f(\mathbf{q}) \right)^2 \frac{1}{2\pi\hbar} \int_{-\infty}^{\infty} dt e^{-i\omega t} \langle e^{-i\mathbf{q} \cdot \mathbf{R}_i(0)} M_i^\perp(0) e^{i\mathbf{q} \cdot \mathbf{R}_j(t)} M_j^\perp(t) \rangle \quad (11)$$

First consider the case for which the magnetic moment is of fixed magnitude and independent of the displacement of the atom. The same analysis can be carried out for the magnetic scattering contribution as has been done above for the purely nuclear case, with the nuclear scattering length being replaced by the perpendicular component of the magnetic moment (times the magnetic form factor). This result indicates that the lattice deformation, i.e. a phonon, also has a magnetic scattering intensity associated with it.

The above statement is, at first sight, surprising. However, as the nuclear density is modulated by the phonon the nucleus will carry with it the magnetisation cloud as defined by its outer electrons in partially filled shells. Consequently the nuclear modulation also gives rise to a modulation of the magnetisation density, which in turn yields a magnetic scattering contribution. It has to be stressed that the excitation is a pure lattice excitation which is inelastic in the nuclear but elastic in the magnetic interaction channel. Thus it does not involve a change of the magnetic subsystem. The magnetic scattering intensity on a phonon is nothing else but the intensity, which has been removed from the Bragg reflections by the *lattice* Debye-Waller factor. For this reason magnetic Bragg reflections are subject to the same Debye-Waller factor associated with nuclear reflections.

The magnetic and nuclear scattering intensities, as seen on a phonon, are experimentally accessible with a spin polarised neutron scattering experiment.

The magnetic signal originates from the magnetic moment which is located on the deformed lattice. If the magnetic moment is stable and follows the nuclear motion without modification then the scattering vector dependence of the magnetic scattering intensity is solely determined by the magnetic form factor. The magnetic form factor is known from static measurements, where the Fourier coefficients of the magnetisation density are experimentally determined from Bragg reflections. The magnetic form factor as seen on the phonon should therefore be a smooth interpolation of the magnetic form factor as seen on Bragg reflections.

However, if the magnetic moment is altered as a result of the lattice modulation the magnetic form factor will deviate from the static interpolation. The simple model discussed here assumes a change of the magnitude of the magnetic moment only, without a change in the spatial extent or symmetry of the magnetisation density. This change arises due to the variation of nearest neighbour separation. Such a change is described by a term of the form $\Delta \cdot \mathbf{q}$. It is to be noted that for long wavelength modulations of the lattice, i.e. as $\mathbf{q} \rightarrow 0$, the lattice is shifted uniformly with essentially no variation of the nearest neighbour separation. Thus one is led to consider a magnetic moment which changes its magnitude according to

$$M_i^\perp = M_i^{(0)} + \left. \frac{dM_i^\perp}{d\Delta \cdot \mathbf{q}} \right|_{\Delta \cdot \mathbf{q}=0} \Delta \cdot \mathbf{q} + \left. \frac{d^2 M_i^\perp}{(d\Delta \cdot \mathbf{q})^2} \right|_{\Delta \cdot \mathbf{q}=0} \frac{(\Delta \cdot \mathbf{q})^2}{2} \quad (12)$$

where $|\Delta \cdot \mathbf{q}|$ measures the local change, at lattice site \mathbf{R}_i , of the distance to nearest neighbour atoms. The average moment $M_i^{(0)} = M^{(0)} \big|_{\Delta \cdot \mathbf{q}=0}$ and its derivatives $M' = \left. \frac{dM_i^{(0)}}{d\Delta \cdot \mathbf{q}} \right|_{\Delta \cdot \mathbf{q}=0}$ and $M'' = \left. \frac{d^2 M_i^{(0)}}{(d\Delta \cdot \mathbf{q})^2} \right|_{\Delta \cdot \mathbf{q}=0}$ are i-independent.

The second derivative of the magnetic moment with respect to the lattice distortion only involves one lattice site index. It has the same formal appearance as the Debye-Waller factor discussed above for the nuclear scattering contribution. This contribution may likewise be considered as a dynamic Debye-Waller factor for the magnetic scattering contribution and can be defined as

$$M_i^\perp = M_i^{(0)} e^{W_{dyn}(\Delta)} \quad (13)$$

with

$$W_{dyn} = \frac{M''}{M^{(0)}} (\Delta \cdot \mathbf{q})^2 \quad (14)$$

Unlike the Debye Waller factor for nuclear scattering which invariably results in a decrease of the scattering intensity of Bragg reflections with increasing scattering vector, for the case of the magnetic scattering contribution on the phonon the magnetic scattering intensity may either increase or decrease, depending on the sign of the 2nd derivative of the magnetic moment with respect to the lattice distortion. It is noted that this dynamic Debye Waller factor becomes equal to 1 as the Bragg reflection is approached as $\Delta \cdot \mathbf{q} \rightarrow 0$ for the time independent lattice.

Collecting the remaining terms up to second order in Δ one obtains, in addition to the scattering contribution identified above for the case without a modulation of the magnetic moment, namely

$$M^{(0)}M^{(0)}(\Delta_i(0) \cdot \mathbf{q})(\Delta_j(t) \cdot \mathbf{q}) \quad (15)$$

terms of the form

$$\begin{aligned} & M'(\Delta_i(0) \cdot \mathbf{q}) \cdot M'(\Delta_j(t) \cdot \mathbf{q}) \\ & + M'(\Delta_i(0) \cdot \mathbf{q}) \cdot M^{(0)}(\Delta_j(t) \cdot \mathbf{q}) \\ & + M^{(0)}(\Delta_i(0) \cdot \mathbf{q}) \cdot M'(\Delta_j(t) \cdot \mathbf{q}) \end{aligned} \quad (16)$$

The scattering vector and energy dependence of these contributions is such that the scattering will occur at the same point in reciprocal space and with the same energy as the one of equation (15). These contributions modify the magnetic scattering as seen on the phonon. As a result of the modulation of the magnetic moment the dynamic magnetic form factor deviates from the interpolation of the static magnetic form factor. The deviation from the value of the static magnetic form factor is a measure of the magnetic moment modulation or instability of the system. For magnetic systems for which the Taylor series expansion in terms of the lattice deformation is valid the size of the experimental signal is determined by the derivatives of the magnetic moment with respect to the nearest neighbour separation. These in turn are related to lattice deformations which can be described using the derivative of the lattice deformation.

For some systems, such as discussed above for an extreme form of vanadium, YMn_2 or invar compounds, the variation of the magnetic moment may be in the form of a discontinuous change from a finite value to zero. If such a modulation occurs as a result of a dynamic lattice modulation the formulation given above in terms of a finite power series in the lattice deformation $\Delta \cdot \mathbf{q}$ is not applicable. While it is to be expected that the experimental signal shows a large deviation of the dynamically measured magnetic form factor as compared to the static one the expansion has to be carried to higher orders. This case, however, is not considered here. It suffices to point out that some experimental observations have been interpreted using such a discontinuous change of the magnetic moment on parts of the distorted lattice [8].

The model given above constitutes a first step towards modelling the experimental data of Steinsvoll et al. [10] and relating the deviations of the dynamically measured magnetic form factor to microscopic changes of the system. The measurement of the magnetic scattering contribution on the phonon is a novel experimental technique with which to explore some dynamical aspects of the magnetic moment and its coupling to the lattice. The description given above will be developed further for the case of invar. Extensive measurements have already been carried out on $Fe_{65}Ni_{35}$ and Fe_3Pt invar compounds, and a significant variation of the dynamically measured magnetic form factor has been seen as compared to the static one. The details of the application of this description to invar compounds will be the subject of future publications.

4 Conclusions

The experimental study of the magnetic scattering contribution on a phonon allows the investigation of the behaviour of the magnetic moment on a distorted lattice. In this way the dynamic behaviour of the magnetic moment, as brought about by the changes in the location of the magnetic atoms due to lattice vibrations, can be assessed. Such changes of the magnetic moment have to be distinguished from the dynamics of the magnetic subsystems, such as spin excitations, which also occur for a system with time independent magnetic moment positions. The change of position of the atom carrying the magnetic moment is a means of experimentally accessing the magnetic moment stability with respect to small positional changes within the system. This technique opens up the possibility of studying some aspects relevant for the question of the formation and stability of magnetic moments in itinerant electron systems. While the variations expected for itinerant electron ferromagnets such as Fe or Ni are small, the experimental investigation of Fe by Steinsvoll et al.[10] indicate a small but systematic deviation of magnetisation contribution on a phonon as compared to the static one. The variation can be expected to be larger for systems close to an instability. Investigations on invar compounds indicate a more substantial change of the magnetic scattering contribution on the phonon than is seen in Fe or Ni.

References

1. T.M. Hattox, J.B. Conklin, J.C. Slater, S.B. Trickey: J. Phys. Chem. Sol. **34**, 1627 (1973)
2. M. Shiga: Physica **B149**, 293 (1988)
3. E.F. Wassermann in *Ferromagnetic Materials*, edited by K.H.J. Buschow and E.P. Wohlfarth, North-Holland (1990)
4. R.J. Weiss: Proc. R. Soc. London **82**, 281 (1963)
5. P. Entel, E. Hoffmann, P. Mohn, K. Schwarz, V.L. Moruzzi: Phys. Rev. **B 47**, 8706 (1993)
6. J.W. Lynn, N. Rosov, M. Acet, H. Bach: J. Appl. Phys. **75**, 6069 (1994)
7. S. Onodera, Y. Ishikawa, K. Tajima : J. Phys. Soc. Jpn. **50**, 1513 (1981)
8. P.J. Brown, I.K. Jassim, K.U. Neumann, K.R.A. Ziebeck: Physica **B 161**, 9 (1989)
9. P.J. Brown, B. Roessli, J.G. Smith, K.U. Neumann, K.R.A. Ziebeck: J. Phys.: Condens. Matt. **8**, 1527 (1996)
10. O. Steinsvoll, R.M. Moon, W.C. Koehler, C.G. Windsor: Phys. Rev. **B24**, 4031 (1981)